



THÈSE DE DOCTORAT

Disques et vents des étoiles chaudes : apport de la spectroscopie et de l'interférométrie multi-bandes

Elisson SALDANHA DA GAMA DE ALMEIDA

Laboratoire J.-L. Lagrange (UMR 7293), Observatoire de la Côte d'Azur

**Présentée en vue de l'obtention du grade de docteur en
Sciences de la Planète et de l'Univers
de l'Université Côte d'Azur**

Thèse dirigée par Armando DOMICIANO DE SOUZA et par Anthony MEILLAND

Soutenue le : 23 novembre 2020

Devant le jury composé de :

Alex CARCIOFI, Professeur, IAG/USP, São Paulo, Brasil
Anthony MEILLAND, Chercheur CR CNRS, Laboratoire Lagrange/OCA, UCA, Nice
Armando DOMICIANO DE SOUZA, Astronome Adjoint, Laboratoire Lagrange/OCA, UCA, Nice
Bruno LOPEZ, Astronome, Laboratoire Lagrange/OCA, UCA, Nice
Evelyne ALECIAN, Chercheur CR CNRS, Université Grenoble Alpes, Grenoble
Jean-Claude BOURET, Chercheur DR CNRS, Laboratoire d'Astrophysique de Marseille, Marseille
Marcelo BORGES FERNANDES, Professeur, Observatório Nacional, Rio de Janeiro, Brasil
Philippe STEE, Chercheur DR CNRS, Laboratoire Lagrange/OCA, UCA, Nice
Sylvia EKSTRÖM, Docteur, Observatoire Astronomique de l'Université de Genève



Disques et vents des étoiles chaudes: apport de la spectroscopie et de l'interférométrie multi-bandes

Jury :

Président du jury :

Marcelo BORGES FERNANDES, Professeur, Observatório Nacional, Rio de Janeiro, Brasil

Rapporteurs :

Evelyne ALECIAN, Chercheur Chargé de Recherche CNRS, Université Grenoble Alpes, Grenoble

Marcelo BORGES FERNANDES, Professeur, Observatório Nacional, Rio de Janeiro, Brasil

Examineurs :

Alex CARCIOFI, Professeur, Instituto de Astronomia, Geofísica e Ciências Atmosféricas/
Universidade de São Paulo, São Paulo, Brasil

Bruno LOPEZ, Astronome, Laboratoire Lagrange/Observatoire de la Côte d'Azur, Université Côte d'Azur, Nice

Jean-Claude BOURET, Chercheur Directeur de Recherche CNRS, Laboratoire d'Astrophysique de
Marseille, Marseille

Philippe STEE, Chercheur Directeur de Recherche CNRS, Laboratoire Lagrange/Observatoire de la
Côte d'Azur, Université Côte d'Azur, Nice

Invités :

Sylvia EKSTRÖM, Docteur, Observatoire Astronomique de l'Université de Genève

Directeur :

Armando DOMICIANO DE SOUZA, Astronome Adjoint, Laboratoire Lagrange/Observatoire de la
Côte d'Azur, Université Côte d'Azur, Nice

Co-directeur :

Anthony MEILLAND, Chercheur Chargé de Recherche CNRS, Laboratoire Lagrange/Observatoire
de la Côte d'Azur, Université Côte d'Azur, Nice

Aos meus pais, Elionai e Sônia, por todo o apoio e carinho.

Acknowledgments/Agradecimentos

I would like to thank my advisors, Armando Domiciano de Souza and Anthony Meilland, for all their support, commitment with my work, and for introducing me to the interferometric journey of hot stars. I also thank you for helping me with the practical stuff of life during my stay in Nice. Thank you a lot for helping me with the heavy baggage when I arrived in Nice!

I thank Yves Rabbia for sharing his time to teach me the theory of stellar interferometry, and also Denis Mourard and Frédéric Morand for giving me the opportunity to learn about interferometric observations with the CHARA/VEGA instrument at Plateau de Calern. I thank Alain Spang for working on the reduction of new VLTI/AMBER data of Rigel (and also for your occasional visits to my office and nice handshakes), Farrokh Vakili for inviting me to study P Cygni using intensity interferometry, and Philippe Stee for participating of my PhD meetings with Armando and Anthony (also for your constructive comments on my paper about *o* Aquarii). Philippe and Farrokh, thank you very much for reading and commenting on my thesis manuscript! I also thank Christine Delobelle, Delphine Saissi, and Sophie Rousset for helping me with the french bureaucracy.

I thank Julieta Sanchez, Fei Hua, and Mircea Moscu for sharing with me good moments during my stay in Nice. Julieta, thank you very much for receiving me at your home in La Plata. Also many thanks for Alban Ceau, Marc-Antoine Martinod, Pierre Janin-Potiron, Romain Laugie, and Vicent Hocdé : thank you for being patient with my French. I hope to meet all you again to have a glass of beer or a cup of coffee. Massinissa Hadjara, thank you for being a very nice neighbor and for the good green grapes!

I would like to thank Alex Carciofi, Bruno Lopez, Evelyne Alecian, Jean-Claude Bouret, Marcelo Borges, Philippe Stee, and Sylvia Ekström for being part of the jury of my thesis and for their constructive comments on my work. Em português, agradeço

ao Alex e Marcelo pelos seus comentários detalhados para a versão final da minha tese. Deixo meu agradecimento ao Marcelo por aceitar ser presidente da minha banca e por me ajudar com os preparativos da defesa online no Observatório Nacional.

Agradeço aos meus pais, Elionai e Sônia, e minha tia Lila, por todo amor e apoio desde sempre. Também aos melhores amigos do mundo : David Campos, Icaro Rossignoli, Marcio Monteiro, Morgana Romão e Poema Portela. Muito obrigado por estarem sempre ao meu lado em todos os momentos, seja online ou de forma presencial. Obrigado também por suportarem minhas reclamações. Poema e Marcio, obrigado por me visitarem em Nice! Pai, mãe e tia Lila, a visita de vocês também está guardada para sempre comigo com muito carinho. Também deixo meu agradecimento à Alinges Lenz pela escuta recente e pelo incentivo para seguir em frente.

Abstract

Hot stars are the main source of ionization of the interstellar medium and its enrichment due to heavy elements. Constraining the physical conditions of their environments is crucial to understand how these stars evolve and their impact on the evolution of galaxies.

Spectroscopy allows to access the physics, the chemistry, and the dynamics of these objects, but not the spatial distribution of these objects. Only long-baseline interferometry can resolve photospheres and close environments, and, combining spectroscopy and interferometry, spectro-interferometry allows to draw an even more detailed picture of hot stars.

The objective of my thesis was to investigate the physical properties of the photosphere and circumstellar environment of massive hot stars confronting multi-band spectroscopic or spectro-interferometric observations and sophisticated non-LTE radiative transfer codes.

My work was focused on two main lines of research. The first concerns radiative line-driven winds. Using UV and visible spectroscopic data and the radiative transfer code CMFGEN, I investigated the weak wind phenomenon on a sample of nine Galactic O stars. This study shows for the first time that the weak wind phenomenon, originally found for O dwarfs, also exists on more evolved O stars and that future studies must evaluate its impact on the evolution of massive stars.

My other line of research concerns the study of classical Be stars, the fastest rotators among the non-degenerated stars, and which are surrounded by rotating equatorial disks. I studied the Be star *o* Aquarii using H α (CHARA/VEGA) and Br γ (VLTI/AMBER) spectro-interferometric observations, the radiative transfer code HDUST, and developing new automatic procedures to better constrain the kinematics of the disk. This multi-band study allowed to draw the most detailed picture of this object and its environment, to test the limits of the current generation of radiative transfer models, and paved the way to my future work on a large samples of Be stars observed with VEGA, AMBER, and the newly available VLTI mid-infrared combiner MATISSE.

Keywords : stars : massive, emission-line, atmospheres, winds, circumstellar matter ; techniques : spectroscopic, interferometric.

Résumé

Les étoiles chaudes sont la principale source d'ionisation du milieu interstellaire et de son enrichissement en éléments lourds. Contraindre les conditions physiques de leur environnement est crucial pour comprendre comment ces étoiles évoluent et leur impact sur l'évolution des galaxies.

La spectroscopie permet d'accéder à la physique, la chimie et la dynamique de ces objets, mais pas à la distribution spatiale de ces objets. L'interférométrie à longue base est la seule technique permettant de résoudre la photosphère et les environnements, et, en combinant spectroscopie et interférométrie, la spectro-interférométrie permet de dresser une image encore plus détaillée des étoiles chaudes.

L'objectif de ma thèse était d'étudier les propriétés physiques de la photosphère et de l'environnement circumstellaire d'étoiles chaudes massives, en confrontant des observations spectroscopiques et spectro-interférométriques sur différents domaines de longueur d'onde à des modèles sophistiqués de transfert radiatif hors-ETL.

Mon travail s'est focalisé sur deux axes. La première concerne les vents radiatifs. En utilisant des données spectroscopiques UV et visible et le code CMFGEN, j'ai étudié le phénomène des vents faibles sur un échantillon de neuf géantes O galactiques. Cette étude montre pour la première fois que le phénomène des vents faibles, trouvé à l'origine pour les naines O, existe également pour des étoiles O plus évoluées et que des prochaines études doivent évaluer leur effet sur l'évolution des étoiles massives.

Mon autre axe de recherche concerne l'étude des étoiles Be classiques, les rotateurs les plus rapides parmi les étoiles non dégénérées et qui sont entourées par des disques équatoriaux en rotation. J'ai étudié l'étoile Be σ Aquarii en utilisant des données spectro-interférométriques obtenues en $H\alpha$ (CHARA/VEGA) et $Br\gamma$ (VLTI/AMBER), le code de transfert radiatif HDUST, et en développant de nouvelles procédures automatiques pour mieux contraindre la cinématique des disques. Cette étude multi-bande a permis d'obtenir la vue la plus complète de cet objet et de son environnement, de tester les limites de la génération actuelle de modèles de transfert radiatif, et d'ouvrir la voie à des travaux futurs sur un échantillon large d'étoiles Be observées avec VEGA, AMBER et MATISSE, le nouvel instrument infrarouge thermique du VLTI.

Mots-clés : étoiles : massive, raie d'émission, atmosphères, vents, matière circumstellaire ; techniques : spectroscopique, interférométrique.

List of Figures

1.1	Schemes of chemical stratification in evolved massive stars (left) and evolved low-intermediate-mass (right) stars.	4
1.2	Modified Conti scenario for the evolutionary scheme of massive stars as a function of zero-age main sequence mass.	5
1.3	Mass-loss rate (left axis, solid line) and stellar mass (right axis, dashed line) as function of age in the Geneva evolutionary model for a non-rotating single star with $M_{\text{ZAMS}} = 60 M_{\odot}$	6
1.4	The R136 open cluster located in the H II region 30 Doradus (Tarantula Nebula) in the Large Magellanic Cloud.	7
1.5	Mass return rate (logarithmic scale) of massive stars as a function of stellar mass.	8
1.6	Amount of dust mass produced by AGB stars and supernovae as a function of progenitor initial mass from Gall et al. (2011b).	9
1.7	Minimum M_{ZAMS} that allows a complete stellar evolution at a certain value of cosmological redshift (z).	10
1.8	Schematic representation of iteration between a photon with linear momentum $h\nu/c$ (energy given by $h\nu$) and a particle of mass m	16
1.9	Ultraviolet spectrum of the O supergiant (type O9.5I) IC 1613-B11 (located in the dwarf galaxy IC 1613) is shown in black line.	19
1.10	Fraction of the radiative acceleration due to each chemical element, compared with the total radiative force (a_{rad}), as a function of distance from the star, in the PoWR model of Sander et al. (2017) to the analysis of ζ Puppis.	21
1.11	Comparison between a initial smooth wind structure (dashed line, modified CAK-theory) and one predicted from time-dependent hydrodynamical simulation from Puls et al. (1993) after 60000 s (solid line)	24
1.12	Mass-loss rate as a function of stellar luminosity at different evolutionary stages of massive stars.	25
1.13	Limits in the HR diagram for acceleration winds due to lines.	27

LIST OF FIGURES

1.14	Boxplot distribution of the projected stellar rotation velocity ($v \sin i$) as a function of spectral type.	28
1.15	Gravity darkening and geometrical oblateness effects due to rotation. . .	35
1.16	Temporal evolution of the linear stellar equatorial velocity (left panel) from Geneva evolutionary models for massive stars with different initial masses. The corresponding angular rotational rate is shown in the right panel.	36
1.17	Rotational rate W of Be-type stars as a function of effective temperature from different studies in the literature.	37
1.18	Comparison between the fraction of stars rotating faster than a minimum value (theoretical fraction in color lines) and the observed fraction of Be stars in Galactic clusters (left panel).	38
1.19	Struve's picture to explain the emission line profiles of Be stars.	41
1.20	Temporal variation from 1986 to 1988 of the observed $H\alpha$ profile (solid black lines) of α Andromedae (B6IIIpe).	42
1.21	Temporal variability of the CQE feature in the He I $\lambda 6678$ line of ϵ Capricorni (B3Ve).	43
1.22	Long-term variability of the $H\alpha$ equivalent width of 28 Tau (B8Vpe). . .	44
1.23	Schemes of different dynamical models to form disks in Be stars.	47
1.24	Model intensity map (projected on the sky) in the K-band from Gies et al. (2007) to the analysis of interferometric data of the Be star γ Cassiopeiae (B0.5IV).	53
1.25	Comparison of Be disks sizes derived in the $H\alpha$ line and in K-band from the CHARA Array interferometric survey of Touhami et al. (2013). . .	54
1.26	Theoretical Be disk formation at different wavelength regions from calculations with code HDUST.	55
2.1	Ratio between the equivalent width measured in He I $\lambda 4471$ and He II $\lambda 4542$ as a function of spectral type of O stars (105 objects).	61
2.2	Visible spectra (~ 4000 - 4700 Å) of O dwarfs (class V) from O9V to O2V. . .	62
2.3	Visible spectra (~ 3800 - 4600 Å) from O9V to A0V stars, covering the entire range of B dwarf stars (B0V-B9V).	63
2.4	Geometric scheme for the formation of P Cygni profiles.	66
2.5	Comparison of UV line formation through the wind extension.	67
2.6	CMFGEN ion fraction of silicon as a function of effective temperature for the parameter space of O supergiant stars.	70
2.7	Effect of varying the effective temperature on the UV and visible regions. .	71

LIST OF FIGURES

2.8	Effect of varying the mass-loss rate on the UV (Si IV $\lambda\lambda$ 1394,1403), visible (H α), and infrared (P γ and Br α) regions.	72
3.1	Schematic of an Airy disk, formed by the phenomenon of diffraction, arising from the incidence of the light wavefronts into a telescope (round pupil).	76
3.2	Comparison between the angular resolution (in milliarcsecond) provided by current single-mirror telescope (blue line; ZIMPOL, IRDIS, VISIR instruments) and interferometric facilities (green line; VEGA/CHARA, MATISSE, VLTI + CHARA instruments, and ALMA), as a function of wavelength.	77
3.3	Scheme for the propagation of light wavefronts through a double-slit screen, the Young's double-slit experiment.	79
3.4	Schematic representing the basic elements of an optical long-baseline interferometer: the telescopes and optical subsystems (relay optics, delay line, and beam combination).	82
3.5	Simulated fringe patterns for objects of different sizes, observed using a two-telescope interferometer.	83
3.6	Schematic of two different cases of spatial and temporal coherence. . .	84
3.7	Schematic of a triplet of telescopes used for measuring closure phase. .	89
3.8	Spectrally dispersed (\sim 2.156-2.175 μ m) fringes of η Carinae measured with VLTI/AMBER in high spectral resolution mode (HR, $R = 12000$) at 26 February 2005.	92
3.9	Different scenarios for the kinematics of a circumstellar disk, calculated using a kinematic model: purely-rotating disk, purely-expanding disk, and a hybrid case, respectively, from the left to the right panels.	94
3.10	Schematic layout of the CHARA Array, installed on the Mount Wilson Observatory (California, USA).	96
3.11	Aerial view of the Very Large Telescope's observing platform, installed at the Cerro Paranal Observatory (Atacama desert, Chile).	98
3.12	Schematic layout of the VLTI Array. The Unit Telescopes (UT) are indicated in red, fixed 8-m telescopes, with stations named from U1 to U4.	99
4.1	Schematic of a plane-parallel geometry.	104
4.2	Line-blanketing effect on the emergent spectrum.	112
4.3	Schematics of the (p,z) coordinate system, which is used in the code CMFGEN to solve the radiative transfer problem (ray-by-ray solution method).	114

LIST OF FIGURES

4.4	Intensity profiles, as a function of the wavelength ($\sim 6530\text{--}6600 \text{ \AA}$, around $H\alpha$), calculated by myself using CMFGEN	115
4.5	Emergent flux (normalized to the continuum), computed from the same CMFGEN model in Fig. 4.4, around the $H\alpha$ line (strong P Cygni profile). 116	
4.6	Distribution of the BeAtlas models with respect to the stellar mass and base disk surface density.	119
4.7	First two rows: intensity maps (128 x 128 pixels) at different values of wavelength close to $Br\gamma$ (from left to right: 2.161, 2.164, 2.165, and 2.166 μ) of two HDUST models, from the BeAtlas grid, with different values of inclination angle: $i = 0$ (first row) and $i = 90^\circ$ (second row).	123
5.1	Comparison between the visibility curves (squared visibility, V^2) of two uniform disks with different values of angular diameter: $\theta_{UD} = 0.1$ mas (black) and 1.0 mas (red).	126
5.2	Left panel: modeling to NPOI observations (interferometric data centered on $H\alpha$) of the Be star σ Aquarii using geometric models.	127
5.3	Example of the graphical interface of LITpro, used in this case to model VLTI/GRAVITY data of Rigel using a uniform disk model: best-fit model with angular diameter of ~ 2.61 mas. See text for discussion.	129
5.4	Geometric modeling, using the software LITpro (Fig. 5.3), of our VLTI/-GRAVITY data of Rigel: squared visibilities at the close-by continuum region ($\sim 2.145\text{--}2.155 \mu\text{m}$) to $Br\gamma$	130
5.5	Chart showing the calculation of the intensity map of the central star plus disk system (total intensity map shown in the bottom) with the kinematic code. See text for discussion.	133
5.6	Comparison between kinematic models, calculated around the $H\alpha$ line, by varying just one selected parameter:	134
5.7	VLTI/AMBER observations in $Br\gamma$ (color lines) of the nova T Pyxidis at different days since the outburst onset (28.76 days in orange and 35.77 days in green).	136
5.8	χ^2 map to VEGA data of σ Aquarii for kinematic models (calculated around $H\alpha$) with different values of disk size (major-axis FWHM of an elliptical Gaussian distribution, in stellar diameter).	137
5.9	Kinematic model disk size (in $Br\gamma$, fit to AMBER data of σ Aquarii) sampled in a MCMC run using EMCEE with 300 walkers and 200 iterations in total.	140

LIST OF FIGURES

6.1	Comparison between parametric HDUST models ($m = 3.0$, left panels) and steady-state non-isothermal HDUST models (non-parametric models, right panels).	213
7.1	VLTI/MATISSE observation of Rigel performed on September 25, 2019.	240
7.2	Intensity profiles from one of our adopted CMFGEN models for Rigel, used as a reference model in our VLTI/GRAVITY proposal.	241
7.3	Simulated visibilities (left panel) and spectra (right panel) in the K-band (GRAVITY wavelength region) from CMFGEN models with different values of mass-loss rate	242
7.5	LITpro best-fit uniform disk models found from fitting our GRAVITY data for Rigel, in the continuum region close to $\text{Br}\gamma$ (left panel) and in the core of $\text{Br}\gamma$ (right panel).	244
7.6	Image reconstruction by Chesneau et al. (2000) of P Cygni large-scale circumstellar environment (up to $\sim 1000 R_\star$) using Observatoire de Haute-Provence (OHP) observations with adaptive optics.	245
7.7	SPHERE simulated observations (raw images) from our reference CMFGEN model for Rigel (with mass-loss rate of $4 \times 10^{-7} M_\odot \text{yr}^{-1}$).	246
7.8	Example of AMBER differential data (red line) of α Arae observed in the Be survey of Meilland et al. (2012).	247
7.9	Left: example of $\text{H}\alpha$ line profiles observed with the VEGA instrument for 17 Be stars of our VEGA survey (34 objects observed in total).	248
7.10	Observation of the Be star α Arae with VLTI/MATISSE from the L-band to the M-band (covering $\sim 3.0\text{-}5.0 \mu\text{m}$).	249
7.11	Preliminary MCMC analysis of VLTI/MATISSE differential data (in the $\text{Br}\alpha$ line) of the Be star α Arae	250
7.12	Geometric modeling of VEGA squared visibilities of the late-type Be star κ Draconis (B6IIIe).	251

List of Tables

1.1	Summary of the stellar parameters of OB-type dwarfs (luminosity class V) from spectral type calibrations in the literature. Parameters for B stars are from Townsend et al. (2004) and O stars from Martins et al. (2005a).	3
2.1	Summary of the main ultraviolet, visible, and infrared line diagnostic used to determine the photospheric and wind parameters of massive stars, in particular, O-type, WR, and B supergiant stars. Adapted from Martins (2011).	69
3.1	Summary of some very first visible and infrared interferometric studies using two-telescope configuration. Reproduced from Léna (2014). . . .	80
3.2	Summary of telescope arrays with spectro-interferometric instruments. Adapted from Hadjara (2017).	95
4.1	Summary of basic characteristics of non-LTE and line-blanketed radiative transfer codes for modeling massive hot stars. Adapted from Chap. 5 of Crivellari et al. (2019)	109
4.2	List of HDUST parameter in the BeAtlas grid. The first row indicates the spectral type corresponding to the stellar mass for B dwarfs (Townsend et al. 2004). All the model are calculated with the following fixed parameters: scale height at the disk base $H_0 = 0.72$, fraction of H in the core $X_c = 0.30$, metallicity $Z = 0.014$, and disk radius = $50 R_{\text{eq}}$. Adapted from Faes (2015)	118

Contents

1	Introduction	1
1.1	OB-type stars	2
1.1.1	Physical properties and stellar evolution	2
1.1.2	Enrichment of the interstellar medium	6
1.2	Radiative line-driven winds	11
1.2.1	The phenomenon of stellar winds	11
1.2.2	Elementary concepts of radiative line-driven winds	13
1.2.3	Radiative winds in the HR diagram	25
1.3	Stellar rotation	29
1.3.1	Effects on the stellar shape	29
1.3.2	Stellar rotational rate and oblateness	31
1.3.3	The von Zeipel effect	33
1.3.4	Fast rotation	35
1.4	The Be phenomenon	40
1.4.1	Characterization and physical origin	40
1.4.2	Variability in Be stars	42
1.4.3	Oe and Ae stars: counterparts to the Be phenomenon?	45
1.5	Circumstellar disks of Be stars	46
1.5.1	Formation and dynamics	46
1.5.2	Geometry and size	52
1.6	Outline of this thesis	56

CONTENTS

2	Stellar spectroscopy	58
2.1	Stellar classification	58
2.2	Line formation in the wind: P-Cygni profiles	64
2.3	Multi-wavelength line diagnostics	68
3	Optical long-baseline stellar interferometry	74
3.1	Why we need high angular resolution observations?	74
3.2	Historical overview	78
3.3	Elementary concepts of OLBI	81
3.4	Light coherence	85
3.5	Interferometric quantities	87
3.5.1	The Zernike-van Cittert theorem	87
3.5.2	Closure phase	89
3.5.3	Visibility calibration	90
3.6	Spectro-interferometry	91
3.7	Spectro-interferometric instruments	95
3.7.1	The CHARA array	95
3.7.2	CHARA/VEGA	97
3.7.3	The VLTI array	97
3.7.4	VLTI/AMBER	100
3.7.5	Comparison between CHARA and VLTI	100
4	Radiative transfer modeling	102
4.1	Elementary concepts of radiative transfer	102
4.2	Overview on radiative transfer codes for hot stars	108
4.3	The code CMFGEN	110
4.4	The code HDUST and the BeAtlas grid	116
4.5	For what CMFGEN and HDUST are suited?	120
4.6	Computational cost of physical models	121

CONTENTS

5	Model fitting of interferometric data	124
5.1	Geometric models	125
5.1.1	Applying the Zernike-van Cittert theorem to analytical models	125
5.1.2	The simplest case: an example of one-component model	125
5.1.3	Adding other components: an example of two-component model	126
5.2	Analytical model fitting: the software LITpro	128
5.2.1	Overview: a tool dedicated to interferometric modeling	128
5.2.2	Example of modeling: VLTI/GRAVITY data of Rigel	129
5.2.3	Limitations: what is the global χ^2 minimum?	130
5.3	The kinematic code	131
5.3.1	Overview: the model parameters	131
5.3.2	Model description: the central star and the circumstellar environment	132
5.3.3	Parameters effects on the interferometric quantities	134
5.3.4	An example of model fitting: AMBER data of the nova T Pyxidis	135
5.4	Kinematic model fitting using MCMC	136
5.4.1	Why use a MCMC fitting-method to the kinematic code?	136
5.4.2	The MCMC method	138
5.4.3	The code EMCEE: a MCMC implementation	138
5.4.4	Using prior information with EMCEE	139
5.4.5	Example of modeling: VLTI/AMBER data of <i>o</i> Aquarii	139
5.4.6	Further improvements	141
6	Published studies	142
6.1	Mini-survey of O stars	143
6.1.1	Problems with the theory of line-driven winds: weak winds	143
6.1.2	Master thesis work	144
6.1.3	Improvements during my PhD	145
6.1.4	Results and conclusions	146

CONTENTS

6.2	The LBV star P Cygni	194
6.2.1	Winds and episodic outbursts of LBVs	194
6.2.2	Intensity interferometry in a nutshell	195
6.2.3	My collaboration with the I2C team	195
6.2.4	Results and conclusions	196
6.3	The Be-shell star <i>o</i> Aquarii	208
6.3.1	Probing the Be phenomenon: why study <i>o</i> Aquarii with interferometry?	208
6.3.2	Observing <i>o</i> Aquarii in the AMBER and VEGA Be surveys . . .	209
6.3.3	A multi-technique modeling approach: from analytical to numerical models	210
6.3.4	Results and conclusions	211
7	Ongoing studies	238
7.1	The radiative line-driven wind of Rigel	238
7.1.1	Rigel: an evolved massive star	238
7.1.2	Multi-band spectro-interferometry: CHARA and VLTI	239
7.1.3	H α intensity interferometry: I2C team	243
7.1.4	Direct imaging: VLT/SPHERE	245
7.2	Classical Be stars	246
7.2.1	Drawing a big picture of Be disks	246
7.2.2	The VEGA and AMBER large surveys	247
7.2.3	First observations with MATISSE	249
7.2.4	Toward a detailed view on Be stars (other than <i>o</i> Aquarii) . . .	251
8	Conclusions and perspectives	253
	Bibliography	257

Chapter 1

Introduction

Contents

1.1	OB-type stars	2
1.1.1	Physical properties and stellar evolution	2
1.1.2	Enrichment of the interstellar medium	6
1.2	Radiative line-driven winds	11
1.2.1	The phenomenon of stellar winds	11
1.2.2	Elementary concepts of radiative line-driven winds	13
1.2.3	Radiative winds in the HR diagram	25
1.3	Stellar rotation	29
1.3.1	Effects on the stellar shape	29
1.3.2	Stellar rotational rate and oblateness	31
1.3.3	The von Zeipel effect	33
1.3.4	Fast rotation	35
1.4	The Be phenomenon	40
1.4.1	Characterization and physical origin	40
1.4.2	Variability in Be stars	42
1.4.3	Oe and Ae stars: counterparts to the Be phenomenon?	45
1.5	Circumstellar disks of Be stars	46
1.5.1	Formation and dynamics	46
1.5.2	Geometry and size	52
1.6	Outline of this thesis	56

1.1. OB-type stars



Stars are unique astrophysical objects to test our understanding about the basic structure of nature. For example, observations of solar neutrinos provided the first clear evidence of the quantum phenomenon called neutrino oscillation, implying that at least one of the neutrino flavors has non-zero mass (e.g., see the Nobel Lecture of McDonald 2016). This disagrees with the so-called Standard Model of elementary particles, and thus opens an entire branch of theoretical research of physics beyond the Standard Model. Conversely, apart from the current understanding of star formation, the study of stars is very well-founded in terms of fundamental physics: combining the background from hydrodynamics, thermodynamics and statistical physics, atomic and molecular physics, and electromagnetism, among others.

The aim of this thesis is to analyse the physical properties and mass loss processes of massive hot stars and study their close environments, ranging from radiatively driven winds (with velocities up to a thousand km s^{-1}) to quasi-stable thin equatorial disks in rotation. For this purpose, different observational techniques and also modeling methods are employed in this work. In this chapter, I overview in details the current understanding about OB-type stars.

1.1 OB-type stars

1.1.1 Physical properties and stellar evolution

O-type stars ($M_{\text{ZAMS}}^1 \gtrsim 17 M_{\odot}$) are subject to extreme physical conditions, showing the highest value of luminosity and effective temperature (T_{eff}) among the canonical

1. Zero-age main sequence mass, the initial stellar mass (onset of the H-burning phase).

1.1. OB-type stars

Table 1.1 – Summary of the stellar parameters of OB-type dwarfs (luminosity class V) from spectral type calibrations in the literature. Parameters for B stars are from Townsend et al. (2004) and O stars from Martins et al. (2005a).

ST	M_{\star} (M_{\odot})	R_{\star} (R_{\odot})	T_{eff} (K)	$\log L_{\star}/L_{\odot}$	ST	M_{\star} (M_{\odot})	R_{\star} (R_{\odot})	T_{eff} (K)	$\log L_{\star}/L_{\odot}$
B9	3.4	2.8	12294	2.20	O9.5	16.5	7.4	30488	4.62
B8	3.8	3.0	13250	2.39	O9	18.0	7.7	31524	4.72
B7	4.2	3.2	14148	2.56	O8.5	19.8	8.1	32522	4.82
B6	4.8	3.5	15355	2.78	O8	22.0	8.5	33383	4.90
B5	5.5	3.8	16726	3.00	O7.5	24.2	8.9	34419	5.00
B4	6.4	4.2	18267	3.24	O7	26.5	9.4	35531	5.10
B3	7.7	4.7	20287	3.52	O6.5	29.0	9.8	36826	5.20
B2.5	8.6	5.0	21566	3.68	O6	31.7	10.2	38151	5.30
B2	9.6	5.4	22887	3.85	O5.5	34.2	10.6	40062	5.41
B1.5	10.8	5.7	24424	4.01	O5	37.3	11.1	41540	5.51
B1	12.5	6.3	26068	4.21	O4	46.2	12.3	43419	5.68
B0.5	14.6	6.9	27948	4.41	O3	58.2	13.8	44616	5.83
B0	17.5	7.7	30201	4.64					

Morgan-Keenan system of stellar classification (Morgan et al. 1943). Based on sophisticated spectral type calibrations (Martins et al. 2005a), a typical late-type O dwarf (O9.5V) has $T_{\text{eff}} \sim 30500$ K and bolometric luminosity $L_{\star} \sim 41700 L_{\odot}$. On the other hand, an earlier and also (supposedly) more evolved O star is expected to have a quite higher effective temperature and luminosity: $T_{\text{eff}} \sim 42600$ K and $L_{\star} \sim 1000000 L_{\odot}$ (e.g., O3I).

With lower effective temperature, B-type dwarfs encompass both the range of intermediate- and high-mass stars, having M_{ZAMS} between $\sim 3 M_{\odot}$ (B9V, $T_{\text{eff}} \sim 12000$ K) and $\sim 18 M_{\odot}$ (B0V, $T_{\text{eff}} \sim 30000$ K). The physical parameters of OB-type dwarf stars are summarized in Table 1.1². Thus, mainly depending on their initial mass, B dwarfs are progenitors of either planetary nebulae ($M_{\text{ZAMS}} \lesssim 8\text{-}9 M_{\odot}$), resulting in white dwarfs as stellar remnant, or core-collapse supernovae that result in neutron stars from the more massive progenitors (e.g., see Fig. 1 of Heger et al. 2003).

Despite being much more abundant than massive stars, based on a typical Salpeter initial mass function (Salpeter 1955), low- and intermediate-mass stars ($M_{\text{ZAMS}} \lesssim 8 M_{\odot}$) are only able to carry the stellar nucleosynthesis up to the core helium-burning phase, resulting in the production of carbon and oxygen during their more evolved phases as asymptotic giant branch (AGB) stars. From Table 1.1, one sees that this applies to B stars among the types B9 and B3. However, massive stars ($M_{\text{ZAMS}} \gtrsim 8 M_{\odot}$) are able to continue the nucleosynthesis in their cores beyond the helium-burning phase up to the production of iron group elements during the silicon-burning phase,

2. In Table 1.1, the quoted value for the initial mass of a B0 dwarf is somewhat larger than for an O9.5 dwarf. We emphasize that this fact is not physically reliable and it happens since the results compiled in this table come from different studies in the literature.

1.1. OB-type stars

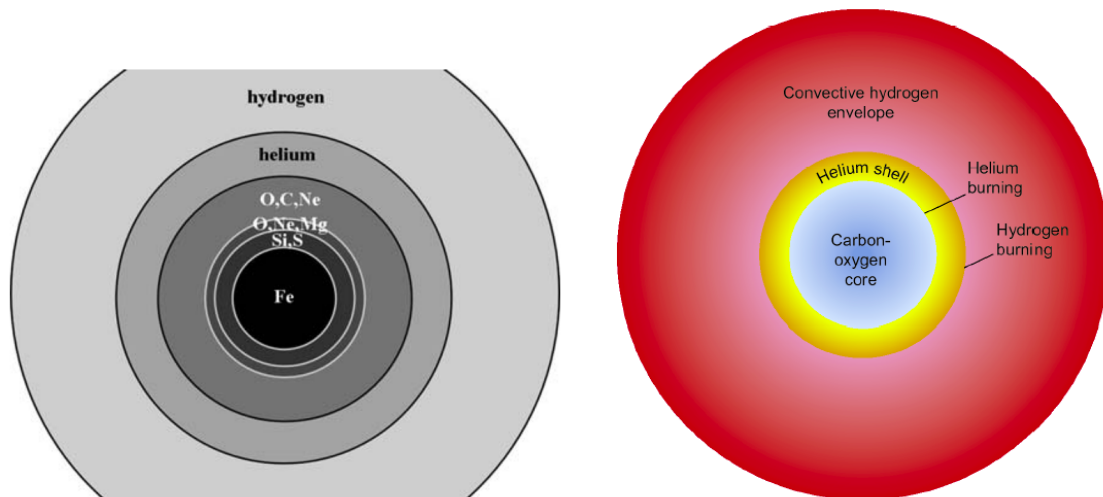


Figure 1.1 – Schemes of chemical stratification in evolved massive stars (left) and evolved low-intermediate-mass (right) stars. Left: reproduced from Maeder (2009). Right: reproduced from Herwig (2005).

resulting in core-collapse supernovae (type II, Ib, or Ic).

Fig. 1.1 presents a basic scheme of the chemical stratification in the structure of evolved massive stars, as well as of evolved low-intermediate-mass stars (AGB phase). One sees that concentric layers are successively composed by lighter elements (as H and He) toward the stellar surface. We stress that this description for the fate of stars according to the initial mass is a simplified picture. For instance, it is still largely unknown the pathways of stars with initial masses between $\sim 8\text{-}10 M_{\odot}$. In this case, depending on the mass loss, they can either evolve to the AGB phase, ending their evolution as planetary nebulae, or evolve up to core-collapse supernovae (e.g., Nomoto 1984, 1987; Jones et al. 2013).

The evolution of massive stars results in different types of supernovae, depending mainly on the initial stellar mass and metallicity (e.g., see Fig. 2 of Heger et al. 2003). In Fig. 1.2, we show the modified Conti scenario for the evolution of single non-rotating stars with solar-metallicity, as a function only of their initial masses (Ekström et al. 2013). This is inspired on the scenario originally proposed by Conti (1975), the first study to propose the evolutionary connection between O-type and Wolf-Rayet stars. Nevertheless, this scheme, presented in Fig. 1.2, is a summary of modern results found by state-of-the-art evolutionary models for massive stars calculated using the Geneva stellar evolution code (Ekström et al. 2012).

From Fig. 1.2, we see that stars with M_{ZAMS} lower than about $30 M_{\odot}$ will end their evolution as red supergiants (T_{eff} up to ~ 4000 K, Levesque et al. 2005), before exploding in type-II supernovae (hydrogen-rich core-collapse supernovae). On the other hand, massive stars with M_{ZAMS} larger than $30 M_{\odot}$ will finish their evolution as Wolf-

1.1. OB-type stars

$M > 60 M_{\odot}$:	$O \rightarrow Of/WNL \rightarrow LBV \rightarrow WNL \rightarrow (WNE) \rightarrow WC \rightarrow SN Ib,c$	WR
$M = 40 - 60 M_{\odot}$:	$O \rightarrow BSG \rightarrow LBV \rightarrow WNL \rightarrow (WNE) \rightarrow WC \rightarrow SN Ib,c$	
$M = 30 - 40 M_{\odot}$:	$O \rightarrow BSG \rightarrow RSG \rightarrow WNE \rightarrow WCE \rightarrow SN Ib,c$	
$M = 25 - 30 M_{\odot}$:	$O \rightarrow (BSG) \rightarrow RSG \rightarrow (YSG?) \rightarrow SN II-L/b$	RSG
$M = 10 - 25 M_{\odot}$:	$O \rightarrow RSG \rightarrow (\text{Ceph. loop for } M < 15 M_{\odot}) \rightarrow RSG \rightarrow SN II-P$	

Figure 1.2 – Modified Conti scenario for the evolutionary scheme of massive stars as a function of zero-age main sequence mass. Reproduced from Ekström et al. (2013).

Rayet stars (T_{eff} up to ~ 200000 K, Tramper et al. 2015), before exploding in type-Ib or type-Ic supernovae (hydrogen-deficient core-collapse supernovae). It is interesting to note that stars with initial masses between 30 and 40 M_{\odot} are expected to loop between the two extreme regions of the HR diagram, passing from the blue to the red supergiant phases and then returning to the blue region of the HR diagram as Wolf-Rayet stars. As pointed out by Ekström et al. (2013), for these more massive stars that can evolve to red supergiants, stellar winds during this phase must be intense enough, in comparison with stars with $10 M_{\odot} < M_{\text{ZAMS}} < 30 M_{\odot}$, to remove the hydrogen from their atmospheres and thus resulting in Wolf-Rayet stars, which show very weak or absent hydrogen lines in their spectra.

We stress that the scheme shown above is based on non-rotating models for single stars with solar-metallicity. Other relevant physical processes, which are not taken into account here, must affect these results: metallicity, rotation, magnetic fields, tidal interaction and mass transfer in binary systems, and more accurate values for the wind mass-loss rate at different evolutionary stages. For instance, it is known that a large fraction (up to $\sim 70\%$) of massive stars are born in multiple system and a significant fraction (up to $\sim 30\%$) of the current single massive stars are in fact merger products from binary system formed in the past (e.g., Sana et al. 2012, 2013a; de Mink et al. 2014). A more detailed discussion on the effects of magnetic field, rotation, and multiplicity, on the evolution of massive stars can be found in Meynet et al. (2011), Meynet et al. (2015), and Sana et al. (2013c), respectively.

In short, our discussion above evidences the importance of mass loss processes on the properties and evolution of massive stars. In particular, Sect. 1.2 is devoted to discuss in details the phenomenon of stellar winds.

As a quantitative example, we show, in Fig. 1.3, how the mass-loss rate of the stellar wind is expected to change as a function of time for a non-rotating single star with $M_{\text{ZAMS}} = 60 M_{\odot}$. These values for the mass-loss rate are taken in account in the Geneva models analysed in Groh et al. (2014). Based on synthetic spectra (calculated with the radiative transfer code CMFGEN) at each evolutionary step, they studied

1.1. OB-type stars

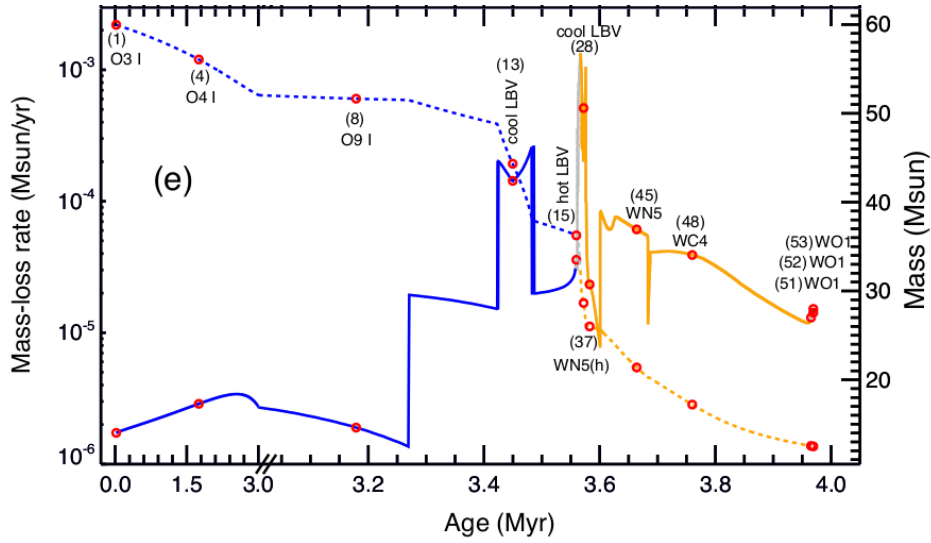


Figure 1.3 – Mass-loss rate (left axis, solid line) and stellar mass (right axis, dashed line) as function of age in the Geneva evolutionary model for a non-rotating single star with $M_{\text{ZAMS}} = 60 M_{\odot}$. Colors encode different evolutionary phases: H-core (blue), H-shell and H+He-shell (gray), and He-core (orange). The evolution of the spectral type predicted by Groh et al. (2014) is also indicated here. Due to the large amount of mass loss since the beginning of the main sequence, the star ends its evolution with about $13 M_{\odot}$. Adapted from Groh et al. (2014).

the spectroscopic properties of a non-rotating single $60 M_{\odot}$ star, evaluating how the spectra type changes as the modeled star evolves from the H-burning phase to the pre-supernova phase.

Interestingly, Groh et al. (2014) showed that a single non-rotating star with $M_{\text{ZAMS}} = 60 M_{\odot}$ must appear in the zero-age main sequence as a O3-4 supergiant (luminosity class I), not as a dwarf star (class V). After that, the star evolves to the LBV and Wolf-Rayet phases before ending its evolution. From Fig. 1.3 one sees that the mass-loss rate changes highly through the evolution, from $\sim 10^{-6} M_{\odot} \text{ yr}^{-1}$ at the beginning of the H-core burning phase, reaching a maximum of $\sim 10^{-3} M_{\odot} \text{ yr}^{-1}$ by the end of the cool LBV phase. Due to the mass loss, this star with an initial mass of $60 M_{\odot}$ will end its evolution with about $13 M_{\odot}$, as a WO1 star until the supernova explosion (Groh et al. 2014).

1.1.2 Enrichment of the interstellar medium

Stars transfer mechanical and radiative energy to the interstellar medium (ISM) by different ways: stellar winds (in addition to episodic mass loss), radiation, and supernovae. In Fig. 1.4, we show the central part of the H II region 30 Doradus (Tarantula Nebula), called R136, in the Large Magellanic Cloud. This region has been widely studied regarding very massive stars ($M_{\text{ZAMS}} \approx 100\text{-}300 M_{\odot}$) and multiplicity properties of massive stars (see, e.g., Crowther et al. 2010; Chené et al. 2011; Sana et al. 2013b).

1.1. OB-type stars



Figure 1.4 – The R136 open cluster located in the H II region 30 Doradus (Tarantula Nebula) in the Large Magellanic Cloud. Imaging from the Hubble Space Telescope/Wide Field Camera instrument in the visible region (photometry in the U-, B-, V-, I-, and H α -bands). This image has field of view of about 46 pc. Source: <https://apod.nasa.gov/apod/ap160124.html>.

From that, we note that R136 is a very crowded stellar environment. In fact, it is the region of highest stellar density in Tarantula Nebula, being populated by a large number of OB-type stars. The spectroscopic analysis of Doran et al. (2013) confirmed about 500 early-type stars in this region. Massive hot stars are the main source of ultraviolet (UV) radiation, ionizing the nebular gas, remnant of the primordial molecular cloud, and then originating H II regions. Moreover, we see that the structure of 30 Doradus is highly shaped due to the interaction of the intense winds and radiation fields from early-type stars with the ISM gas.

Therefore, it is conspicuous the importance of massive stars in the enrichment of the ISM, both from a physical (transfer of kinematic energy) and chemical (production and transfer of metals) views. Abbott (1982a) was one of the first quantitative studies to investigate the effects of the winds of massive stars on the ISM. This author evaluated the mechanical and radiative energy contribution from O-type, BA supergiants, and Wolf-Rayet stars to the enrichment of the ISM within a distance of ~ 3 kpc. He found that these stars transfer mass (by means of winds) and radiation to the ISM at a rate of $9 \times 10^{-5} M_{\odot} \text{ yr}^{-1} \text{ kpc}^{-2}$ and $2 \times 10^{38} \text{ erg s}^{-1} \text{ kpc}^{-1}$, respectively.

Fig. 1.5 shows the results found by Castor (1993) for the rate of mass that is injected into the interstellar medium as a function of initial stellar mass. This rate (in units of $M_{\odot} \text{ yr}^{-1} \text{ kpc}^{-2}$) is weighted by the initial mass function from Garmany et al. (1982).

1.1. OB-type stars

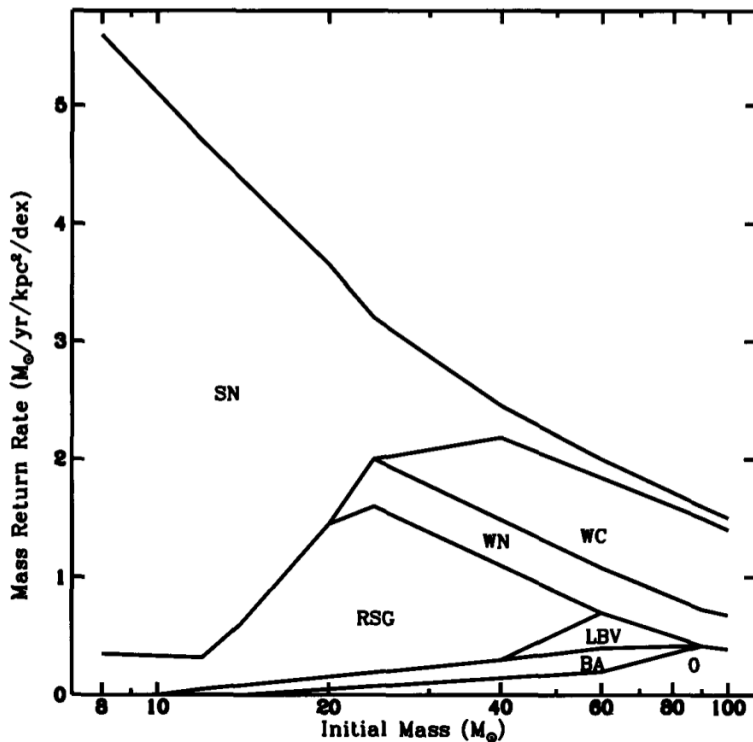


Figure 1.5 – Mass return rate (logarithmic scale) of massive stars as a function of stellar mass. The evolutionary phases are indicated at the different regions here: O-type, BA supergiant, luminous blue variable (LBV), red supergiant (RSG), carbon Wolf-Rayet (WC), and nitrogen Wolf-Rayet (WN) stars. The region of core-collapse supernovae is indicated by SN. The stellar mass is shown in logarithmic scale. Apart from the stellar mass that returns to the interstellar medium due to supernovae, the peak of mass return comes from stars with initial mass of about $40 M_{\odot}$ during the Wolf-Rayet phase. Reproduced from Lamers & Cassinelli (1999).

In short, it expresses the contribution to the enrichment of the ISM given the initial mass through the different evolutionary phases of massive stars. First, notice that stars with $M_{\text{ZAMS}} \sim 8\text{-}10 M_{\odot}$ will transfer mass to the ISM mainly at the end of their evolutionary paths, when exploding in core-collapse supernovae of type-II (Fig. 1.2). Despite having less intense winds than the more massive stars, these stars with $M_{\text{ZAMS}} \sim 8\text{-}10 M_{\odot}$ also significantly contribute to the mass return to the ISM, taking the SN contribution into account, since they are more numerous in comparison with the more massive objects. Apart from the mass injection by means of supernovae, the largest individual contribution to the enrichment of the ISM comes from stars with initial masses of $\sim 40 M_{\odot}$ during their evolutionary stages as Wolf-Rayet stars.

However, as pointed out in Sect. 1.1.1, B dwarfs encompasses both intermediate-mass (M_{ZAMS} of $\sim 3 M_{\odot}$, type B9) and high-mass stars (M_{ZAMS} of $\sim 18 M_{\odot}$, type B0). These lower-mass B stars will then evolve to the AGB phase. Our discussion above was focused on the contribution of massive stars to the enrichment of the ISM, but AGB stars are also important contributors of gas and dust to the ISM by their intense winds. Due to winds, mainly during the AGB phase, a star with M_{ZAMS} of $\sim 4 M_{\odot}$ is expected

1.1. OB-type stars

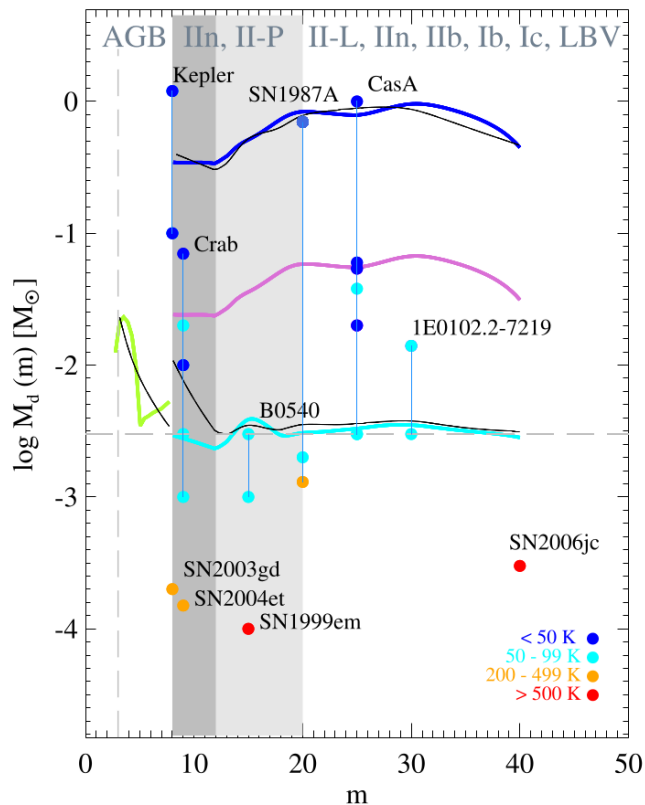


Figure 1.6 – Amount of dust mass produced by AGB stars and supernovae as a function of progenitor initial mass from Gall et al. (2011b). The theoretical curve for AGB stars is shown in green, while the curves for supernovae are shown in blue, pink, and cyan according to the dust production efficiency that is used in the models. Measured values for supernovae remnants are shown in colored points according to different values of dust temperature. Further details on these theoretical curves and measured values are found in Sect. 7.2 of Gall et al. (2011b). See text for discussion. Reproduced from Gall et al. (2011b).

to loose about 80% of its initial mass (e.g., Cummings et al. 2016).

AGB stars are responsible to about the half of the recycled gas that is used in the star formation process (e.g., Maeder 1992), and they are important sources of dust in the Universe (see, e.g., Valiante et al. 2009; Gall et al. 2011b, and references therein). Fig. 1.6 shows the predictions from Gall et al. (2011b) for the amount of dust yield both by AGB stars and supernovae. These theoretical curves are compared with measured values for supernovae remnants from the literature. Here, the theoretical curves for supernovae are calculated considering different regimes of dust production efficiency, which is related to the total amount of dust injected into the ISM (see Eq. 21 of Gall et al. 2011a). From that, one sees that the amount of dust produced by AGB stars is somewhat comparable to the one by supernovae regardless of the different theoretical scenarios that are analysed by these authors.

In addition, Fig. 1.7 shows the minimum initial stellar mass for a star dying at a certain epoch (expressed in terms of cosmological redshift z). Considering the onset of star formation at $z = 10$, just very massive stars with mass up to $\sim 100 M_{\odot}$ are able to

1.1. OB-type stars

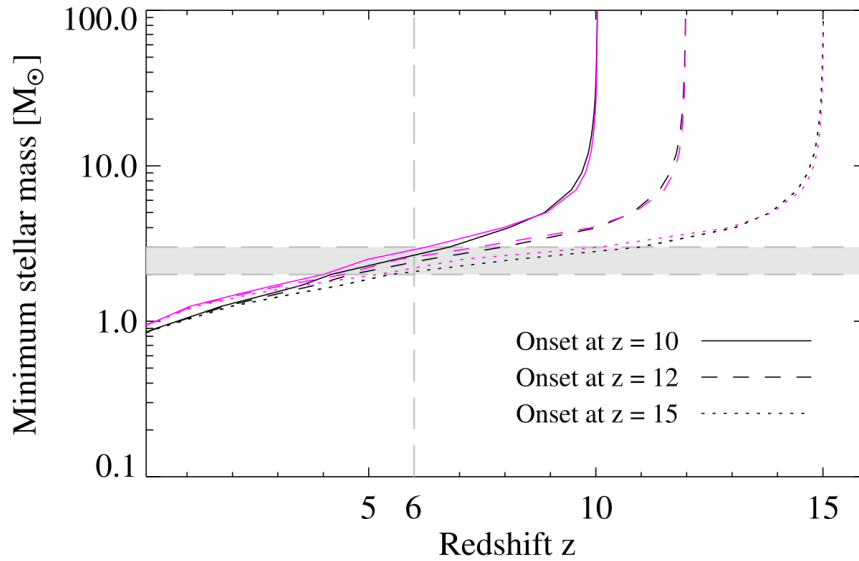


Figure 1.7 – Minimum M_{ZAMS} that allows a complete stellar evolution at a certain value of cosmological redshift (z). Stellar formation starts on three different value of redshift: $z = 10$ (solid line), $z = 12$ (dashed line), and $z = 15$ (dotted line). Black lines corresponds to stellar metallicity $Z = 0.001$ and pink lines to $Z = 0.040$. The gray region indicates the minimum initial mass ($\sim 2\text{-}3 M_{\odot}$) for stars contributing (in this case, during the AGB phase) to the injection of dust into the ISM in the early Universe ($z = 6$). Reproduced from Gall et al. (2011b).

contribute to the enrichment of the ISM at this epoch (Gall et al. 2011b).

Based on Fig. 1.7, we see that only stars with M_{ZAMS} larger than $\sim 3 M_{\odot}$ are able to pollute the ISM at the epoch $z = 6$ (Universe with age of $\sim 10^9$ yr). Stars with initial mass lower than this threshold evolve in time-scales longer than the age of the Universe at $z = 6$. In short, OB-type dwarfs are the progenitors of the sources of the ISM gas and dust at the early Universe.

In conclusion, massive star are rare due to the initial mass function and also to their shorter lifetimes of $\sim 10^6\text{-}10^8$ Myr. As a rough estimate, there are only $\sim 14000\text{-}18000$ O-type stars in the Galaxy (Maíz Apellániz et al. 2013). Despite their rarity, these stars are important because they enrich physically and chemically the ISM with their strong outflows, since the beginning of the main sequence until evolved stages as BSG, RSG, LBV, and Wolf-Rayet stars. Moreover, they are progenitors of more exotic astrophysical objects, neutron stars and black holes, that are connected to high-energy astrophysical phenomena, as gamma-ray bursts and gravitational waves (e.g., Gehrels & Razzaque 2013; Abbott et al. 2016).

1.2 Radiative line-driven winds

1.2.1 The phenomenon of stellar winds

Stellar winds are characterized by a continuous process of mass loss from the stellar atmosphere (i.e., the photosphere³). The reader should pay attention here to the property of continuity because massive stars lose mass by means of other mechanisms during their evolution, such as supernovae or episodic mass eruptions that eject a large amount of matter in a limited amount of time (time-scale of years), as the giant mass loss eruption that occurred at P Cygni (LBV star, spectral type B1-2Ia) in the 17th century (see, e.g., Israelian & de Groot 1999; Smith 2014).

The mass-loss rate (\dot{M}) and the terminal velocity (v_∞) are the main fundamental parameters to describe the hydrodynamics of the wind. With respect to a larger astrophysical context, it is important to constrain the real values for these two parameters in massive stars because they directly provide the kinematic energy injected into the interstellar medium through winds by the wind power P_W (Abbott 1982a):

$$P_W = \frac{1}{2} \dot{M} v_\infty^2. \quad (1.1)$$

The mass-loss rate is defined as the quantity of mass that the star loses via winds per unit time:

$$\dot{M} = -\frac{dM_\star}{dt}, \quad (1.2)$$

where M_\star is the stellar mass (expressed as a function of time).

The terminal velocity is the wind velocity that is reached at a sufficiently large distance from the stellar surface ($r \rightarrow \infty$) for enabling null-acceleration (as a result of null-force) on the wind.

These two basic parameters of the wind, \dot{M} and v_∞ , are related to each one by the equation of mass continuity:

$$\dot{M} = 4\pi r^2 \rho(r) v(r), \quad (1.3)$$

where $\rho(r)$ is the wind density structure and $v(r)$ is the wind velocity structure for a certain distance r from the center of the star ($r \geq R_\star$).

Eq. 1.3 stands in the case of a stationary (i.e., time-independent, $\frac{\partial v(r,t)}{\partial t} = 0$), smooth, and spherically symmetrical wind. It expresses the conservation of mass through the wind, that is, the same quantity of mass (gas) flows, per unit time, through

3. Throughout this thesis, the terms “(stellar) atmosphere” and “extended atmosphere” are occasionally used to design the photosphere and the circumstellar environment, respectively.

1.2. Radiative line-driven winds

a sphere with area given by $4\pi r^2$ (at any value of r).

Based on solutions for the momentum equation of the wind from Castor et al. (1975), the wind velocity structure, $v(r)$, is usually parameterized in the literature by the so-called β -law approximation:

$$v(r) = v_0 + (v_\infty - v_0) \left(1 - \frac{R_\star}{r}\right)^\beta, \quad (1.4)$$

where R_\star is the stellar radius, v_0 is the velocity at the photosphere (i.e., the base of the wind is set at the photosphere), and r is given as a function of R_\star . Considering that $v_\infty \gg v_0$, Eq. 1.4 can be approximated as follows:

$$v(r) = v_\infty \left(1 - \frac{R_\star}{r}\right)^\beta. \quad (1.5)$$

Thus, given the terminal velocity v_∞ , the wind velocity is fully parameterized by the exponent β . Based on spectroscopic and hydrodynamical studies, β is typically found around 0.8-1.0 for O dwarfs (luminosity class V) stars (e.g., Bouret et al. 2013; Muijres et al. 2012). On the other hand, β can reach larger values up to ~ 2.0 -3.0 in OB supergiants (e.g., Crowther et al. 2006; Martins et al. 2015). From Eq. 1.5, we note that higher values of β implies that the wind accelerates slower. Curé & Rial (2004) investigated the effect of rotation on the wind acceleration of massive stars, and they verified that solutions for slow velocity winds are acceptable in the case of fast rotators, having rotational velocities higher than about 75% the critical value (Sect. 1.3.2). This could be in part one possibility to explain such large values of β that are typically observed in more evolved massive stars.

We point out that winds are common in different types of stars: both in young and evolved low-mass stars (e.g., T-Tauri, solar-type, and AGB stars) and in young and evolved massive stars. Despite being created by different physical mechanisms, this means that winds happens virtually in all types of stars, having different effects on stellar evolution depending on the intensity of the mass-loss rate.

For instance, the Sun shows a stable outflow that is well characterized by a quiescent mass-loss rate of $\sim 10^{-14} M_\odot \text{ yr}^{-1}$ and a terminal velocity of $\approx 400 \text{ km s}^{-1}$ (e.g., Sturrock et al. 1986). The solar wind is driven by gas pressure due to the high temperature of the solar corona (e.g., Noble & Scarf 1963). Parker (1958) was the first to show quantitatively that a static solar corona is impossible, introducing the term “stellar wind”. Further details on coronal winds can be found in Chapter 5 of Lamers & Cassinelli (1999). For a better comparison with these values mentioned for the Sun, O-type stars show mass-loss rates up to $\sim 10^{-6} M_\odot \text{ yr}^{-1}$ and terminal velocities up to $\approx 3000 \text{ km s}^{-1}$ for the earlier spectral types (e.g., O3-4): their mass-loss rates are 10^8 times larger than

1.2. Radiative line-driven winds

in winds of solar-type stars during the main sequence.

More generally, intermediate- and low-mass stars develop winds with higher mass-loss rates just during evolved (more luminous) evolutionary phases, such as the AGB phase. In this case, mass-loss rates vary from $\sim 10^{-7} M_{\odot} \text{ yr}^{-1}$ at the initial AGB phase up to $\sim 10^{-4} M_{\odot} \text{ yr}^{-1}$ at the end of the AGB phase. This later and more intense wind phase is called as the AGB super-wind phase (Renzini 1981; Bowen & Willson 1991). It is thought that such very slow winds (v_{∞} up to $\sim 30 \text{ km s}^{-1}$) showing a large amount of mass loss are driven during the AGB phase as follows (e.g., Höfner & Andersen 2007): pulsations transfer gas from the stellar surface to the outer atmospheric layers, where the temperature is low enough to enable the formation of dust grains. From that, the radiative pressure on the coupled system of gas and dust grains (carbonaceous or silicates) drives a steady outflow. The reader interested on further details regarding the mass loss of AGB stars is referred to the review of Höfner & Olofsson (2018).

In short, intermediate- and low-mass stars are important to the enrichment of the interstellar medium, as discussed in Sect. 1.1.2, but this contribution is limited to later evolutionary phases. Their contribution is also limited in terms of heavy elements: they will mostly enrich the ISM with the injection of carbon, nitrogen, and oxygen. On the other hand, winds of massive stars are relevant during all their evolutionary phases, since the main sequence phase up to their later stages. Due to their high effective temperatures and luminosities, up to $\sim 10^6$ times the solar luminosity, OB-type stars are able to develop radiative line-driven winds, as discussed below.

1.2.2 Elementary concepts of radiative line-driven winds

Radiative line-driven winds means that the wind acceleration arises from the scattering of the stellar continuum flux by line transitions of (mainly) elements heavier than hydrogen and helium, creating spectral absorption and emission lines. Such photon-matter interaction transfers linear momentum from the stellar radiation field to the gas that composes the photosphere and the wind, and thus dropping the assumption of hydrostatic equilibrium for the stellar atmosphere.

This mechanism for driving winds is not limited to massive hot stars, such as OB dwarfs, OBA supergiants, LBVs, and WR stars. After the post-AGB phase, low- and intermediate-mass stars will develop radiative-line driven winds during the phase as central stars of planetary nebula (CSPN) (e.g., Cerruti-Sola & Perinotto 1985; Prinja 1990). Despite having quite low luminosities, when compared with massive stars, CSPNs show very high effective temperature, reaching extreme values as high as $\sim 150000 \text{ K}$ (e.g., Herald & Bianchi 2011; Keller et al. 2011). Moreover, the line-driven mechanism is promising to explain the origin of winds in the accretion disks of

1.2. Radiative line-driven winds

quasars (e.g., Shlosman et al. 1985; Proga et al. 2000). Concerning the massive stars with low T_{eff} , as the RSGs, the mechanisms for the wind acceleration are thought to be quite similar to the ones described for AGBs stars in Sect. 1.2.1: a combination of stellar pulsations and radiative pressure on the coupled system of gas and dust grains (that are formed in outer atmospheric layers).

Considering the simplest case of stationary winds, and that the only forces exerted are due the gravity, the gas pressure gradient, and the radiation, the momentum equation of a radiation line-driven wind is expressed as follows:

$$v \frac{dv}{dr} = -\frac{GM_{\star}}{r^2} + \frac{1}{\rho} \frac{dp(r)}{dr} + g_{\text{rad}(r)}, \quad (1.6)$$

where G is the gravitational constant, M_{\star} is the stellar mass, and p is the gas pressure. Assuming the case of a ideal gas with isothermal temperature T , the state equation is described by:

$$p(r) = \frac{RT}{\mu} \rho(r), \quad (1.7)$$

where $\sqrt{\frac{RT}{\mu}}$ is the isothermal sound speed in the wind, R is the ideal gas constant and μ is the mean molecular weight of the gas ($\mu = 0.602$ for an atmosphere with solar-metallicity).

On the right hand of Eq. 1.6, the first two terms are common when describing the hydrodynamics of different types of stellar winds. However, the third-term in the equation of motion represents the total radiative acceleration acting on the wind and is expressed as follows:

$$g_{\text{rad}}(r) = g_e(r) + g_{\text{line}}(r), \quad (1.8)$$

since this results from the momentum transfer by two different ways of photon-atom interaction:

- (i) g_e is the radiative acceleration due to Thomson scattering (i.e., elastic scattering of photons by electrons, the contribution from the continuum opacity).
- (ii) g_{line} is the contribution due to line opacity (bound-bound transitions).

In addition, free-free and bound-free transitions also contribute to the radiative force due to continuum opacity (see, e.g., Eq. 26 of Sander et al. 2015).

Note that both terms are explicitly written here as a function of r . The first term in Eq. 1.8 is given by:

$$g_e(r) = \frac{\kappa_e L_{\star}}{4\pi r^2 c}, \quad (1.9)$$

1.2. Radiative line-driven winds

where κ_e is the opacity for electron scattering, L_\star is the stellar luminosity, and c is the light speed in the vacuum. The term κ_e is dependent on the gas metallicity and also the degree of gas ionization that typically ranges from ~ 0.28 to $0.35 \text{ cm}^2\text{g}^{-1}$ in early-type stars.

From Eq. 1.9, the Eddington parameter Γ_e is defined as the ratio between the radiative acceleration contribution from Eq. 1.9 and the gravitational acceleration $g(r)$, which is given by GM_\star/r^2 :

$$\Gamma_e = \frac{g_e(r)}{g(r)} = \frac{\kappa_e L_\star}{4\pi GM_\star c}, \quad (1.10)$$

where M_\star is the stellar mass.

Physically, this parameter expresses how close a star is to the gravitationally unbound limit ($\Gamma_e \rightarrow 1$, the so-called classical Eddington limit), just considering the radiative force due to electron scattering. From that, most massive hot stars have Γ_e up to a factor of 2 lower than the Eddington limit. In advance of discussion, one sees, from Fig. 1.10, that electron scattering contributes much more to the radiative force at the base of the wind (photosphere) than at large distances through the wind. As these stars display strong winds, this evidences the large contribution from line opacity (g_{line}) to the total radiative force in Eq. 1.8.

The density stratification $\rho(r)$ in the momentum equation is related to the velocity $v(r)$ by the equation of mass continuity (Eq. 1.3). Given a certain value for the mass-loss rate (constant term in Eq. 1.3), the momentum equation can be re-written replacing the term $\rho(r)$ by $\dot{M}/(4\pi r^2 v(r))$. Therefore, the hydrodynamics of the wind is fully described by Eqs. 1.3 and 1.7 together with Eq. 1.6⁴.

Clearly, the evaluation of the radiative acceleration due to line transitions imposes the biggest challenge to solve the equation of motion of the wind. Consider the absorption of a photon of frequency ν_0 by an atom with mass m of the stellar atmosphere, and the subsequently re-emission of a photon by this same atom. The variation of the atom's radial linear momentum p_r (in the same direction of the initially absorbed photon path) is given by:

$$\Delta p_r = m\Delta v_r = \frac{h\nu_0}{c}(1 - \cos \alpha), \quad (1.11)$$

where α is the angle formed by the initially absorbed photon path and the subsequent re-emitted photon path (as represented in Fig. 1.8). Thus, in the particular case of $\alpha = 0$, that is, the re-emitted photon has the same direction of the initially absorbed

4. Note that the state equation (Eq. 1.7) was assumed for an isothermal wind. However, it is not a realistic approximation since the temperature and the mean molecular weight must be radially dependent (see., e.g., Sander et al. 2017).

1.2. Radiative line-driven winds

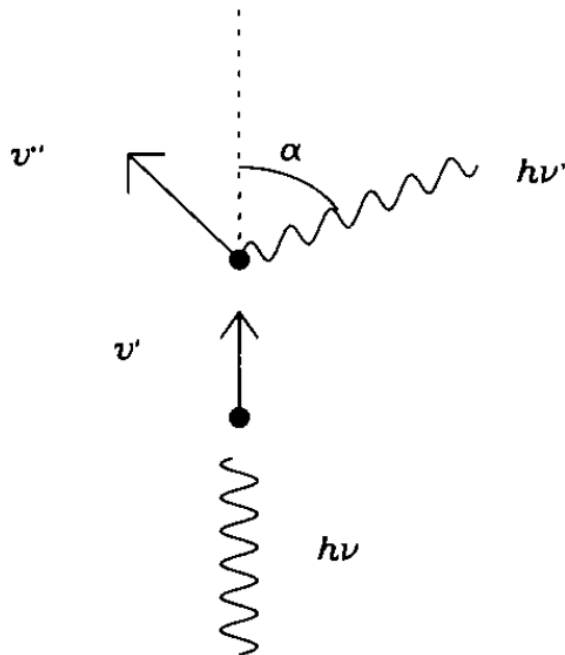


Figure 1.8 – Schematic representation of interaction between a photon with linear momentum $h\nu/c$ (energy given by $h\nu$) and a particle of mass m . The particle has velocity v' due to the gain of momentum by absorbing the photon. The velocity of the particle will change to v'' after re-emitting a photon with linear momentum $h\nu'/c$, which forms an angle α with respect to the initial photon's path (linear momentum $h\nu/c$). See text for discussion. Reproduced from Lamers & Cassinelli (1999).

photon, the atom does not present any net gain of radial linear momentum. On the other hand, the maximum gain of momentum is achieved when the photon is re-emitted in the particular case of opposite direction ($\alpha = 180^\circ$): $\Delta p_r = \frac{2h\nu_0}{c}$.

One of the basic idea behind the transfer of momentum in radiative line-driven winds is that, statistically, the photon re-emission must follow approximately an isotropic distribution. Thus, after a large number of iterations with photons with linear momentum $h\nu/c$ coming from the radial direction (as indicated in Fig. 1.8), we can evaluate the mean variation of linear momentum of this atom of mass m , by the integration of Eq. 1.11 over 4π radian (sphere) as follows⁵:

$$\langle \Delta p_r \rangle = \frac{h\nu_0}{c} \frac{1}{4\pi} \int_0^\pi 2\pi(1 - \cos \alpha) \sin \alpha d\alpha. \quad (1.12)$$

Here, we found that the mean variation of the linear momentum, due to the interaction with photons with ν_0 coming from a certain direction, is given by the following expression:

$$\langle \Delta p_r \rangle = \frac{h\nu_0}{c}. \quad (1.13)$$

5. We point out a small mistake in the lower ($-\pi/2$) and upper ($\pi/2$) limits of the integration shown in Eq. 8.5 of Lamers & Cassinelli (1999)

1.2. Radiative line-driven winds

Thus, the radiative force due to lines that is exerted on a volume element of the wind with mass Δm , during an interval Δt , can be written as follows:

$$g_{\text{line}} = \sum_{i=1}^N \frac{\langle \Delta p_r \rangle_i}{\Delta m \Delta t}, \quad (1.14)$$

where i denotes different line transitions participating in the transfer of linear momentum to the gas.

Despite being didactic, the formulation of the line-radiative acceleration as shown above is not useful to evaluate the wind momentum equation. Lucy & Solomon (1970) was one of the first works to attempt this task and to determine the mass-loss rate of massive hot stars from first principles (i.e., solving the momentum equation). These authors identified the absorption resonance lines⁶ in the ultraviolet region of ion metals, such as Si IV, C IV, and N V, as the mechanism to break the hydrostatic equilibrium in the atmosphere of these stars. By setting regularity condition at the sonic point of the wind⁷, they introduced the so-called reversing moving layer theory, which was recently updated considering more sophisticated non-LTE (Local Thermodynamics Equilibrium) radiative transfer calculations (see Lucy 2007, 2010b,a). One of the main findings of this pioneer work was to estimate an upper limit on the mass-loss rate for line-driven winds due to the contribution from just one line:

$$\dot{M} \lesssim \frac{L_{\star}}{c^2}. \quad (1.15)$$

As one could expect, the mass-loss rate of radiative line-driven winds is dependent on the stellar luminosity: higher values of mass-loss rate must be achieved for the more luminous stars. This result found by Lucy & Solomon (1970) can be explained using a simple physical argument as follows.

Consider that just one absorption line in certain rest-frame ν_0 contributes to the radiative acceleration and the wind is optically very thick in such line. The latter hypothesis, i.e., optically very thick line, means that all the photons with ν_0 are absorbed in the wind. Thus, we will have the following quantity of linear momentum that is transferred from the radiation field to the wind:

$$\dot{M} v_{\infty} = \frac{1}{c} \int_{\nu_0}^{\nu_0(1+v_{\infty}/c)} 4\pi R_{\star}^2 F_{\nu}^* d\nu, \quad (1.16)$$

where F_{ν}^* is the stellar flux in the frequency ν at the stellar radius.

Due to the Doppler effect, Eq. 1.16 states that photons with frequency between

6. Lines formed due to the electron transition between the ground energy level and the first excited state.

7. Considering an isothermal wind, the sonic point is defined by the distance r_s in the wind where the velocity is equal to the isothermal sound speed, i.e., $v(r = r_s) = \sqrt{RT/\mu}$.

1.2. Radiative line-driven winds

ν_0 and $\nu_0(1 + v_\infty/c)$ contribute to the formation of the spectral line with frequency rest-frame frequency ν_0 . Thus, we integrate Eq. 1.16 through the whole wind extension, i.e., from the base of the wind with $v(r) = 0$ up to the outermost wind region where $v(r) = v_\infty$. This equation expresses the gain of linear momentum of the wind, $\dot{M}v_\infty$, due to the absorbed radiation (on the right hand of Eq. 1.16).

Note that the velocity stratification in wind (see, again, Eq 1.5) is important regarding the wind acceleration of massive hot stars, which have high values of terminal velocities up to $\sim 3000 \text{ km s}^{-1}$. As a result of the Doppler effect, photons with frequencies higher than ν_0 will be absorbed through the whole wind extension, also contributing to form such a line: in the outermost part of the wind, photons launched from the stellar surface with rest-frame $\nu_0(1 + v_\infty/c)$.

Therefore, the Doppler effect enables to keep the wind driving due to lines even up to large distances from the stellar surface.

Within a good approximation, we can assume F_ν^* as constant inside the integration interval in frequency, writing Eq. 1.16 as follows:

$$\dot{M}v_\infty \sim \frac{4\pi R_\star^2 F_{\nu_0}^* \nu_0 v_\infty}{c^2}, \quad (1.17)$$

where $F_{\nu_0}^*$ is the stellar flux in the rest-frame frequency ν_0 .

Assuming a black body radiation for the stellar flux and that our adopted optically very thick lines happens in the intensity maximum peak⁸, $F_{\nu_0}^* \nu_0 \sim 0.62\sigma T_{\text{eff}}^4$, where σ is the Stefan-Boltzmann constant. Thus, from Eq. 1.17 and the Stefan-Boltzmann equation:

$$L_\star = 4\pi\sigma R_\star^2 T_{\text{eff}}^4, \quad (1.18)$$

we have the following estimation for the mass-loss rate due to such very thick line:

$$\dot{M} \lesssim 0.62 \frac{L_\star}{c^2} \sim \frac{L_\star}{c^2}. \quad (1.19)$$

For sure, Eq. 1.19 must be seen just as rough estimation for the maximum value of \dot{M} , assuming here that all the stellar luminosity is used to accelerate the wind. Massive hot stars present winds that are driven by a large number of lines. Thus, the resulting mass loss of a wind driven by N_{thick} very thick lines can be expressed as:

$$\dot{M} \sim N_{\text{thick}} \frac{L_\star}{c^2}, \quad (1.20)$$

since these transitions are independent among themselves.

8. This is a reasonable assumption since hot stars emit the most part of their energy in the UV and the relevant lines to drive the wind are formed in this spectral region.

1.2. Radiative line-driven winds

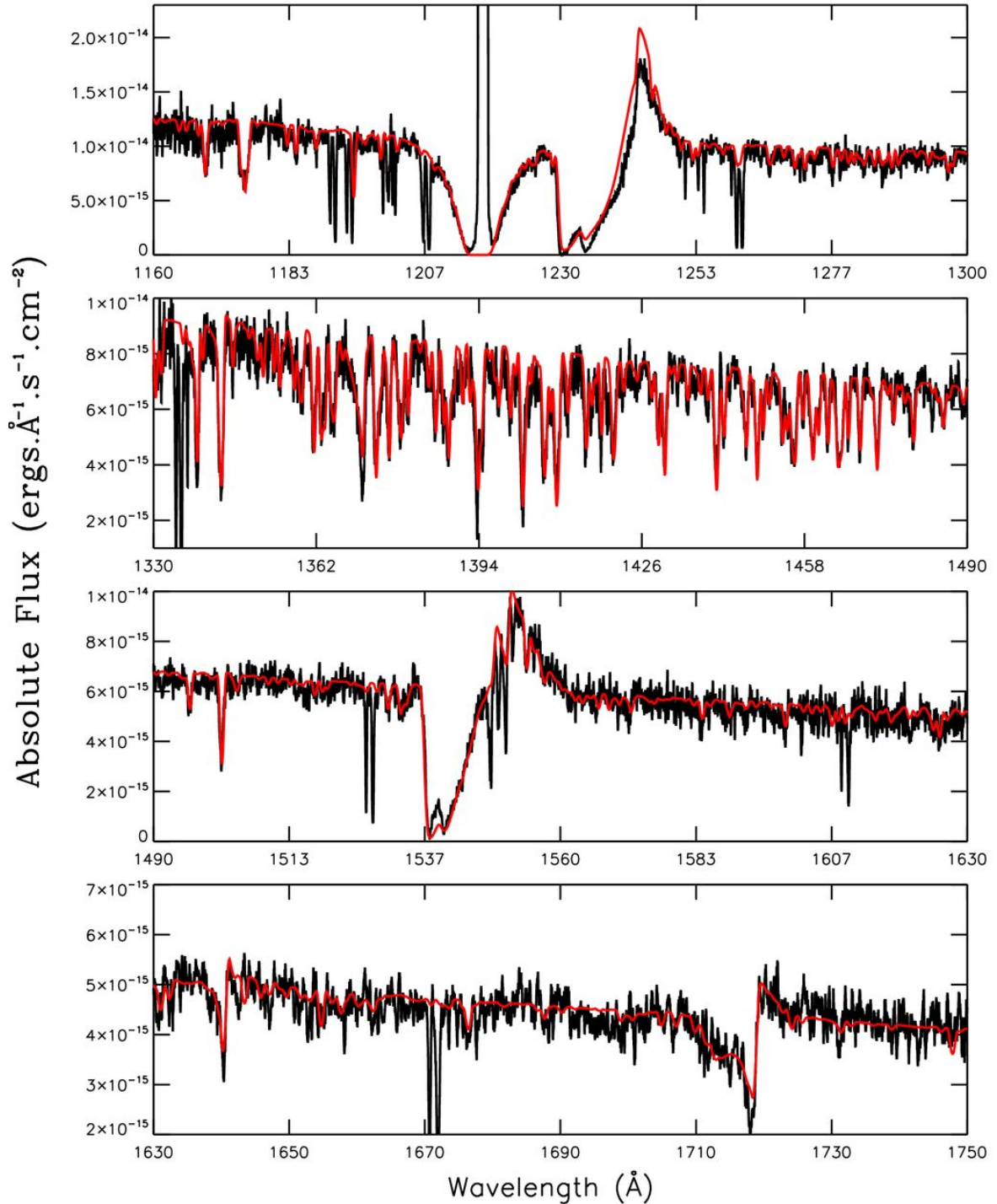


Figure 1.9 – Ultraviolet spectrum of the O supergiant (type O9.5I) IC 1613-B11 (located in the dwarf galaxy IC 1613) is shown in black line. The best-fit CMFGEN found by Bouret et al. (2015) is shown in red line. See text for discussion. Reproduced from Bouret et al. (2015).

1.2. Radiative line-driven winds

In Fig. 1.9, we show spectroscopic data from the Copernicus and the International Ultraviolet Explorer (IUE) satellites, covering the region of $\sim 1100\text{-}1760$ Å, for the early O supergiant IC 1613-B11 (O9.5I). The best-fit radiative transfer model from Bouret et al. (2015), calculated with the code CMFGEN, is also shown here. Later, we discuss in details about this code in Sect. 4.3. From fitting the observed spectrum and the spectral energy distribution using CMFGEN, these authors derived the following parameters for this star $T_{\text{eff}} = 30000$ K, $\log g = 3.25$, $\log L_{\star}/L_{\odot} = 5.45$, $\dot{M} = 1.5 \times 10^{-8} M_{\odot} \text{ yr}^{-1}$, and $v_{\infty} = 1300 \text{ km s}^{-1}$, among other stellar and wind parameters.

Most spectral lines seen in Fig. 1.9 are formed in the photosphere, being useful to probe the stellar parameters such as the effective temperature. The usage of spectroscopy to derive the stellar and wind parameters will be better discussed in Sect. 2. These transitions are mainly due to heavy elements from the iron group (e.g., iron, nickel, and cobalt), forming the so-called iron forest in the ultraviolet region.

Furthermore, one sees that other lines are formed showing both absorption and emission components, such as N V $\lambda 1240$, C IV $\lambda\lambda 1548,1551$, and N IV $\lambda 1718$. These lines have a significant fraction of formation in the wind and thus displaying the so-called P Cygni profiles (Sect. 2.2). As discussed above, Lucy & Solomon (1970) calculated the theoretical mass-loss rate for a O-type star based only on resonant transitions (as C IV $\lambda\lambda 1548,1551$). From Eq. 1.19, one sees that the limit mass-loss rate due to a very thick line is $\dot{M} = 2.0 \times 10^{-8} M_{\odot} \text{ yr}^{-1}$, being somewhat larger than the value derived from Bouret et al. (2015) of $\dot{M} = 1.5 \times 10^{-8} M_{\odot} \text{ yr}^{-1}$ for IC 1613-B11 ($\log L_{\star}/L_{\odot} = 5.45$).

Indeed, from Fig. 1.9, we see that a large amount of lines of metals contribute to the transfer of linear momentum to the stellar atmosphere, and then to the wind driving in a O-type star. In this work, Bouret et al. (2015) analysed three O-type stars in low-metallicity galaxies. First, since the momentum transfer is mainly due to the interaction of the radiation with metal ions, as one may expect the mass-loss rate is scaled to the stellar metallicity: lower metallicity, and thus smaller opacity in the important lines to accelerate the wind, means lower values of mass-loss rate and also terminal velocity. This dependence between the wind basic parameters and the stellar metallicity is very well supported both from theoretical predictions (e.g., Vink et al. 2001; Lucy 2012) and spectroscopic modeling (Mokiem et al. 2007b; Bouret et al. 2003). For example, Mokiem et al. (2007b) derived the relation of $\dot{M} \propto Z^{0.83 \pm 0.16}$ based on the analysis of O stars and early-B supergiants in the Galaxy and in the Magellanic Clouds.

A quantitative example of the contribution by each chemical element to the total radiative acceleration is presented in Fig. 1.10. These calculations were performed by Sander et al. (2017) to analyse the Galactic O supergiant ζ Puppis (O4I) using the

1.2. Radiative line-driven winds

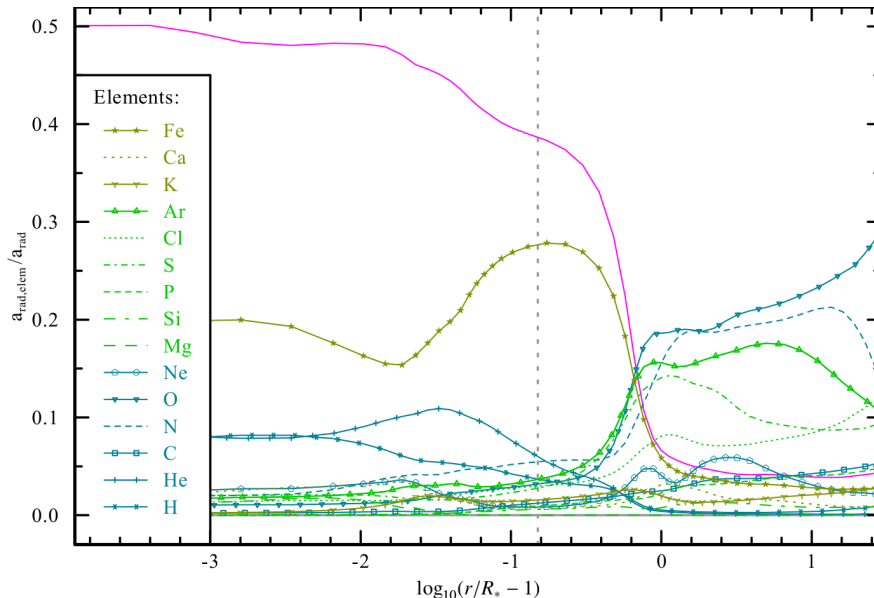


Figure 1.10 – Fraction of the radiative acceleration due to each chemical element, compared with the total radiative force (a_{rad}), as a function of distance from the star, in the PoWR model of Sander et al. (2017) to the analysis of ζ Puppis. The gray dashed line indicates the critical point of the wind ($r \sim 1.16 R_{\star}$) for the solution of the hydrodynamic equation (Eq. 13 of Sander et al. 2017), corresponding, in this case, to the sonic point. The contribution from electron scattering (continuum) is shown in pink solid color. Note how the continuum contribution to the total radiative force decreases toward larger distances in the wind region. Together with the line acceleration due to iron, the continuum mainly contributes to transfer momentum in the innermost part of the wind. Carbon, nitrogen, and oxygen have a more important role to sustain the wind acceleration at larger distances from the stellar surface. Adapted from Sander et al. (2017).

radiative transfer code Potsdam Wolf-Rayet (PoWR, Hamann 1985, 1986; Gräfener et al. 2002; Hamann & Gräfener 2003; Sander et al. 2017). From Eq. 1.8, in addition to the line contribution, we need to take into account the radiative acceleration due to Thomson scattering. This is shown, in Fig. 1.10, in pink line, and one sees how clearly the acceleration due to the electron scattering becomes much less important, in comparison with the contribution due to lines, toward larger distances from the photosphere (e.g., $r > 2 R_{\star}$).

Moreover, the acceleration contribution due to hydrogen and helium is also clearly less important than the ones from heavy elements, as iron, carbon, nitrogen, and oxygen. Interestingly, considering a solar-like chemical abundance, one may note that all these relevant elements (metals) to the wind driving compose about just about 1% of the stellar atmosphere (or even less in low metallicity environments such as for IC 1613-B11). This means that the bulk of the material (typically, hydrogen and helium), composing the photosphere and the wind, are not the principal source of momentum transfer to drive a steady outflow.

We can only to explain the wind driving based on effect of Coulomb coupling. In short, atoms of hydrogen and helium are not mainly accelerated by lines, but by the

1.2. Radiative line-driven winds

electric field originated from the heavy ions. This process results in a slowing down of the metals and creates a steady outflow of the wind. Since this implies in reducing the acceleration of the heavy ions, the efficiency of the Coulomb coupling is measured in terms of two characteristic time-scales: t_s is the time-scale to slow-down the heavy ions due to the Coulomb coupling and t_d is the time-scale to increase the velocity of the metal ions due to gain of momentum by line transitions. As shown by Lucy & Solomon (1970), it is necessary to satisfy the condition $t_s < t_d$ to have an efficient process of Coulomb coupling, and then driving a steady outflow. In terms of basic stellar and wind parameters, this condition is satisfied if:

$$\frac{L_* v_\infty}{M} < 5.9 \times 10^{16}. \quad (1.21)$$

For more details, we refer the reader to the Section 8.1.2 of Lamers & Cassinelli (1999). As pointed out by these authors, despite being satisfied for O-type stars, this condition stated in Eq. 1.21 for the phenomenon of Coulomb coupling may not be satisfied in the case of late B and A dwarfs (see, e.g., Babel 1995, 1996). As we will discuss in Sect. 1.2.3, radiative line-driven winds are not expected on late B-type stars.

Despite being a ground-breaking work to explain the mechanism of mass-loss on massive hot stars, Lucy & Solomon (1970) could not provide an accurate quantitative prediction for the mass-loss rate. As commented above, these authors computed the radiative acceleration in the wind due to a few resonance lines. From our previous discussion, a large number of lines (both optically thin and thick) indeed are contributing to the net momentum transfer in the wind of these stars.

Castor et al. (1975) was the first to develop a formalism to take into account the acceleration contribution from a large ensemble of lines. This is the so-called CAK-theory for radiative line-driven winds and it has been updated and extended by a series of works (e.g., Abbott 1982b; Pauldrach et al. 1986; Shimada et al. 1994; Kudritzki 2002; Curé et al. 2011). For essentially the same stellar parameters, the CAK-theory predicts a mass-loss rate of about 10^2 times larger than the one predicted by the work of Lucy & Solomon (1970).

In the CAK-theory, the distribution function of lines N contributing to the radiative acceleration, is approximated by a power-law as follows:

$$\frac{dN}{d\kappa} \sim \left(\frac{\kappa}{\kappa_0} \right)^{\alpha-2}, \quad (1.22)$$

where κ is the line opacity and κ_0 is a normalization constant such as $\kappa_0 \frac{dN}{d\kappa} = 1$. Here, the constant α is given in the interval between 0 and 1. Physically, $\alpha = 0$ would mean purely a contribution from optically thin lines and $\alpha = 1$ from optically thick lines.

1.2. Radiative line-driven winds

In addition, based on the Sobolev approximation⁹, Castor et al. (1975) showed the following relation for the radiative force due to lines g_{line} :

$$g_{\text{line}} \sim \left(\frac{1}{\rho} \frac{dv}{dr} \right)^\alpha. \quad (1.23)$$

From Eq. 1.22 and 1.23, the CAK-theory proposes to express g_{line} as a function of radiative acceleration due to electron scattering:

$$g_{\text{line}} = g_e M(t), \quad (1.24)$$

where the variable $M(t)$ introduced in the formalism of Castor et al. (1975) is the so-called the force multiplier, and it gives the ratio between the line radiative force and the radiative force due to the continuum, reaching up to $\sim 10^4$ (e.g., see. Fig. 8.8 of Lamers & Cassinelli 1999). $M(t)$ is defined as follows:

$$M(t) = kt^{-\alpha} s^\delta \sim \left(\frac{1}{\rho} \frac{dv}{dr} \right)^\alpha, \quad (1.25)$$

where the term s , later introduced by Abbott (1982b) to taken into account ionization effects, is dependent on the electron density and the geometrical dilution factor, and thus being dependent on the distance from the star (see Eq. 8.86 of Lamers & Cassinelli 1999). The constants k , α , and δ are the so-called force multiplier parameters and the variable t is the optical depth parameter:

$$t \sim \rho \frac{dr}{dv}. \quad (1.26)$$

One may note that the definition of the optical depth parameter is related to the distance at the wind, where lower values means larger distances from the photosphere, i.e., $M(t)$ changes at each value of distance in the wind. Typical values of α lies between 0.45 and 0.65, depending on the stellar parameters, such as the effective temperature. Physically, this means that both optically thin ($\alpha = 0$) and thick lines ($\alpha = 1$) contribute to the wind acceleration. For a literature compilation of values for the force multiplier parameters, we refer the reader to Table 8.2 in Sect. 8.6.1 of Lamers & Cassinelli (1999).

Lastly, from the CAK-theory, we have the following scaling relations for the mass-loss rate (see, e.g., Puls et al. 2008):

9. Introduced by Sobolev (1960), this method simplifies the radiative transfer treatment in stellar winds. For a given value of frequency and direction, the Sobolev approximation treats the photon-particle interaction as happening at a certain value of optical depth in the wind (Sobolev optical depth point). Likewise, the Sobolev approximation works in terms of an extended region in the wind to happen the photon-particle interaction (defined by the Sobolev length). Further details about the Sobolev approximation can be found in Sect. 8.4 of Lamers & Cassinelli (1999)

1.2. Radiative line-driven winds

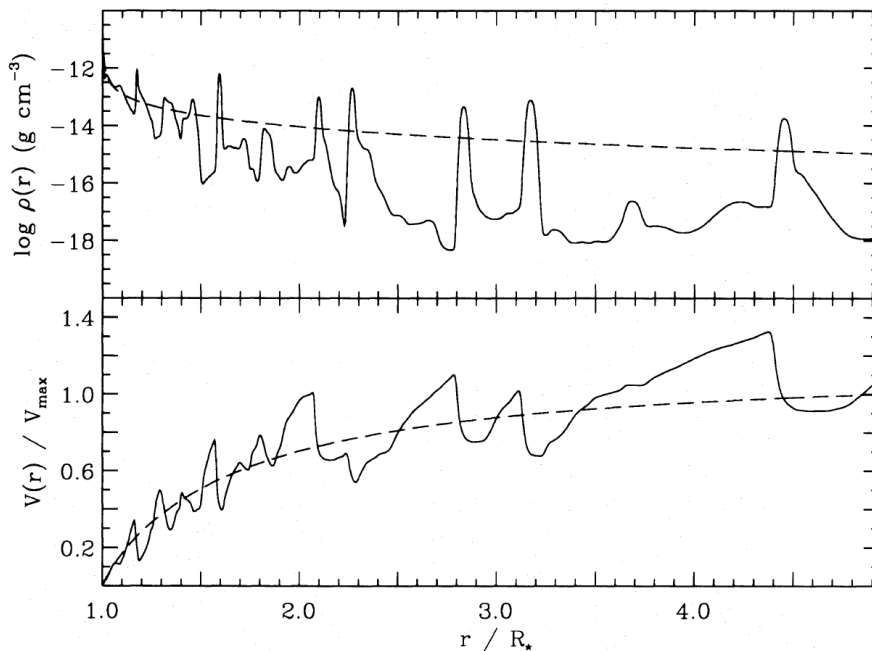


Figure 1.11 – Comparison between a initial smooth wind structure (dashed-line, modified CAK-theory) and one predicted from time-dependent hydrodynamical simulation from Puls et al. (1993) after 60000 s (solid line). See text for discussion. Reproduced from Puls et al. (1993).

$$\dot{M} \sim (kL_*)^{1/\alpha'} (M(1 - \Gamma_e))^{1-1/\alpha'}, \quad (1.27)$$

where $\alpha' = \alpha - \delta$ and Γ_e is the Eddington factor (Eq. 1.10).

The terminal velocity is simply given by Eq. 1.5 with $\beta = 0.5$ in the standard CAK-theory. As discussed in Sect. 1.2.1, more recent theoretical works, such as Curé & Rial (2004) that investigate the effects of rotation on the solution for the wind acceleration, are able to derive quite larger values of β , in this case being compatible to the spectroscopic results found for OB-supergiants.

Finally, we point out that massive stars does not have smooth stationary winds, as simplified in the CAK-theory described above. It is well-established that massive stars, such as O-type, Wolf-Rayet, and LBV stars, have inhomogeneous and variable winds, that is, their wind density structures show local fluctuations, deviating from a smooth distribution, due to the agglomeration of matter, forming clumps of matter (see, e.g., Eversberg et al. 1998; Bouret et al. 2005; Markova et al. 2005; Lépine & Moffat 2008).

For instance, the amount of X-ray emission and the appearance of discrete absorption component in the P-Cygni profiles are understood as arising from wind inhomogeneity. In Fig. 1.11, we show the comparison between the velocity and density structures from an modified version of the CAK-theory (homogeneous winds) and the results found by Puls et al. (1993) for non-homogeneous winds (time-dependent hydrodynamical simulations). From the theoretical point-of-view, the formation of local agglomeration

1.2. Radiative line-driven winds

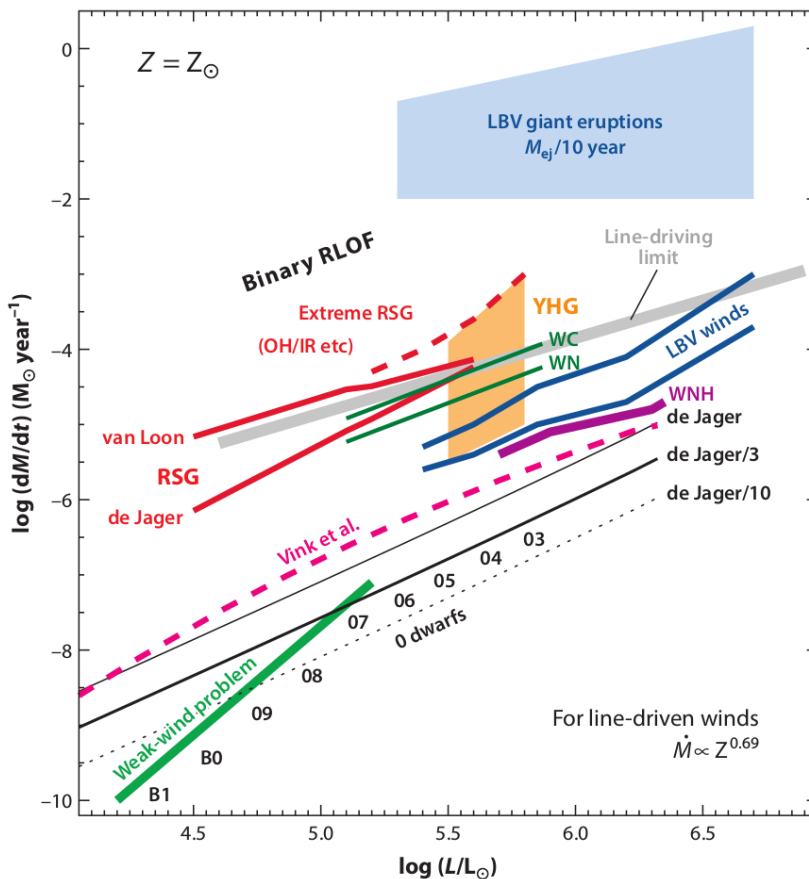


Figure 1.12 – Mass-loss rate as a function of stellar luminosity at different evolutionary stages of massive stars. This diagram compiles both theoretical and spectroscopic (measured) mass-loss rates for massive stars in the Galaxy. The gray line indicates the estimated maximum mass-loss rate of a line-driven wind given by $\sim L_*/c^2$ (Eq. 1.19). The green line indicates the measured mass-loss rates using atmosphere models of O-type stars for which are found weak winds. See text for discussion. Reproduced from Smith (2014).

of material in the wind is understood to arise from intrinsic instabilities in the line force (e.g., Owocki et al. 1988; Owocki 1992, and reference therein).

1.2.3 Radiative winds in the HR diagram

Fig. 1.12 provides an overview of the mass loss in massive stars as a function of luminosity. This diagram clarifies how the mass-loss rate of stellar winds changes with respect to their evolution. Here, both theoretical and measured mass-loss rates are given for OB-type stars, red/yellow supergiants, luminous blue variable, and Wolf-Rayet stars. As expected for radiative line-driven winds, we see that the mass-loss rate increases toward higher luminosity. Late O dwarfs (O9V) show $\dot{M} \sim 10^{-10}$ - $10^{-9} M_\odot \text{ yr}^{-1}$, while the wind is drastically stronger in Wolf-Rayet and luminous blue variable stars with \dot{M} up to 10^{-5} - $10^{-3} M_\odot \text{ yr}^{-1}$, reaching the mass loss limit for line-drive winds (gray line).

In addition, the largest rate of mass transfer that are expected in Roche-lobe overflow

1.2. Radiative line-driven winds

in binary systems is shown too. It is also indicated the quantity of mass that is ejected by episodic eruption in luminous blue variable stars. As previously commented, due to lower values of effective temperature, winds from cool evolved massive stars are driven differently to the ones in massive hot stars (radiative line-driven winds). Nevertheless, note that the mass-loss rate also scales with the stellar luminosity since these cool evolved massive stars have radiative-dust driven winds (empirical prescriptions from de Jager et al. 1988; van Loon et al. 2005). Extreme RSGs are the most luminous objects among RSGs, having the stronger winds (comparable to the ones found in LBVs). The stellar wind is so intense in extreme RSGs that the central star is obscured in the visible region, resulting in strong maser emission from OH, silicates, and H₂O (OH/IR star), and infrared excess due to dust grains (e.g., Smith et al. 2001; Decin et al. 2006).

For OB-type dwarf stars, both predicted and measured (derived from spectroscopic analysis) mass-loss rates are given in Fig. 1.12. The theoretical prediction for the mass-loss rate from Vink et al. (2000, 2001) is shown in pink dashed color. For comparison, the empirical prescription from de Jager et al. (1988) is also indicated with different scales in order to account the effects due to wind clumping in the models used to measure the values shown in green line. Here, it is highlighted the expected region of the so-called weak wind problem.

The phenomenon of weak winds is characterized by measured mass-loss rates that are much lower, by up to two orders of magnitude, than the theoretical values from Vink et al. (2000). This astrophysical problem is one of the main topics of this thesis and will be discussed in details in Sect. 6.1, in the context of my work about giant O-type stars.

We see that just the earliest B-type stars are indicated in Fig. 1.12 (B0 and B1). This corresponds to the most massive B stars with initial masses between ~ 13 and $18 M_{\odot}$. In later B stars, much lower mass-loss rates are expected due to lower values of stellar luminosity. For a better visualisation, we show, in Fig. 1.13, the results from Abbott (1979) for the wind dynamics across the HR diagram. There are three region to be highlighted here:

- (i) The shaded region, which encompasses the most luminous and hotter stars, indicates the case of radiative-line driven winds that are self-initiated due to the instabilities in the stellar atmosphere. For these stars, hydrostatic atmospheres are not reliable physical solutions for the equation of motion. Note that these results from Abbott (1979) indicate that stars with initial masses higher than $\sim 10 M_{\odot}$ necessarily have stellar winds driven by lines.
- (ii) For stars lying between the shaded region and the “wind limit” line, both hydrostatic atmospheres and radiative winds are reliable solutions. In this case,

1.2. Radiative line-driven winds

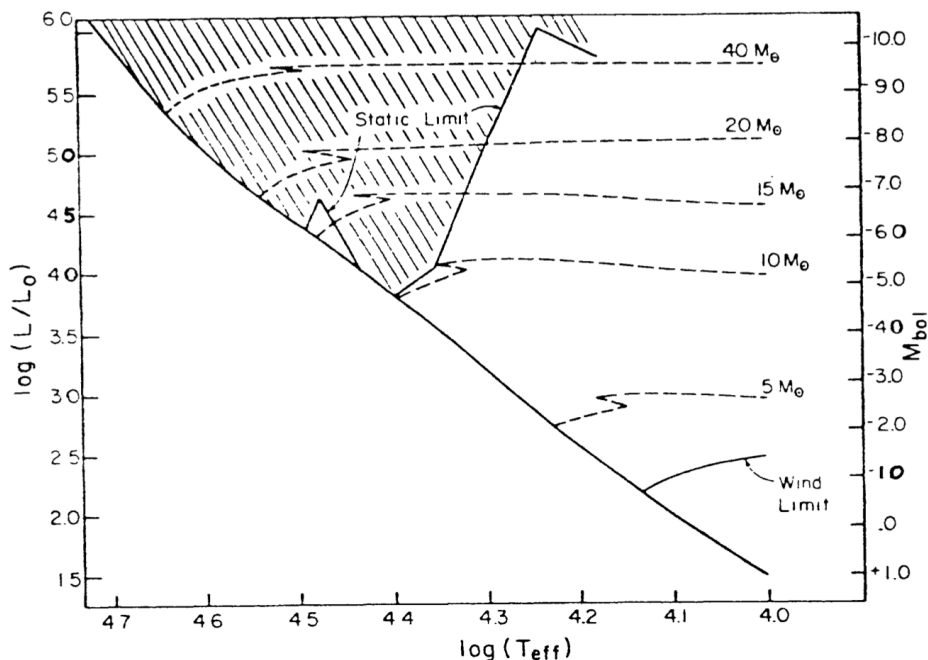


Figure 1.13 – Limits in the HR diagram for acceleration winds due to lines. Evolutionary tracks for stars with different initial masses are shown in dashed lines with the ZAMS region (solid line across the HR diagram). Stars with high enough luminosity and effective temperature are able to ignite and sustain winds driven by lines (dashed region). Note that stars with initial mass higher than $\sim 10 M_\odot$ (B2V) must develop radiative line-driven winds. Reproduced from Abbott (1979).

radiative line-driven winds can be sustained, once ignited, but these stars have too low luminosities to self-initiate line-driven winds.

- (iii) Lastly, it is impossible to self-initiate or sustain a radiative line-driven winds in stars below the “wind limit” line.

As indicated in Fig. 1.13, the lowest initial mass between the regimes of “static limit” and “wind limit” is somewhat lower than $5 M_\odot$, thus corresponding to B6-B9 dwarfs with $L_\star \sim 600\text{-}160 L_\odot$. We point out that these results from Abbott (1979) have been updated by a series of more recent studies. Using more sophisticated atmosphere models (e.g, non-LTE), Kr̄tička (2014) showed that B-type stars with T_{eff} lower than ~ 15000 K cannot self-initiate or sustain radiative line-driven winds. This is in fair agreement with the results from Abbott (1979) that indicate $T_{\text{eff}} \sim 17000$ K. As found by Kr̄tička (2014), considering solar-like abundances, the hotter B stars ($T_{\text{eff}} = 30000$ K) present homogeneous radiative wind with \dot{M} of $\sim 2.0 \times 10^{-9} M_\odot \text{ yr}^{-1}$, while this value is decreased to $\sim 7.0 \times 10^{-13} M_\odot \text{ yr}^{-1}$ for B stars with $T_{\text{eff}} = 16000$ K.

This means that physical mechanisms other than line-driving, such as rotation, are needed in order remove material from the atmospheres of the less massive B stars. In Fig. 1.14, we plot the distribution of the measured $v \sin i$ as a function of spectral type for main sequence stars ranging from M9 to O4. For sure, this quantity is dependent on

1.2. Radiative line-driven winds

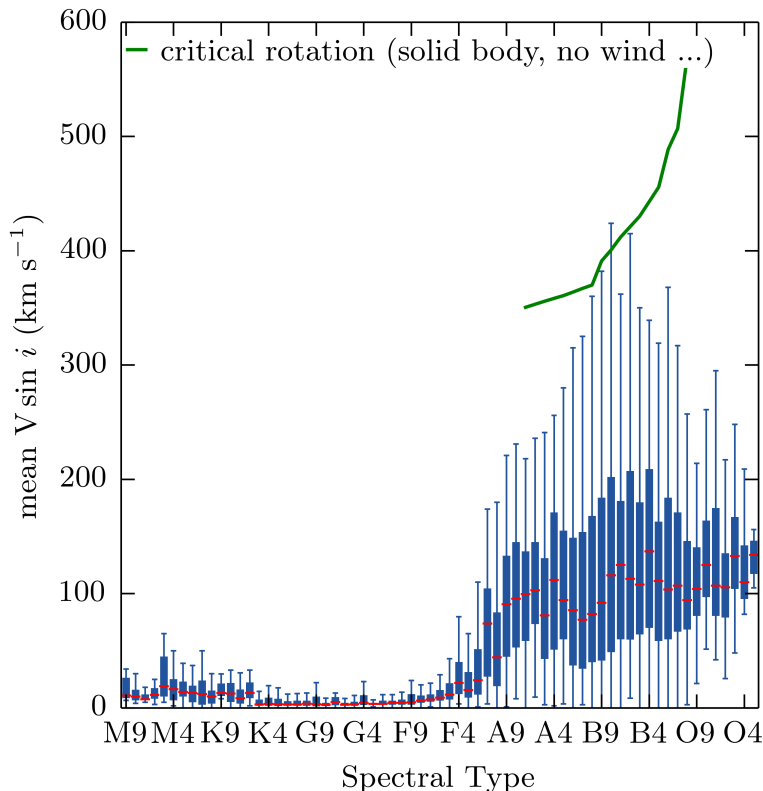


Figure 1.14 – Boxplot distribution of the projected stellar rotation velocity ($v \sin i$) as a function of spectral type. The mean value of $v \sin i$ is indicated in red and the interquartile range in blue boxes. The predicted value of critical rotation for the earlier types is shown in green line. Note that late-type stars (M-F types) rotates much more slower than the early-type stars (A-O types). Also note that B stars rotates closer to the critical value than O stars. Source: http://aa.oma.be/stellar_rotation

the stellar inclination angle (i). Nevertheless, since there is no correlation between i and the spectral type, we must consider this distribution as a real trend for the equatorial stellar velocity as a function of spectral type.

First, we clearly see that low-mass stars rotate much slower than the massive ones of type B and O. This happens due to a very efficient process of magnetic braking that removes a large quantity of angular momentum from the star (Schatzman 1962; Weber & Davis 1967). Low-mass stars have convective dynamo in their outer layers that create a dipolar magnetic field that is extended beyond the stellar surface. The stellar wind is coupled to the magnetic field lines, forcing the wind to co-rotate with the star, and thus decreasing the stellar rotation due to the conservation of angular momentum.

As one can see from Fig. 1.14, the mean value of $v \sin i$ starts to increase near the spectral type F4 up to values higher than $\sim 100 \text{ km s}^{-1}$. This can be understood since the presence of a convection layer is expected for low-mass stars up to this spectral type, but not for the more massive ones. Nevertheless, strong magnetic field have been detected for about 7-10% of OBA-type stars, with intensity ranging from $\sim 10^2$ to 10^4 G. Due to their rarity, long-term stability (up to decades), and simple dipolar topology,

1.3. Stellar rotation

it is understood that massive stars can have fossil magnetic field, that is, originated from the primordial molecular cloud that formed the star (see, e.g., Neiner et al. 2015; Shultz et al. 2018, and references therein). For further details about magnetic field in massive stars, see the series of paper from the Magnetic in Massive Stars (MiMeS) survey (Wade et al. 2016a) and the B fields in OB stars (BOB) survey (Morel et al. 2015).

Fig. 1.14 also evidences that the highest values of stellar rotation are found for late B stars. The value of the outliers in the boxplot distribution decreases from the B9 stars to the more massive of type O4. As discussed above, the stellar wind intensity increases with the spectral type for OB stars: the more massive O stars lose more efficiently angular momentum through stellar winds than the B stars, and then resulting in lower rotational velocities. Indeed, some late-type B stars (around B9-B7) rotates so fast that they are close to the critical value of rotation.

Such fast rotation modifies the physical properties of the stellar interiors and surfaces (e.g., Maeder & Meynet 2005; Brott et al. 2011). For massive stars, it can lead to a break of spherical symmetry of radiative winds (e.g., Müller & Vink 2014). In the most extreme cases, such as for classical Be stars (Sect. 1.4), it can lead to the formation of dense circumstellar disks at the equatorial plane (Sect. 1.5). In the following section, we introduce the effects of rotation on the stellar surface and their consequences in the case of fast rotation.

1.3 Stellar rotation

1.3.1 Effects on the stellar shape

Considering a non-rotating star under the Roche model (e.g., Domiciano de Souza et al. 2002; Ekström et al. 2008), the equipotential surface at a distance r from the center of the star is due to the gravitational potential energy:

$$\Phi(r) = -\frac{GM_r}{r}, \quad (1.28)$$

where G is the universal gravitational constant and M_r is the stellar mass inside the distance r .

Thus, the gravity acceleration g is given by the gradient of the potential energy:

$$\vec{g}(r) = -\vec{\nabla}\Phi(r) = \frac{GM_r}{r^2}\hat{r}. \quad (1.29)$$

This quantity Φ is not affected by rotation. Thus, taking into account the potential V due to the centrifugal force in a rotating star, the total equipotential surface Ψ is

1.3. Stellar rotation

simply modified as follows:

$$\Psi(r, \theta) = \Phi(r) + V(r, \theta). \quad (1.30)$$

Here, the centrifugal potential V introduced by rotation is:

$$V(r, \theta) = -\frac{\Omega^2 \varpi^2(r, \theta)}{2}, \quad (1.31)$$

where Ω is the angular velocity that is constant along the distance r and $\varpi = r \sin \theta$, being θ the co-latitudinal angle formed between the stellar rotational axis and position \vec{r} . Hence, the quantity ϖ gives the distance from the position \vec{r} to the rotational axis.

Eq. 1.30 is then expressed as follows:

$$\Psi(r, \theta) = -\frac{GM_r}{r} - \frac{\Omega^2 r^2 \sin^2 \theta}{2}. \quad (1.32)$$

Ψ defines the shape of the stellar surface for a rotating star with angular velocity Ω , and is constant at certain point defined by r and θ (equipotential surface). Since the centrifugal force is null over the polar axis ($\theta = 0$, so $V = 0$), it is useful to express Eq. 1.32 as function of polar radius R_p :

$$\Psi(r = R_p, \theta = 0) = \text{constant} = \frac{GM_\star}{R_p} = \frac{GM_\star}{R(\theta)} + \frac{\Omega^2 R(\theta)^2 \sin^2 \theta}{2}, \quad (1.33)$$

where M_\star is the stellar mass and $R(\theta)$ is the stellar radius expressed as a function of co-latitude. For simplicity, the dependence of R on θ is omitted in the following.

The acceleration at the stellar surface is then modified by the inclusion of rotation as follows:

$$\vec{g}_{\text{eff}}(R, \theta) = -\vec{\nabla} \Psi(R, \theta), \quad (1.34)$$

$$\vec{g}_{\text{eff}}(R, \theta) = \left(-\frac{GM_\star}{R^2} + \Omega^2 R \sin^2 \theta \right) \hat{r} + \left(\Omega^2 R \sin \theta \cos \theta \right) \hat{\theta}. \quad (1.35)$$

\vec{g}_{eff} is called the effective surface acceleration and its modulus $g_{\text{eff}} = |\vec{g}_{\text{eff}}|$ is then given by:

$$g_{\text{eff}}(R, \theta) = \sqrt{\left(-\frac{GM_\star}{R^2} + \Omega^2 R \sin^2 \theta \right)^2 + \left(\Omega^2 R \sin \theta \cos \theta \right)^2}. \quad (1.36)$$

In the case of a non-rotation star ($\Omega = 0$, thus $R(\theta) = R_p = R_\star$), Eq. 1.36 is simply reduced to the case of the acceleration due just to the gravitational field (Eq. 1.29, $r = R_\star$):

1.3. Stellar rotation

$$g = \frac{GM_{\star}}{R_{\star}^2}. \quad (1.37)$$

1.3.2 Stellar rotational rate and oblateness

First, we define the critical velocity, also called the break-up velocity. This happens when the modulus of gravitational force is equal to the modulus of centrifugal force at the stellar equator. In this case, any radial contribution (in the same direction of the centrifugal force) to the equation of motion, as due to the radiative force, implies the break of the hydrostatic equilibrium of the stellar atmosphere, and thus mass loss. This means that the effective surface acceleration is null at the equator if the star rotates at critical velocity. Thus, from Eq. 1.36, we have:

$$\Omega_{\text{crit}} = \sqrt{\frac{GM_{\star}}{R_{\text{eq,crit}}^3}}, \quad (1.38)$$

where $R_{\text{eq,crit}}$ is the stellar equatorial radius in the case of critical rotation $\Omega = \Omega_{\text{crit}}$.

Using this value of angular velocity in Eq. 1.33, we see that the equatorial radius is 3/2 times larger than the polar one if $\Omega = \Omega_{\text{crit}}$:

$$\frac{R_{\text{eq,crit}}}{R_{\text{p,crit}}} = \frac{3}{2}, \quad (1.39)$$

where $R_{\text{p,crit}}$ is the polar radius in critical rotation.

One useful quantity that is commonly used in the literature is the (angular) rotational rate w defined as follows:

$$\omega = \frac{\Omega}{\Omega_{\text{crit}}}, \quad (1.40)$$

in order to express how close a certain star with angular velocity Ω is to the break-up limit. Conversely, this also can be expressed in terms of linear rotational velocity v_{rot} and v_{crit} :

$$v_{\text{crit}} = \Omega_{\text{crit}} R_{\text{eq,crit}}, \quad (1.41)$$

where v_{crit} is the linear equatorial velocity in the case of critical rotation. Thus, the angular and linear rotational rates are related to each other as follows:

$$\frac{\Omega}{\Omega_{\text{crit}}} = \frac{v_{\text{rot}}}{v_{\text{crit}}} \frac{R_{\text{eq,crit}}}{R_{\text{eq}}}, \quad (1.42)$$

where R_{eq} is the actual equatorial radius and v_{rot} the actual linear equatorial rotational velocity.

1.3. Stellar rotation

Another useful quantity, which is related to the rotational rate, is the stellar oblateness f (e.g., Domiciano de Souza et al. 2002; Ekström et al. 2008) that is defined as the ratio between the equatorial and polar stellar radii:

$$f = \frac{R_{\text{eq}}}{R_{\text{p}}}. \quad (1.43)$$

Finally, another common quantity used in literature (e.g., Espinosa Lara & Rieutord 2011; Domiciano de Souza et al. 2018) to express the stellar oblateness is by the flattening parameter ϵ :

$$\epsilon = 1 - \frac{R_{\text{p}}}{R_{\text{eq}}}. \quad (1.44)$$

From Eq. 1.33, considering $\theta = \pi/2$ (stellar equator):

$$\frac{GM_{\star}}{R_{\text{p}}} = \frac{GM_{\star}}{R_{\text{eq}}} + \frac{\Omega^2 R_{\text{eq}}^2}{2}. \quad (1.45)$$

Thus, we find the following relation between the stellar oblateness f and the polar radius R_{p} :

$$R_{\text{p}} = \left(\frac{GM_{\star}}{\Omega} \right)^{1/3} \left(\frac{2(f-1)}{f^3} \right)^{1/3}. \quad (1.46)$$

From Eqs. 1.38 and 1.39, the angular critical velocity Ω_{crit} can also be expressed in terms of the polar radius:

$$\Omega_{\text{crit}} = \sqrt{\left(\frac{2}{3} \right)^3 \frac{GM_{\star}}{R_{\text{p,crit}}^3}}. \quad (1.47)$$

Therefore, from Eqs. 1.46 and 1.47, the angular rotational ratio and the stellar oblateness are related as follows:

$$\frac{\Omega}{\Omega_{\text{crit}}} = \sqrt{\left(\frac{3R_{\text{p,crit}}}{2R_{\text{p}}} \right)^3 \frac{2(f-1)}{f^3}}. \quad (1.48)$$

At the critical case, with $\Omega = \Omega_{\text{crit}}$ and $R_{\text{p}} = R_{\text{p,crit}}$, we found $f = 3/2$, in agreement with Eq. 1.39.

Note, from Eq. 1.48, that is necessary to know the value of the polar radius at the critical value in order to relate the rotational rate and the stellar oblateness. However, in good approximation, $R_{\text{p,crit}} \sim R_{\text{p}}$, being a better assumption as the stellar rotational velocity approaches the break-up case (e.g., see Fig. 2 of Ekström et al. 2008). Therefore, Eq. 1.48, can be expressed as the following approximation:

1.3. Stellar rotation

$$\frac{\Omega}{\Omega_{\text{crit}}} \sim \sqrt{\left(\frac{3}{2}\right)^3 \frac{2(f-1)}{f^3}}. \quad (1.49)$$

Alternatively, another definition, presented by Rivinius et al. (2013), for the rotational rate W is given with respect to the Keplerian circular orbital velocity v_{orb} at the stellar equator:

$$v_{\text{orb}} = \sqrt{\frac{GM_{\star}}{R_{\text{eq}}}}, \quad (1.50)$$

being W defined as follows:

$$W = \frac{v_{\text{rot}}}{v_{\text{orb}}}. \quad (1.51)$$

As pointed out by Rivinius et al. (2013): “it defines what velocity boost is required for a given star to launch material into the closest possible orbit, i.e., just above the photosphere at the equator”. Despite not being widely used in the literature, one advantage of this definition relies on its independence on the assumed stellar rotating model. Notice that the previous definition ω , given by Eqs. 1.38 and 1.40, is based on the Roche model.

1.3.3 The von Zeipel effect

Under the assumption of LTE¹⁰, and radiative equilibrium (i.e., all the energy is transported by radiation in the star), the flux $F(r)$ at the certain distance r of the stellar interior is given by:

$$F(r) = \frac{L_r}{4\pi r^2} = -C_{\text{rad}} \frac{dT}{dr}, \quad (1.52)$$

where L_r is the stellar luminosity at r , and the coefficient of radiative conductivity C_{rad} is defined as follows:

$$C_{\text{rad}} = \frac{4acT^3}{3\kappa\rho}, \quad (1.53)$$

where κ and ρ are the local opacity and mass volume density, $a = 4\sigma/c$, T is the local temperature following a black body distribution.

In the case of a star rotating with constant angular velocity Ω , the transport of radiative flux, given by the temperature gradient, is then modified as follows:

10. Good approximation for stellar interiors as the temperature gradient is typically small over a mean free path (see, e.g., Maeder 2009). Further details on the hypothesis of local thermodynamics equilibrium will be provided in Sect. 4.1.

1.3. Stellar rotation

$$\vec{F}(\Omega, \theta) = -C_{\text{rad}} \vec{\nabla} T(\Omega, \theta), \quad (1.54)$$

being analogous to Eq. 1.52, but as a function of Ω and the co-latitude.

The equipotentials and isobars (i.e., lines of constant pressure in the star) coincide in the case of star rotating like a solid body. This means that the temperature and density in the star are expressed as a function only of the equipotential, thus we can rewrite Eq. 1.54 using Eq. 1.34:

$$\vec{F} = -C_{\text{rad}} \frac{dT}{d\Psi} \vec{\nabla} \Psi = C_{\text{rad}} \frac{dT}{d\Psi} \vec{g}_{\text{eff}}, \quad \vec{F} = -C_{\text{rad}} \frac{dT}{dP} \vec{\nabla} P = -\rho C_{\text{rad}} \frac{dT}{dP} \vec{g}_{\text{eff}}, \quad (1.55)$$

where the term $\rho C_{\text{rad}} \frac{dT}{dP}$ is constant at a certain equipotential surface Ψ and the relation between the pressure gradient ($\vec{\nabla} P$) and the effective acceleration, $\vec{\nabla} P / \rho = -\vec{\nabla} \Psi = \vec{g}_{\text{eff}}$, states the hydrostatic equilibrium in the star.

Note that Eq. 1.55 is valid at a certain distance r . At the stellar surface, the so-called von Zeipel theorem (von Zeipel 1924) states the following relation between the radiative flux and the effective surface acceleration:

$$\vec{F}(\Omega, \theta) = -\frac{L_{\star}}{4\pi GM_{\star}} \vec{g}_{\text{eff}}(\Omega, \theta) \propto \vec{g}_{\text{eff}}(\Omega, \theta), \quad (1.56)$$

where $\frac{L_{\star}}{4\pi GM_{\star}}$ comes from the evaluation of the constant (for a certain distance r) $\rho C_{\text{rad}} \frac{dT}{dP}$ at the stellar surface (see, e.g., Sect. 4.2.2 of Maeder 2009).

Hence, the von Zeipel theorem states that the radiative flux is proportional to the effective surface acceleration. This effect is also called in the literature as gravity darkening, or von Zeipel effect.

One very important consequence from the von Zeipel theorem is the relation between the effective temperature and surface acceleration at a certain co-latitudinal angle. From the relation between the radiative flux and luminosity (Eq. 1.52), and the Stefan-Boltzmann theorem (Eq. 1.18), the von Zeipel theorem says that:

$$T_{\text{eff}}(\Omega, \theta) = \sqrt[4]{\frac{L_{\star}}{4\pi\sigma GM_{\star}}} \sqrt[4]{g_{\text{eff}}(\Omega, \theta)} \propto \sqrt[4]{g_{\text{eff}}(\Omega, \theta)}, \quad (1.57)$$

being the effective temperature dependent on the co-latitude.

We stress that this relation $T_{\text{eff}} \propto g_{\text{eff}}^{0.25}$, found by von Zeipel (1924), is valid under the hypothesis of a uniformly rotating star in radiative equilibrium. However, barotropicity and radiative equilibrium are incompatible hypotheses at the same time in order to describe a rotating star (see, Eddington 1925; Rieutord & Espinosa Lara 2009, and references therein). For instance, Lucy (1967) found $T_{\text{eff}} \propto g_{\text{eff}}^{0.08}$ for the gravity darkening

1.3. Stellar rotation

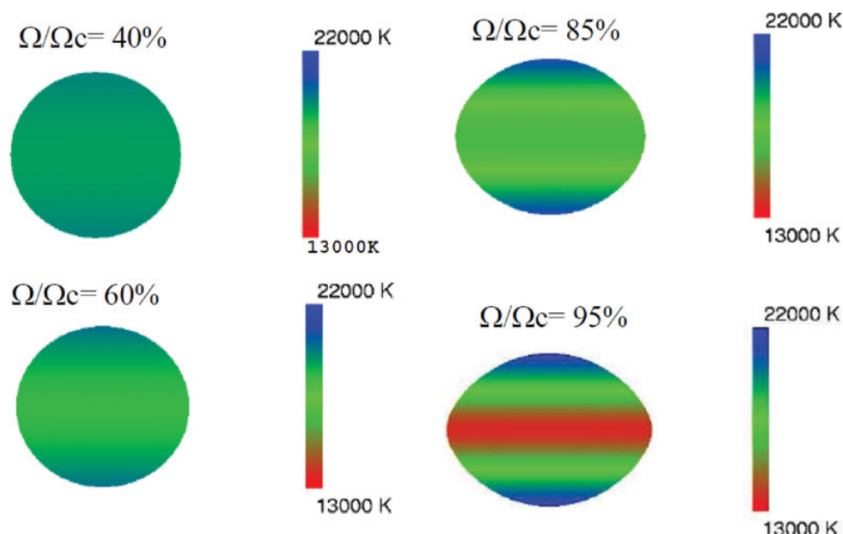


Figure 1.15 – Gravity darkening and geometrical oblateness effects due to rotation. Roche models for a solid body computed for different values of equatorial stellar velocity from $\Omega/\Omega_{\text{crit}} = 0.40$ up to $\Omega/\Omega_{\text{crit}} = 0.95$. The effective temperature is indicated by color bars. For the faster rotating star model, the effective temperature stratification reaches a difference of ~ 9000 K with respect to the stellar pole and equator. Reproduced from Martayan et al. (2011).

effect, when considering a convective envelope (i.e., dropping the assumption of radiative equilibrium). More generally, this effect follows the relation $T_{\text{eff}} \propto g_{\text{eff}}^{\beta}$, where the exponent β is lower than 0.25 (e.g., van Belle et al. 2006; Monnier et al. 2007; Hadjara et al. 2018; Domiciano de Souza et al. 2018). This means that the von Zeipel theorem, as originally stated, is likely to overestimate the difference of temperature between the pole and the equator. A more recent version of the gravity darkening effect is given by Espinosa Lara & Rieutord (2011)

1.3.4 Fast rotation

From Eq. 1.36, we note that the effective acceleration is stratified with respect to the co-latitudinal angle θ . At the stellar surface, the maximum value of effective acceleration is reached at the pole, while it decreases toward higher values of co-latitudinal angle down to the equator due to rotation. From the von Zeipel theorem, the effective temperature is then larger at the pole than at the equator, considering a rotating star model (Eq. 1.57). Also note that this effect increases with Ω (up to Ω_{crit}).

For example, in Fig. 1.15, we show results calculated under the Roche approximation of a solid body for different values of rotational rate $\Omega/\Omega_{\text{crit}}$ ranging from 0.40 up to 0.95. First, the effect of geometrical oblateness is clear as Ω approaches its critical value. Moreover, we also clearly see how the von Zeipel effect increases toward higher values of $\Omega/\Omega_{\text{crit}}$. While a star with lower rotational velocity ($\Omega/\Omega_{\text{crit}} = 0.40$) shows a fairly homogeneous effective temperature, the effective temperature is highly stratified,

1.3. Stellar rotation

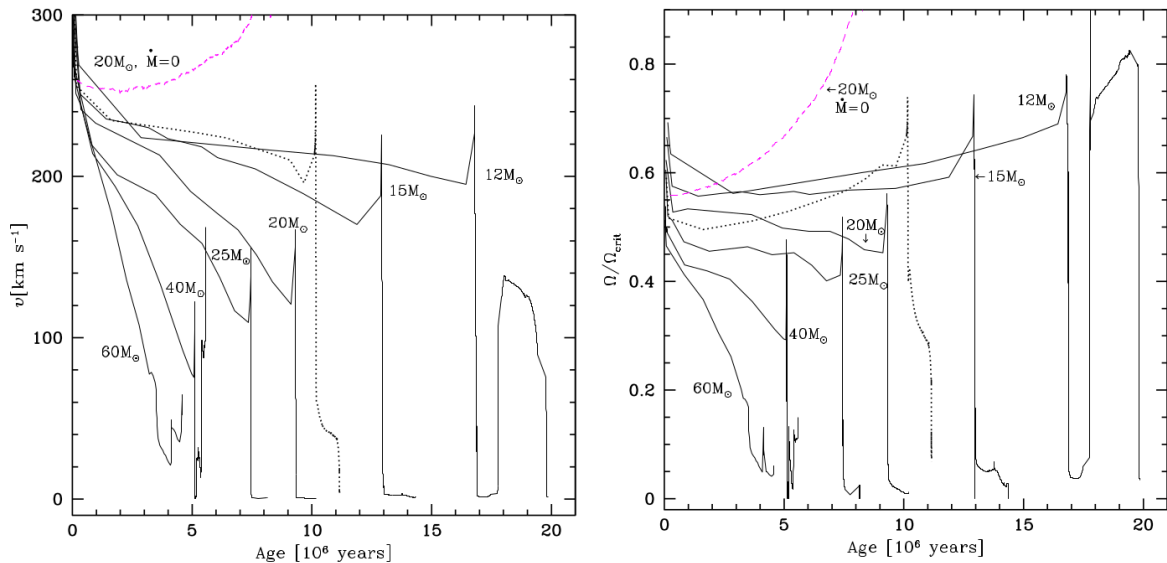


Figure 1.16 – Temporal evolution of the linear stellar equatorial velocity (left panel) from Geneva evolutionary models for massive stars with different initial masses. The corresponding angular rotational rate is shown in the right panel. Stellar winds are taken in account in the models shown in solid black line, but not in pink line ($20 M_{\odot}$, $\dot{M} = 0$). A star with initial mass of $12 M_{\odot}$ (B1V) ends the main sequence phase with a high rotational rate ($\Omega/\Omega_{\text{crit}} \sim 0.8$), while O-type stars will have quite lower values of rotational rate due to stronger stellar winds. Reproduced from Meynet & Maeder (2000).

with respect to θ , for stellar rotation close to the critical value. For the highest value of equatorial rotational velocity ($\Omega/\Omega_{\text{crit}} = 0.95$), the effective temperature reaches ~ 22000 K at the stellar pole and ~ 13000 K at the equator.

As discussed in Sect. 1.2.3, from an observational point-of-view, B-type stars are much more likely to be fast rotators than O-type stars. In addition, Fig. 1.16 shows the variation of the linear equatorial velocity, and the respective angular rotational rate, according to the stellar lifetime in Geneva evolutionary models. These results are presented for massive stars with different initial masses from $12 M_{\odot}$ (around the type B1V) up to $60 M_{\odot}$ (O3V).

First, we note how $\Omega/\Omega_{\text{crit}}$ drastically evolves for a $20 M_{\odot}$ model, when not taking into account the loss of angular momentum due to the stellar winds ($\dot{M} = 0$, pink dashed line). In this case, $\Omega/\Omega_{\text{crit}}$ increases up to the critical limit around the end of the main sequence phase (around the age of 8 Myr). We stress that such result is valid for a solid rotating model, meaning instantaneous transport of angular momentum from the center of star to the surface (constant Ω as a function of r , as discussed in Sect. 1.3.2). When taking diffusive processes in account in the stellar interior, the increase of the rotational velocity must be smaller in this case. On the other hand, considering the same initial mass of $20 M_{\odot}$, but taking into account the removal of angular momentum by winds, $\Omega/\Omega_{\text{crit}}$ gradually decreases up to the end of the main sequence phase. This effect is stronger as the initial mass is larger due to higher values of mass-loss rate, even during the main sequence phase.

1.3. Stellar rotation

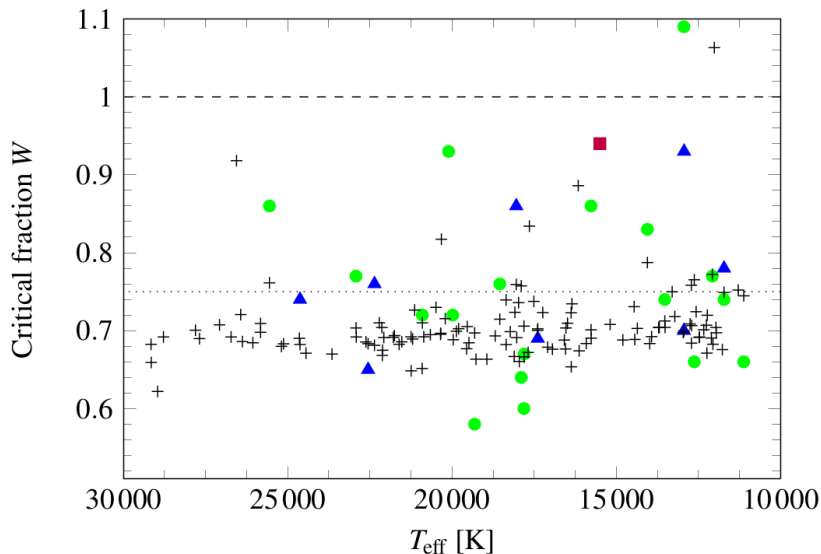


Figure 1.17 – Rotational rate W of Be-type stars as a function of effective temperature from different studies in the literature. Black crosses: Frémat et al. (2005). Green points: Rivinius et al. (2006). Blue triangles: Meilland et al. (2012). Red square (Achernar, B6V): Domiciano de Souza et al. (2012). The mean value of W is shown in dotted line and the critical case is indicated in dashed line. Despite the lack of clear correlation between W and the effective temperature, late-type Be stars tend to have higher values of rotational rate than the earlier Be stars. Reproduced from Rivinius et al. (2013)

For the lowest mass star with $M_{\text{ZAMS}} = 12 M_{\odot}$, we see that the rotational rate increases during the main sequence evolution up to about $\Omega/\Omega_{\text{crit}} = 0.8$. This happens due to the very low mass-loss rates by stellar winds in comparison with the other models for more massive stars shown here. Moreover, one can see the high decrease of $\Omega/\Omega_{\text{crit}}$ after the H-burning phase due to the growth of the stellar radius. Further details on these models can be found in Meynet & Maeder (2000).

The discussion above clarifies how the stellar rotation is important to remove angular momentum, in particular for B stars. Interesting, a $12 M_{\odot}$ model, having a weak stellar wind (low \dot{M}), are more likely to reach the break-up limit and then to lead to a large amount of mass loss toward the end of the main sequence due to fast rotation.

Among the early-type stars, Be stars are well-known to present the highest rotational velocities (e.g., see Slettebak 1966, 1970, and references therein), and then enhanced gravity darkening and geometrical oblateness effects. This means that the stellar rotation is important to break the hydrostatic equilibrium in the atmosphere of Be stars. Indeed, Be stars also present larger (by up to ~ 10 times) values of mass-loss rates than “normal” B-type stars, that is, which have never shown the Be phenomenon (e.g., Prinja 1989).

In Fig. 1.17, we provide a compilation of literature results for the rotational rate (W , Eq. 1.51) of Be stars as a function of effective temperature. These results are obtained by different types of methodologies, based both on spectroscopic (Frémat et al. 2005; Rivinius et al. 2006) and interferometric analyses (Domiciano de Souza et al. 2012;

1.3. Stellar rotation

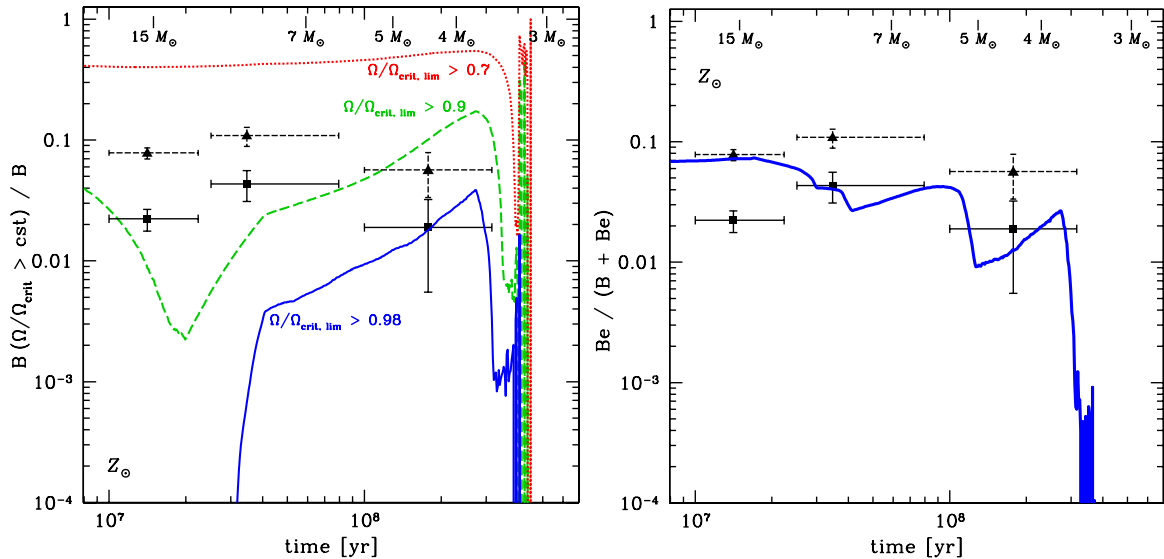


Figure 1.18 – Comparison between the fraction of stars rotating faster than a minimum value (theoretical fraction in color lines) and the observed fraction of Be stars in Galactic clusters (left panel). The age of the cluster is indicated in the bottom horizontal axis, corresponding to the lifetime of stars with different initial masses (top horizontal axis). In the right panel, the theoretical fraction, calculated assuming a dependence between $\Omega/\Omega_{\text{crit}}$ and the effective temperature, is also compared with data. See text for discussion. Reproduced from Granada et al. (2013).

Meilland et al. 2012). One sees that Be stars are fast rotators (mean value of $W \sim 0.75$), but they are not necessarily rotating close to the critical case ($W = 1$). Thus, in addition to the centrifugal force due to rotation, other mechanisms, as the radiative force and pulsations, are needed to explain the mass loss in Be stars that are rotating well below the break-up case.

Moreover, we also note the lack of clear correlation between the rotational rate and the effective temperature. However, still from Fig. 1.17, cooler Be stars seems to be more likely close to the critical value than the hotter objects. This could be understood since the stellar wind are stronger in the hotter Be stars than in the cooler ones, then removing a large amount of angular momentum during the evolution in the main sequence.

Indeed, the dependence of the rotational rate of Be stars and stellar parameters (such as the effective temperature) is still an open issue in the literature, affecting our understating about the Be phenomenon itself. Interferometric surveys of Be stars could not provide a clear correlation between the stellar rotation and the effective temperature (e.g., Meilland et al. 2012; Cochetti et al. 2019). Nonetheless, as stressed by these authors, more precise determinations of the rotational rate of Be stars are needed to better clarify this issue. On the other hand, from the statistical analysis of Cranmer (2005), late-type Be stars (with $T_{\text{eff}} \lesssim 21000$ K) are more likely to rotate closer to the critical value than the earlier objects.

1.3. Stellar rotation

These results from Cranmer (2005) are supported by other more recent studies as Huang et al. (2010) and Granada et al. (2013). In Fig. 1.18, we show the results from Granada et al. (2013) for the temporal evolution of the fraction of stars rotating faster than a certain threshold. Their prediction from Geneva evolutionary models are compared with the observed fraction of Be stars, that is, $\text{Be}/(\text{Be} + \text{B})$, in Galactic clusters. Despite the few observational data, one sees that their theoretical fraction of Be stars can fairly reproduce the observed trend for Be stars (right panel), when considering a dependence of the rotational rate and the effective temperature, assuming the results of Cranmer (2005).

In short, rotation is likely to be a major source of mass loss in late-type Be stars, when compared with the earlier ones. One could expect this fact since earlier Be stars have higher luminosities, and thus a larger contribution from the radiative force to break the hydrostatic equilibrium of the stellar atmosphere.

Lastly, Martayan et al. (2006) and Martayan et al. (2007b) found that the rotational rates of Be stars are higher in the Large Magellanic Cloud (LMC) and SMC, in comparison with the Galaxy: up to $\sim 75\text{-}100\%$ of the critical value in the SMC (lower metallicity than the Galaxy and LMC). From Fig. 1.17, one sees a lower limit of about 60%. Again, this effect could be expected since the mass-loss rate of the stellar wind is smaller as the stellar metallicity is reduced, and thus the process of removing angular momentum from star by winds is less efficient. This effect on stellar rotation explains the different fractions of Be stars that are observed in the Galaxy and in lower metallicity environments, as the LMC and SMC. From the few observational data shown in Fig. 1.18 for the fraction of Be stars in Galactic clusters, one sees that the highest value is about 10%. Indeed, larger studies found that the fraction of Be stars is about 17%, considering both late and early-type B stars (Zorec & Briot 1997). On the other hand, the fraction of Be stars is quite enhanced up to 40% in the SMC (e.g., Martayan et al. 2007a; Bodensteiner et al. 2020). In short, these observational facts emphasize the relation between fast rotation and the occurrence of the Be phenomenon.

In conclusion, as they are the faster rotators among all the non-degenerate stars, Be stars are unique objects to better understand the effects of near-critical rotation on the stellar structure and evolution, as well as on the mass-loss mechanism in early-type stars. In the following section, we discuss in details the so-called Be phenomenon.

1.4 The Be phenomenon

1.4.1 Characterization and physical origin

Classical Be stars are B-type stars in the main sequence phase (luminosity class from III-V) that show, or showed at some time, Balmer lines in emission (e.g., Rivinius et al. 2013). Other spectral lines of He I and low ionized metal such as Fe II are also found in emission (see Fig. 1.19). The Be phenomenon is found in the entire range of spectral type of B stars: M_{ZAMS} from $\sim 3 M_{\odot}$ for B9 stars ($T_{\text{eff}} \sim 12000$ K) up to $\sim 18 M_{\odot}$ for B0 stars with $T_{\text{eff}} \sim 30000$ K (Townsend et al. 2004).

As pointed out by Rivinius et al. (2013), this definition for classical Be stars is made in order to exclude other early-type stars with Balmer lines in emission, as the Oe and Ae-type stars, since it is still an open question in literature whether these objects present such spectral features due to the same physical origin of classical Be stars. This question will be discussed in details in Sect. 1.4.3. Furthermore, another group of peculiar B stars, the so-called B[e] stars, also show Balmer lines in emission. Here, the qualifier “[]” indicates that these stars show in the visible region permitted and forbidden emission lines due to metals, such as Fe II and O I, in addition to strong Balmer emission lines (e.g., Zickgraf et al. 1986). Stars showing the B[e] phenomenon form a highly inhomogeneous group of objects and such characteristics are found in supergiant stars, young stellar objects, symbiotic binaries, and compact planetary nebulae (see, e.g., Lamers et al. 1998).

In addition to this peculiar spectral feature of emission-lines, Be stars also have other important observational characteristics that distinguish them to the “normal” B-type stars. They present a large excess in the spectral energy distribution from the infrared up to the radio region, that is, that cannot be explained as being originated from a pure-photospheric contribution (e.g., Gehrz et al. 1974; Cote & Waters 1987; Waters et al. 1991). Moreover, the majority of Be stars present non-null intrinsic polarization in emission-lines and in the continuum region (see, e.g., Coyne 1976; Wood et al. 1997).

All these observational characteristics of Be stars are well explained as arising from a dust-free gaseous thin equatorial disk that is supported by rotation with a very small radial velocity of a few km s^{-1} (e.g., Rivinius et al. 1999; Stee 2011). In order to explain the double-peaked Balmer emission in Be stars, Struve (1931) was the first to propose that these stars are surrounded by an equatorial gaseous disk due to their fast rotation.

A basic scheme of the Struve’s picture is presented in Fig. 1.19. Here, we present the observed spectra of Be stars seen under different inclination angles: from close to the pole-on case (HD 5223) to close to the edge-on case (*o* Aquarii). We see how the morphology of the double-peaked emission-lines changes as a function of inclination angle. While HD 5223 shows a single-peaked $\text{H}\alpha$ profile, the Be-shell star *o* Aquarii

1.4. The Be phenomenon

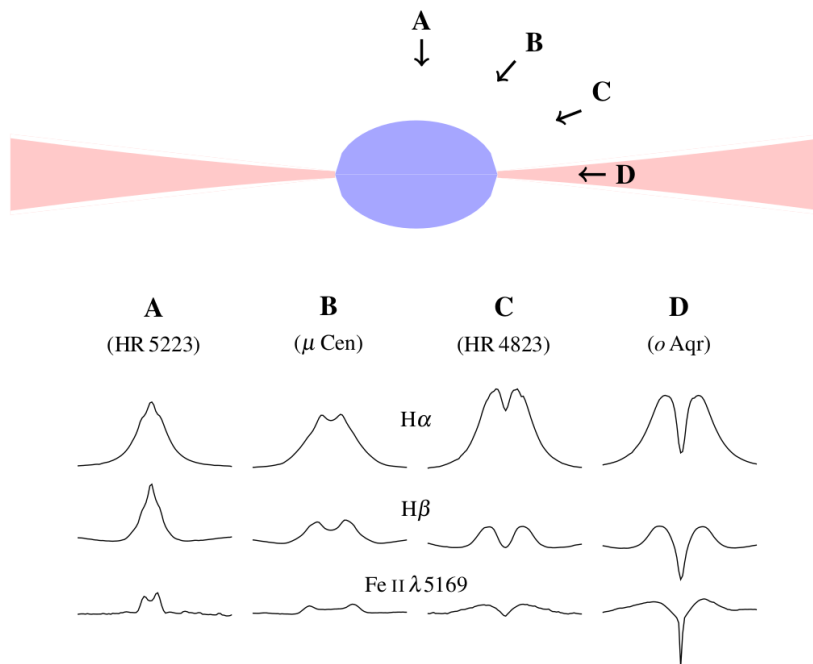


Figure 1.19 – Struve’s picture to explain the emission line profiles of Be stars. Observed spectral profiles are shown for Be stars seen under different values of inclination angle, from the pole-on case (HD 5223) up to the edge-on case (*o* Aquarii). Note how the H α profile of *o* Aquarii shows highly broadened peaks due to the circumstellar disk velocity field. See text for discussion. Reproduced from Rivinius et al. (2013).

shows a broadened double-peaked H α profile due to the disk rotation. For the case of *o* Aquarii, the very deep absorption in the core of the H α line arises from the large amount of column density in the observer’s line of sight through a large extension of disk.

As stressed in the first paragraph of this section, the part “or showed at some time” is important for the description of the Be stars. Such phenomenon is intrinsically transient as the circumstellar disks pass by different phases of dissipation and rebuilt due to mass injection from the central star. Once classified as Be star, a star will remain so in the future, even with the absence of emission-lines in its spectrum in observations a posteriori.

For example, we show, in Fig. 1.20, the temporal variation of the H α line profile of the Be-shell star *o* Andromedae (B6IIIpe) from Clark et al. (2003). These authors analysed H α spectroscopic data taken over a long period of about 17 years (from 1985 to 2002) in order to better constrain the disk variability for this star. To illustrate the time-scale variability of the H α line profile due to changes on the disk, they present observations taken over a period of 2 years (between 1986 and 1988).

Their mean spectra taken from 1985 is shown in dashed line as a reference for a H α line profile formed (almost) purely in the stellar atmosphere, that is, none or very weak contribution due to the circumstellar material. These authors verified that the

1.4. The Be phenomenon

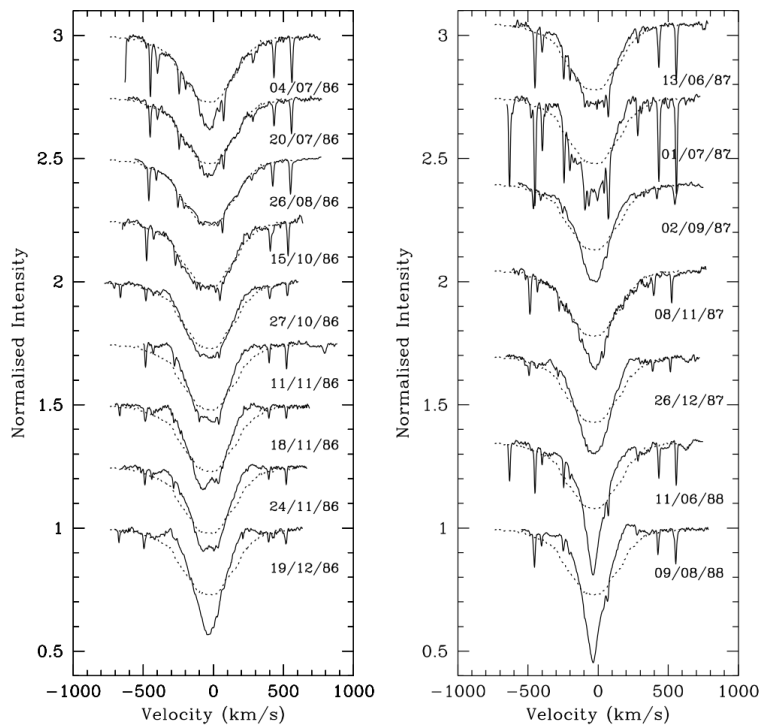


Figure 1.20 – Temporal variation from 1986 to 1988 of the observed $H\alpha$ profile (solid black lines) of *o* Andromedae (B6IIIpe). The mean $H\alpha$ profile from observations taken in 1985 is shown in dotted black line, being well reproduced by a pure photospheric model. Note the transition from the B-shell type to the Be-shell type between 1987 and 1988 due to a new accretion phase of the circumstellar disk. See text for discussion. Reproduced from Clark et al. (2003).

$H\alpha$ line profile is very stable during the year of 1985 and can be well-modeled as a pure photospheric line. It is clear from this modeling that *o* Andromedae was passing by a normal B-type phase during 1985. As pointed out by Clark et al. (2003), the transition from the B phase to the B-shell phase occurs during 1986, and finally, in 1988, the Be(-shell) phase is onset, characterized by a distinguishable emission observed in the $H\alpha$ line wings (in comparison with the pure photospheric model).

1.4.2 Variability in Be stars

In the case of *o* Andromedae, we see that the $H\alpha$ profile is significantly variable within a time-scale of about 2 years, due to mass injection from the central star to rebuild the circumstellar disk (Clark et al. 2003). More generally, Be stars are known to present variability in a wide range of time-scales, from hours up to several decades, based on different types of observables (photometry, polarimetry, spectroscopy). Such large range of time-scales is well understood as arising from different physical phenomena from both the stellar atmosphere and the circumstellar material. For a more comprehensive discussion, we refer the reader to the review of Rivinius et al. (2013).

The shortest variations in Be stars with a time-scale of hours to days concern H

1.4. The Be phenomenon

and He lines and photometric data are due to non-radial stellar pulsations (see, e.g., Rivinius et al. 2003). Such short-term variability is more likely to be verified in the earlier Be stars than in the later spectral types since the amplitude of pulsations is larger for earlier-type B stars than for the later ones (e.g., Percy et al. 2004; Baade et al. 2016).

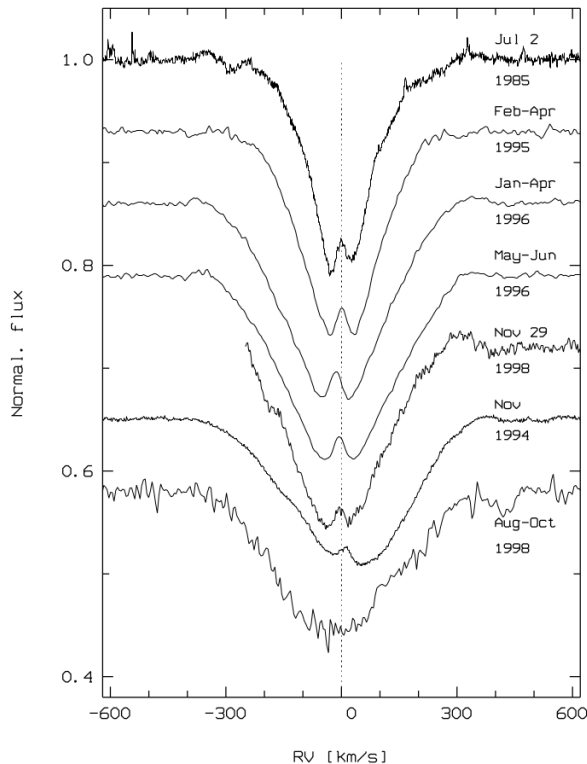


Figure 1.21 – Temporal variability of the CQE feature in the He I $\lambda 6678$ line of ϵ Capricorni (B3Ve). See text for discussion. Reproduced from Rivinius et al. (1999).

Be stars also often exhibit variation of the Violet-to-Red (V/R) peak ratio with time-scales ranging from months to over a decade (e.g., Rivinius et al. 2006). This quantity is given by the ratio between the relative flux (to the continuum) in the blueward and redward emission-peaks maxima (usually in $H\alpha$). The shorter V/R variations (time-scale of months) are understood as arising from binarity effects, while the longer ones (time-scale of years) are well explained by the precession of one-armed density waves in the circumstellar disk (Okazaki 1991, 1997).

The edge-on Be star ι Aquarii, discussed in Fig. 1.19, has never presented longer-term V/R variability (e.g., Rivinius et al. 2006). Rivinius et al. (2006) also verified central quasi-emission (CQE) in the Mg II $\lambda 4481$ line of this star. This spectral feature appears in certain line profiles as of He I, Fe II, and Mg II. Despite being shown as a “bump” in emission, these features are understood as a pure geometrical effect that can arise (under certain conditions, depending on the disk opacity and size in the continuum) in a (quasi-)Keplerian-rotating disk seen close to the edge-on case (Hanuschik 1995;

1.4. The Be phenomenon

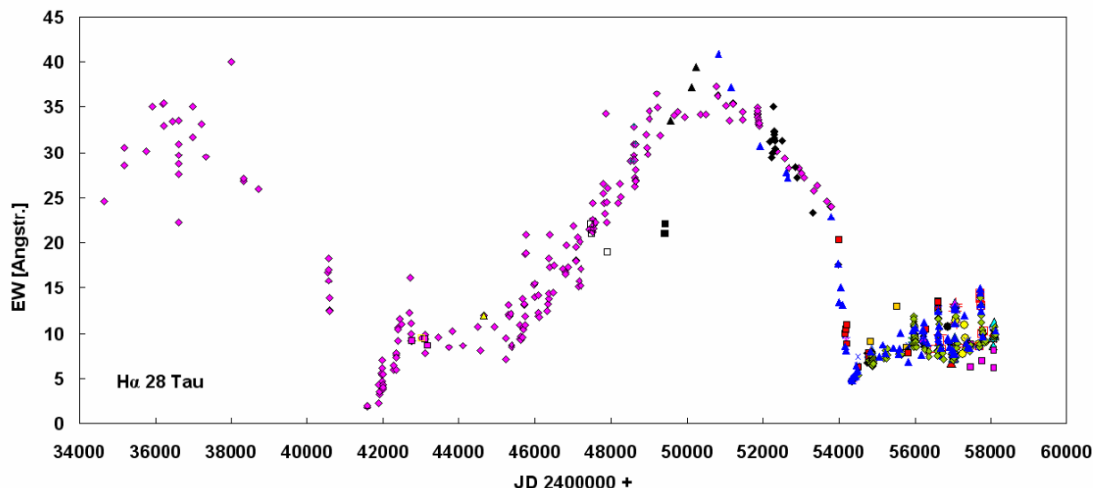


Figure 1.22 – Long-term variability of the H α equivalent width of 28 Tau (B8Vpe). Observations are taken from about 1953 up to 2018. See text for discussion. Reproduced from Pollmann (2018).

Rivinius et al. 1999). However, as pointed out by Rivinius et al. (2006), it is very unlikely, considering the same period of time, to observe CQEs and variability in the V/R ratio. This happens since the occurrence of this feature requires very low radial velocities in the disk.

Fig. 1.21 shows the variability of CQE in the He I λ 6678 line of the Be star ϵ Capricorni (B3Ve). The spectra are ordered to show the temporal variation of strengthen of the CQE feature: strongest CQE in the top (1985) and the absence of CQE in the bottom (1998). As suggested by Rivinius et al. (1999), such a temporal variation of the CQE feature must be related to changes on the disk structure: CQEs in the spectra of Be stars are more likely to happen during the accretion phase of the circumstellar disk.

Finally, another quantity of interest to address the temporal changes of Be disks is the equivalent width (EW) of H α and also other Balmer lines (e.g., Dachs et al. 1986; Mennickent 1991; Jones et al. 2011).

The line equivalent width, within the interval of wavelength λ_0 and λ_f , is calculated as follows:

$$EW = \int_{\lambda_0}^{\lambda_f} \left(1 - \frac{F_\lambda}{F_0} \right) d\lambda, \quad (1.58)$$

where F_0 is the continuum flux around the spectral line and F_λ is the line flux.

For emission-lines, EW , as defined above, is negative, but in this case sometimes the absolute value (positive) of EW is considered, as in Fig. 1.22 where we show the measured H α equivalent width of the binary Be star 28 Tau (Pleione, B8Vpe) covering about 65 years of observations, showing a high long-term variability in H α .

The understanding of long-term variability in H α of 28 Tau is still an open question

1.4. The Be phenomenon

in literature. As initially proposed by Hirata (2007), the change on the observed $H\alpha$ profile of 28 Tau would arise from a geometric effect due to the disk precession around the central star because of the presence of a secondary component. The observations of Pollmann (2018) support this interpretation since these authors found a high correlation between the variation of the central absorption component of $H\alpha$ and the minima of the V/R ratio.

However, based on the analysis of the full width at half maximum (FWHM) in the $H\alpha$ line, Nemravová et al. (2010) argued that such a huge variation in $H\alpha$ arises from structural changes on the disk, i.e., passing from a dissipation phase to a growing phase between about 1993 and 2012. Note, from Fig. 1.22, that the $H\alpha$ equivalent width decreases between 1993 (MJD = 49000) and 2006 (MJD = 54000), and then increases again between 2006 and 2012 (MJD = 56000). Nevertheless, it is conspicuous how the change on the disk density, by a binary companion or by the disk evolution (growth and dissipation phases) affects this observable in the $H\alpha$ line.

1.4.3 Oe and Ae stars: counterparts to the Be phenomenon?

As pointed out, in Sect. 1.4.1, other hot stars with spectral type beyond the B-type can present double-peaked Balmer emission lines. Despite being more rare than in B stars, this is also observed in fast rotators with adjacent type to B stars: late (around O8-9) O-type (e.g., Negueruela et al. 2004; Golden-Marx et al. 2016; Li et al. 2018) and early (around A0-1) A-type stars (e.g., Monin et al. 2003; Bohlender 2016). This could suggest that these stars are the high and low-mass analogs of the Be phenomenon, that is, they also have decretion circumstellar disks in rotation due to mass injection from the central star during the main sequence phase.

Golden-Marx et al. (2016) verified a much larger fraction of Oe/O stars in the Small Magellanic Cloud (SMC) of 0.26 ± 0.04 , in comparison with the one found in the Galaxy of 0.03 ± 0.01 . To date, they found the earliest Oe stars (type O6) known in the both galaxies. This is important to better understand the Be phenomenon itself as it concerns the role of stellar winds, which are weaker as the stellar metallicity is reduced, to allow the process of growth and dissipation of circumstellar disks even in such more massive stars (O-type). Based on the results from these authors, this means that in the SMC even O6 stars, which have stronger winds than the later O stars, could form a circumstellar disk due to the less intense winds in comparison with early O stars but in the Galaxy.

Furthermore, Ae/An stars are known to present very weak emission in the $H\alpha$ line wings. More recent, the results from Bohlender (2016) also support this scenario of counterpart to the Be phenomenon, but as the lower-mass analogs of the Be phenomenon.

1.5. Circumstellar disks of Be stars

About 15% of the stars of their large sample of A-type stars (~ 400 stars) show shell or emission features in the $H\alpha$ line. They verified that the incidence of such features decreases toward the earlier A-type stars and also according to lower values of $v \sin i$.

Despite these evidences discussed above, this scenario for Oe and Ae/An stars, as being the more and less massive extensions of classical Be stars, is still an open question in literature. For instance, the spectro-polarimetric study of peculiar O stars by Vink et al. (2009) detected depolarization “line effects” in $H\alpha$ for just one out of five Oe stars of their sample. However, such incidence in classical Be stars is quite larger up to $\sim 55\%$ as an evidence of their asymmetric circumstellar envelopes (Vink et al. 2002). As pointed out by Rivinius et al. (2013), some Ae/An stars should be composed of pre-main sequence objects, as Herbig stars. In this case, their disks are not created by material that is ejected from the stellar surface, but star-forming disks showing infrared excess due to dust (e.g., Jamialahmadi et al. 2015).

1.5 Circumstellar disks of Be stars

1.5.1 Formation and dynamics

Different dynamical model tried to explain the disk formation of Be stars, as shown schematically in Fig. 1.23.

First, based on the theory of radiative line-driven winds introduced by Lucy & Solomon (1970) and Castor et al. (1975) for massive hot stars, Bjorkman & Cassinelli (1993) presented the first quantitative physical model in order to explain the circumstellar disk formation in Be stars, the so-called wind-compressed disk (WCD) model.

To explain the formation of a circumstellar disk, the WCD model just needs a fast rotating star and a radiative line-driven wind. Hence, the wind streamlines are distorted due to fast rotation, forcing the outflow to be confined around the stellar equatorial plane and thus forming a disk. In this case, the mass-loss rate and the terminal velocity are scaled to the stellar rotational velocity Ω and the co-latitudinal angle θ as follows:

$$\dot{M}(\Omega, \theta) \propto (1 - \Omega^2 \sin^2 \theta)^{1-1/\alpha'}, \quad (1.59)$$

$$v_\infty(\Omega, \theta) \propto (1 - \Omega^2 \sin^2 \theta)^{1/2}, \quad (1.60)$$

where α' is defined from the force multiplier parameter from the CAK-theory as presented in Sect. 1.2.2. Thus, this results that \dot{M} is increased, while v_∞ is decreased, as θ tends to $\pi/2$ (stellar equator).

Despite being a benchmark work to predict quantitatively the disk dynamics in Be

1.5. Circumstellar disks of Be stars

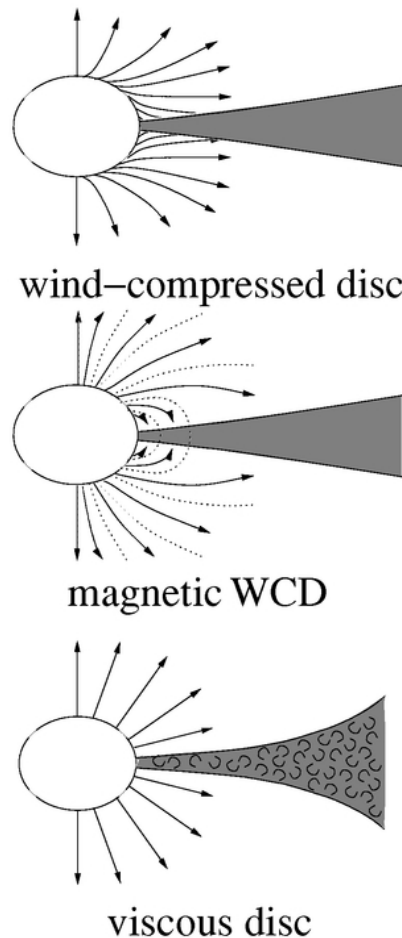


Figure 1.23 – Schemes of different dynamical models to form disks in Be stars. The stellar wind streamlines are represented by rows. See text for discussion. Reproduced from Porter & Rivinius (2003)

stars, the WCD model is invalid. As discussed in Section 1.3.4, the gravity darkening effect highly impacts the stellar properties in the case of fast rotators, as the case of Be stars. Owocki et al. (1996) and Owocki et al. (1998) showed that the inclusion of non-radial forces (arising from the finite size of star) and gravity darkening lead to a significant reduction of the equatorial mass-loss, and then preventing the formation of a high density disk as predicted by the WCD model.

Therefore, just from a theoretical point-of-view, the WCD is ruled out when taking into account more realistic physical assumptions in the hydrodynamical simulations of Be disks. Nevertheless, Cassinelli et al. (2002) modified the original WCD model, including dipolar stellar magnetic fields, being then called magnetic WCD model (Fig. 1.23). In this case, in addition to the ram pressure due to the stellar winds, the magnetic field lines also contribute to confine the circumstellar material around the equator. In order to affect the wind structure in Be stars, this model only need a relatively weak magnetic field of the order of $\sim 10^2$ G.

As discussed in Sect. 1.2.3, magnetic fields have already been detected in OBA-type

1.5. Circumstellar disks of Be stars

stars, but their detection in Be stars proved to be quite elusive. Some studies have reported measurements of weak fields ($\lesssim 150$ G) in Be stars (e.g., Yudin et al. 2011), while others point out that these measurements are spurious (Bagnulo et al. 2012). To date no firm evidence of magnetic fields was found for Be stars. Such an absence of magnetic field in Be stars poses a question if fast rotation would prevent the stability of a dipolar magnetic field in these stars (e.g., Wade et al. 2016b; Wade & Neiner 2018). In short, this lack of observational evidence of dipolar magnetic fields in Be stars is an important problem to support the magnetic WCD model.

Taken at face value, the WCD model implies that the circumstellar disk has an azimuthal velocity field $v_\phi(r)$:

$$v_\phi(r) = v_{\text{rot}}(r/R_\star)^{-1}, \quad (1.61)$$

where v_{rot} is the rotational velocity at the base of the disk. This arises from the assumption that the angular momentum is radially conserved through the disk.

On the other hand, if we consider that the disk dynamics is driven by gas turbulent viscosity, from the balancing of the gravitational and centrifugal force on an element of the disk, this would imply that the disk rotates in a Keplerian fashion as follows:

$$v_\phi(r) = v_{\text{rot}}(r/R_\star)^{-1/2}. \quad (1.62)$$

To date, all the different types of observables strongly support this last scenario of a Keplerian rotating disk in Be stars.

The first clear direct determination of a Keplerian disk around Be stars was found by Meilland et al. (2007b) for α Arae (B3Ve), from the modeling of VLTI/AMBER spectro-interferometric data in the K-band using the radiative transfer code SIMECA (Stee & de Araujo 1994; Stee et al. 2008). In addition to several spectroscopic and interferometric works (see, e.g., Stee & Meilland 2012; Rivinius et al. 2013, and references therein), more recent spectro-interferometric analyses, as the VLTI/AMBER surveys of Be stars from Meilland et al. (2012) and Cochetti et al. (2019), provided strong evidence for a Keplerian disk rotation in almost all their Be star samples.

This fact directly supports the last model presented in Fig. 1.23, the so-called viscous decretion disk (VDD) model (Lee et al. 1991; Okazaki 2001; Bjorkman & Carciofi 2005). In the VDD model, given that mass is removed from the stellar surface to the Keplerian orbit at the base of the disk, the material will then be transported outward due to viscous diffusion. This same model is also able to explain the hydrodynamics of the disk in young stellar objects (e.g., Pringle 1981; Balbus 2003), with the only difference that the flow is inward in that case (accretion disk instead of decretion disk in Be stars). Said differently, the disk dynamics of Be stars is viscously-driven and then described

1.5. Circumstellar disks of Be stars

by the Navier-Stokes equations (see, Eq. 3.1 to 3.4 of Carciofi 2011).

Clearly, one quantity of interest is the disk volume mass density $\rho(r, z, t)$, which is expressed as a function of position (in cylindrical coordinates) and time. From that, the disk surface mass density $\Sigma(r, t)$ is then defined:

$$\Sigma(r, t) \equiv \int_{-\infty}^{+\infty} \rho(r, z, t) dz. \quad (1.63)$$

From the Navier-Stokes equations, we can write a diffusion equation for the disk surface density (e.g., Pringle 1981):

$$\frac{\partial \Sigma(r, t)}{\partial t} = \frac{1}{r} \frac{\partial}{\partial r} \left[\frac{\frac{\partial}{\partial r} (r^2 \Sigma(r, t) \alpha c_s^2)}{\frac{\partial}{\partial r} (r^2 \Omega)} \right], \quad (1.64)$$

where c_s is the disk isothermal sound speed that is given by:

$$c_s = \sqrt{\frac{k_B T}{\mu m_H}}, \quad (1.65)$$

where k_B is the Boltzmann constant, μ is the mean molecular weight of the gas, m_H is the hydrogen mass, and T is isothermal electron temperature. Ω is the angular frequency of disk rotation. Lastly, α is the so-called Shakura-Sunyaev's viscous parameter. The kinematic viscosity ν of Be disks is typically parameterized in terms of α (Shakura & Sunyaev 1973):

$$\nu = \alpha c_s H, \quad (1.66)$$

where H is the isothermal disk scale height:

$$H(r) = H_0 \left(\frac{r}{R_{\text{eq}}} \right)^{3/2}, \quad (1.67)$$

and H_0 is the scale height at the disk base,

$$H_0 = c_s R_{\text{eq}} \left(\frac{GM_\star}{R_{\text{eq}}} \right)^{-1/2}. \quad (1.68)$$

In Eq. 1.66, α is defined between 0 and 1. This parameter can be understood as a scale to the evolution of the disk dynamics: larger values of α mean that the disk growth or dissipate in a shorter time-scale (see, e.g., Hauboiss et al. 2012), and then the variation of α will affect the observables predicted from the VDD model (e.g., see Fig. 5 of Carciofi 2011). Therefore, α is related to the so-called viscous diffusion timescale t_{diff} given by:

$$t_{\text{diff}} = \frac{r^2}{\nu} = \frac{r^2}{\alpha c_s H}, \quad (1.69)$$

1.5. Circumstellar disks of Be stars

expressing the typical time-scale for changes on the density structure due to viscosity. This quantity must be taken with caution as it does not represent the time-scale for the disk growth. As pointed out by Haubojs et al. (2012), considering their VDD model simulations with $\alpha = 1.0$, it is needed about 30 years to reach 95% of the limit density at $10 R_\star$, while $t_{\text{diff}} = 1.7$ years at this same distance in the disk. Then the value of t_{diff} (at a certain distance) is quite smaller than the one to the disk to reach (almost) the steady-state regime.

In the particular case of steady-state regime¹¹, we are able to solve analytically Eq. 1.64 for an isothermal disk as follows (Okazaki 2007):

$$\Sigma(r) = \frac{\dot{M} v_{\text{orb}} R_\star^{1/2}}{3\pi\alpha c_s^2 r^{3/2}} \left(\sqrt{\frac{R_0}{r}} - 1 \right), \quad (1.70)$$

where \dot{M} is the rate of mass injection to the disk and is assumed constant in this derivation for $\Sigma(r)$. R_0 is an integration constant that is related to the extension of the disk.

Due to the complexity of the radial density profile of Be disks, for example, being affected by presence of a binary companion (Panoglou et al. 2016), one common approach in the literature is to parameterize $\rho(r, z)$ using a power-law approximation, based on a vertically isothermal disk:

$$\rho(r, z) = \rho_0 \left(\frac{R_{\text{eq}}}{r} \right)^m \exp \left(\frac{-z^2}{2H(r)^2} \right), \quad (1.71)$$

where ρ_0 is the volume density at the disk base (at $r = R_{\text{eq}}$ and $z = 0$). Hence, apart from the stellar parameters¹², the density profile is fully described by just two parameters: ρ_0 and m (the density law exponent).

From Eq. 1.63, the volume and surface density profiles are related to each other by:

$$\rho(r, z) = \frac{\Sigma(r)}{H(r)\sqrt{2\pi}} \exp \left(\frac{-z^2}{2H(r)^2} \right). \quad (1.72)$$

Conversely, the surface density profile $\Sigma(r)$ can also be parameterized by a power-law approximation:

$$\Sigma(r) = \Sigma_0 \left(\frac{R_{\text{eq}}}{r} \right)^n, \quad (1.73)$$

where Σ_0 is the surface density at the disk base. Since the scale height $H(r) \propto r^{3/2}$,

11. Assuming $\frac{\partial \Sigma(r, t)}{\partial t} = 0$ and no-null mass injection from the central star to the disk.

12. The temperature T , which is used to calculate H_0 (Eq. 1.68) is usually adopted as a fraction of the effective temperature (e.g., Carciofi & Bjorkman 2006)

1.5. Circumstellar disks of Be stars

from Eq. 1.71 the volume (m) and surface (n) density law exponents are related to each other by¹³:

$$n = m - 1.5. \quad (1.74)$$

Finally, the volume and surface densities at the disk base are related as follows:

$$\rho_0 = \Sigma_0 \sqrt{\frac{GM_\star}{2\pi c_s^2 R_{\text{eq}}^3}}. \quad (1.75)$$

From this simple parameterization for the disk density, models with radial density exponent $m = 3.5$ mimic the analytical solution for the steady-state regime, when considering a vertical isothermal disk (Eq. 1.70). We emphasize that it is not reliable to characterize the whole disk extension by a single value of radial density law exponent (e.g., Haubois et al. 2012). Nevertheless, circumstellar disks passing by distinguishable phases of growth or dissipation must present quite different values of m . A growing disk will have a value of m in the interval of ~ 3.5 - 5.0 , while $m \sim 1.5$ - 3.5 indicates a dissipation phase (e.g., Vieira et al. 2017).

In short, once the material is ejected from the central star to the disk, the VDD model is able to explain the outflow dynamics in the disk in terms of turbulent viscosity. One can note that a clear weakness of this model is the inability to explain the mechanism of mass loss in these stars. As commented above, the VDD formulation requires the assumption of the rate of mass injection from the star to the disk. As already commented in Section 1.3.4, the own high rotational rate of Be stars is recognized as a source of force to pull out material from the star, possibly more important for the later Be stars.

Lastly, we point out here some possible departures from the VDD model. First, some interferometric studies found deviations from a disk Keplerian rotation (c.f., Eq. 1.62) in Be stars. From modeling spectro-interferometric VLTI/AMBER data (K-band) and the Pa β line profile using the code SIMECA, Meilland et al. (2007a) determined disk velocity law of $\beta = -0.32 \pm 0.1$ for κ Canis Majoris (B2IVe). On the other hand, analysing AMBER data of better quality for this star, the subsequent analysis from Meilland et al. (2012) provided a better agreement with the Keplerian picture from the VDD model, showing $\beta = -0.5 \pm 0.2$. Delaa et al. (2011) also found a value of β around -0.3 ($\beta = -0.35 \pm 0.05$) for the Be star ψ Persei (B3Ve) from the analysis of spectro-interferometric data in the H α line from the CHARA/VEGA instrument. From the analysis of AMBER data, Cochetti et al. (2019) found at least one clear departure of $\beta = -0.5$ for 228 Eri (B2Vne) with $\beta = -0.35 \pm 0.05$.

Furthermore, a series of works about Be stars that present fairly stable disks (in

13. We point out that some authors define these variables in the opposite way: m as the surface density law exponent and n the volume density law exponent (e.g., Haubois et al. 2012)

1.5. Circumstellar disks of Be stars

the time-scale of decades) found clear deviations from the canonical value of $m = 3.5$ for the steady-state regime. For example, Klement et al. (2015) found $m = 2.9$ for the late-type Be star β Canis Minoris (B8Ve) and Correia Mota (2019) derived $m = 2.44_{-0.16}^{+0.27}$ for α Ara (B2Vne). Thus, the radial density exponent is consistently equal or than 3.0 for these Be stars with stable disks. From analysing the temporal variation of the disk density, Vieira et al. (2017) identified a slightly extended range of $m = 3.0$ -3.5 for the steady-state regime. This indicates that the standard theory is either incorrect or incomplete, since it predicts that (vertically) isothermal steady-state disks (considering a single star) should have $m = 3.5$. One possibility to explain this fact could rely on both non-isothermal and binarity effects in the disk structure (see, e.g., Carciofi & Bjorkman 2008; Panoglou et al. 2016; Cyr et al. 2017).

1.5.2 Geometry and size

As discussed above, the disk density is fairly well described considering a simple structure given by Eq. 1.72 (power law + vertical Gaussian fall-off). For instance, using radiative transfer models, under the approximation of Eq. 1.72 in the VDD model, Touhami et al. (2011) were able to well explain the spectral energy distribution for a large sample of Be stars (130 objects). As one may expect, the disk density distribution is related to the disk physical extension. As pointed out by Rivinius et al. (2013), this quantity is rather difficult to be derived, unless in the case of a truncated disk (due to a binary companion), and it has no unambiguous determination for Be stars up to date.

Nevertheless, based on interferometric observations, a series of papers have been presented results for the size of the emitting region of Be disks at certain specific spectral regions (e.g., Quirrenbach et al. 1997; Gies et al. 2007; Meilland et al. 2012; Touhami et al. 2013; Dalla Vedova et al. 2017; Cochetti et al. 2019). One challenge imposed by Be stars disks comes from the inability to resolve them using single aperture telescopes. Currently, optical long-baseline interferometry is the only technique able to achieve sufficiently high spatial resolution in order to directly constrain the geometry of Be disks, which are typically extended up to a few milliarcseconds in the visible and infrared regions (see, e.g., Chesneau et al. 2012; Stee & Meilland 2012). This observational technique will be explained in details in Chapter 3.

Since the size of the emitting region of the disk is a proxy to its physical extension, this first quantity will be called the disk size, or disk extension, in the remaining of this thesis. The disk size can be understood in terms of the so-called pseudo-photosphere (see, e.g., Carciofi & Bjorkman 2006; Carciofi 2011). As suggested by the term employed to this region, the circumstellar disk will play like an extension to the stellar atmosphere,

1.5. Circumstellar disks of Be stars

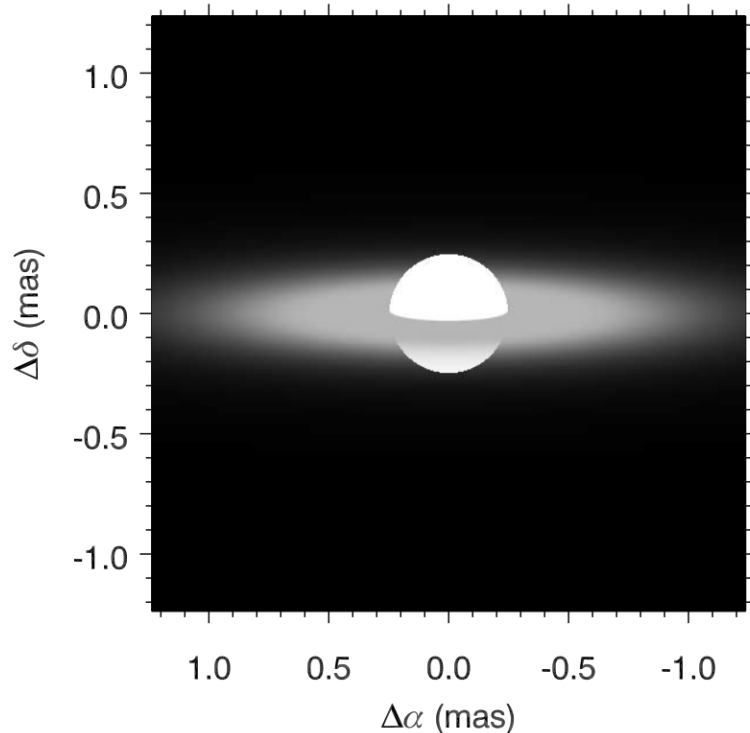


Figure 1.24 – Model intensity map (projected on the sky) in the K-band from Gies et al. (2007) to the analysis of interferometric data of the Be star γ Cassiopeiae (B0.5IV). In this model, these authors assumed $i = 80^\circ$ for the central star (represented by a uniform disk distribution). The disk density law is assumed by $\rho = 7.2 \times 10^{-11} \text{ g cm}^{-3}$ and $n = 2.7$. See text for discussion. Adapted from Gies et al. (2007).

as it becomes optically thick, contributing to the line formation region (and to the continuum). The pseudo-photosphere is then defined as the circumstellar disk region that is optically opaque to the radiation in the continuum or in line, being wavelength dependent.

Fig. 1.24 shows the intensity image in the K-band, projected on the sky, from simple radiative transfer models (based on the approach of Hummel & Vrancken 2000) of Gies et al. (2007) to interpret interferometric data. Here, these authors also employed the density law in the disk given by Eq. 1.72 and they assume a simple uniform disk intensity distribution for the central star. For this model, close to the edge-on case ($i = 80^\circ$), one can clearly see how the disk intensity falls toward larger distances, following approximately a Gaussian distribution, as expected since the mass density law in the disk is assumed according to Eq. 1.72 in the calculations by these authors.

In comparison with radiative transfer calculations, geometric models are a much simpler approach to estimate the disk extension based on fitting interferometric observables. In this case, analytical functions are used to represent the intensity contribution from the central star and from the circumstellar disk. Typically, the disk intensity distribution is modelled as following a Gaussian distribution (see, e.g. Touhami et al.

1.5. Circumstellar disks of Be stars

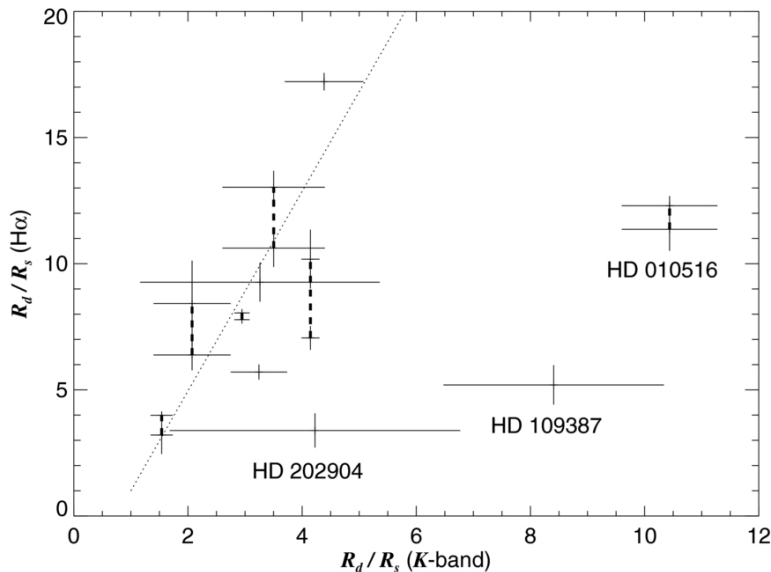


Figure 1.25 – Comparison of Be disks sizes derived in the H α line and in K-band from the CHARA Array interferometric survey of Touhami et al. (2013). The linear fit to the data is shown in dotted line. Note that the disk extension is usually larger in the H α line than in the K-band region. Reproduced from Touhami et al. (2013).

2013). Thus, one useful quantity to estimate the disk extension is the FWHM of a Gaussian distribution, expressing the region of the disk where most part ($\sim 80\%$) of emission is formed in a certain wavelength channel (see, e.g., Delaa et al. 2011; Meilland et al. 2012; Cochetti et al. 2019). A comprehensive compilation of literature results for Be disks sizes, from the H α line up to the radio region at 2 cm, is found in Tables 1 and 2 of Rivinius et al. (2013).

The understanding of Be disks extension at different wavelength regions is still an open issue in the literature. For example, Gies et al. (2007) derived the angular sizes of four Be stars (γ Cas, ϕ Per, ζ Tau, and κ Dra) in the K-band using simple geometric models to fit interferometric data measured with the CHARA/CLASSIC instrument. They showed that the disks of these stars were significantly larger (by up to ~ 1.5 - 2.0 times) in the H α line than in near-infrared region (K-band, enclosing the Br γ line). These authors explained that in terms of a larger opacity in H α than in the K-band region, resulting in a more extended disk at lower densities toward larger distances. Such a trend of larger disk sizes in H α than in the K-band is also verified by the interferometric Be survey of Touhami et al. (2013) as shown in Fig. 1.25. Here, Touhami et al. (2013) compare the disk size (R_d/R_s) in the H α line to their results found in the K-band. This quantity for the disk size is defined as the ratio between the angular size of the Gaussian ellipse (representing the disk) and the uniform disk (representing the star) in their best-fit geometric models. Apart from a few cases, one clearly sees that the most part of their Be star sample show a quite larger disk extension in H α than in K-band with the highest discrepancy up to ~ 4 times.

1.5. Circumstellar disks of Be stars

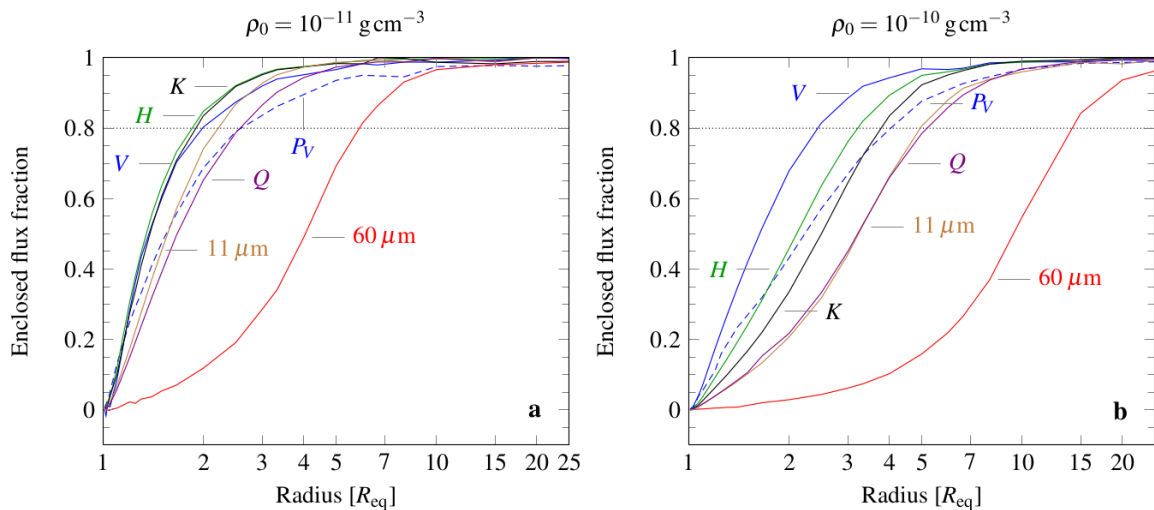


Figure 1.26 – Theoretical Be disk formation at different wavelength regions from calculations with code HDUST. Results from model with have different base disk densities of $\rho_0 = 10^{-11} \text{ g cm}^{-3}$ (left panel) and $\rho_0 = 10^{-10} \text{ g cm}^{-3}$ (right panel). For the HDUST model with higher ρ_0 , $\sim 50\%$ of the disk emitting region is formed within $\sim 10 R_{\text{eq}}$ in $60 \mu\text{m}$. See text for discussion. Reproduced from Rivinius et al. (2013).

On the other hand, some studies have found larger or similar Be disk extension in $\text{Br}\gamma$, when compared with $\text{H}\alpha$. Using the code SIMECA, Stee & Bittar (2001) theoretically investigated the formation region of different lines in Be disks based on typical stellar and disk parameters for both early and late-type Be stars. Interestingly, their simulations support that the disk size can be up 2 times larger in the $\text{Br}\gamma$ line than in the $\text{H}\alpha$ line. Moreover, Carciofi (2011) using the radiative transfer code HDUST found that Be disks can have a quite similar V- and K-bands formation regions.

Fig. 1.26 shows the formation region of the disk emission at different spectral bands using HDUST. Here, Rivinius et al. (2013) presented their results from HDUST models with different base disk densities of $\rho_0 = 10^{-11} \text{ g cm}^{-3}$ and $\rho_0 = 10^{-10} \text{ g cm}^{-3}$. One sees that the formation regions of the V and K-bands are quite similar in the lower density model, while the denser model shows a larger emitting region in the K-band. Moreover, both cases show a larger disk emitting region toward the far-infrared region ($60 \mu\text{m}$) in comparison with the visible and near-infrared regions. Considering the higher density model, about the half of the disk emission is formed at $10 R_{\text{eq}}$ in $60 \mu\text{m}$, while the same fraction of flux is reached at less than $2 R_{\text{eq}}$ in the V-band. Overall, these results can be interpreted in terms of the definition of the disk pseudo-photosphere. One may expect to have a larger pseudo-photosphere, at a certain wavelength, for the model with higher disk density. Indeed, we see that at all the considered wavelength regions, the disk formation is shifted toward larger distances due to a larger pseudo-photosphere of the disk in the model with higher density.

Lastly, more recently, Cochetti et al. (2019) determined the disk size for a large

sample of Be stars (26 objects) using a kinematic model to interpret their VLTI/AMBER data. This model is described in details in Sect. 5.3. However, when comparing their results to the ones found by previous studies but in $H\alpha$, these authors could not verify a clear correlation between the disk size in the $H\alpha$ and $Br\gamma$ lines. As pointed out by these authors, it is important to constrain the disk extension from the analysis of quasi-contemporaneous observations in both spectral regions since the circumstellar environments of Be stars can be highly variable in a short period of time.

1.6 Outline of this thesis

As discussed above, despite the success of the CAK-theory to explain different observational features of winds of massive hot stars, further efforts are still needed to better understand their fundamental parameters. As pointed out in Sect. 1.2.3, certain classes of O-type stars show large discrepancies between the predicted and measured (from spectroscopy) mass-loss rates (weak winds). In addition, it is still hard to conciliate the results for the mass-loss rates of massive hot stars obtained at different spectral regions (as UV, visible, and infrared).

Regarding Be stars, the VDD theory is also able to reproduce several types of observables for these stars, but the mechanisms underlying the mass loss process on Be stars are still not very well understood. Our discussion in Sect. 1.5.1 evidences the importance of a more detailed characterization on the properties of Be stars, as their rotational rate and disk physical parameters, to draw a better picture of the Be phenomenon.

In this thesis, I address these questions above, investigating both the physical properties of massive hot stars with radiative line-driven winds and rotating equatorial disks.

In Chaps. 2 and 3, I discuss the two main observational techniques used in this thesis: spectroscopy and spectro-interferometry. Chap. 4 discusses some basic concepts of radiative transfer modeling, focusing on the two radiative transfer codes used in this thesis to interpret the spectroscopic and interferometric datasets: CMFGEN and HDUST. Lastly, less complex modeling tools to interpret interferometric data are also discussed in Chap. 5.

The results found in this thesis are discussed in Chap. 6. In Sect. 6.1, I discuss my UV and visible spectroscopic study of giants O-type stars, in the context of the so-called weak wind phenomenon, using CMFGEN to determine their stellar and wind parameters. In Sect. 6.2, I discuss my collaboration using CMFGEN to interpret first $H\alpha$ -band intensity interferometric observations of the LBV star P Cygni, and then to estimate its distance. Lastly, in Sect. 6.3, I discuss my CHARA/VEGA and VLTI/VLTI

1.6. Outline of this thesis

spectro-interferometric study on the Be star *o* Aquarii. For this purpose, I used modeling tools of increasing complexity to constrain both the morphology, kinematics and physics of its disk and central star. My ongoing and near-future studies about winds and disks of massive hot stars are discussed in Chap. 7.

In the end, Chap. 8 gives an overview on the main findings of this thesis and some broader perspectives to study the environments of massive hot stars.

Chapter 2

Stellar spectroscopy

Contents

2.1	Stellar classification	58
2.2	Line formation in the wind: P-Cygni profiles	64
2.3	Multi-wavelength line diagnostics	68

2.1 Stellar classification

Since the discovery of spectral lines in the solar spectrum by Joseph von Fraunhofer in 1814¹, a series of schemes have been developed to classify the stellar spectra, mainly based on the observation of spectral lines in the visible region, to draw a better picture on the physics underlying the stellar atmospheres.

One of the first systematic studies on stellar classification was performed by Angelo Secchi in the middle of the 19th century. He classified the spectra of about 4000 stars, and then introducing the so-called Secchi classes that grouped the stars as early-type (class I, showing strong hydrogen lines) and late-type (class II, showing lines of metals and weak hydrogen lines). It is interesting to note that the terms early-type (for hotter stars) and late-type (for cooler stars) were originally coined due to a wrong understanding about stellar evolution (based on the Kelvin-Helmholtz mechanism²), meaning that the cooler stars would be necessarily more evolved than the hotter ones. Secchi included other classes, as III (modernly, M-type stars) and IV (carbon stars).

1. In fact, William Wollaston was the first, in 1802, to report absorption lines in the solar spectrum, but Fraunhofer performed a deeper analysis of the solar spectrum, identifying more than 500 different spectral absorption lines: afterward named as the Fraunhofer lines (e.g., see page 330 of Pannekoek 1961).

2. At the beginning of the 20th century, it was thought that the Kelvin-Helmholtz mechanism explained the stellar radiation. Eddington (1926) was the first to correctly propose that nuclear fusion is the source of the stellar radiation.

2.1. Stellar classification

Also interestingly, Secchi was the first to observe the spectrum (in the $H\beta$ line) of a Be star, γ Cassiopeiae, in 1866 (Secchi 1866). More generally, Secchi grouped these stars, which display Balmer emission lines, as being of class V (e.g., see pages 450-452 of Pannekoek 1961).

More fundamental systems were developed at Harvard College Observatory from 1885 until the beginning of the 20th century, namely, the Harvard classification system, that was led by the astronomers Williamina Fleming and Annie Jump Cannon. The letters employed in the Harvard system resulted in the current classification of O-B-A-F-G-K-M-types. Until her death in 1941, Cannon had classified up to about 395000 stellar spectra. For a more comprehensive overview on the history of stellar classification, we refer the reader to Chap. 40 of Pannekoek (1961) and Chap. 1 of Gray & Corbally (2009).

Today, the most used system is the so-called Yerkes or Morgan-Keenan-Kellman (MKK) system (Morgan et al. 1943). It was updated with inclusion of standard stars, in order to define prototypes of the spectral classes, by the Morgan Keenan (MK) system (Johnson & Morgan 1953). Basically, this is a two-dimensional scheme with the stars grouped by the canonical spectral types, O, B, A, F, G, K, and M, and numerical suffix from 0 to 9. The second dimension relies on luminosity class of the star: V (dwarfs), IV (sub-giants), III (giants), II (bright giants), I (supergiants³). The luminosity class was introduced in order to take into account stars with approximately the same effective temperature in the HR diagram, but with different values of luminosity. In addition, several spectral qualifiers have been used, such as “e” for emission line stars (including classical Be stars). We refer the reader to Table 3 of Sota et al. (2011) for an extensive list of the stellar qualifiers.

Despite having other meanings, one can see that the nomenclature of letters and roman numerals used in the Morgan-Keenan system is inherited from previous works on stellar classification. The MK system expresses different physical properties of the stars. The spectral types from O to M correspond to a decreasing sequence of effective temperature, as firstly understood by the benchmark work of Payne (1925). The Roman numerals correspond to a luminosity sequence, more luminous (and presumably more evolved) stars toward the class I. Fixing the luminosity class V (beginning of the H-burning phase), the dwarf stars also correspond to a sequence of higher stellar radius and mass toward the hotter objects (see Table 1.1 for the OB-type dwarfs).

The original MK system have been revised and extended by a series of works (e.g., Morgan & Keenan 1973; Morgan et al. 1978; Kirkpatrick 2005). With respect to O-type stars, Walborn (1971) introduced the O3 class to the MK system. Originally, the

3. As for the giant classes, the luminosity class I is sub-divided in Ia (more luminous) and Ib (less luminous) supergiants. It is also extended to class 0 for the hypergiant stars (Keenan 1971, 1973).

2.1. Stellar classification

MK system had the types O5 and O9, as the earliest and the latest ones for O stars, respectively. Later, the spectral types O3.5 and O2 were defined by Walborn et al. (2002), mainly based on the relative ratio strength between N III and N IV emission-lines. To date, the O2-type class is the earliest one in the MK system, corresponding to main sequence stars with the highest values of effective temperature, $T_{\text{eff}} \sim 55000$ K (Walborn et al. 2004; Mokiem et al. 2007a).

In addition to the canonical MK system, other spectral types have been taken into account, as the type W for classical Wolf-Rayet stars (e.g., Smith 1968), presented in Figs. 1.2 and 1.3. Due to their strong winds, Wolf-Rayet stars have hydrogen depleted atmospheres, and thus very weak, or absent, hydrogen lines in their visible spectrum, which is mainly composed of broad and strong emission-lines due to helium and metals as CNO (e.g., see Fig. 1 of Crowther 2007). WR stars are classified as: WN (strong N lines), WC (strong C lines and absence of N lines), and more rarely, WO (both strong C and O lines) (e.g., van der Hucht et al. 1981; Figer et al. 1997).

From our discussion in Sect. 1.1.1, these subtypes of WR stars correspond to distinguish evolutionary stages of massive stars. From Fig. 1.3, notice the predicted sequence $\text{WN} \rightarrow \text{WC} \rightarrow \text{WO}$ by Groh et al. (2014) for a non-rotating star model with initial mass of $60 M_{\odot}$. This comes from the on-going process of mass loss by winds that strip the material of the stellar atmosphere, and then revealing the chemical products created by different core-burning phases. The subtype WN/C is understood as an intermediate evolutionary phase between WN and WC stars (Conti & Massey 1989). Interestingly, due to their high effective temperature, low-mass stars at very late evolutionary stages, as CSPNs (see Sect. 1.2.2), present visible spectra similar to the one of massive stars. In particular, hydrogen-deficient CSPNs essentially show WR-type spectra and then are classified as [WR] stars⁴.

With respect to the other evolved stages of massive stars, RSGs show spectral type M or K (around F, G, A-types for yellow or warm supergiants) with luminosity class I or 0 (e.g., Neugent et al. 2010; Messineo et al. 2018). On the other hand, LBV stars cover a larger range of spectral types, from types O and B ($T_{\text{eff}} \sim 12000\text{-}30000$ K), during the quiescent phase, to the types G and F ($T_{\text{eff}} \sim 7000\text{K}$) during the eruptive phase (e.g., Humphreys & Davidson 1994, and reference therein). In short, it can be a hard task to distinguish them from other evolved stars that also occupy similar regions in the upper HR diagram, as yellow supergiants and also B[e] supergiants (e.g., Humphreys 2003; Humphreys et al. 2017).

The spectral type classification of O stars is mainly based on the relative strength line of both neutral and ionized helium. In particular, He I $\lambda 4471$ and He II $\lambda 4542$

4. In this case, brackets are used to indicate that they are low-mass stars, instead of classical WR stars (van der Hucht et al. 1981).

2.1. Stellar classification

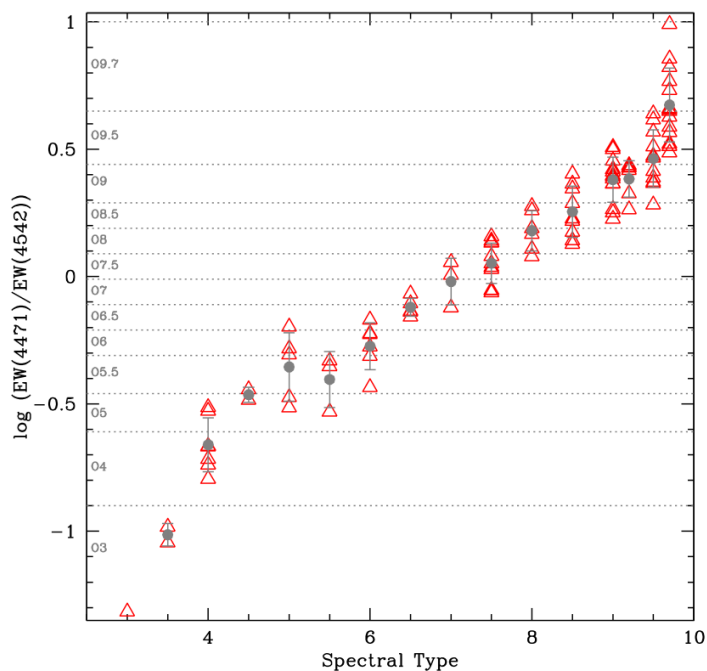


Figure 2.1 – Ratio between the equivalent width measured in He I $\lambda 4471$ and He II $\lambda 4542$ as a function of spectral type of O stars (105 objects). The ratio for each star is shown in red triangle and the mean values are shown in gray point within the error bars. The dashed gray lines indicate the limits of the ratio according to the spectral type. Overall, the ratio $EW(\text{He I } \lambda 4471)/EW(\text{He II } \lambda 4542)$ increases toward O-type stars with lower effective temperature, toward the type O9.7. Reproduced from Martins (2018).

are the most important ones as spectral type criteria, which is supplemented by other helium lines such as He I $\lambda 4144$, He II $\lambda 4200$, and He I $\lambda 4388$ (e.g., Plaskett & Pearce 1931; Abt et al. 1968; Conti & Alschuler 1971; Mathys 1989; Walborn & Fitzpatrick 1990; Sota et al. 2011).

Fig. 2.1 presents the ratio between the equivalent width (EW) calculated in He I $\lambda 4471$ and He II $\lambda 4542$, as a function of spectral type, from O9.7 to O3. Here, there is no distinction among the luminosity classes, covering from the class V to Ia. The ratio $EW(\text{He I } \lambda 4471)/EW(\text{He II } \lambda 4542)$ increases for O-type stars with lower effective temperatures. This can be understood since the He I $\lambda 4471$ intensity decreases, while the He II $\lambda 4542$ intensity increases, toward the hotter O stars, resulting from the ionization balance of He I and He II, as shown in Fig. 2.2 (dwarf O stars). From Fig. 2.2, one sees that the He I $\lambda 4144$, He I $\lambda 4388$, and He I $\lambda 4471$ lines vanish for the objects earlier than O4-3.5 due to the high degree of ionization in the atmosphere ($T_{\text{eff}} \gtrsim 43500$ K).

On the other hand, Fig. 2.2 also shows that the He II $\lambda 4686$ intensity tends to decrease as the effective temperature increases. Indeed, He II $\lambda 4686$ is not very useful as a spectral type criteria for O stars but can be used as a luminosity class criterion (e.g., Martins 2018). He II $\lambda 4686$ is quite sensitive to the wind parameters (as the mass-loss rate and clumping factor), and thus used as a diagnostic to determine, or investigate

2.1. Stellar classification

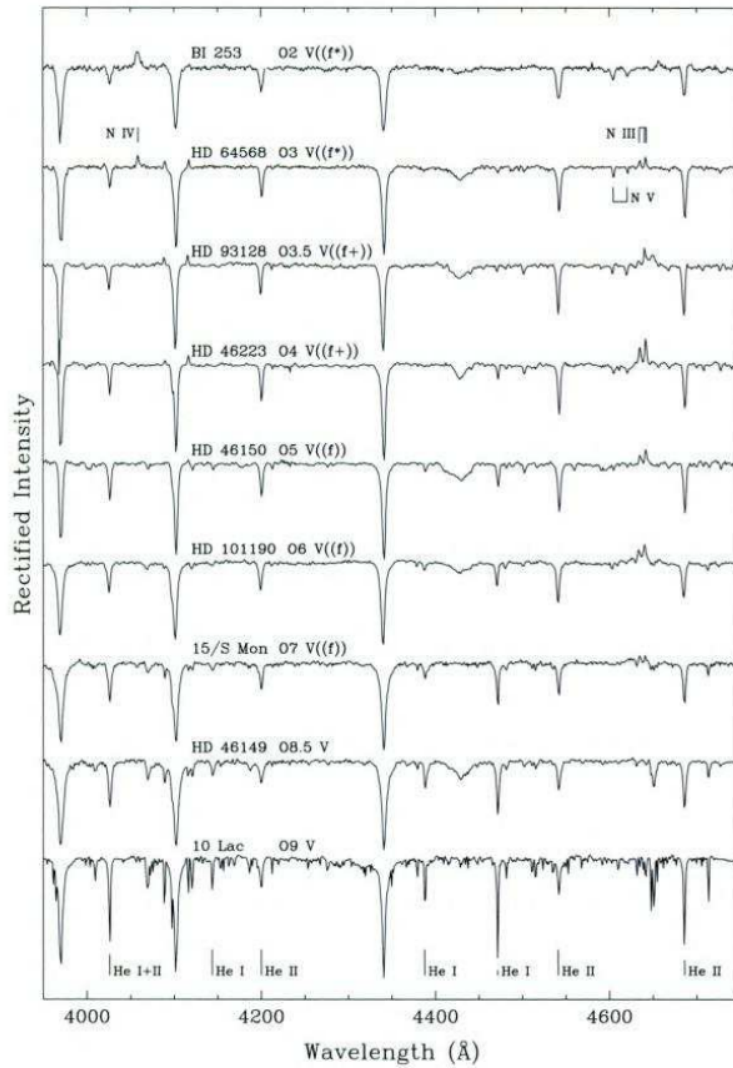


Figure 2.2 – Visible spectra ($\sim 4000\text{--}4700$ Å) of O dwarfs (class V) from O9V to O2V. Note how the He II $\lambda 4542$ line strengthens in absorption toward the earlier objects, while He I $\lambda 4471$ line strengthens in absorption toward the later objects. See text for discussion. Reproduced from Gray & Corbally (2009).

theoretically, the wind parameters of O stars (e.g., Martins 2011; Sundqvist et al. 2011; Tramper et al. 2014). This line goes from absorption, as shown in Fig. 2.2, to emission in the more luminous O stars as the early-type supergiants, which have stronger winds. For example, see Fig. A.6 of Bouret et al. (2015), showing the visible spectrum of HD 16691 (O4If⁵).

Originally, in the MKK and MK systems, the distinction between O- and B-type stars was set by the absence of lines due to ionized helium in the spectrum of B0 stars. In this case, the B spectral class was defined to encompass stars showing He I lines, but not He II lines, in the visible region (e.g., Morgan et al. 1943). Nevertheless, modern spectroscopic data revealed (weak) He II lines in the B-class around the B0-type (e.g.,

5. The spectral qualifier “f” means that N III $\lambda 4634\text{--}4640\text{--}4642$ and He II $\lambda 4686$ are in emission.

2.1. Stellar classification

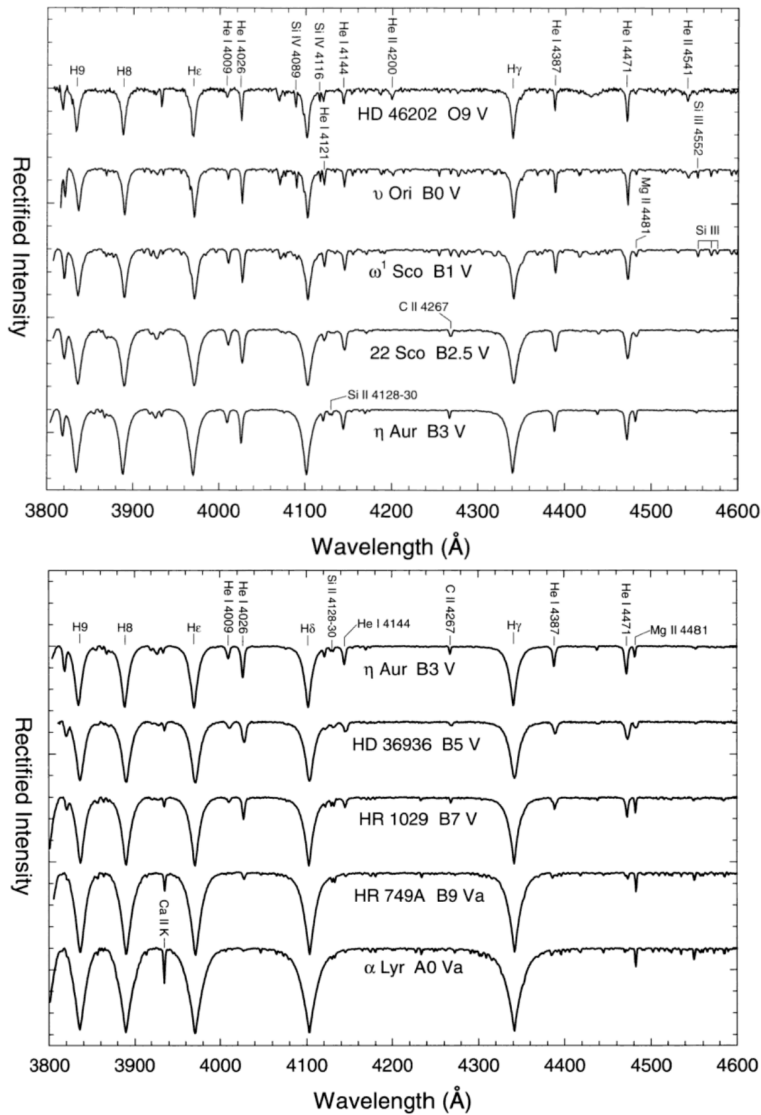


Figure 2.3 – Visible spectra ($\sim 3800\text{-}4600$ Å) from O9V to A0V stars, covering the entire range of B dwarf stars (B0V-B9V). Note that the He II $\lambda 4542$ line becomes weaker toward the later spectral type, vanishing in the spectrum of B1 stars. Also see how the Balmer lines become stronger from O stars toward the A0 stars. See text for discussion. Reproduced from Gray & Corbally (2009).

Walborn 2008).

The visible spectra of stars with spectral types from O9V to A0V are shown in Fig. 2.3. This covers practically the same wavelength region as in Fig. 2.2, but extending the spectral type toward objects later than O9V. One can clearly see He II $\lambda 4542$ in the spectrum of the shown B0V star (ν Orionis), but not for later-types. The intensity of neutral helium lines decreases from the type O to B, and the He I lines vanish around the type A0. Due to lower values of effective temperature, spectral features in the visible spectrum of metallic ions, mainly, Si, C, N, and O, are used as spectral type criteria for B stars. In particular, the relative ratio strengths between silicon lines at different ionization stages is important for that since they are quite sensitive to

2.2. Line formation in the wind: P-Cygni profiles

the variation of effective temperature, such as Si IV λ 4089, Si II λ 4124-4131, and Si III λ 4552-4567-4574 (e.g., Kilian et al. 1991b,a).

Besides the lines due to helium and metallic ions, the hydrogen Balmer lines also are rather important as a spectral type criteria. Considering the dwarf class, and a pure photospheric contribution, the Balmer lines strengthen from the O-type through the B-type, reaching a maximum around the type A0-A2, and then becoming weaker for later-types. In a qualitative way, the atmosphere of O stars are so hot that most part of hydrogen is either ionized or at high energy states. On the other hand, most part of hydrogen is in the ground energy state in M-type stars ($T_{\text{eff}} \sim 2000\text{-}4000$ K, Allard & Hauschildt 1995). The maximum fraction of hydrogen atoms populating the second energy level is reached for $T_{\text{eff}} \sim 10000\text{-}9000$ K, corresponding to A0-A2-type stars. For a quantitative discussion, in the framework of the LTE approximation, see, for example, Sect. 7.2 of Böhm-Vitense (1989).

For more details concerning the spectral classification of O stars in the visible, we refer the reader to a series of papers from the Galactic O-Star Catalog⁶ (GOSC Maíz Apellániz et al. 2013) and the Galactic O-star Spectroscopic Survey (GOSSS Maíz Apellániz et al. 2011). To date, these projects provide detailed classification for about 590 O stars (see, Sota et al. 2011, 2014; Maíz Apellániz et al. 2016, 2018). In addition to the visible region, the morphology of ultraviolet lines are also used as spectral classification of OB-type stars (see, e.g., Walborn et al. 1985; Rountree & Sonneborn 1991; Walborn et al. 1995). We refer the interested reader to Heck (1987) for a detailed discussion on ultraviolet spectral classification both for hot and cool stars.

2.2 Line formation in the wind: P-Cygni profiles

The spectral lines formed in the stellar wind can be found in pure-absorption, pure-emission, or with components in blueward absorption and redward emission. As discussed in Sect. 1.2.2, the latter is the so-called P Cygni line profile. These profiles are unequivocal spectral signatures of strong winds around hot massive stars. We point out that the same cannot be stated for pure-emission lines. They can be mainly formed in the stellar atmosphere, for example, as the N III $\lambda\lambda$ 4634, 4640, 4641 lines that are found in emission in Of stars (Mihalas & Hummer 1973).

Similarly, inverse P Cygni profiles, that is, redward absorption and blueward emission components, are unequivocal spectral signatures of inward flows toward the central star. Both P Cygni and inverse P Cygni line profiles are found in the spectrum of pre-main sequence objects, T-Tauri and Herbig Ae/Be stars, due to a complex interplay

6. Available at <https://gosc.cab.inta-csic.es/>

2.2. Line formation in the wind: P-Cygni profiles

between outward (winds) and inward (accretion disk) flows found in these objects (e.g., Alencar & Basri 2000; Deleuil et al. 2004; Cauley & Johns-Krull 2014).

P Cygni profiles were first observed in the spectrum of the LBV star P Cygni, showing a large number of them (up to about 140) in the visible and near-infrared regions (e.g., Struve 1935; Struve & Roach 1939; Beals 1953; Burbidge & Burbidge 1955). The understanding of the nature of these profiles comes from the 1930s, with McCrea (1929) proposing that P Cygni profiles observed in novae arise from an expanding shell. This suggestion was followed by a series of studies by Carlyle Smith Beals (Beals 1929, 1930, 1932, 1935), explaining that such spectral feature, also observed in the spectrum of WR stars and η Carinae (another LBV star), originates from “continuous ejection of gaseous material from the star” (Beals 1929). Later, Beals (1953) published an extensive catalogue of early-type stars, covering spectral types from O5 to A4, which showed P Cygni-like spectra in the visible region.

Followed by other observational studies (e.g., Wilson 1958; Underhill 1958), these results supported that strong winds are indeed a common phenomenon among early-type stars, instead of an anomalous or very particular phenomenon of some stars as P Cygni. Soon after, this picture was confirmed by the very first UV spectroscopic observations from Morton (1967b,a), which revealed strong and broad P Cygni profiles of Si IV, C V, and N V, in the UV spectrum ($\sim 1200\text{--}1600$ Å) of OB supergiants, arising from high values of effective temperature (highly ionized wind) and also of mass-loss rate and terminal velocity. Subsequently, UV spectroscopic observations were technically improved by means of the Copernicus and IUE satellites that allowed more systematic analysis of early-type stars (e.g., Underhill 1975; Morton 1976; Snow & Morton 1976; Henrichs et al. 1983; Prinja & Howarth 1986; Howarth & Prinja 1989). Regarding the IUE studies about early-type stars, the interested reader can see the reviews of Cassinelli & Lamers (1987), Willis & Garmany (1987), and Snow & Stalio (1987) about OB, WR, and Be stars, respectively. In short, all these spectroscopic studies discussed above set the conditions to develop and verify the radiative line-driven wind theory from Lucy & Solomon (1970) and Castor et al. (1975).

In a qualitative way, the formation of P Cygni line profiles is understood in terms of the flux contribution from different regions in the stellar wind, apart from the photospheric contribution to the line formation in a certain rest-frame frequency ν_0 (likely forming a pure-absorption line). For that, we show a geometric scheme (star plus wind) in Fig. 2.4. Here, we consider the simplest case of a spherically symmetric expanding shell around the star, following the wind velocity law as described in Eq. 1.5.

From the Doppler effect, both the absorption and emission components of a certain P Cygni line profile (transition with rest-frame frequency ν_0), arise from the interaction between the wind and photons emitted from the star with frequencies higher or equal

2.2. Line formation in the wind: P-Cygni profiles

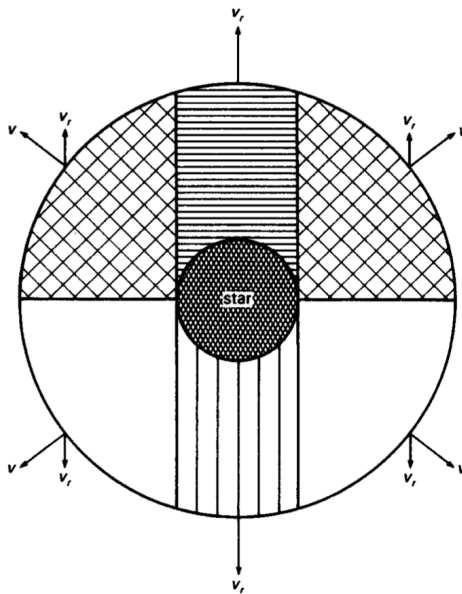


Figure 2.4 – Geometric scheme for the formation of P Cygni profiles. The star is represented by the central dark region that is surrounded by an expanding shell (wind). V denotes the wind velocity and V_r is the radial component, which is parallel to the line of sight of the observer. An asymmetric P Cygni profile is then formed by the superposition of the radiation arising from all these regions. Examples of observed P Cygni profiles in the spectrum of O-type stars were previously shown in Fig. 1.9, and Fig. 2.5 shows examples of theoretical P Cygni profiles in C IV $\lambda\lambda$ 1548,1550. Reproduced from Böhm-Vitense (1989).

to ν_0 . At the distance r in the wind, a photon has frequency ν_{obs} :

$$\nu_{\text{obs}} = \nu_0 - \nu_0 \frac{v(r)}{c}, \quad (2.1)$$

as observed from the stellar surface (rest-frame). Hence, photons emitted from the star with ν'_0 :

$$\nu'_0 = \nu_0 + \nu_0 \frac{v(r)}{c}, \quad (2.2)$$

will contribute at r to the transition with frequency ν_0 , and thus ν'_0 ranges from ν_0 ($v(r = R_*) \sim 0$) up to $\nu_0 + v_\infty/c$.

First, the absorption component of the P Cygni profile originates from the scattering of photons in the wind region in front of the star, toward the line of sight of the observer (vertical dashed area in Fig. 2.4). The redward part of the absorption component is formed close to the stellar surface ($v(r)$ close to zero so ν'_0 close to ν_0), while the blueward one is formed in the outermost wind region (up to v_∞). If the wind column density is high enough so the absorption component can be found saturated, that is, having null flux.

The wind region represented by the white and cross-hatched areas in Fig. 2.4 will thus contribute to the emission component due to the scattering of photons toward the observer. In this case, note that the emission arises from distances in the wind with

2.2. Line formation in the wind: P-Cygni profiles

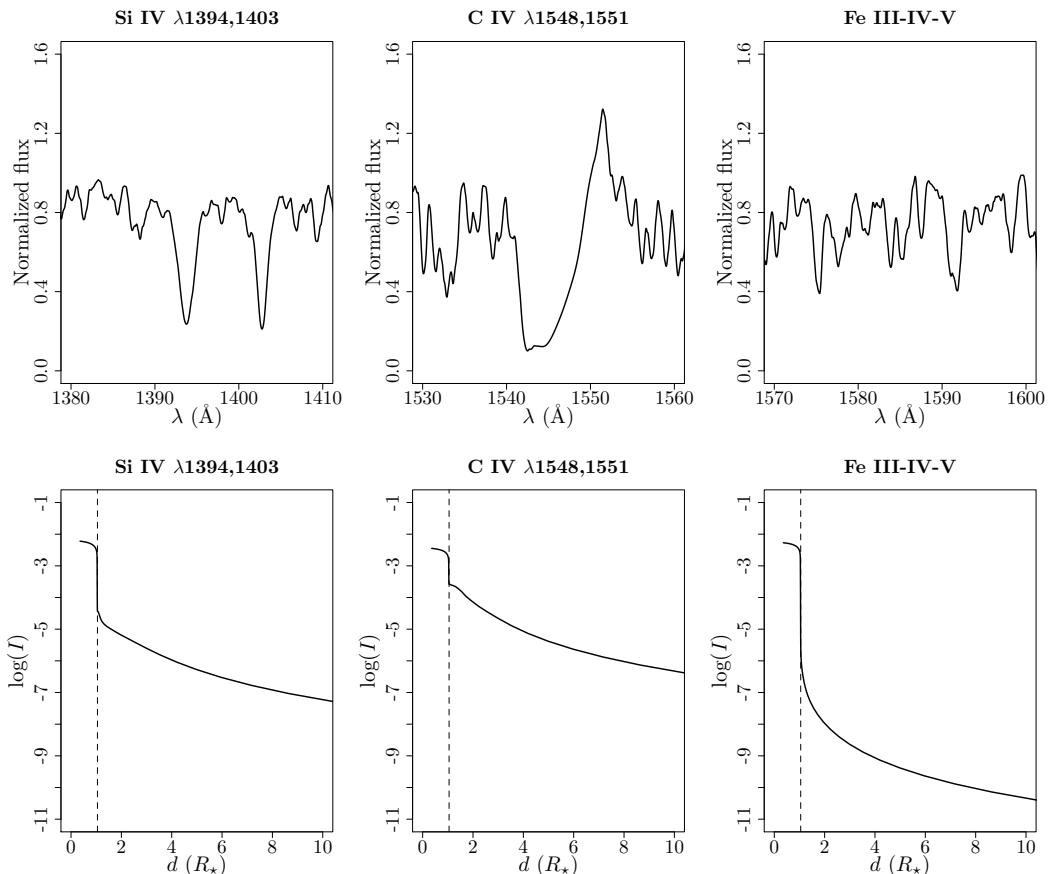


Figure 2.5 – Comparison of UV line formation through the wind extension. The top panels show synthetic line profiles in the UV, calculated by myself, using CMFGEN with parameters as follows: $\log(L_*/L_\odot) = 5.12$, $T_{\text{eff}} = 30600$ K, $\log g = 3.50$, $R_* = 13 R_\odot$, $M_* = 20 M_\odot$, $\dot{M} = 1.5 \times 10^{-9} M_\odot \text{ yr}^{-1}$, and $v_\infty = 1300 \text{ km s}^{-1}$. The bottom panels show the intensity, within the same spectral regions indicated in the top panels, as a function of radial distance from the center of the star. The dashed lines indicate the start of the wind region in the model. Intensity unit is in $\text{erg}/(\text{cm}^2 \text{ s Hz sr})$. Note the large drop of intensity at the base of the wind for the spectral region encompassing mainly just Fe lines. See text for discussion.

velocities, with respect to the observer, ranging from $-v_\infty$ to v_∞ , due to the contribution from both wind hemispheres. This same effect does not happen regarding the formation of the absorption component because a portion of the wind region, in the line of sight of the observer, is occulted by the star (horizontal dashed line), and then this region of the wind does not contribute to the observed P Cygni profile.

From adding the contributions of all these different parts of the wind to the emerging spectrum, an asymmetric P Cygni profile is formed, showing a blueshifted absorption component and a emission component with a peak close to the rest-frame frequency (slightly shifted to the red part of the spectrum), as shown for C IV $\lambda \lambda 1548,1551$ in Fig. 2.5.

Since P Cygni profiles are formed by scattering, when radiative or collisional processes are dominant in the wind, its absorption component will be thus filled-in due

2.3. Multi-wavelength line diagnostics

to the photons created in the wind (“true emission”). Thus, instead of forming a P Cygni profile, these processes could result in the formation of a pure-emission line. The resonance transitions, such as, P v $\lambda\lambda$ 1118,1128, N v λ 1240, Si iv $\lambda\lambda$ 1394,1403, and C iv $\lambda\lambda$ 1548,1550, for O and early B stars, are expected to show the strongest P Cygni profiles in the ultraviolet since these transitions have short lifetimes and then occurring more frequently. On the other hand, due to lower values of effective temperature, resonance lines produced by singly ionized metals, such C, Mg, Al, Si, and Fe are relevant in the formation of P Cygni in late B and early A supergiants.

The discussion above is only a qualitative picture of P Cygni profiles. For instance, since the ionization fractions are expected to change through the wind, depending on the stellar and wind parameters, a certain metal ion, which produces a certain line, may not occur up to the largest distance in the wind (where $v = v_\infty$). This would result in a less broad P Cygni profile. A deeper discussion about the formation of P Cygni profiles can be found in Sect. 2.2 of Lamers et al. (1999).

To illustrate, in a quantitative way, the formation of P Cygni profiles in the winds of hot stars, Fig. 2.5 shows synthetic lines from a radiative transfer model calculated using code CMFGEN (Sect. 4.3): around Si iv $\lambda\lambda$ 1394,1403, C iv $\lambda\lambda$ 1548,1551, and also a narrow spectral region that is mainly composed of lines of iron group elements, specially Fe iv (considering the parameters of this model).

For each one of the presented wavelength regions, we also show the intensity as a function of distance from the center of star. One clearly sees that C iv $\lambda\lambda$ 1548,1551 forms a fully developed P Cygni profile, while Si iv $\lambda\lambda$ 1394,1403 is in absorption due to the low value of mass-loss rate adopted in this model ($\dot{M} = 1.5 \times 10^{-9} M_\odot \text{ yr}^{-1}$), considering the set of stellar parameters here (with $T_{\text{eff}} \sim 30000 \text{ K}$). Nevertheless, even in this case, Si iv $\lambda\lambda$ 1394,1403 shows a significant line intensity through the wind extension, unlike the intensity of the iron lines that suddenly drops at the base of the wind since these lines are mainly formed in the stellar atmosphere. On the other hand, in advance of discussion, one sees, from Fig. 2.8, that fully developed P Cygni profiles are also formed in Si iv $\lambda\lambda$ 1394,1403, but when considering a much larger value of mass-loss rate in the model ($\dot{M} = 2.5 \times 10^{-7} M_\odot \text{ yr}^{-1}$).

2.3 Multi-wavelength line diagnostics

Due to their high effective temperature ($T_{\text{eff}} \gtrsim 10000 \text{ K}$), hot stars emit most part of their radiative energy in the UV region, resulting in highly ionized environments around these objects. Their UV spectra are composed of a large number of narrow photospheric lines (often called the UV iron forest) and a few strong resonance lines, which are mainly formed in the wind. As discussed in Sect. 1.2.2, in general, the iron

2.3. Multi-wavelength line diagnostics

Table 2.1 – Summary of the main ultraviolet, visible, and infrared line diagnostic used to determine the photospheric and wind parameters of massive stars, in particular, O-type, WR, and B supergiant stars. Adapted from Martins (2011).

Parameter	Ultraviolet	Visible	Infrared
T_{eff}	Iron forest (Fe III-IV-V-VI)	He I $\lambda 4471$ and He II $\lambda 4542$ Si II $\lambda 4124$, Si III $\lambda 4552$, and Si IV $\lambda 4116$	He I $\lambda 2.112$ and He II $\lambda 2.189$
$\log g$	—	H α , H β , H γ , and H δ	Br γ
\dot{M}	P V $\lambda\lambda$ 1118,1128 N V $\lambda 1240$ Si IV $\lambda\lambda$ 1394,1403 C IV $\lambda\lambda$ 1548,1550 N IV $\lambda 1718$	H α and He II $\lambda 4686$	Pf γ , Br α , and Br γ
v_{∞}	P V $\lambda\lambda$ 1118,1128 N V $\lambda 1240$ Si IV $\lambda\lambda$ 1394,1403 C IV $\lambda\lambda$ 1548,1550 N IV $\lambda 1718$	H α , H β , H γ , and He I $\lambda 4471$ (if strong winds)	He I $\lambda 2.058$, He I $\lambda 2.112$, and Br γ (if strong winds)
f_{∞}	P V $\lambda\lambda$ 1118,1128 O V $\lambda 1371$ N IV $\lambda 1718$	H α and He II $\lambda 4686$	Br10 and Br11

lines are rather relevant to the radiative acceleration in the wind sub-sonic region (that is, velocity lower than the sonic point of the wind⁷), while the contribution from C, N, O, and Si to the radiative acceleration increases toward larger distances from the stellar surface. Moreover, hydrogen recombination lines, such as, H α (visible), Br γ (K-band), and Br α (L-band), are also naturally important diagnostics for the determination of the stellar and wind parameters for a large fraction of hot stars (which are not H-depleted).

Quantitative spectroscopy relies on the determination of the stellar and wind parameters by modeling the observed spectrum by means of radiative transfer models, as calculated using the code CMFGEN, previously discussed in Figs. 1.9 and 2.5. In Table 2.1, we summarize the principal line diagnostics in the ultraviolet, visible, and infrared regions, used to determine the effective temperature (T_{eff}), surface gravity ($\log g$), mass-loss rate (\dot{M}), terminal velocity (v_{∞}), and the wind clumping (f_{∞}) of O-type, WR, and also B supergiant stars.

In the following, we focus our discussion on the stellar effective temperature and the wind mass-loss rate. For that, we use state-of-the-art radiative transfer models, calculated with the code CMFGEN. Further details on multi-wavelength quantitative spectroscopy of hot stars can be found in Martins (2011), extending the discussion of this section to the analysis of surface magnetic field, surface chemical abundance, projected rotational velocity, and macroturbulence.

The effective temperature is one of the main stellar parameters affecting the wind properties. This happens since this parameter impacts the wind ionization structure. In

⁷. See footnote 4 in Sect. 1.2.2

2.3. Multi-wavelength line diagnostics

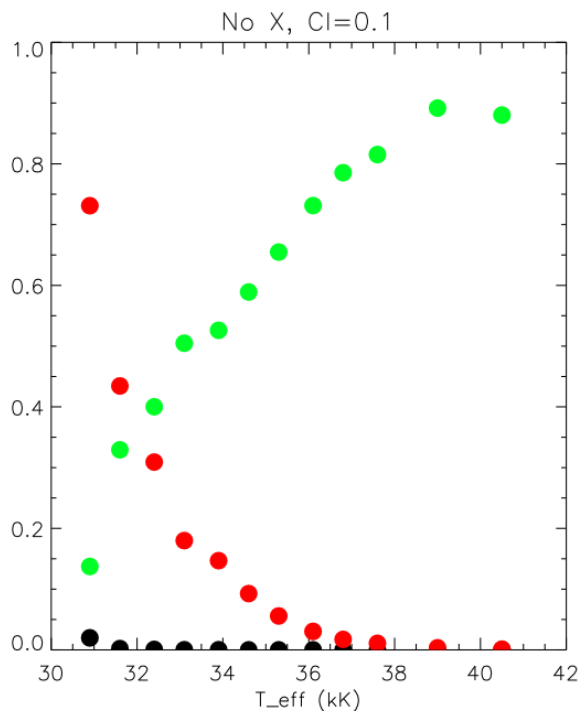


Figure 2.6 – CMFGEN ion fraction of silicon as a function of effective temperature for the parameter space of O supergiant stars. Black: Si III. Red: Si IV. Green: Si V. In the top, it is indicated the level of wind clumping ($f_\infty = 0.1$) and the absence of X-Rays in the models. Adapted from Austin (2011).

Fig. 2.6, we show the ionization fraction of silicon, calculated with CMFGEN, according to the variation of the effective temperature. Here, the model parameter space is set typically for O supergiants, as investigated by Austin (2011). In this case, the fraction of Si IV increases toward lower values of T_{eff} . Note how practically all silicon is found in the higher ionization stage considered here (Si V) for higher values of effective temperature (up to $T_{\text{eff}} \sim 40000$ K).

Looking the synthetic spectra, in advance, as shown in Fig. 2.7, one sees how the Si IV $\lambda\lambda 1394, 1403$ is significantly affected by varying the effective temperature. In this case, when considering a lower value of T_{eff} , closer to 30000 K, Si IV $\lambda\lambda 1394, 1403$ shows a larger line width, resulting from a larger wind contribution. In short, this means that reliable estimations for the wind mass-loss rate depend on accurate constrains on T_{eff} .

In a more quantitative way, this can be understood since the intensity of the line profile due to a certain atomic specie (ion), that is related to the optical depth for such wavelength region, depends both on the mass-loss rate and the ion fraction. For instance, considering Si IV, under the Sobolev approximation⁸ the optical depth (in this case, denoted as τ_{SiIV}) is then directly proportional to the mass-loss rate, the chemical abundance of abundance of silicon (ϵ_{Si}), and to the Si IV fraction (q_{SiIV}): $\tau_{\text{SiIV}} \propto \dot{M} q_{\text{SiIV}} \epsilon_{\text{Si}}$.

8. See footnote 6 in Sect. 1.2.2.

2.3. Multi-wavelength line diagnostics

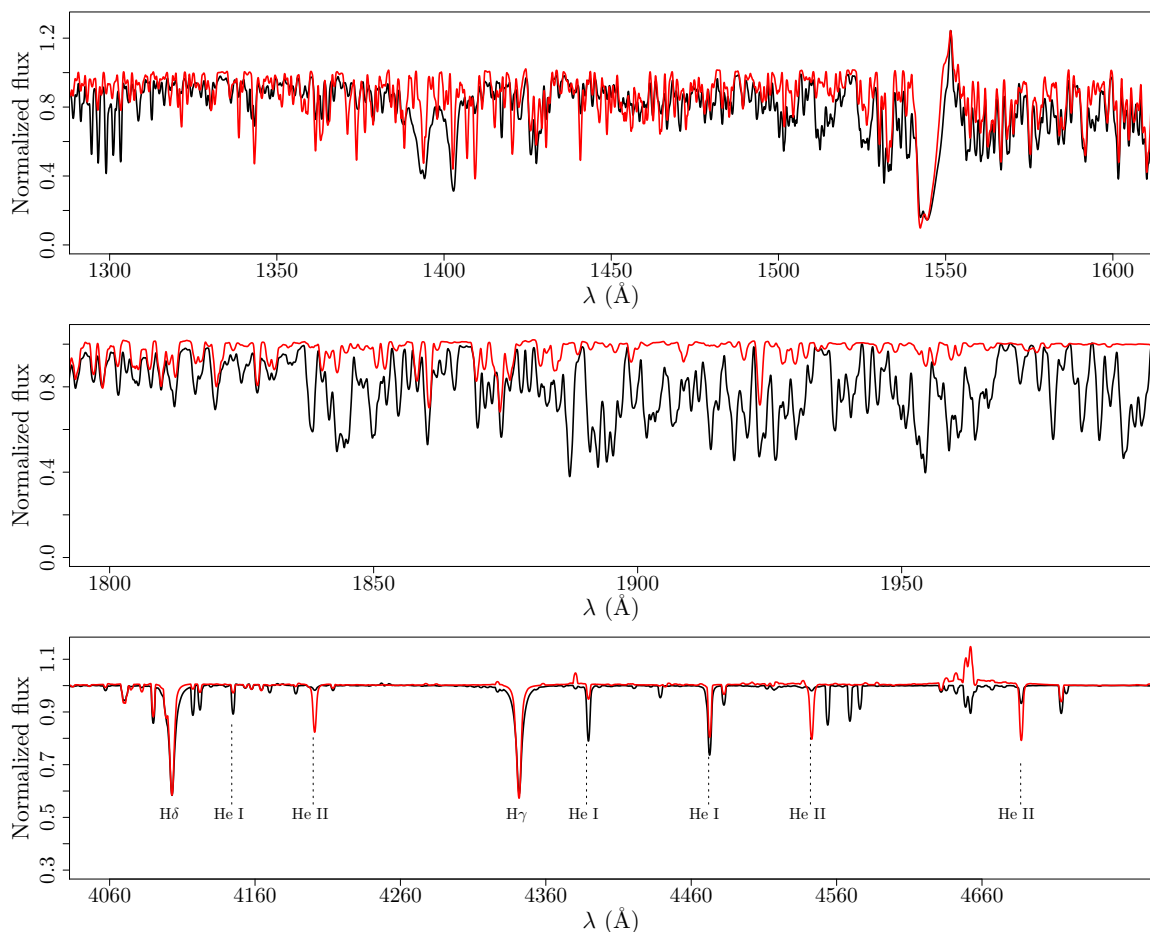


Figure 2.7 – Effect of varying the effective temperature on the UV and visible regions. Synthetic spectra are shown for two CMFGEN models, calculated by myself, with different values of effective temperature: $T_{\text{eff}} = 27500$ K (black) and $T_{\text{eff}} = 37500$ K (red). All the other parameters are fixed according to the model shown in Fig. 2.5. See text for discussion.

From Section 2.1, it is conspicuous that the main diagnostics of the effective temperature are based on the ionization balances of helium and silicon lines in the visible spectrum. The lines of He I $\lambda 4471$ and He II $\lambda 4542$, and Si II $\lambda 4124$, Si III $\lambda 4552$, and Si IV $\lambda 4116$ are particularly important to determine the T_{eff} of O- and B-type stars, respectively.

In Fig 2.7, we compare the synthetic spectra from two different CMFGEN models, covering the UV (~ 1200 - 2000 Å) and visible regions (~ 4050 - 4750 Å). The parameter values of these models are the same than the ones shown in Fig. 2.5, but with $T_{\text{eff}} = 27500$ K and $T_{\text{eff}} = 37500$ K.

As one can see from Fig. 2.7, such a high contrast between the synthetic spectra, both in the UV and visible, is due to the high difference in T_{eff} , namely, 10000 K. In particular, in the UV, the highest effects are seen in the iron forest around 1850-2000 Å (in this case, mainly composed of Fe III lines). In the visible, the strongest effects are seen in the He I $\lambda 4471$ and He II $\lambda 4542$ lines, as discussed above, as the parameters

2.3. Multi-wavelength line diagnostics

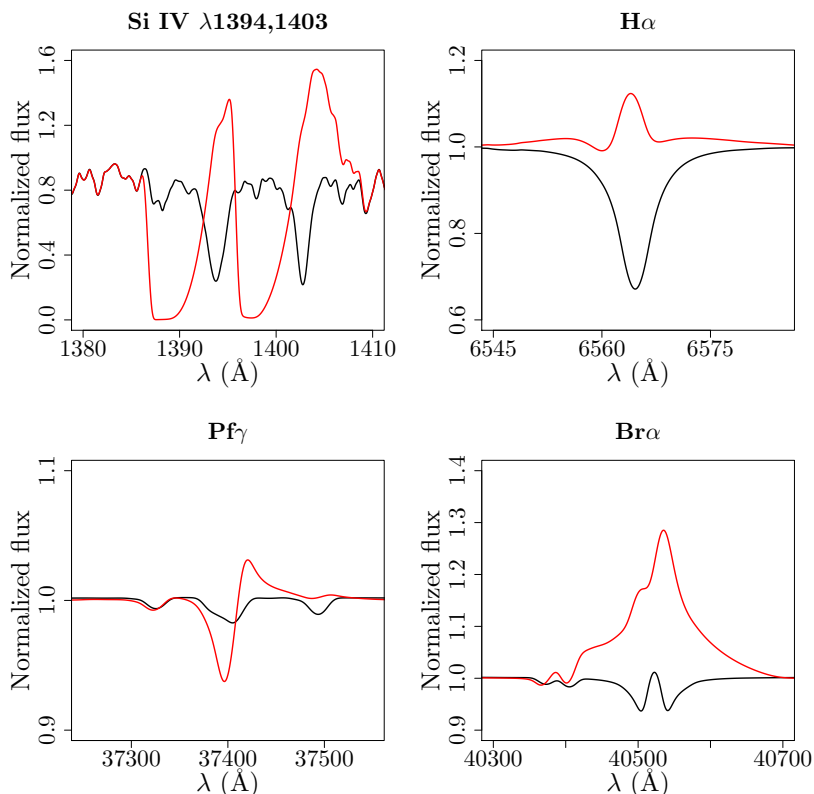


Figure 2.8 – Effect of varying the mass-loss rate on the UV (Si iv $\lambda\lambda$ 1394,1403), visible ($H\alpha$), and infrared ($Pf\gamma$ and $Br\alpha$) regions. Synthetic spectra are shown for two CMFGEN models, calculated by myself, with different values of \dot{M} : $\dot{M} = 1.5 \times 10^{-9} M_{\odot} \text{ yr}^{-1}$ (black) and $\dot{M} = 2.5 \times 10^{-7} M_{\odot} \text{ yr}^{-1}$ (red). All the other parameters are fixed according to the model shown in Fig. 2.5. Note how all these diagnostic lines for the mass-loss rate are highly affected by just varying this parameter in the models.

of these models are tuned for the analysis of O-type stars. The T_{eff} of O stars is generally determined from such quantitative spectroscopic analysis, with uncertainties of ~ 1000 - 2000 K, from the fit to the visible He I-II lines, and somewhat larger values of ~ 2000 - 4000 K from the fit purely based on the iron forest in the ultraviolet (e.g., Repolust et al. 2004; Martins et al. 2004; Holgado et al. 2018).

Overall the T_{eff} derived, in separate way, from the UV iron forest lines and the visible helium lines agrees fairly well (e.g., using the code CMFGEN as in Hillier et al. 2003; Martins et al. 2005b). However, significant differences are still reported in the literature. For example, Bianchi & Garcia (2002) derived quite lower values of T_{eff} of O stars from the ultraviolet, of about ~ 6000 K, when compared with the values derived from the visible spectrum. This points out the current need of a multi-wavelength approach in order to better constrain such a fundamental stellar parameter, allowing us to achieve lower uncertainties on the determination of the wind properties, as discussed above.

Regarding the wind parameters, the line diagnostics for the mass-loss rate and the terminal velocity are essentially the same in the UV region. However, as discussed

in Sect. 2.2, depending on the stellar and wind parameters, it is possible to observe saturated P Cygni profiles (mainly in the objects of stronger winds), and in this case, the terminal velocity can be unambiguously derived by adjusting the blueward extension of their absorption component, while the wind mass-loss rate will affect highly the P Cygni intensity overall, and thus its morphology. As shown in Table 2.1, the hydrogen and helium lines, found in the visible and infrared, are useful to estimate the terminal velocity of objects with strong stellar wind, as WR and early B-supergiant stars, showing \dot{M} as high as $10^{-5} M_{\odot} \text{ yr}^{-1}$. Furthermore, these lines are also used as diagnostics for the determination of the wind mass-loss rate.

In Fig. 2.8, we compare synthetic profiles in the UV, visible, and infrared, computed from two CMFGEN models, in this case, only varying the mass-loss rate: $\dot{M} = 1.5 \times 10^{-9} M_{\odot} \text{ yr}^{-1}$ (black) and $\dot{M} = 2.5 \times 10^{-7} M_{\odot} \text{ yr}^{-1}$ (red). As in the previous example, for the effective temperature, all the other parameters are fixed with the same values as those of the model presented in Fig. 2.5. These lines shown here are one of the main mass-loss diagnostics presented in Table 2.1, and it is conspicuous their high sensitive to the variation of the mass-loss rate (of about 2 orders of magnitude).

We point out that UV resonance lines, such as Si IV $\lambda\lambda$ 1394,1403, forming P-Cygni profiles in the model with the highest \dot{M} in Fig. 2.8, respond differently to the change in \dot{M} than the hydrogen recombination lines. As resonance lines, their intensity (I) is directly proportional to the local density in the wind, i.e., $I \propto \rho$. On the other hand, the intensity of recombination lines, as H α , Pf γ , and Br γ , shown in Fig. 2.8, depends on the square of ρ , $I \propto \rho^2$, since the formation of these lines requires the interaction of two particles (an electron and an ion).

This fact above is relevant with respect to the estimation of the \dot{M} of massive stars with weaker winds, having $\dot{M} \sim 10^{-10}$ - $10^{-9} M_{\odot} \text{ yr}^{-1}$. Despite the less accurate modeling of their ionization structure, in comparison to the H lines, the UV resonance lines better trace \dot{M} for low-density wind regimes, as the H and He recombination lines are typically formed in the wind region closer to the stellar surface (larger wind density) than the UV resonance lines. However, recombination lines will be more useful as mass-loss diagnostics of stronger (denser) winds, showing $\dot{M} \sim 10^{-8}$ - $10^{-7} M_{\odot} \text{ yr}^{-1}$ (see, e.g., Puls et al. 2008; Marcolino et al. 2009).

A multi-wavelength quantitative spectroscopic approach, that is, using spectral lines formed in different wavelength regions, to better constrain the real rates of mass-loss in massive stars, is one of the main objective of this thesis. This issue will be discussed in details, in Sect. 6.1, when presenting our results for the wind parameters of O-type stars, concerning the so-called weak wind problem, firstly discussed in Sect. 1.2.3.

Chapter 3

Optical long-baseline stellar interferometry

Contents

3.1	Why we need high angular resolution observations?	74
3.2	Historical overview	78
3.3	Elementary concepts of OLBI	81
3.4	Light coherence	85
3.5	Interferometric quantities	87
3.5.1	The Zernike-van Cittert theorem	87
3.5.2	Closure phase	89
3.5.3	Visibility calibration	90
3.6	Spectro-interferometry	91
3.7	Spectro-interferometric instruments	95
3.7.1	The CHARA array	95
3.7.2	CHARA/VEGA	97
3.7.3	The VLTI array	97
3.7.4	VLTI/AMBER	100
3.7.5	Comparison between CHARA and VLTI	100

3.1 Why we need high angular resolution observations?

In the previous chapter, we highlighted the power of spectroscopy to characterize the stellar and circumstellar properties of massive hot stars.

3.1. Why we need high angular resolution observations?

However, due to the very low values of stellar angular size, we usually are not able to retrieve information about the spatial intensity distribution of the star and of its environments projected across the sky, purely based on the analysis of line profiles. Nevertheless, one possibility, using spectroscopic data, in order to indirectly resolve the structure of stellar surfaces relies on the so-called Doppler imaging technique (e.g., Vogt et al. 1987). On the other hand, this technique works optimally for fast rotators, with intermediate values of inclination angle, preferentially between $\sim 20^\circ$ - 70° , arising ambiguities on the polar locations for stars seen close to edge-on (e.g., Strassmeier 2002).

Spatial resolution means the ability to resolve, that is, distinguish, different points of the observed object's image. The angular resolution provided by a single-mirror telescope depends on its mirror's diameter (D) and the observing wavelength (λ), being usually approximated by the so-called Rayleigh criterion:

$$\theta_{\text{res}}^{\text{diffraction}} = 1.22 \frac{\lambda}{D} \sim \frac{\lambda}{D}. \quad (3.1)$$

This simple estimation for the angular resolution of a telescope comes from the diffraction limit imposed by the interference of the incident light wavefronts of an unresolved object across the telescope aperture. Considering a uniformly-illuminated circular aperture, with diameter D , the diffraction pattern is described by an Airy disk, with brightness, $I(\rho)$, given as follows:

$$I(\rho) = \left(\frac{\pi D^2}{4} \right)^2 \left[\frac{2J_1(\pi \rho D)}{\pi \rho D} \right]^2, \quad (3.2)$$

where ρ is the radial distance from the center of the Airy disk and J_1 is the first order Bessel function of the first kind (e.g., see Chap. 9 of Abramowitz M. 1972).

As shown in Fig. 3.1, the Airy disk pattern has a central bright region with a diameter of $\sim 2.44 \frac{\lambda}{D}$. Thus, the factor 1.22, in Eq. 3.1, which is the radius of the Airy disk's first zero (first dark ring), expresses the ability to separate two point source images at the focal plane of the telescope.

As pointed out, in Fig. 3.1, the Airy disk pattern results from the observation of an unresolved object, a point source, describing then the ideal (i.e., without instrumental and atmospheric effects) point spread function (PSF) of a circular single-mirror telescope. Even considering a single-mirror telescope, we stress that the PSF changes according to the employed aperture geometry for the telescope pupil (e.g., as shown in Fig. 2 of Millour 2014).

We also stress that the angular resolution of a telescope, as approximated by Eq. 3.1, does not take into account the optics wavefront aberrations nor atmospheric turbulence effects on the focal plane image, which can drastically reduce the telescope's capacity

3.1. Why we need high angular resolution observations?

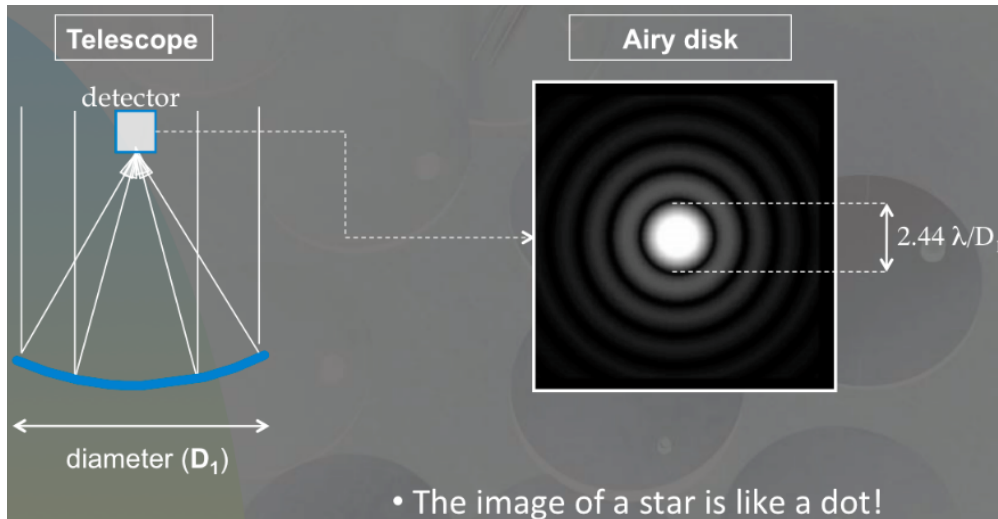


Figure 3.1 – Schematic of an Airy disk, formed by the phenomenon of diffraction, arising from the incidence of the light wavefronts into a telescope (round pupil). The light wavelength is given by λ and the telescope principal mirror by D_1 . The Airy disk’s central bright region has a diameter of $\sim 2.44\lambda/D$. See text for discussion. Reproduced from Surdej (2019).

to spatially resolve an object. To overcome this problem, adaptive optics systems have been extensively developed since the end of the 1990’s in order to reduce the image blur due to the atmospheric turbulence. For example, in the visible spectral region, without the use of adaptive optics, the spatial resolution of a 10-m telescope would be equivalent of a 10-cm mirror telescope. Details about this technique can be found in the reviews of Beckers (1993) and Davies & Kasper (2012).

Nevertheless, the current generation of 10-m class telescopes are only able to resolve the nearest supergiant stars. For instance, we consider Achernar that is the brightest ($V = 0.46$) and nearest Be star with a distance of 42.8 pc (van Leeuwen 2007). Achernar has an equatorial angular diameter of ~ 1.99 mas, considering the linear equatorial radius of $\sim 9.16 R_{\odot}$, and a mean angular diameter of 1.77 mas when taking into account its geometrical oblateness (Domiciano de Souza et al. 2014). From Eq. 3.1, considering $\lambda = 6563 \text{ \AA}$ (centered at the $H\alpha$ line) and a 8-m telescope, as the Unit Telescopes at the ESO/VLT facility, we find that $\theta_{\text{res}} \sim 0.02$ arcsecond, that is, 20 milliarcseconds. This is one order of magnitude larger than the angular diameter of Achernar projected onto the sky.

Thus, even considering the nearest Be star, this shows the impossibility to obtain finer spatial information of its surface, using such a large single-mirror telescope as provided by the ESO Unit Telescopes. In addition, as discussed in Sects. 1.4 and 1.5, Be stars possess transient or stable (within a certain time-scale) circumstellar disks with emitting envelope extension reaching up to a few milliarcseconds in angular size. Therefore, in addition to spectral resolution, this evidences the necessity of spatial resolution in order to constrain the physical properties of Be stars, and more generally

3.1. Why we need high angular resolution observations?

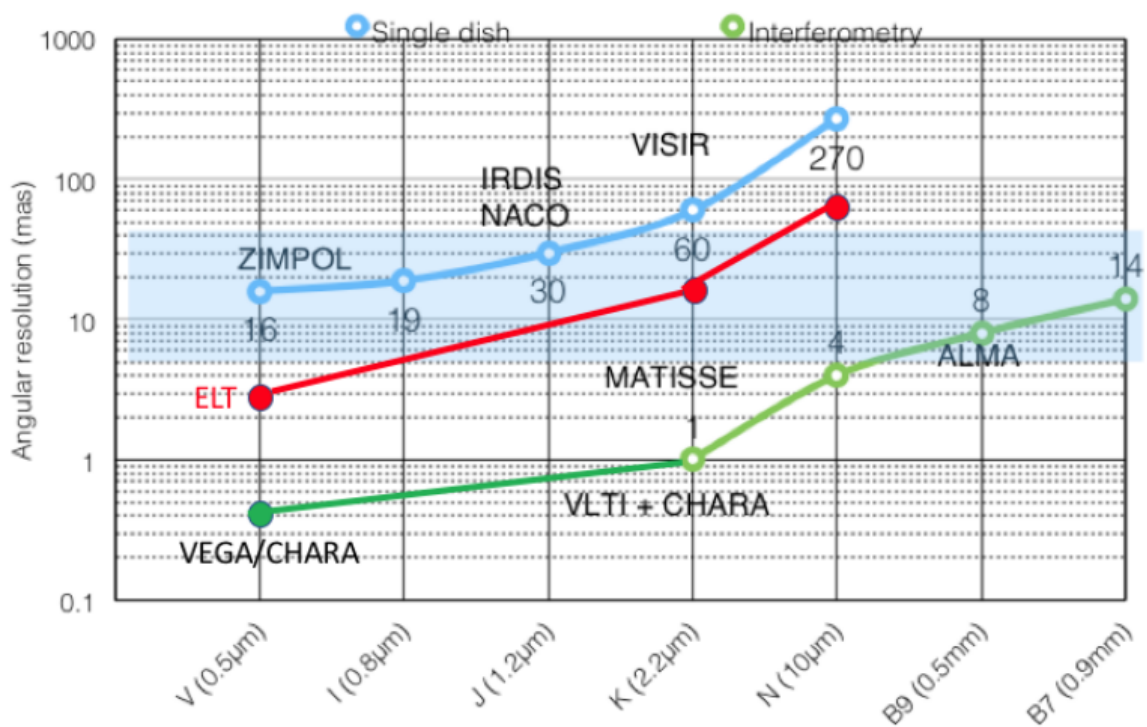


Figure 3.2 – Comparison between the angular resolution (in milliarcsecond) provided by current single-mirror telescope (blue line; ZIMPOL, IRDIS, VISIR instruments) and interferometric facilities (green line; VEGA/CHARA, MATISSE, VLTI + CHARA instruments, and ALMA), as a function of wavelength. The blue region indicates a similar range of angular resolution that is achieved by both the current facilities and the future ones, as the Extremely Large Telescope (ELT, 39-m telescope) in red line. See text for discussion. Reproduced from Mourard & Nardetto (2019).

of massive stars, and their environments (composed of winds, disks, or both of them).

To date, interferometry is the only technique that enables to overcome the limitations of angular resolution imposed by the aperture size of current single-mirror telescopes, and allowing us to resolve the surface and the environment of massive stars, which typically have angular sizes as low as ~ 1 and 10 mas, respectively. In this case, by combing the light-beams from different single-mirror telescopes in order to obtain interference fringes, the angular resolution can now be approximated by the distance B_{proj} of a pair of telescopes, projected onto the sky in the direction of the observed object, that is, the projected baseline length, replacing D in Eq. 3.1 by:

$$\theta_{\text{res}}^{\text{interf}} \sim \frac{\lambda}{B_{\text{proj}}}. \quad (3.3)$$

We thus achieve a spatial resolution as provided by the diffraction-limit of a “synthesized telescope” with its mirror diameter equal to the projected baseline length of the telescope array.

Fig. 3.2 compares the spatial resolution provided by different single-mirror telescopes and by interferometric facilities, as a function of wavelength, from the visible to the

3.2. Historical overview

millimetric region. First, we note how the ability to spatially resolve is typically reduced toward longer wavelength (in agreement with Eqs. 3.1 and 3.3). Moreover, to date, one sees that the highest angular resolution, in the visible band (including the $H\alpha$ line) are obtained using the CHARA/VEGA instrument, reaching a maximum resolution of $\sim 0.3\text{-}0.4$ mas. Meanwhile, the CHARA (such as CLASSIC) and VLTI instruments (such as MATISSE) provide the highest ones in the near-infrared (including the $Br\gamma$ line) and in the mid-infrared (including the $Br\alpha$ line).

Fig. 3.2 also shows the possible synergies between the single-mirror telescopes and interferometric facilities. For example, the ELT array will be able to obtain similar value of angular resolution (~ 3 mas) in the visible than the current VLTI/MATISSE instrument in the N-band, as well as the Atacama Large Millimeter Array (ALMA), allowing us to compare the properties of the objects studied then under the same level of spatial resolution in different spectral channels (visible, mid-infrared, and sub-millimeter regions).

3.2 Historical overview

Optical long-baseline interferometry (OLBI) means the use of optical systems to combine the light received from separate pairs of telescopes in order to obtain fringe patterns. As pointed out by Monnier (2003b), the term “optical” used here indicates the implementation of such optical system to manipulate the collected light, instead of indicating the wavelength domain of the observations. Currently, OLBI is limited in the spectral channels from the optical/visible region (~ 400 nm) to the mid-infrared (~ 10 μm). Further details on the history of stellar interferometry can be found in Lawson (2000) and Léna (2014).

The basis for stellar interferometry comes from the demonstration of the wave properties of the light by Thomas Young in 1801. Fig. 3.3 shows the basic scheme of the so-called Young’s double slit experiment. Under certain condition, as it will be discussed in more details in Sect. 3.3, an interference pattern composed of bright and dark fringes arises from the interaction of the light waves originating from the two slits.

As indicated in Fig. 3.3, each point of a light wavefront works like his own source of spherical waves, following the Huygens-Fresnel principle, originally proposed by Christiaan Huygens in 1678. This allows to explain an interference pattern resulting from the combination of overlapping light waves, which are originated from the two slits. Considering the simplest case of a monochromatic light source, that is, fixing the light wavelength, the angular separation between the fringes can then be expressed as a function of distance between the two slits. For a certain constant distance from the slits to the pattern screen, a larger distance between the slits implies larger separation

3.2. Historical overview

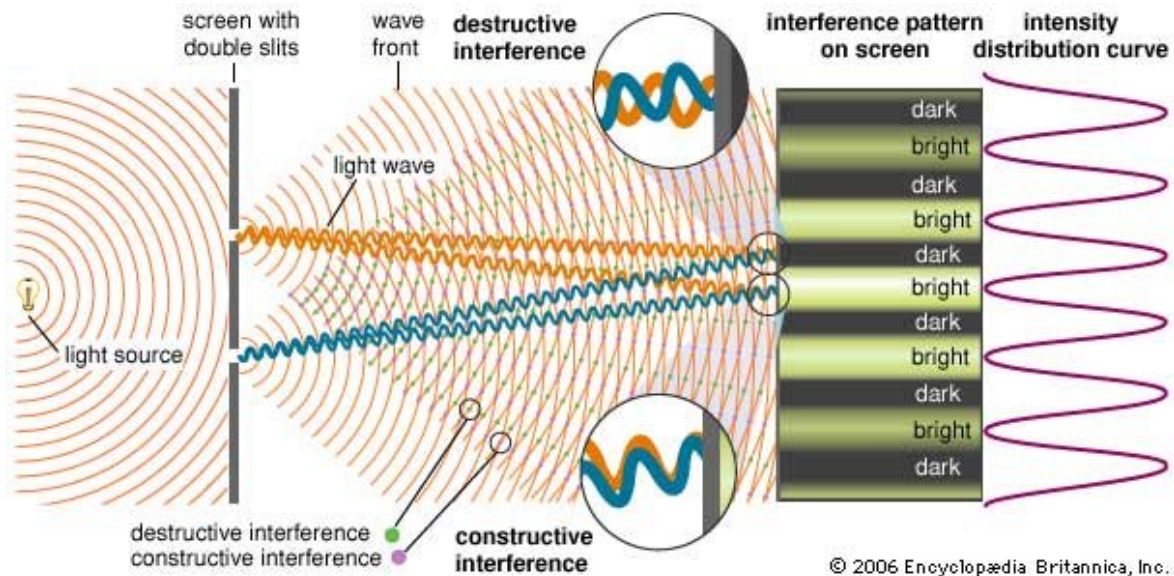


Figure 3.3 – Scheme for the propagation of light wavefronts through a double-slit screen, the Young’s double-slit experiment. For simplification, the light source is considered monochromatic with wavelength λ . By the Huygens–Fresnel principle, each point of a light wavefront behaves itself as a own source of spherical waves. The light interference happens according to the difference in phase between different wavefronts. Complete constructive interference happens when the path difference is equal to λ , or a integer multiple of that, while complete destructive interference happens when the path difference is equal to $\lambda/2$, or a integer multiple of that. Interference fringes (bright and dark bands) are then formed by the superposition of the overlapping light waves propagating toward the screen. Source: <https://www.britannica.com/>.

between the interference fringes, a lower contrast of the fringes.

Based on the Young’s double-slit experiment, Hippolyte Fizeau was the first to propose, in 1868, the measurement of stellar diameters by the observation of interference fringes, using slits in front of the telescope principal mirror. Until then, it was considered an impossible task to measure stellar diameters for stars other than the Sun. As figured out by Fizeau, the contrast of the fringes will be a function of both the angular diameter of the star and the slits separation.

The first successful implementation of this method was the measurement of the diameters of the Jupiter’s moons (angular size of ~ 1 arcsecond) by Michelson (1891), using the 12-inch refractor at Lick Observatory. Three decades later, Michelson & Pease (1921) finally managed to measure the first angular diameter of a star (other than the Sun) using the 2.5-m refractor at Mount Wilson Observatory in California. To increase the angular resolution, they mounted a 20-foot beam (6 m) equipped with mirrors over the telescope structure. Thanks to this modification, they measured the angular diameter of the red supergiant star Betelgeuse, finding an angular size of ~ 47 mas with an uncertainty of about 10%.

Due to both instrumental and atmospheric effects, later interferometric works had a quite limited quality in measuring fringes for a larger sample of stars. This drastically

3.2. Historical overview

Table 3.1 – Summary of some very first visible and infrared interferometric studies using two-telescope configuration. Reproduced from Léna (2014).

Year	Instrument/baseline	Location	Observation	Wavelength	Resolution
1970	6 m	Pulkovo (Crimea)	Orbit of Capella	Visible	~1 mas
1974	I2T/12 m	Calern (France)	Vega	Visible	1 mas
1974	ISI/5.5 m	Kitt Peak (Arizona)	Mercury	10.6 μm	200 mas
1986	I2T/8 to 25 m	Calern (France)	γ Cas envelope	H α	1.4 mas
1986	SUSI/11 m	Narrabri (Australia)	Sirius diameter	Visible	1 mas
1986	COAST/6 m	Cambridge (UK)	Orbit of Capella	Visible	10 mas
1988	MarkIII/12 m	Mt. Wilson (California)	Diameter of 4 stars	Visible	1 mas

limited the pioneer studies of stellar interferometry to longer wavelengths, for which the manipulation of the light to obtain interference is easier than in the visible/infrared. From 1940's to the beginning of the 1970's, most part of the interferometric works were performed using radio interferometers, for example, using the Five Kilometer Array (Ryle 1950). This happens since the coherence time-scale, allowing interference, is dependent on the light wavelength. In the practice, for grounded-based observations, resulting from the atmospheric turbulence, the coherence time-scale is limited to very short value of $\sim 10^0$ - 10^1 ms in the visible, when compared with the radio domain, reaching up to several minutes (e.g., see Table 2 of Monnier & Allen 2013).

In 1974, Antoine Labeyrie was the first to directly combine coherently the visible light received by separate telescopes in order to measure interference fringes, using the *Interféromètre à 2 Télescopes* (I2T) interferometer (Plateau de Calern, France), providing an upper limit of 5 mas for the stellar diameter of Vega (Labeyrie 1975). This ground-breaking work established the modern technique of OLBI, and then reviving the stellar interferometry at the visible and infrared wavelengths.

Still using the I2T interferometer, Thom et al. (1986) was the first to spatially resolve the circumstellar environment of a classical Be star, γ Cassiopeiae, measuring an extension of 3.6 mas in the H α line. Still observing in H α , Mourard et al. (1989) was one of the first spectro-interferometric studies to find evidences of a rotating disk in γ Cassiopeiae, with the *Grand Interféromètre à 2 Télescopes* (GI2T) interferometer, also installed on Plateau de Calern. Stee et al. (1995) were the first to interpret GI2T spectro-interferometric observations of γ Cassiopeiae using a radiative transfer model (code SIMECA). Later, Vakili et al. (1997) provided the first spectro-interferometric observations of the LBV star P Cygni, using the GI2T interferometer, in the H α and HeI $\lambda 6678$ emission lines. In addition to constraining the extension of P Cygni' wind

3.3. Elementary concepts of OLBI

in these lines, these authors found evidences of inhomogeneities in its winds based on differential phase measurements in H α . Some of these early results, together with other remarkable ones found using two-telescope interferometry, are listed in Table 3.1.

3.3 Elementary concepts of OLBI

Fig. 3.4 shows the principal components of an optical interferometer. From that, we point out that the capability to spatially resolve the object is dependent on the projected baseline length, B_{proj} , defined as follows:

$$B_{\text{proj}} = B \sin \theta, \quad (3.4)$$

where B is the linear baseline length between the pair of telescopes, and θ is the angle formed between the baseline vector, \hat{B} , and the line of sight toward the object. If the baseline is perpendicular to the line of sight, we have $B_{\text{proj}} = B$.

Moreover, one sees that a geometrical delay, τ_g (time unit), naturally arises from interferometry since the light wavefronts are collected at different times by each telescope forming the array, being given as follows:

$$\tau_g = \frac{\vec{B} \cdot \hat{s}}{c}, \quad (3.5)$$

where \vec{B} is the baseline vector and \vec{s} is a unit vector in the direction of the source. This quantity, τ_g , is related to the optical path difference (OPD) in the interferometer, $\text{OPD} = \tau_g c$.

The optical system used to send the light to the beam combination facility, where the interference is indeed performed, is represented in the bottom of the schematic in Fig. 3.4. At first glance, it may sound an easy task, but several technical issues are related to this process. For instance, it is necessary to transport the collected light through nearly vacuum pipes, or to employ a dispersion compensator, in order to overcome the effect of spectral dispersion due to the long distances that the light must travel between the telescope and the beam combiner (e.g., ten Brummelaar 1995).

In addition, the optical system also contains movable delay lines, which are needed to compensate the geometrical delay, as discussed above, originating in the sidereal motion of the source, as shown in Eq. 3.5. This change in the optical path difference is rather important concerning the own phenomenon of light interference, in order to allow the formation of fringes, as it is discussed below.

As stated in the previous section, an interferometer measures the interference fringe pattern produced by the combination of the light-beams received by a pair of telescopes. Said differently, an interferometer is then sensitive to the degree of coherence of the

3.3. Elementary concepts of OLBI

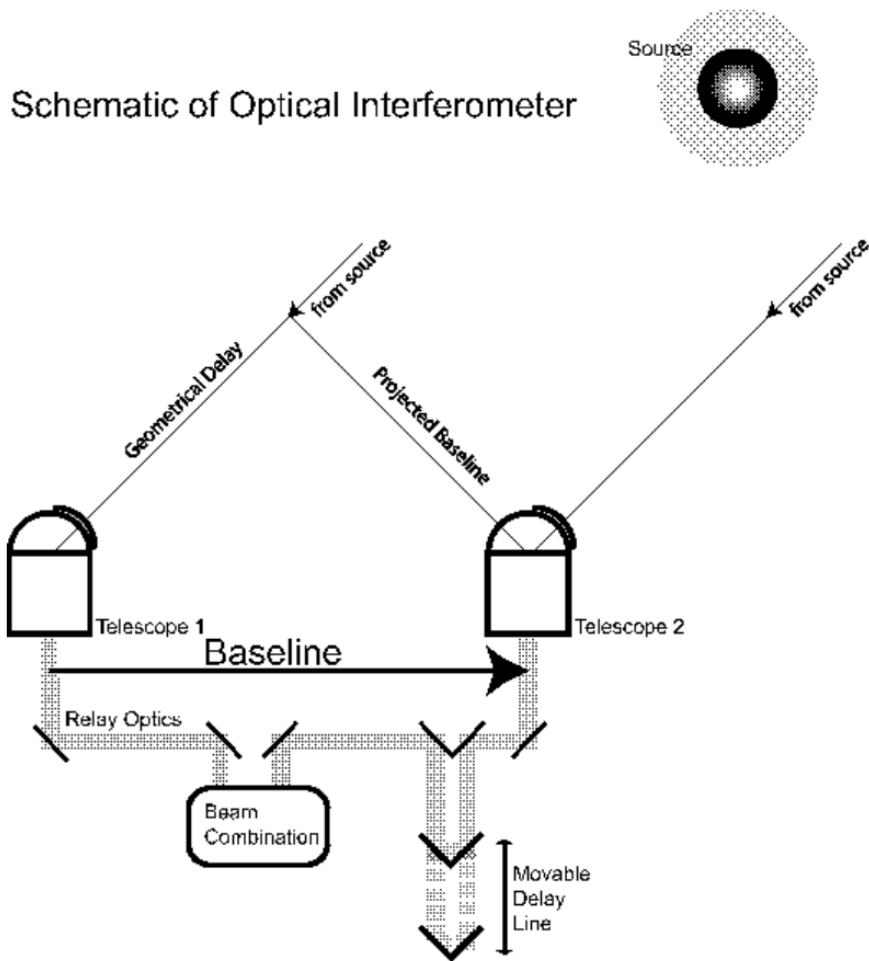


Figure 3.4 – Schematic representing the basic elements of an optical long-baseline interferometer: the telescopes and optical subsystems (relay optics, delay line, and beam combination). See text for discussion. Reproduced from Monnier (2003b).

light wavefronts received by a pair of telescopes.

The concept of coherence is very useful in order to understand the phenomenon of interferometry. If two light wavefronts show the same phase difference, the same wavelength, and the same waveform, they are said to be coherent. Ideally, light interference pattern happens under such condition. For this reason, the Young's double-slit experiment works optimally (to produce interference patterns) using a laser source, a highly coherent light source, since its radiation beam is highly directional, that is, spatially narrow, and also nearly monochromatic. On the other hand, a conventional light bulb works like a highly incoherent source of light since it is composed of a wide range of wavelengths (in the visible region, $\sim 3000\text{-}7000 \text{ \AA}$) and also emitted in many directions away from the source.

For instance, as a thought experiment, imagine raindrops falling on a lake. Here, each raindrop works like a source of (mechanical) waves in the water, and thus, at each point of the lake, the resulting wavefronts are formed by the superposition of all these

3.3. Elementary concepts of OLBI

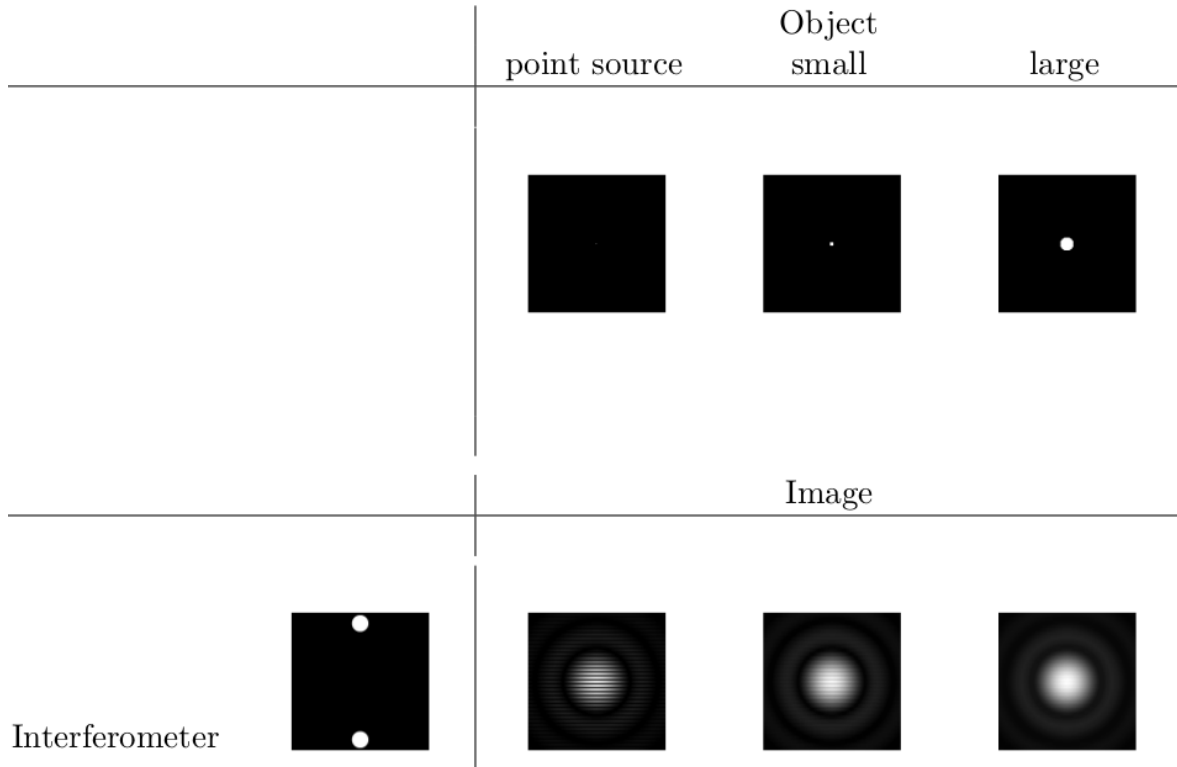


Figure 3.5 – Simulated fringe patterns for objects of different sizes, observed using a two-telescope interferometer. In the first column, we show the ideal case of a completely spatially unresolved source (point source). Note how the contrast of the interferometric fringes changes due to the change on the degree of coherence of the light, between the two telescopes, as the object’s size increases and begins to be resolved by the interferometer. See text for discussion. Adapted from Millour (2014)

wave sources. Since the raindrops reach the lake in a random way, both in space and time, one might expect that the wavefronts, at different points on the lake, are highly uncorrelated, not showing a constant phase difference. In this case, we say that the wave sources are incoherent.

From that, we point out that the concept of coherence works in the domain of space and time. Spatial coherence measures the correlation between the wave phase at different points along the transverse direction of the light propagation, and then stating how uniform is the phase wave. Ideally, a point source produces waves that are perfectly coherent in the spatial domain. Moreover, this means that some level of incoherence is always introduced when we are able to spatially resolve the object (as a star), as the different parts of the (resolved) object begins to work independently, thus incoherent sources of light, lacking a constant phase relationship between the waves emitted by them.

Returning to the Young’s double-slit experiment, interference fringes are lost when the distance between the pinholes are larger than a certain value r_c :

$$r_c = \frac{\lambda}{\theta}, \quad (3.6)$$

3.3. Elementary concepts of OLBI

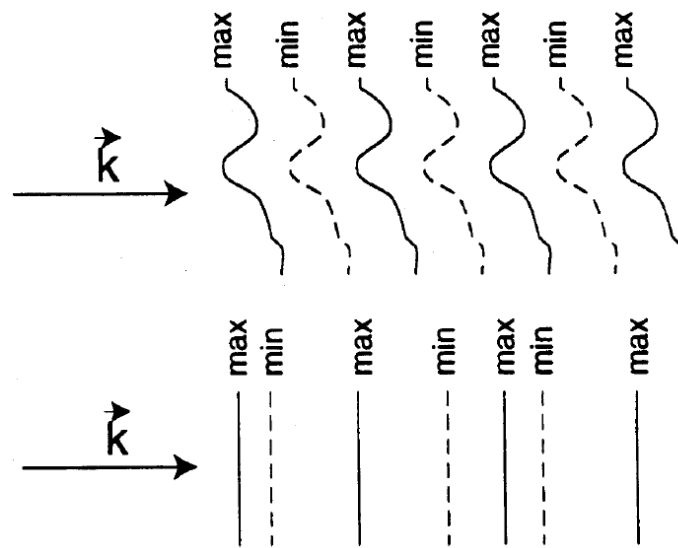


Figure 3.6 – Schematic of two different cases of spatial and temporal coherence. The vector \hat{k} sets the direction of light propagation. In the top, there are shown highly temporally coherent waves, but also highly incoherent in the space domain. In the bottom, the opposite case is illustrated: the waves are highly coherent in the space domain, but highly incoherent in the time domain. Source: <https://www.brown.edu>.

where θ is the angular diameter of the source. This critical value, r_c , is called the coherence distance of the source (e.g., see page 95 of Labeyrie et al. 2006).

As discussed in Sect. 3.2, the implementation of this method, in order to measure stellar diameters, founded the field of stellar interferometry at the end of the 19th century.

In Fig. 3.5, we show simulations of fringe patterns measured by a two-telescope interferometer, for different cases of spatial resolution, a completely unresolved source (i.e., point source), and also other cases with larger objects up to a fully resolved one. One sees here how the fringes are blurry, showing a lower contrast, as the object is resolved, associated to the decrease in the level of coherence of light collected by the two telescopes (due to the increase of the object's size projected onto the sky). Conversely, considering an object with fixed angular size, we are able to measure fringes produced under different degrees of light coherence by varying the baseline length and orientation.

In Sect. 3.3, the Young's double-slit experiment was discussed assuming a monochromatic light source, that is, emitting light described, ideally, by just one given value of wavelength. For sure, this description is quite unrealistic for natural light sources, since most astrophysical objects are indeed polychromatic sources of light, emitting a non-monochromatic wave packet (or also called as wave train).

This fact above is important concerning the concept of coherence since we need to deal now with wavefronts that are composed by multiple frequencies. Temporal coherence measures the correlation between the wave phase at different points in the

3.4. Light coherence

own direction of the light propagation. In Fig. 3.6, we illustrate somewhat extreme cases of coherence: spatially coherent and temporally incoherent waves, and the opposite case, temporally coherent and spatially incoherent waves. Thus, some level of temporal incoherence is always introduced by the polychromatic nature of the light sources because the phase waves are displaced, in the direction of the light propagation, due to the different values of wavelengths that result in the wave packet. In short, the degree of temporal coherence of the source is related to its spectral purity, and, for sure, to the instrumental spectral bandwidth of the observations.

In the practice, polychromatic light can be well described by a spectral band of wavelength width $\Delta\lambda$, centered at a certain value of wavelength λ_0 (the maximum peak of the light intensity). One characteristic time-scale, τ_c , can then be defined in order to allow temporal coherence:

$$\tau_c = \frac{1}{\Delta\nu} = \frac{\lambda_0^2}{c\Delta\lambda}, \quad (3.7)$$

where c is the light speed in vacuum and $\Delta\nu$ is the frequency width corresponding to $\Delta\lambda$.

Physically, this quantity describes the effective oscillation time of a wave packet composed of non-monochromatic light. From that, the length-scale for temporal coherence, l_c , associated to τ_c , is then defined as follows:

$$l_c = c\tau_c = \frac{\lambda_0^2}{\Delta\lambda}, \quad (3.8)$$

being called as the coherence length.

These characteristic scales above are rather important concerning the operation of a interferometer. Looking the parameter l_c , the geometrical delays between the beams, that is, the OPD, must be set to values lower than l_c to allow the occurrence of fringe patterns. This shows the importance of the movable delays lines, discussed above (Fig. 3.4), in order to maintain the optical path difference, that changes with the time, lower than such critical length-scale, during the observations.

3.4 Light coherence

In the following section, we deal with the fundamental interferometric quantities, which are extracted from the measurement of fringes. For that, firstly, a more quantitative description of light coherence is needed. We consider the electric field \vec{E} component of an electromagnetic wave, in 3 dimensions, as follows:

$$\vec{E}(\vec{r}, t) = \vec{E}_0 \exp[i(\vec{k} \cdot \vec{r} - \omega t)]. \quad (3.9)$$

3.4. Light coherence

Here, the position $\vec{r} = x\hat{x} + y\hat{y} + z\hat{z}$, in Cartesian coordinates, $|\vec{E}_0|$ is the amplitude of the electric field, $|\vec{k}| = k = 2\pi/\lambda$ is the wavenumber, $w = 2\pi c/\lambda$ is the angular frequency, that is, $w = ck$, and λ , as usual, is the light wavelength.

The light intensity I , as measured by a detector, is then given by the superposition of the wavefronts coming from different positions \vec{r}_i :

$$I = \left\langle \left\| \sum_i \vec{E}(\vec{r}_i, t - \tau_i) \right\|^2 \right\rangle, \quad (3.10)$$

where τ_i is the delay time of the wavefronts coming from \vec{r}_i , and the use of brackets denotes the temporal average of the electric fields \vec{E} over t . As defined above, for sure, the light intensity is a real number.

The coherence function, $\Gamma_{i,j}$, quantifies the correlation between the light wavefronts \vec{E} received from each pair of positions, denoted by \vec{r}_i and \vec{r}_j , with a delay time τ :

$$\Gamma_{i,j}(\tau) = \left\langle \vec{E}(\vec{r}_i, t - \tau) \vec{E}^*(\vec{r}_j, t) \right\rangle, \quad (3.11)$$

where the use of asterisk denotes the complex conjugate.

Therefore, using Eq. 3.10, the light intensity is expressed as a function of degree of coherence $\Gamma_{i,j}$, as follows:

$$I = \sum_i \Gamma_{i,i}(0) + \sum_{i,j} \left[\Gamma_{i,j}(\tau_i - \tau_j) + \Gamma_{i,j}^*(\tau_i - \tau_j) \right]. \quad (3.12)$$

Considering the simplest case of two wavefronts, received by a single pair of telescopes of an interferometer, denoted here by the indices “1” and “2”, Eq. 3.12 takes the form of:

$$I = I_1 + I_2 + \Gamma_{1,2}(\tau) + \Gamma_{1,2}^*(\tau), \quad (3.13)$$

being the delay $\tau = \tau_i - \tau_j$ from Eq. 3.12. In addition, in this case, the correlation function, Eq. 3.11, can be simplified as:

$$\gamma_{1,2}(\tau) = \frac{\Gamma_{1,2}(\tau)}{\Gamma_{1,1}(0) + \Gamma_{2,2}(0)}. \quad (3.14)$$

Here, the correlation function, $\gamma_{1,2}$, is normalized by the total intensity that is collected by the array of two telescopes: $I_1 + I_2 = \Gamma_{1,1}(0) + \Gamma_{2,2}(0)$.

Lastly, from Eqs. 3.13 and 3.14, the intensity I can be written as follows (considering a 1D interferograph):

$$I(x) = [I_1(x) + I_2(x)][1 + \Re(\gamma_{1,2}(\tau))]. \quad (3.15)$$

3.5 Interferometric quantities

3.5.1 The Zernike-van Cittert theorem

Eq. 3.15 is often called the interferometric equation, that is, describing the interferometric fringe patterns formed by each array of two telescopes.

Taking the real part of the correlation function $\gamma_{1,2}(\tau)$, in the interferometric equation, we have:

$$\Re(\gamma_{1,2}(\tau)) = V \cos\left(\frac{2\pi x}{\lambda} + \phi\right), \quad (3.16)$$

where V denotes the modulus of $\gamma_{1,2}$, $V = |\gamma_{1,2}|$, and ϕ is the phase of $\gamma_{1,2}$. Note that the fringe pattern itself is related to the cosine term in Eq. 3.16.

Typically, the quantity $\gamma_{1,2}$, a complex number, is called as the (normalized) complex visibility, often denoted by \tilde{V} . In a more general way, the complex visibility can be written as follows:

$$\tilde{V}(u, v, \lambda) = |\tilde{V}(u, v, \lambda)| \exp[i\phi(u, v, \lambda)], \quad (3.17)$$

where u and v are the spatial frequencies of the projected baseline (B_{proj}):

$$\frac{B_{\text{proj}}}{\lambda} = \sqrt{u^2 + v^2}. \quad (3.18)$$

First, as written in Eq. 3.17, the complex visibility is explicitly dependent on the observing wavelength. Moreover, note that the spatial frequencies, defining the called uv plan of the observations, are themselves dependent on λ (Eq. 3.18).

The real quantities V and ϕ are the visibility amplitude and visibility phase of the fringe pattern. However, they are often simply called in literature, respectively, visibility and phase, and these terms are also used in the remaining of this thesis.

The discussion above clarifies why we stated, in the previous section, that an interferometer is sensitive to the degree of coherence of the light, which is received by the telescope array. Thus, these are the most fundamental quantities – the visibility and phase – that can be retrieved from the measurement of a fringe pattern using an OLBI.

Concerning the fringe pattern, while the phase is related of the position of the fringes, the visibility is a measurement of the fringe contrast. It was firstly defined by Michelson (1890) as follows:

$$V = |\gamma_{1,2}| = |\tilde{V}| = \frac{I_{\text{max}} - I_{\text{min}}}{I_{\text{max}} + I_{\text{min}}}, \quad (3.19)$$

where I_{max} is the maximum fringe intensity (related to the bright bands) and I_{min} is

3.5. Interferometric quantities

the minimal one (related to the dark bands). Note that, as defined in Eq. 3.19, the visibility is normalized as a function of intensity, ranging between 0 and 1.

Here, the ideal case of $V = 1$ means an object that is fully unresolved by the interferometer, that is, ideally, a monochromatic point source. The other ideal case, $V = 0$, means that the object is fully resolved by the interferometer, and then the interferometric fringes completely disappear. For example, see, again, Fig. 3.5. From that, the visibility of the star is dropping, in the different cases, shown from the left to right panels, as the degree of spatial resolution is increased (in this case, due to the change of the object's angular size on the sky).

Up to this point, it must be clear that the fringe pattern encodes information on the spatial intensity distribution of the object (projected onto the sky). We can say that the essential goal of OLBI is to measure fringes under different degrees of coherence, showing visibilities between the two ideal cases, as described above, in order to obtain finer spatial information on the intensity distribution of the object. However, how could we retrieve such information from the measurement of the complex visibility?

The “ace in the hole” of interferometry is the so-called Zernike-van Cittert theorem (van Cittert 1934; Zernike 1938):

$$\tilde{V}(u,v)_\lambda = \frac{\int \int S(\alpha,\delta)_\lambda \exp[-2i\pi(u\alpha + v\delta)] d\alpha d\delta}{S_\lambda^{\text{total}}}, \quad (3.20)$$

where α and δ are the usual angular coordinates in the sky, and $S(\alpha,\delta)_\lambda$ is the brightness distribution of the source (projected onto the sky).

Thus, the Zernike-van Cittert theorem relates the complex visibility to the Fourier transform of the source brightness distribution. Also note that, in principle, given $\tilde{V}(u,v)_\lambda$, we are thus able to retrieve $S(\alpha,\delta)_\lambda$ from the inverse Fourier transform of $\tilde{V}(u,v)_\lambda$ ¹.

Note that, as defined above, the complex visibility is normalized by the total source brightness:

$$S_\lambda^{\text{total}} = \int \int S(\alpha,\delta)_\lambda d\alpha d\delta. \quad (3.21)$$

As explicitly set in Eq. 3.20, the Zernike-van Cittert theorem works for each value of wavelength. Apart from the dependence on λ from the spatial coordinates u and v in the Fourier plan (Eq. 3.18), $S(\alpha,\delta)$ can be highly dependent on λ , so \tilde{V} must also change with respect to the wavelength. For simplicity, this dependence of the

1. Despite the apparent simplicity of this description, in the practice, it is indeed a hard task to perform an image reconstruction of the observed source, both from an observational and modeling point-of-views. For instance, see Millour et al. (2012), Thiébaud & Young (2017), and references therein.

3.5. Interferometric quantities

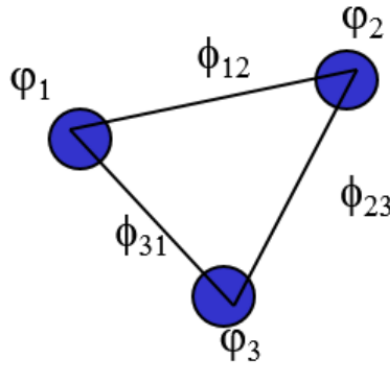


Figure 3.7 – Schematic of a triplet of telescopes used for measuring closure phase. The atmospheric phase, introduced in the fringe measurement, on each telescope, is indicated by ϕ_1 , ϕ_2 , and ϕ_3 . The true phase of the object is also indicated by Φ_{12} , Φ_{23} , and Φ_{31} . See text for discussion. Reproduced from Mourard & Nardetto (2019).

Zernike-van Cittert theorem on the wavelength will be omitted in the remaining of this section.

Besides the own technical issues related to the quality of the fringe measurements, due to instrumental and atmospheric effects, one of the biggest challenges of interferometric studies relies on filling the uv plan in order to retrieve finer spatial information about the object, covering different values of spatial frequencies (in the Fourier domain). This means recording fringes under different degrees of coherence. In practice, this task requires multiple observations performed using different arrays configurations (different baseline lengths and orientations on the sky).

3.5.2 Closure phase

We point out that the true information about the object’s phase is indeed lost, when measuring fringes with ground-based telescopes.

This happens due to the alteration or disturbance of the wavefronts by the atmosphere, as the atmospheric turbulence displaces the received wavefronts, destroying the object phase signal. This is known as the piston effect. Fortunately, it is possible to partially overcome this issue by the measurement of another quantity, the closure phase, which is related to the phase, but measured using different triplets of telescopes (Fig. 3.7).

For this purpose, it is necessary to employ an array composed of at least three telescopes, as indicated in Fig. 3.7. From that, Φ_{12} , Φ_{23} , and Φ_{31} would correspond to the object fringe phases that would be measured by each pair of telescopes without atmospheric effects. The phases that are, in fact, measured by each baseline, denoted here by ψ , are then:

3.5. Interferometric quantities

$$\begin{aligned}
\psi_{12} &= \Phi_{12} + \phi_1 - \phi_2, \\
\psi_{23} &= \Phi_{23} + \phi_2 - \phi_3, \\
\psi_{31} &= \Phi_{31} + \phi_3 - \phi_1,
\end{aligned}
\tag{3.22}$$

where ϕ is the piston effect introduced by the atmospheric turbulence in wavefronts collected by each telescope.

From Eq. 3.22, one sees that the piston effect can be cancelled by the sum of ψ_{12} , ψ_{23} , and ψ_{31} , and thus, defining the closure phase CP :

$$CP = \psi_{12} + \psi_{23} + \psi_{31}, \tag{3.23}$$

that is, a certain triplet configuration is associated to one measurement of closure phase.

This interferometric quantity is important, for example, to the study of circumstellar environments, as it provides information on the amount of asymmetry of the object. Considering that the object is at least partially resolved, the measurement of CP traces the photocenter of the object projected onto the sky (e.g., see Monnier 2003a). For instance, considering a center-symmetric intensity map, as arising from a spherically symmetric outflow, the measured CP would be null (equivalently, equal to -180° or $+180^\circ$). On the other hand, in this case, any departure from a center-symmetric intensity map would result in non-zero closure phases (ranging between -180° and $+180^\circ$). Further details on the mathematical description of closure phases can be found in Monnier (2000) and Monnier (2003a).

3.5.3 Visibility calibration

Concerning the visibility of a certain target, we are able to estimate its true, or absolute, visibility by also observing close stars (in angular size) to the target, in order to overcome atmospheric and instrumental effects, using the called transfer function TF :

$$TF = \frac{V_{\text{obs}}^{\text{cal}}}{V_{\text{true}}^{\text{cal}}}, \quad 0 \leq TF \leq 1, \tag{3.24}$$

where $V_{\text{obs}}^{\text{cal}}$ is the measured visibility of the calibrator star and $V_{\text{true}}^{\text{cal}}$ is its (true) absolute visibility.

The estimation of the true visibility of the target, $V_{\text{true}}^{\text{target}}$, is then given by:

$$V_{\text{true}}^{\text{target}} = \frac{V_{\text{obs}}^{\text{target}}}{TF}, \tag{3.25}$$

where $V_{\text{obs}}^{\text{target}}$ is the measured visibility of the target object.

3.6. Spectro-interferometry

Note that $V_{\text{true}}^{\text{cal}}$ is a prior information to be used in Eq. 3.24. Thus, it is a good practice to select (nearly) unresolved sources, that is, $V_{\text{true}}^{\text{target}} \sim 1$, for a certain interferometric configuration, or with a very accurate determination of angular diameter. To further details on interferometric calibration, we refer the interested reader to Percheron (2008).

3.6 Spectro-interferometry

Spectro-interferometry, also called differential interferometry (Petrov 1989), or self-phase-referencing interferometry (Woillez et al. 2012), means that the measured fringes patterns are dispersed along the spectral dimension using a spectrograph. This technique was first used with the I2T interferometer by Koechlin et al. (1979) to detect differential phase effects on Capella..

In Fig. 3.8, we show the interference fringes of the LBV star η Carinae observed in high spectral resolution mode ($R = 12000$) with the VLTI/AMBER instrument in the K-band ($\sim 2.156\text{-}2.175 \mu\text{m}$, including the Br γ line). One clearly sees how the contrast of the fringes is lower in Br γ (brighter region), that is, showing a lower value of visibility, when compared with the close-by continuum, due to the larger flux contribution from its strong wind in Br γ than in the continuum. Indeed, looking the near-infrared spectrum of η Carinae, one can find a strong and broad Br γ emission-line, indicating then a significant line formation through the wind region (e.g., see Fig. 2 of Weigelt et al. 2007).

It is important to stress that spectro-interferometry enables to access much more information than the one provided by single-band interferometry, but performed sequentially at different spectral bands. Spectro-interferometry introduces new quantities: the differential visibility and differential phase (including here the closure phase).

Considering a narrow region in wavelength, one might expect that the atmospheric effects on the wavefronts are roughly the same. Thus, we are able to retrieve information of the object, in a certain spectral line, relatively to other reference measurement simultaneously observed, at a wavelength close to the line. Usually, the continuum region, close to the line, is chosen as the wavelength of reference in order to calculate the differential quantities (see Fig. 3.9). Nevertheless, this choice can have some caveats, for example, a Be disk can contribute up to 20% of the total continuum emission, being thus relatively significant when compared with the flux contribution from the central star (see, e.g., Stee & de Araujo 1994). In advance of discussion, we stress, however, that this problem does not stand in our study of the Be star σ Aquarii, showing a flux contribution from the disk in the H α close-by continuum of 0 up to 6% (see Table 2 of de Almeida et al. 2020).

3.6. Spectro-interferometry

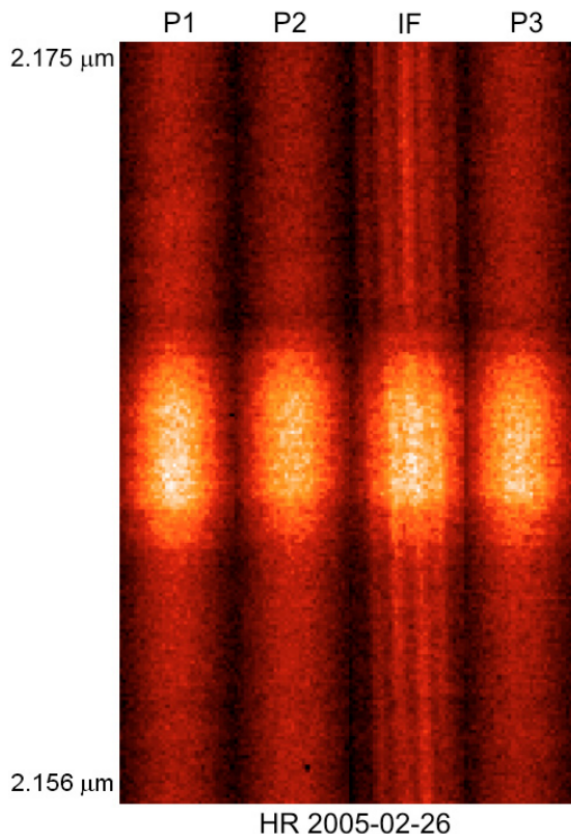


Figure 3.8 – Spectrally dispersed ($\sim 2.156\text{--}2.175\ \mu\text{m}$) fringes of η Carinae measured with VLTI/AMBER in high spectral resolution mode (HR, $R = 12000$) at 26 February 2005. The spectrally dispersed fringe signal is shown in IF, while the photometric calibration signals from the three telescopes are shown from P1 to P3. Note that the bright regions are associated with the Doppler-broadened $\text{Br}\gamma$ emission ($2.166\ \mu\text{m}$). Reproduced from Weigelt et al. (2007).

Furthermore, having measurements of differential visibilities, and also of absolute visibilities (as given by Eq. 3.25), for example, observed at a close-by continuum region to the spectral line, we are thus able to retrieve information on the absolute visibility of the object with spectral resolution.

As pointed out in Sect. 3.1, interferometric observations are needed in order to measure the geometry and extension of the stellar surfaces and their environments. Attempting this task is much harder, or simply impossible, using single-mirror telescopes, being marginally feasible just for the nearer and brighter objects (such as red giants and AGB stars), and using others high angular resolution techniques, as with the instruments of VLT/SPHERE (see, e.g., Kervella et al. 2015; Ohnaka et al. 2016; Khouri et al. 2016). A detailed overview on the SPHERE instruments can be found in Beuzit et al. (2019).

Combining simultaneously the power of spectroscopy and interferometry, spectro-interferometry is one of the most suitable observational methods for the analysis of stellar environments. In addition to information about the spatial distribution of their

3.6. Spectro-interferometry

environments, as provided by non-spectrally-dispersed interferometry, this technique also allows us to probe its kinematics by observing certain spectral lines, for example, as $H\alpha$, $Br\gamma$, and $Br\gamma$. Furthermore, as discussed in Sect. 2.3 (see, again, Table 2.1), these lines are the most sensitive to probe the physical conditions (as the local density that is related to the mass-loss rate) of the atmospheres and environments of massive hot stars.

For example, we show, in Fig. 3.9, three different scenarios for a stellar environment, that is, having different kinematics: a purely-rotation Keplerian disk, a purely-expanding disk (i.e., an equatorial outflow), and a mixed case between these extreme cases. These models are calculated using a kinematic code presented in details in Meiland et al. (2012) and Cochetti et al. (2019). In short, in this case, as shown in Fig. 3.9, the intensity map, representing the flux contribution due to the circumstellar environments is assumed as a simple uniform disk following these kinematics mentioned above. Details on this kinematic code will be properly addressed in Sect. 5.3.

From Fig. 3.9, one sees that the morphology of the observed synthetic line profiles, calculated in $H\alpha$, are very similar among all the different kinematical scenarios, apart from the line wings. Nevertheless, it is important to stress that the $H\alpha$ wings of hot stars, as the Be stars, can be highly affected by non-kinematic line-broadening, as due to non-coherent scattering (e.g., Hummel & Dachs 1992; Delaa et al. 2011). Moreover, the emission line profile will be affected by changing the geometry representing the circumstellar disk in the model, for example, a Gaussian distribution, instead of the simplest case of a uniform disk.

In short, disentangling the kinematics of these environments, only based on spectroscopy, is clearly a difficult task.

In addition to the spectral line profiles, Fig. 3.9 also shows the predicted differential interferometric observables, the differential visibility and phase, in the $H\alpha$ line. Here, two different cases are shown, one for an interferometry baseline aligned along the disk major-axis, and other for baseline perpendicular to the disk major-axis. From that, one clearly sees, due to the ability of spatial resolution, how both the differential visibility and phase are sensitive to different considered kinematics, and to the different baseline configuration with respect to the object. For instance, considering the interferometer baseline perfectly aligned along the disk major-axis (purely-expanding disk case, middle panel of Fig. 3.9) results in null value of phase since the projected velocity of the envelope is null through all the disk extension, being then the photocenter of the object unshifted in the sky regardless the value of wavelength.

3.6. Spectro-interferometry

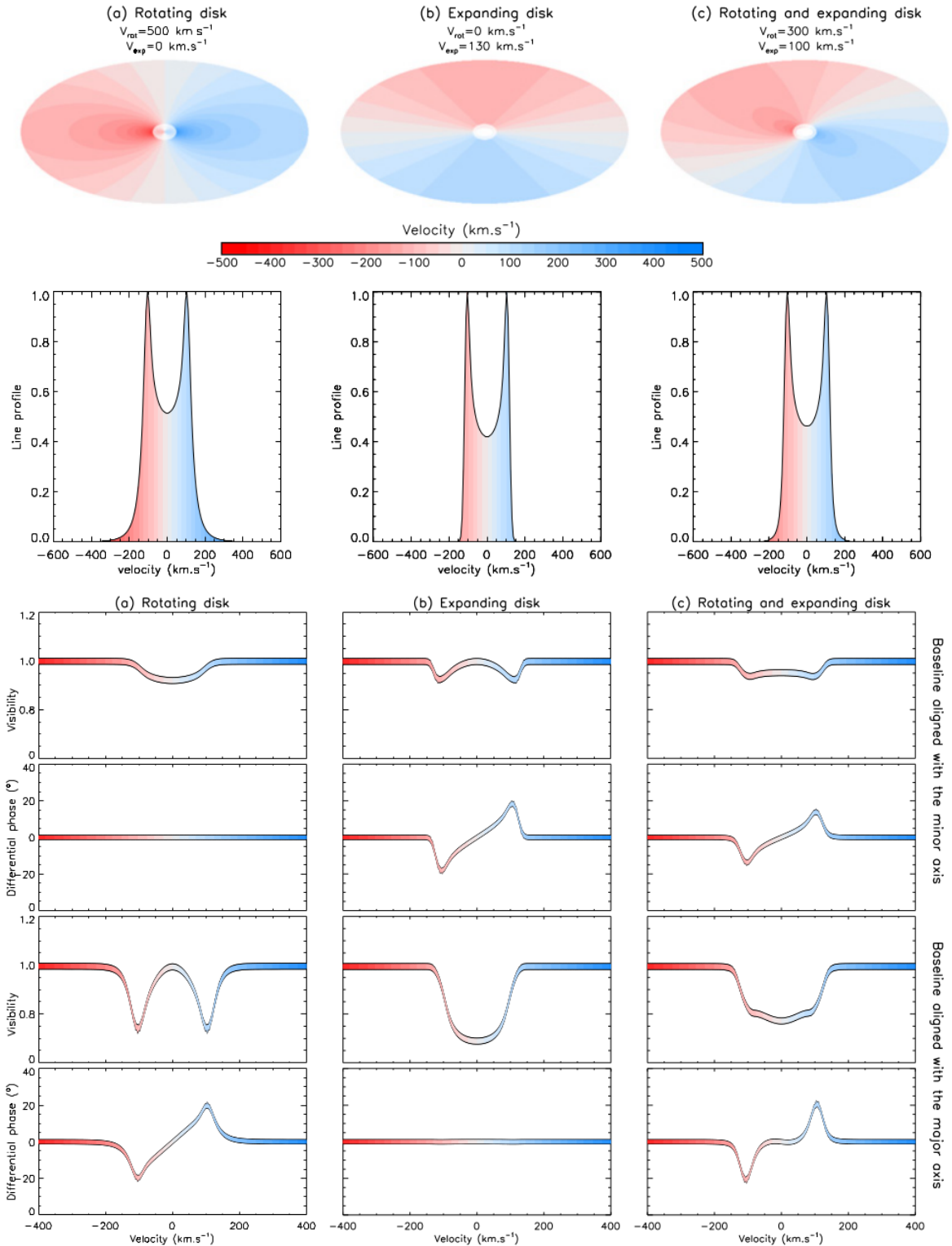


Figure 3.9 – Different scenarios for the kinematics of a circumstellar disk, calculated using a kinematic model: purely-rotating disk, purely-expanding disk, and a hybrid case, respectively, from the left to the right panels. The top panels show the iso-velocity maps for these different models. For each one of these models, the synthetic H α line profile is shown in the second row. The synthetic differential interferometric quantities, the visibility and phase, are also shown, but for two extreme cases of interferometer baseline alignment, with respect to the circumstellar disk major-axis. See text for discussion. Reproduced from Meilland & Stee (2014).

3.7. Spectro-interferometric instruments

Table 3.2 – Summary of telescope arrays with spectro-interferometric instruments. Adapted from Hadjara (2017).

Array	Location	Year	N ^o of telescopes	B_{\max} (m)	λ (μm)
NPOI ^a	Anderson Mesa (USA)	1994–	6	435	0.45-0.85 (B-I)
CHARA ^b	Mount Wilson (USA)	2001–	6	331	0.45-2.50 (B-K)
VLTI ^c	Cerro Paranal (Chile)	2001–	4	202	1.2-13.0 (J-N)
ISI ^d	Mount Wilson (USA)	1988–	3	70	8-13 (N)
SUSI ^e	Narrabri (Australia)	1991–	2	640	0.4-0.9 (B-I)
†PTI ^f	Mount Palomar (USA)	1995–2008	2	110	1.5-2.4 (H-K)
†KECK-I ^g	Mauna Kea (USA)	2003-2012	2	85	2.2-10.0 (K-N)

^a Navy Precision Optical Interferometer.

^b Center for High Angular Resolution Astronomy.

^c Very Large Telescope Interferometer.

^d Berkeley Infrared Spatial Interferometer.

^e Sydney University Stellar Interferometer.

^f Palomar Testbed Interferometer.

^g Keck Interferometer.

† Discontinued.

3.7 Spectro-interferometric instruments

Table 3.2 summarizes the current (and recently discontinued) observational facilities with high spectral resolution spectro-interferometric instruments. In addition to their location and operating date, the number of telescope configuration, maximum baseline length, and the wavelength range (and the corresponding photometric bands) are also shown here. In particular, we point out that the CHARA and VLTI Arrays host the current state-of-the-art spectro-interferometric instruments.

In the following sections, we briefly describe some of the instruments hosted on these arrays, in particular, the CHARA/VEGA and VLTI/AMBER spectro-interferometric instruments, since large sets of data observed with these instruments are analysed in this thesis (Sect. 6.3).

3.7.1 The CHARA array

The Center for High Angular Resolution Astronomy (CHARA²) is an optical-interferometric array, owned by Georgia State University, located at Mount Wilson Observatory, California (USA).

CHARA is composed of six 1-m class telescopes, forming a Y-shape array, as shown in Fig. 3.10, in order to optimize the uv plan coverage. The light from the telescopes are sent through vacuum pipes to a recombining laboratory equipped with fixed and movable delay lines. In total, there are 15 different baseline configurations, formed by

2. <http://www.chara.gsu.edu/>

3.7. Spectro-interferometric instruments

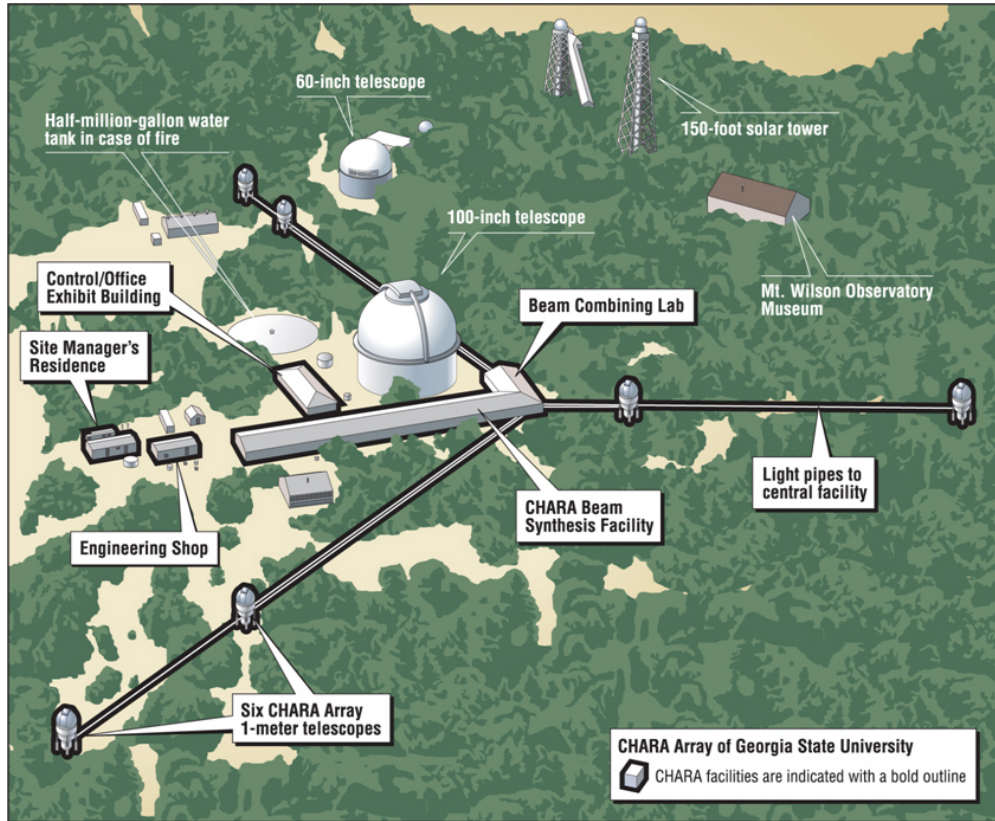


Figure 3.10 – Schematic layout of the CHARA Array, installed on the Mount Wilson Observatory (California, USA). Source: <http://www.chara.gsu.edu/>.

each pair of two telescopes, being the S2-S1 configuration the shortest with ~ 34 m, while E2-S1 is the largest one with ~ 331 m (see the maximum baseline length in Table 3.2). A full list describing the CHARA baseline configuration can be found in Table 1 of ten Brummelaar et al. (2005). Further technical details on the elements composing the CHARA Array also are described in ten Brummelaar et al. (2005).

Currently, six spectro-interferometric are working at CHARA, operating in the near-infrared or in visible region, namely:

- (i) CLASSIC and CLIMB: JHK-bands (Ten Brummelaar et al. 2013)
- (ii) JouFLU³: K-band (Coudé du Foresto et al. 2003; Scott et al. 2013)
- (iii) MIRC-X⁴: JH-bands (Monnier et al. 2004; Anugu et al. 2018)
- (iv) PAVO⁵: 6300-9500 Å (Ireland et al. 2008)

3. Acronym for “Jouvence of FLUOR”, being the Fiber Linked Unit for Optical Recombination (FLUOR) an older near-infrared instrument (see references above).

4. An upgrade of the Michigan Infrared Combiner (MIRC) instrument (see references above).

5. Acronym for “Precision Astronomical Visible Observations”.

3.7. Spectro-interferometric instruments

(v) VEGA⁶: 4800-8500 Å (Mourard et al. 2009)

Jointly, these instruments were used, from 2005 to date, in about 90 refereed articles, ranging from the study of circumstellar disks in low and massive stars up to the characterization of exoplanets.

Among other on-going instrumental projects, we point out the Fibered spectrally Resolved Interferometer – New Design (FRIEND) instrument, a new visible beam-combiner, covering the spectral interval of $\sim 6200\text{-}8500$ Å (Martinod et al. 2018). This spectro-interferometric instrument was designed to overcome certain limitations of the VEGA instrument, as unreliable estimations of closure phase (see, e.g., Mourard et al. 2012). It was mainly a test instrument for the future six-telescope visible combiner SPICA at CHARA (Mourard et al. 2017).

3.7.2 CHARA/VEGA

Despite these limitations, VEGA (Visible spEctroGraph and polArimeter, Mourard et al. 2009) is a unique instrument with respect to the capability of combining both high spatial resolution (up to $\sim 0.3\text{mas}$) and high spectral resolution (up to $R = 30000$ in the high resolution mode) in the visible domain. Currently, VEGA can combine simultaneously up to four beams operating at different wavelengths from 4500 Å to 8500 Å, that is, including the H α line, being particularly important to perform spectro-interferometric studies of massive hot stars and their environments. As a non-exhaustive list of works on these objects, based on VEGA observations, see Chesneau et al. (2010), Meilland et al. (2011), Delaa et al. (2011), Stee et al. (2012), and Mourard et al. (2015), for example⁷.

Together with PAVO, mentioned above, VEGA is one of the two visible spectro-interferometric instruments on CHARA. One clear advantage of VEGA, with respect to PAVO ($R = 30$), relies on its high instrumental spectral resolution (R). To date, it is the only instrument operating at CHARA with a spectral resolution high enough to resolve narrow spectral features such as atomic and molecular lines, in short, offering three spectral modes: $R = 1000$ (LR, low resolution mode), $R = 6000$ (MR, medium resolution mode), and $R = 30000$ (HR, high resolution mode).

3.7.3 The VLTI array

The Very Large Telescope Interferometer (VLTI) is the interferometric mode of the Very Large Telescope (VLT), located at Cerro Paranal Observatory in the Atacama

6. Acronym for “Visible spEctroGraph and polArimeter”.

7. A full list of refereed articles, using the VEGA instrument, can be found in the web-site: <https://www.oca.eu/fr/publications-vega>.

3.7. Spectro-interferometric instruments



Figure 3.11 – Aerial view of the Very Large Telescope’s observing platform, installed at the Cerro Paranal Observatory (Atacama desert, Chile). The 4 fixed 8-m telescopes and the 4 movable 1.8-m telescopes are shown here. Source: <https://www.eso.org/>.

desert. It is owned by the European Southern Observatory (ESO), an intergovernmental consortium, founded on 1962, actually composed of 16 state-members⁸. Fig. 3.11 shows an aerial view of the ESO/VLT facility. The interested reader can see Blaauw (1991) for a historical overview of ESO.

Despite the initial objection, during the 1970’s, of the astronomical community to the implementation of a large interferometric facility, the same was rapidly encouraged by successful works with optical long-baseline interferometers in the 1980’s, for example, as with the GI2T (Plateau de Calern, France), a direct upgrade from the pioneer I2T interferometer. As pointed in Sect. 3.2, the GI2T was the first interferometric facility used to successfully probe the circumstellar environments of hot stars. In short, ESO approved the construction of the VLT project, also including a interferometric model (VLTI), in 1987 (see Sect. 5 of Léna 2014).

The VLTI Array is composed of four fixed 8.2-m telescopes, called as Unit Telescopes (UTs), in addition to four movable 1.8-m telescopes, called as Auxiliary Telescopes (ATs). A layout of the VLTI baselines is shown in Fig 3.12. The shortest baseline configuration (B0-C0) has about 8 m, while the largest one has about 202 m (B5-J6). One clear advantage of employing movable telescopes for interferometry is to increase the number

8. Further details can be found in <https://www.eso.org/public/about-eso/memberstates/>.

3.7. Spectro-interferometric instruments

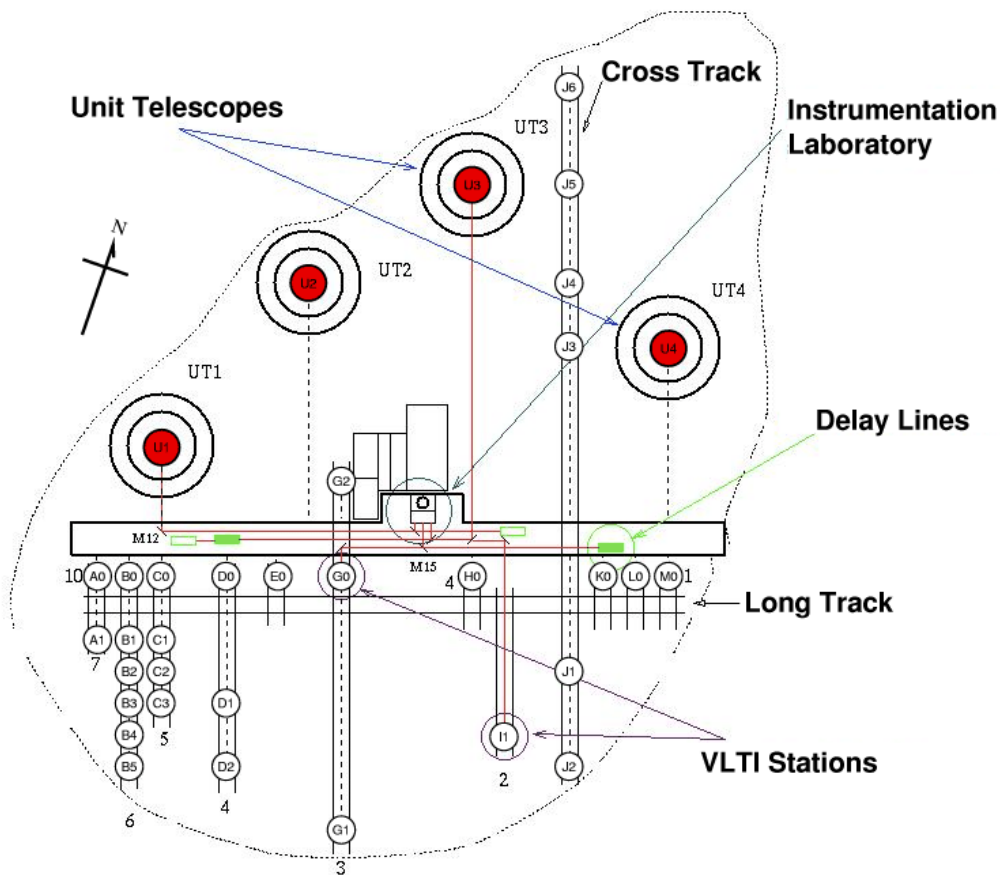


Figure 3.12 – Schematic layout of the VLTI Array. The Unit Telescopes (UT) are indicated in red, fixed 8-m telescopes, with stations named from U1 to U4. The possible positions of the Auxiliary Telescopes (AT), 1.8-m telescopes, have stations named from A0 to M0. Source: <https://www.eso.org/>.

of possible baseline configurations, reaching up to 518 different configurations with VLTI in total. Then the ability of covering the uv plan is drastically improved in this case, when compared with facilities using fixed telescopes as CHARA. A complete list of the baselines on VLTI can be found in the web-site for the “VLTI Station Position Technical Data”, hosted by ESO: <https://www.eso.org/observing/etc/doc/viscalc/vltistations.html>.

The VINCI beam-combiner started to be built in 1998 and it was the first VLTI instrument measuring interference fringes in 2001, in the near-infrared (K-band). This was an instrument designed to test and tune the performance of the VLTI Array (see, e.g., Kervella et al. 2000; Glindemann et al. 2002). Despite being essentially a test instrument for VLTI, observations with VINCI resulted in a significant number of studies. Regarding the photosphere and environments of hot stars, for example, see Domiciano de Souza et al. (2003), Domiciano de Souza et al. (2005), Kervella (2007).

From that, followed the instruments MIDI (mid-infrared, N-band) in 2003 and AMBER (JHK-bands, Petrov et al. 2007) in 2004. They are called as the VLTI first generation of interferometric instruments. For a summary of their characteristics,

3.7. Spectro-interferometric instruments

for example, see Table 2 of Richichi & Percheron (2005). The VLTI second generation is composed by GRAVITY (K-band, Gravity Collaboration et al. 2017) and MATISSE (LMN-bands, Lopez et al. 2014) instruments, with first light very recently in 2016 and 2018, respectively.

In summary, these instruments were employed in a large number works, to date, up to about 460 referee articles in total. From them, just PIONIER⁹, GRAVITY, and MATISSE are still working, being the others decommissioned. Also, note that all the instruments installed on VLTI operate, or operated, in the near-infrared (JHK-bands), such as AMBER and GRAVITY, or longer wavelengths up to the mid-infrared region, such as MATISSE (LMN-bands) and MIDI (N-band).

In addition to these references above, as a non-exhaustive list of work on hot stars with VLTI instruments, we also refer the reader to Meilland et al. (2007b), Meilland et al. (2007a), Domiciano de Souza et al. (2007), Meilland et al. (2012), Weigelt et al. (2016), and Cochetti et al. (2019), being all these latter ones based on VLTI/AMBER observations.

3.7.4 VLTI/AMBER

The Astronomical Multi-BEam combineR (AMBER, Petrov et al. 2007) was a three beam combiner operating in the H- and K-bands, with three spectral resolution models: $R = 35$ (LR), $R = 1500$ (MR), and $R = 12000$ (HR). It was the instrument installed at VLTI offering the highest spectral resolution thanks to its HR mode, and thus the most adapted to study gaseous circumstellar environment in emission lines.

Despite being a decommissioned instrument, by the end of 2017, a large number of observations performed with AMBER are still used in very recent works about circumstellar environments (e.g., Koutoulaki et al. 2018; Cochetti et al. 2019; Adam & Ohnaka 2019; Ohnaka et al. 2019; Hadjara et al. 2019), and it yielded the largest number of articles among the VLTI instruments to date.

3.7.5 Comparison between CHARA and VLTI

With respect to CHARA (Sect. 3.7.1), we point that one caveat of VLTI (Sect. 3.7.3) relies on its shorter maximum baseline length, of about 202 m, allowing us to reach lower angular resolutions than the ones with the CHARA Array (baselines up to ~ 331 m). Furthermore, currently, there are no spectro-interferometric instrument, operating at the visible region, installed on the VLTI Array. As discussed above, to date, all the VLTI instruments work from the near- to the mid-infrared region. For instance, see

9. It is a 4-telescope visitor spectro-interferometric instrument at VLTI (H-band, Le Bouquin et al. 2011), constituting a gap between the first and second VLTI generations.

the interesting science cases pointed out by Millour et al. (2018) for a future visible spectro-interferometric instrument on VLTI.

On the other hand, VLTI offers larger (1.8-m and 8-m mirror), and also movable telescopes, instead of the 1-m fixed telescopes on CHARA. As pointed out above, the usage of the movable auxiliary telescopes of VLTI allows us to reach up to 518 different baseline configurations, instead of the 15 baselines with CHARA. For sure, this results in a better coverage of the uv plane. In addition, VLTI has shorter baselines, of about 8m, the ones on CHARA, of about 34 m, and then mapping smaller spatial frequencies in the Fourier space.

In conclusion, the spectro-interferometric instruments currently mounted on CHARA and VLTI are thus complementary in order to perform more detailed interferometric studies on hot stars, in the framework of a multi-wavelength approach, covering both the visible and the near-infrared regions, at different levels of angular resolution. This complementary task, relying both on CHARA and VLTI observations, is part of the objective of this thesis, when studying the surface and environment of the Be star α Aquarii (Sect. 6.3).

Chapter 4

Radiative transfer modeling

Contents

4.1	Elementary concepts of radiative transfer	102
4.2	Overview on radiative transfer codes for hot stars	108
4.3	The code CMFGEN	110
4.4	The code HDUST and the BeAtlas grid	116
4.5	For what CMFGEN and HDUST are suited?	120
4.6	Computational cost of physical models	121

4.1 Elementary concepts of radiative transfer

Stellar radiation flux contains information on the physics and chemistry of the matter composing the photosphere and the circumstellar environment, as the emergent radiation field results from the interaction of the photons with both of them. The goal of radiative transfer modeling is to explain such radiation field in terms of (almost) fundamental parameters, for the photosphere, such as the stellar luminosity, effective temperature, surface gravity, and for the circumstellar environment, such as the mass-loss rate, the density, and the velocity field.

This is usually a hard task to be performed. As result of the interaction photon-particle, both the radiation and gas fields are modified in the end, being thus a coupled problem to be solved. This means that, in order to predict, as precisely as possible, the stellar radiation, a stellar atmosphere model must also describe the state of the gas, that is, to know how are distributed the atoms over bound and free states, and thus requiring knowledge on the thermodynamics and hydrodynamics of the gas.

Before setting the radiative transfer problem itself, some quantities of interest are discussed in the following. The specific (or also called monochromatic) intensity is defined as follows:

4.1. Elementary concepts of radiative transfer

$$I_\nu = \frac{dE_\nu}{dA dt d\Omega d\nu}, \quad (4.1)$$

and thus describing the amount of energy dE going through an surface dA from light beams with frequency ranging between ν and $\nu + d\nu$, forming an solid angle $d\Omega$, per unit time dt . Besides the own dependence on the light's frequency, also note that the intensity depends on the spatial direction due to the dependence on the solid angle.

Another very useful related quantity is the specific flux F_ν :

$$F_\nu = \int_0^{2\pi} \int_0^\pi I_\nu(\theta, \phi) \cos \theta \sin \theta d\theta d\phi, \quad (4.2)$$

where θ and ϕ are the usual spherical coordinates. This is the net amount of energy that is emitted by the star at the frequency ν .

Formally, the radiative flux comes from the moments of the specific intensity:

$$M_\nu^n = \frac{1}{2} \int_{-1}^{+1} I_\nu \mu^n d\mu, \quad (4.3)$$

where M_ν^n is the moment of n-th order and $\mu = \cos \theta$ (Fig. 4.1). The so-called Eddington Flux, H_ν , is then derived from first moment of the intensity (M_ν^1):

$$H_\nu = \frac{1}{2} \int_{-1}^{+1} I_\nu \mu d\mu, \quad (4.4)$$

and is related to the specific flux (Eq. 4.2) by:

$$F_\nu = 4\pi H_\nu. \quad (4.5)$$

Another very useful quantity, which is used for solving the radiative transfer problem (e.g., see Eq. 2 of Hillier & Miller 1998), is derived from the zero-order intensity moment (M_ν^0):

$$J_\nu = \frac{1}{2} \int_{-1}^{+1} I_\nu d\mu, \quad (4.6)$$

being J_ν the mean intensity, at a certain position and wavelength, evaluated over all the directions.

Note that the spatial information – how the energy flow is angularly distributed (θ, ϕ) – is lost in the definition of flux, in Eq. 4.2, when compared with Eq. 4.1, due to the integration on solid angle. This means that the flux is the most natural quantity to be addressed by (unresolved) spectroscopy, being this the case for stars, while interferometry is sensible to the intensity distribution of the star (across the sky).

Furthermore, unlike the intensity, the flux is dependent on the distance to the source. Thus, by the energy conservation and the Stefan-Boltzmann theorem (Eq. 1.18):

4.1. Elementary concepts of radiative transfer

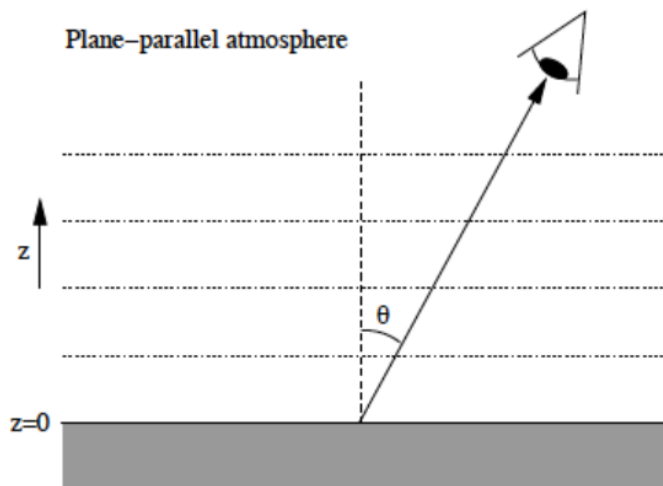


Figure 4.1 – Schematic of a plane-parallel geometry. The position is set by the distance z and the angle θ that is formed between the normal vector (vertical dashed line) to the surface of the stellar atmosphere and the light array propagation (toward an observer).

$$L_{\star} = 4\pi R_{\star}^2 F = 4\pi d^2 F_{\text{obs}},$$

$$F_{\text{obs}} = \left(\frac{R_{\star}}{d}\right)^2 F, \quad (4.7)$$

where, as usual, L_{\star} and R_{\star} are the stellar bolometric luminosity and radius, F is the emergent flux at the stellar surface, and F_{obs} the observed flux at the distance d to the star.

In Eq. 4.7, since we are dealing with the bolometric luminosity L_{\star} , the flux quantities are integrated in frequency:

$$F = \int_0^{\infty} F_{\nu} d\nu. \quad (4.8)$$

In the most general form, the equation of radiative transfer can be expressed as follows (see Eq. 26 in Chap. 2 of Mihalas 1978):

$$\frac{1}{c} \frac{\partial I_{\nu}}{\partial t} + \vec{\nabla} \cdot (I_{\nu} \vec{n}) = \eta_{\nu} - \chi_{\nu} I_{\nu}, \quad (4.9)$$

where \vec{n} is the vector setting the position where the radiative field is evaluated.

The quantities η_{ν} and χ_{ν} are the emission and the absorption coefficients, respectively. These coefficients share a common origin, in the way that they are related to Eq. 4.1, but stating, respectively, the quantity of energy that is added or removed to a light beam through the medium. Note that they are themselves dependent on the

4.1. Elementary concepts of radiative transfer

frequency.

The emission coefficient η_ν is defined as follows:

$$dE_\nu = \eta_\nu dV d\Omega d\nu dt, \quad (4.10)$$

having dimensions of $\text{erg cm}^{-3} \text{sr}^{-1} \text{Hz}^{-1} \text{s}^{-1}$ (CGS system).

The absorption coefficient χ_ν is given by:

$$dI_\nu = -\chi_\nu I_\nu ds, \quad (4.11)$$

where ds is the distance travelled by the light beam, and χ_ν has dimension of cm^{-1} in the CGS system. Usually the absorption coefficient is also called as the opacity of the medium. One useful quantity, related to the absorption coefficient, is the mean free path:

$$l_\nu = \frac{1}{\chi_\nu}. \quad (4.12)$$

Eq. 4.12 sets the typically distance that a photon travels (freely) within consecutive processes of interaction with the gas particles of the atmosphere.

In addition, another important quantity, but related to the opacity χ_ν of the medium, is the optical depth τ_ν :

$$\tau_\nu = \int_0^s \chi_\nu ds', \quad (4.13)$$

being evaluated through a distance s . This quantity is useful as it depends both of the distance length travelled by the light and of the medium opacity. When $\tau_\nu \gg 1$, the medium is said to be optically thick (at a certain value of frequency), while a optically thin medium has $\tau_\nu \ll 1$.

We are able to simplify the radiative transfer equation (Eq. 4.9) considering the case of a stationary atmosphere, and thus assuming that:

$$\frac{\partial I_\nu}{\partial t} = 0. \quad (4.14)$$

Furthermore, other important simplification is provided when assuming a plane-parallel geometry for the atmosphere. Fig. 4.1 shows a schematic of a plane-parallel geometry. The atmosphere is composed of parallel planes and a constant value θ , which is formed between the light ray (seen toward the observed) and the normal to the surface of the atmosphere. Considering the usual Cartesian coordinates, and following the schematic of Fig. 4.1, we thus have:

4.1. Elementary concepts of radiative transfer

$$\frac{\partial I_\nu}{\partial x} = \frac{\partial I_\nu}{\partial y} = 0, \quad (4.15)$$

and

$$\vec{n}_z \cdot \vec{n} = \cos \theta = \mu. \quad (4.16)$$

This means that, for a certain direction (given by $\cos \theta$), the solution of the radiative transfer equation is dependent only of the variable z . Then the left hand of Eq. 4.9 is simplified to:

$$\mu \frac{dI_\nu}{dz} = \eta_\nu - \chi_\nu I_\nu. \quad (4.17)$$

Usually the radiative transfer equation is expressed as a function of the optical depth. For that, it is introduced the called source function, S_ν , defined in terms of the emission and absorption coefficients, as follows:

$$S_\nu = \frac{\eta_\nu}{\chi_\nu}. \quad (4.18)$$

Physically, the source function can be interpreted as the amount of energy emitted along a photon mean free path (Eq. 4.12).

From Eq. 4.13, we have that:

$$d\tau_\nu = \chi_\nu ds, \quad (4.19)$$

being $s = z/\mu$

Thus, from Eqs. 4.18 and 4.19, the equation of radiative transfer for the stationary and plane-parallel case is then reformulated as follows (Eq. 1.27 of Rybicki & Lightman 1986):

$$\frac{dI_\nu}{d\tau_\nu} = S_\nu - I_\nu, \quad (4.20)$$

being $I_\nu = I_\nu(\tau_\nu, \theta)$.

Consider that the light array travels through the atmosphere from a optical depth τ_2 to τ_1 , being $\tau_2 > \tau_1$ ¹. Thus, the formal solution of Eq. 4.20 is given as follows:

$$I_\nu(\tau_1, \mu) = I_\nu(\tau_2, \mu) \exp [-(\tau_2 - \tau_1)/\mu] + \frac{1}{\mu} \int_{\tau_1}^{\tau_2} S_\nu(\tau_\nu) \exp [-(\tau'_\nu - \tau_1)/\mu] d\tau'_\nu. \quad (4.21)$$

Note that the solution provided by Eq. 4.21 is not valid for an extended atmosphere,

1. For simplicity, when specifying a certain value of optical depth, we remove the ν index, but we keep using this index when expressing the variable (τ_ν).

4.1. Elementary concepts of radiative transfer

as formed by winds and disks on massive hot stars, having an extension much larger than R_\star (up to 10^1 - $10^2 R_\star$). However, it is a good approximation to model the photosphere (hydrostatic region) since its extension is very small in comparison with R_\star . As will be latter discussed (Sect. 4.2), atmosphere models for hot stars must solve the equation of radiative transfer using a spherical geometry, instead of plane-parallel geometry, in order to be able to explain the line-formation in the circumstellar envelope.

Also note that, as formulated in Eq. 4.20, the solution for the radiative transfer problem is specified by knowing the source function $S_\nu(\tau_\nu)$. In this case, one important simplification is provided in terms of the so-called hypothesis of local thermodynamic equilibrium (LTE).

In LTE, we assume that the source function, at any point of the atmosphere, is given by the Planck distribution $B_\nu(T(\tau_\nu))$:

$$S_\nu(\tau_\nu) = B_\nu(T(\tau_\nu)) = \frac{2h\nu^3}{c^2} \frac{1}{\exp[h\nu/k_B T] - 1}, \quad (4.22)$$

being k_B the constant Boltzmann and T the (local) temperature in the atmosphere.

As stated above, $T = T(\tau_\nu)$, that is, this assumption works locally in the atmosphere, being valid at each point in the atmosphere. It does not states that the entire extension of atmosphere is modeled as having a unique value of temperature. Quite the contrary, in general, the temperature decreases outwards the photosphere. Indeed, as shown in Eq. 1.52 (LTE case), the radiative flux is dependent on the radial gradient of the temperature.

In the end, one sees how this latter hypothesis simplifies the solution of the radiative transfer problem. From Eq. 4.22, the source function (at a certain depth point) only depends on temperature. Thus, by knowing the temperature structure of the atmosphere, Eq. 4.21 can be solved. This means that the state of the gas is set by the Maxwell-Boltzmann and Saha distributions, described, locally, by a single value of temperature. The LTE approximation works well when the gas density of the atmosphere is high enough, meaning a larger opacity, and then a shorter mean free path of the gas particles and photons. In good approximation, this physical condition ensures that both the radiation and gas fields share, locally, the same value of temperature (holding for the Planck, Maxwell-Boltzmann, and Saha distributions).

For instance, LTE is a reasonable approach to model the solar photosphere: it is well-known that a LTE radiative transfer modeling is able to reproduce well the solar spectrum (e.g., Holweger 1967; Kurucz 1991, 2005). Nevertheless, even regarding the solar spectrum, a non-LTE approach is mandatory for the analysis of certain spectral lines, being particularly important for accurate determinations of chemical abundances (e.g., see Grevesse et al. 2010, 2012; Amarsi et al. 2020, and references

4.2. Overview on radiative transfer codes for hot stars

therein).

However, it is a complete different scenario when dealing with the atmospheres of massive hot stars. Even considering the photospheric region, these stars have much lower values of mass density, when compared with main sequence low-mass stars, such as the Sun.

For instance, massive O-type stars have $M_{\text{ZAMS}} \gtrsim 8 M_{\odot}$, but, at the same, radius much larger than the Sun, up to $14 R_{\odot}$ (for a O3 dwarf, Table 1.1). As a very crude estimation, the mass density is linearly proportional to the mass, but inversely proportional to the cube of the radius. Thus, following this approximation, the density in the photosphere of a O3 dwarf is lower by a factor of 10^2 than the solar case. In this case, LTE is a very bad hypothesis to model the photosphere, as the radiative processes begins to be more important than the collisional processes in the transport of energy. Furthermore, the winds and disks around these stars also can not be modelled under LTE, as the density quickly drops in the extended atmosphere in comparison with the hydrostatic region (photosphere).

In conclusion, the radiative transfer problem for massive hot stars must be treated, both for the photosphere and extended atmosphere, without the assumption of LTE, that is, requiring a non-LTE treatment. This means that the equation describing the radiation field and the state of the gas must be treated simultaneously. Despite being valid for the particular case of plane-parallel geometry, one sees, from Eq. 4.20, that the radiative transfer problem itself is dependent on the state of the gas (that affects the source function). On the other hand, the LTE approximation makes the source function equal to a very simple expression (Eq. 4.22).

In the following section, we discuss the principal atmosphere model codes for massive hot stars.

4.2 Overview on radiative transfer codes for hot stars

Non-LTE radiative transfer modeling is a central part of this thesis, allowing us to perform a quantitative analysis of both spectroscopic and (spectro-)interferometric data, in terms of fundamental parameters of the photosphere and the circumstellar environment. Despite being widely used for spectroscopic analysis, the use of radiative transfer codes, such as CMFGEN and HDUST, to interpret multi-wavelength spectro-interferometric observations is however still somewhat scarce and quite recent in the literature (e.g., Meilland et al. 2007b,a; Domiciano de Souza et al. 2004, 2005; Chesneau et al. 2010, 2012).

4.2. Overview on radiative transfer codes for hot stars

Table 4.1 – Summary of basic characteristics of non-LTE and line-blanketed radiative transfer codes for modeling massive hot stars. Adapted from Chap. 5 of Crivellari et al. (2019)

Code	Geometry	Line-blanketing	Radiative transfer	Temperature structure	Wavelength range	Major application	Execution time	Comments	Basic references
TLUSTY	Plane-parallel	Yes	Observer's frame	Radiative equilibrium	No limitations	Hot stars with negligible winds	Hours	No winds	Hubeny & Lanz (1995)
CMFGEN	Spherical	Yes	CMF	Radiative equilibrium	No limitations	OBA-stars, WR, CSPN, SNe	Hours	Start model required	Hillier & Miller (1998)
PoWR	Spherical	Yes	CMF	Radiative equilibrium	No limitations	WR, O-stars	Hours	—	Gräfener et al. (2002)
FASTWIND	Spherical	Approx.	CMF and Sobolev approx.	e ⁻ thermal balance	Visible and IR	OB-stars, early A-sgs	Up to 0.5h	User-specified atomic models	Puls et al. (2005)
WM-basic	Spherical	Yes	Sobolev approx.	e ⁻ thermal balance	UV	Hot stars with dense winds, SNe	1-2h	No clumping	Pauldrach et al. (2001)

This modern and physically consistent methodology was also employed in this thesis, combining both spectroscopic and interferometric observations to extract the physical properties of the photospheres of hot stars and their circumstellar environments. I worked using radiative transfer models on all the topics of this thesis. I used a pre-calculated grid of HDUST models to interpret multi-wavelength spectro-interferometric data (CHARA/VEGA and VLTI/AMBER data) of the Be star *o* Aquarii (Sect. 6.3). In addition, I worked using the code CMFGEN to perform a detailed multi-wavelength (UV and visible) spectroscopic modeling of O-type stars (Sect. 6.1), and also, when collaborating to model recent H α intensity interferometry measurements of P Cygni (Sect. 6.2). A detailed discussion on CMFGEN and HDUST (and the BeAtlas grid) are provided in Sect 4.3 and 4.4.

Nevertheless, we stress that other radiative transfer codes are used in the literature for the analysis of hot stars. For instance, the code Postdam Wolf-Rayet (PoWR, Sect. 1.2.2) provides a similar treatment to the one by CMFGEN (Table 4.1), being also well suited to model the extended atmosphere of hot and massive stars, such as O-type and Wolf-Rayet stars (see, e.g., Hamann et al. 2008; Maryeva & Abolmasov 2012, and references therein). In comparison with HDUST, the code BEDISK (Sigut & Jones 2007), and its complementary code BERAY (Sigut 2011), also have been employed to investigate the physical properties of Be star disks (e.g., Halonen et al. 2010; Arcos et al. 2018; Sigut 2018).

In advance of discussion, HDUST is not included, in Table 4.1, since it provides a statistical method for solving the radiative transfer equation, jointly to the radiative and statistical equilibrium equations. In addition, to date, HDUST provides a fully hydrogen composition (for gaseous environments), and then not taking into account line-blanketing effects due to heavy elements (which are discussed in the next section).

Table 4.1 provides a global picture of state-of-the-art non-LTE line-blanketed radia-

4.3. The code CMFGEN

tive transfer codes, which are used for the analysis of hot massive stars. From Table 4.1, TLUSTY (Hubeny & Lanz 1995; Lanz & Hubeny 2003, 2007) is the only code with a plane-parallel geometry, and, hence, suited to model lines formed (almost) in the photosphere. This means that TLUSTY is dedicated to the (photospheric) analysis of hot stars with less strong winds, such as B dwarfs (and late O dwarfs, if the primary focus is to determine the photospheric parameters). Also, note that the TLUSTY solution is performed in the observer’s frame since it is a purely photospheric model code, that is, taking into account only the hydrostatic region of the atmosphere.

Furthermore, the code FASTWIND (Santolaya-Rey et al. 1997; Puls et al. 2005) was originally designed to provide an approximate treatment of line-blanketing. This means that a group of lines of ‘explicit elements’ (e.g., H, He, C, N, O, and others) is treated in the comoving frame (CMF), while most part of the lines due to ‘background elements’ (mostly from the iron group) are treated using the Sobolev approximation. Using this approach, FASTWIND is able to provide a realistic line synthesis for hot stars, comparable to one provided by more robust codes, such as CMFGEN (see, e.g., Massey et al. 2013). Nevertheless, recent efforts have been made for a fully consistent treatment of line-blanketing with FASTWIND, by means of treating all the lines in the CMF approach (Puls 2017), and thus allowing a realistic line synthesis in the UV region. Note that only the visible and infrared regions are indicated for FASTWIND in Table 4.1. Further details on atmosphere model codes of massive hot stars can be found in the review of Sander (2017).

Finally, note that all the codes for extended atmosphere, listed in Table 4.1, use a spherically symmetric geometry, being thus 1-D models. This is a very fair assumption for stellar winds of non-rotating single stars. On the other hand, such codes cannot reproduce the break of spherical symmetry that is introduced by fast rotation, such as the formation of equatorial disks around classical Be stars. As it will be discussed in Sect. 4.4, such geometric limitation is well overcome by the code HDUST due to its alternative method, in comparison with the CMF approach, to solve the radiative transfer problem.

4.3 The code CMFGEN

CMFGEN² (Hillier & Miller 1998) is a state-of-the-art non-LTE radiative transfer code, which was originally developed to study the properties of massive hot stars, such as WR and LBV stars (e.g., Hillier & Miller 1999; Dessart et al. 2000; Hillier et al. 2001). Nevertheless, it also has been widely used for the analysis of central stars of planetary nebula (e.g., Marcolino et al. 2007), OB-type (e.g., Bouret et al. 2012), and, more recently, core-collapse supernovae (e.g., Dessart et al. 2016). CMFGEN has been

2. Acronym for comoving frame general.

4.3. The code CMFGEN

currently updated by D. J. Hillier (University of Pittsburgh, USA) and is publicly available³

CMFGEN iteratively solves the radiative transfer equation and the statistical and radiative equilibrium equations in the comoving frame, in a simultaneous way. The assumption of radiative equilibrium, used to constrain the temperature structure, means that all the energy in the atmosphere is fully transported by radiation, that is, neglecting conduction and convection. In this case, all the (radiative) energy that is absorbed at a volume of the atmosphere is equal to the total energy that is emitted at the same volume. Formally, holding for each point of the atmosphere, this can be expressed as follows:

$$\int_0^{\infty} \chi_{\nu}(J_{\nu} - S_{\nu}) d\nu = 0. \quad (4.23)$$

As discussed in Sect. 4.1, holding LTE, the state of the gas is given by the local temperature (and the particle density). In this case, the statistical equilibrium equations are described by the Maxwell-Boltzmann and Saha distributions. In the non-LTE approach, as using CMFGEN, “in a simultaneous way” (as stated above) means that the radiative transfer equation and the ones of statistical and radiative equilibrium equation form a coupled problem to be solved. Whereas the statistical equilibrium equations, describing the populations, depends on the radiation field, the radiation field also depends on the solution of the statistical equilibrium equations. Then a simultaneous solution of them is needed. Further details on the expressions of the statistical equilibrium equations in non-LTE can be found in Sect. 5.5 of Mihalas (1978).

From a practical point-of-view, CMFGEN requires a start model (see Table 4.1), providing an initial guess of the populations. After a number of iterations (for example, 60), from the correction of the populations, a new converged model can be found when the radiation field and the populations satisfied simultaneously the radiative transfer equation and the statistical equilibrium equations (under radiative equilibrium) for the new input parameters. The reader can found details on the solution methods of CMFGEN in Sect. 3 of Hillier & Miller (1998).

The input parameters in CMFGEN have been discussed in details in a series of works. In short, as a non-extensive list, these are the main parameters to define the atmosphere model: in addition to the chemical composition, the stellar luminosity, effective temperature, gravity surface acceleration, radius, mass, mass-loss rate, wind clumping factor, terminal velocity, and wind velocity law exponent. The reader can find further details in Groh (2011), Hillier (2012), Appendix B of Martins (2004), and

3. CMFGEN website: <http://kookaburra.phyast.pitt.edu/hillier/web/CMFGEN.htm>.

4.3. The code CMFGEN

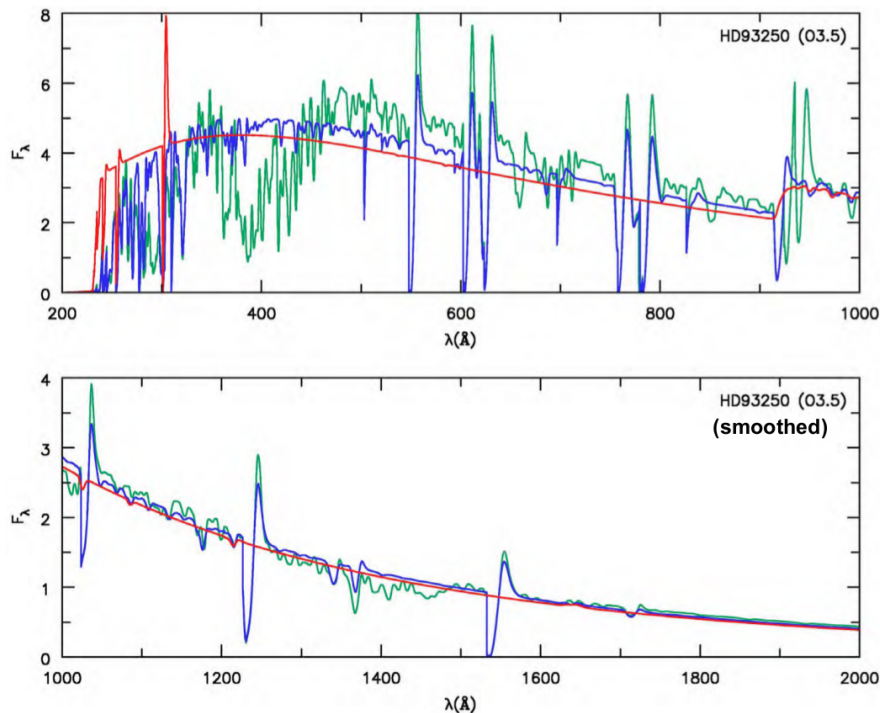


Figure 4.2 – Line-blanketing effect on the emergent spectrum. Comparison among three CMFGEN models with the following chemical compositions: H + He (red), H + He + CNO (blue), and H + He + CNO + Fe group elements (green). All the models have the following parameters: $\log L_*/L_\odot = 6.11$, $T_{\text{eff}} = 45700$ K, $\log g = 4.0$, $R_* = 18.3 R_\odot$, $\dot{M} = 5.6 \times 10^{-7} M_\odot \text{ yr}^{-1}$, and $v_\infty = 3000$ km s $^{-1}$. This set of physical parameters fairly describes the spectrum of HD 93250 (spectral type O4). See text for discussion. Reproduced from Groh (2011).

in the reference manual of CMFGEN, which is available in the CMFGEN website (see footnote 3 of this chapter).

In the following, we summarize some of the principal characteristics of CMFGEN:

- (i) It assumes a stationary spherically symmetric wind. Currently, CMFGEN does not solve the radiative transfer equations in a consistent way with the wind hydrodynamics. This means that the wind density and velocity structures must be provided, they are input parameters of the model. The density is given by Eq. 1.3, while Eq. 1.4 sets the velocity law in its simplest form. Nevertheless, somewhat more complex velocity laws can be adopted, for example, a two-component β velocity law, describing the inner and outer regions of the wind (see., e.g., Hillier & Miller 1999). However, more recently, CMFGEN allows a temporal dependent treatment of the radiative transfer and statistical equations (non-stationary outflow), being useful to model the light curves and spectra of supernovae (e.g., see, again, Dessart et al. 2016).
- (ii) CMFGEN allows us to include a large quantity of atomic species in the modeling, namely, ions of: H, He, C, N, O, F, Ne, Na, Mg, Al, Si, P, S, Cl, Ar, K, Ca, Ti, Cr, Mn, Fe, Co, and Ni. Fig. 4.2 compares the synthetic spectrum in the

4.3. The code CMFGEN

UV from CMFGEN models with different chemical compositions: H + He, H + He + CNO, and H + He + CNO + Fe group elements. The parameters are set according to a O4 star (HD 93250). One sees that the proper modeling of the UV region for such a hot star demands the inclusion of elements heavier than helium. This is also needed in order to treat the so-called line-blanketing effect that is “exactly” treated in CMFGEN. The larger opacity introduced by metals blocks the radiation and then increases the temperature at the inner region of the atmosphere (backwarming effect). This affects not just the lines, but the continuum region itself (as shown in Fig. 4.2). This means that models with the inclusion of metals (as realistically as possible) requires lower values of effective temperature to reproduce the same ionization (as without metals). Thus, it impacts the determination of the effective temperature: line-blanketed models (correctly) downward the inferred T_{eff} of hot stars (e.g., see Najarro et al. 2006, and references within).

- (iii) As discussed in Sect. 1.2.2, intrinsic instabilities in the line force creates non-homogeneous winds (i.e., “clumps” in the wind density structure), and thus originating significant emission of X-Rays due to shocks in the wind of massive hot stars (e.g., see Oskinova 2016, and references within). X-Ray emission must be taken into account in order to reproduce, as realistically as possible, the ionization balance in the wind, and then the spectral lines (in particular the ones formed in the UV, which are important wind diagnostics). CMFGEN enables to take the Auger ionization into account (Cassinelli & Olson 1979; Olson & Castor 1981) by X-Rays (see Sect. 6 of Hillier & Miller 1998). Lastly, the wind clumping is modelled in CMFGEN in terms of a volume filling factor $f(r)$:

$$f(r) = f_{\infty} + (1 - f_{\infty})e^{-\frac{v(r)}{v_{\text{initial}}}}, \quad (4.24)$$

being f_{∞} and v_{initial} the (input) free parameters chosen to include the effect of clumping. This simple parameterization assumes that the interclump medium is void and that the wind clumps are smaller in comparison with the photon mean-free path for all the values of wavelength (called microclumping approximation).

Physically, v_{initial} means the location in the wind where the formations of clumps begins to be important, and f_{∞} gives the value of clumping at larger distances, that is, $f(r \rightarrow \infty)$, with lower values of f_{∞} meaning more structured winds. From Eq. 4.24, f is set to unity when $f_{\infty} = 1.0$ (homogeneous wind, no clumps).

Taking into account the volume filling factor $f(r)$, the wind density (Eq. 1.3) is then modified as follows:

4.3. The code CMFGEN

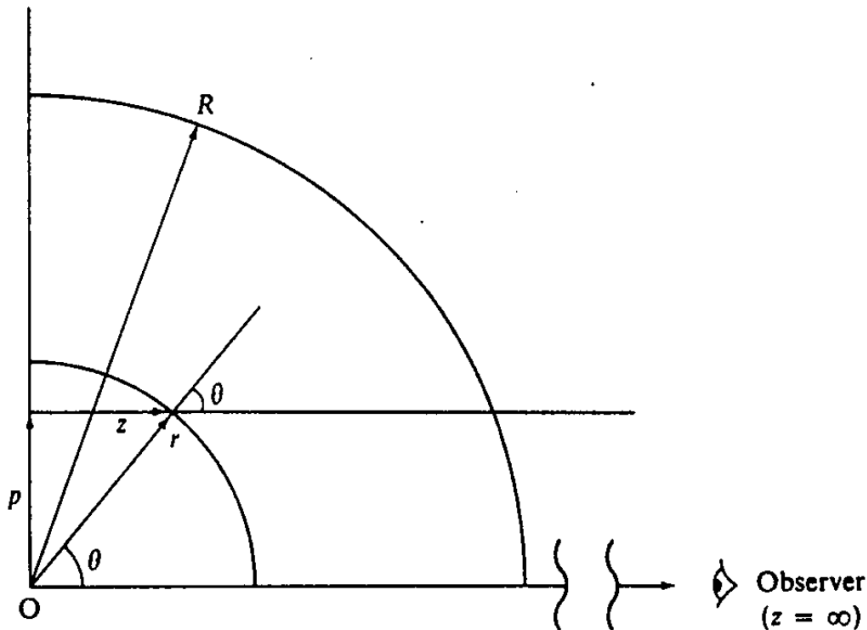


Figure 4.3 – Schematics of the (p, z) coordinate system, which is used in the code CMFGEN to solve the radiative transfer problem (ray-by-ray solution method). The coordinate p is called as the impact parameter, measuring the perpendicular distance to the rays given by the direction z . The coordinates (p, z) are related to the polar ones (r, θ) by: $z = r \cos \theta$, $p = r \sin \theta$, and $r = \sqrt{p^2 + z^2}$. For instance, Fig. 4.4 shows the theoretical intensity (as a function of wavelength) for each value of p from a model calculated using CMFGEN. Further details on the ray-by-ray solution method can be found in Sect. 5.3.2 of Crivellari et al. (2019). Reproduced from Mihalas (1978).

$$\rho(r) = \frac{\dot{M}}{4\pi r^2 v(r) f(r)}. \quad (4.25)$$

Several spectroscopic studies on hot stars showed that the inclusion of clumping is needed to determine realistic values of mass-loss rates for hot stars winds. In short, the inclusion of wind clumping in the models implies downward revisions on their wind mass-loss rates by a factor up to ~ 10 , when compared with the values derived using homogeneous wind models (e.g., Bouret et al. 2003; Repolust et al. 2004; Bouret et al. 2012).

In order to calculate the predicted visibility, it is needed a description of the intensity as a function of distance from the center of the star (impact parameter p , see Fig. 4.3) for a certain value of wavelength. In Fig. 4.4, we show the intensity profiles, as a function of wavelength (around the $H\alpha$ line), for each value of impact parameter, calculated using CMFGEN. A certain agglomeration of profiles is seen closer to the photosphere since the grid points of the model are not equally spaced in the photosphere and in the wind. In particular, this model was calculated in the context of my work about P Cygni (Sect. 6.2).

One sees that $H\alpha$ is forming a strong P Cygni profile, related to the high value of

4.3. The code CMFGEN

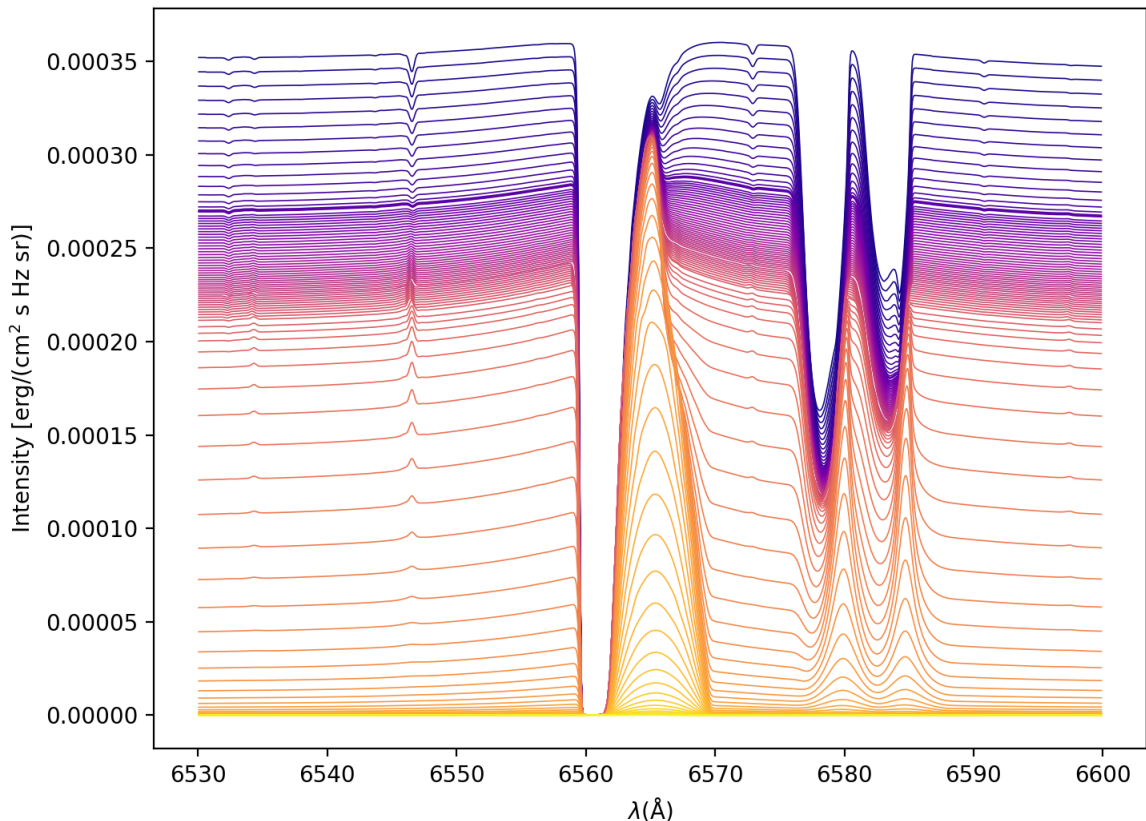


Figure 4.4 – Intensity profiles, as a function of the wavelength ($\sim 6530\text{--}6600\text{ \AA}$, around $\text{H}\alpha$), calculated by myself using CMFGEN with the following stellar and wind parameters: $\log L_{\star}/L_{\odot} = 5.73$, $T_{\text{eff}} = 18700\text{ K}$, $\log g = 2.3$, $R_{\star} = 70.6 R_{\odot}$, $\dot{M} = 1.0 \times 10^{-5} M_{\odot} \text{ yr}^{-1}$, and $v_{\infty} = 185\text{ km s}^{-1}$. Intensity profiles are shown for each value of distance from the center of the star (in total, 115 points). Lighter (toward yellow) I versus λ profiles come from larger distances through the wind region (extension of $50 R_{\star}$). See text for discussion.

mass-loss rate ($\dot{M} = 1.0 \times 10^{-5} M_{\odot} \text{ yr}^{-1}$). In Fig. 4.4, lower values of intensity in the continuum (close-by $\text{H}\alpha$) come from larger distances in the model (wind region). Note how $\text{H}\alpha$ is filled in emission toward larger distances. Moreover, weak spectral features around $\text{H}\alpha$, such as the $\text{C II } \lambda\lambda 6580, 6585$ doublet, are formed in pure-absorption in the photosphere (dark intensity profiles), but in emission through the wind (light intensity profiles).

From Fig. 4.4, we are able to create an image cube, describing the intensity map of the object for each value of wavelength, and then predict the model visibility from the Fourier transform of the intensity map (valid for each value of wavelength). Since CMFGEN is essentially a 1-D model, it is needed to take into account the geometry of the model (spherically symmetric wind) in order to interpolate an image (2-D).

Also notice that the resulting spectrum (Fig. 4.5), around $\sim 6530\text{--}6600\text{ \AA}$, is computed by adding the different intensity curves shown in Fig. 4.4. For example, the emergent spectrum in $\text{C II } \lambda\lambda 6580, 6585$ forms two weak P Cygni profiles (note the shift, in wavelength, between the absorption and emission contributions).

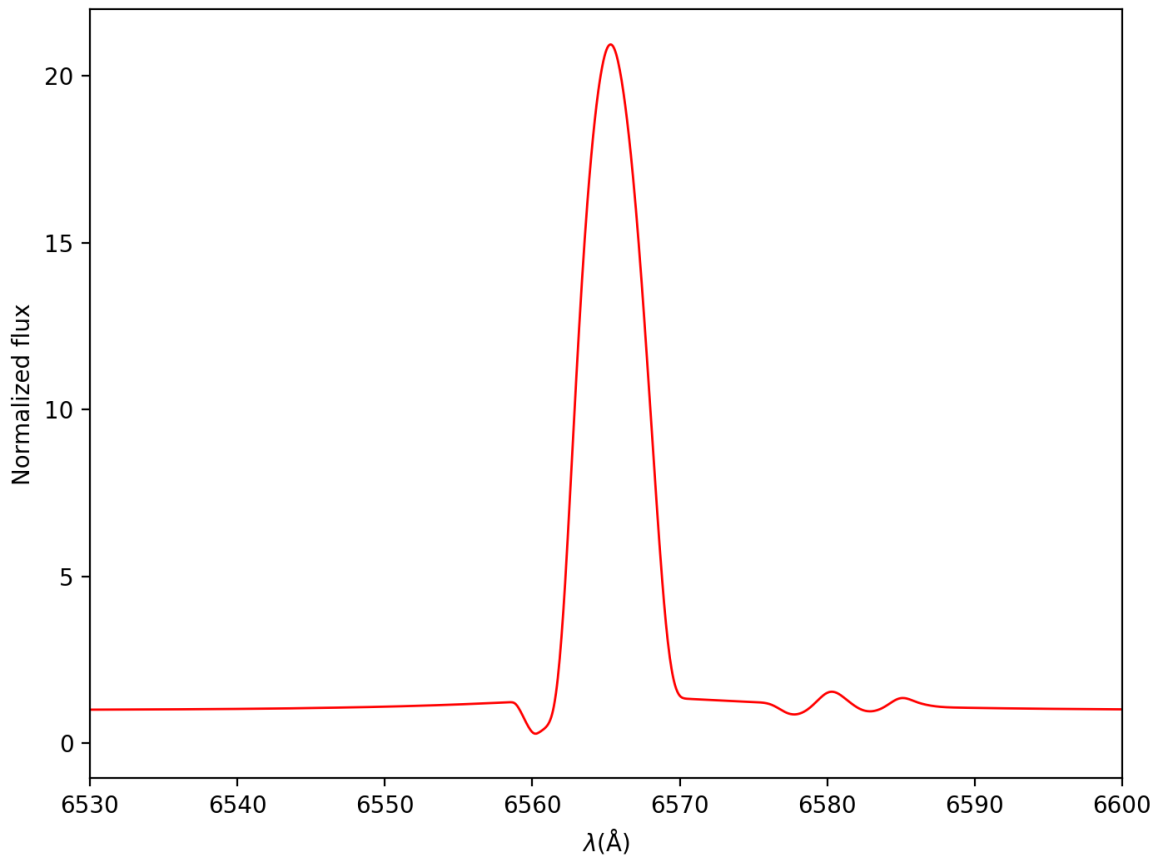


Figure 4.5 – Emergent flux (normalized to the continuum), computed from the same CMFGEN model in Fig. 4.4, around the $H\alpha$ line (strong P Cygni profile). Note that $C\ II\ \lambda\lambda 6580, 6585$ lines also form P Cygni profiles but very weak in comparison with the $H\alpha$ transition.

Of course, the variation of the mass-loss rate in the model will impact the intensity profiles, especially in $H\alpha$. Fixing all the other parameters, increasing \dot{M} implies a stronger P Cygni profile, with a more intense emission component⁴.

In short, despite the high computational cost (as will be discussed in Sect. 4.6), this shows how radiative transfer modeling is a powerful tool to probe the physical conditions of circumstellar environments. From a set of (almost) fundamental physical and chemical parameters, it can be used to model spectroscopic and (spectro-)interferometric data at different transitions.

4.4 The code HDUST and the BeAtlas grid

One alternative to CMF-based codes, which explicitly (numerically) solve the radiative transfer and statistical equilibrium equations in the comoving frame, relies on Monte Carlo method. In this case, the radiation field is reconstructed by classifying

4. Note that, in this case, the absorption component of the P Cygni profile in $H\alpha$ is saturated, that is, null intensity.

4.4. The code HDUST and the BeAtlas grid

the photons packages by position, propagation, direction, and wavelength. This allows us to solve the radiative transfer problem self-consistently in a statistical sense. In particular, the Monte Carlo method is a very useful when dealing with the radiative transfer in more complex geometries than the 1-D assumption as in CMFGEN, and other CMF-based codes, for radiative winds (see, again, Table 4.1).

HDUST (Carciofi & Bjorkman 2006, 2008) is a state-of-the-art 3-D non-LTE radiative transfer code that solves the radiative transfer and statistical equilibrium equations using the Monte Carlo method. The Monte Carlo method implemented in HDUST largely follows the one developed by Lucy (2002, 2003, 2005), which ensures the condition of radiative equilibrium, differing with respect to the process of atom-photon interaction (see Sect. 2 of Carciofi & Bjorkman 2006).

In HDUST, the circumstellar environment can be treated under arbitrary 3-D geometry and kinematics. This provides a suitable approach to model both winds and disks around hot stars. For purely-gaseous environment, such as in Be disks, the chemical composition is assumed by atomic hydrogen (and free electrons). As suggested by its name, besides a hydrogen gaseous composition, HDUST also allows us to take into account the opacity of dust grains, following the so-called Mie theory (see Carciofi et al. 2004). This is particularly relevant for the analysis of objects such as B[e] stars, which have gaseous and dusty environments. In short, HDUST has been successfully used in a series of studies to interpret different observational properties of Be and B[e] stars. For instance, see Bjorkman & Carciofi (2005), Carciofi et al. (2010), Klement et al. (2015), and Domiciano de Souza et al. (2015).

In this thesis, all the HDUST models analysed are part of the BeAtlas project (Faes 2015; Correia Mota 2019). This model grid have been developed by D. M. Faes, B. C. Mota, and A. C. Carciofi (Universidade de São Paulo, Brazil) in particular for the analysis of the Be disks, as well as the central star.

In the models of BeAtlas, the kinematics of the disk is adopted as following a Keplerian rotation (Eq. 1.62), according to the VDD scenario (Sect. 1.5.1). BeAtlas is composed of ~ 14000 models with images (specific intensity maps), SEDs, and spectra calculated in natural and polarized light, over several spectral regions, including the H α and Br γ lines, and also the K-band region. Hence, it is very suitable for interpreting spectro-interferometric data, such as from CHARA/VEGA and VLTI/AMBER. Besides the purely theoretical investigation by Faes (2015) of differential phase signatures for Be disks, this thesis provides to date the first application of BeAtlas for the spectro-interferometric analysis of a Be star (Sect. 6.3).

Table 4.2 shows the parameter spaces covered in BeAtlas. We stress that these values correspond to the BeAtlas grid developed by Faes (2015), being this version employed in the present thesis. BeAtlas models with finer parameter steps have been

4.4. The code HDUST and the BeAtlas grid

Table 4.2 – List of HDUST parameter in the BeAtlas grid. The first row indicates the spectral type corresponding to the stellar mass for B dwarfs (Townsend et al. 2004). All the model are calculated with the following fixed parameters: scale height at the disk base $H_0 = 0.72$, fraction of H in the core $X_c = 0.30$, metallicity $Z = 0.014$, and disk radius = $50 R_{\text{eq}}$. Adapted from Faes (2015)

Parameter	Value
Spectral type	B0.5, B1, B1.5, B2, B2.5, B3, B4, B5 B6, B7, B8
M_\star (M_\odot)	14.6, 12.5, 10.8, 9.6, 8.6, 7.7, 6.4, 5.5 4.8, 4.2, 3.8
i (deg)	0.0, 27.3, 38.9, 48.2, 56.3, 63.6, 70.5 77.2, 83.6, 90.0
Oblateness (R_{eq}/R_p)	1.1, 1.2, 1.3, 1.4, 1.45
Σ_0 (g cm^{-2}) ^a	0.02, 0.05, 0.12, 0.28, 0.68, 1.65, 4.00
m ^b	3.0, 3.5, 4.0, 4.5 + non-isothermal

^a Surface density at the base of the disk.

^b Disk mass density law exponent. “non-isothermal” stands for HDUST models computed without the assumption of isothermal disk scale height.

calculated by Correia Mota (2019).

Since we are dealing with a pre-calculated model grid, a BeAtlas-based analysis is, at least at a certain level, biased by the limited parameter space and selected parameter values of the grid, which are not homogeneously distributed (for example, see Fig. 4.6). From that, one sees a gap of models with higher values of Σ_0 , as the stellar mass decreases since convergence issues with HDUST arises in this case (see Sect. 3.4.2 of Correia Mota 2019). Nevertheless, this particular limitation in the grid is not expected to highly affect the analysis of Be disks since late-type Be stars (i.e., lower stellar mass) are more likely to have less dense disks (see Vieira et al. 2017; Arcos et al. 2017).

In total, five physical parameters vary in the grid. Three out of five parameters describe the central star: the stellar mass, stellar oblateness, inclination angle. Each value of R_{eq}/R_p is uniquely related to W , assuming that the central star is a rigid rotator under the Roche model. From Table 4.2, these values of R_{eq}/R_p correspond to $W = 0.447, 0.663, 0.775, 0.894, \text{ and } 0.949$, respectively. We recall the reader that the rotational W is defined according to Eq. 1.51. Since rotational effects are relevant for the analysis of Be stars, the gravity darkening effect⁵ is included in the BeAtlas

5. See, again, Sects. 1.3.3 and Sect. 1.3.4.

4.4. The code HDUST and the BeAtlas grid

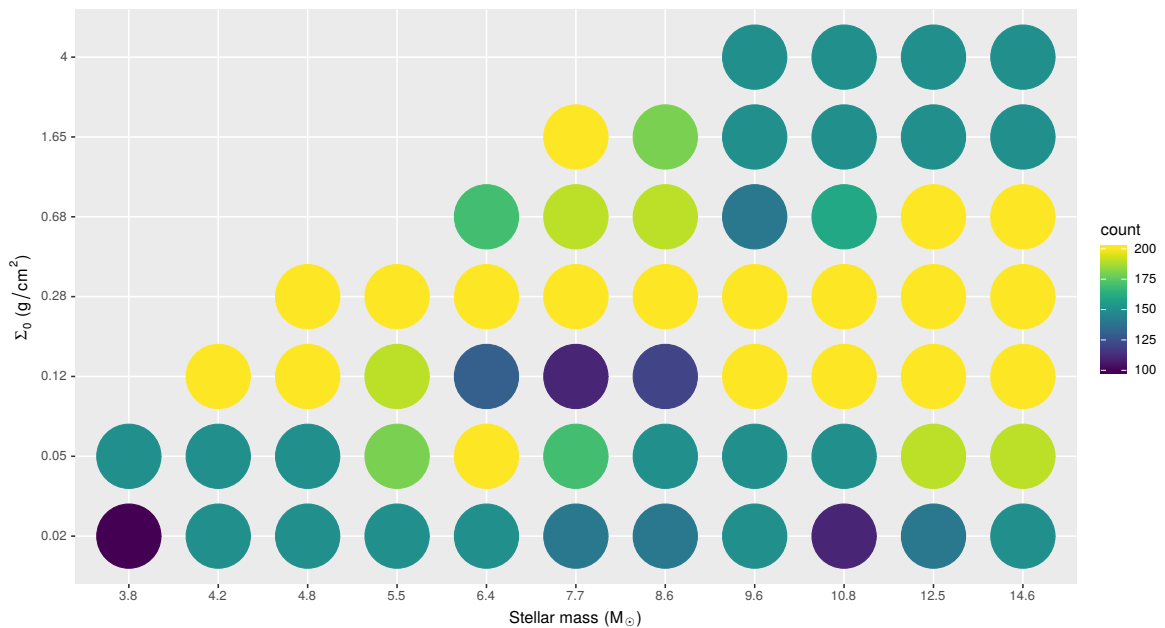


Figure 4.6 – Distribution of the BeAtlas models with respect to the stellar mass and base disk surface density. Note the absence of models with high values of base disk density for the lower stellar mass. See text for discussion.

models following the prescription from Espinosa Lara & Rieutord (2011).

The polar stellar radius R_{pol} is obtained from each combination of stellar mass and stellar oblateness. For example, models with $M_{\star} = 3.4 M_{\odot}$ have R_{pol} between ~ 3.36 and $3.37 R_{\odot}$ for the different values of rotational rates considered in the grid (between 0.447 and 0.949, respectively). For $M_{\star} = 14.6 M_{\odot}$, the polar radius is ~ 7.50 and $\sim 7.38 R_{\odot}$ for these extreme values of W . The stellar mass and rotational rate also define the value of the stellar rotational velocity v_{rot} . For $M_{\star} = 3.4 M_{\odot}$, we have $v_{\text{rot}} \sim 160$ and 300 km s^{-1} for $W = 0.447$ and 0.949 . For $M_{\star} = 14.6 M_{\odot}$, $v_{\text{rot}} \sim 210$ and 420 km s^{-1} for these same values of rotational rate.

Regarding the disk properties, the last two parameters in Table 4.2 are parameterizations for the density structure of the VDD model description: the base surface density (Σ_0) and the radial density exponent (m). More generally, two kinds of disk models are found in the BeAtlas grid:

- (i) Non-isothermal steady-state models: self-consistent solution of the viscous diffusion equation considering a steady-state disk, that is, a null temporal variation of the disk density:

$$\frac{\partial \Sigma(r,t)}{\partial t} = 0, \quad (4.26)$$

considering a non-null mass injection in the disk, $\Sigma_{\text{in}} \neq 0$.

Then the radial (surface) disk density is described by the mass-loss rate \dot{M}

4.5. For what CMFGEN and HDUST are suited?

and the Shakura-Sunyaev's viscous parameter α , as given by Eq. 1.70.

- (ii) Parametric models: it is assumed an isothermal disk scale height (Eq. 1.67). In this case, the radial disk density is parameterized by the base disk density Σ_0 , corresponding to different values of \dot{M} , and the density law exponent n , as given by Eq. 1.73.

We recall the reader that each value of n are related to the (volume) density law exponent by Eq. 1.74, as well as Σ_0 and ρ_0 are related to each other by Eq. 1.75

In Sect. 6.3, our analysis is based on the parametric models of BeAtlas, as the non-isothermal (hydrodynamically self-consistent) models currently cover a quite limited range of parameter values, with α fixed at 0.5, composing a small fraction of the grid ($\sim 14\%$) from Faes (2015). Further details on self-consistent models using HDUST can be found in Carciofi & Bjorkman (2008) and Klement et al. (2015).

In conclusion, the range of values for Σ_0 and m in BeAtlas encompass somewhat extreme cases in the literature for the circumstellar disk of Be stars. The listed values of Σ_0 correspond to ρ_0 from $\sim 10^{-12}$ g cm $^{-3}$ to $\sim 10^{-10}$ g cm $^{-3}$. Parametric models with $m = 3.5$ are equivalent to the steady-state solution of the viscous diffusion equation considering an isothermal disk scale height. Thus, regarding the mass density law exponent m , models with $m > 3.5$ would represent a disk passing by an accretion phase, while the ones with $m < 3.5$ a disk in an ongoing process of dissipation (see, e.g., Haubois et al. 2012; Vieira et al. 2017).

Finally, Fig. 4.7 compares the intensity map around the Br γ of two BeAtlas models with different values of inclination angle: a perfectly pole-on ($i = 0$) and one seen edge-on ($i = 90^\circ$). All the other parameters are fixed, as indicated in Fig. 4.7. From that, note how the disk emitting envelope is much larger in the Br γ line than in the close-by continuum (first three columns of the top panels), and then affecting the predicted value of differential visibility (simulated to a AMBER triplet configuration, bottom panels).

4.5 For what CMFGEN and HDUST are suited?

From our previous discussion, both CMFGEN and HDUST are state-of-the-art codes, used in a series of works on hot massive stars. Despite being a very limited metric of impact, up to date, the basic reference of CMFGEN (Hillier & Miller 1998) have been cited in ~ 820 papers, while the one of HDUST (Carciofi & Bjorkman 2006) have received ~ 150 citations. For sure, there is a time-delay between these two codes, but such discrepancy can be understood in terms of a larger applicability of CMFGEN, which, for example, fully takes into account the effect of line-blanketing,

4.6. Computational cost of physical models

while HDUST is currently limited to hydrogen composition, when considering a pure gaseous environment. In addition, unlike HDUST⁶, CMFGEN is publicly available.

The code CMFGEN allows us to include several chemical elements (at different levels of ionization), and for each one the lines are treated in a “exact” way, that is, computed from solving in the comoving frame the radiative transfer, statistical and radiative equilibrium equation simultaneously. For instance, from our discussion of Fig. 4.2, one sees how unsuitable is HDUST in order to model the wind of an early-type O star (physical parameters for a O4 star in Fig. 4.2) due the absence of metals in the evaluation of the opacity, being this issue less severe for B-type stars (showing lower values of effective temperature).

On the other hand, unlike CMFGEN, HDUST allows to take into account the opacity due to dust grains, being this a very important feature, among the massive hot stars, when modeling the environments of B[e] supergiants. Nevertheless, we point out that current efforts have been made to include several chemical elements, beyond the hydrogen (and free electron) gas composition, in the modeling with HDUST (HDUST3, Carciofi et al. 2017).

In addition, HDUST does not take the task of explicitly solve the radiative transfer equations, providing a statistical approach, by a Monte Carlo method, to find the radiative field and state of the gas. In particular, one caveat of Monte Carlo radiative transfer codes relies on convergence issues when dealing with the calculation of optically thick lines, as the number of interaction particle-photon is increased due to a larger opacity of the medium.

However, the use of a Monte Carlo approach introduces a much higher flexibility on the modeled geometry. Again, all the CMF-based codes, shown in Table 4.1 assume a spherical symmetric outflow. Thus, for example, HDUST is very suited to model the environment of a Be star, formed by an equatorial disk (and possibly, in addition to a polar wind), due to complex geometry in this case. This is a proper task to be performed using a Monte Carlo-based code, such as HDUST. Lastly, unlike CMFGEN, notice that HDUST is able to predict the degree of light polarization as a result of the asymmetric geometry of the envelope. Nevertheless, efforts have been made to implement non-LTE CMF codes for hot stars beyond the 1-D geometry. For example, based on CMFGEN, see the code of Busche & Hillier (2005).

4.6 Computational cost of physical models

Due to the complexity of solving the radiative transfer problem, under the non-LTE treatment, both CMFGEN and HDUST take several hours to convergence a single

6. For access and collaborations with HDUST, contact A. C. Carciofi.

4.6. Computational cost of physical models

model.

Considering the non-parallelized version of CMFGEN⁷, it must be needed ~ 6 -12 hours of computing time in order to convergence a single CMFGEN model, allocating ~ 2 -3 GB of RAM memory. However, these reference values are highly dependent on the chosen solution method, the number of atomic species that are included in the modeling, as well as, the number of iterations and depth points that are chosen by the user to calculate the photosphere and wind⁸.

Furthermore, since in practices it is required a start CMFGEN model, in order to estimate the populations, for sure, the convergence time (as the convergence itself) depends on how the parameters are changed in the new model, compared with the start model. For instance, including more heavy elements in the model, and thus increasing the number of equations to be solved, increases the allocation of memory and it can lead to a computing time for up to more than one day. For comparison, the code FASTWIND demands about 1 to 10 minutes to converge a model (Table 4.1), as it works using the Sobolev approximation to treat a large number of lines (mainly of the iron group).

In short, both Monte Carlo- (as HDUST) and CMF- (as CMFGEN) based codes have a significant computational cost. Hence, it is impossible to implement a “real-time” fitting process using these codes. For example, considering the time of 6 hours for converging a CMFGEN model, and employing a Markov Chain Monte Carlo method (as will be latter discussed in Sect. 5.4), with 180000 tested samples of parameters, it would be needed ~ 120 years for searching the best-fit parameters that explain the data!

As will be discussed in Chap. 5, this issue described above can be overcome using analytical and simple numerical model, having a computational cost of a few seconds, or much less than that.

In conclusion, obtaining the “best-fit” models, using the CMFGEN and HDUST codes, relies on physical insights from the user in order to change a specific parameter of interest for comparison with the data, and typically requiring to compute a large number of models (for example, ~ 50) to obtain the best-fit model. Alternatively, one can use a pre-calculated model grid (as the BeAtlas grid, discussed in Sect. 4.4). However, this approach is also biased with respect to exploration of the parameter space in order to better explain the data. Regarding CMFGEN, current efforts have been made to calculate large public model grids, and then requiring the use of CPU clusters (e.g., Zsargo et al. 2013; Fierro et al. 2015; Zsargo et al. 2017).

7. Currently, it is possible to install a parallelized version of CMFGEN. This leads to faster calculations by up to a factor of 2-3 times when using 4 processors.

8. For instance, models for O stars typically must be computed using a total of ~ 60 -80 depth points for the photosphere plus wind structure. See the description for the control file MODEL_SPEC in the CMFGEN manual.

4.6. Computational cost of physical models

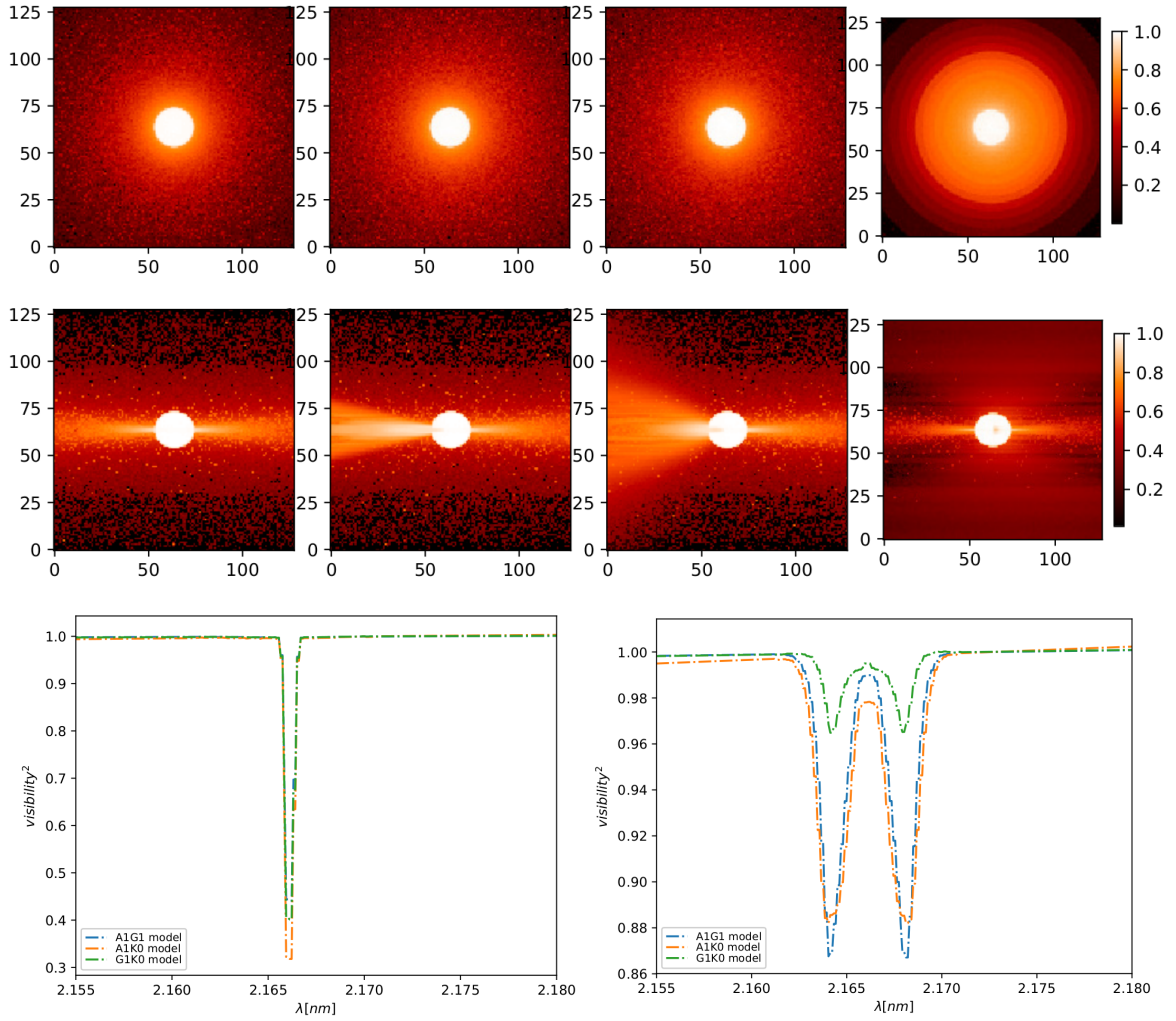


Figure 4.7 – First two rows: intensity maps (128 x 128 pixels) at different values of wavelength close to Br γ (from left to right: 2.161, 2.164, 2.165, and 2.166 μ) of two HDUST models, from the BeAtlas grid, with different values of inclination angle: $i = 0$ (first row) and $i = 90^\circ$ (second row). All the other parameters are fixed as follows: $M_\star = 14.6 M_\odot$ (type B0.5), $R_{\text{eq}}/R_p = 1.1$, $\Sigma_0 = 0.5 \text{ g cm}^{-2}$, and $m = 3.0$ (see Table 4.2). The flux/pixel scale is shown in arbitrary units. Simulated VLTI/AMBER visibilities from these 2 models are shown in the last row: $i = 0$ (left panel) and $i = 90^\circ$ (right panel). See text for discussion.

Chapter 5

Model fitting of interferometric data

Contents

5.1	Geometric models	125
5.1.1	Applying the Zernike-van Cittert theorem to analytical models	125
5.1.2	The simplest case: an example of one-component model	125
5.1.3	Adding other components: an example of two-component model	126
5.2	Analytical model fitting: the software LITpro	128
5.2.1	Overview: a tool dedicated to interferometric modeling	128
5.2.2	Example of modeling: VLTI/GRAVITY data of Rigel	129
5.2.3	Limitations: what is the global χ^2 minimum?	130
5.3	The kinematic code	131
5.3.1	Overview: the model parameters	131
5.3.2	Model description: the central star and the circumstellar environment	132
5.3.3	Parameters effects on the interferometric quantities	134
5.3.4	An example of model fitting: AMBER data of the nova T Pyxidis	135
5.4	Kinematic model fitting using MCMC	136
5.4.1	Why use a MCMC fitting-method to the kinematic code?	136
5.4.2	The MCMC method	138
5.4.3	The code EMCEE: a MCMC implementation	138
5.4.4	Using prior information with EMCEE	139
5.4.5	Example of modeling: VLTI/AMBER data of <i>o</i> Aquarii	139
5.4.6	Further improvements	141

5.1 Geometric models

5.1.1 Applying the Zernike-van Cittert theorem to analytical models

Despite not being able to constrain the physical conditions in the photosphere and the envelope, such as the density and temperature structures, as well its kinematics, geometric models are useful modeling tools to study the geometry of the central star and its environment (e.g., see Berger, J.-P. 2003).

This is the simplest possible approach to interpret interferometric data. As discussed in Sect. 3.5.1, the so-called Zernike-van Cittert theorem (Eq. 3.20) relates the brightness of the source projected on the sky to the degree of the light coherence measured by the interferometer at given wavelength and spatial frequencies. For comparison with observational interferometric quantities, the intensity distribution of the star is modeled by a simple analytical function and then the complex visibility calculated by applying the Zernike-van Cittert theorem, that is, a Fourier transform applied to the stellar intensity map on the sky.

In the following, we discuss just some simplified cases of geometric modeling, but before setting the problem itself, it is useful to remind the reader about some basic properties of Fourier transform (FT), linking the brightness distribution and the interferometric quantities, as follows:

1. Addition property: $\text{FT} \{I_1(\alpha, \beta) + I_2(\alpha, \beta)\} = \tilde{V}_1(u, v) + \tilde{V}_2(u, v)$.
2. Similarity property: $\text{FT} \{I_1(a\alpha, b\beta)\} = \frac{1}{|ab|} \tilde{V}_1(u/a, v/b)$.
3. Translation property: $\text{FT} \{I_1(\alpha - \alpha_0, \beta - \beta_0)\} = \tilde{V}_1(u, v) \exp[2\pi i(u\alpha_0 + v\beta_0)]$.
4. Convolution property: $\text{FT} \{I_1(\alpha, \beta) \otimes I_2(\alpha, \beta)\} = \tilde{V}_1(u, v) \tilde{V}_2(u, v)$.

In the equations above, $\tilde{V}(u, v)$ denotes the complex visibility without taking into account the scaling factor due to the total intensity of the source, that is, it is not normalized. On the other hand, we remind the reader that $\tilde{V}(u, v)$, as expressed by Eq. 3.20, is the complex visibility normalized by the total intensity of the source. The functions I_1 and I_2 denote two different intensity maps and the notation of the variables stands as used in Sect. 3.5, a , b , α_0 , and β_0 are constants, and the convolution operator is denoted by “ \otimes ”.

5.1.2 The simplest case: an example of one-component model

The simplest possible geometric modeling scenario consistent of assuming that the stellar intensity is described by a uniform disk. In this case, the (squared) visibility of

5.1. Geometric models

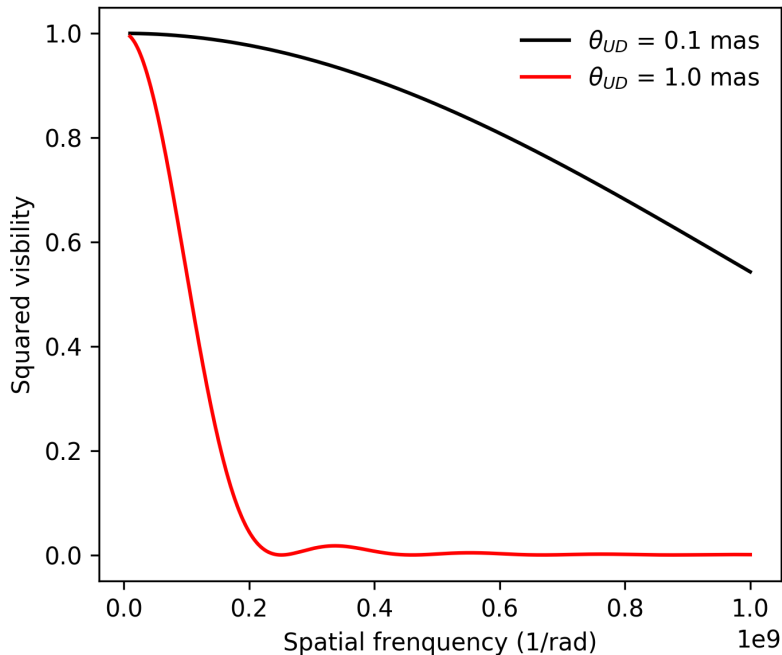


Figure 5.1 – Comparison between the visibility curves (squared visibility, V^2) of two uniform disks with different values of angular diameter: $\theta_{UD} = 0.1$ mas (black) and 1.0 mas (red).

a uniform disk with angular diameter θ is given by a first-order Bessel function of the first kind, J_1 :

$$V_{UD}^2 = \left(\frac{2J_1(\pi\theta\sqrt{u^2 + v^2})}{\pi\theta\sqrt{u^2 + v^2}} \right)^2, \quad (5.1)$$

where the variables u and v are the spatial frequency coordinates (Eq. 3.18). In the case of a uniform disk, since the intensity map of the object is center-symmetric the phase's component of the complex visibility is null, simplifying it to a real number.

For instance, Fig. 5.1 shows V_{UD}^2 for uniform disks of different angular diameters. From that, notice the visibility lobes from the Bessel function for the larger uniform disk, while the smaller one is barely resolved at lower spatial frequencies (V_{UD}^2 close to 1).

5.1.3 Adding other components: an example of two-component model

Somewhat more complex model configurations, that is, with higher number of free parameters, can be employed. For instance, Fig. 5.2 shows the geometric modeling by Sigut et al. (2015) to NPOI visibilities of the Be star α Aquarii.

5.1. Geometric models

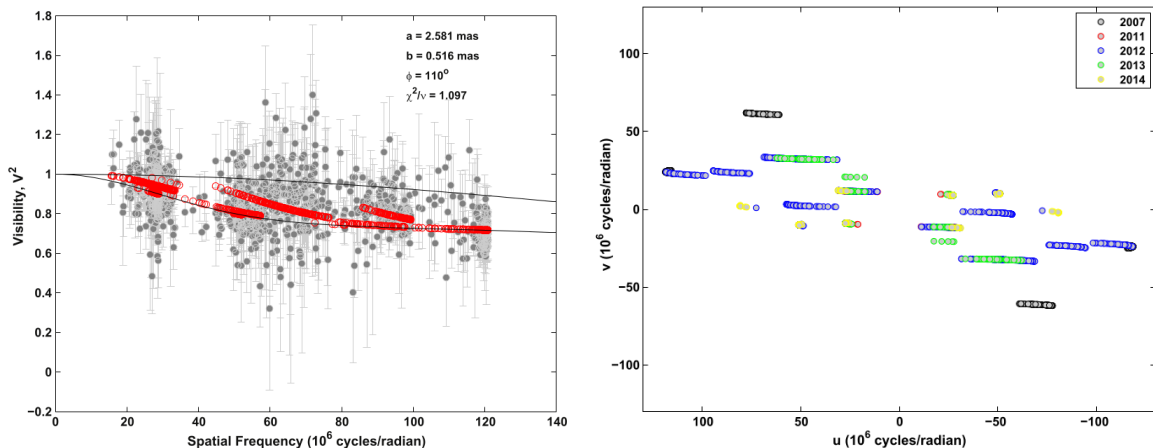


Figure 5.2 – Left panel: modeling to NPOI observations (interferometric data centered on $H\alpha$) of the Be star σ Aquarii using geometric models. The best-fit model to V^2 is shown in red points (simulated visibilities for each value of spatial frequency): a two-component geometric model composed by a uniform disk and an elliptical Gaussian distribution (axial ratio $r = 0.2$). The visibilities of the major and minor axes of the fitted elliptical Gaussian (values provided in the figure, a and b , respectively) are shown in black solid lines. a and b correspond to the major and minor axes (Full width at half maximum) of the Gaussian distribution. $\phi = 110^\circ$ is the major-axis position angle of the disk on the sky. The corresponding uv plan coverage of the observations is shown in the right panel. Reproduced from Sigut et al. (2015).

Their best-fit model (reduced χ^2 of 1.097) is a two-component geometric model: a 0.22 mas uniform disk contributing to 86% of the total flux, representing the photosphere, plus an elliptical Gaussian, representing the flux contribution from the disk, with parameters indicated in Fig. 5.2.

From Fig. 5.2, their second component contributes to about 14% of the total flux (see Table 3 of Sigut et al. 2015). They found a disk major-axis Full width at half maximum (FWHM) of ~ 2.58 mas, corresponding to $\sim 11.6 D_\star$, under their assumption of 0.22 mas for the stellar diameter, with position angle of 110° .

Following the addition property of Fourier transform, in such a two-component geometric approach, in this case above, the total model visibility, V_{total} , is then expressed as (see Eq. 6 of Sigut et al. 2015):

$$V_{\text{total}} = F_\star V_{\text{UD}}(0.22 \text{ mas}) + (1 - F_\star) V_{\text{GB}}. \quad (5.2)$$

In Eq. 5.2, F_\star is the (normalized) flux contribution from the central star, and then $1 - F_\star$ the one from the disk. $V_{\text{UD}}(0.22 \text{ mas})$ is given by Eq. 5.1 for $\theta = 0.22$ mas, while the visibility from the elliptical Gaussian distribution is described by (e.g., see Tycner et al. 2006):

$$V_{\text{GB}}(s) = \exp \left[-\frac{(\pi a s)^2}{4 \ln 2} \right], \quad (5.3)$$

where a is the major-axis Full width at half maximum (FWHM) of the Gaussian, and

5.2. Analytical model fitting: the software LITpro

the variable s is defined as follows:

$$s = \sqrt{r^2(u \cos \phi - v \sin \phi)^2 + (u \sin \phi + v \cos \phi)^2}, \quad (5.4)$$

where ϕ and r are respectively the major-axis position angle and axial ratio (a/b) of the disk, represented by the Gaussian, following the same notation as in Fig. 5.2. Note that for a circular Gaussian distribution ($r = 1$, non-flattened), s is simply replaced by the term $\sqrt{u^2 + v^2}$, as in Eq. 5.1 for the uniform disk.

5.2 Analytical model fitting: the software LITpro

5.2.1 Overview: a tool dedicated to interferometric modeling

LITpro¹ (Tallon-Bosc et al. 2008) is a model-fitting software for visible and infrared interferometric data developed by the Jean-Marie Mariotti Center (JMMC). It allows us to combine multiple geometric model components and to derive the model parameters that minimizes the reduced χ^2 to data. In order to search for the local χ^2 minimum, this modeling software is based on a Levenberg-Marquardt algorithm in combination with a Trust Region method. Details on these numeric methods can be found in Tallon-Bosc et al. (2008) and references within.

The data is read by LITpro in the OI Exchange Format (OI-FITS Pauls et al. 2005), allowing to store, following the OIFITS notation: squared visibilities (VIS2), amplitude and phase of complex visibility (VISAMP and VISPHI), amplitude and phase of bispectrum (T3AMP and T3PHI). It allows to include data from several OIFITS files, reorganizing the arrays in the memory in order to make the data analysis more efficient. LITpro has been updated and currently improved by JMMC and is publicly available², in addition to many other softwares² dedicated to optical interferometry that also are supported by JMMC³.

LITpro has several built-in functions to be chosen by the user to the data analysis, such as uniform and elliptical disk and uniform and elliptical Gaussian distributions, which are of interest to interpret interferometric data of Be stars. The complete list of available models in LITpro can be found in the LITpro Reference Guide (Table 1) in the LITpro website (see footnote 2 of this chapter). For instance, somewhat more complex models are allowed, such as limb-darkened disk model, which are of interest to evaluate the limb-darkening effect using interferometric data (e.g., see Nardetto et al. 2016, and references within). It is important to stress that LITpro works directly in

1. Acronym for Lyon Interferometric Tool prototype.

2. LITpro website: <http://www.jmmc.fr/litpro>

3. See <http://www.jmmc.fr/english/the-jmmc/who-are-we/>.

5.2. Analytical model fitting: the software LITpro

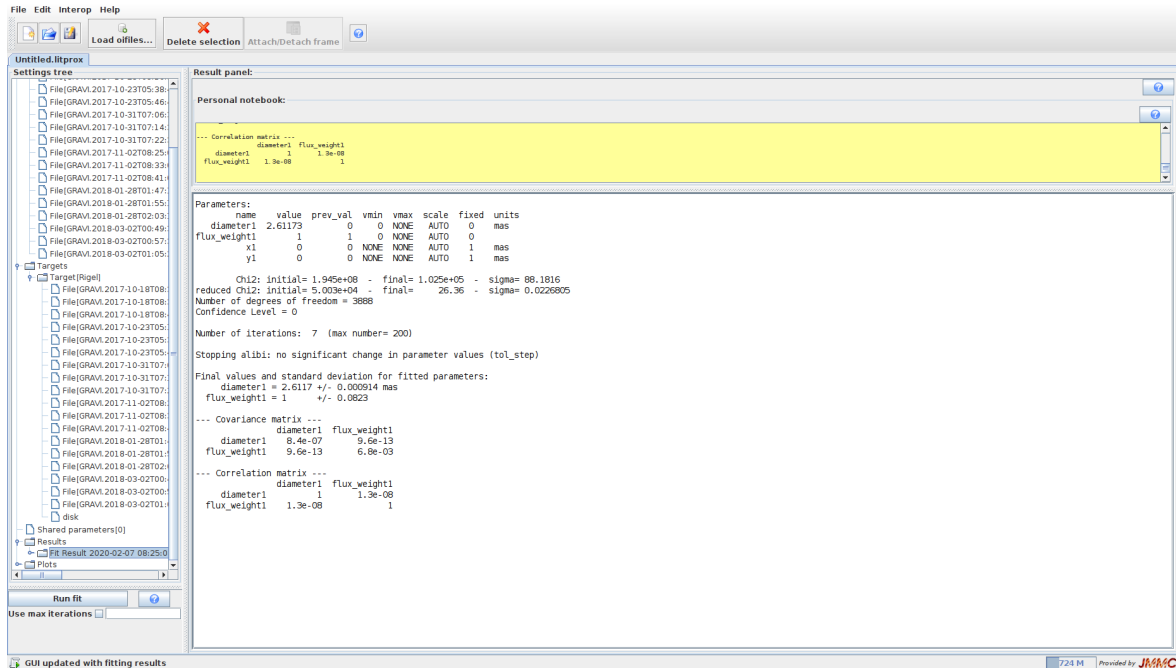


Figure 5.3 – Example of the graphical interface of LITpro, used in this case to model VLTI/GRAVITY data of Rigel using a uniform disk model: best-fit model with angular diameter of ~ 2.61 mas. See text for discussion.

the Fourier space, using the analytical solutions of the Fourier transform for the chosen built-in functions.

5.2.2 Example of modeling: VLTI/GRAVITY data of Rigel

For instance, Fig. 5.3 shows the graphic interface of LITpro (version 1.0.16). It works using Graphic User Interface in JAVA language. In this case, we consider a simple uniform disk to model our VLTI/GRAVITY squared visibility (absolute visibility) of the B supergiant Rigel (see Sect. 7.1.2). The fitted-visibility curve to our data is shown in Fig. 5.4. This is the visibility at the close-by continuum region, $\sim 2.145\text{-}2.155 \mu\text{m}$, to the $\text{Br}\gamma$ line.

Considering a uniform disk, the best-fit model, $\theta \sim 2.61$ mas, is very efficiently found by LITpro, as just 7 iterations are needed to be performed from a total of 200 maximum iterations that were chosen in this case. The large value of minimum reduced χ^2 (~ 26) comes from the unrealistic very low error bars considered in the fitting. However, one sees how the minimum χ^2 is well constrained around $\theta = 2.61$ mas (see the left panel of Fig. 5.4).

In addition to the example above, I extensively used the software LITpro in my spectro-interferometric study on the Be star *o* Aquarii, as will be discussed in Sect. 6.3. In advance of discussion, the best-fit geometric models to VEGA calibrated data of *o* Aquarii are presented in Fig. 2 of de Almeida et al. (2020), as well as Table 1 of

5.2. Analytical model fitting: the software LITpro

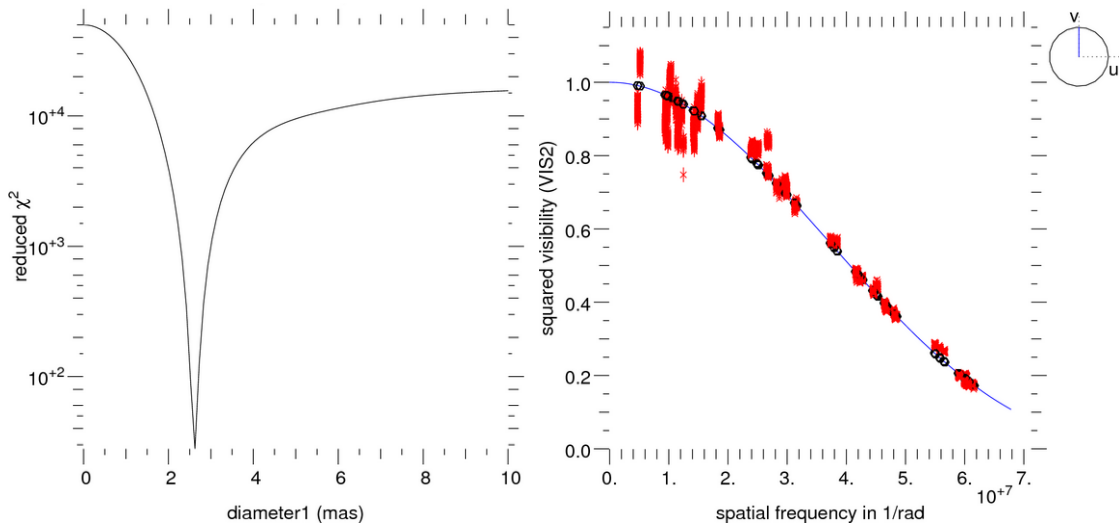


Figure 5.4 – Geometric modeling, using the software LITpro (Fig. 5.3), of our VLTI/GRAVITY data of Rigel: squared visibilities at the close-by continuum region ($\sim 2.145\text{--}2.155 \mu\text{m}$) to $\text{Br}\gamma$. The χ^2 -map delivered by LITpro is shown in the left panel. The GRAVITY data (red points) is compared with the fitted geometric model (open points, blue line) in the right panel. See text for discussion.

the same article shows the summary of the results for the (angular) extension of its photosphere and circumstellar disk, based on that data and LITpro modeling.

5.2.3 Limitations: what is the global χ^2 minimum?

Since LITpro is a robust fitting-tool that uses a Levenberg-Marquardt algorithm, it allows us to find local χ^2 minimum, or, minima, to explain the data, based on the partial derivatives of the selected functions to model the data.

From Fig. 5.4, one sees that the global minimum using a uniform disk model is easily found (around $\theta = 2.61 \text{ mas}$) in this case. However, discriminate the global minimum among several local minima can be a much harder task to be performed, especially considering more complex models, and ultimately the own data. More generally, this is one major difficulty of non-linear model fitting methods, as the Levenberg-Marquardt method.

Lastly, as a practical point-of-view, we point out that the results found by LITpro are somewhat sensitive to the initially adopted parameter values. Some tools have been developed to guide the user to find the global minimum (as the χ^2 -map shown Fig. 5.4). To verify if LITpro is not indeed converging to a particular local minimum solution, the user should test different adoptions for the initial values of the model parameters.

5.3 The kinematic code

5.3.1 Overview: the model parameters

The kinematic code was developed by A. Meilland (Observatoire de la Côte d’Azur) with the particular purpose of constraining the geometry and kinematics of circumstellar disks using spectro-interferometric data (Sect. 3.6), especially of Be stars.

It was firstly used by Delaa et al. (2011) to model VEGA observations of the Be stars 48 Persei and ϕ Persei, and since then it has been extensively used in other interferometric studies of Be stars (e.g., Meilland et al. 2011, 2012; Jamialahmadi et al. 2015; Cochetti et al. 2019). The interested reader can find a broader discussion on this code in these references above.

More recently, the kinematic code was also employed to interpret the VEGA and AMBER spectro-interferometric data of o Aquarii, presented in this thesis (Sect. 6.3). In advance of discussion, a summary of our best-fit kinematic models (to VEGA and AMBER data) is found in Table 2 of de Almeida et al. (2020).

Before discussing on how the kinematic code works, a full list of parameters of the kinematic model is given as follows:

- (i) The global simulation parameters: size of the simulation in pixels ($n_x = n_y$), field of view in stellar diameter (fov), number of wavelength (n_λ), central wavelength of the emission line (λ_0), step in wavelength ($\delta\lambda$), and spectral resolution (R).
- (ii) The global geometric parameters: stellar radius (R_\star), distance (d), inclination angle (i), and disk major-axis position angle (PA).
- (iii) The disk continuum parameters: disk major-axis FWHM in the continuum (a_c), disk continuum flux normalized by the total continuum flux (F_c).
- (iv) The disk emission line parameters: disk major-axis FWHM in the line (a_l) and line equivalent width (EW).
- (v) The global kinematic parameters: stellar rotational velocity (v_{rot}), expansion velocity at the photosphere (v_0), terminal velocity (v_∞), exponent of the expansion velocity law (γ), and exponent of the rotational velocity law (β).

Thus, in the total, 13 parameters describe the geometry and kinematics of the central stars and the disk.

5.3.2 Model description: the central star and the circumstellar environment

This codes uses simple geometric models to describe the emissions from the star and its environment, but taking into account the Doppler effect on the considered spectral channel (line), being thus suited to model spectro-interferometric data (see, again, Fig. 3.9).

The flux contribution from the star is modelled as a uniform disk, while the circumstellar disk is modelled as two (elliptical) Gaussian distributions: one for the disk emission in the continuum and the other for the disk emission in the line.

The disk intensity map in the line is computed taking into account the Doppler effect in the considered spectral channel due to the disk velocity of expansion and rotation. The expansion velocity is parameterized as follows:

$$v_{\text{radial}}(r) = v_0 + (v_\infty - v_0) \left(1 - \frac{R_\star}{r}\right)^\gamma. \quad (5.5)$$

We aware the reader that Eq. 5.5 is indeed Eq. 1.4 (Sect. 1.2.1), and thus following the CAK-theory, but changing the variable β in Eq. 1.4 to γ (as in the parameter list in Sect. 5.3.1). This notation for the wind velocity-law in Sect. 1.2.1 follows the practices in the literature of radiative line-driven winds (e.g., Puls et al. 2009). As described below, this change is done because the variable β is used here (and in de Almeida et al. 2020) to describe the rotational velocity law.

The rotational velocity of the disk in the kinematic model is given by a simple power law with exponent β :

$$v_{\text{azimuthal}}(r) = v_{\text{rot}} \left(\frac{r}{R_\star}\right)^\beta. \quad (5.6)$$

Note that, as Be disks show very slow expansion velocity, the parameters v_0 and v_∞ can be set zero ($v_{\text{azimuthal}} \gg v_{\text{radial}}$).

Taking into account Eqs. 5.5 and 5.6, the resulting velocity field, v_{proj} , along the observer's line of sight (ϕ) is then computed as follows:

$$v_{\text{proj}} = (v_{\text{azimuthal}} \sin \phi - v_{\text{radial}} \cos \phi) \sin i. \quad (5.7)$$

We remind the reader that i is defined as the stellar inclination angle (Sect. 5.3.1). From v_{proj} , iso-velocity maps ($R(x, y, \lambda, \delta\lambda)$), projected along the line of sight, are calculated for each considered spectral channel:

5.3. The kinematic code

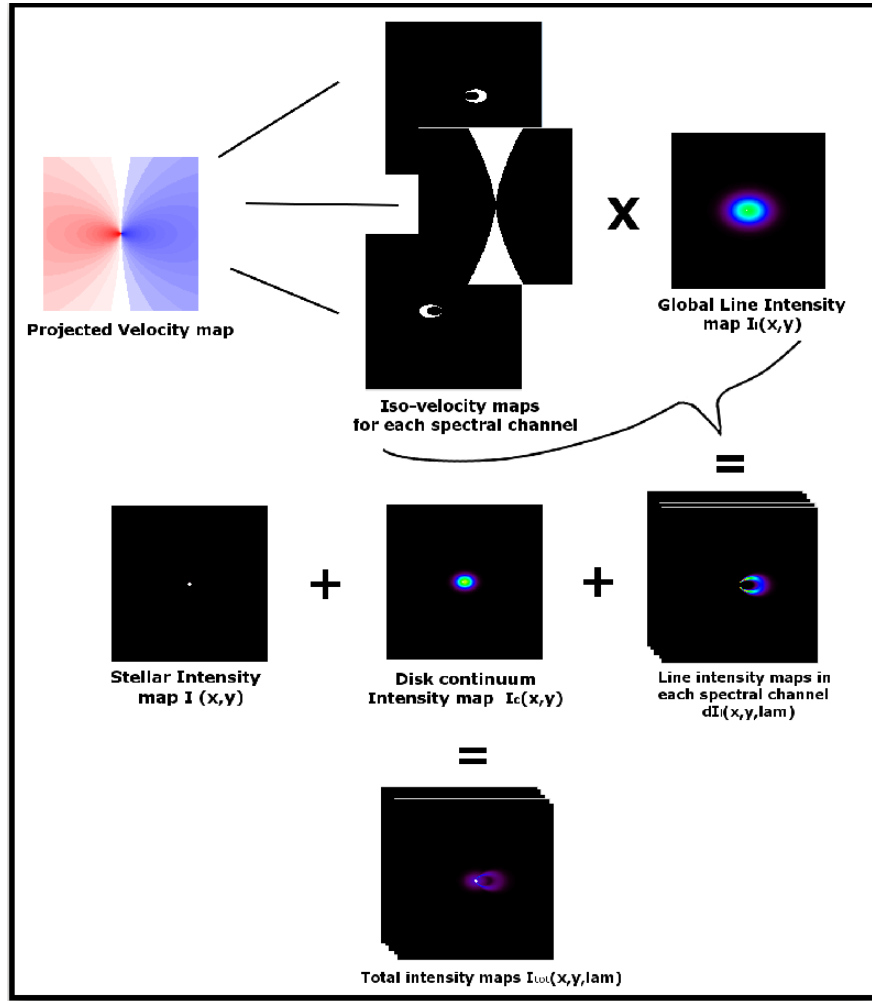


Figure 5.5 – Chart showing the calculation of the intensity map of the central star plus disk system (total intensity map shown in the bottom) with the kinematic code. See text for discussion.

$$R(x, y, \lambda, \delta\lambda) = \frac{1}{\sigma\sqrt{2\pi}} \exp \left[\left(-\frac{v_{\text{proj}}(x, y) - v_{\text{doppler}}(\lambda)}{\sqrt{2}\sigma} \right)^2 \right], \quad (5.8)$$

where x and y are the coordinates of the object (projected on the sky), and v_{doppler} is the Doppler displacement in the line profile, with σ given by:

$$\sigma = \frac{\delta\lambda c}{2\lambda\sqrt{2\ln 2}}. \quad (5.9)$$

Finally, the total intensity map (I_{total}) can be calculated as follows:

$$I_{\text{total}} = I_{\star}F_{\star} + I_c^{env}F_c + R(x, y, \lambda, \delta\lambda)I_{\text{line}}EW, \quad (5.10)$$

where I_{\star} is the star intensity (constant brightness, a uniform disk), I_c^{env} is the circumstellar intensity in the continuum. The parameters F_{\star} and F_c are, respectively, the stellar and disk continuum fluxes normalized by the total continuum flux, and the other

5.3. The kinematic code

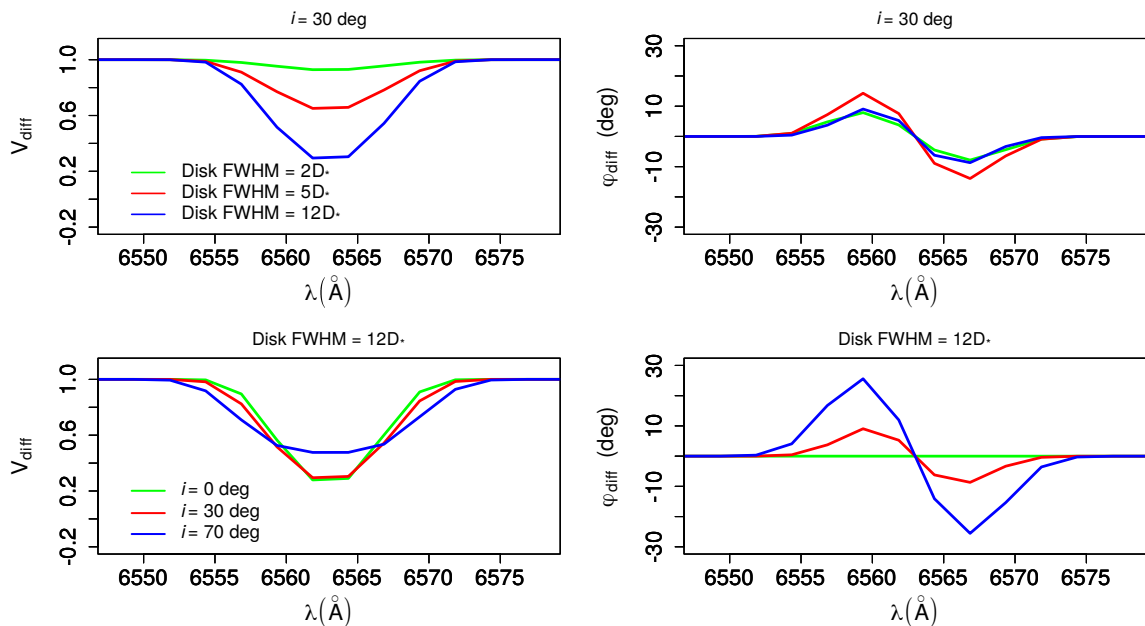


Figure 5.6 – Comparison between kinematic models, calculated around the $H\alpha$ line, by varying just one selected parameter: the disk size in the line (top panels, FWHM from 2 to 12 D_* with i fixed at 30°) and the stellar inclination angle (bottom panels, i from 0 to 70° with FWHM fixed at 12 D_*). Simulated differential visibility and phase for one of our CHARA/VEGA measurements of α Aquarii. Note how the variation of these parameters changes the visibility and phase in a different way. See text for discussion.

variables were described so far (see the list of parameters shown at the beginning of this section). The last term of 5.10 corresponds to the circumstellar disk intensity in the spectral line. Further details on Eqs. 5.7, 5.8, and 5.10 can be found in Delaa et al. (2011).

A schematic of the calculation with the kinematic mode is presented in Fig. 5.5. In the end, an image cube (intensity map for each value of wavelength) of the modeled star plus disk system is calculated and then the interferometric quantities, as a function of wavelength, are extracted by applying the discrete Fourier transform using a fast Fourier transform algorithm⁴ to the intensity maps at each value of wavelength.

5.3.3 Parameters effects on the interferometric quantities

An example of observables (differential interferometric quantities and the spectrum in $H\alpha$) using the kinematic code was presented in Fig. 3.9 (Sect. 3.6).

In Fig. 5.6, we compare kinematic models, calculated in the $H\alpha$ line, with different values of disk size in the $H\alpha$ line (a_l) and stellar inclination angle (i). All the other parameters are fixed, then the effects of these two parameters can be easily seen in the

4. Currently, the kinematic code is written in IDL language. Details about the IDL implementation of the fast Fourier transform algorithm can be found at <https://www.harrisgeospatial.com/docs/FFT.html>.

predicted differential visibility and phase in $H\alpha$. From that, in general, one sees how the drop in visibility is more affected by varying the extension of the disk in the kinematic model, while the differential phase is more affected by changing the inclination.

As expected, a disk with a larger extension shows a larger drop in visibility. In particular, when considering $i = 0$, and thus no Doppler effect in the line, with $v_{\text{proj}} = 0$ (see Eq. 5.7), the differential phase is equal to zero as the photocenter of the system (star plus disk) is symmetric in the line (and in the continuum). Nevertheless, notice that varying i will also affect the visibility width and drop in the line. A more comprehensive discussion on the effects of the kinematic model parameters on the visibility and phase can be found in Sect. 5.3.2 of Meilland et al. (2012) and Sect. 3.1 of Cochetti et al. (2019).

5.3.4 An example of model fitting: AMBER data of the nova T Pyxidis

Despite being widely used in studies about Be stars, the kinematic code can also be applied to the interferometric analysis of other stellar sources.

For instance, Fig. 5.7 shows the results of Chesneau et al. (2011) to modeling AMBER differential data (in the $\text{Br}\gamma$ line) of the nova object T Pyxidis⁵ observed at different days from the outburst (about one week of difference). In this case, Chesneau et al. (2011) used a modified version of the kinematic code, as presented in Sect. 5.3.2, just considering radial expansion of the novae shell (with two components, polar and equatorial velocities).

From Fig. 5.7, one sees how the AMBER visibility drops in $\text{Br}\gamma$ as the circumstellar material evolves since the outburst onset. Despite being dependent on the specific baseline configuration, an inverse S-shaped phase is observed for this object, being successfully modelled using the kinematic code with different values of polar and equatorial velocities for the two observations at different epochs (see Chesneau et al. 2011).

In short, based on the kinematic code, the study Chesneau et al. (2011) provided the first direct access to the morphology and kinematics of novae at an early-stage from the first days of the explosion. This is one of the outstanding questions in astrophysics. One remarkable result found by these authors is that novae shell expand in a bipolar-shape since the very early-stage, instead of a spherically symmetric outflow, in line with some previous studies of novae using interferometry (e.g., Chesneau et al. 2007).

5. Novae are outbursts ignited by thermonuclear fusion on the surface of white dwarfs due to material transferred from an evolved close binary companion, a red giant star (e.g., see Bode & Evans 2008).

5.4. Kinematic model fitting using MCMC

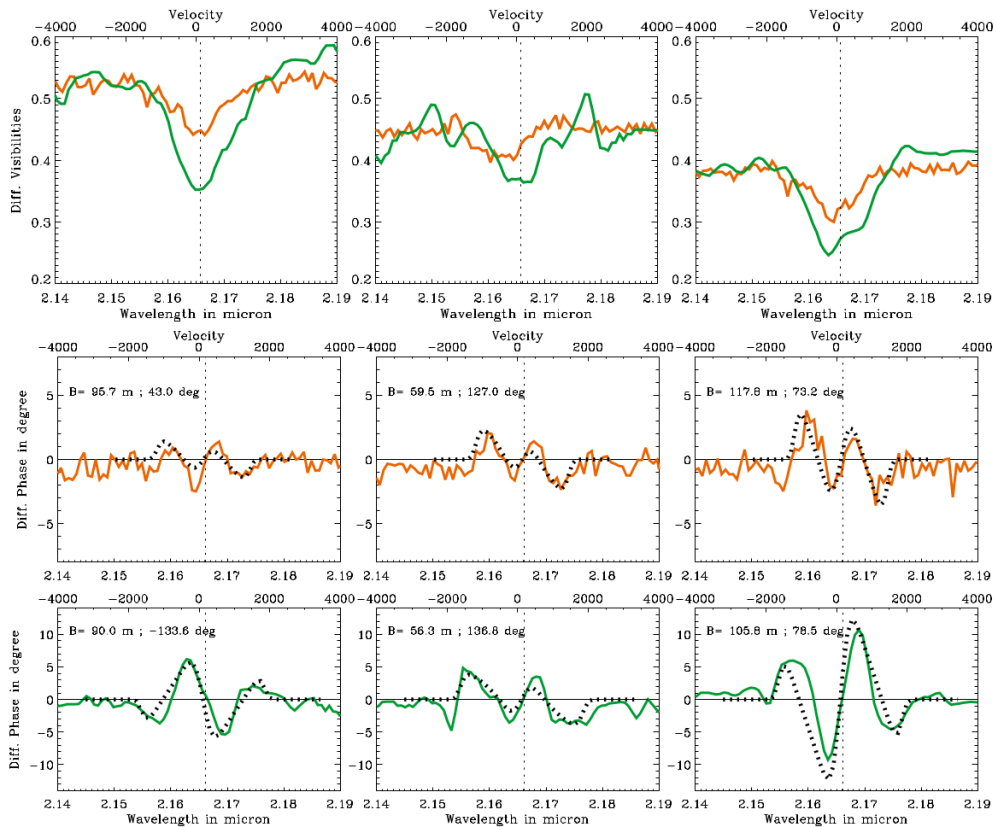


Figure 5.7 – VLTI/AMBER observations in Br γ (color lines) of the nova T Pyxidis at different days since the outburst onset (28.76 days in orange and 35.77 days in green). The best-fit kinematic models of Chesneau et al. (2011) to one each of these observations is shown dashed-line. See text for discussion. Adapted from Chesneau et al. (2011).

5.4 Kinematic model fitting using MCMC

5.4.1 Why use a MCMC fitting-method to the kinematic code?

When dealing with just one free parameter, such as in the geometric modeling with a uniform disk (Eq. 5.1), the best estimate parameter to the data can be easily found, considering that the parameter space was sufficiently well explored for finding the global minimum (if it exists) to the data. However, this task becomes harder as the number of free parameters of our analytical model increases. As discussed in Sect. 5.3, the kinematic model has a total of 13 free parameters.

For example, we show, in Fig. 5.8, the χ^2 map of kinematic models, calculated around H α , to model our VEGA dataset of *o* Aquarii, varying just one parameter: the disk FWHM major-axis in H α (a_l , in stellar diameters). In Fig 5.8, all the other model parameters are fixed. Here, v_0 , v_∞ , and γ are fixed at zero. One sees that the reduced χ^2 is minimized at $a_l \sim 9.5 D_\star$, with $\chi^2 = 4.5$. However, is this indeed the real minimum χ^2 to explain our dataset and then $a_l = 9.5 D_\star$ the best estimate? Of course, this result depends on the assumptions for the other parameters, which are fixed here.

5.4. Kinematic model fitting using MCMC

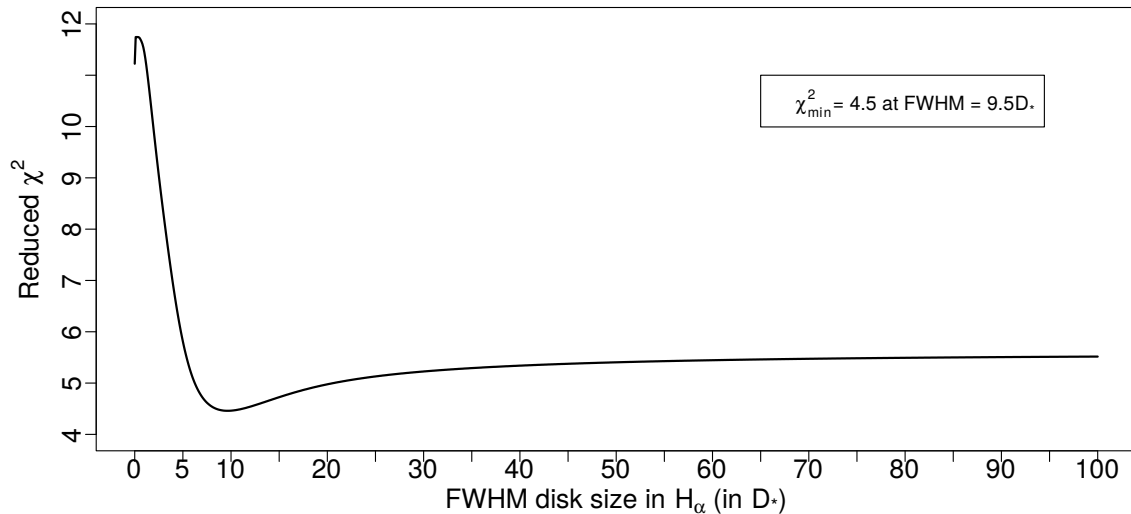


Figure 5.8 – χ^2 map to VEGA data of *o* Aquarii for kinematic models (calculated around $H\alpha$) with different values of disk size (major-axis FWHM of an elliptical Gaussian distribution, in stellar diameter). All the other parameters are fixed, as follows: $R_\star = 3.7 R_\odot$, $d = 134$ pc, $i = 60^\circ$, $PA = 110^\circ$, $a_c = 0$, $F_c = 0$, $EW = 19$ Å, $v_{\text{rot}} = 450$ km s $^{-1}$, and $\beta = -0.5$ (see Sect. 5.3.1).

Answering this question above demands to explore the parameter spaces of our kinematic code, this can be a hard task when dealing with more complex analysis than the one presented in Fig. 5.8 (one free parameter). For instance, varying the parameter values also in 1000 regular steps, as in Fig. 5.8 for the disk size, yields to the calculation of 10^{15} kinematic models, being this an unpractical task to performed.

In conclusion, it is conspicuous the necessity of a wiser approach to explore the model parameter spaces and finding the set of best-fit parameters that explain the data. All the previous studies on Be stars cited at the beginning of Sect. 5.3.1, employ the kinematic code by varying manually their parameters in order to find the best-fit parameters and their associated uncertainties, and then being biased by the very limited number of model tests to their datasets.

We could approach this question above in terms of the same fitting-method of LITpro (Sect. 5.2), that is, employing a Levenberg-Marquardt method to constrain the kinematic model parameters. However, as discussed in Sect. 5.2.3, one major problem of this fitting-method relies on possibly getting stuck at local minima that are far-away from the global minimum to explain the data. Such common issue of frequentist approaches, as the Levenberg-Marquardt method, can be overcome by employing a Bayesian statistical inference technique, as the so-called Markov-Chain Monte Carlo (MCMC) method that is discussed below.

5.4.2 The MCMC method

This issue above can be overcome using a MCMC fitting procedure. The MCMC method is a way to estimate the probability density function of the model parameters by sampling the parameter spaces. Then MCMC is inherently a Bayesian statistical inference method, that is, relying on the so-called Bayes’ theorem (e.g., see Sect. 3.8 of Feigelson & Babu 2012).

One of its main advantages is to allow us to infer the best-fit parameters and their associated uncertainties by directly calculating statistics, such as the mean and standard deviation, as well as the median and quartiles, from the probability density function. Also, as being a Bayesian inference method, it allows us to find the best-fit parameters based on prior information about the object of science, both from an empirical and theoretical point-of-view.

The basic idea behind MCMC is to perform a random walk covering the model parameter spaces, in a way that the probability of a “walker” to arrive at a certain set of parameter values is proportional to the probability density function. The random walk is performed by following a Markov Chain. This means that the selection of the next successive point to be covered depends only on the immediate previous state of the chain.

5.4.3 The code EMCEE: a MCMC implementation

In this section we implemented an automatic-fitting procedure to the kinematic model using the code EMCEE⁶ (Foreman-Mackey et al. 2013). It is a MCMC implementation in Python, based on the MCMC method of Goodman & Weare (2010). EMCEE is more efficient and simpler to use than more traditional MCMC methods, such as the ones based on the Metropolis-Hastings algorithm (see, e.g., Foreman-Mackey et al. 2013). For example, considering a N -dimensional parameter space, these latter MCMC codes require the evaluation of $\sim N^2$ tuning parameters, while this problem is limited to just one or two parameters in EMCEE, such as by setting a number of walkers. Then EMCEE has been more widely used in a series of astrophysical studies⁷. In particular, it has been used in some recent works on stellar spectroscopy and interferometry (see, e.g., Monnier et al. 2012; Domiciano de Souza et al. 2014; Sanchez-Bermudez et al. 2017; Mossoux et al. 2018; Bouchaud et al. 2020).

Denoting y as the predicted model value and x the observed one, the likelihood function p_{like} of the model is given by the following quantity (see Eq. 3.67 of Feigelson

6. Publicly available package. See the EMCEE website: <https://emcee.readthedocs.io/en/stable/>.

7. A list of astrophysical studies using EMCEE can be found at <https://EMCEE.readthedocs.io/en/stable/testimonials/>.

5.4. Kinematic model fitting using MCMC

& Babu 2012):

$$p_{\text{like}} = \frac{1}{\sqrt{2\pi}\sigma} \exp \left[-\frac{(y_i - x_i)^2}{2\sigma^2} \right], \quad (5.11)$$

where σ is the standard deviation of the data. Thus, following the definition of model χ^2 , and apart from a constant, the (logarithm) of the likelihood function is given by:

$$\ln p_{\text{like}} = -\frac{\chi^2}{2}. \quad (5.12)$$

From Eq. 5.12, one sees that the maximization of the likelihood function means to minimize the model χ^2 .

5.4.4 Using prior information with EMCEE

Instead of working on the search of the maximum likelihood function, a MCMC method works with the posterior probability function (denoted here by p_{post}) from Bayesian inference. This means that the tested sample by MCMC is sensitive to preset information given by a prior probability function p_{prior} :

$$\ln p_{\text{post}} = \ln p_{\text{like}} + \ln p_{\text{prior}}. \quad (5.13)$$

Such a prior probability function typically can be set by physical conditions known to our problem. For example, based on the projected rotational velocity, $v \sin i$, we can define p_{prior} as follows:

$$p_{\text{prior}} = -w \left(\frac{[(v \sin i)_{\text{model}} - (v \sin i)_{\text{obs}}]^2}{2\sigma^2} \right), \quad (5.14)$$

where the $(v \sin i)_{\text{model}}$ is simply calculated from the sampled MCMC values for v_{rot} and i of the kinematic model, and $(v \sin i)_{\text{obs}}$ is the prior information. Here, the variable w denotes an arbitrary weight on the prior probability function, and σ the error bar on the measured value of $v \sin i$.

Note that $w = 0$ means to set Eq. 5.13 equal to 5.12, this being the simplest case. As will be discussed in Sect. 6.3, this particular prior function is included in our modeling of *o* Aquarii data using the EMCEE code to find the best-fit kinematic model parameters.

5.4.5 Example of modeling: VLT/AMBER data of *o* Aquarii

Fig. 5.9 shows the results for the disk emitting size in Br γ from one of our MCMC tests to fit the AMBER data of *o* Aquarii (Sect. 6.3) using the kinematic model. Notice that this MCMC run quickly converges to the value of ~ 11.8 stellar diameters for the disk extension in Br γ of the Be star *o* Aquarii.

5.4. Kinematic model fitting using MCMC

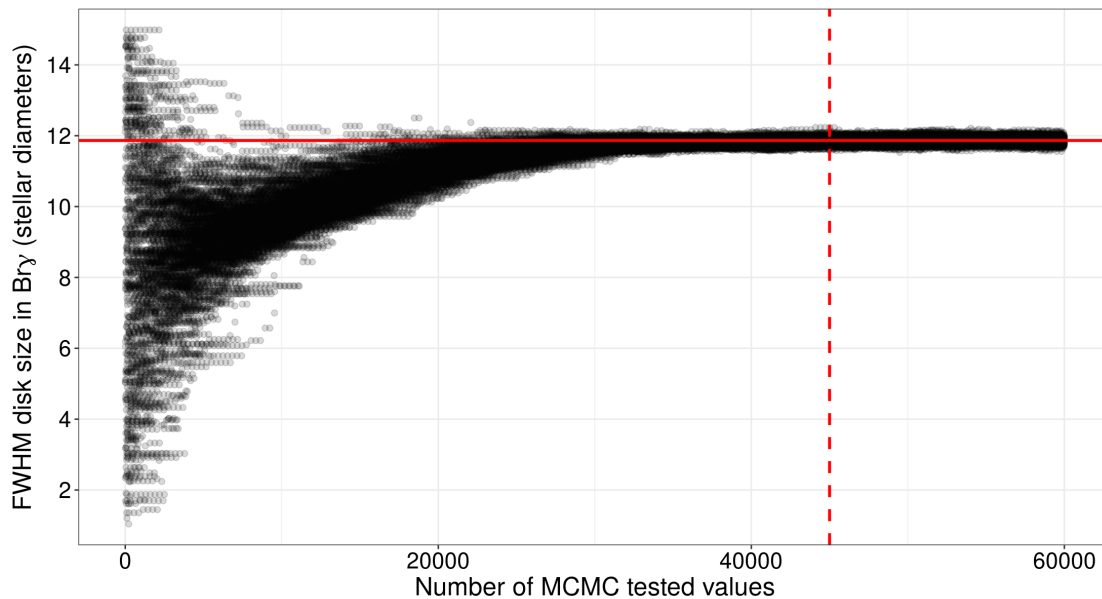


Figure 5.9 – Kinematic model disk size (in $\text{Br}\gamma$, fit to AMBER data of α Aquarii) sampled in a MCMC run using EMCEE with 300 walkers and 200 iterations in total. The vertical dashed red line marks the end of the burn-in phase of the MCMC run. The horizontal solid red line marks the value of disk size equal to $11.8 D_{\star}$. See text for discussion.

More generally, the quantity of parameter samples in the EMCEE run is controlled by the total number of walkers and iterations performed in each walker: N^w of walkers multiplied by N^i of iterations. Since we chosen 300 walkers and 200 iterations in the MCMC run shown in Fig. 5.9, the number of tested values for a_{line} ($\text{Br}\gamma$) is equal to 60000.

The calculation of the statistics to find the best estimate is performed after the burn-in phase of the run (150 iterations in this case), that is, all the values tested before that are discarded in the determination of the best-fit parameters. The acceptance fraction (a_f), in each walker, is an important parameter to evaluate if the MCMC sampling represents the posterior distribution of the model parameters well. In each walker, the acceptance fraction expresses the ratio between the accepted steps and the total number of steps. For instance, if a_f is very close to one, this means that almost all the proposed steps are accepted in the MCMC run and then the tested values are highly independent among them, producing chains that are not representative to the target's posterior distribution. As a rule of thumb, the acceptance fraction, at least the averaged value among all the walkers, should be $\sim 0.2-0.5$ (see Foreman-Mackey et al. 2013, and references within). The mean a_f is ~ 0.56 in our MCMC run showed in Fig. 5.9.

5.4.6 Further improvements

Lastly, some coding improvements are needed for a better computational performance of our MCMC fitting procedure.

Since the kinematic code is written in the IDL language, the current MCMC fitting code employs a Python library (pIDLy⁸) to run the kinematic code. One con of this procedure comes from the execution time that is needed to calculate a single kinematic mode. For instance, it can take ~ 6 and 9s to simulate the interferometric quantities for a large sample of VEGA and AMBER observations, as presented in this thesis⁹. Although still a feasible approach in terms of time, in this case, a robust MCMC run using a large number of walkers and iterations, such as 300 and 200, requires a computation time of about 4 and 6 days.

As our MCMC code was written in Python, it is needed to employ specific Python libraries to import the outputs from the kinematic code (IDL), and then wasting computing time to perform this process. A natural solution for a better performance on the computing time is then to re-write the kinematic in Python language. Currently, we have been working on MCMC tests with the kinematic code written in Python. This improvement in terms of coding will be useful for our future project on a large VEGA and AMBER¹⁰ survey of Be stars (Sect. 7.2).

8. Available at <https://pypi.org/project/pIDLy/>

9. These computing times stand for calculations were performed using CPU clusters from the CentOS 7.

10. As discussed in Sect. 3.7.4, despite the decommissioning of the VLTI/AMBER instrument in 2017, several studies on hot stars have been performed since then.

Chapter 6

Published studies

Contents

6.1	Mini-survey of O stars	143
6.1.1	Problems with the theory of line-driven winds: weak winds	143
6.1.2	Master thesis work	144
6.1.3	Improvements during my PhD	145
6.1.4	Results and conclusions	146
6.2	The LBV star P Cygni	194
6.2.1	Winds and episodic outbursts of LBVs	194
6.2.2	Intensity interferometry in a nutshell	195
6.2.3	My collaboration with the I2C team	195
6.2.4	Results and conclusions	196
6.3	The Be-shell star <i>o</i> Aquarii	208
6.3.1	Probing the Be phenomenon: why study <i>o</i> Aquarii with interferometry?	208
6.3.2	Observing <i>o</i> Aquarii in the AMBER and VEGA Be surveys	209
6.3.3	A multi-technique modeling approach: from analytical to numerical models	210
6.3.4	Results and conclusions	211

This chapter presents the results that I obtained during my PhD on three different studies about massive hot stars. They are presented here in chronological order of publication.

Sect. 6.1 discusses my first-authored A&A paper (de Almeida et al. 2019, hereafter Paper I) on spectroscopic analysis of O-type stars. An early summary about this topic is published in the proceedings of the XV Latin American Regional IAU Meeting (da G. de Almeida et al. 2017) and is also presented in Sect. 6.1. Sect. 6.2 discusses my co-authored MNRAS paper (Rivet et al. 2020, hereafter Paper II) on intensity

interferometry of the LBV star P Cygni. Lastly, Sect. 6.3 discusses my first-authored A&A paper (de Almeida et al. 2020, hereafter Paper III) on spectro-interferometry of the Be star *o* Aquarii.

This study about *o* Aquarii is the principal paper of my thesis, for which I devoted most part of my work time during the PhD from learning about interferometric observations to their interpretation using different modeling methods (Chaps. 4 and 5).

6.1 Mini-survey of O stars

6.1.1 Problems with the theory of line-driven winds: weak winds

From the discussion in Chap. 1, O stars lose a significant fraction of mass through radiative line-driven winds during their short lifetimes. This affects their physical properties across the HR diagram such the stellar rotation and chemical surface abundances. However, although the theoretical bases of line-driven winds were set around half a century ago, it is still uncertain what are the real mass-loss rates among different luminosity classes of late- and early-type O stars. Based on spectroscopic analysis performed at different wavelength regions, the values of mass-loss rate for these stars seem to (at least partially) diverge, as discussed below.

This paper investigates the so-called weak wind phenomenon, also called as the weak wind problem (e.g., Martins et al. 2005b; Marcolino et al. 2009; Muijres et al. 2012). As pointed out by Puls et al. (2009), it is one of the main open issues in the massive star literature. As discussed in Sect. 1.2.3, this problem is found for late O dwarfs (O8-9V stars) being characterized by a large disagreement between the mass-loss rates derived from UV spectroscopic studies and the values that are predicted based on hydrodynamical simulations (Vink et al. 2000, 2001), the latter ones are larger by up to two orders of magnitude.

It is still not completely clear if the weak wind problem only arises based on the analysis of UV spectra of O stars. Marcolino et al. (2009) verified that the UV mass-loss rates, that is, determined from fitting UV spectra, for their sample of five late O dwarfs match the observed $H\alpha$ profiles well in overall. On the other hand, both their final models (with UV mass-loss rates) and the theoretical mass-loss rates using the recipe from Vink et al. (2000) are able to reproduce fairly well the observed $H\alpha$ profiles for two out of their five objects. This means that with respect to the visible region, both models with lower (from spectroscopy) and higher (from theory) mass-loss rates are somewhat indistinct for these stars.

Furthermore, some studies claim that only X-ray observations could provide reliable

6.1. Mini-survey of O stars

estimates of the mass-loss rate for late O dwarfs (see Oskinova 2016, and references within). In this case, for a low-density wind, as in late O dwarfs, the bulk of the wind would be in a hot gas state, filling a much larger volume than the cool gas. This would prevent us from deriving the real mass-loss rate based purely on the modeling of UV and visible spectra. Currently, this is a debatable question regarding weak winds due to the low statistics of analysed objects with X-ray spectra: it is partially supported by some studies (e.g., Huenemoerder et al. 2012), while other studies do not support this idea. For instance, Cohen et al. (2014) found a weak wind for the late O dwarf ζ Ophiuchi (O9.7V), deriving a mass-loss rate of $\sim 1.5 \times 10^{-9} M_{\odot} \text{ yr}^{-1}$ from modeling X-ray line profiles. This result is in line with the mass-loss rate determined by Marcolino et al. (2009) for this star, namely, $\sim 1.6 \times 10^{-9} M_{\odot} \text{ yr}^{-1}$ (mass-loss rate derived from fitting UV lines). On the other hand, the mass loss recipe of Vink et al. (2000) predicts a mass-loss rate of the order of $10^{-7} M_{\odot} \text{ yr}^{-1}$ for ζ Ophiuchi (Marcolino et al. 2009).

Lastly, state-of-the-art stellar evolution models (e.g., Ekström et al. 2012; Meynet et al. 2015) use the mass-loss recipe of Vink et al. (2000, 2001) for the wind of massive stars during the H-burning phase, and thus being likely overestimated for the less luminous massive stars. In short, these questions above show the current importance of investigating the phenomenon of weak winds on O stars, demanding a multi-wavelength spectroscopic analysis of their wind properties.

6.1.2 Master thesis work

I started to work on this project during my Master thesis (de Almeida 2016) under the supervision of W. L. F. Marcolino (Observatório do Valongo, Brazil). We aimed to investigate weak winds among Galactic late-type O giant stars (O8-9.5III). These stars are somewhat more evolved objects than dwarfs and have luminosities around the critical value proposed in the literature of $\log(L_{\star}/L_{\odot}) \approx 5.2$, for which the weak wind problem seems to begin (onset of weak winds). So far, this problem has only been reported in late O and early B dwarfs (see Hillier 2020, and references within). We performed a detailed UV and visible spectroscopic analysis using sophisticated non-LTE atmosphere models calculated with the code CMFGEN of nine O8-O9.5III stars, namely: HD 156292, HD 24431, HD 105627, HD 116852, HD 153426, HD 218195, HD 36861, HD 115455, and HD 135591.

For this purpose, we used high resolution UV and visible spectra to derive the stellar and wind properties of our sample. The UV spectra were observed with the International Ultraviolet Explorer (IUE) telescope, using the Short Wavelength Prime (SWP)

6.1. Mini-survey of O stars

instrument¹. The spectra cover the wavelength interval of $\sim 1200\text{--}1975$ Å. As discussed in Sect. 2.3, this spectral region is important for the determination of the physical properties of O-type stars, which display lines formed both in the photosphere (the so-called UV iron forest) and in the wind region (such as N v $\lambda 1240$, Si iv $\lambda\lambda 1394, 1403$, C iv $\lambda\lambda 1548, 1551$ and N iv $\lambda 1718$). For the visible data, covering the H α line, we observed six stars of our sample using the FEROS spectrograph mounted at the ESO/MPG 2.2 m telescope in La Silla (Chile) from March 17 to 22, 2016. For the other three stars of our sample, we used public visible data obtained with the CFHT/ESPADONS and 2-m T el escope Bernard Lyot/NARVAL instruments.

This allowed us to probe the weak wind phenomenon on massive stars others than O dwarfs, based on a multi-wavelength quantitative spectroscopic approach, that is, using radiative transfer models (CMFGEN) to fit both the UV and visible (H α) observed spectra. Furthermore, combined UV and visible spectroscopic studies focusing on stellar and wind properties of late O giants are still somewhat scarce in the literature. To date, the study of Mahy et al. (2015) performed one of the most comprehensive UV and visible spectroscopic analysis of late O giants in the Galaxy, also using the code CMFGEN: five objects in total, but with UV spectra available for only two out of these five stars.

6.1.3 Improvements during my PhD

I did the bulk of the work on this topic during my Master thesis, but I substantively improved the analysis during my PhD thesis, in particular, based on suggestions provided by J.-C. Bouret (Observatoire de Marseille, France). These improvements are summarized in the following:

- (i) Determination of the stellar and wind parameters from the visible region for the complete star sample (Sects. 2 and 4 of Paper I). Previously, in de Almeida (2016), this was performed for the most part of the sample (seven out of nine objects), leaving to be performed for two stars (HD 24431 and HD 218195). Regarding the wind properties, this was particularly important for checking our mass-loss rates (derived using UV lines) to the observed H α line profile for all the star sample.
- (ii) Inclusion of more atomic species to evaluate their effects on the spectroscopic modeling, especially regarding the UV region (Sect. 4.1 of Paper I). Namely, at the end, the following ions were added to our basic CMFGEN models (Table 2 of Paper I): C II, N II, O II, Ne II, Ne III, Ne IV, Ne V, P IV, P V, S III, S IV, Ar III, Ar IV, Ar V, Ar VI, Cr III, Cr IV, Cr V, Cr VI, Ni III, Ni IV, Ni V, Ni VI. Due to the

1. Public data available in the Barbara A. Mikulski Archive for Space Telescopes (MAST): <https://archive.stsci.edu/iue/>

6.1. Mini-survey of O stars

high computational cost of including so much more elements, this was performed based on our best-fit CMFGEN model for one star of our sample (HD 116852).

- (iii) Analysis of the spectral energy distribution (SED) for all the stars of our sample, using Gaia DR2 parallaxes (Gaia Collaboration et al. 2018), and then exploring possible effects due to interstellar extinction (Sect. 4.2.1 of Paper I). Previously, we have adopted the luminosities values for each star based on sophisticated calibration for O stars provided by Martins et al. (2005a), without checking the predicted SED from our best-fit CMFGEN models in comparison with observations.
- (iv) Comparison between the mass-loss rates determined in Paper I with the theoretical values of Vink et al. (2000) and Lucy (2010b,a) (Sect. 4.3.2 of Paper I). Previously, all the comparison between our results on the wind mass-loss rate and the predicted values was relied on the study of Vink et al. (2000).
- (v) Evaluation of binary effects on the H α line profiles for three stars (spectroscopic double-lined binary systems) of our sample: HD 156292, HD 153426, and HD 156292 (Sect. 5.2 of Paper I). For that, multi-epoch public FEROS data of these stars were collected. We recall the reader that CMFGEN provides a spherically symmetric wind modeling. In short, as discussed in Sect. 5.2 of Paper I, the H α wings seems to be indeed affected by the binary nature of these stars. Nevertheless, our determined mass-loss rates are unlikely biased by binary effects, as the H α line core (sensitive to the wind mass-loss rate) is not substantively affected.
- (vi) Analysis of luminosity effects on the line profiles, in particular, Si IV $\lambda\lambda$ 1394,1403, C IV $\lambda\lambda$ 1548,1551, in order to evaluate possible changes on the determination of the mass-loss rates of our star sample (Sect. 5.3.3 of Paper I). As discussed in Sect. 2.1, the Si IV $\lambda\lambda$ 1394,1403 line profiles are well-known to be sensitive to the luminosity class of O stars.

6.1.4 Results and conclusions

Further details on the observational data used in this study, as well as on the modeling assumptions using CMFGEN, are found in Sects. 2 and 3.1 of Paper I, respectively. The UV and visible line-diagnostics used to derive the fundamental stellar (e.g., effective temperature and surface gravity acceleration) and wind parameters (mass-loss rate and terminal velocity) are discussed in details in Sect. 3.2. The determined parameters for all the nine stars of our sample of late-type O giants are shown in Table 3 of Paper I.

Figs. 12 and 13 of Paper I compare our derived mass-loss rates for late O giants

6.1. Mini-survey of O stars

with the values predicted from the theoretical works discussed above. In addition to our results, spectroscopic mass-loss rates found in the literature for others O stars with different luminosity (dwarfs, early giants, and supergiants²) are also compared. First, we point out that the spectroscopic mass-loss rates shown in these figures are unclumped mass-loss rates, they are equal to the clumped mass-loss rates (i.e., derived using clumped models) multiplied by a factor of $1/\sqrt{f_\infty}$ (clumping filling factor, Eq. 4.24).

For our results, this conversion factor is ~ 3.14 since the f_∞ was fixed at 0.1 in the modeling of all the star sample. Despite being not realistic to consider unclumped (i.e., a homogeneous density structure) winds for O stars, we need to consider unclumped mass-loss rates (Table 3 of Paper I), when comparing our results with the theoretical mass-loss rates of Vink et al. (2000) and Lucy (2010a), since these theoretical studies do not take wind clumping into account. Following the notation used in Paper I, the mass-loss rates predicted using the recipes from Vink et al. (2000) and Lucy (2010a) are denoted here by \dot{M}_{Vink} and \dot{M}_{Lucy} , respectively.

Comparing the spectroscopic results from the literature with \dot{M}_{Vink} (Fig. 12 of Paper I), weak winds are found in late O dwarfs with $\log(L_\star/L_\odot) \lesssim 5.2$. These stars show spectroscopic mass-loss rate $\sim 10^{-9} M_\odot \text{ yr}^{-1}$, while the values for \dot{M}_{Vink} reach up to $10^{-7} M_\odot \text{ yr}^{-1}$. On the other hand, the spectroscopic mass-loss rates for the more luminous OB star (supergiants, luminosity class I) are in line with the values predicted using the mass-loss recipe of Vink et al. (2000).

As discussed above, our results for the mass-loss rate are also compared with the theoretical values using Lucy (2010a) (Fig. 13 of Paper I). We found that the predictions from Lucy (2010a) provide a better match to our determined mass-loss rates of late O giants, when compared with \dot{M}_{Vink} . This result is in line with previous studies on late O dwarfs, showing a better agreement between the \dot{M}_{Lucy} and the mass-loss rates derived from spectroscopy (Lucy 2010a). In this case, the weak wind problem is substantially attenuated, with discrepancies up to ~ 1.0 dex between \dot{M}_{Lucy} and the derived \dot{M} for our star sample.

However, one sees that study of Lucy (2010a) underestimates the mass-loss rates for OB supergiants, for which Vink's predictions are in line with the spectroscopic results. The results found in Figs. 12 and 13 are summarized in Fig. 14 of Paper I, where the discrepancies between the spectroscopic and theoretical mass-loss rates are compared among the different classes of OB stars. It is hard to compare the predictions of Vink et al. (2000) with the ones from Lucy (2010a) because they employ different approaches. While Vink et al. (2000) find \dot{M} that is globally (through the wind) consistent with the conservation of energy, Lucy (2010a) predicts indeed the mass-loss rate from first principles (solving the wind momentum equation). Nevertheless, the values of \dot{M}_{Vink} for

2. Here, early-type B supergiants are also included in the analysis.

6.1. Mini-survey of O stars

OB supergiants are supported by more recent hydrodynamical simulations from Muijres et al. (2012).

The UV synthetic lines from our final models are compared with the ones using \dot{M}_{Vink} for all the star sample (Fig. 15 of Paper I). We limited this spectral analysis to mass-loss rates using Vink et al. (2000) since these theoretical values are widely used in the literature in comparison with Lucy (2010a). Again, we remind the reader that our final models considered in this comparison use unclumped mass-loss rates. All the other parameters in the models are fixed according to Table 3 of Paper I. In short, when using \dot{M}_{Vink} in the CMFGEN models, the synthetic Si IV $\lambda\lambda$ 1394,1403 line profiles are systematically much more intense than the observed spectra. With respect to C IV $\lambda\lambda$ 1548,1551, the models with \dot{M}_{Vink} display saturated line profiles, in contrast with the observations for the HD 24431, HD 105627, and HD 153426 (unsaturated profiles in C IV $\lambda\lambda$ 1548,1551). This means that the predictions using Vink et al. (2000) are ruled out based on the modeling of the UV spectra of our star sample.

Fig. 16 of Paper I provides an analogous comparison to the one performed in Fig. 15, but for the H α line. As discussed in details in Sect. 5.1 of Paper I, the situation when modeling the H α line is somewhat more complex than in the analysis of UV region. Considering our UV mass-loss rates (within the derived error bars), we are able to reproduce the observed H α profile for four objects of our sample, while the models using \dot{M}_{Vink} highly misfit the observed data in H α for 5 objects of our sample.

Nevertheless, these discrepancies found between the models with \dot{M}_{Vink} and observations are clearly enhanced in comparison to the results found from Marcolino et al. (2009) for O8-9.5V stars. While their sample of late O dwarfs has a mean value of $\sim 9.0 \times 10^{-8} M_{\odot} \text{ yr}^{-1}$ for \dot{M}_{Vink} , our sample of late O giants has mean \dot{M}_{Vink} six times higher than that ($\sim 5.0 \times 10^{-7} M_{\odot} \text{ yr}^{-1}$). Since the H α line profile is more sensitive on the mass-loss rate regime of $\dot{M} \gtrsim 10^{-7} M_{\odot}$ (Sect. 2.3), we were able to provide a better check for the Vink’s predictions for our sample with respect to the fit to the H α line.

Regarding the simultaneous fit to the UV and visible (H α) spectra, weak winds are favoured by our study when compared with the predicted mass-loss rates for late O giants in overall.

From Sect. 6 of Paper I: “in conclusion, our results indicate the weak wind phenomenon in O8-9.5III stars. It is the first time that weak winds are found for spectral types other than O8-9.5V. Despite our efforts, we are not able to model at the same time both the UV wind diagnostic lines and the H α profile for all the stars of our sample. This issue could be solved by investigations regarding macroclumping implementation in the modeling with CMFGEN and potential H α variability (as observed in late OB supergiants) among late O giants. Apart from this problem, low \dot{M} (weak winds) are

6.1. Mini-survey of O stars

avored to model the spectra (UV + optical regions) of late O dwarfs and giants in comparison with values provided by theory. In other words, the measured mass-loss rates of these stars are systematically lower than the predictions of Vink et al. (2000). This is important as they are low luminosity O stars (latter spectral types), implying that the majority of the O-type stars must undergo a weak wind phase. Therefore, we suggest that the mass-loss recipe in the majority of modern stellar evolution codes must severely overestimate \dot{M} during the H-burning phase. Further investigations are needed to evaluate the consequences of this in terms of physical parameters for massive stars (e.g., angular momentum and CNO surface abundances).”

We precisely identified the luminosity region of $\log(L_*/L_\odot) \approx 5.2$ as critical for weak winds, but we were not able to address the physical causes for that in this paper. In short, Muijres et al. (2012) found that their simulations for O stars fail to drive a wind for the late-type O dwarfs due to the lack of Fe v lines at the base of wind for these stars, when compared with the earlier O stars. More recently, Vilhu & Kallman (2019) suggested that weak winds can be explained in terms of a velocity-porosity (vorocity) effect of the wind stratification (clumps) for the later O dwarfs. Indeed, to date it is still an open issue in the literature and further investigations are needed on the physical causes of weak winds.

Another interesting issue raised from weak wind regards the so-called modified wind momentum-luminosity relation for massive hot stars. The modified wind momentum (D_{mom}) was firstly introduced by Kudritzki et al. (1995):

$$D_{mom} = \dot{M}v_\infty\sqrt{R_*}, \quad (6.1)$$

being the term “modified” used for this quantity due to the stellar radius $\sqrt{R_*}$, apart from the wind momentum ($\dot{M}v_\infty$).

As shown by the Kudritzki et al. (1995), this quantity for radiative-line driven winds is expected to scale with the stellar luminosity:

$$\log(D_{mom}) = a \log(L_*/L_\odot) + b, \quad (6.2)$$

where the linear and angular coefficients above are specifically dependent on the spectral type and metallicity.

This relation has been supported by subsequent spectroscopic studies (e.g., Puls et al. 1996; Kudritzki et al. 1999; Mokiem et al. 2007a,b), and it simply states that more luminous massive stars are likely to have more intense wind (larger wind momentum), as expected from the CAK-theory.

Thus, based on prior information about D_{mom} , for instance, from theoretical investigations (e.g., Vink et al. 2000, 2001), one could be able to estimate the stellar

6.1. Mini-survey of O stars

luminosity. This is particularly important as independent tool to estimate distances, up to Mega-parsec scales, as will also be discussed in Sect. 6.2 (Paper II). As supported by Paper I, this relation should be taken with caution since it breakdowns at $\log(L_*/L_\odot) \approx 5.2$, when compared with the theoretical relation predicted from Vink et al. (2000) (see Fig. 11 of Paper I).

Despite focusing our discussion here on the weak wind problem, other interesting issues were found by Paper I, also deserving further investigations. For instance, our best-fit models overestimate the emission component of C IV $\lambda\lambda$ 1548,1551 for all the star sample. As discussed in Sect. 3.1 of Paper I, the wind velocity law exponent β was initially fixed at 1.0 in our analysis based on previous results found for O-type stars (Sect. 1.2). However, we needed to reduce β from 1.0 to very low values, namely, ~ 0.3 . Such low values of β are unreliable since they are not acceptable at all in the framework of line-driven winds (standard CAK-theory).

Therefore, we were just able to reduce the discrepancies between our final models ($\beta = 1.0$) and data when taking into account a fuller ion composition in the models, but in addition to a high value of photospheric microturbulence (up to 20-30 km s⁻¹). On the other hand, such a high value of microturbulence is not expected at all for late O giants stars (Sect. 4.1 of Paper I). Moreover, this latter adoption on the microturbulence prevents us from determining T_{eff} by the UV and visible lines in a self-consistent way. Fixing the photospheric microturbulence at 10 km s⁻¹, the fit to the emission component of C IV $\lambda\lambda$ 1548,1551 of our star sample seems to be improved just when setting $\beta \sim 0.3$ (see Fig. 10 of Paper I). One possibility to explain this issue could rely on the quite simple β parameterization used in Paper I (following Eq. 1.5).

Probing the weak wind phenomenon in Galactic O-type giants

E. S. G. de Almeida^{1,2}, W. L. F. Marcolino², J.-C. Bouret³, and C. B. Pereira⁴

¹ Observatoire de la Côte d’Azur, Université Côte d’Azur, CNRS, Laboratoire Lagrange, France
e-mail: elisson.saldanha@oca.eu

² Observatório do Valongo, Universidade Federal do Rio de Janeiro, Rio de Janeiro, Brazil

³ Aix-Marseille Université, CNRS, CNES, LAM, Laboratoire d’Astrophysique de Marseille, Marseille, France

⁴ Observatório Nacional/MCTIC, Rio de Janeiro, Brazil

Received 18 September 2018 / Accepted 12 February 2019

ABSTRACT

Aims. Analyses of Galactic late O dwarfs (O8–O9.5V stars) raised the “weak wind problem”: spectroscopic mass-loss rates (\dot{M}) are up to two orders of magnitude lower than the theoretical values. We investigated the stellar and wind properties of Galactic late O giants (O8–O9.5III stars). These stars have luminosities $\log(L_\star/L_\odot) \sim 5.2$, which is the critical value (onset of weak winds) proposed in the literature.

Methods. We performed a spectroscopic analysis of nine O8–O9.5III stars in the ultraviolet (UV) and optical regions using the model atmosphere code CMFGEN.

Results. Stellar luminosities were adopted using calibrations from the literature. Overall, our model spectral energy distributions agree well with the observed ones considering parallaxes from the latest *Gaia* data release (DR2). The effective temperature derived from the UV region agrees well with the ones from the optical. As expected, the analysis of the Hertzsprung–Russell (HR) diagram shows that our sample is more evolved than late O dwarfs. From the UV region, we found $\dot{M} \sim 10^{-8} - 10^{-9} M_\odot \text{ yr}^{-1}$ overall. This is lower by $\sim 0.9 - 2.3$ dex than predicted values based on the (global) conservation of energy in the wind. The mass-loss rates predicted from first principles, based on the moving reversing layer theory, agree better with our findings, but it fails to match the spectroscopic \dot{M} for the most luminous OB stars. The region of $\log(L_\star/L_\odot) \sim 5.2$ is critical for both sets of predictions in comparison with the spectroscopic mass-loss rates. CMFGEN models with the predicted \dot{M} (the former one) fail to reproduce the UV wind lines for all the stars of our sample. We reproduce the observed H α profiles of four objects with our \dot{M} derived from the UV. Hence, low \dot{M} values (weak winds) are favored to fit the observations (UV + optical), but discrepancies between the UV and H α diagnostics remain for some objects.

Conclusions. Our results indicate weak winds beyond the O8–9.5V class, since the region of $\log(L_\star/L_\odot) \sim 5.2$ is indeed critical to the weak wind phenomenon. Since O8–O9.5III stars are more evolved than O8–9.5V, evolutionary effects do not seem to play a role in the onset of the weak wind phenomenon. These findings support that the \dot{M} (for low luminosity O stars) in use in the majority of modern stellar evolution codes must be severely overestimated up to the end of the H-burning phase. Further investigations must evaluate the consequences of weak winds in terms of physical parameters for massive stars (e.g., angular momentum and CNO surface abundances).

Key words. stars: massive – stars: atmospheres – stars: fundamental parameters – stars: winds, outflows – stars: mass-loss

1. Introduction

With their high effective temperatures ($\gtrsim 30$ kK) and intense radiation fields ($L_\star \lesssim 10^6 L_\odot$), massive O-type stars have a huge impact on the interstellar medium through ionizing photons (e.g., Abbott 1982) and strong line-driven outflows ($\lesssim 10^{-6} M_\odot \text{ yr}^{-1}$). After they leave the main sequence, O stars evolve to become objects such as red supergiants, luminous blue variables, and Wolf–Rayet stars, depending on the initial mass (Meynet et al. 2011). Therefore, they are also progenitors of type II–Ib–Ic supernovae, neutron stars, black holes, long gamma-ray bursts (e.g., Gehrels & Razzaque 2013), and possibly gravitational wave events at low metallicity (Abbott et al. 2016).

Despite having been studied for several decades, exciting findings regarding O stars have been reported in the literature in recent years. For example, it is still unclear why about 10% of O stars have been found to possess surface magnetic fields (Grunhut et al. 2017). Moreover, it has been argued that O stars form almost exclusively in multiple systems (Sana et al. 2014). As is the case for magnetic fields, the effects of binary interactions (e.g., tides, mass transfer, and mergers) on stellar evolution are complex and constitute a hot topic in the literature (see,

e.g., Keszthelyi et al. 2017; de Mink et al. 2014). The instability inherent in line-driven winds is another critical issue; it induces the far from smooth density and velocity structures – inhomogeneities – that present a challenge to hydrodynamics and to implementation in atmosphere codes (e.g., Sundqvist et al. 2014; Sundqvist & Puls 2018). Such inhomogeneities directly affect the mass-loss rate obtained for these stars, and with likely evolutionary consequences.

Another open question that has been called urgent in the massive star community (e.g., Puls et al. 2009) is the so-called weak wind problem¹. It is characterized by a large discrepancy between theoretical predictions for the mass-loss rates (\dot{M}) of O8–O9V stars – provided by Vink et al. (2000, 2001) – and the results obtained from spectroscopic analyses using atmosphere models (e.g., Martins et al. 2005a; Marcolino et al. 2009). The “measured” (i.e., derived using atmosphere models) mass-loss rates of late-type O dwarfs (O8–9.5V stars) are up to two orders of magnitude lower than the predicted ones.

¹ We use the term “problem” throughout the text to state the disagreement between spectroscopic and predicted mass-loss rates.

The first results regarding weak winds were presented almost three decades ago, showing a significant difference (approximately a factor of 5–10) between spectroscopic and predicted \dot{M} for the faintest O stars (e.g., Chlebowski & Garmany 1991). However, one of the first quantitative findings about the weak wind problem with modern photosphere-wind unified models came from Bouret et al. (2003) and Martins et al. (2004). These authors investigated O dwarfs in the Small Magellanic Cloud and found weak mass-loss on the order of $10^{-9} - 10^{-8} M_{\odot} \text{ yr}^{-1}$ (in O6-O9.5V stars). An important question raised by these results was the role played by the low metallicity environment (like the Small Magellanic Cloud) and the youth of the sample stars. Later, Martins et al. (2005a) and Marcolino et al. (2009) presented spectroscopic analyses using optical and ultraviolet data for a total of 17 Galactic O dwarfs and inferred much lower mass-loss rates than predicted for the late-type objects (O8-9V). The discrepancies found reached up to two orders of magnitude. This ruled out an environmental effect due to metallicity. Overall, these results indicated that weak winds concern a particular range of stellar luminosity, corresponding to late O dwarfs, namely $\log(L/L_{\odot}) \sim 4.5-5.0$.

Interestingly, one of the most recent hydrodynamical results regarding O stars (Muijres et al. 2012) fails to drive winds for low luminosity O stars (O6.5V and later). Muijres et al. (2012) identified the absence of physical solutions for their hydrodynamical approach as resulting from the lack of Fe V at the basis of the wind for this spectral range. This is notable since P-Cygni profiles are observed in the UV spectra of these stars. It exposes our lack of knowledge about the force that maintains the wind at this luminosity range. Moreover, such discrepancy between the hydrodynamical² mass-loss rates of Vink et al. (2000) and results from atmosphere models is currently a serious question because the most modern evolutionary models use the predicted values of Vink et al. (2000) during the main sequence phase (e.g., Ekström et al. 2012; Meynet et al. 2015). Stated differently, the mass-loss rate of the majority of massive stars (low luminosity) at the main sequence is severely overestimated in most evolution models. The mass range affected is around 20–25 M_{\odot} , that is, the mass range of late O dwarfs. The evolutionary consequences of this fact up to the end of the main sequence are as yet unknown.

We aim to investigate the weak wind phenomenon among more evolved O stars for the first time. We are particularly interested in late O giants because of their luminosity – $\log(L_{\star}/L_{\odot}) \sim 5.2$ – which seems to define the outset of the weak wind problem. So far, this problem has only been reported in O8-9.5V stars. We performed a quantitative analysis of nine Galactic late-type O giants (O8-9.5III) using ultraviolet and optical data to derive their main stellar and wind physical parameters. Our analysis increases the number of O8-9.5III stars analyzed in the literature through a quantitative approach in the UV and visible spectral regions. Up to date, Mahy et al. (2015) is one of the most comprehensive works deriving the stellar and wind parameters of Galactic late O giants, combining UV and visible spectra: five objects in total, with UV data for two out of five stars.

This paper is organized as follows. In Sect. 2, we present the observational data used in our analysis. In Sect. 3, we present the code to generate the non-LTE expanding atmosphere models (CMFGEN). The code assumptions and our methodology for

the analysis of the UV and optical data are discussed. In Sect. 4, we first present the derived stellar and wind parameters and our fits (Sect. 4.1). Then, we analyze the energy spectral distribution, the photospheric parameters, and the evolutionary status of our sample in Sect. 4.2. The wind parameters and the weak wind phenomenon are analyzed in detail in Sect. 4.3. After, we discuss the derivation of \dot{M} from the UV in comparison with the optical region (from H α) in Sect. 5.1. In Sect. 5.3, we evaluate the effect of different parameters (e.g., CNO abundances) on the \dot{M} diagnostics. Finally, our conclusions are presented in Sect. 6.

2. Observations

Our sample contains nine Galactic late O giants. They belong to the O8-9.5III spectral types, according to the classification provided by the Galactic O-Star Catalog (GOSC, Maíz Apellániz et al. 2013). We present them in Table 1. Three stars of our sample are double-lined spectroscopic binaries (HD 156292, HD 153426, and HD 115455), and we discuss in Sect. 5.2 possible binary effects on the analysis. Two stars of our sample have a classification outside the luminosity class III: HD 116852 (O8.5II-III) and HD 135591 (O8IV). We initially included these objects in the analysis based on an outdated GOSC classification, O9III for HD 116852 and O7.5III for HD 135591 (Maíz-Apellániz et al. 2004). Nevertheless, HD 116852 and HD 135591 have expected stellar parameters (such as bolometric luminosity and effective temperature) consistent with the rest of our sample of giants. The known population of O8-9.5 giants is close to sixty stars (Maíz Apellániz et al. 2013). From an observational point of view, our analyzed spectra have a fairly good morphological homogeneity. We consider our sample representative and it corresponds to $\sim 25\%$ of the late O giants with available spectra from the IUE/Short-Wavelength Prime (SWP) instrument.

We used high-resolution ($\Delta\lambda \sim 0.2 \text{ \AA}$) data from the International Ultraviolet Explorer (IUE) satellite³. We focused on the $\sim 1200 - 1975 \text{ \AA}$ interval (SWP instrument). This region contains the most important photospheric and wind lines useful to our purposes (e.g., iron forest, N V $\lambda 1240$, Si IV $\lambda 1394, 1403$, C IV $\lambda 1548, 1551$, and N IV $\lambda 1718$). When available, we co-added different observations for the same target in order to achieve a better signal-to-noise ratio (S/N). In addition, we used IUE/ Long-Wavelength Prime (LWP) data ($\sim 1900-3125 \text{ \AA}$) and UBVJHK photometry in the analysis of the spectral energy distribution of our sample.

We also acquired high-resolution optical spectroscopic data for six stars of the sample: HD 156292, HD 105627, HD 116852, HD 153426, HD 115455, and HD 135591. The observations were done with the FEROS spectrograph (resolving power $R = 48\,000$) at the ESO/MPG 2.2 m telescope in La Silla (Chile) from 17 to 22 March of 2016. Technical details about FEROS can be found in Kaufer et al. (1999, 2000). The exposure times varied from 80 to 420 s. The spectra cover the interval $\sim 3500-9200 \text{ \AA}$, and the S/N achieved is about 100 for all the stars. Furthermore, we used high-resolution optical data for HD 36861 from the NARVAL spectrograph ($R = 75\,000$) at the 2 m Telescope Bernard Lyot on Pic du Midi (France), covering $\sim 3700-6800 \text{ \AA}$. For HD 24431 and HD 218195, we used public data from the Magnetism in Massive Stars (MiMeS) survey (Wade et al. 2016) obtained using the ESPADONS instrument ($R = 68\,000$) at the

² We note that the mass-loss rates predicted by Vink et al. (2000) are not rigorously hydrodynamical since the authors do not explicitly solve the wind equation through simulations. Nevertheless, Vink et al. (2000) provide \dot{M} using a global energy argument, where the conservation of energy is globally satisfied in the wind for solely one value of \dot{M} . For more details, see Vink et al. (1999).

³ Public data available in the Barbara A. Mikulski Archive for Space Telescopes (MAST): <https://archive.stsci.edu/iue/>

Table 1. Star sample and photometric/spectroscopic data.

Star	HD 156292	HD 24431	HD 105627	HD 116852	HD 153426	HD 218195	HD 36861 A (λ Orionis A)	HD 115455	HD 135591
Spec. type	O9.7III	O9III	O9III	O8.5II-III((f))	O8.5III	O8.5III Nstr	O8III	O8III((f))	O8IV((f))
Spec. bin.	SB2	–	–	–	SB2	–	–	SB2	–
Member.	NGC 6322	Sh 2-205 Cam OB1	–	–	Sh 2-2	Cep OB1	Sh 2-264 Collinder 69 Ori OB1	RCW 75 Cen OB1	ASCC 79
Johnson U	7.101	6.507	7.270	8.380	6.650	7.657	2.196	7.400 ^(a)	4.442
Johnson B	7.773	7.117	8.182	8.380	7.610	8.650	3.218	8.170 ^(a)	5.372
Johnson V	7.509	6.745	8.140	8.470	7.470	8.357	3.405	7.970 ^(a)	5.457
Johnson R	–	6.360 ^(a)	–	–	–	–	–	–	–
Johnson I	–	6.100 ^(a)	–	–	–	–	–	–	–
2MASS J	6.944	5.917	7.985	8.720	7.057	7.755	3.735 ^(b)	7.469	5.554
2MASS H	6.886	5.826	8.030	8.789	7.056	7.708	3.769 ^(b)	7.442	5.566
2MASS Ks	6.855	5.839	8.069	8.795	7.027	7.735	3.876 ^(b)	7.454	5.616
$E(B - V)$	0.52	0.63	0.30	0.17	0.40	0.55	0.07	0.46	0.17
Dist. (pc)	1833 ⁺²⁷⁰ ₋₂₀₈	823 ⁺⁶² ₋₅₄	2541 ⁺²⁸⁷ ₋₂₃₄	22 726 _{-12 766} 2857 ₋₁₉₅₆ ^(c)	2163 ⁺²⁶⁹ ₋₂₁₅	1588 ⁺²⁷⁶ ₋₂₀₄	417 ⁺¹⁰ ₋₁₀	2266 ⁺²⁷¹ ₋₂₁₉	836 ⁺¹³⁷ ₋₁₀₃
SWP N ^o	16 218	30 166	20 623	09332	01517 07827-28 07828	26 975	46 234 46 237 46 241 46 245 46 247	16 087	48 294
SWP date	1982-Jan-31	1987-Jan-26	1983-Aug-06	1980-Jun-20	1978-May-10 1980-Jan-31 1980-Jan-31	1985-Oct-24	1992-Nov-12 1992-Nov-12 1992-Nov-12 1992-Nov-12	1982-Jan-21	1993-Aug-03
LWP N ^o	–	10 024	16 537	15 610	06841	06987	15 311	–	25 759
LWP date	–	1987-Jan-26	1983-Aug-06	1989-May-27	1980-Feb-02	1985-Oct-25	1989-Apr-05	–	1993-Jun-17
Vis. inst.	FEROS	ESPADONS	FEROS	FEROS	FEROS	ESPADONS	NARVAL	FEROS	FEROS
Vis. date	2016-Mar-23	2011-Nov-07	2016-Mar-18	2016-Mar-18	2016-Mar-18	2011-Jul-05	2007-Sep-21	2016-Mar-18	2016-Mar-18

Notes. Spectral types, spectroscopic binary classification, and memberships are from [Sota et al. \(2014\)](#). Photometric data are from [Maíz-Apellániz et al. \(2004\)](#) with exception to the specific references. Color excesses are calculated considering intrinsic colors calibrated by spectral type from [Martins & Plez \(2006\)](#). Distances are from [Gaia Collaboration \(2018\)](#). For HD36861, we adopted the distance from the mean *Gaia* DR2 parallaxes for the components C and D, as in [Gordon et al. \(2018\)](#). Distance from [van Leeuwen \(2007\)](#) for HD 116852 is shown too. All distances are obtained from the direct inversion of the measured parallaxes. We list information about the analyzed data in the UV (SWP and LWP number and observation date) and in the visible (instrument name/observation date) regions.

References. ^(a)[Ducati \(2002\)](#), ^(b)[Cutri et al. \(2003\)](#), ^(c)[van Leeuwen \(2007\)](#).

Canada-France-Hawaii Telescope (USA). The optical data of our sample were analyzed in a second step in our methodology, thus allowing us to check the consistency of the results derived from a pure ultraviolet analysis (e.g., effective temperature and mass-loss rate).

3. Atmosphere models

3.1. Code

We used the code CMFGEN ([Hillier & Miller 1998](#)) to derive the stellar and wind properties of the late-type O giant stars of our sample. It allows us to solve the radiative transfer, statistical and radiative equilibrium equations in a spherically symmetric outflow. It includes, for example, the effects of line blanketing, clumping, and Auger ionization by X-rays, and provides realistic spectra from the UV to the middle infrared.

The code requires an initial estimate of the hydrostatic structure. For this purpose, we used a grid of non-LTE plane-parallel models computed with the code TLUSTY ([Hubeny & Lanz 1995](#)), based on the OSTAR2002 grid ([Lanz & Hubeny 2003](#)). The sampling steps of our grid are ~ 500 K in effective temperature and ~ 0.25 dex in surface gravity. When necessary, we interpolated on T_{eff} and $\log(g)$. For the wind, we used a standard β velocity law, in the form $v(r) = v_{\infty} \left(1 - \frac{R_{*}}{r}\right)^{\beta}$, which is smoothly connected to the hydrostatic density structure just above the sonic point.

Initially, we used the following assumptions in the modeling for all the stars of our sample:

(i) We adopted standard solar abundances ([Grevesse et al. 2010](#)) for all the chemical elements. Later, we performed tests concerning the effects of CNO abundance changes on the derivation of the mass-loss rate (Sect. 5.3.1). The atomic species

Table 2. Number of levels, super-levels, and bound-bound transitions for each atomic species included in our basic models.

Ion	Full levels	Super-levels	b-b transitions
H I	30	30	435
He I	69	69	905
He II	30	30	435
C III	243	99	5528
C IV	64	64	1446
N III	287	57	6223
N IV	70	44	440
N V	49	41	519
O III	104	36	761
O IV	64	30	359
O V	56	32	314
Mg II	44	36	348
Si III	50	50	232
Si IV	66	66	1090
S V	144	37	1673
Fe III	607	65	5482
Fe IV	1000	100	25 241
Fe V	1000	139	25 173
Fe VI	1000	59	24 798

Notes. CMFGEN approach for a faster computational treatment. For more details see, for example, Hillier & Miller (1998).

included in each model and their number of energy levels are shown in Table 2, together with the total number of computed bound-bound transitions.

(ii) We assumed $\beta = 1.0$ for the wind velocity structure. Values of $\beta = 0.8 - 1.0$ are recognized as typical for O stars since they are supported both from spectroscopic modeling (e.g., Bouret et al. 2013) and hydrodynamical predictions (e.g., Muijres et al. 2012). As we will show later (Sect. 4.3.1), lower values for this parameter provide a better fit to the observed C IV $\lambda\lambda 1548, 1551$ profiles in late O giants.

(iii) All models include the effects of X-rays (energy interval of 0.1–1.0 keV) produced in the wind with the canonical value for O-type stars of $\log(L_X/L_{\text{BOL}})$ approximately -7.0 (e.g., Sana et al. 2006; Rauw et al. 2015). We adopted the value of $\log(L_X/L_{\text{BOL}}) = -7.0 \pm 0.1$. In fact, two objects of our sample have observed values for $\log(L_X/L_{\text{BOL}})$ in the literature: HD 36861 (λ Orionis A) and HD 135591. The first has determinations of -6.96 (Berghoefter et al. 1996) and -6.81 (Nazé 2009), while the latter one shows -7.14 (Berghoefter et al. 1996).

(iv) Wind clumping was included by default in the models. In CMFGEN, a volume filling factor is used according to the formula $f(r) = f_\infty + (1 - f_\infty)e^{-\frac{v(r)}{v_{\text{initial}}}}$ (microclumping approximation). The free parameters v_{initial} and f_∞ are the onset velocity of clumping and the filling factor value at $r \rightarrow \infty$, respectively. We adopted $v_{\text{initial}} = 30 \text{ km s}^{-1}$ and $f_\infty = 0.1$ (e.g., Bouret et al. 2003; Martins et al. 2005a). It is important to note that “clumped models” imply underestimation of the derived mass-loss rates in comparison with “unclumped models” (see, e.g., Martins 2011). When needed, we scaled our mass-loss rates by a factor of $1/\sqrt{f_\infty}$ (~ 3.16) to compare them with unclumped results from the literature.

(v) In CMFGEN, a depth-dependent microturbulence velocity is used to compute the emergent spectrum (formal solution). It is parameterized as $\xi_i(r) = \xi_i^{\text{min}} + (\xi_i^{\text{max}} - \xi_i^{\text{min}})\frac{v(r)}{v_\infty}$, where ξ_i^{min} and ξ_i^{max} are the minimum and maximum microturbulence

velocities. As in Mahy et al. (2015), we fixed $\xi_i^{\text{min}} = 10 \text{ km s}^{-1}$ and ξ_i^{max} is set to $0.1v_\infty$. In Sect. 4.1, we discuss the effect of this assumption particularly on the analysis of the effective temperature.

3.2. Diagnostics for the photospheric and wind parameters

First, we performed the analysis of all objects using the UV data set alone. Ultraviolet spectroscopy is suitable to investigate the weak wind phenomenon since the most traditional mass-loss diagnostic in the optical (H α line) is found to be insensitive for the analysis of mass losses lower than $\sim 10^{-8} - 10^{-7} M_\odot \text{ yr}^{-1}$ (e.g., Puls et al. 2008; Martins 2011). Thereafter, we extended the analysis to the visible region, comparing with the results derived from the UV (e.g., for T_{eff} and \dot{M}).

We have used typical line diagnostics in the optical and UV for the determination of the photospheric and wind properties – the effective temperature T_{eff} , surface gravity $\log(g)$, projected rotational velocity $v \sin i$, mass-loss rate (\dot{M}), and terminal velocity v_∞ (e.g., Martins et al. 2004; Marcolino et al. 2009; Mahy et al. 2015). The spectroscopic parameters are obtained through a direct comparison between the synthetic spectrum and the data. The uncertainty for each parameter is inferred in a conservative way: the upper and lower limits for each parameter do not provide an acceptable “by eye” fit to the data (as, e.g., in Marcolino et al. 2009). We provide examples for the derivation of T_{eff} and of \dot{M} below.

In the following we summarize our methodology in more detail:

(i) The bolometric luminosity $\log(L_\star/L_\odot)$ was adopted according to the spectral type of each star of our sample. We used the calibrations for Galactic O stars provided by Martins et al. (2005b) adopting conservative error bars, namely, ± 0.2 dex in $\log(L_\star/L_\odot)$. Since Martins et al. (2005b) provide results for luminosity classes V, III, and I, we use mean values among these classes for the stars with intermediate classification, such as HD 116852 (II-III) and HD 135591 (IV). We initially chose this assumption because the astrometric distances derived from the HIPPARCOS parallaxes are highly uncertain for most of our sample. For O stars, the discrepancy between the HIPPARCOS distances and the ones predicted from the spectral type is notorious (e.g., Schröder et al. 2004). The total amplitude of 0.4 dex in $\log(L_\star/L_\odot)$ uncertainty covers a significant deviation in terms of spectral types from O9.5III to O6.5III (Martins et al. 2005b). In Sect. 4.2.1, we discuss this assumption for the stellar luminosity, using recent astrometric results from Gaia Collaboration (2018).

(ii) The effective temperature T_{eff} was derived by the ionization balance method through the intensity of the Fe III-IV-V lines in the ultraviolet, especially Fe III and Fe V. In the optical, it was derived by the relative intensity of the He I and He II profiles, mainly He I $\lambda 4471$ and He II $\lambda 4542$. Additional lines for consistency checking include He I $\lambda 4144$, He II $\lambda 4200$, He I $\lambda 4713$, He I $\lambda 4920$, He I $\lambda 5016$, and He II $\lambda 5412$.

We emphasize that we have inferred independent values for the temperature using the ultraviolet and optical separately. In Fig. 1, we illustrate the derivation of T_{eff} for one of the stars of our sample, HD 156292. The first three panels show the models for the determination of the effective temperature (considering the error bars) in the ultraviolet. The bottom panels show the same three models in the optical region for He I $\lambda 4471$, He II $\lambda 4542$, and He II $\lambda 5412$. It is conspicuous that the same effective temperature fits both the UV and the visible spectra.

(iii) The surface gravity $\log(g)$ was initially adopted according to the spectral type using the calibrations of

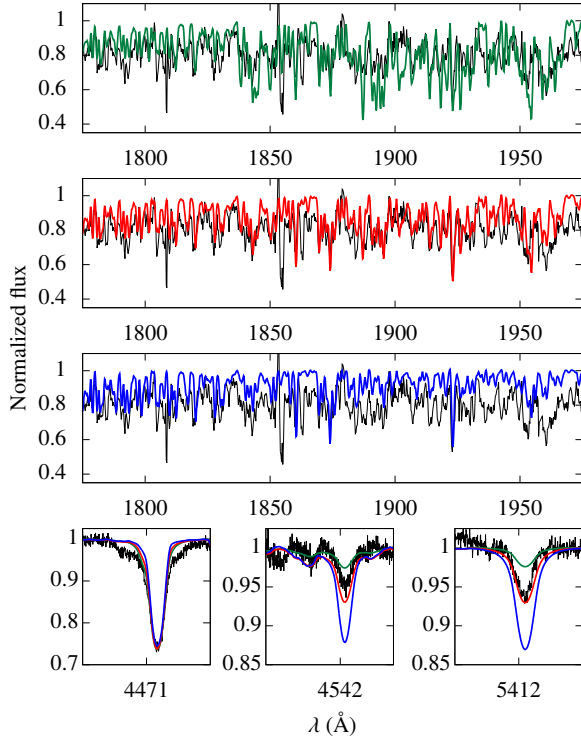


Fig. 1. Determination of $T_{\text{eff}}^{\text{UV}}$ for HD 156292 (O9.7III). The IUE spectrum is in black. In the UV, most features are due to Fe IV ($\sim 1775\text{--}1840$ Å) and Fe III (≥ 1840 Å). Models are shown in green ($T_{\text{eff}}^{\text{UV}}$ lower limit), red (final model), and blue ($T_{\text{eff}}^{\text{UV}}$ upper limit). In the *bottom panels*, these models are shown for T_{eff} diagnostics in the optical (He I $\lambda 4471$, He II $\lambda 4542$, and He II $\lambda 5412$).

Martins et al. (2005b). After the UV analysis, we checked the fits for the wings of the Balmer lines, mainly H γ and H β , for all our sample.

(iv) The stellar radius R_{\star} of each object follows from the Stefan–Boltzmann equation for a specific T_{eff} and $\log(L_{\star}/L_{\odot})$,

$$R_{\star} = \sqrt{\frac{L_{\star}}{4\pi\sigma T_{\text{eff}}^4}}, \quad (1)$$

where $\sigma \equiv$ Stefan–Boltzmann constant.

The spectroscopic M_{\star} is found from the gravity law

$$M_{\star} = \frac{gR_{\star}^2}{G}, \quad (2)$$

where G is the universal gravity constant.

The error bars for R_{\star} are calculated from the uncertainties in $\log(L_{\star}/L_{\odot})$ (highest contribution to the error propagation on the radius) and for M_{\star} from the uncertainties in R_{\star} (highest contribution to the error propagation on the mass), being thus underestimated values.

(v) The projected rotational velocity $v \sin i$ was initially adopted from Howarth et al. (1997), and modified when needed in order to provide a better fitting to the observed broadening. We analyzed the broadening of UV Fe III–IV–V transitions, as well as of weak metal lines and He I transitions in the optical. We stress here that macroturbulence is not accounted for in our models. We are aware that the inclusion of macroturbulence must provide a better overall fit to the optical data, but it does not have a significant impact on the wind parameters. Thus, our values of $v \sin i$, in fact, express the total line broadening and they must be seen as upper limits.

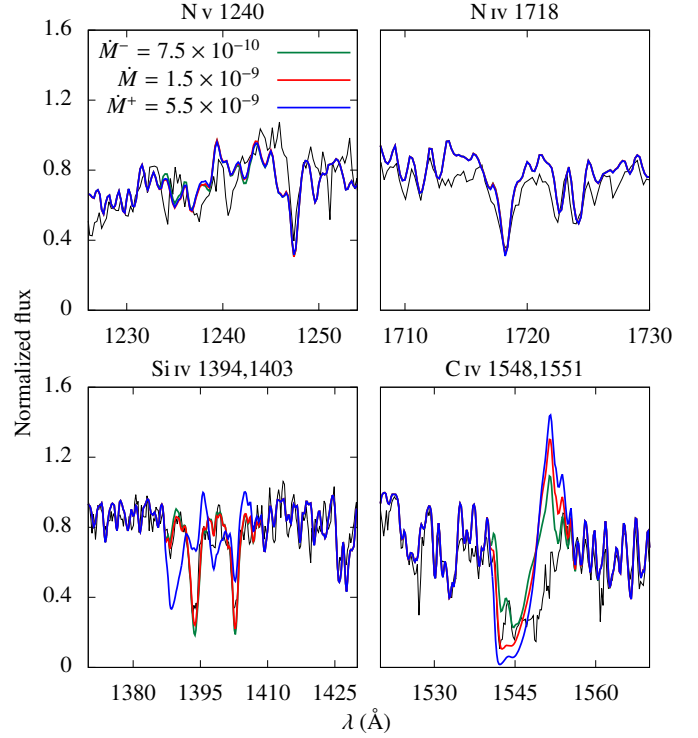


Fig. 2. Determination of \dot{M} for HD 156292 from the UV lines. The IUE spectrum is in black. We show the models in green (lower limit on \dot{M}), red (final model), and blue (upper limit on \dot{M}). Mass-loss rate unit is in $M_{\odot} \text{ yr}^{-1}$. We note that Si IV $\lambda\lambda 1394,1403$ and C IV $\lambda\lambda 1548,1551$ are the most useful lines for the analysis of the wind mass loss in late O giants. All the models have v_{∞} fixed in 1300 km s^{-1} .

(vi) The wind terminal velocity v_{∞} is derived from fitting the blueward extension (formed up to $v_{\infty} + \xi_t^{\text{max}}$) of the absorption component of the C IV $\lambda\lambda 1548,1551$ profile. Overall, we are able to provide a very reasonable fit to the observed blueward extension of C IV $\lambda\lambda 1548,1551$ with our adopted value of $\xi_t^{\text{max}} = 0.1v_{\infty}$.

(vii) The mass-loss rate \dot{M} was determined by fitting the intensity of the ultraviolet P-Cygni profiles Si IV $\lambda\lambda 1394,1403$ and C IV $\lambda\lambda 1548,1551$. The H α profile was also used to infer \dot{M} , allowing us to compare with the values derived from the UV. In Fig. 2, we illustrate the determination of the wind mass loss of HD 156292 from the UV lines. The model parameters are fixed except the mass-loss rate. The lines N v $\lambda 1240$ and N iv $\lambda 1718$ are much less sensitive to the variation in \dot{M} than the lines due to Si iv and C iv. Nevertheless, they provide at most constraints on the mass-loss rate. For example, models with $\dot{M} \sim 10^{-7} M_{\odot} \text{ yr}^{-1}$ provide stronger nitrogen lines than the observed ones in our sample. For HD 156292, the modeling provided by our lower limit on \dot{M} is quite close to our final model. Such uncertainty is due to the discrete absorption components in the observed C IV $\lambda\lambda 1548,1551$ of HD 156292, which are not included in our modeling. In any case, it would imply an overestimated \dot{M} and thus provides a proper comparison with the theoretical values for this star.

4. Results

We present the stellar and wind parameters derived for our sample in Table 3. Effective temperature determined through the analysis of Fe III–IV–V (ultraviolet) is denoted as $T_{\text{eff}}^{\text{UV}}$, while the values obtained by He I–II (optical) are denoted by $T_{\text{eff}}^{\text{opt}}$. For

Table 3. Summary of the results for the stellar and wind parameters.

Parameter	HD 156292	HD 24431	HD 105627	HD 116852	HD 153426	HD 218195	HD 36861	HD 115455	HD 135591
Spectral type	O9.7III	O9III	O9III	O8.5II-III((f))	O8.5III	O8.5III Nstr	O8III	O8III((f))	O8IV((f))
$\log(L_*/L_\odot)$	5.12 ± 0.20	5.17 ± 0.20	5.17 ± 0.20	5.33 ± 0.20	5.24 ± 0.20	5.24 ± 0.20	5.30 ± 0.20	5.30 ± 0.20	5.10 ± 0.20
$T_{\text{eff}}^{\text{UV}}$ (kK) ^(a)	$31.0^{+2.0}_{-3.0}$	33.0 ± 3.0	$33.0^{+1.5}_{-2.0}$	$32.5^{+2.0}_{-2.5}$	32.0 ± 2.0	33.0 ± 2.0	33.5 ± 2.5	$34.0^{+3.5}_{-1.5}$	35.0 ± 2.5
$T_{\text{eff}}^{\text{opt}}$ (kK) ^(b)	30.0 ± 2.0	32.5 ± 1.5	$33.0^{+1.5}_{-2.0}$	$33.0^{+2.0}_{-2.5}$	35.0 ± 1.0	35.0 ± 1.5	$35.0^{+2.0}_{-1.5}$	$34.0^{+2.0}_{-1.5}$	36.0 ± 1.5
$\log(g)$	3.50 ± 0.10	3.75 ± 0.10	3.50 ± 0.10	3.50 ± 0.10	3.55 ± 0.10	3.55 ± 0.10	3.60 ± 0.10	3.57 ± 0.10	3.75 ± 0.10
R_* (R_\odot)	$13.0^{+3.7}_{-2.3}$	$11.9^{+3.5}_{-2.2}$	$11.9^{+3.5}_{-2.2}$	$14.7^{+4.3}_{-2.7}$	$13.7^{+4.0}_{-2.5}$	$12.9^{+3.7}_{-2.4}$	$13.4^{+3.9}_{-2.4}$	$13.0^{+3.8}_{-2.4}$	$9.7^{+2.8}_{-1.8}$
M_* (M_\odot)	$19.6^{+11.1}_{-7.0}$	$28.9^{+16.8}_{-10.6}$	$16.3^{+9.5}_{-6.0}$	$25.0^{+14.5}_{-9.1}$	$24.3^{+14.1}_{-8.9}$	$21.5^{+12.5}_{-7.9}$	$26.1^{+15.1}_{-9.5}$	$22.9^{+13.3}_{-8.4}$	$19.4^{+11.2}_{-7.1}$
$v \sin i$ (km s ⁻¹)	100	80	160	120	110	80	75	70	80
v_∞ (km s ⁻¹)	1300 ± 200	2300 ± 300	2100 ± 300	2100 ± 300	2400 ± 300	2000 ± 200	2000 ± 200	2300 ± 300	2100 ± 300
\dot{M}_{derived} ($M_\odot \text{ yr}^{-1}$) ^(c)	$1.50^{+4.00}_{-0.75} \times 10^{-9}$	$2.5^{+7.5}_{-1.5} \times 10^{-9}$	$4.0^{+16.0}_{-2.5} \times 10^{-9}$	$6.0^{+19.0}_{-4.5} \times 10^{-8}$	$4.5^{+10.5}_{-2.5} \times 10^{-9}$	$1.00^{+2.50}_{-0.75} \times 10^{-8}$	$2.5^{+3.5}_{-2.2} \times 10^{-8}$	$5.0^{+10.0}_{-3.0} \times 10^{-9}$	$2.00^{+6.00}_{-1.85} \times 10^{-8}$
$\dot{M}_{\text{unclumped}}$ ($M_\odot \text{ yr}^{-1}$) ^(d)	$4.8^{+12.6}_{-2.5} \times 10^{-9}$	$7.9^{+23.7}_{-4.7} \times 10^{-9}$	$1.3^{+5.0}_{-0.8} \times 10^{-8}$	$1.90^{+6.00}_{-1.43} \times 10^{-7}$	$1.4^{+3.4}_{-0.8} \times 10^{-8}$	$3.2^{+7.8}_{-2.4} \times 10^{-8}$	$7.9^{+11.1}_{-7.0} \times 10^{-8}$	$1.6^{+3.2}_{-1.0} \times 10^{-8}$	$6.30^{+18.70}_{-5.83} \times 10^{-8}$
\dot{M}_{Vink} ($M_\odot \text{ yr}^{-1}$) ^(e)	$2.6^{+0.5}_{-0.3} \times 10^{-7}$	$5.4^{+0.5}_{-0.3} \times 10^{-7}$	$5.4^{+0.8}_{-0.7} \times 10^{-7}$	$6.6^{+1.1}_{-1.0} \times 10^{-7}$	$4.2^{+0.7}_{-0.6} \times 10^{-7}$	$5.4^{+0.8}_{-0.8} \times 10^{-7}$	$5.8^{+1.0}_{-0.7} \times 10^{-7}$	$7.1^{+1.2}_{-0.9} \times 10^{-7}$	$3.5^{+0.5}_{-0.5} \times 10^{-7}$
\dot{M}_{Lucy} ($M_\odot \text{ yr}^{-1}$) ^(f)	$2.1^{+1.4}_{-0.7} \times 10^{-8}$	$1.2^{+0.8}_{-0.4} \times 10^{-8}$	$7.1^{+4.9}_{-2.4} \times 10^{-8}$	$9.8^{+6.5}_{-3.3} \times 10^{-8}$	$4.2^{+2.9}_{-1.4} \times 10^{-8}$	$5.9^{+3.9}_{-2.0} \times 10^{-8}$	$5.0^{+3.3}_{-1.7} \times 10^{-8}$	$6.5^{+4.3}_{-2.2} \times 10^{-8}$	$1.3^{+0.8}_{-0.5} \times 10^{-8}$
$\log(D_{\text{mom}}^{\text{unclumped}})$ ^(g)	$26.15^{+0.56}_{-0.48}$	$26.60^{+0.60}_{-0.40}$	$26.74^{+0.72}_{-0.40}$	$27.98^{+0.62}_{-0.60}$	$26.90^{+0.52}_{-0.35}$	$27.16^{+0.52}_{-0.61}$	$27.56^{+0.38}_{-0.92}$	$26.92^{+0.47}_{-0.40}$	$27.41^{+0.60}_{-1.12}$
$\log(D_{\text{mom}}^{\text{Vink}})$ ^(e)	$28.03^{+0.49}_{-0.49}$	$28.12^{+0.49}_{-0.49}$	$28.12^{+0.49}_{-0.49}$	$28.32^{+0.49}_{-0.49}$	$28.25^{+0.49}_{-0.49}$	$28.25^{+0.49}_{-0.49}$	$28.36^{+0.49}_{-0.49}$	$28.36^{+0.49}_{-0.49}$	$28.10^{+0.49}_{-0.49}$

Notes. Solar units and g unit are in the cgs system. Modified wind momenta (D_{mom}) are calculated using the mass-loss rate and terminal velocity in the cgs system and the radius in solar unit. ^(a)Determined from the UV region (Fe III-IV-V lines). ^(b)Determined from the optical region (He I-II lines). ^(c)Mass-loss rate using $f_\infty = 0.1$. ^(d) $\dot{M}_{\text{unclumped}} = \frac{\dot{M}_{\text{derived}}}{\sqrt{f_\infty=0.1}} \sim 3.16 \dot{M}_{\text{derived}}$. ^(e)Calculated from Vink et al. (2000). ^(f)Calculated from Lucy (2010a). ^(g) $D_{\text{mom}}^{\text{unclumped}} = v_\infty \sqrt{R_*} \dot{M}_{\text{unclumped}}$.

a proper comparison with the theoretical values, we list our unclumped mass-loss rates ($\dot{M}_{\text{unclumped}}$). Unclumped modified wind momenta ($\log(D_{\text{mom}}^{\text{unclumped}})$) are calculated using $\dot{M}_{\text{unclumped}}$.

In Table 3, we denote \dot{M}_{derived} as our mass-loss rate derived with the inclusion of clumping (adopted value of $f_\infty = 0.1$), while $\dot{M}_{\text{unclumped}}$ is calculated from $\dot{M}_{\text{derived}} / \sqrt{f_\infty} = 0.1 \sim 3.16 \dot{M}_{\text{derived}}$. In the rest of this paper, we will keep referring to the clumped values as \dot{M}_{derived} and to the unclumped ones as $\dot{M}_{\text{unclumped}}$.

The mass-loss rate \dot{M}_{Vink} is the theoretical rate from the mass-loss recipe of Vink et al. (2000). It was calculated considering $T_{\text{eff}}^{\text{UV}}$, the derived M_* , and adopting the ratio $v_\infty/v_{\text{esc}} = 2.6$. Accordingly, we provide values for $\log(D_{\text{mom}}^{\text{Vink}})$ that were calculated from $\log(L_*/L_\odot)$. We find that our mass-loss rates (\dot{M}_{derived}) are systematically lower than the predictions of Vink et al. (2000) by ~ 0.9 – 2.2 dex. The discrepancy is reduced to ~ 0.4 – 1.7 dex considering the unclumped values for the mass-loss rate ($\dot{M}_{\text{unclumped}}$).

We also present in Table 3 the mass-loss rates predicted by the hydrodynamical approach of Lucy (2010a), namely, the moving reversing layer theory (Lucy & Solomon 1970). We performed bivariate linear interpolation in the model grid provided by Lucy and we computed mass fluxes J for the sample taking $\log(g)$ and $T_{\text{eff}}^{\text{UV}}$ into account. Values for \dot{M}_{Lucy} were then obtained from our values for the stellar radii (see Eq. (3) in Lucy 2010b). We see a significant reduction in the discrepancy regarding the predicted mass-loss rates from Lucy (2010a). The values for \dot{M}_{derived} are lower⁴ by ~ 0.2 – 1.5 dex. However, we note that \dot{M}_{Lucy} is overestimated (up to ~ 1.0 dex) in comparison with $\dot{M}_{\text{unclumped}}$ for most of our sample. More details will be discussed later in the paper.

4.1. Spectral modelling

We present the fits to the UV and optical spectra of each object of our sample in Appendices A and B, respectively. All the fits

⁴ However, note that \dot{M}_{derived} is higher than \dot{M}_{Lucy} by ~ 0.1 dex for HD 135591.

presented in the appendices use the UV mass-loss rate and $T_{\text{eff}}^{\text{UV}}$ (see Table 3). In the rest of this paper, we also only present models with the effective temperature derived from the UV region. This approach is followed in this paper, since we extensively used our final models with $T_{\text{eff}}^{\text{UV}}$ in the analysis of degeneracy tests for the \dot{M} derivation. Our principal tests (such as for T_{eff}) will be discussed in detail in Sect. 5.3. Here, as an example, we present the final model for HD 156292 in Fig. 3. Overall, we achieve a very reasonable fit to the UV and optical data simultaneously. Additional details and observed discrepancies are discussed below.

Despite our efforts, a perfect fit to the observed spectra is elusive. In the UV (see Figs. A.1–A.9), the spectrum below $\sim 1240 \text{ \AA}$ is affected by geocoronal emission and severe interstellar H I absorption that is not taken into account here. We also note the presence of interstellar lines created by low ionized metals, neglected in our models. From the atlas of Dean & Bruhweiler (1985), the most common ones found in the IUE (SWP) spectra are: S II $\lambda 1259$, Si II $\lambda 1260$, O I $\lambda 1302$, Si II $\lambda 1304$, C II $\lambda 1334$, C II $\lambda 1306$, Si II $\lambda 1527$, Fe II $\lambda 1608$, C I $\lambda 1656$, C I $\lambda 1657$, C I $\lambda 1658$, Al II $\lambda 1657$, Si II $\lambda 1808$, Al III $\lambda 1855$, and Al III $\lambda 1863$. Several of them can be identified in our stars.

The N V $\lambda 1240$ wind profile is not reproduced in some stars of our sample (e.g., see Fig. A.6 for HD 218195). However, this transition is known to be very sensitive to the X-ray luminosity from the wind and to the N/H abundance. In Fig. 4, we show the behavior of the UV wind lines due to the variation in X-ray luminosity (± 1.0 dex) in the modeling of HD 218195. We found that our mass-loss diagnostics (Si IV $\lambda \lambda 1394, 1403$ and C IV $\lambda \lambda 1548, 1551$) are not strongly affected by such variation in X-ray in the parameter space of O8–9.5III. Thus, our results for \dot{M} are unlikely biased by X-ray effects. On the other hand, it is clear that N V $\lambda 1240$ is much more affected. Therefore, we did not consider it for the mass-loss rate determination.

Overall, our synthetic profiles of S V $\lambda 1502$ (in absorption) are stronger than the observations. Since this line is very sensitive to the microturbulence velocity at the photosphere, we tested different set of values for ξ_t^{min} from our assumption of 10 – 30 km s^{-1} . For example, we show in Fig. 5 our model for

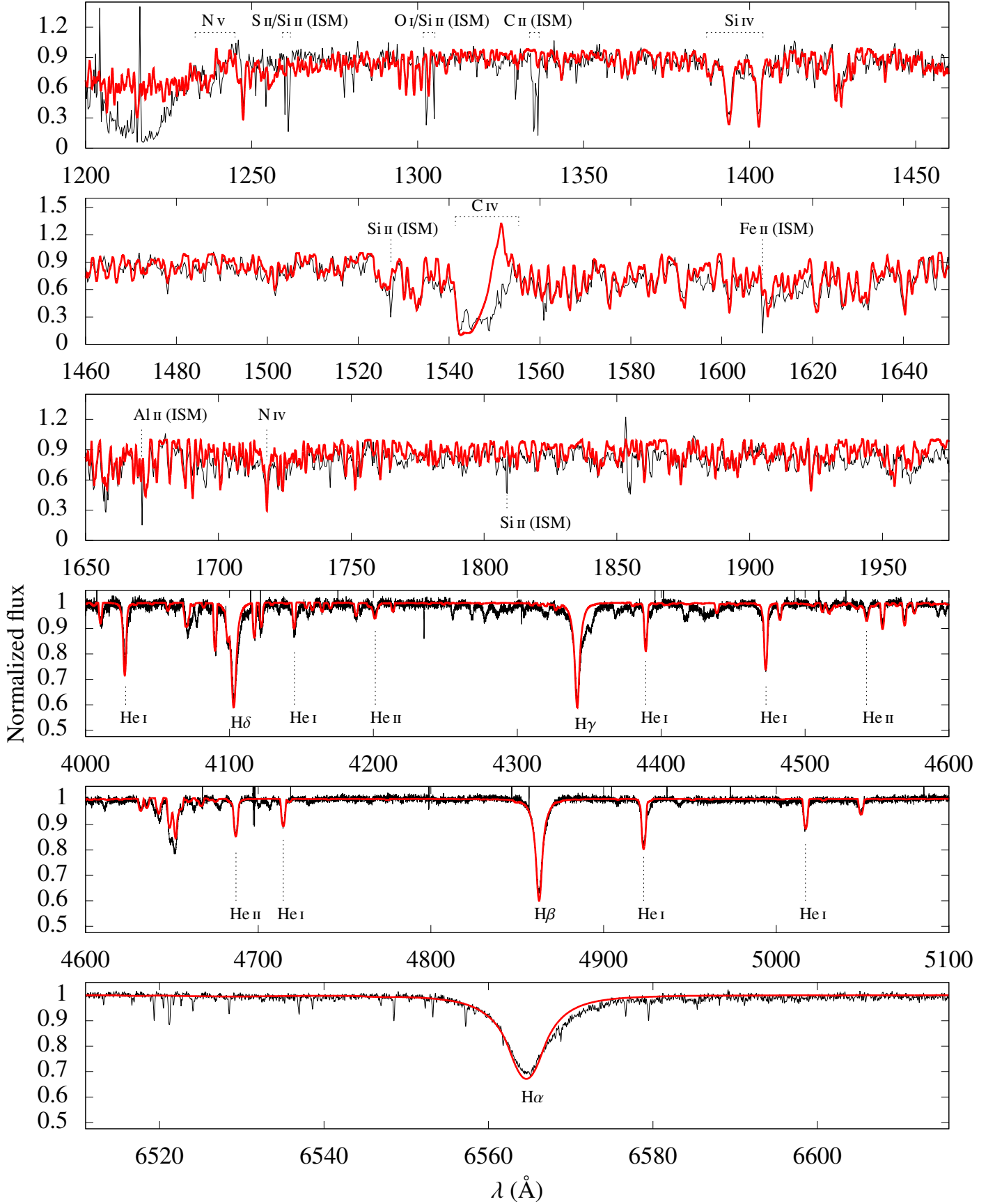


Fig. 3. Modeling (red) of HD 156292 (O9.7III) in the UV and optical. The IUE and FEROS data are shown in black. The effective temperature is derived from fitting the UV region (see $T_{\text{eff}}^{\text{UV}}$ in Table 3). We obtain a good fit to both the UV and optical observed spectra. In addition to the stellar and wind diagnostics, we list some interstellar (ISM) lines. In this case, $H\alpha$ is well reproduced with our \dot{M} derived from the UV. Discussion can be found in the text.

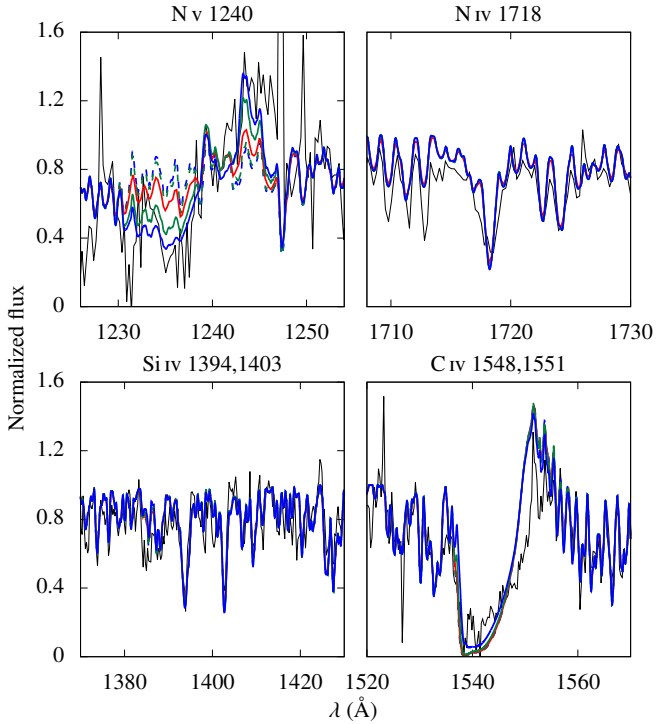


Fig. 4. Models with different X-ray fluxes compared to the IUE spectrum (black line) of HD 218195. All the other parameters are fixed. These models have the following $\log(L_X/L_{\text{BOL}})$: -7.96 (blue dashed), -7.49 (green dashed), -7.00 (solid red), -6.49 (solid green), and -6.00 (solid blue). Our final model for HD 218195 is shown in red line (typical X-ray luminosity for O stars). We note how the modeling of N v $\lambda 1240$ is sensitive to the inclusion of X-Rays, while Si iv $\lambda\lambda 1394,1403$ and C iv $\lambda\lambda 1548,1551$ are almost unchanged.

HD 116852 computed with $\xi_t^{\text{min}} = 10, 20, \text{ and } 30 \text{ km s}^{-1}$. It is necessary to increase ξ_t^{min} from 10 up to 30 km s^{-1} to reproduce the observed S v $\lambda 1502$. On the other hand, T_{eff} diagnostic lines in the UV and in the visible are misfitted considering a microturbulence velocity higher than 10 km s^{-1} . Thus, it is not possible to obtain a consistent fit simultaneously to the Fe III-IV-V lines and to the He I-II lines with this suggested higher ξ_t^{min} .

In addition to our basic model (atomic species shown in Table 2), we also compare in Fig. 5 models computed with the inclusion of the following species in order to test possible effects due to line blanketing: C II, N II, O II, Ne II, Ne III, Ne IV, Ne V, P IV, P V, S III, S IV, Ar III, Ar IV, Ar V, Ar VI, Cr IV, Cr V, Cr VI, Ni III, Ni IV, Ni V, and Ni VI. Our results regarding the modeling of S v $\lambda 1502$ are unchanged. Still from Fig. 5, one sees that the C IV $\lambda\lambda 1548,1551$ profile from our final model (solid red line) has an emission component stronger than observed. In advance of the discussion, this issue is systematic in our sample. We are not able to reproduce the observed emission component by just considering our models with a fuller account of species, we need a higher ξ_t^{min} up to $20\text{--}30 \text{ km s}^{-1}$ to better reproduce the observed emission. As discussed above, despite being able to fit the S v $\lambda 1502$ line, such high photospheric microturbulence prevents a self-consistent analysis of the effective temperature both from the UV and the visible for our sample. Therefore, we present our results with the default value of $\xi_t^{\text{min}} = 10 \text{ km s}^{-1}$.

We point out that [Holgado et al. \(2018\)](#) provide limits on the photospheric microturbulence from optical spectroscopic analysis to four stars of our sample: HD 24431 ($\xi_t^{\text{min}} > 18 \text{ km s}^{-1}$), HD 218195 ($\xi_t^{\text{min}} > 18 \text{ km s}^{-1}$), HD 36861 ($\xi_t^{\text{min}} > 11 \text{ km s}^{-1}$),

and HD 135591 ($\xi_t^{\text{min}} < 8 \text{ km s}^{-1}$). From Figs. A.2, A.6, A.7, and A.9, our final models for HD 24431 and HD 218195 (high ξ_t^{min}) overestimate the observed emission component of C IV $\lambda\lambda 1548,1551$ practically as much as in the cases of HD 36861 and HD 135591 (low ξ_t^{min}). Thus, even considering these estimations for the microturbulence, we are not able to explain our systematic overestimation of the emission component in C IV $\lambda\lambda 1548,1551$ by just regarding ξ_t^{min} . This issue concerning C IV $\lambda\lambda 1548,1551$ will be discussed in terms of the wind velocity in Sect 4.3.1.

In the optical, it is conspicuous that our models do not reproduce the features of C III $\lambda 4647 - 4650 - 4651$ (see Figs. B.1–B.9). For HD 105627, HD 116852, and HD 115455, they are barely produced by our models. In contrast, the final models for HD 36861 and HD 135591 show these profiles in emission, while the data reveal them in absorption. For HD 156292 and HD 153426, the synthetic lines are in absorption but weaker than observed. We note, however, that these lines are quite sensitive to radiative transfer details in the extreme UV – such as the lack of robust atomic data for these transitions – as already pointed out by [Martins & Hillier \(2012\)](#). Recent efforts on a better carbon atomic model, using the code FASTWIND ([Puls et al. 2005](#)), were presented by [Carneiro et al. \(2018\)](#). Thus, despite being sensitive to \dot{M} , C III $\lambda 4647 - 4650 - 4651$ must not be used as diagnostics for this parameter.

4.2. Stellar properties

4.2.1. Spectral energy distribution

The spectral energy distribution (SED) for all the stars of our sample are presented in Fig. 6. We included the effect of interstellar medium (ISM) extinction in the synthetic SEDs using the reddening law from [Cardelli et al. \(1989\)](#) with $R_V = 3.1$. The color excess $E(B-V)$ (Table 1) was assumed according to the calibrated intrinsic colors $(B-V)_0$ from [Martins & Plez \(2006\)](#). We compare the data with our synthetic SEDs scaled to take into account the *Gaia* DR2 parallaxes ([Gaia Collaboration 2016, 2018](#)): with $1/(\pi + \sigma_\pi)$ in solid green, $1/\pi$ in solid red, and $1/(\pi - \sigma_\pi)$ in solid blue. Synthetic SEDs taking into account HIPPARCOS parallaxes ([van Leeuwen 2007](#)) are shown in dotted lines for HD 116852. For HD 36861 (λ Ori A), the distance from the *Gaia* DR2 parallaxes is 271_{-35}^{+47} pc. As in [Gordon et al. \(2018\)](#), we adopted the distance of 417 ± 10 pc from the mean of the parallaxes for components C and D, since the *Gaia* DR2 parallaxes for HD 36861 have large error bars. Furthermore, different methods in the literature provide a distance estimation for this star up to ~ 400 pc (e.g., [van Leeuwen 2007](#); [Maíz Apellániz et al. 2008](#); [Mayne & Naylor 2008](#); [Maíz Apellániz & Barbá 2018](#)).

From Fig. 6, we verify that our models provide a very reasonable fit to the observed SEDs overall (e.g., for HD 156292). Again, these luminosity values (Table 3) are adopted given the spectral type using the calibrations of [Martins et al. \(2005b\)](#). $\log(L_\star/L_\odot)$ is fixed here for each star, thus we are not taking the error bar in $\log(L_\star/L_\odot)$ into account in this analysis. We tested possible effects on the SED fit due to our adoptions on the color excess (Table 1) and on the total to selective extinction ratio ($R_V = 3.1$). In Table 4, we compare this assumption on R_V with the values derived from [Wegner \(2003\)](#) since our sample has six objects in common with this work: HD 24431, HD 105627, HD 153426, HD 36861, HD 115455, and HD 135591. The color excess $E(B-V)$ in [Wegner \(2003\)](#) is adopted considering intrinsic colors from [Wegner \(1994\)](#). There are no large discrepancies between these literature results and the adopted value of R_V in

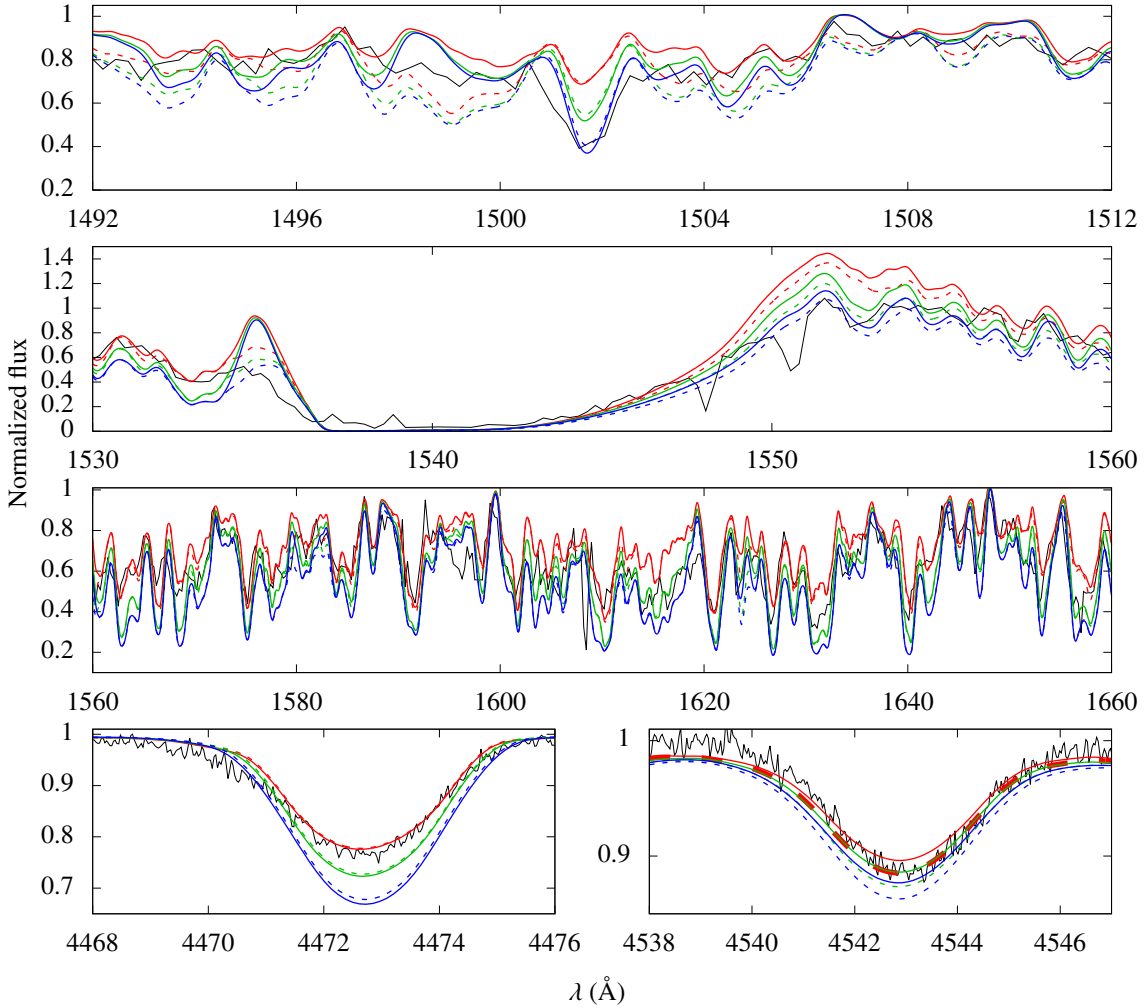


Fig. 5. Effect of ξ_t^{\min} in the T_{eff} analysis (HD 116852). Models with $\xi_t^{\min} = 10, 20,$ and 30 km s^{-1} are shown respectively in red, green, and blue. The IUE and FEROS data are shown in black. Models with a fuller account of atomic species are shown by dashed lines. The model with $\xi_t^{\min} = 10 \text{ km s}^{-1}$ and a fuller account of species (dashed red line) is shown with thicker lines in He II $\lambda 4542$ since it is overlapped with the basic model $\xi_t^{\min} = 20 \text{ km s}^{-1}$ (solid green). Line S V $\lambda 1502$ is reproduced by our model with the highest photospheric microturbulence velocity. The emission component of C IV $\lambda \lambda 1548, 1551$ is also better reproduced with a higher ξ_t^{\min} up to $20\text{--}30 \text{ km s}^{-1}$. However, T_{eff} diagnostics are misfitted in this case. It is not possible to fit simultaneously He I $\lambda 4471$ and He II $\lambda 4542$ considering $\xi_t^{\min} = 20\text{--}30 \text{ km s}^{-1}$. Our conclusions are unchanged regardless of the improved atomic in the modeling.

our analysis. One of the highest discrepancies is found for HD 36861 ($R_V \sim 2.5$), but with a large error bar compatible with $R_V \sim 3.1$. For these six stars, we present two sets of model SEDs in Fig 6: one with our adopted values for the extinction parameters and another one with the parameters (without the error bars) from Wegner (2003). For HD 36861, we show four different sets of models, including the one with the extinction parameters from Wegner (2003), as discussed below. Both sets of extinction parameters provide very reasonable fits to the observed SEDs, in particular to the shape of the 2200 \AA bump for the targets with IUE/LWP data. Thus, the analysis of the stellar luminosity is unlikely biased by our adoption of $R_V = 3.1$. Despite individual departures from this value, other studies in the literature support that $R_V \sim 3.1$ is a reasonable assumption for galactic O-type stars (e.g., Majaess et al. 2016).

The highest discrepancy in Fig. 6 is seen for HD 116852: we underestimate the data in ~ 1.5 dex (solid red line). Taking distances from van Leeuwen (2007) into account, our model overestimates the observations in ~ 0.5 dex (dashed red line). From both Gaia Collaboration (2018) and van Leeuwen (2007), the parallax

π has the same order of magnitude of σ_π . There is no model shown with distance $1/(\pi - \sigma_\pi)$ in both cases due to negative parallax values. We stress that the direct inversion of the Gaia DR2 parallax is a reasonable distance estimator for stars with $\sigma_\pi/\pi \lesssim 0.2$ (Bailer-Jones et al. 2018). Eight out of nine stars of our sample have $\sigma_\pi/\pi \lesssim 0.2$ from the Gaia DR2 release. HD 116852 is the only exception with a high ratio $\sigma_\pi/\pi \sim 1.3$. Therefore, this discrepancy for HD 116852 is more likely due to an unreliable distance estimation, using the direct inversion of π , than due to our adopted luminosity of $\log(L_\star/L_\odot) = 5.33$ for this star. Still from Fig. 6, the distance needed to fit the SED is ~ 4.8 kpc with $\log(L_\star/L_\odot) = 5.33$ (dashed red line). This result is in agreement with the spectroscopic distance of 4.8 kpc derived by Sembach & Savage (1994) for HD 116852. The closest astrometric result to this distance is provided by the lower limit on π from ESA (1997), giving an upper limit on the distance of ~ 3.6 kpc.

In the case of HD 36861 and HD 218195, the difference between our model and the observations is stronger in the UV than in the near-infrared. For HD 218195, it reaches up to ~ 1.0 dex in the UV continuum. For example, we show in Fig. 6

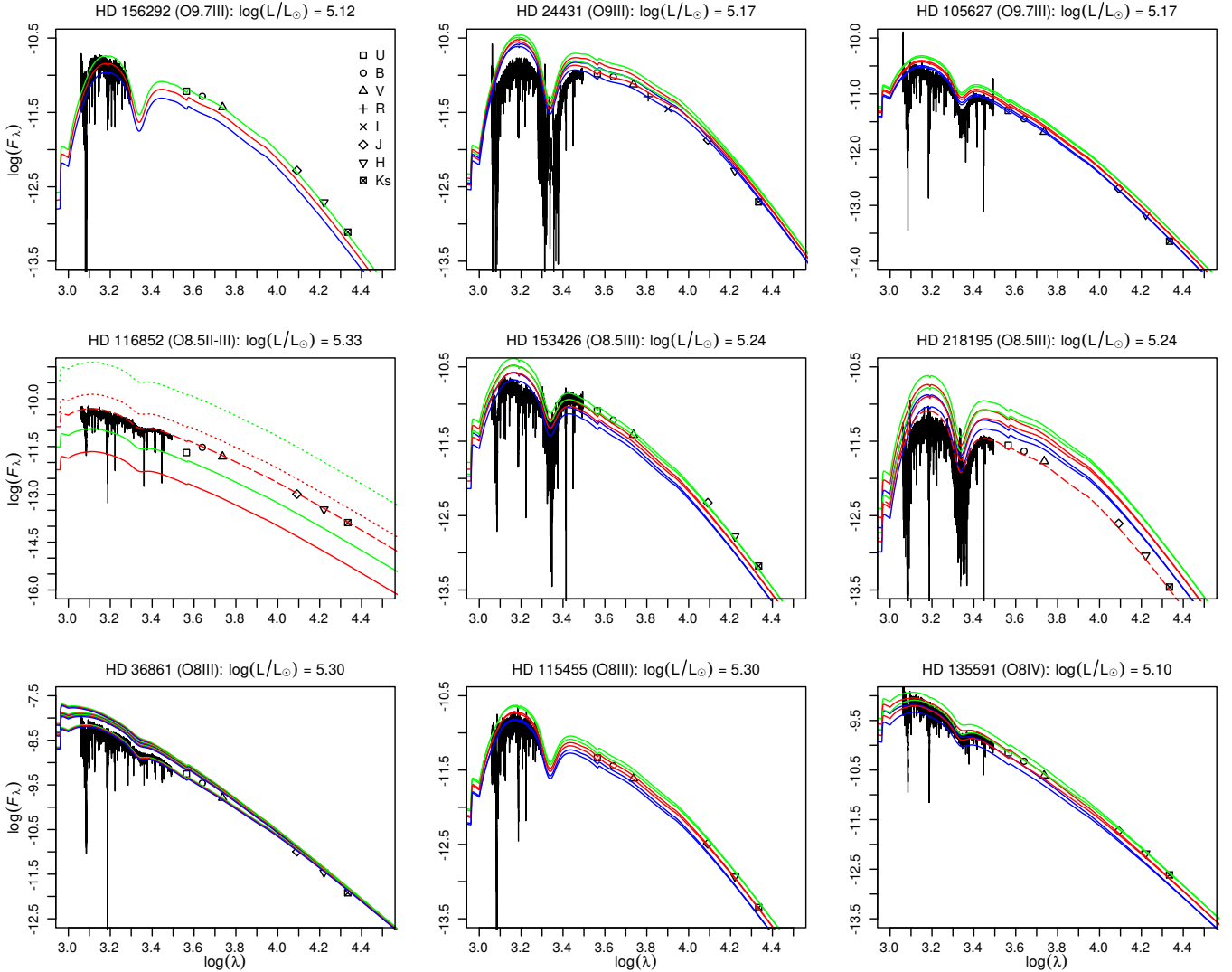


Fig. 6. Model SEDs (color lines) compared to the observed ones (black). The IUE/SWP+LWP and photometric data are listed in Table 1. Flux unit is in $\text{erg cm}^{-2} \text{s}^{-1} \text{\AA}^{-1}$ and wavelength is in \AA . Model SEDs in solid lines are computed with distances from *Gaia* DR2: $1/(\pi + \sigma_\pi)$ (green), $1/\pi$ (red), $1/(\pi - \sigma_\pi)$ (blue). Model SEDs taking into account HIPPARCOS distances are shown in dotted lines (HD 116852). For the stars listed in Table 4, we show two sets of models with different values of $E(B - V)$ and R_V from our assumption and from Wegner (2003). For HD 36861, there are shown four sets of models with different extinction parameters, including one with $E(B - V)$ and R_V from Wegner (2003). For HD 218195, we compare two sets of models with different values of $E(B - V)$. For HD 116852 and HD 218195, SED models considering the distances of 4.8 and 2.5 kpc are shown in red dashed line. See text for discussion.

two sets of models (solid lines) for HD 218195 computed with the same distance and with slightly different values of $E(B - V)$: 0.55 and 0.60. The latter corresponds to the selective extinction adopted by Patriarchi et al. (2001) for this star, using intrinsic colors from Wegner (1994). Considering this color excess different from our assumption, we are able to reproduce better the SED shape in the continuum UV and to diminish the discrepancy in the UVB-bands. In addition, we are able to improve significantly our fit (red dashed line) taking into account the spectroscopic distance of ~ 2.5 kpc found by Maíz Apellániz & Barbá (2018) for HD 218195. This distance is somewhat larger than the value from *Gaia* DR2 parallaxes (~ 1.6 kpc). In this case, we use the extinction parameters from Maíz Apellániz & Barbá (2018) for this star ($E(B - V) = 0.54$ and $R_V = 3.2$), but they are very close to our adopted values. For HD 36861, we show four sets of SED models with different extinction parameters: our adopted values, derived from Wegner (2003), from Gordon et al. (2018), and from Maíz Apellániz & Barbá (2018). In this case, our SED

models encompass the observed one by just considering different values for $E(B - V)$ and R_V . An analysis of ISM reddening is beyond the scope of this paper, nevertheless we point out that uncertainties in our adopted values for $E(B - V)$ can explain certain differences between our models and the observed SED.

Therefore, despite uncertainties regarding the implementation of ISM reddening in the models and the distance estimations, we conclude that the luminosities provided in Martins et al. (2005b) are in fair agreement with the observations of O8-9.5III stars. Considering our adopted $E(B - V)$, it is necessary to decrease $\log(L_\star/L_\odot)$ in ~ 0.5 dex for HD 218195. This reduction in luminosity would place this star in the late O dwarfs' loci in the HR diagram. However, no evidence supports such uncertainty in the spectral classification. Nevertheless, a lower $\log(L_\star/L_\odot)$ implies downward revision of \dot{M} for HD 218195 to re-fit the observed Si IV $\lambda\lambda 1394, 1403$. In this case, our inferred mass-loss rates for this star are at most overestimated due to the adopted luminosity.

Table 4. Comparison between our adopted ISM extinction parameters ($R_V = 3.1$) to the total to selective extinction ratio derived by Wegner (2003) for stars in common with our sample.

Star	HD 24431	HD 105627	HD 153426	HD 36861 A (λ Orionis A)	HD 115455	HD 135591
$E(B - V)^{(a)}$	0.63	0.30	0.40	0.07	0.46	0.17
$E(B - V)^{(b)}$	0.65	0.31	0.43	0.09	0.47	0.22
$R_V^{(b)}$	3.46 ± 0.06	3.24 ± 0.16	3.19 ± 0.16	2.46 ± 0.60	3.29 ± 0.13	3.57 ± 0.18

Notes. ^(a)Adopted in this work (see Table 1). ^(b)From Wegner (2003).

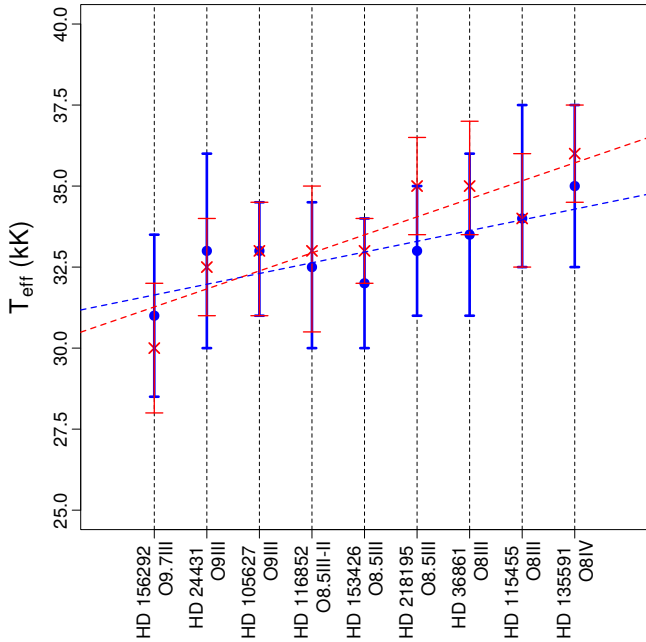


Fig. 7. Comparison between effective temperatures obtained from the UV versus optical for all our sample. The stars are ordered from the later to the earlier types. The effective temperature derived from the UV and the optical regions are shown, respectively, by circles (blue) and crosses (red). We show weighted least squares fits to the UV T_{eff} (dashed blue line) and to the optical T_{eff} (dashed red line). We note the good agreement between them and the trend of higher T_{eff} towards earlier spectral types.

4.2.2. Photospheric parameters

In the following, we analyze the UV and optical effective temperatures inferred for all objects of our sample in Fig. 7. We find good agreement between the effective temperatures derived from the iron forest lines in the ultraviolet and from the helium lines in the visible region. The highest discrepancy (2000 K) is seen for HD 218195. However, even in this case, the ultraviolet and optical results are consistent within the error bars. The expected trend of higher temperatures towards earlier spectral classes (from O9.7III to O8IV) is confirmed: for a better visualization, we provide two linear regressions in Fig. 7 to the UV and optical T_{eff} in function of the spectral type. We find only two objects (HD 156292 and HD 24431) with $T_{\text{eff}}^{\text{opt}}$ lower than $T_{\text{eff}}^{\text{UV}}$. Others results in the literature find good agreement for T_{eff} derived from the UV and the optical spectra using the code CMFGEN (e.g., Hillier et al. 2003; Martins et al. 2005a). Therefore, our results confirm the viability of the determination of the effective temperature for O giants solely through the ultraviolet, despite its relatively high error bars.

We compare our photospheric parameters with the ones found by Martins et al. (2015a)⁵ as our sample shows four objects in common with them: HD 24431, HD 153426, HD 218195, and HD 36861. We verify a good agreement for the effective temperature. These authors derived the following values for T_{eff} , respectively: 33 500, 34 000, 34 000, and 35 000 K. Our values ($T_{\text{eff}}^{\text{opt}}$) differ in 1000 K for all these stars. Such differences are inside our error bars on $T_{\text{eff}}^{\text{opt}}$ and it is also the typical uncertainty from Martins et al. (2015a).

For $\log(g)$, we derived the same value for HD 24431, but overall our values are lower (up to 0.25 dex) than the ones found in Martins et al. (2015a). Here, the lowest discrepancy is 0.15 dex for HD 36861 ($\log(g) = 3.75$ from Martins et al. 2015a) and the highest one is 0.25 dex for HD 218195 ($\log(g) = 3.80$ from Martins et al. 2015a). This discrepancy for HD 218195 is explained considering our different values between $T_{\text{eff}}^{\text{UV}}$ (33 000 K) and $T_{\text{eff}}^{\text{opt}}$ (35 000 K). From our tests using $T_{\text{eff}}^{\text{opt}}$, it is necessary to increase $\log(g)$ up to ~ 3.8 to re-fit the wings of the Balmer lines. We are aware that the effective temperature derived from the UV lines is less precise than the ones derived from the optical analysis. Nonetheless, as discussed above, these independent determinations of T_{eff} are in overall good agreement, attesting that our measured T_{eff} from the UV are reliable. Thus, such discrepancies must not impact the derivation of the mass-loss rate for the stars of our sample.

Regarding $v \sin i$, our values are systematically larger in comparison with Martins et al. (2015a). These discrepancies are expected, as we do not include macroturbulence in the modeling and these authors include it. In any case, we stress that the effective temperature has the highest potential of affecting our mass-loss analysis.

4.2.3. HR diagram

After deriving the stellar and wind parameters, we analyzed our sample in the HR diagram along with results from the literature for different classes of O-type stars. We used evolutionary tracks and isochrones from Ekström et al. (2012). The tracks were computed considering solar metallicity ($Z = 0.014$) and $v_{\text{initial}}/v_{\text{critical}} = 0.4$ (Ekström et al. 2012).

We present the results in Figs. 8 and 9. We show evolutionary tracks for the initial masses (M_{ZAMS}) of 20, 25, 28, 32, 40, and 60 M_{\odot} , as well as isochrones for the ages (t) of $10^{6.0}$, $10^{6.5}$, $10^{6.6}$, $10^{6.7}$, $10^{6.8}$, $10^{6.9}$ yr. Results concerning dwarfs (O3.5-9.5V) are from Martins et al. (2005a) and Marcolino et al. (2009). The OB supergiants (O3-9.7I and B0-0.5I) are from Repolust et al. (2004), Mokiem et al. (2005), Crowther et al. (2006), and Bouret et al. (2012). The early-type giants (O5-7.5III) are from Repolust et al. (2004) and Mokiem et al. (2005). Additionally, results for

⁵ Martins et al. (2015a) do not provide results for the wind parameters as their focus is on surface abundances for O stars.

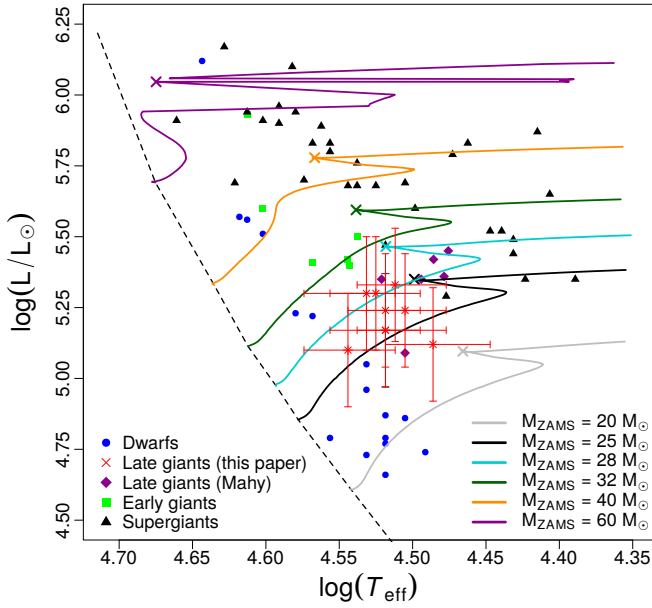


Fig. 8. Evolutionary tracks (in color lines) for samples of O dwarfs, giants, and supergiants. For each model, the central H exhaustion is indicated by crosses. The zero-age line is in dashed black. Stars are grouped by different symbols and colors. Our sample (red crosses) has initial masses (M_{ZAMS}) ranging around $25\text{--}28 M_{\odot}$. Late O giants are closer to the end of the main sequence phase than the dwarfs.

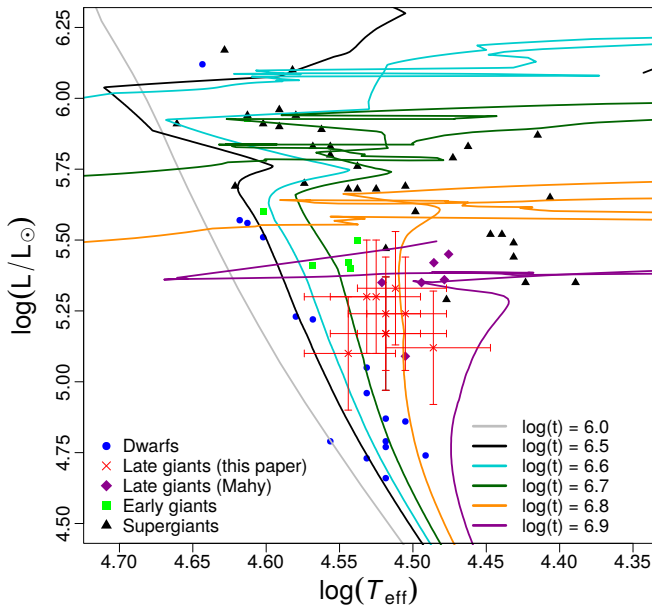


Fig. 9. Same as in Fig. 8, but showing the isochrones. The bulk of the late O giants show ages ranging around $10^{6.7}\text{--}10^{6.8}$ yr.

late O giants (six stars O8-9.5III in total, excluding giants earlier than O7) from Mahy et al. (2015) are shown too. There are no objects in common between Mahy et al. (2015) and our sample.

As expected, O dwarfs, giants, and supergiants occupy different loci in the HR diagram. In particular, our sample of late O giants populate a narrow region due to the low dispersion in luminosity (adopted) and effective temperature (from UV): $\log(L_{\star}/L_{\odot}) \sim 5.1\text{--}5.3$ and $\log(T_{\text{eff}}) \sim 4.50\text{--}4.55$. The bulk of our sample shows initial (evolutionary) masses of $\sim 25\text{--}28 M_{\odot}$ and ages of $\sim 10^{6.7}\text{--}10^{6.8}$ yr. The star of our sample with the

lowest T_{eff} , HD 156292, has initial mass between 20 and $25 M_{\odot}$ (being closer to the latter) and age between $10^{6.8}$ and $10^{6.9}$ yr. In contrast, the O5-7.5III stars correspond to different intervals of mass and age, with $M_{\text{ZAMS}} \sim 32\text{--}60 M_{\odot}$ and $t \sim 10^{6.6}\text{--}10^{6.7}$ yr, and hence they are more massive and younger than our sample, as expected from the spectral classification. We see that the late giants of Mahy et al. (2015) populate the region around our sample despite the two stars that are close to the edge of our upper limits on $\log(L_{\star}/L_{\odot})$. Indeed, Mahy et al. (2015) noted the discrepancies between their luminosities and the spectral-type calibration of Martins et al. (2005b). They argue that this trend is related to their methodology for the derivation of the luminosity, and thus slightly affecting the analysis on the HR diagram.

The dwarfs considered here present a larger interval in mass and age ($\sim 25\text{--}60 M_{\odot}$ and $t \sim 10^{6.0}\text{--}10^{6.8}$), since they encompass a larger range of spectral types (from O9.5V to O3.5V). This is the same as for the OB supergiants that spread over the whole diagram in T_{eff} , implying $M_{\text{ZAMS}} \sim 25\text{--}60 M_{\odot}$ and $t \sim 10^{6.5}\text{--}10^{6.9}$ yr. We recall here that the O dwarfs with $\log(L_{\star}/L_{\odot}) < 5.2$ present the weak wind problem and correspond to the O8-9.5V spectral types. For these stars, we observe masses of $\sim 20\text{--}25 M_{\odot}$ and ages around $10^{6.7}$ yr. In fact, as expected, we can perceive a clear division in ages between dwarfs, giants, and supergiants from Fig. 9.

In conclusion, we corroborate the literature results showing that O giants are slightly more evolved objects than the dwarfs, being closer to the end of the main sequence phase (e.g., Mahy et al. 2015; Martins et al. 2015a). Our sample is described on the HR diagram as a descent of O dwarfs with $\log(L_{\star}/L_{\odot}) \sim 5.0$, corresponding to the spectral types O6.5-8V. These O dwarfs are the onset of the weak wind problem. Thus, weak winds in O giants would imply that this phenomenon is not exclusively associated to younger stars on the main sequence. The bulk of our sample is halfway between the O dwarfs' loci and the end of the H-burning phase, thus weak winds could persist up to end of the main sequence before undergoing the supergiant phase. We stress that OB supergiants do not present the weak wind phenomenon (e.g., Bouret et al. 2012).

4.3. Wind properties

4.3.1. Wind velocity law

As previously mentioned, the emission component of the CIV $\lambda\lambda 1548, 1551$ P-Cygni profile is overestimated in our models. Different parameters can affect this profile, for example, the carbon abundance, mass-loss rate, X-ray flux, and wind velocity structure. However, we only found better fits by changing this last, more specifically, the β parameter. Tests performed with other parameters did not change the profile in the desired way and/or produced undesired effects in other parts of the spectrum. It is possible to decrease the emission to the observed level by decreasing the mass-loss rate or the carbon abundance⁶. On the other hand, the absorption component of the P-Cygni decreases too much in comparison with the observations. It is beyond the scope of this paper to derive CNO abundances for late O giants. Nevertheless, we discuss in Sect. 5.3.1 the effects of CNO abundances on the determination of \dot{M} from the UV.

We have tried different values for the β parameter in the velocity law. In Fig. 10, we compare our final models ($\beta = 1.0$) to models recalculated with lower β values around 0.3. Our tests

⁶ A lower carbon abundance is actually expected as O stars evolve (e.g., Martins et al. 2015a).

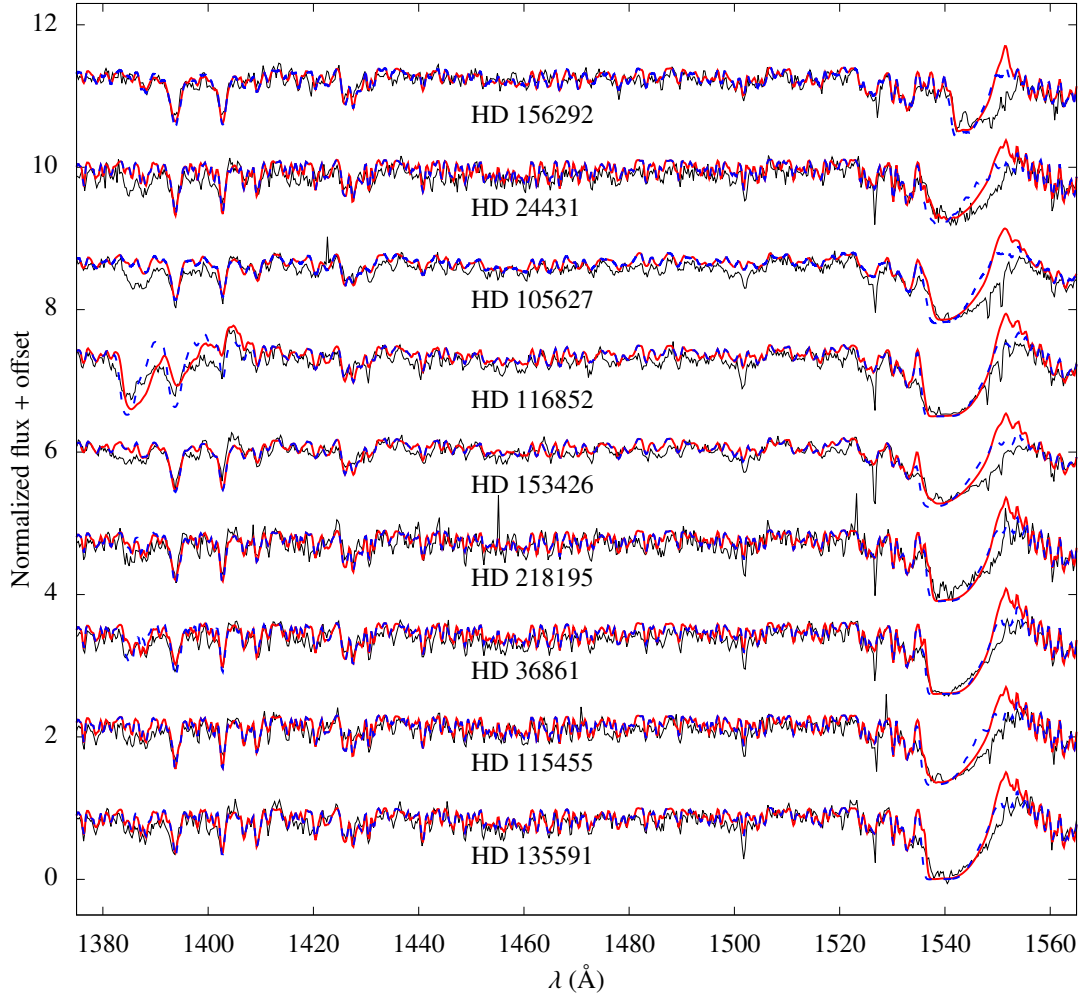


Fig. 10. Final models for $\beta = 1.0$ (red) and tests with $\beta \sim 0.3$ (dashed blue) for each star in the UV. Here, $\beta = 0.35$ for HD 24431 and HD 115455 due to model convergence issues with $\beta = 0.3$. For the other stars, $\beta = 0.3$. The IUE spectra are in black. The emission component of C IV $\lambda\lambda 1548,1551$ is better modeled with $\beta \sim 0.3$.

are limited to this value because we could not reach model convergence below $\beta \lesssim 0.3$ ⁷. Overall, the fit to the observed profiles is improved with a $\beta \sim 0.3$. The emission component of the profiles decreases in comparison with $\beta = 1.0$ models and provides a better match to the observations. We see that the effects of varying β on the Si IV $\lambda\lambda 1394,1403$ profiles are not significant. The exception is for HD 116852, but this modification of the spectral lines due to β is much smaller than the changes created by the limits on \dot{M} of this star.

In the framework of the Sobolev approximation, the variation in β impacts differently on line formation in the inner and outer regions of the wind. In the inner wind, the Sobolev length is proportional to $(\frac{dv}{dr})^{-1}$. That is, a lower β (higher gradient) implies a smaller interaction region: we have less absorption and emission at low velocities (close to the line center). This can be seen in the C IV $\lambda\lambda 1548,1551$ profiles in Fig. 10. On the other hand, the Sobolev length is proportional to $\frac{r^2}{v}\beta^{-1}$ in the outer wind. By decreasing β , we have a larger interaction region at high velocities (far from the line center). This is also observed in Fig. 10 (more absorption), but the effect is lower compared to the decrease in emission.

⁷ Indeed, we could not reach convergence even with $\beta = 0.3$ for some stars (HD 24431 and HD 115455), but it worked with a slightly higher value $\beta = 0.35$ – 0.40 .

Low values for β , as suggested by our fits, are uncommon from the spectroscopic modelling of O stars: most O stars have β close to unity (dwarfs) or even higher, up to ~ 2.0 – 3.0 in supergiants (see, e.g., Crowther et al. 2006; Martins et al. 2015b). Moreover, there are hydrodynamical results showing $\beta \sim 1.0$ – 0.9 for O8–9.5 giants (Muijres et al. 2012). Therefore, our tests suggesting very low values of β are an artifact of our modeling assumptions, they do not represent a viable solution to the wind velocity structure of O-type stars. We recall that we assumed a standard β velocity law to describe the wind region. One possibility relies on less simple parameterizations for wind velocity structure, for example, a two-component β velocity describing separately the inner and outer regions of the wind (e.g., Hillier & Miller 1999). Thus, a deeper investigation is needed, but it is beyond the scope of this paper.

4.3.2. Mass-loss rates: weak winds

In this section, we compare the mass-loss rates determined from atmospheric models with the ones predicted by Vink et al. (2000) and Lucy (2010a). First, we consider the $\log(D_{\text{mom}})$ versus $\log(L_{\star}/L_{\odot})$ diagram in Fig. 11. Our results for late O giants are presented along with dwarfs, giants, and supergiants of different spectral classes from the literature. We do not include here the results of Mahy et al. (2015) since they derived v_{∞} for just

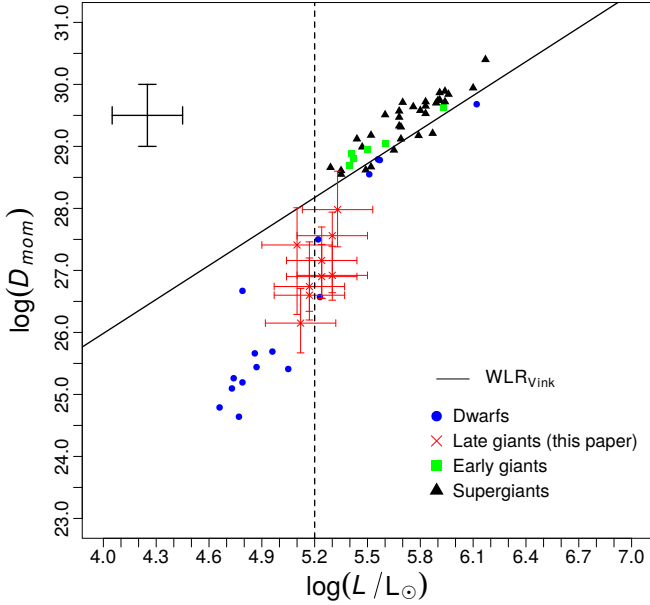


Fig. 11. Wind momentum-luminosity diagram for O dwarfs, giants, and supergiants. Colors and geometric figures stand as in Fig. 8, our results are shown in red crosses. Our results are derived from the UV analysis. All the spectroscopic results consider (or are scaled to) unclumped \dot{M} . The theoretical relation of Vink et al. (2000) is in solid black. We mark $\log(L_*/L_\odot) = 5.2$ in dashed black line, and representative error bars for the literature results are shown in the top left.

two objects out of six late O giants. All spectroscopic results in Figs. 11–14 consider homogeneous wind models: the literature results with clumping were scaled by a factor of $1/\sqrt{f_{\text{cl}}}$.

The weak wind phenomenon is seen for the late O dwarfs (O8–9.5V) with $\log(L_*/L_\odot) \lesssim 5.2$. Their modified momentum are up to two orders of magnitude lower than the theoretical relation of Vink et al. (2000). The late O dwarf closest to the predicted value – $\log(L_*/L_\odot) \sim 4.8$ and $\log(D_{\text{mom}}) \sim 26.6$ – had its mass-loss rate derived by Martins et al. (2005a) as a conservative upper limit value. For the most luminous stars with $\log(L_*/L_\odot) \gtrsim 5.2$, there is a good agreement between the measured and predicted values. Our results fall below the values expected from theory, even considering the error bars. Only one object of our sample (HD 116852) marginally agrees with the wind momentum-luminosity relation from Vink et al. (2000). Hence, we conclude that late O giants also present winds weaker than predicted by theory. The discrepancy is more severe for O8 giants (HD 156292, O9.7III, lowest D_{mom}) and is attenuated towards O9 giants (HD 116852, O8.5II–III, highest D_{mom}). It suggests a gradual change from “weak” to “normal” winds (agreement with predictions) for the stars of our sample.

In Fig. 12, we present a direct comparison between the spectroscopic \dot{M} and the predicted ones using Vink et al. (2000). Stars are divided by colors and geometric symbols as in Fig. 11. In addition, we include here the results of Mahy et al. (2015) for O8–9.5III stars for which mass-loss rates were determined (five out of six stars). It reflects the same basic conclusions obtained from the wind momentum-luminosity diagram in Fig. 11. Nevertheless, the mass-loss range and the types of O stars for which the radiative wind theory is successful are conspicuous. We note that the sample of late O giants from Mahy et al. (2015) tends to agree better with the predictions of Vink et al. (2000), but we still observe the weak wind problem here: three out of five stars in good agreement and two stars presenting significant

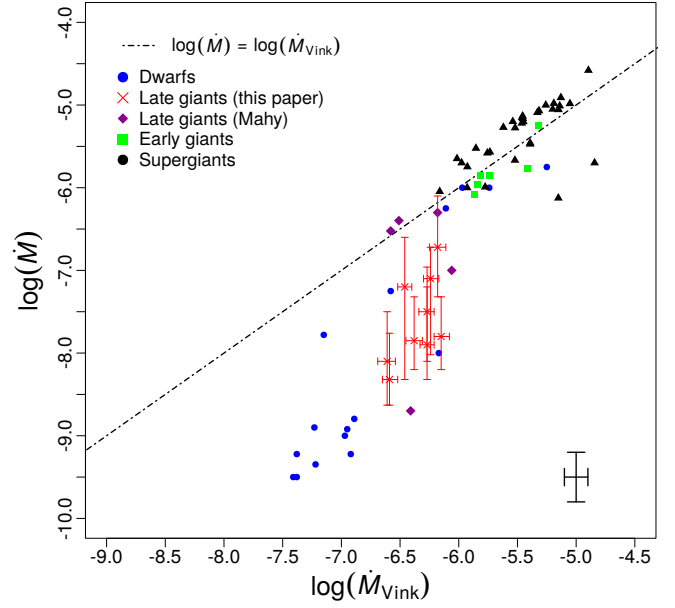


Fig. 12. Comparison between the spectroscopic \dot{M} and the ones predicted from Vink et al. (2000) for O dwarfs, giants, and supergiants. Colors and geometric figures stand as in Fig. 8, our results are shown in red crosses. One-to-one relation is shown in dotted-dashed line, and representative error bars for the literature results are shown in the bottom right. O8–9 dwarfs (weak winds) are shown in blue points. We see that late O giants also present weak winds.

deviations (with one clear weak wind star). Since Mahy et al. (2015) derived mass-loss rates using UV and $H\alpha$, we will discuss this question in more detail in Sect. 5.1.

Furthermore, we performed the same comparison but with the hydrodynamical predictions of Lucy (2010a) for Galactic O stars. These predictions are made in the framework of the most recent updated version of the moving reversing layer theory (Lucy & Solomon 1970). In short, for given stellar parameters, the equation of motion has physical solution for a certain value of mass flux J that satisfies null effective gravity surface at the critical point of the wind. In a previous work, Lucy (2010b) found that the discrepancies between the measured \dot{M} for late O dwarfs (Marcolino et al. 2009) and their predictions are significantly reduced up to about one order of magnitude. In Fig. 13, we present a comparison between the derived \dot{M} (by atmosphere models) and the ones calculated using the predicted mass fluxes given by Lucy (2010a) for almost the same sample presented in Fig. 12.

The grid of Lucy (2010a) provides mass fluxes for stars with $3.00 \leq \log(g) \leq 4.50$. Thus, we excluded some OB supergiants (six objects) that were analyzed in the previous comparison with \dot{M}_{Vink} . From the literature sample presented in Fig. 12, we excluded stars with $\log(g) < 2.95$. For stars with $2.95 \leq \log(g) \leq 3.00$ (three objects), we calculated the mass fluxes (and then \dot{M}_{Lucy}) considering $\log(g) = 3.00$. Interestingly, we observe a better agreement between the spectroscopic and predicted values for the mass-loss rates of low-luminosity objects (late O dwarfs and giants). However, the most part still have \dot{M} values about 0.5–1.0 dex lower than \dot{M}_{Lucy} . In contrast to the previous comparison with Vink et al. (2000), the predictions of Lucy (2010a) for high-luminosity OB stars – $\log(L_*/L_\odot) \gtrsim 5.2$ – are lower than the mass-loss rates obtained by atmosphere models. For a better visualization, we present again these results in an alternative form in Fig. 14. We see that \dot{M}_{Lucy} underestimates the mass

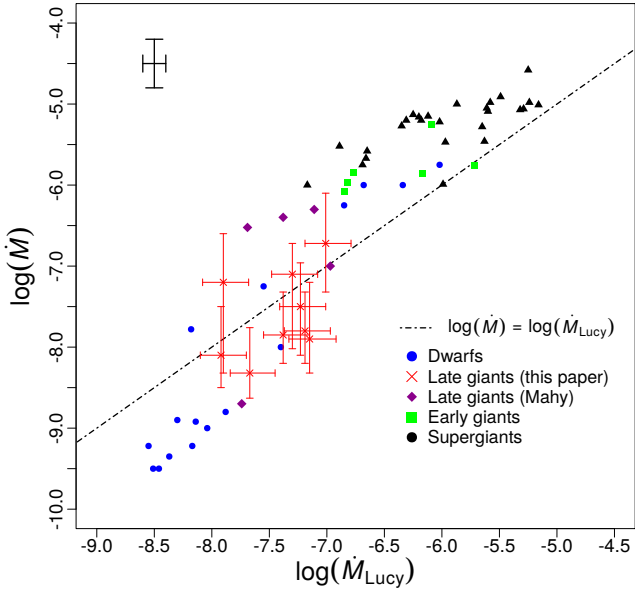


Fig. 13. Same as Fig. 12, but comparing with theoretical \dot{M} from Lucy (2010a). The weak wind problem is significantly lessened to about one order of magnitude. On the other hand, the discrepancy here for the luminous OB stars (shown in triangles) is increased in comparison with Vink et al. (2000).

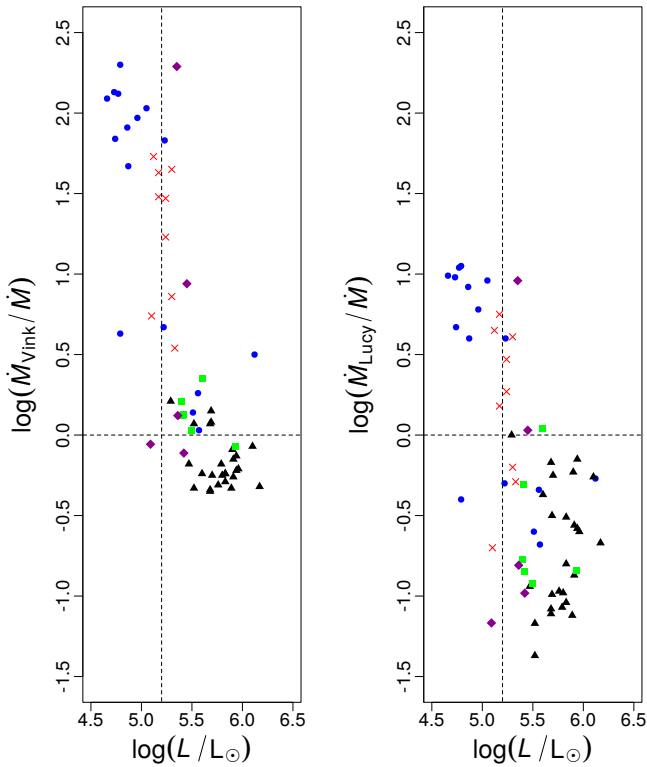


Fig. 14. Difference (as a function of luminosity) between the measured \dot{M} (clumped) and their theoretical values by Vink et al. (2000) on the left, and by Lucy (2010a) on the right. Symbols stand as presented in Fig. 8, our results are shown in red crosses. The luminosity value of $\log(L_*/L_\odot) = 5.2$ and the match between the spectroscopic and theoretical \dot{M} are indicated by dashed black lines. We note that \dot{M}_{Lucy} attenuates the weak wind problem, but it increases the discrepancy to the spectroscopic \dot{M} in $\log(L_*/L_\odot) \gtrsim 5.2$.

loss of OB stars with $\log(L_*/L_\odot) \gtrsim 5.2$ practically as much as it overestimates for objects with $\log(L_*/L_\odot) \lesssim 5.2$.

In conclusion, Figs. 11 and 12 indicate that late O giants exhibit weak winds. As O8-9.7III objects are more evolved than late O dwarfs, we naturally exclude evolutionary effects as the reason for weak winds. Put differently, O stars with luminosities lower than $\log(L_*/L_\odot) \sim 5.2$ must have weak winds through the H-burning phase. Furthermore, the predictions from Lucy (2010a) attenuate the weak wind problem both for late O dwarfs and for late giants. However, these theoretical values clearly fail (in comparison with Vink et al. 2000) to predict the mass-loss rates for more luminous OB stars, such as OB supergiants, early dwarfs, and early giants. We stress here that the predictions of Vink et al. (2000) are in good agreement with the hydrodynamical simulations of Muijres et al. (2012) for O stars with $\log(L_*/L_\odot) \gtrsim 5.2$, while the latter fails to predict \dot{M} for objects below this luminosity region. It is hard to compare the predictions of Vink et al. (2000) with the ones from Lucy (2010a) because they employ different approaches: the first find \dot{M} that is globally (in the wind) consistent with the conservation of energy, while Lucy (2010a) predicts the mass loss from first principles (i.e., solving the equation of motion). Nevertheless, it is remarkable that the region of $\log(L_*/L_\odot) \sim 5.2$ shows to be critical for both of them (in comparison with the spectroscopic \dot{M}).

5. Discussion

5.1. Mass-loss rates: UV versus visible

In this section, we compare our final models to the ones computed using \dot{M}_{Vink} , regarding the spectral modeling in the ultraviolet and optical regions. Throughout this section, we only compare our results with the predictions from Vink et al. (2000) because they are currently used in most modern stellar evolution codes. In the previous discussion, all \dot{M} for the objects of our sample were derived from the UV analysis. Overall, our synthetic H α profiles have deeper cores than the observations, indicating the need to increase the \dot{M} parameter in our models.

Regarding O8-9.5V stars, Marcolino et al. (2009) found that their UV \dot{M} produce H α profiles in absorption, in relatively good agreement with observations. Moreover, they show that in three (out of five) objects the predicted \dot{M} (Vink) implies a shallower H α line, in contrast to the data. For the other two stars, the difference between the final models and \dot{M}_{Vink} is minor against the observations. We show below that such discrepancies in H α are higher for O8-9.5III stars.

First, in Fig. 15, we compare our final models with models using the mass-loss rates from Vink et al. (2000) in the UV region. All models with \dot{M}_{Vink} are computed with $f_\infty = 1.0$ because Vink et al. (2000) do not take clumping into account. These values of \dot{M}_{Vink} are higher than our unclumped \dot{M} from UV up to about two orders of magnitudes (Table 3). Our best fits to the observations consider clumping ($f_\infty = 0.1$, see Sect. 3). We recall, however, that Fig. 15 would be virtually identical by preserving $\dot{M}/\sqrt{f_\infty}$ constant for each star. All the other physical parameters are fixed. The synthetic profiles of Si IV $\lambda\lambda 1394, 1403$ using \dot{M}_{Vink} are systematically more intense than the data for all objects. Regarding C IV $\lambda\lambda 1548, 1551$, it is difficult to distinguish between our final mass-loss rates and the ones predicted by Vink for stars with saturated profiles (e.g., HD 116852). On the other hand, in HD 24431, HD 105627, and HD 153426 the predicted rates saturate the profiles in contrast to the observations. Hence, we conclude that models considering \dot{M}_{Vink} are not able to fit the UV mass-loss diagnostics of late O giants.

Our analysis of the H α profile is presented in Fig. 16. Again, models with \dot{M}_{Vink} are computed without clumping. However,

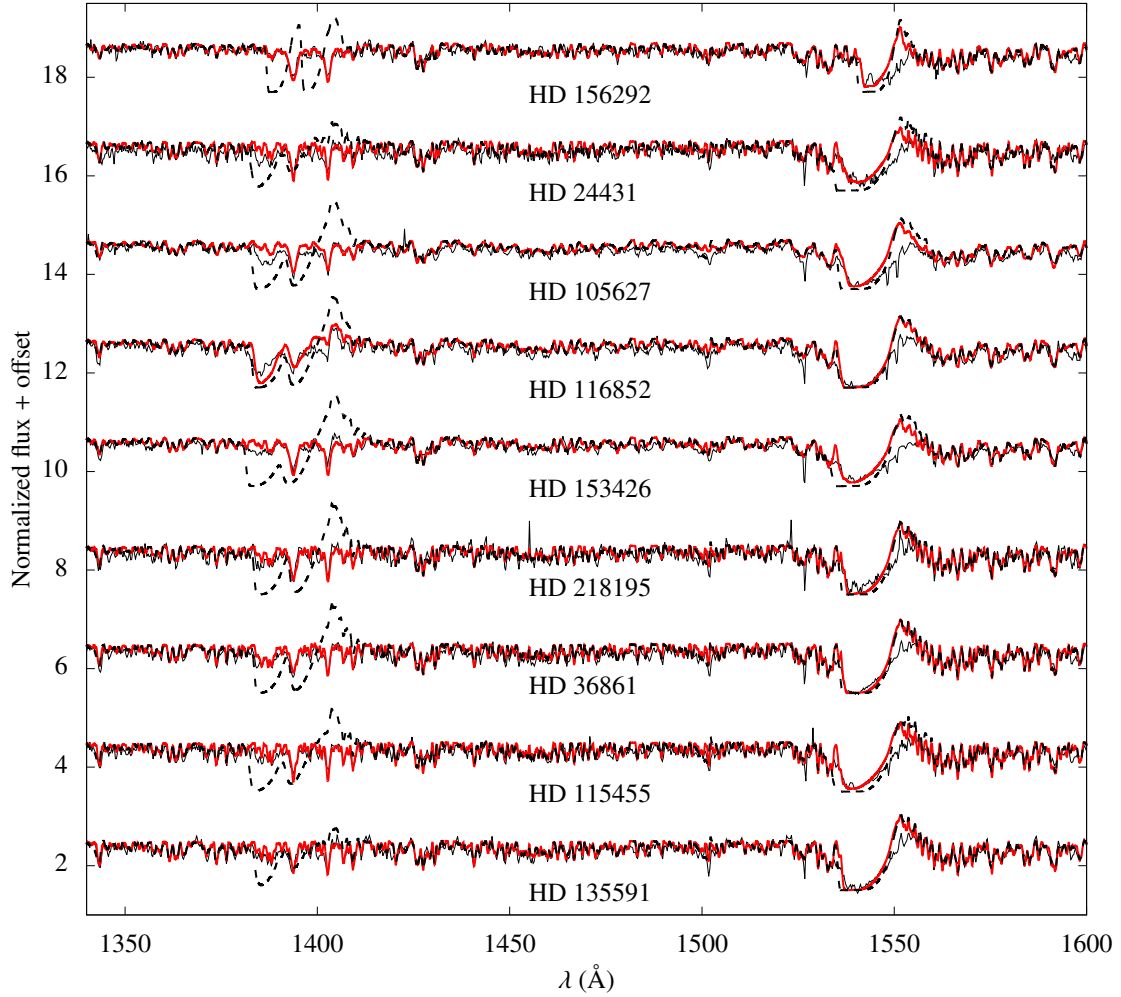


Fig. 15. Comparison between the final models and the ones computed using the hydrodynamical mass-loss rates of Vink et al. (2000) in the UV region. The IUE spectra are in solid black, and the star name is indicated right below its spectrum. All the final models (\dot{M} from the UV) are in red, while \dot{M}_{Vink} is in dashed black. Our final models have clumping ($f_{\infty} = 0.1$), while the models with \dot{M}_{Vink} are unclumped. We note how \dot{M}_{Vink} overestimates the intensity in Si IV $\lambda\lambda 1394, 1403$ for all our sample. C IV lines also become saturated in a few cases, in contrast to the observations.

in this case, we have four “types” of models:

(i) with UV mass loss (solid red). We present “models (i)” for all the stars of our sample. These models have $f_{\infty} = 0.1$.

(ii) With UV upper mass loss (solid blue). We show “models (ii)” only for HD 116852 and HD 135591 because we are able to reproduce (or to overestimate) with them the observed H α . We do not present our UV upper limit on \dot{M} for the other stars, since they produce practically the same H α profile as “models (i)” in this case. These models have $f_{\infty} = 0.1$.

(iii) With Vink’s mass loss (dashed black). As for “models (i)”, “models (iii)” are shown for all the stars of our sample. We use unclumped models because Vink et al. (2000) do not take clumping into account.

(iv) With mass loss derived from fitting the H α profile (dashed red). “Models (iv)” are shown only for those stars for which we do not fit H α in any of the above cases. For example, we present this type of model for HD 218195, since neither models with our UV \dot{M} , our UV upper \dot{M} , nor \dot{M}_{Vink} are able to fit the observed H α profile. These models have $f_{\infty} = 0.1$.

We note that the synthetic profiles calculated with \dot{M}_{Vink} produce H α somewhat more strongly than the observed profiles for five stars of our sample: HD 156292, HD 105627, HD 218195, HD 36861, and HD 135591. We observe that the discrepancies

for O8-9III are higher than the ones found by Marcolino et al. (2009) for late dwarfs. This can be explained in terms of a higher H α sensitivity for $\dot{M} \gtrsim 10^{-7} M_{\odot} \text{ yr}^{-1}$. In fact, our sample has an average \dot{M}_{Vink} of $\sim 5.0 \times 10^{-7} M_{\odot} \text{ yr}^{-1}$, while the O8-9V star sample in Marcolino et al. (2009) has an average value of $\sim 9.0 \times 10^{-8} M_{\odot} \text{ yr}^{-1}$ for the predicted \dot{M} .

From Fig. 16, the H α profiles of HD 156292 and HD 105627 are well fitted by our final models: \dot{M} derived from fitting the UV resonance lines of Si IV and C IV. For the other seven stars, our UV mass-loss rates show a deeper core in H α . We see that the profiles of HD 24431, HD 116852, and HD 115455 are fitted considering the mass-loss rate from Vink et al. (2000). However, for HD 116852, our UV upper limit on \dot{M} (solid blue line) also reproduces H α . It happens because all our models – used to derive \dot{M} – have the inclusion of clumping, while the models with \dot{M}_{Vink} are unclumped. Still regarding the mass-loss upper limit from UV, we are also able to fit the H α data of HD 135591. Thus, our \dot{M} derived from the UV (“models (i)” plus “models (ii)”) are consistent with the observed H α profile of four stars out of nine.

For the other three objects (HD 153426, HD 218195, HD 36861), we need to increase \dot{M} up to $\sim 10^{-7} M_{\odot} \text{ yr}^{-1}$ to fill their core. Our models show H α insensitive for $\dot{M} \sim 10^{-8} -$

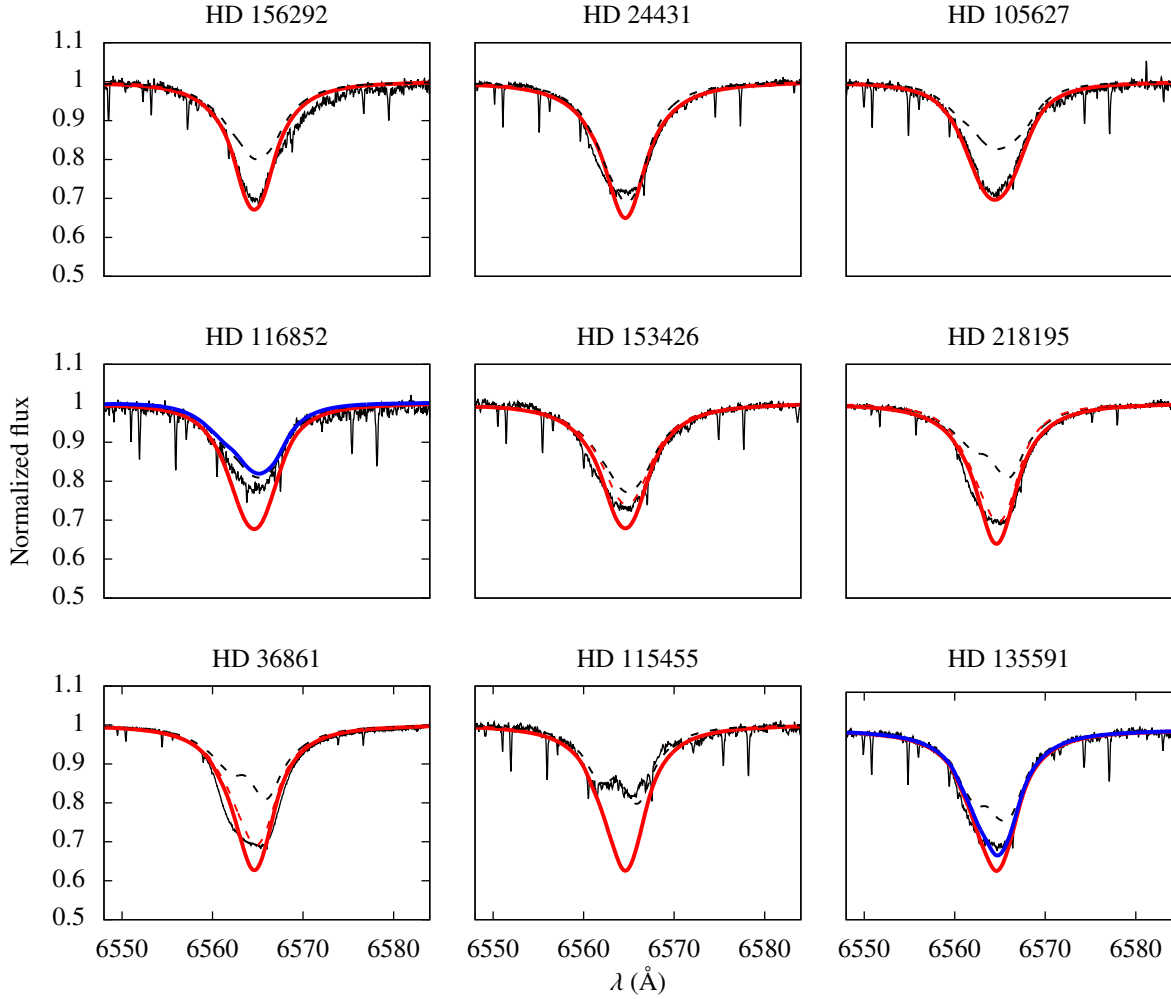


Fig. 16. Mass-loss rates from fitting $H\alpha$. Our final models (UV \dot{M}) are shown in solid red: “models (i)”. Upper limits on UV \dot{M} that encompass the observed $H\alpha$ line are shown in blue for some stars: “models (ii)”. Models with \dot{M}_{vink} are presented in dashed black: “models (iii)”. Again, only the models with \dot{M}_{vink} are homogeneous. When none of the previous models are able to adjust the $H\alpha$ intensity, we provide a new \dot{M} determination from fitting $H\alpha$ (dashed-red): “models (iv)”. The text gives further details concerning the notations “models (i–iv)”.

$10^{-7} M_{\odot} \text{ yr}^{-1}$, similarly to results found in the literature for late O dwarfs (e.g., Martins et al. 2012). Since the $H\alpha$ data for these three stars tend to be reproduced by just varying \dot{M} in CMFGEN, we consider that these deeper observed profiles are unlikely to be due to circumstellar or interstellar contamination. Nonetheless, such cases of contamination have been reported in the literature for early and late O dwarfs (see, e.g., Martins et al. 2005a). Another observational issue in this analysis could be due to $H\alpha$ variability for the stars in our sample, potentially impacting the determination of \dot{M} from this transition. For example, Martins et al. (2015b) investigated the spectral variability in the optical region in early OB supergiants and late O dwarfs. They found strong profile variability in $H\alpha$ for the supergiants, while the dwarfs do not exhibit any sign of variability. Hence, it would be necessary to investigate this issue in detail for an intermediate luminosity class such as the giants. Moreover, we performed different tests (e.g., changing the number of depth points and including additional ions) to solve this discrepancy between the models with \dot{M} from fitting the UV and the $H\alpha$ data, but the situation was not improved at all. Thus, we conclude that our models cannot fit simultaneously the UV and optical wind signatures in about half of our sample.

As mentioned in Sect. 4.3.2, \dot{M} found by Mahy et al. (2015) tend to be closer to the predicted values using the mass-loss

recipe of Vink et al. (2000). This can be explained since their mass-loss analysis is only complete concerning the visible spectra: they have IUE/SWP data only for two out of the six O8–9.5III stars in their sample. Even so, we still see one unequivocal late giant in their sample that shows the weak wind phenomenon: HD 191878 (type O8III). For this object, Mahy et al. (2015) derived $\dot{M} = 2.0 \times 10^{-9} M_{\odot} \text{ yr}^{-1}$ (unclumped CMFGEN model) by simultaneously fitting the UV spectrum and the $H\alpha$ line. Regarding Galactic O3–9.5V stars, Martins et al. (2012) also found a disagreement using CMFGEN between the UV mass-loss rates and the ones derived from the fitting of $H\alpha$. They found the most severe disagreements for the O8–9V stars. Their \dot{M} derived from the UV region are up to two orders of magnitude lower than \dot{M} from $H\alpha$, being this latter closer to \dot{M}_{vink} . Thus, we verify a similar trend in our sample. One of the possibilities stressed by Martins et al. (2012) to explain this issue is the neglect of macroclumping in the modeling with CMFGEN. The literature shows that accounting for macroclumping reduces more significantly the intensity in the UV lines than in $H\alpha$ (e.g., Oskinova et al. 2007; Sundqvist et al. 2011; Sundqvist & Puls 2018). Martins et al. (2012) pointed out that the inclusion of macroclumping could lead to a better agreement between \dot{M} from the UV and $H\alpha$ fittings, since the UV values would be reduced in this case. On the other hand, it also implies that \dot{M}

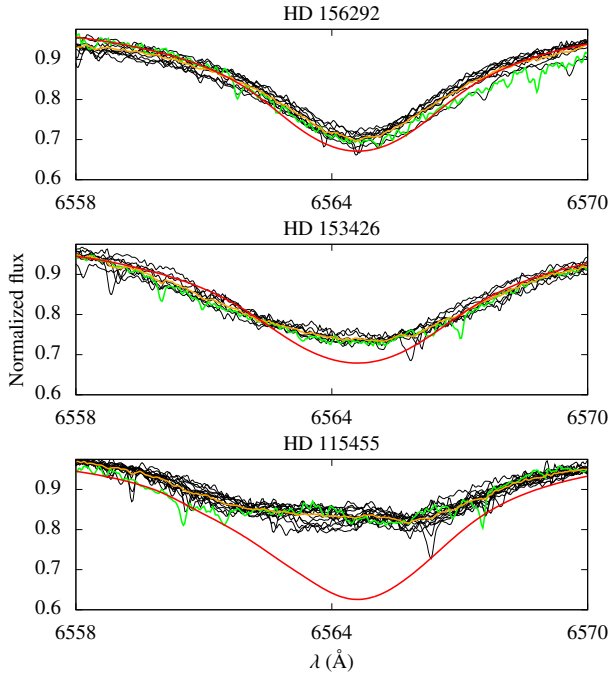


Fig. 17. Effect of binarity on the $H\alpha$ profile of the SB2 systems in our sample: HD 156292, HD 153426, and HD 115455. Archival FEROS data are shown in black. Our observed spectrum for each star is shown in green. Best-fit CMFGEN model derived from the UV is shown in red. The observed spectra are shifted in λ to match the line core of the model. The mean spectra among all the observations is shown in orange. The observed spectra are on average more intense from HD 156292 towards HD 115455.

predicted neglecting clumping (such as the Vink’s value for HD 116852 in Fig. 16) must overestimate the real rates.

In short, \dot{M} computed using the recipe of Vink et al. (2000) are not able to fit the UV resonance lines for any of the stars of our sample. Lower \dot{M} are supported in four out of nine stars considering simultaneously the fitting of the UV and the optical regions, so, in this sense, favoring the weak wind phenomenon in late O giants. Besides possible effects resulting from our physical assumptions in the modeling, environmental contamination, and spectroscopic variability, we need to increase the UV mass loss of about half of our sample to find a better modeling of $H\alpha$. These higher \dot{M} values from $H\alpha$ are incompatible with the UV modeling. Hence, we have a partial agreement between \dot{M} derived from the fitting to the UV resonance lines and to the $H\alpha$ line. Again, this issue between the UV and the visible analyses is also present in the literature for O dwarfs and deserves further study.

5.2. Mass-loss rates: binary effects

As previously commented, three stars of our sample are spectroscopic double-lined binary systems: HD 156292, HD 153426, and HD 156292 (see Table 1). In Fig. 17, we compare our models (derived from fitting the UV region) to multi-epoch FEROS spectra of HD 156292, HD 153426, and HD 115455 in the $H\alpha$ line. Apart from the spectra that are modeled in this paper for each of these stars (listed in Table 1), the observed spectra in this figure are retrieved from the ESO Science Archive Facility (Phase 3). The dates of the observations are shown in Table 5 with orbital phases calculated considering T_0 from our observations. The orbital periods P_{orb} of HD 156292, HD 153426, and HD 115455 are, respectively, 4.94 days, 22.40 days, and 15.08

Table 5. Observation log for the FEROS data of HD 156292, HD 153426, and HD 115455 analyzed in Fig. 17.

UTC (start time)	MJD (start time)	ESO program	ϕ
HD 156292			
2016-03-23T09:00:47.612	57470.37555106	096.A-9027(A)	$\equiv 0$
2015-04-04T06:35:39.030	57116.27475729	089.D-0975(A)	-0.680
2012-06-20T07:17:03.206	56098.30350933	089.D-0975(A)	-0.747
2012-05-21T06:52:16.748	56068.28630495	089.D-0975(A)	-0.824
2009-05-05T05:48:32.002	54956.24203706	083.D-0589(A)	-0.934
2009-05-04T04:45:08.265	54955.19801233	083.D-0589(A)	-0.145
2009-05-03T06:19:11.026	54954.26332206	083.D-0589(A)	-0.335
2009-05-02T06:58:08.837	54953.29038006	083.D-0589(A)	-0.531
2008-05-14T08:54:46.852	54600.3713756	081.D-2008(A)	-0.973
2005-06-25T08:24:03.531	53546.35004087	075.D-0061(A)	-0.337
HD 153426			
2016-03-18T09:15:25.182	57465.38570813	096.A-9027(A)	$\equiv 0$
2015-04-04T06:07:00.909	57116.25487163	089.D-0975(A)	-0.586
2012-06-19T07:36:40.433	56097.31713464	089.D-0975(A)	-0.075
2012-05-21T06:08:58.157	56068.25622867	089.D-0975(A)	-0.372
2011-05-18T06:42:56.653	55699.27982237	087.D-0946(A)	-0.844
2009-05-25T09:24:12.238	54976.39180831	083.D-0589(B)	-0.116
2008-05-14T08:02:44.235	54600.3352342	081.D-2008(A)	-0.904
2005-06-26T08:28:32.329	53547.35315196	075.D-0061(A)	-0.912
HD 115455			
2016-03-18T04:28:43.671	57465.18661656	096.A-9027(A)	$\equiv 0$
2007-06-15T23:58:03.854	54266.99865572	079.D-0564(B)	-0.081
2007-05-27T04:31:13.627	54247.18835217	079.D-0564(C)	-0.395
2007-05-24T03:49:08.750	54244.15912905	079.D-0564(B)	-0.596
2007-04-22T06:11:41.302	54212.25811692	079.D-0564(B)	-0.711
2007-04-21T05:39:19.139	54211.23563818	079.D-0564(A)	-0.779
2007-04-19T05:24:50.083	54209.22557966	079.D-0564(A)	-0.913
2007-04-19T05:05:31.858	54209.21217428	079.D-0564(A)	-0.913
2007-04-01T04:56:14.188	54191.20571977	079.D-0564(B)	-0.107
2006-08-22T23:42:49.633	53969.98807446	077.B-0348(A)	-0.777
2006-08-21T23:24:36.329	53968.97542048	077.B-0348(A)	-0.844
2006-08-20T23:22:12.614	53967.97375711	077.B-0348(A)	-0.911
2006-08-19T23:22:41.721	53966.97409399	077.B-0348(A)	-0.977
2006-08-18T23:36:52.296	53965.98393861	077.B-0348(A)	-0.043
2005-01-03T07:28:56.719	53373.31176758	074.D-0300(A)	-0.344

Notes. Our observed spectra are shown in bold. Orbital phases (ϕ) are calculated considering the epoch time T_0 ($\phi = 0$) from our observation.

days (Sota et al. 2014). The orbital phases are fairly uniformly distributed from about 0.1 to 1.0.

As discussed in the previous section, we are able to provide an acceptable fit to $H\alpha$ in HD 156292, considering our parameters derived from the UV. On the other hand, we need to increase our UV mass-loss rates for HD 153426 and HD 115455 to fit their $H\alpha$ spectra. From Fig. 17, we see how the morphology of the $H\alpha$ profiles changes due to different orbital configuration of these binary systems. Our failure to reproduce the shape of both $H\alpha$ wings, in particular HD 156292, can be explained due to the binary nature of the system. Furthermore, the line core is also affected with the intensity varying by about 2–3%. For HD 153426 and HD 115455, our model with UV \dot{M} fails to reproduce the observed $H\alpha$ profiles regardless of the epoch time.

Still from Fig. 17, one sees that the averaged spectra, among all the observations for each of these three stars, and ours observed spectra are very similar. Therefore, our $H\alpha$ analysis (considering just our observed spectra) and conclusions presented in Sect. 5.1 are unchanged. Binarity is not affecting the $H\alpha$ line cores in a significant way in the SB2 stars of our sample.

Regarding the wind profiles in the UV region, we cannot perform a similar analysis since there is just one IUE/SWP

spectrum for each of these three stars. However, we see that the observed profiles of Si IV $\lambda\lambda 1394,1403$ and C IV $\lambda\lambda 1548,1551$ are fairly similar in morphology in the overall sample (see, e.g., Fig. 10). This reflects in the determination of the mass-loss rate from fitting these lines: we obtain a relatively uniform range of \dot{M} values from $\sim 10^{-9}$ to $10^{-8} M_{\odot} \text{ yr}^{-1}$, with a trend for higher \dot{M} for more luminous objects, as expected. HD 116852 presents a clear morphological exception, with developed P-Cygni profiles in Si IV $\lambda\lambda 1394,1403$. However, this object has the highest luminosity of our sample, being of luminosity class II-III, and the highest \dot{M} derived from fitting the UV lines. Additionally, this star is not classified as a binary in the literature. So, this exception in morphology is very unlikely due to binary effects. We stress that our failure to reproduce the emission component of C IV $\lambda\lambda 1548,1551$ seems to be independent of the binary status our sample. For example, the final model for HD 156292 overestimates the observed emission component of this line practically as much as in the case of HD 105627 (no binary status). Thus, our results do not support that such an issue arises due to binary effects.

We are aware that disentangling of the observed spectra would be the most appropriate method to evaluate quantitatively possible effects of binarity on our results, but this technique is beyond the scope of this paper. Nevertheless, these results indicate that our mass-loss rates, derived from fitting the UV wind lines and the H α line, are unlikely biased by binary effects. Moreover, our models provide reasonable fits to the observed SED, and the effective temperature derived from the UV and the visible regions are in good agreement, showing a trend of higher T_{eff} towards the earlier stars (O8). This reflects in the analysis of the HR diagram, where our sample's loci are consistent with other results in the literature for O dwarfs, giants, and supergiants.

5.3. Mass-loss rates: degeneracies

Here, we investigate the effects of different stellar parameters on the UV line diagnostics for the mass-loss rate. The computational effort required by CMFGEN hinders degeneracy tests for several parameters simultaneously (e.g., CNO abundances, T_{eff} , and luminosity). Therefore, we calculated the effects of a specific parameter on the \dot{M} diagnostics, leaving all others fixed. We present results separately for CNO abundances (ϵ_{CNO}), T_{eff} , and $\log(L_{\star}/L_{\odot})$.

5.3.1. CNO abundances

Compared with main sequence objects, evolved O stars present an enhanced N/H together with depleted C/H and O/H ratios at their surfaces (see, e.g., Martins et al. 2015a, and references therein). Deviations from the solar CNO abundance have a potential impact on the determination of the mass-loss rates for the stars of our sample. In particular, a very low C/H ratio affects directly the C IV $\lambda\lambda 1548,1551$ profile, decreasing its strength⁸. Thus, we proceeded as follows to evaluate abundance effects on our results:

(i) Martins et al. (2015a) derived CNO abundances for 74 O stars of different luminosity classes through spectral modeling with CMFGEN. Our sample has four stars in common with them: HD 24431, HD 153426, HD 218195, and HD 36861. For these

⁸ The Sobolev optical depth for C IV is directly proportional to the product $\dot{M}q_{\text{CIV}}\epsilon_{\text{C}}$, where q_{CIV} is the ion fraction of C IV (see, e.g., Lamers et al. 1999).

objects, we re-computed our final models (Table 3) using the values given by Martins et al. (2015a) for C/H, N/H, and O/H.

(ii) For HD 156292, HD 105627, HD 116852, HD 115455, and HD 135591, for which there is no detailed abundance analysis, we chose to adopt the lowest C/H, highest N/H, and lowest O/H values among the late O giants found in Martins et al. (2015a), namely: C/H = 0.7×10^{-4} , N/H = 1.6×10^{-4} , and O/H = 1.1×10^{-4} . This approach is obviously conservative. Our main concern is about C/H, because it is expected to be lower than the solar value, impacting C IV $\lambda\lambda 1548,1551$.

(iii) We then analyzed the effects of non-solar CNO values in the modeling of the UV mass-loss diagnostics, revising, when necessary, the mass-loss rates to re-fit the observed spectra.

(iv) The revised mass-loss rates were evaluated again in the log(\dot{M}) versus log(\dot{M}_{Vink}) diagram, allowing us to compare them with the previous \dot{M} using solar abundances.

We show in Fig. 18 the final models with solar abundances in comparison with the ones using the results from Martins et al. (2015a). The considered ϵ_{CNO} are listed in Table 6. The C IV $\lambda\lambda 1548,1551$ profiles of four stars are affected by a lower carbon abundance, becoming weaker than the observed: HD 156292, HD 24431, HD 105627, and HD 115455. For these objects, we re-determined their \dot{M} , which are indicated in Table 6. For three out these stars, we have adopted conservative low values of C/H. That is, these new inferred \dot{M} are likely overestimated due to our adoption. The above results are summarized in Fig. 19, where we present again the measured \dot{M} and the ones according to Vink et al. (2000). It is clear that our conclusions regarding weak winds in late O giants are not changed due to possible affects created by CNO abundances. Some points shift toward to the expected mass-loss rates, but the changes are minor overall.

5.3.2. Effective temperature

Reliable effective temperatures are mandatory to derive the wind parameters. Depending on the model parameters range, changes in T_{eff} can modify the ionization structure in the wind (e.g., Austin & Prinja 2011), directly affecting the wind lines. Here, we analyze the effect of different T_{eff} values on the mass-loss rate. For simplicity, we present only results for HD 156292 (O9.7III) and HD 116852 (O8.5II-III). These two stars have extreme values of mass-loss rate among the objects of our sample. The \dot{M} of HD 116852 is higher than the \dot{M} of HD 156292 by a factor of 40.

In Figs. 20 (HD 116852) and 21 (HD 156292), we show the fits to the two main UV diagnostics of \dot{M} considered in this paper. We present the synthetic wind profiles corresponding to the upper and lower limits of the mass-loss rates for these stars, with T_{eff} fixed (upper panels). For comparison, we also present the synthetic wind profiles corresponding to the upper and lower limits for T_{eff} , with fixed \dot{M} (lower panels). These values for the effective temperature were derived from the UV region, allowing us to develop a more conservative analysis since they have higher error bars than the ones found from fitting the He I-II lines in the optical.

For HD 156292, we do not see significant changes in Si IV $\lambda\lambda 1394,1403$ and C IV $\lambda\lambda 1548,1551$ with different values for T_{eff} . We note that in the case of HD 116852:

(i) Variation in T_{eff} affects the Si IV $\lambda\lambda 1394,1403$ transition but not C IV $\lambda\lambda 1548,1551$ that is saturated.

(ii) We need to increase \dot{M} to re-fit the Si IV $\lambda\lambda 1394,1403$ profiles.

(iii) This new (larger) mass-loss rate lies within the error bars already provided by our final \dot{M} : this can be seen from the

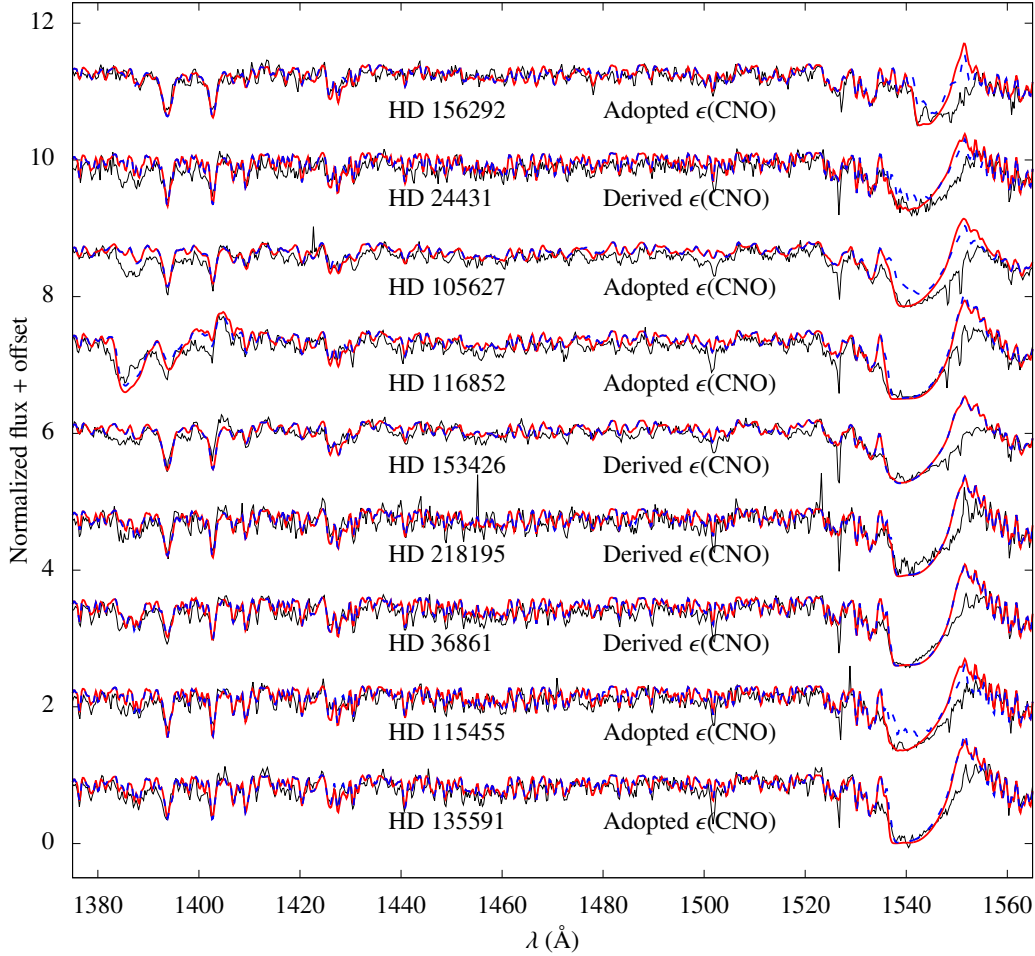


Fig. 18. Final models for all our sample considering solar abundances (red). Re-computed models using ϵ_{CNO} from Martins et al. (2015a) are in dashed blue. IUE data are in black. We indicate, right above each spectrum, whether ϵ_{CNO} is a determination from Martins et al. (2015a) or an adoption based on their results (see text for details). We note that the highest effects in C IV $\lambda\lambda 1548, 1551$ are due to the adopted ϵ_{CNO} .

Table 6. CNO affects on the mass-loss rates of all the sample.

Star	$\dot{M}_{\text{derived}}^{(a)}$ ($M_{\odot} \text{ yr}^{-1}$)	$\dot{M}_{\text{revised}}^{\text{CNO}}$ ($M_{\odot} \text{ yr}^{-1}$)	C/H, N/H, O/H ($\times 10^{-4}$)
HD 156292	$1.5^{+4.0}_{-0.75} \times 10^{-9}$	$3.0^{+2.5}_{-1.5} \times 10^{-9}$	* 0.7, 1.6, 1.1
HD 24431	$2.5^{+7.5}_{-1.5} \times 10^{-9}$	$5.0^{+5.0}_{-2.5} \times 10^{-9}$	1.3, 0.8, 3.9
HD 105627	$4.0^{+16.0}_{-2.5} \times 10^{-9}$	$1.0^{+2.0}_{-0.6} \times 10^{-8}$	* 0.7, 1.6, 1.1
HD 116852	$6.0^{+19.0}_{-4.5} \times 10^{-8}$	✓	* 0.7, 1.6, 1.1
HD 153426	$4.5^{+10.5}_{-2.5} \times 10^{-9}$	✓	2.9, 1.0, 4.6
HD 218195	$1.0^{+2.5}_{-0.75} \times 10^{-8}$	✓	2.0, 5.0, 4.6
HD 36861	$2.5^{+3.5}_{-2.2} \times 10^{-8}$	✓	2.2, 1.5, 4.7
HD 115455	$5.0^{+10.0}_{-3.0} \times 10^{-9}$	$1.5^{+2.0}_{-1.0} \times 10^{-8}$	* 0.7, 1.6, 1.1
HD 135591	$2.0^{+6.0}_{-1.85} \times 10^{-8}$	✓	* 0.7, 1.6, 1.1

Notes. Revised mass-loss rates are denoted by $\dot{M}_{\text{revised}}^{\text{CNO}}$. The tick symbol (✓) stands for star without changes in \dot{M} . In the last column, the asterisk symbol (*) stands for adopted ϵ_{CNO} . The \dot{M}_{derived} were determined using solar ϵ_{CNO} from Grevesse et al. (2010): C/H = 2.7×10^{-4} , N/H = 0.7×10^{-4} , and O/H = 4.9×10^{-4} . ^(a)Same notation as in Table 3.

amplitude of the profile variations corresponding to the error bars on \dot{M} .

(iv) The strongest effect on Si IV $\lambda\lambda 1394, 1403$ is due to the lower limit of T_{eff} . In this case, we need to decrease \dot{M} to fit again the Si IV $\lambda\lambda 1394, 1403$ profiles.

Therefore, we do not need to revise upward the UV mass-loss rate due to uncertainties in T_{eff} . The error bars on the mass-loss

rates are conservative enough to encompass uncertainties due to T_{eff} .

5.3.3. Stellar luminosity

It is well known that the luminosity class affects the Si IV $\lambda\lambda 1394, 1403$ lines of O-type stars (Walborn & Panek 1984; Howarth & Prinja 1989; Pauldrach et al. 1990). These lines are almost photospheric in O9.5 dwarfs, while O supergiants show fully P-Cygni profiles in Si IV $\lambda\lambda 1394, 1403$. Here, we evaluate the impact of our luminosity adoptions, from Martins et al. (2005b), on the derivation of \dot{M} . As discussed in Sect. 4.2.1, these values of $\log(L_{\star}/L_{\odot})$ match well the observed SEDs for the most part of our sample, considering astrometric measures from Gaia Collaboration (2018). For this purpose, we analyze the cases of HD 156292 and HD 116852 again. As discussed above, these stars possess, respectively, the lowest and highest density wind in our sample – $\dot{M} = 1.5 \times 10^{-9} M_{\odot} \text{ yr}^{-1}$ and $\dot{M} = 6.0 \times 10^{-8} M_{\odot} \text{ yr}^{-1}$. They are also extreme cases in luminosity, respectively: $\log(L_{\star}/L_{\odot}) = 5.12$ (lowest value) and $\log(L_{\star}/L_{\odot}) = 5.33$ (highest value).

We show the fits to the UV mass-loss diagnostics in Figs. 22 (HD 116852) and 23 (HD 156292). As in Figs. 20 and 21, the models corresponding to the upper and lower limits of the mass-loss rates are shown in the upper panels. Here, they have the

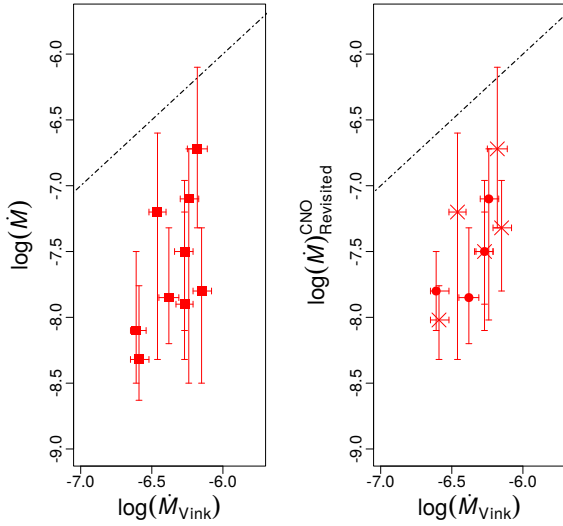


Fig. 19. Effects of ϵ_{CNO} in the $\log(\dot{M})$ versus $\log(\dot{M}_{\text{Vink}})$ diagram. On the left are previous results using the solar chemical abundance (shown in Fig. 12). On the right are revised \dot{M} taking different CNO values into account. Circles indicate stars with exact ϵ_{CNO} from Martins et al. (2015a). Crosses indicate stars for which we adopted extreme ϵ_{CNO} based on the results of Martins et al. (2015a). Our conclusions about weak wind in late O giants are not affected due to CNO abundances.

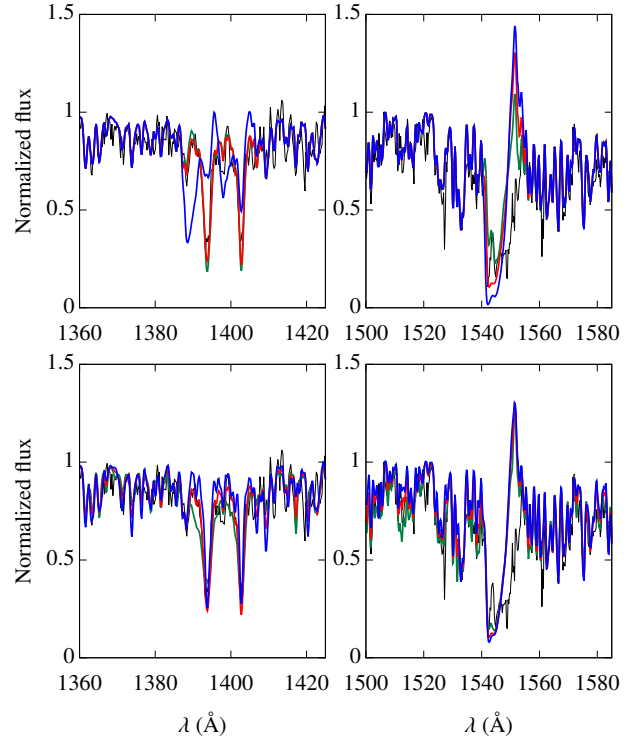


Fig. 21. Same analysis as in Fig. 20, but for HD 156292 (O9.7III). Final model (red) with $\dot{M} = 1.5 \times 10^{-9} M_{\odot} \text{ yr}^{-1}$ and $T_{\text{eff}} = 31\,000$ K. *Top panels:* models with the limits on \dot{M} ($7.5 \times 10^{-10} M_{\odot} \text{ yr}^{-1}$ in green and $5.5 \times 10^{-9} M_{\odot} \text{ yr}^{-1}$ in blue): fixed $T_{\text{eff}} = 31\,000$ K. *Bottom panels:* models with the limits on T_{eff} (28 000 K in green and 33 000 K in blue): fixed $\dot{M} = 1.5 \times 10^{-9} M_{\odot} \text{ yr}^{-1}$. We note that the error bars of T_{eff} do not produce any significant changes in the considered mass-loss diagnostics.

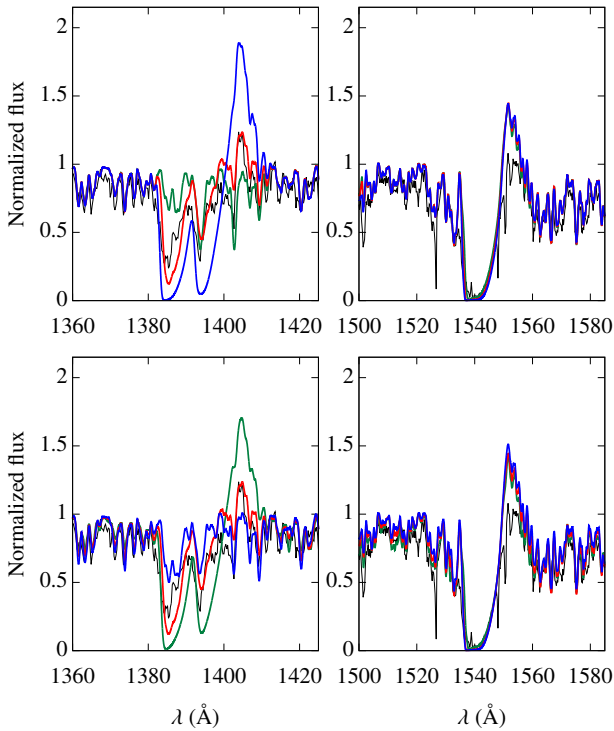


Fig. 20. Effect of T_{eff} on the UV mass-loss diagnostics Si IV $\lambda\lambda 1394, 1403$ and C IV $\lambda\lambda 1548, 1551$. We show the analysis for HD 116852 (O8.5II-III) with $T_{\text{eff}}^{\text{UV}}$. In all panels, our final model is shown in red: $\dot{M} = 6.0 \times 10^{-8} M_{\odot} \text{ yr}^{-1}$ and $T_{\text{eff}} = 32\,500$ K. *Top panels:* models with the limits on \dot{M} ($1.5 \times 10^{-8} M_{\odot} \text{ yr}^{-1}$ in green and $2.5 \times 10^{-7} M_{\odot} \text{ yr}^{-1}$ in blue): fixed $T_{\text{eff}} = 32\,500$ K. *Bottom panels:* models with limits on T_{eff} (30 000 K in green and 34 500 K in blue): fixed $\dot{M} = 6.0 \times 10^{-8} M_{\odot} \text{ yr}^{-1}$. We note that the error bars of \dot{M} are conservative enough to account for the effects due to variation in T_{eff} .

luminosity fixed for each case. In the lower panels, we present the synthetic profiles for models with variation in stellar luminosity within our adopted error bars of 0.2 in $\log(L_{\star}/L_{\odot})$ and fixed \dot{M} .

For HD 156292, we do not see any significant changes in Si IV $\lambda\lambda 1394, 1403$ and C IV $\lambda\lambda 1548, 1551$ with different values of luminosity ($\log(L_{\star}/L_{\odot}) = 4.92$ and 5.32). On the other hand, we note that in the case of HD 116852:

(i) Variation in $\log(L_{\star}/L_{\odot})$, from 5.08 to 5.48, affects the Si IV $\lambda\lambda 1394, 1403$ transition but not C IV $\lambda\lambda 1548, 1551$, which is saturated.

(ii) The strongest effect on Si IV $\lambda\lambda 1394, 1403$ is due to the lower limit on $\log(L_{\star}/L_{\odot})$. In this case, we need to decrease \dot{M} in order to re-fit the Si IV $\lambda\lambda 1394, 1403$ profiles.

(iii) The upper limit on luminosity provides an acceptable fit to the Si IV $\lambda\lambda 1394, 1403$ within the error bars provided to \dot{M} .

Hence, as in the case of the effective temperature, we do not need to revise our UV mass-loss rates to higher values due to the uncertainties (± 0.2 dex) in the luminosity.

6. Conclusions

We presented a quantitative analysis of nine late O giant stars (O8–O9.5III) using non-LTE atmosphere models computed with the code CMFGEN. We used archival high-resolution UV (IUE/SWP) and recent optical data (FEROS, NARVAL, and ESPADONS) to determine the main photospheric and wind parameters for each star of our sample. We analyzed the results in the context of the weak wind phenomenon. Our main findings and conclusions are summarized as follows:

(i) Overall, we achieved good fits to the UV and optical data. The bulk of our sample has parameters in the following ranges: $\log(L_{\star}/L_{\odot}) \sim 5.10 - 5.30$, $T_{\text{eff}} \sim 30\,000 - 35\,000$ K,

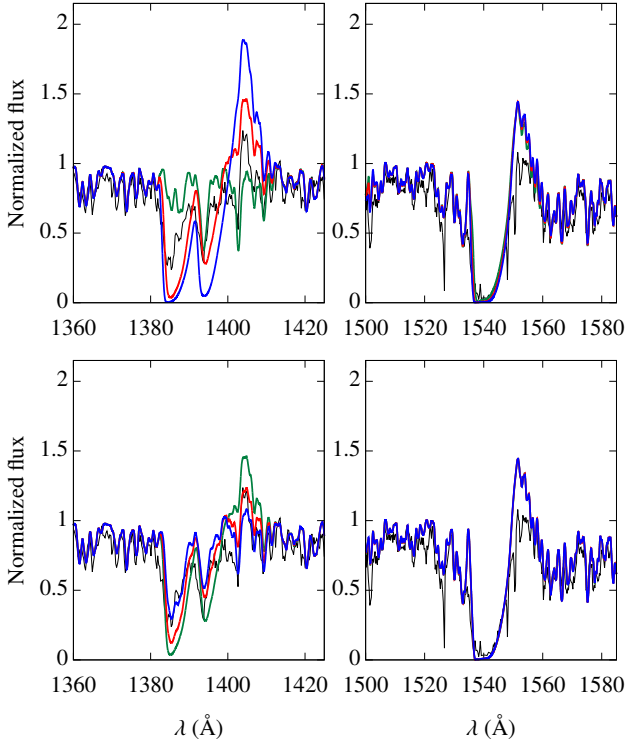


Fig. 22. Stellar luminosity effect on the UV mass-loss diagnostics Si IV $\lambda\lambda 1394,1403$ and C IV $\lambda\lambda 1548,1551$. We show the analysis for HD 116852 with $T_{\text{eff}}^{\text{UV}}$. In all panels, the final model is shown in red: $\dot{M} = 6.0 \times 10^{-8} M_{\odot} \text{ yr}^{-1}$ and $\log(L_{\star}/L_{\odot}) = 5.33$. *Top panel:* models with the limits on \dot{M} ($1.5 \times 10^{-8} M_{\odot} \text{ yr}^{-1}$ in green and $2.5 \times 10^{-7} M_{\odot} \text{ yr}^{-1}$ in blue): fixed $\log(L_{\star}/L_{\odot}) = 5.33$. *Bottom panel:* models with the limits on $\log(L_{\star}/L_{\odot})$ (5.13 in green and 5.53 in blue): fixed $\dot{M} = 6.0 \times 10^{-8} M_{\odot} \text{ yr}^{-1}$. We note that the error bars of \dot{M} are conservative enough to account for effects due to variation in luminosity.

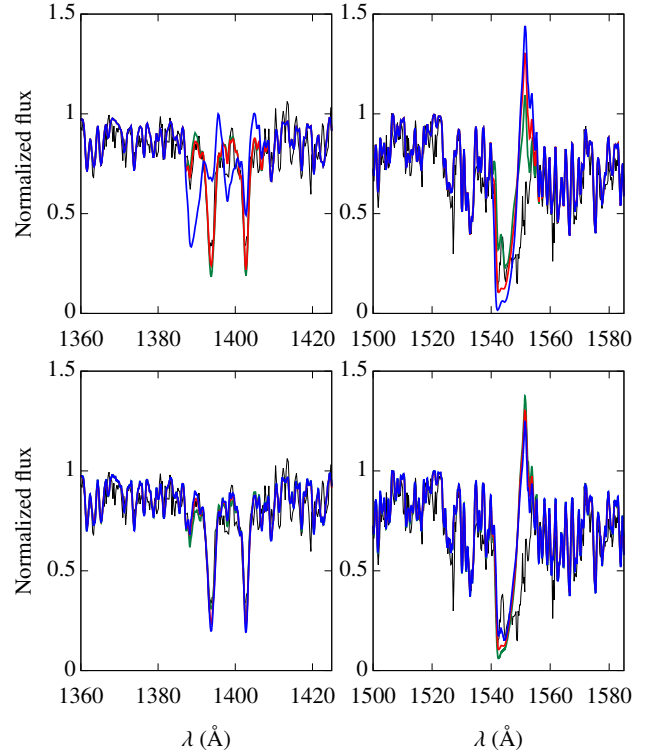


Fig. 23. Same analysis as in Fig. 22, but for HD 156292. Final model (red) with $\dot{M} = 1.5 \times 10^{-9} M_{\odot} \text{ yr}^{-1}$ and $\log(L_{\star}/L_{\odot}) = 5.12$. *Top panel:* models with the limits on \dot{M} ($7.5 \times 10^{-10} M_{\odot} \text{ yr}^{-1}$ in green and $5.5 \times 10^{-9} M_{\odot} \text{ yr}^{-1}$ in blue): fixed $\log(L_{\star}/L_{\odot}) = 5.12$. *Bottom panel:* models with the limits on $\log(L_{\star}/L_{\odot})$ (4.92 in green and 5.32 in blue): fixed $\dot{M} = 1.5 \times 10^{-9} M_{\odot} \text{ yr}^{-1}$. We note that the error bars of $\log(L_{\star}/L_{\odot})$ do not produce any significant changes on the UV diagnostics for \dot{M} .

$\log(g) \sim 3.50 - 3.60$, $v_{\infty} \sim 2000 - 2400 \text{ km s}^{-1}$, and $\dot{M} \sim 10^{-9} - 10^{-8} M_{\odot} \text{ yr}^{-1}$.

(ii) It is reliable to derive the main physical properties of late O giants – T_{eff} , R_{\star} , M_{\star} , \dot{M} , and v_{∞} – solely from UV spectrum (IUE/SWP data, $\sim 1100 - 2000 \text{ \AA}$), considering that values for the bolometric luminosity and surface gravity are adopted. The main mass-loss diagnostics for O8-9.5 giants are Si IV $\lambda\lambda 1394,1403$ and C IV $\lambda\lambda 1548,1551$.

(iii) Overall, our model SEDs reproduce well the observed ones considering parallaxes from Gaia Collaboration (2018) and van Leeuwen (2007). The highest discrepancies are explained by unreliable distance estimations and uncertainties in the ISM extinction. Thus, the calibrated $\log(L_{\star}/L_{\odot})$ given by Martins et al. (2005b) is a good assumption for late O giants.

(iv) We determined T_{eff} separately from the UV (Fe III-V lines) and the optical (He I-II lines). These independent measurements for T_{eff} agree well. For both of them, the expected tendency of higher values of T_{eff} was obtained, as we go from later (O9.5III) towards earlier (O8III) spectral types.

(v) The emission component of C IV $\lambda\lambda 1548,1551$ is systematically overestimated by our models. We are able to improve the fits with ξ_t^{min} up to $20 - 30 \text{ km s}^{-1}$ together with a fuller accounting of atomic species. Our improved model in terms of species is not sufficient to explain this discrepancy. However, such higher values for the photospheric microturbulence prevent a self-consistent T_{eff} analysis from the UV and optical for the stars of our sample. Considering the adoption of $\xi_t^{\text{min}} = 10 \text{ km s}^{-1}$, our

tests show that the fits are only improved by using a considerably lower β in the velocity law, namely, of ~ 0.3 . These values are not common among O stars. Dwarfs usually present values close to unity while OB supergiants may present larger values, such as $\beta \gtrsim 3.0$. We consider that this very low β value is likely due to the simple β parameterization used in this paper, that is, they must be an artifact of our modeling assumption with CMFGEN. A deeper investigation regarding this issue is required.

(vi) We analyzed literature results for O dwarfs, giants, and supergiants with our ones in the HR diagram. The loci of these stars are different in the diagram. We estimated ages for the giants of our sample and confirmed that they are more evolved than dwarfs. The bulk of our sample has ages of $10^{6.7} - 10^{6.8} \text{ yr}$ and evolutionary masses of $M_{\text{ZAM}} \sim 25 - 28 M_{\odot}$. These values of mass are consistent with the recent findings of Martins et al. (2017), which determined spectroscopic masses around $25 - 40 M_{\odot}$ for O7-8 giants. Our spectroscopic masses ($M_{\star} \sim 16 - 26 M_{\odot}$) are in marginal agreement with the evolutionary masses.

(vii) The mass-loss rates obtained from the UV analysis were compared with different theoretical works. Considering clumped \dot{M} , our values are considerably lower than the values predicted from Vink et al. (2000) by a factor of $\sim 0.9 - 2.3$ dex. The discrepancy is reduced to $\sim 0.4 - 1.7$ dex in comparison with our unclumped \dot{M} , still being severe since it reaches up to about two orders of magnitude. That is, late O giants also present weak winds, like late O dwarfs. The disagreement between our results and the predicted values by theory is lessened as we go from

O9.5III to O8III objects. Thus, the region of $\log(L_*/L_\odot) \sim 5.2$ seems critical for the weak wind phenomenon.

(viii) We also compared our results with the theoretical \dot{M} from Lucy (2010a). The predictions of Lucy (2010a) are better in comparison with \dot{M}_{Vink} for low luminosity objects. The weak wind problem is considerably attenuated (where Vink's predictions are worst), with discrepancies up to ~ 1.0 dex. On the other hand, they underestimate the mass-loss rates for OB supergiants (where Vink's predictions work well). The physical reason for these discrepancies should be investigated in detail, but it is beyond the scope of this paper. We verified that the region of $\log(L_*/L_\odot) \sim 5.2$ seems to be critical for both the predictions from Vink et al. (2000) and Lucy (2010b).

(ix) The mass-loss rates predicted from Vink et al. (2000) largely overestimate the intensity in Si IV $\lambda\lambda 1394, 1403$ for all our sample. These values of \dot{M} also overestimate the C IV $\lambda\lambda 1548, 1551$ for our stars with non-saturated profiles. For H α , a good part of our sample (five out of nine stars) shows overestimated profiles using \dot{M}_{Vink} . The mass loss from Vink et al. (2000) is able to fit the observed H α for three objects: HD 24431, HD 116852, and HD 115455.

(x) We checked the fits to the H α profiles using our mass-loss rates inferred from the UV diagnostics. We found excellent fits for two objects (HD 156292 and HD 105627) and for another two stars the upper limit on \dot{M} also provide reasonable fits (HD 116852 and HD 135591). However, for five objects, we could not fit H α even considering the UV upper limits on the \dot{M} : HD 24431, HD 218195, HD 36861, HD 153426, and HD 115455. Despite our efforts, in these stars our models fail to reproduce simultaneously all the wind diagnostics considered here (UV and optical).

(xi) Regarding the simultaneous fitting to the UV and H α spectra, weak winds in O8-9.5III are favored in comparison with the values from Vink et al. (2000). We fit the UV and optical spectra of four out of nine stars of our sample. Models with \dot{M}_{Vink} are able to reproduce the H α data for three out of nine objects, but they fail to reproduce the UV wind lines for all our sample. We needed to revise upward the UV \dot{M} to model the H α profiles in about half of our sample. This issue regarding the UV and optical modeling with CMFGEN is also found in works about O dwarfs. It is still an open question in the literature.

(xii) Our results show that effects of binarity on the UV and optical analyses are unlikely to change our conclusions about the weak wind phenomenon in late O giants. Moreover, we performed different tests to address the impact of stellar parameters on the mass-loss rates derivation from the UV wind lines. We also found that the depletion of C/H, caused by evolutionary effects in late O giants, is not enough to modify our conclusions regarding the weak winds. The same is valid for the effects of T_{eff} and L_* on the UV wind diagnostics.

In conclusion, our results indicate the weak wind phenomenon in O8-9.5III stars. It is the first time that weak winds are found for spectral types other than O8-9.5V. Despite our efforts, we are not able to model at the same time both the UV wind diagnostic lines and the H α profile for all the stars of our sample. This issue could be solved by investigations regarding macroclumping implementation in the modeling with CMFGEN and potential H α variability (as observed in late OB supergiants) among late O giants. Apart from this problem, low \dot{M} (weak winds) are favored to model the spectra (UV + optical regions) of late O dwarfs and giants in comparison with values provided by theory. In other words, the measured mass-loss rates of these stars are systematically lower than the predictions of Vink et al. (2000). This is important as they are low luminosity O stars

(latter spectral types), implying that the majority of the O-type stars must undergo a weak wind phase. Therefore, we suggest that the mass-loss recipe in the majority of modern stellar evolution codes must severely overestimate \dot{M} during the H-burning phase. Further investigations are needed to evaluate the consequences of this in terms of physical parameters for massive stars (e.g., angular momentum and CNO surface abundances).

Acknowledgements. We would like to thank the anonymous referee for comments that helped to improve the paper. E.S.G. de Almeida thanks the "Ville de Nice" (Nice, France) for the financial support to this work through the "Bourse Doctorale Olivier Chesneau" during the period of 2016-2019. E.S.G. de Almeida thanks the CAPES Agency (Brazil) for the financial support to this work through MSc grant during the period of 2015-2016. E.S.G. de Almeida thanks A. Domiciano de Souza, A. Meilland, and P. Stee for reading the original manuscript. W.L.F. Marcolino acknowledges CNPq for the PQ grant (307152/2016-2). Based on observations collected at the European Southern Observatory under ESO programme 096.A-9027(A). Based on data obtained from the ESO Science Archive Facility under request numbers 389364, 389364, and 389372. Some of the data presented in this paper were obtained from the Mikulski Archive for Space Telescopes (MAST). STScI is operated by the Association of Universities for Research in Astronomy, Inc., under NASA contract NAS5-26555. Support for MAST for non-HST data is provided by the NASA Office of Space Science via grant NNX13AC07G and by other grants and contracts. This work has made use of data from the European Space Agency (ESA) mission *Gaia* (<https://www.cosmos.esa.int/gaia>), processed by the *Gaia* Data Processing and Analysis Consortium (DPAC, <https://www.cosmos.esa.int/web/gaia/dpac/consortium>). Funding for the DPAC has been provided by national institutions, in particular the institutions participating in the *Gaia* Multilateral Agreement. This research has made use of the SIMBAD database, operated at CDS, Strasbourg, France.

References

- Abbott, D. C. 1982, *ApJ*, 263, 723
- Abbott, B. P., Abbott, R., Abbott, T. D., et al. 2016, *ApJ*, 818, L22
- Austin, M. J., & Prinja, R. K. 2011, in *Active OB Stars: Structure, Evolution, Mass Loss, and Critical Limits*, eds. C. Neiner, G. Wade, G. Meynet, & G. Peters, *IAU Symp.*, 272, 600
- Bailer-Jones, C. A. L., Rybizki, J., Fouesneau, M., Mantelet, G., & Andrae, R. 2018, *AJ*, 156, 58
- Berghoefter, T. W., Schmitt, J. H. M. M., & Cassinelli, J. P. 1996, *A&AS*, 118, 481
- Bouret, J.-C., Lanz, T., Hillier, D. J., et al. 2003, *ApJ*, 595, 1182
- Bouret, J.-C., Hillier, D. J., Lanz, T., & Fullerton, A. W. 2012, *A&A*, 544, A67
- Bouret, J.-C., Lanz, T., Martins, F., et al. 2013, *A&A*, 555, A1
- Cardelli, J. A., Clayton, G. C., & Mathis, J. S. 1989, *ApJ*, 345, 245
- Carneiro, L. P., Puls, J., & Hoffmann, T. L. 2018, *A&A*, 615, A4
- Chlebowski, T., & Garmany, C. D. 1991, *ApJ*, 368, 241
- Crowther, P. A., Lennon, D. J., & Walborn, N. R. 2006, *A&A*, 446, 279
- Cutri, R. M., Skrutskie, M. F., van Dyk, S., et al. 2003, *VizieR Online Data Catalog: II/246*
- Dean, C. A., & Bruhweiler, F. C. 1985, *ApJS*, 57, 133
- de Mink, S. E., Sana, H., Langer, N., Izzard, R. G., & Schneider, F. R. N. 2014, *ApJ*, 782, 7
- Ducati, J. R. 2002, *VizieR Online Data Catalog: II/237*
- Ekström, S., Georgy, C., Eggenberger, P., et al. 2012, *A&A*, 537, A146
- ESA 1997, *The HIPPARCOS and Tycho catalogues. Astrometric and photometric star catalogues derived from the ESA HIPPARCOS Space Astrometry Mission* (Noordwijk, Netherlands: ESA Special Publications Division), 1200
- Gaia Collaboration (Prusti, T., et al.) 2016, *A&A*, 595, A1
- Gaia Collaboration (Brown, A. G. A., et al.) 2018, *A&A*, 616, A1
- Gehrels, N., & Razaque, S. 2013, *Front. Phys.*, 8, 661
- Gordon, K. D., Gies, D. R., Schaefer, G. H., et al. 2018, *ApJ*, 869, 37
- Gruesse, N., Asplund, M., Sauval, A. J., & Scott, P. 2010, *Ap&SS*, 328, 179
- Grunhut, J. H., Wade, G. A., Neiner, C., et al. 2017, *MNRAS*, 465, 2432
- Hillier, D. J., & Miller, D. L. 1998, *ApJ*, 496, 407
- Hillier, D. J., & Miller, D. L. 1999, *ApJ*, 519, 354
- Hillier, D. J., Lanz, T., Heap, S. R., et al. 2003, *ApJ*, 588, 1039
- Holgado, G., Simón-Díaz, S., Barbá, R. H., et al. 2018, *A&A*, 613, A65
- Howarth, I. D., & Prinja, R. K. 1989, *ApJS*, 69, 527
- Howarth, I. D., Siebert, K. W., Hussain, G. A. J., & Prinja, R. K. 1997, *MNRAS*, 284, 265
- Hubeny, I., & Lanz, T. 1995, *ApJ*, 439, 875
- Kaufer, A., Stahl, O., Tubbings, S., et al. 1999, *The Messenger*, 95, 8

- Kauffer, A., Stahl, O., Tubbesing, S., et al. 2000, in *Optical and IR Telescope Instrumentation and Detectors*, eds. M. Iye & A. F. Moorwood, *Proc. SPIE*, **4008**, 459
- Keszthelyi, Z., Wade, G. A., & Petit, V. 2017, in *The Lives and Death-Throes of Massive Stars*, eds. J. J. Eldridge, J. C. Bray, L. A. S. McClelland, & L. Xiao, *IAU Symp.*, **329**, 250
- Lamers, H. J. G. L. M., Haser, S., de Koter, A., & Leitherer, C. 1999, *ApJ*, **516**, 872
- Lanz, T., & Hubeny, I. 2003, *ApJS*, **146**, 417
- Lucy, L. B. 2010a, *A&A*, **524**, A41
- Lucy, L. B. 2010b, *A&A*, **512**, A33
- Lucy, L. B., & Solomon, P. M. 1970, *ApJ*, **159**, 879
- Mahy, L., Rauw, G., De Becker, M., Eenens, P., & Flores, C. A. 2015, *A&A*, **577**, A23
- Maíz Apellániz, J., & Barbá, R. H. 2018, *A&A*, **613**, A9
- Maíz-Apellániz, J., Walborn, N. R., Galué, H. Á., & Wei, L. H. 2004, *ApJS*, **151**, 103
- Maíz Apellániz, J., Alfaro, E. J., & Sota, A. 2008, ArXiv e-prints [arXiv:0804.2553]
- Maíz Apellániz, J., Sota, A., Morrell, N. I., et al. 2013, in *Massive Stars: From alpha to Omega*, **198**
- Majaess, D., Turner, D., Dékány, I., Minniti, D., & Gieren, W. 2016, *A&A*, **593**, A124
- Marcolino, W. L. F., Bouret, J.-C., Martins, F., et al. 2009, *A&A*, **498**, 837
- Martins, F. 2011, *Bull. Soc. Roy. Sci. Liège*, **80**, 29
- Martins, F., & Hillier, D. J. 2012, *A&A*, **545**, A95
- Martins, F., & Plez, B. 2006, *A&A*, **457**, 637
- Martins, F., Schaerer, D., Hillier, D. J., & Heydari-Malayeri, M. 2004, *A&A*, **420**, 1087
- Martins, F., Schaerer, D., Hillier, D. J., et al. 2005a, *A&A*, **441**, 735
- Martins, F., Schaerer, D., & Hillier, D. J. 2005b, *A&A*, **436**, 1049
- Martins, F., Mahy, L., Hillier, D. J., & Rauw, G. 2012, *A&A*, **538**, A39
- Martins, F., Hervé, A., Bouret, J.-C., et al. 2015a, *A&A*, **575**, A34
- Martins, F., Marcolino, W., Hillier, D. J., Donati, J.-F., & Bouret, J.-C. 2015b, *A&A*, **574**, A142
- Martins, F., Simón-Díaz, S., Barbá, R. H., Gamen, R. C., & Ekström, S. 2017, *A&A*, **599**, A30
- Mayne, N. J., & Naylor, T. 2008, *MNRAS*, **386**, 261
- Meynet, G., Georgy, C., Hirschi, R., et al. 2011, *Bull. Soc. Roy. Sci. Liège*, **80**, 266
- Meynet, G., Chomienne, V., Ekström, S., et al. 2015, *A&A*, **575**, A60
- Mokiem, M. R., de Koter, A., Puls, J., et al. 2005, *A&A*, **441**, 711
- Muijres, L. E., Vink, J. S., de Koter, A., Müller, P. E., & Langer, N. 2012, *A&A*, **537**, A37
- Nazé, Y. 2009, *A&A*, **506**, 1055
- Oskinova, L. M., Hamann, W.-R., & Feldmeier, A. 2007, *A&A*, **476**, 1331
- Patriarchi, P., Morbidelli, L., Perinotto, M., & Barbaro, G. 2001, *A&A*, **372**, 644
- Pauldrach, A. W. A., Kudritzki, R. P., Puls, J., & Butler, K. 1990, *A&A*, **228**, 125
- Puls, J., Urbaneja, M. A., Venero, R., et al. 2005, *A&A*, **435**, 669
- Puls, J., Vink, J. S., & Najarro, F. 2008, *A&ARv*, **16**, 209
- Puls, J., Sundqvist, J. O., Najarro, F., & Hanson, M. M. 2009, *AIP Conf. Ser.*, **1171**, 123
- Rauw, G., Nazé, Y., Wright, N. J., et al. 2015, *ApJS*, **221**, 1
- Repolust, T., Puls, J., & Herrero, A. 2004, *A&A*, **415**, 349
- Sana, H., Rauw, G., Nazé, Y., Gosset, E., & Vreux, J.-M. 2006, *MNRAS*, **372**, 661
- Sana, H., Le Bouquin, J.-B., Lacour, S., et al. 2014, *ApJS*, **215**, 15
- Schröder, S. E., Kaper, L., & Lamers, H. J. G. L. M., & Brown, A. G. A. 2004, *A&A*, **428**, 149
- Sembach, K. R., & Savage, B. D. 1994, *ApJ*, **431**, 201
- Sota, A., Maíz Apellániz, J., Morrell, N. I., et al. 2014, *ApJS*, **211**, 10
- Sundqvist, J. O., & Puls, J. 2018, *A&A*, **619**, A59
- Sundqvist, J. O., Puls, J., Feldmeier, A., & Owocki, S. P. 2011, *A&A*, **528**, A64
- Sundqvist, J. O., Puls, J., & Owocki, S. P. 2014, *A&A*, **568**, A59
- van Leeuwen, F. 2007, *A&A*, **474**, 653
- Vink, J. S., de Koter, A., & Lamers, H. J. G. L. M. 1999, *A&A*, **350**, 181
- Vink, J. S., de Koter, A., & Lamers, H. J. G. L. M. 2000, *A&A*, **362**, 295
- Vink, J. S., de Koter, A., & Lamers, H. J. G. L. M. 2001, *A&A*, **369**, 574
- Wade, G. A., Neiner, C., Alecian, E., et al. 2016, *MNRAS*, **456**, 2
- Walborn, N. R., & Panek, R. J. 1984, *ApJ*, **280**, L27
- Wegner, W. 1994, *MNRAS*, **270**, 229
- Wegner, W. 2003, *Astron. Nachr.*, **324**, 219

Appendix A: Final models: ultraviolet

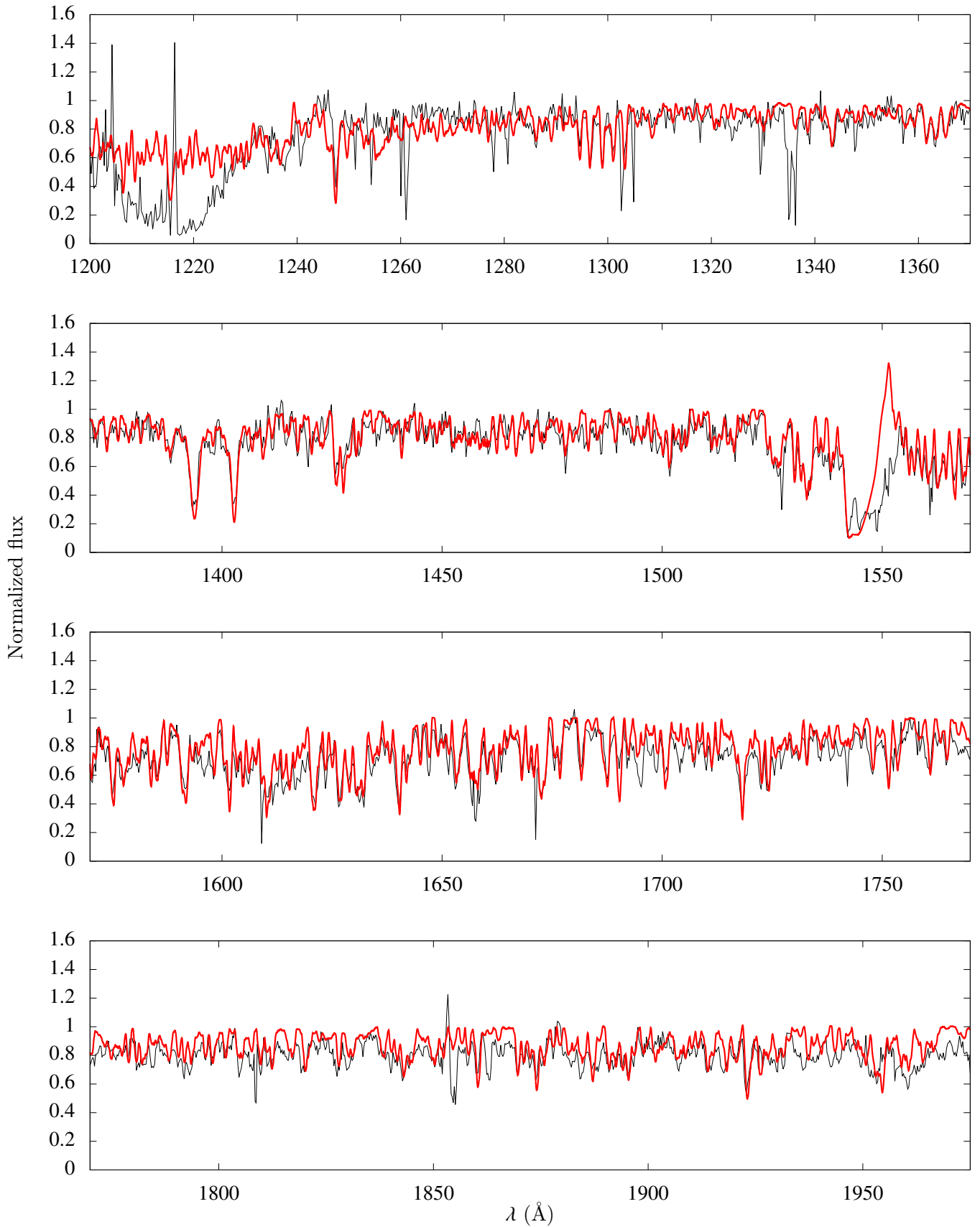


Fig. A.1. Final CMFGEN model with $T_{\text{eff}}^{\text{UV}}$ (red) for HD 156292 in the UV. The IUE/SWP spectrum is shown in black. Model parameters are listed in Table 3.

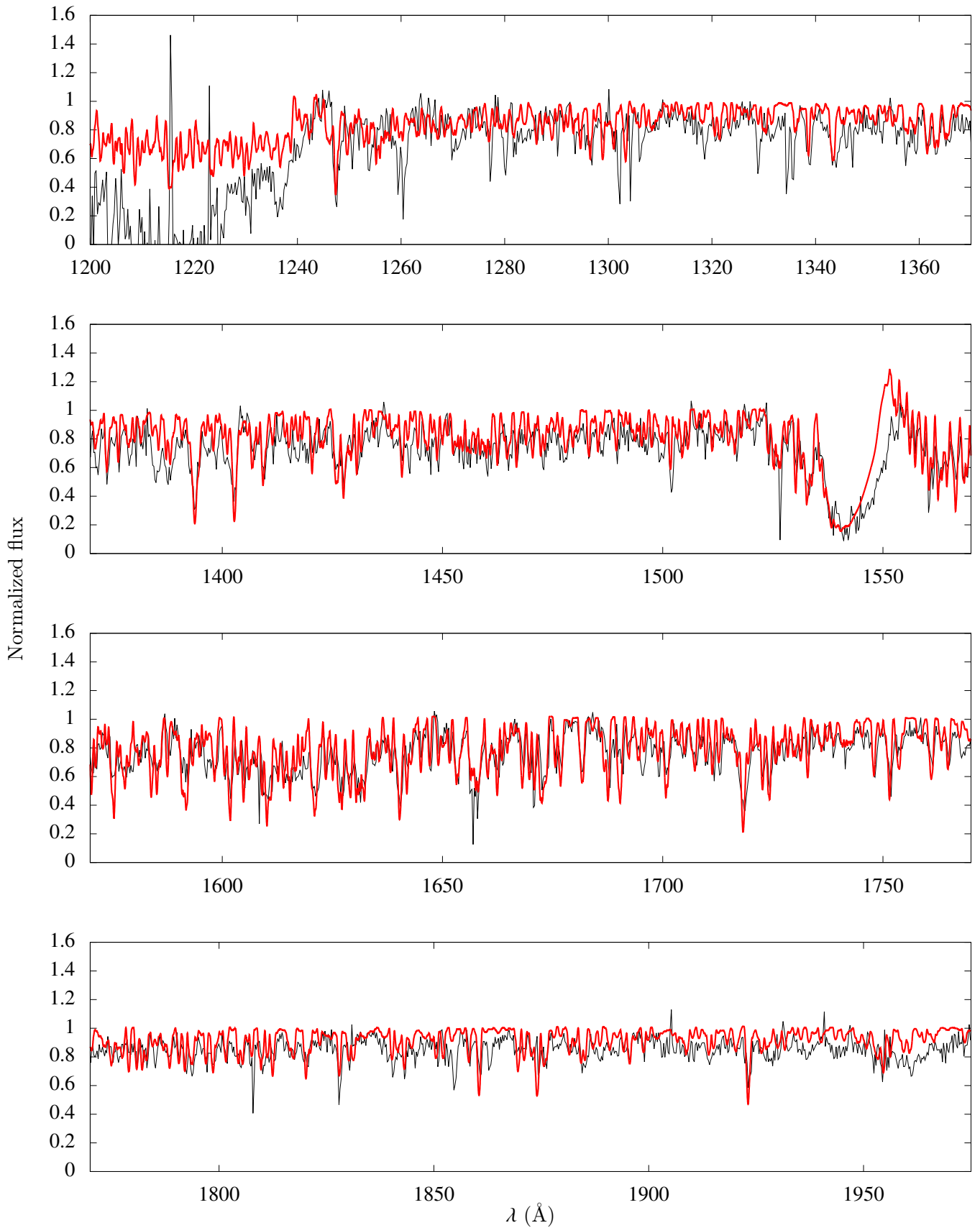


Fig. A.2. Final CMFGEN model with $T_{\text{eff}}^{\text{UV}}$ (red) for HD 24431 in the UV. The IUE/SWP spectrum is shown in black. Model parameters are listed in Table 3.

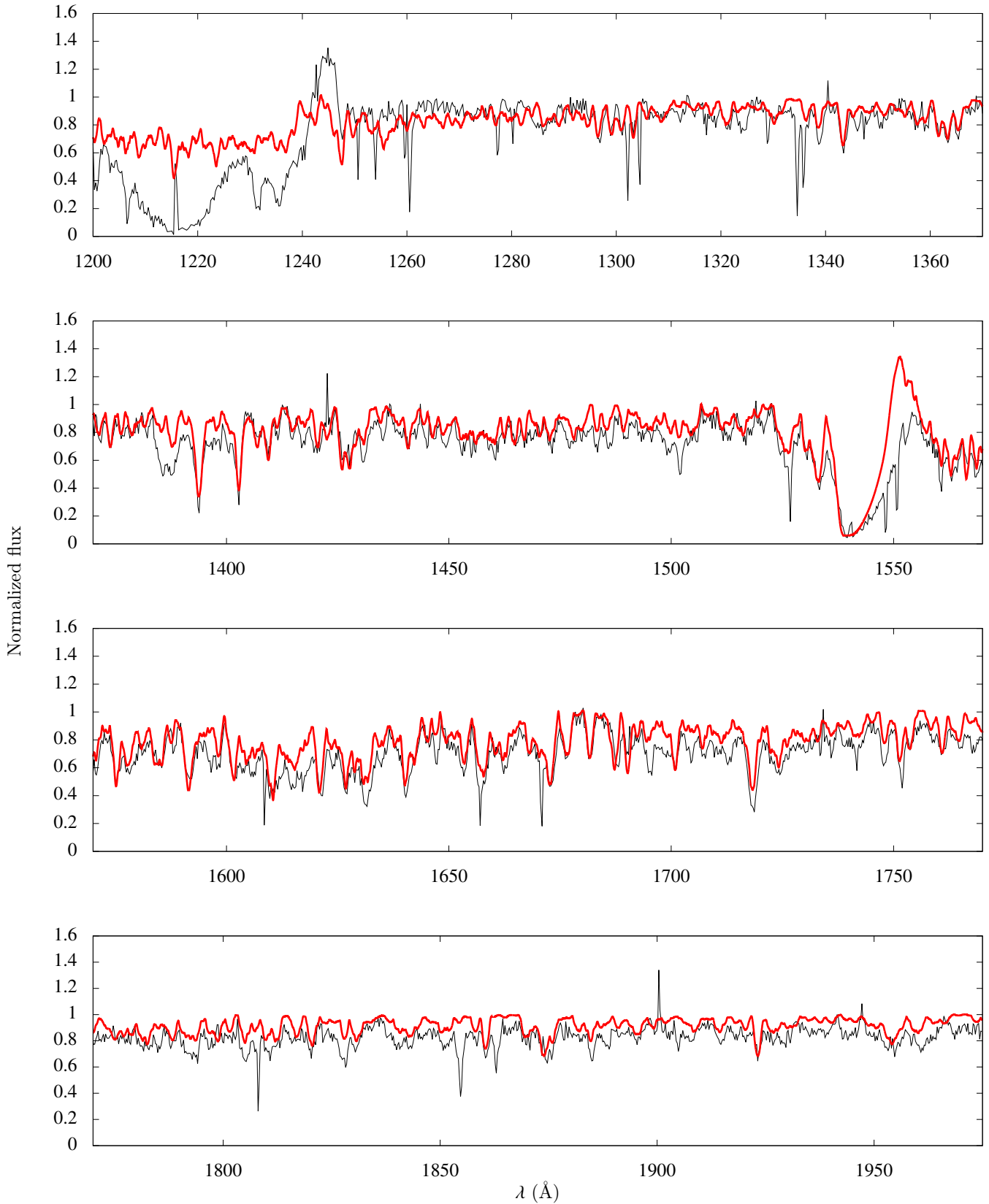


Fig. A.3. Final CMFGEN model with $T_{\text{eff}}^{\text{UV}}$ (red) for HD 105627 in the UV. The IUE/SWP spectrum is shown in black. Model parameters are listed in Table 3.

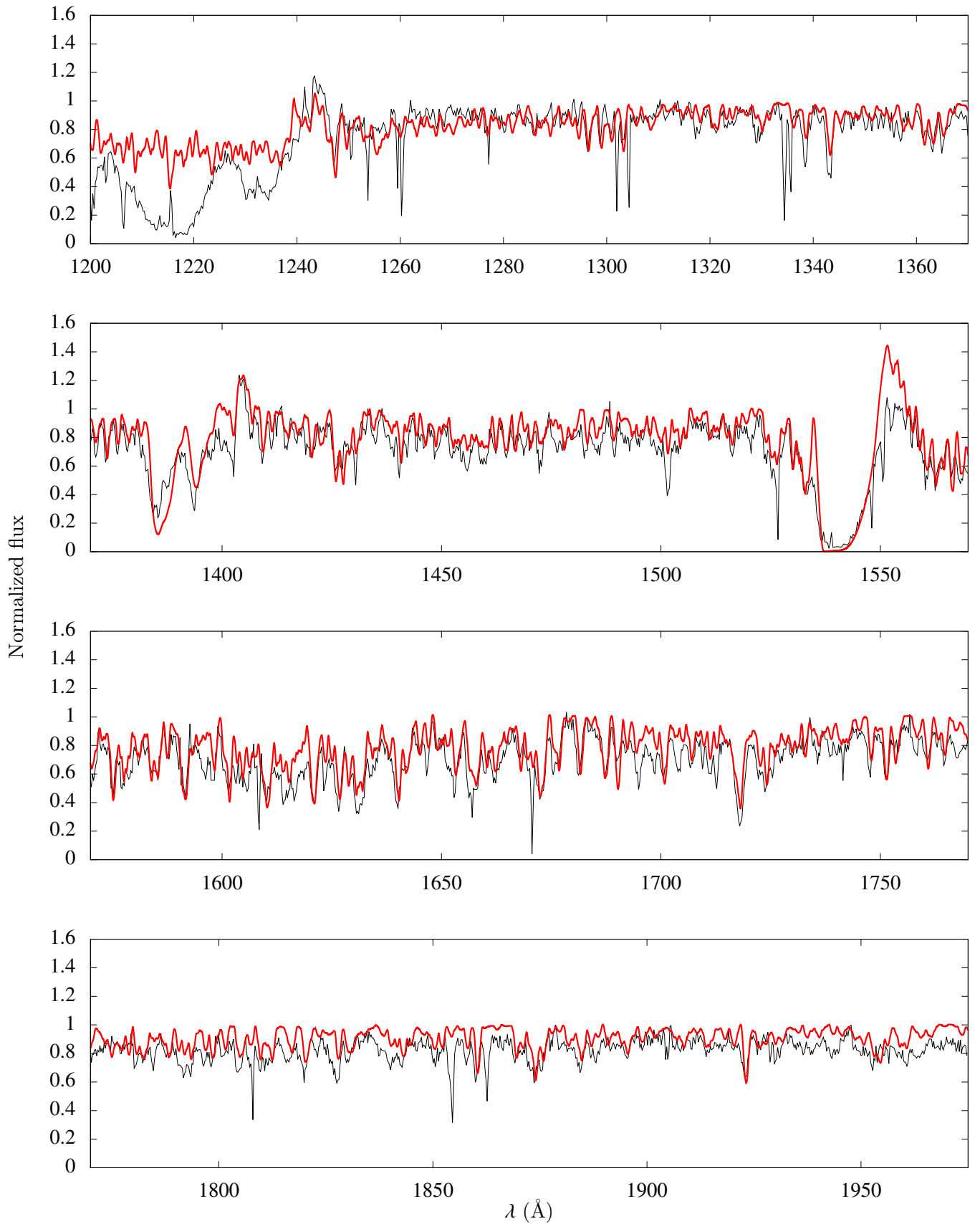


Fig. A.4. Final CMFGEN model with $T_{\text{eff}}^{\text{UV}}$ (red) for HD 116852 in the UV. The IUE/SWP spectrum is shown in black. Model parameters are listed in Table 3.

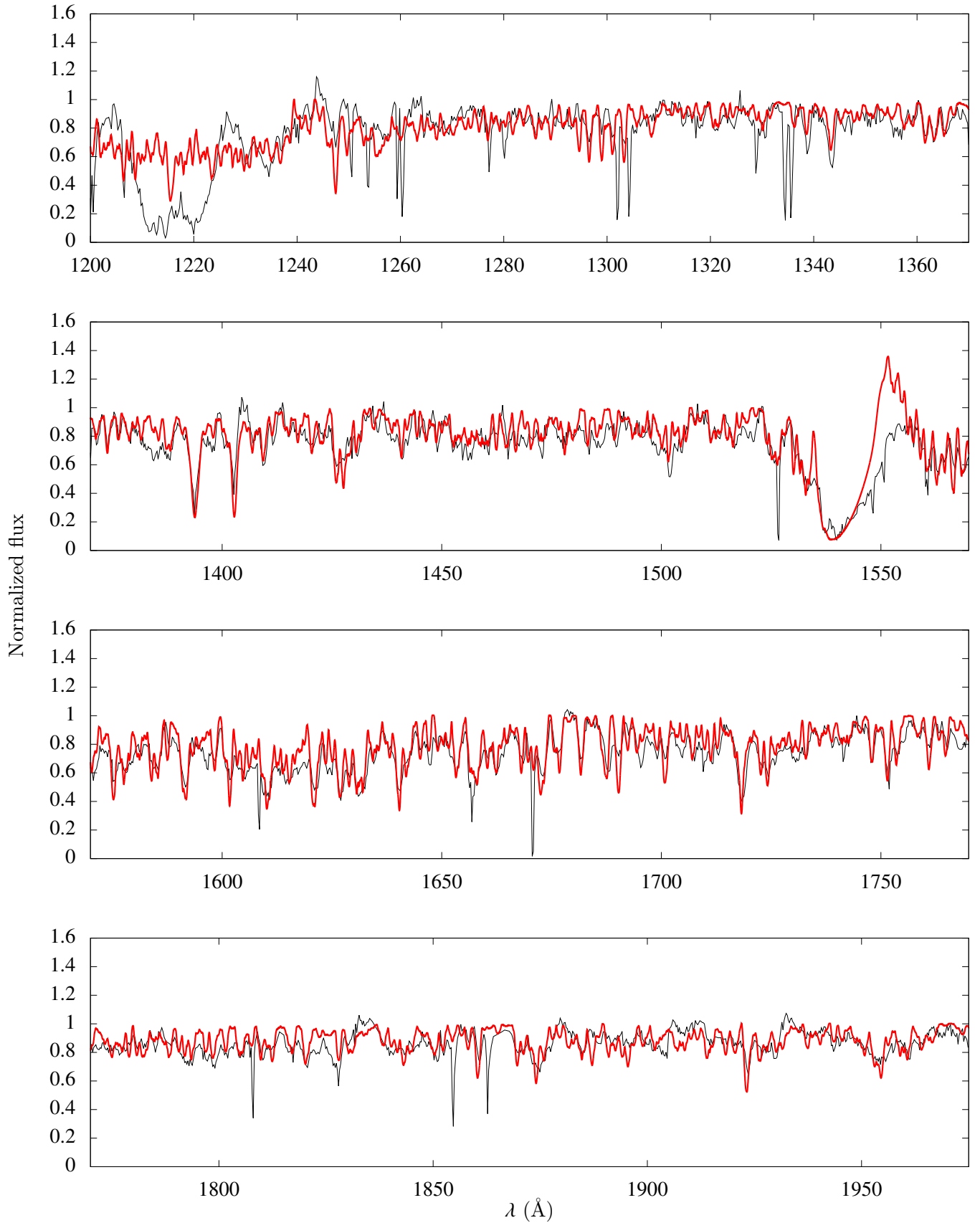


Fig. A.5. Final CMFGEN model with $T_{\text{eff}}^{\text{UV}}$ (red) for HD 153426 in the UV. The IUE/SWP spectrum is shown in black. Model parameters are listed in Table 3.

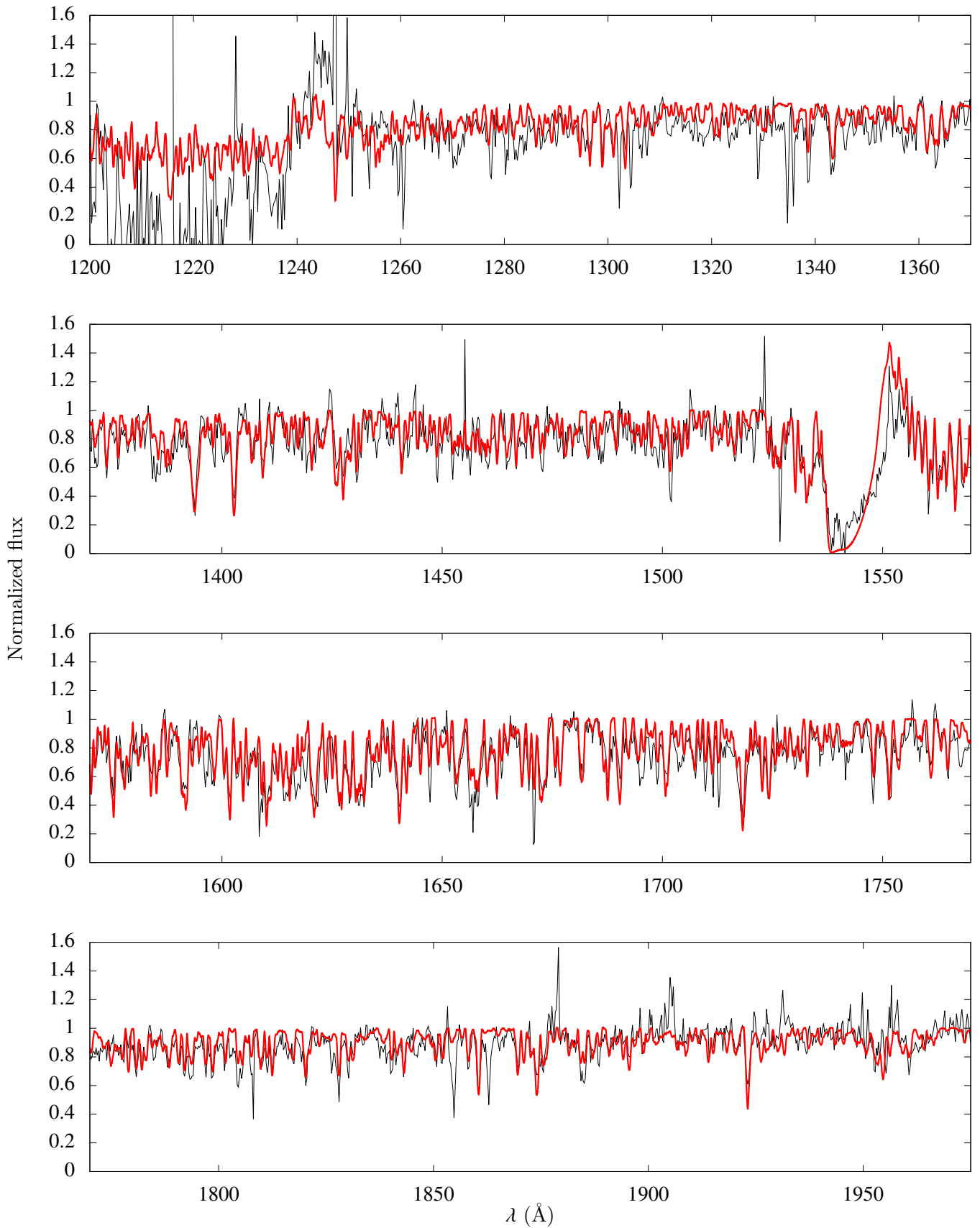


Fig. A.6. Final CMFGEN model with $T_{\text{eff}}^{\text{UV}}$ (red) for HD 218195 in the UV. The IUE/SWP spectrum is shown in black. Model parameters are listed in Table 3.

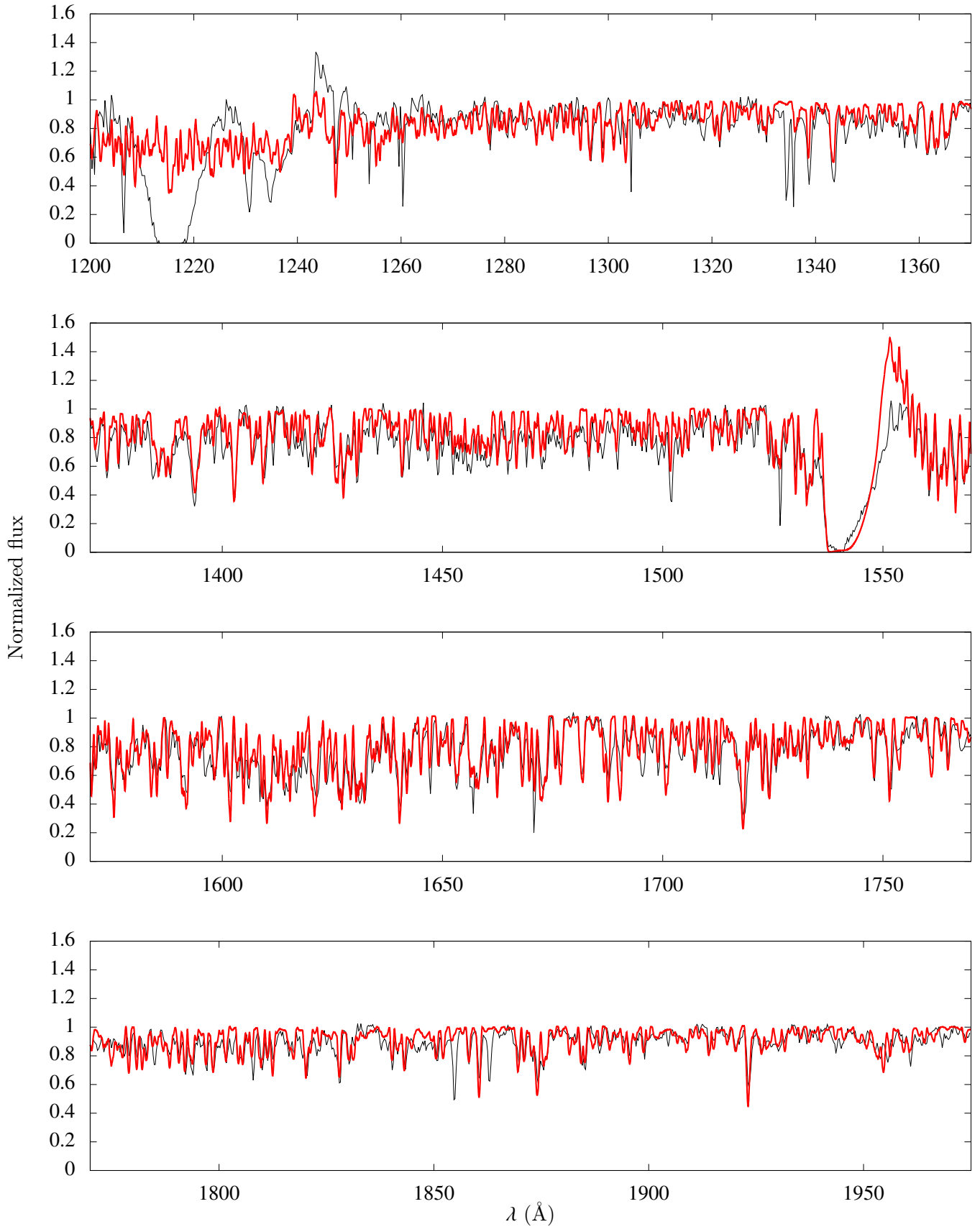


Fig. A.7. Final CMFGEN model with $T_{\text{eff}}^{\text{UV}}$ (red) for HD 36861 in the UV. The IUE/SWP spectrum is shown in black. Model parameters are listed in Table 3.

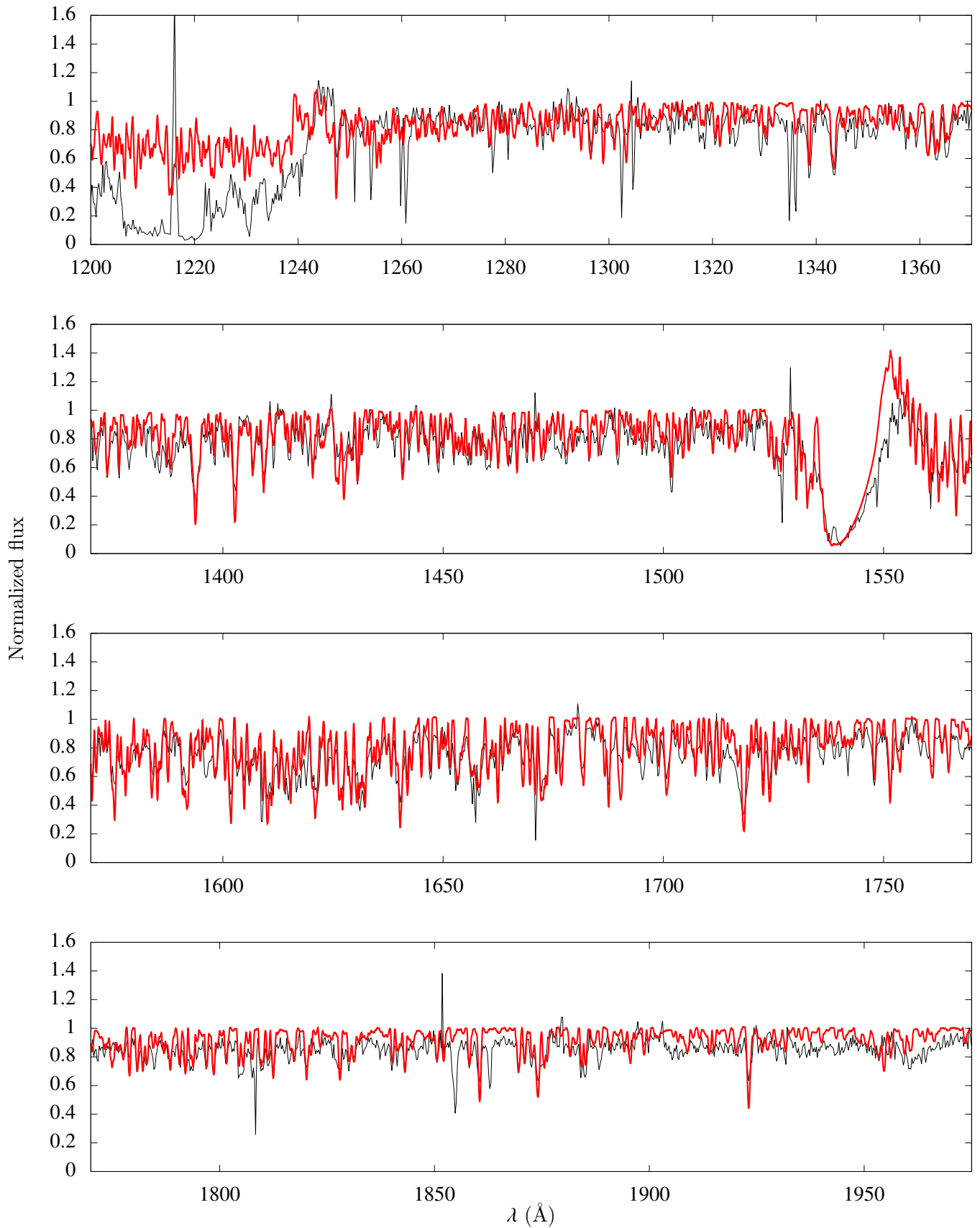


Fig. A.8. Final CMFGEN model with $T_{\text{eff}}^{\text{UV}}$ (red) for HD 115455 in the UV. The IUE/SWP spectrum is shown in black. Model parameters are listed in Table 3.

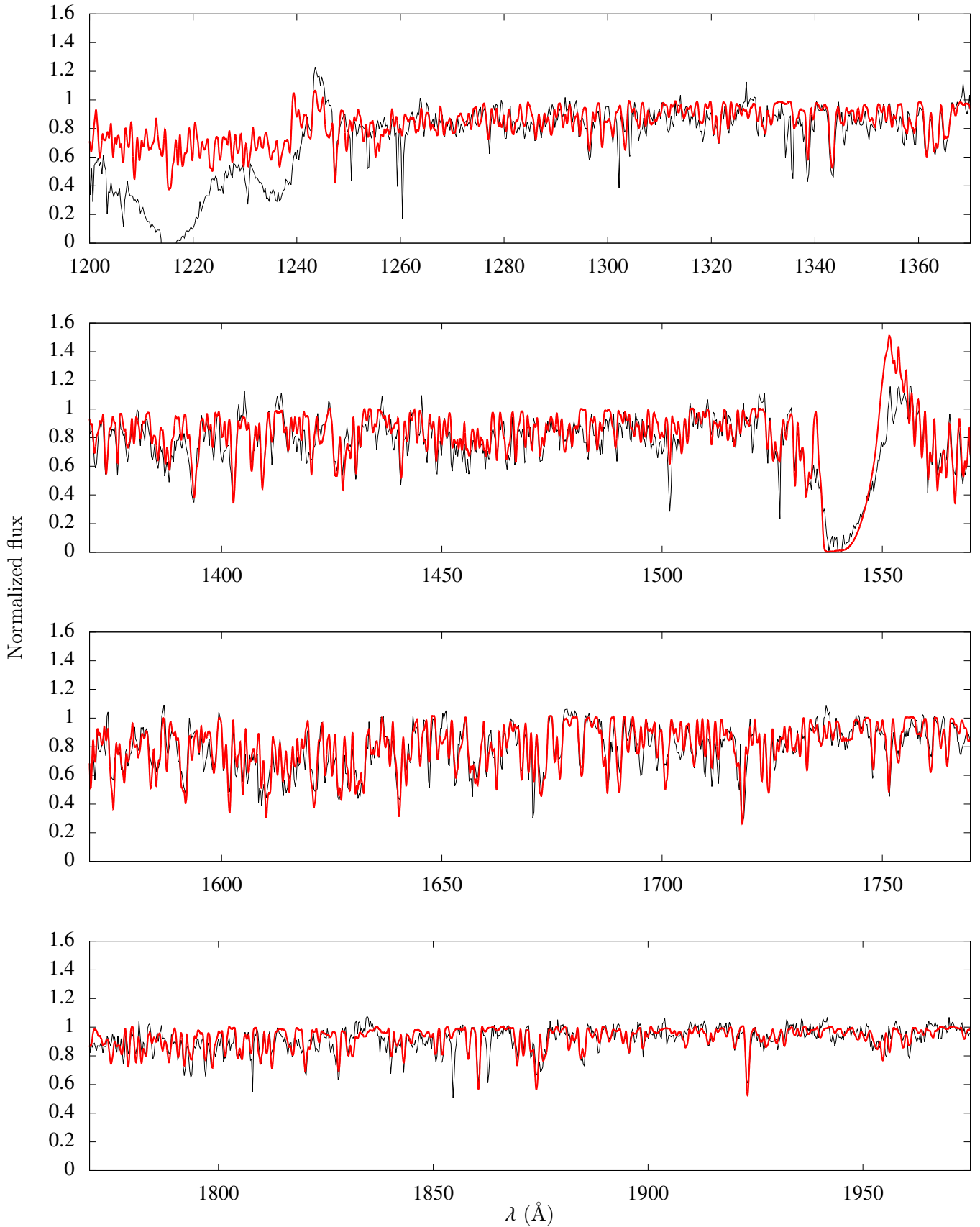


Fig. A.9. Final CMFGEN model with $T_{\text{eff}}^{\text{UV}}$ (red) for HD 135591 in the UV. The IUE/SWP spectrum is shown in black. Model parameters are listed in Table 3.

Appendix B: Final models: optical

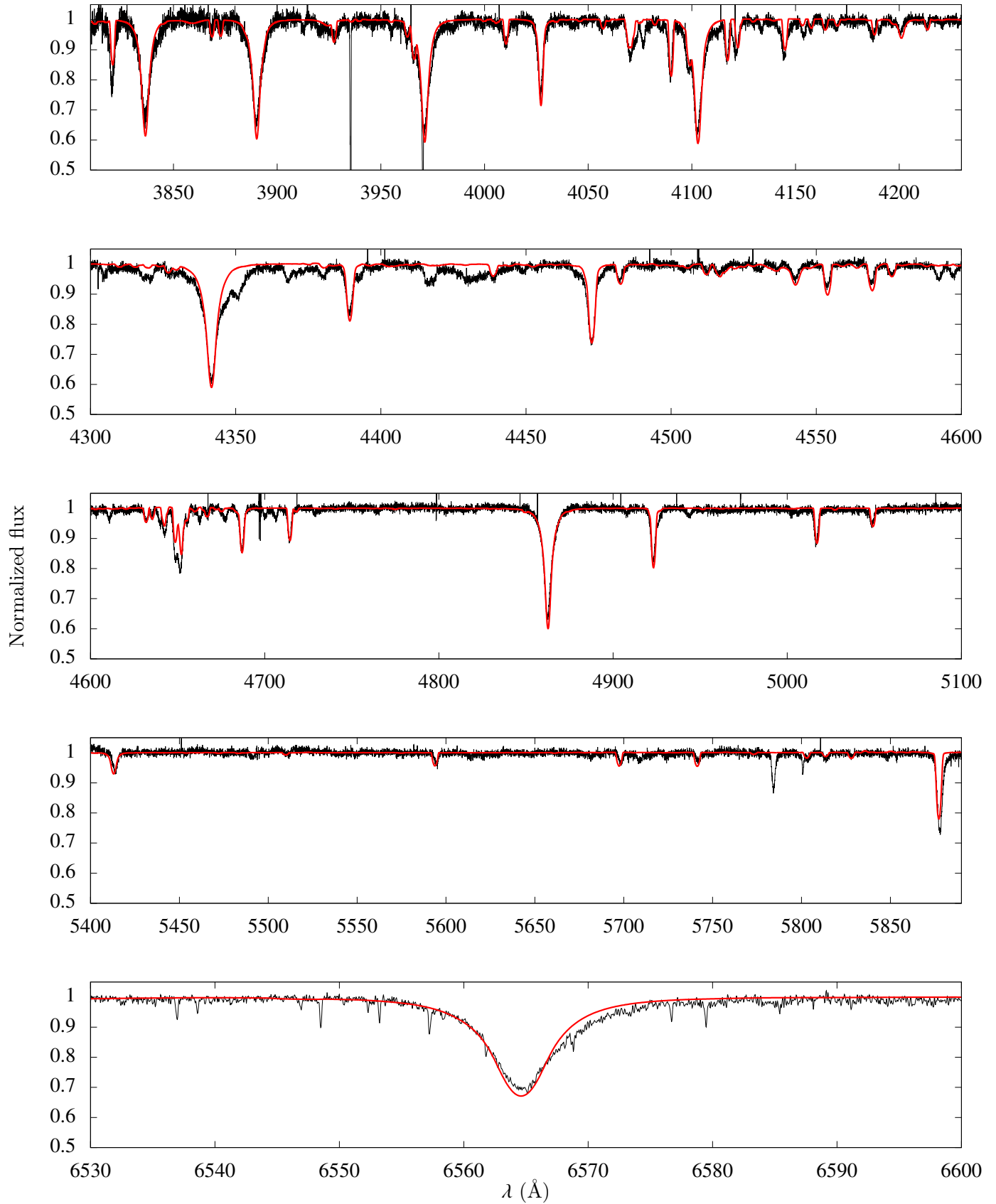


Fig. B.1. Final CMFGEN model with $T_{\text{eff}}^{\text{UV}}$ (red) for HD 156292 in the optical. The FEROS spectrum is shown in black. Model parameters are listed in Table 3.

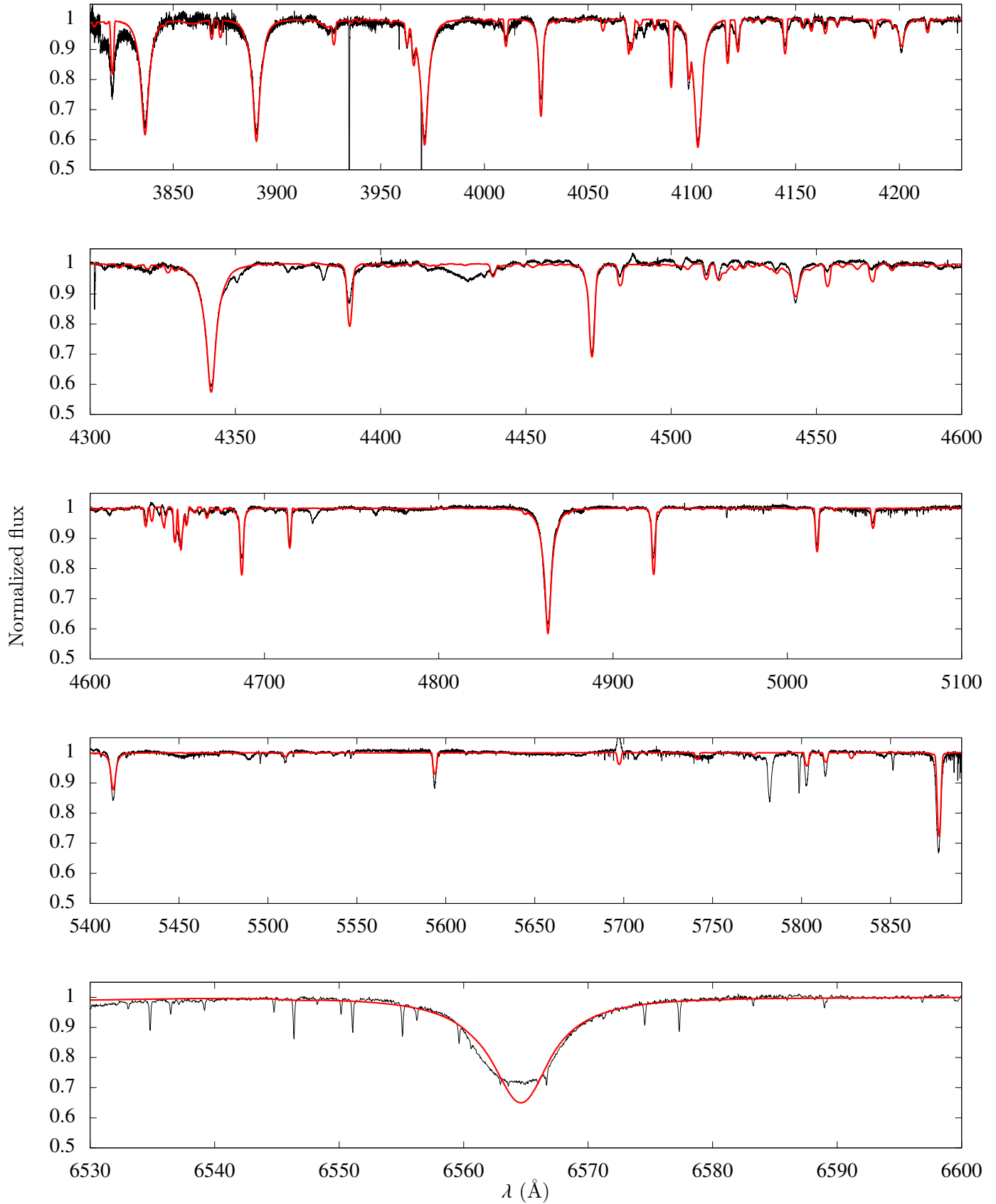


Fig. B.2. Final CMFGEN model with $T_{\text{eff}}^{\text{UV}}$ (red) for HD 24431 in the optical. The ESPADONS spectrum is shown in black. Model parameters are listed in Table 3.

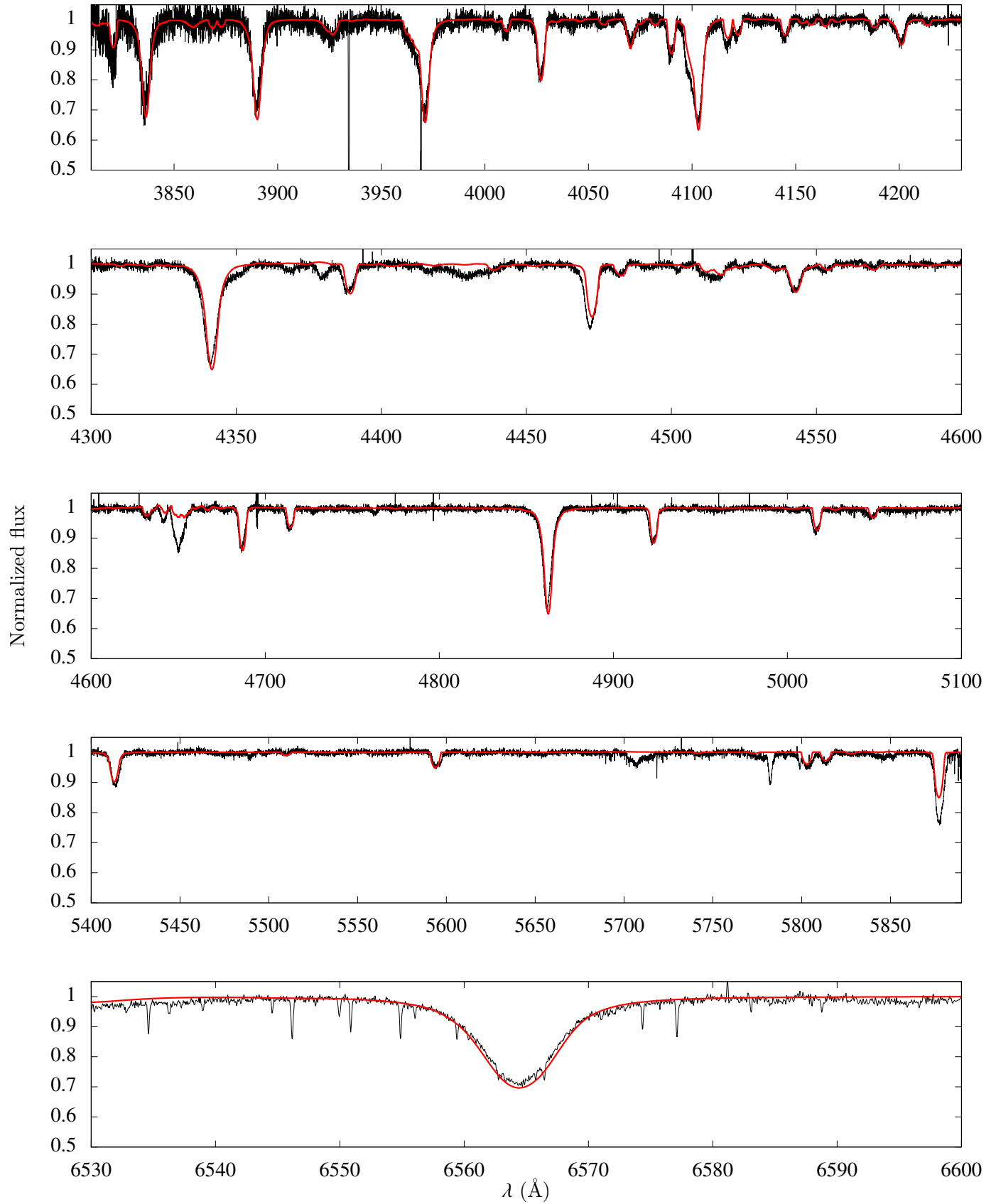


Fig. B.3. Final CMFGEN model with $T_{\text{eff}}^{\text{UV}}$ (red) for HD 105627 in the optical. The FEROS spectrum is shown in black. Model parameters are listed in Table 3.

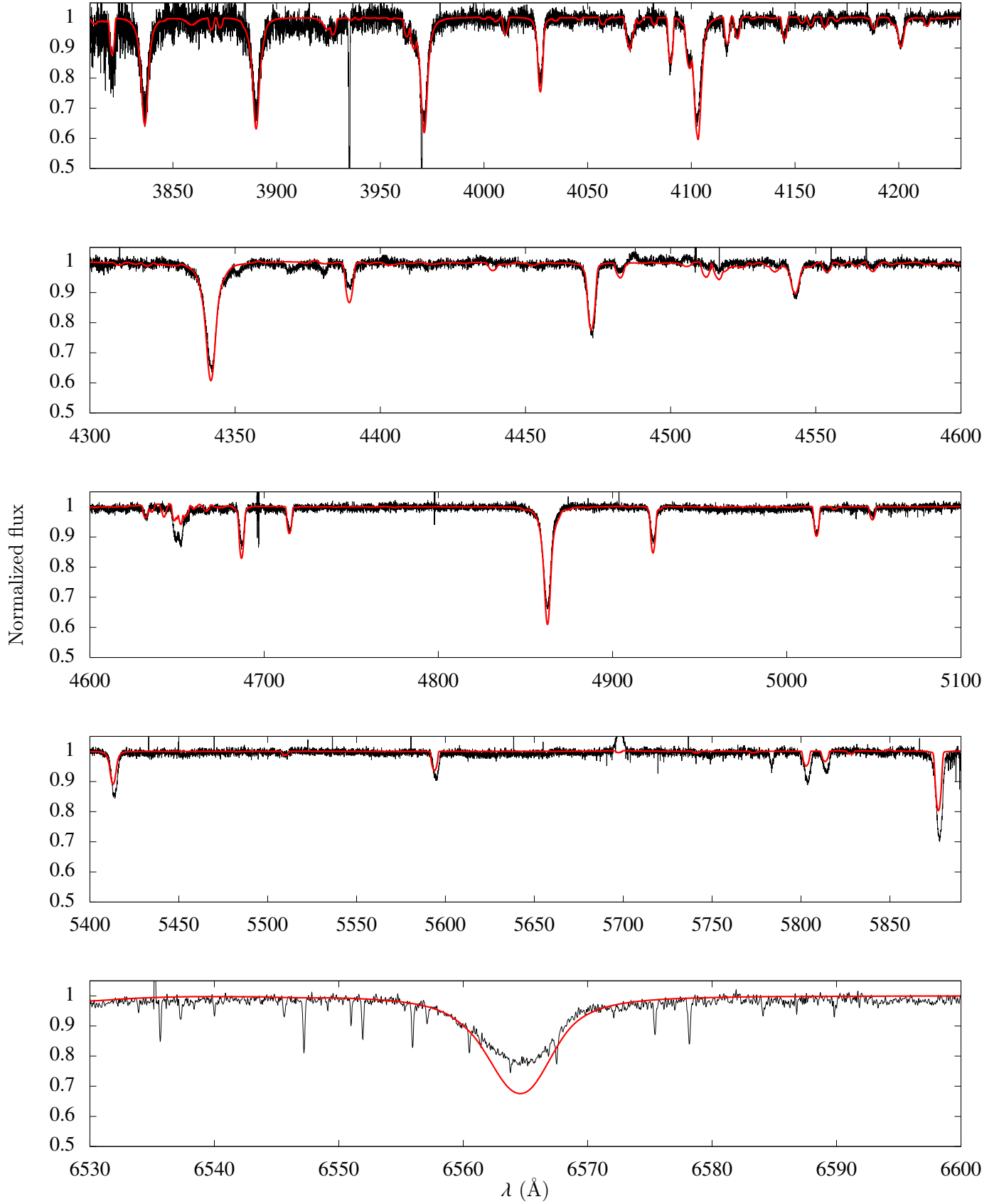


Fig. B.4. Final CMFGEN model with $T_{\text{eff}}^{\text{UV}}$ (red) for HD 116852 in the optical. The FEROS spectrum is shown in black. Model parameters are listed in Table 3.

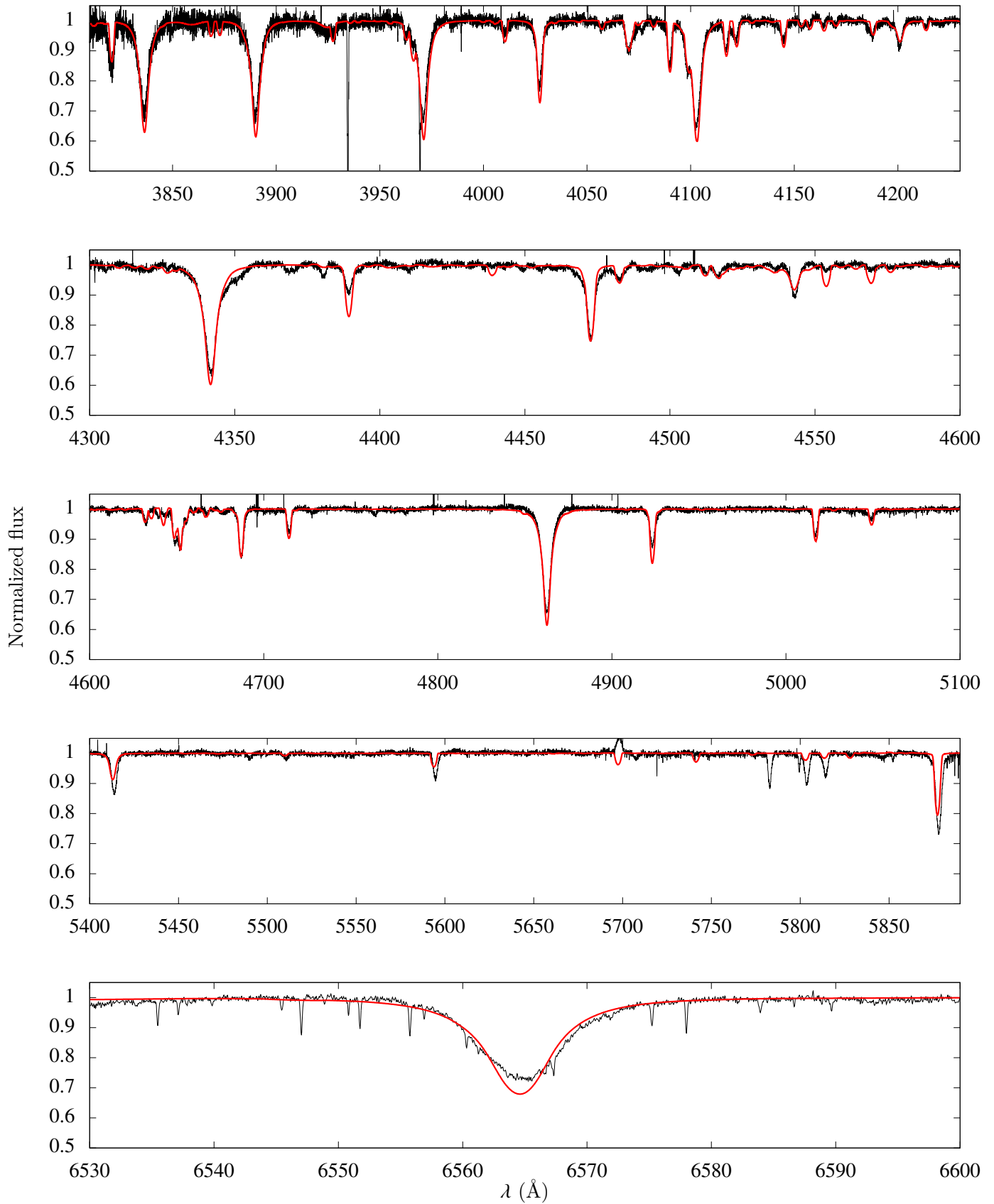


Fig. B.5. Final CMFGEN model with $T_{\text{eff}}^{\text{UV}}$ (red) for HD 153426 in the optical. The FEROS spectrum is shown in black. Model parameters are listed in Table 3.

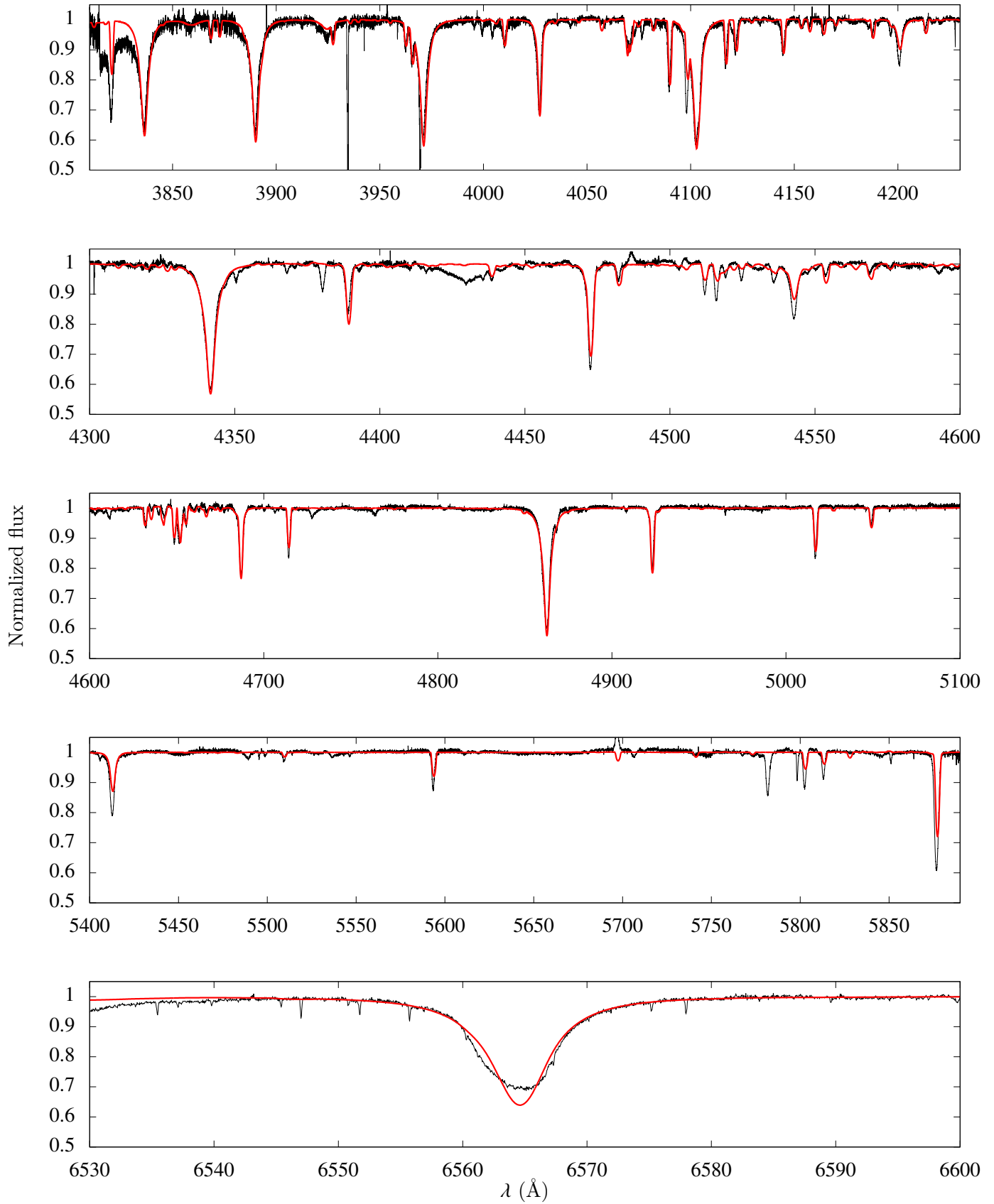


Fig. B.6. Final CMFGEN model with $T_{\text{eff}}^{\text{UV}}$ (red) for HD 218195 in the optical. The ESPADONS spectrum is shown in black. Model parameters are listed in Table 3.

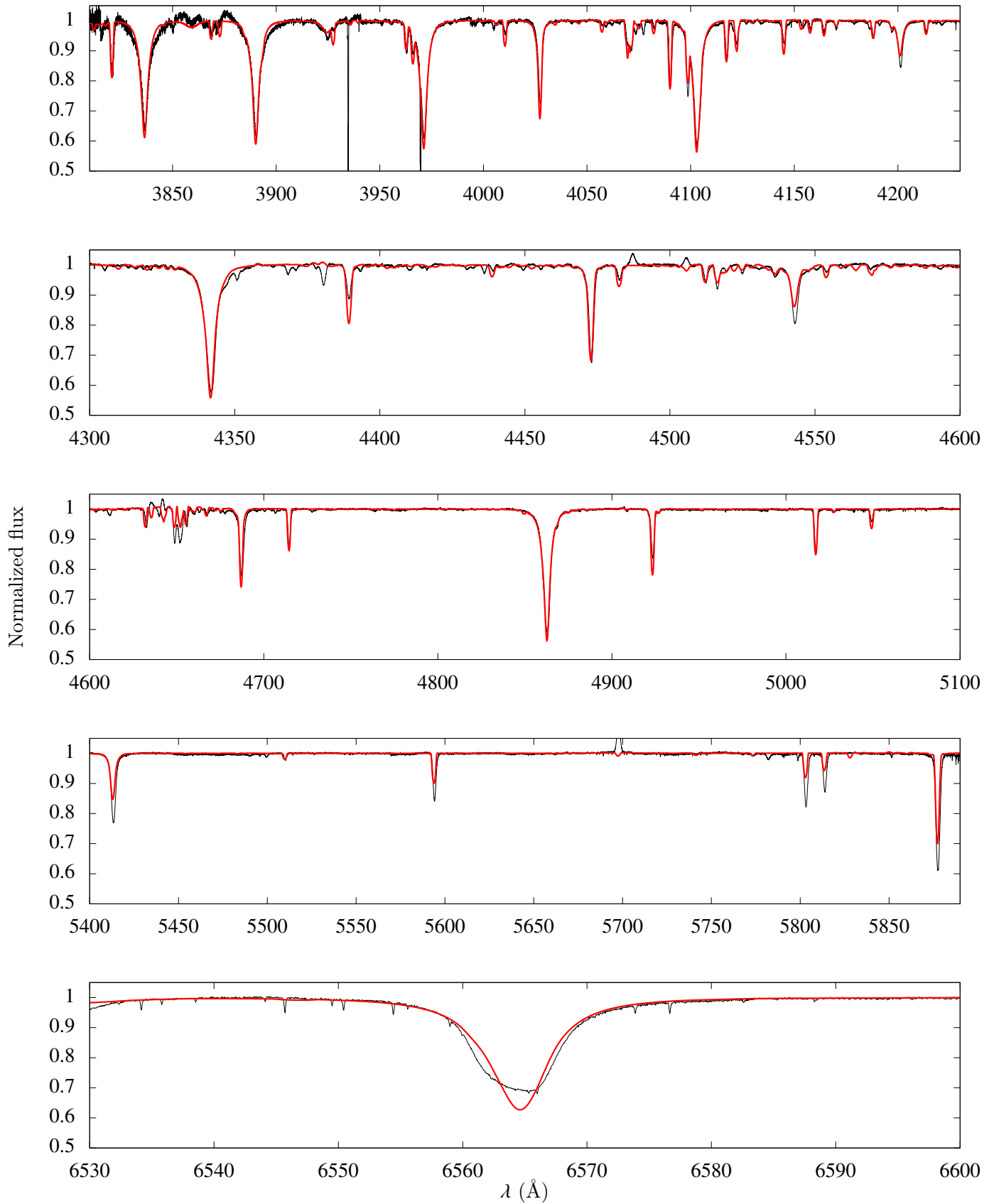


Fig. B.7. Final CMFGEN model with $T_{\text{eff}}^{\text{UV}}$ (red) for HD 36861 in the optical. The NARVAL spectrum is shown in black. Model parameters are listed in Table 3.

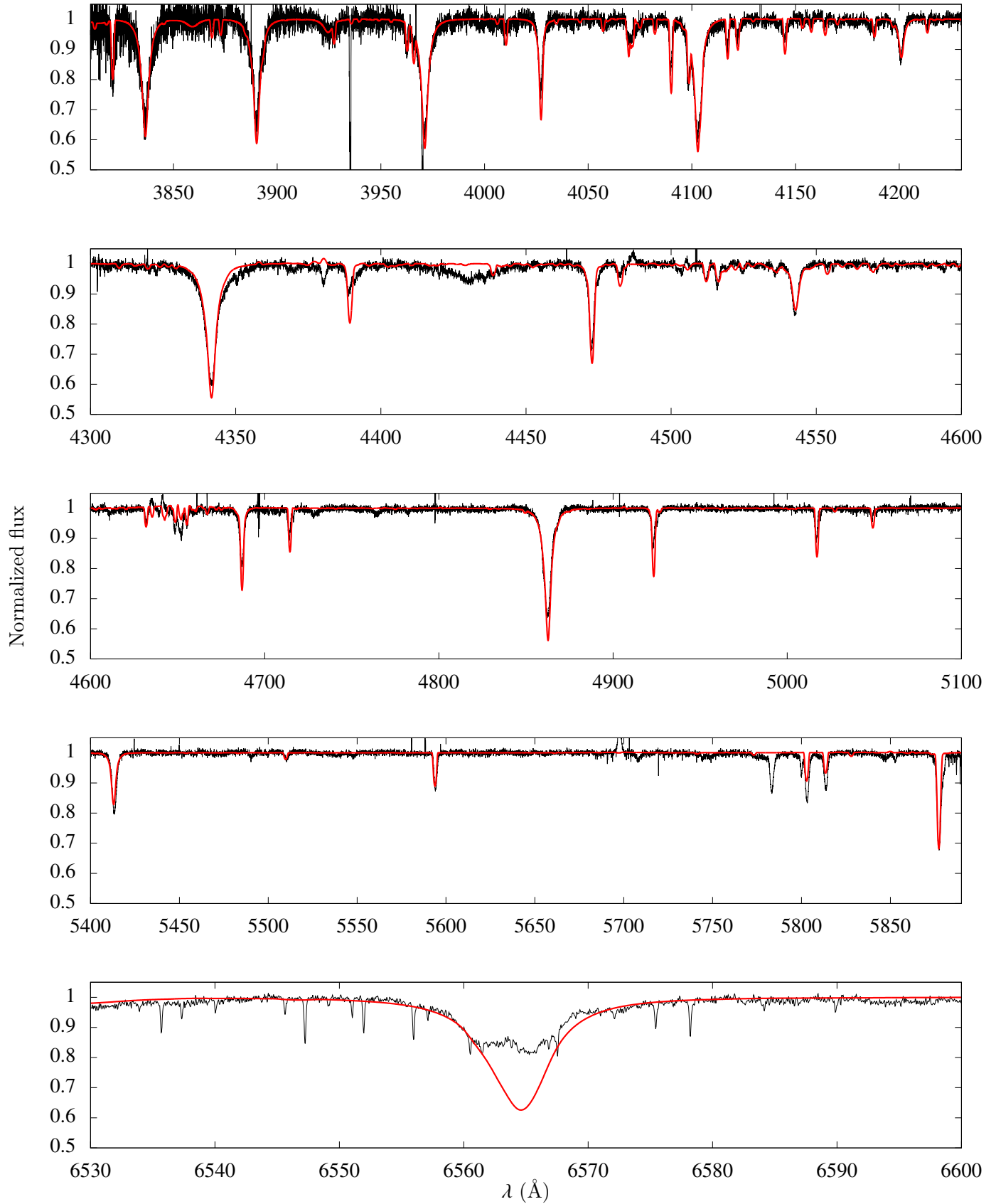


Fig. B.8. Final CMFGEN model with $T_{\text{eff}}^{\text{UV}}$ (red) for HD 115455 in the optical. The FEROS spectrum is shown in black. Model parameters are listed in Table 3.

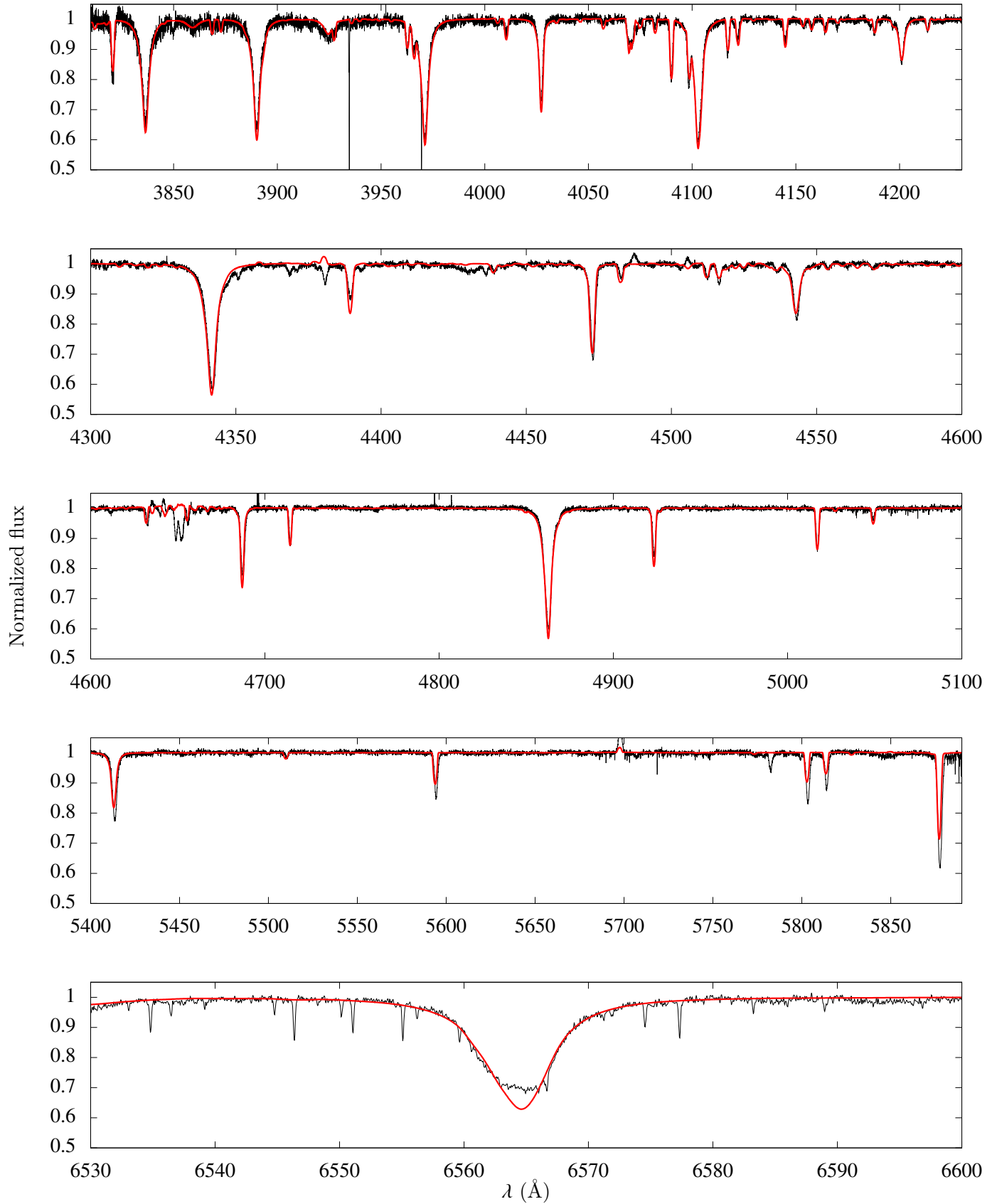


Fig. B.9. Final CMFGEN model with $T_{\text{eff}}^{\text{UV}}$ (red) for HD 135591 in the optical. The FEROS spectrum is shown in black. Model parameters are listed in Table 3.

LATE O GIANTS AND THE WEAK WIND PROBLEM

Elisson S. da G. de Almeida^{1,2}, Wagner L. F. Marcolino², and Claudio B. Pereira³

We analysed O giants through UV and optical spectroscopy using the code CMFGEN. We conclude that these stars show weak winds and are at the transition region in luminosity for such issue.

We performed a spectroscopic modelling of 9 Galactic late O giants (O8-9.5III). We used high resolution UV data from the IUE telescope and optical data from the FEROS and NARVAL instruments. We derived the principal stellar winds physical parameters of the sample, i.e., the \dot{M} and v_∞ . For this, we analysed sophisticated non-LTE atmosphere models computed by the code CMFGEN (Hillier & Miller 1998). We are interested about these stars because of their luminosity region at $\log(L_*/L_\odot) \approx 5.2$, which seems to define the beginning of the called weak wind problem (e.g., Martins et al. 2005; Marcolino et al. 2009), where the \dot{M} derived by atmospheric modelling are orders of magnitude lower than the hydrodynamical predicted values (Vink et al. 2000) for late O dwarfs (O8-9.5V). In order to obtain the stellar and wind parameters, we used the following line diagnostics: (i) UV: Fe III-IV-V (T_{eff}), P-Cygni profiles of C IV $\lambda\lambda 1548, 1551$ (\dot{M} and v_∞), and Si IV $\lambda\lambda 1394, 1403$ (\dot{M}); (ii) optical: He I-II (T_{eff}), Balmer series ($\log g$), weak metal lines and He I ($v \sin i$), and H α (\dot{M}). We developed a detailed analysis of possible relevant degeneracies between the \dot{M} and stellar parameters (such as T_{eff} , CNO abundances, and microturbulence field) and found that the determined limits for \dot{M} are robust to uncertainties on the stellar properties. There is an overall agreement between the UV and optical analyses. However, for 3 stars we do not find agreement between the modelling of H α and UV. In the Fig. 1, we show the comparison between the determined \dot{M} and the predicted values \dot{M}_{Vink} for different types of OB stars. The dwarfs with weak winds are below $\log(L/L_\odot) \approx 5.2$ (balls). Note the overall agreement between the predicted and the derived \dot{M} for the most luminous OB stars. Our results for O giants are shown in red squares. We

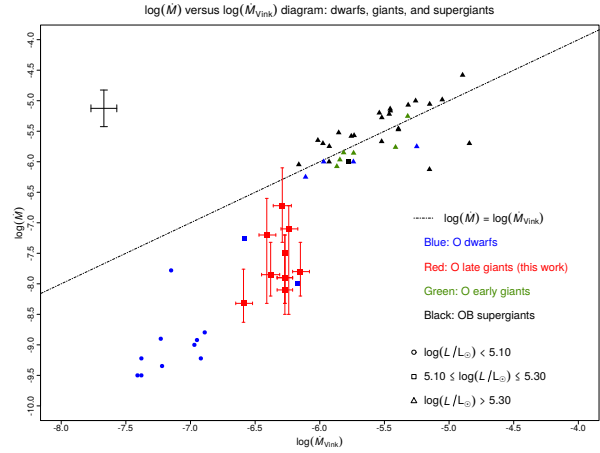


Fig. 1. Representative error bars for the literature results: O dwarfs (Martins et al. 2005; Marcolino et al. 2009), O early giants and OB supergiants (references within Mokiem et al. 2007).

conclude that O8-9.5III also exhibit the weak wind problem and confirm the region of $\log(L_*/L_\odot) \approx 5.2$ as critical for the weak winds. These results are the first to show this issue besides the types O8-9.5V. We analysed our sample in the HR diagram together to literature results for O dwarfs and supergiants and we verified the more evolved status of the former in comparison with the late dwarfs. Therefore, we attest that the weak winds are not due to evolutionary effects.

REFERENCES

- Hillier, D. J., & Miller, D. L. 1998, ApJ, 496, 407
 Marcolino, W. L. F., Bouret, J.-C., Martins, F., et al. 2009, A&A, 498, 837
 Martins, F., Schaerer, D., Hillier, D. J., et al. 2005, A&A, 441, 735
 Mokiem, M. R., de Koter, A., Vink, J. S., et al. 2007, A&A, 473, 603
 Vink, J. S., de Koter, A., & Lamers, H. J. G. L. M. 2000, A&A, 362, 295

¹Laboratoire Lagrange, UMR 7293, Université de Nice-Sophia Antipolis, CNRS, Observatoire de la Côte d’Azur, 06108 Nice, France (Elisson.Saldanha@oca.eu).

²Observatório do Valongo, Universidade Federal do Rio de Janeiro, 20080-090 Rio de Janeiro, Brazil.

³Observatório Nacional, 20921-400 Rio de Janeiro, Brazil.

6.2 The LBV star P Cygni

6.2.1 Winds and episodic outbursts of LBVs

P Cygni (HD 193237, B1Iape³) is one of the most observed LBV stars, for which extensive models have been developed (e.g., Lamers et al. 1983; Najarro et al. 1997; Najarro 2001; Richardson et al. 2013). P Cygni is a prototype of the LBV stars, also called as S Doradus variables.

These stars evolved from the more massive O-type stars ($M_{\text{ZAMS}} \gtrsim 40 M_{\odot}$; Table 1.2) and display photometric and spectroscopic variability covering a wide range of timescales from weeks to years and over centuries (e.g., Lamers 1995; Markova et al. 2001b; Richardson et al. 2011). LBVs possess the strongest radiative line-driven winds among the hot massive stars, with mass-loss rates typically ranging from $\sim 10^{-5}$ up to $10^{-3} M_{\odot} \text{ yr}^{-1}$ (Fig. 1.12)⁴.

In addition, they undergo violent episodic mass loss, ejecting a much larger amount of material than the mass loss process by stellar winds. It is understood that η Carinae (another LBV star, more luminous than P Cygni) ejected an astonishing quantity of material, $\sim 15\text{-}20 M_{\odot}$, due to a giant eruption that lasted about a whole decade during the 19th century (Smith & Owocki 2006). We point out that the mechanisms linked to LBV eruptions are not well known yet. Nevertheless, one possibility relies on a continuum-driven outburst arising when deep photospheric layers occasionally exceed the Eddington limit (see Eq. 1.10), and then the radial velocity in the photosphere suddenly increases to high values up to about 200 km s^{-1} (e.g., Guzik et al. 1997; Cox et al. 1998).

As discussed in Sect 1.2.1, P Cygni also passed by two eruptions during the 17th century, reaching a maximum of brightness of $V \sim 3$ and a subsequent drop up to $V \sim 6$. The condensation of dust grains in its circumstellar environment could explain such a drop in the visual magnitude (see Israelian & de Groot 1999, and references within). Since then the visual magnitude is more or less constant around the mean value of 4.82, but showing a gradual decrease in the visual magnitude of $\sim 0.15 \text{ mag/century}$ (de Groot & Lamers 1992). Indeed, the analysis of historical observations of P Cygni by these authors provided the first direct evidence of evolution in the HR diagram. Markova et al. (2001a) showed that P Cygni’s effective temperature is slowly decreasing by a rate of $\sim 12 \text{ K yr}^{-1}$. This is consistent with the picture that P Cygni evolves toward the red part of the HR diagram, lying between the shell hydrogen burning phase and the core helium phase (e.g., El Eid & Hartmann 1993).

3. The suffix “ep” is used to designate emission lines with peculiarity.

4. For example, P Cygni has a wind mass-loss rate in the order of $10^{-5} M_{\odot} \text{ yr}^{-1}$ (e.g., Najarro 2001).

6.2. The LBV star P Cygni

Moreover, the wind mass-loss rate of P Cygni is known to vary by $\sim 19\%$ over a period of about 7 years of short S Doradus phase. This affects its apparent stellar radius (Markova et al. 2001a), thus being relevant for interpreting interferometric observations of this star. Therefore, our discussion above shows that quasi-contemporaneous photometric and spectroscopic observations are needed to correctly interpret interferometric observations of LBV stars.

6.2.2 Intensity interferometry in a nutshell

The technique of intensity interferometry is distinct from the OLBI technique, which is used in Paper III, as it is based on the so-called Hanbury Brown and Twiss effect (Hanbury Brown 1956; Brown & Twiss 1956). Unlike OLBI, in the technique of intensity interferometry, the light received by a separate pair of telescopes is not brought together using optical systems, measuring the degree of correlation of the photon fluxes, instead of electric fields, as in the case of OLBI.

These pioneer works of Robert Hanbury Brown and Richard Twiss resulted in the development of intensity interferometers working from the visible up to longer wavelengths in the sub-millimetric and radio regions. For instance, the Narrabri 200-m baseline interferometer (Hanbury Brown et al. 1967a) provided the first interferometric catalogue of angular diameters for 32 early-type stars with spectral types from O7 to F8, observed in the visible (Hanbury Brown et al. 1974). This instrument had a lasting impact in the field of stellar high angular resolution observations by means of systematic measurements of stellar diameters, in particular for hot and massive stars (e.g., Hanbury Brown et al. 1967b, 1970; Davis et al. 1970; Code et al. 1976).

6.2.3 My collaboration with the I2C team

Using the technique of intensity interferometry (see Sect. 3.2), the visibility of P Cygni was measured using a two-telescope array (1-m class telescopes) mounted at the Centre Pédagogique Planète et Univers (C2PU/Observatoire de la Côte d’Azur) facility at the Plateau de Calern, France. This project on stellar intensity interferometry is called as Intensity Interferometry at Calern (I2C, Lai et al. 2018; Rivet et al. 2018) and is composed by a multidisciplinary group of researchers, comprising both astrophysicists and cold-atom physicists from Observatoire de la Côte d’Azur and Institute de Physique de Nice (Université Côte d’Azur). In addition to P Cygni, a few bright stars have been recently observed by the I2C team (see Guerin et al. 2017, 2018): Rigel (B8Iae), Vega (A0Va), Capella (G8III + G0III), Arcturus (K0III), Gomeisa (F5IV-V), and Pollux (K0III).

I have collaborated to this project by calculating a small set of radiative transfer

6.2. The LBV star P Cygni

models using the code CMFGEN, and then analysing these intensity interferometric observations of P Cygni centered on the H α emission line.

In particular, we were interested in determining the distance of P Cygni from modeling its visibility curve. Despite being well-studied for a long time, the exact distance of P Cygni is a current issue. As summarized in Table 1 of Turner et al. (2001), different distance determination methods provide distances varying between ~ 1.2 kpc and 2.3 kpc for this star. More recently, Gaia global astrometry mission (Data Release 2) finds a distance of 1.36 ± 0.24 kpc (Gaia Collaboration et al. 2018). However, this result is unlikely very accurate as P Cygni is too much bright for the normal scanning operation with Gaia, as it was optimally designed to observe fainter sources with a visual magnitude higher than ~ 11 .

6.2.4 Results and conclusions

For this purpose, we compared our H α visibility data with the predicted visibility from sophisticated non-LTE radiative transfer models calculated using the code CMFGEN. We point out that a spherically symmetric wind is a good assumption for P Cygni (e.g., Richardson et al. 2011), and CMFGEN was used on some previous spectroscopic and interferometric studies about P Cygni (e.g., Richardson et al. 2013; Najarro 2001). Following the approach of Richardson et al. (2013), we adopted the basic stellar and wind parameters of our CMFGEN model from the results of Najarro (2001). This latter study provided a detailed spectroscopic modeling of P Cygni from the ultraviolet to the mid-infrared region. The values of the fundamental parameters in our CMFGEN model are shown in Table 4 of Paper II. In particular, I computed approximately 30 different models for fixing the set of parameters for this study, as well as performing some additional modeling tests.

As an independent cross-check validation of our physical model, the synthetic spectrum of our model is compared with quasi-simultaneous observed spectrum of P Cygni in the visible region⁵. In short, we are able to match the visible spectrum of P Cygni fairly well (see Fig. 5 of Paper II). Despite being an interferometric study focused on H α observations, we used a complex chemical composition for the atmosphere of P Cygni, as in Najarro (2001). The basic atomic our CMFGEN model is shown in Table 3 of Paper II. From that, in addition to the strong H and He P Cygni profiles, our CMFGEN is also able to reproduce weak metal lines in the visible spectrum of P Cygni, such as the C II $\lambda 6580$ and $\lambda 6585$ lines (close to H α). Unlike the atomic data used in the CMFGEN models of Paper I (Sect. 6.1), we needed to include low-ionisation species,

5. Public data retrieved from the Astronomical Ring for Access to Spectroscopy (ARAS) database: <http://www.astrosurf.com/aras/>.

6.2. The LBV star P Cygni

as of C, N, O, and Fe in the models for P Cygni due to its lower effective temperature ($T_{\text{eff}} \sim 18700$ K) in comparison with late O giants ($T_{\text{eff}} \sim 30000$ - 35000 K).

From matching the observed visibility curve with the predicted one using CMFGEN, we estimated the distance of P Cygni as $d = 1.56 \pm 0.25$ kpc (Fig. 7 of Paper II). Despite being a fit based on just two visibilities measurements, note that we are able to find an error bar on P Cygni's distance that is comparable (compatible within the error bars) to the one from the Gaia DR2 parallaxes, namely, 1.36 ± 0.24 kpc. In short, the results found by Paper II indicate a smaller value of distance for P Cygni in comparison with the most adopted value for this star in the literature of ~ 1.8 kpc.

In conclusion, despite the current technical limitation on the technique of intensity interferometry, Paper II shows that intensity interferometry in the $H\alpha$ -band allows us to retrieve useful information on the fundamental parameter of the central star and its environments.

Furthermore, this study relies on a quite unusual interpretation of interferometric quantities. For instance, the interferometric data of the Be star ι Aquarii (Sect. 6.3) was interpreted considering a fixed value of distance from the Gaia DR2 parallax. As will be discussed in Sect. 7.1.3, we aim to apply the modeling method of Paper II to analyse intensity interferometric observations of other bright massive stars such as Rigel. Thus, Paper II sets an independent calibration method for estimating distances, being particularly interesting for evolved (bright) stars.

Lastly, this method also can be used as an independent check to the modified wind momentum-luminosity relation (Sect. 6.1), another distance determination method, but based on the wind fundamental parameters of massive stars. This is currently important since, as discussed in Sect. 6.1, Paper II evidences problems with respect to the theoretical modified wind momentum-luminosity relation for low luminous O stars.

Intensity interferometry of P Cygni in the H α emission line: towards distance calibration of LBV supergiant stars

J.-P. Rivet,¹★ A. Siciak,² E. S. G. de Almeida,¹ F. Vakili,^{1,3} A. Domiciano de Souza,¹
M. Fouché,² O. Lai¹,¹ D. Vernet,⁴ R. Kaiser² and W. Guerin¹2★

¹Laboratoire Lagrange, Observatoire de la Côte d'Azur, CNRS, Université Côte d'Azur, F-06304 Nice, France

²Institut de Physique de Nice, CNRS, Université Côte d'Azur, F-06560 Valbonne, France

³Department of Physics, Shahid Beheshti University, Shahid Shahriari Square, Tehran 19839 69411, Iran

⁴UMS Galilée, Observatoire de la Côte d'Azur, CNRS, Université Côte d'Azur, F-06304 Nice, France

Accepted 2020 February 25. Received 2020 February 20; in original form 2019 December 10

ABSTRACT

We present intensity interferometry of the luminous blue variable P Cyg in the light of its H α emission performed with 1 m-class telescopes. We compare the measured visibility points to synthesized interferometric data based on the CMFGEN physical modelling of a high-resolution spectrum of P Cyg recorded almost simultaneously with our interferometry data. Tuning the stellar parameters of P Cyg and its H α linear diameter, we estimate the distance of P Cyg as 1.56 ± 0.25 kpc, which is compatible within 1σ with 1.36 ± 0.24 kpc reported by the *Gaia* DR2 catalogue of parallaxes recently published. Both the values are significantly smaller than the canonic value of 1.80 ± 0.10 kpc usually adopted in literature. Our method used to calibrate the distance of P Cyg can apply to very massive and luminous stars both in our Galaxy and neighbouring galaxies, and can improve the so-called wind momentum–luminosity relation that potentially applies to calibrate cosmological candles in the local Universe.

Key words: techniques: interferometric – stars: distances – stars: massive – stars: winds, outflows.

1 INTRODUCTION

The purpose of this paper is to show that, even with its present limitations, intensity interferometry can provide new and useful information on the fundamental stellar parameters and the mechanisms that govern the physics of massive stars and their mass-loss: more precisely on the luminous blue variable (LBV) archetype star P Cyg (HD193237) (Najarro 2001).

Intensity interferometry (hereafter II), as imagined by Hanbury Brown and Twiss in the 1950s (Hanbury Brown & Twiss 1956), culminated in the early 1970s by providing the first systematic catalogue of the angular diameter (in the visible) of 32 stars observed with the Narrabri 200 m-baseline interferometer (Hanbury Brown, Davis & Allen 1974). In addition to this, Hanbury Brown and his team explored different phenomenological effects, such as flattening of rapidly rotating stars, close binary stars and their parameters (Herbison–Evans et al. 1971), scattering effects occurring in the massive wind of blue supergiants and emission carbon line extent of a Wolf–Rayet star (Hanbury Brown et al. 1970). An extensive review of these experiments is described by Hanbury Brown in his book on the Narrabri interferometer (Hanbury Brown 1974), which stopped

operating in the early seventies. More contemporary, Cherenkov arrays of telescopes have been considered to revive II with much larger collectors in size and much longer baselines, aiming at stellar surface imaging by aperture synthesis interferometry on a much broader class of targets (Dravins 2016; Kieda et al. 2019a, b). Successful demonstrations of II with Cherenkov telescopes have been reported very recently (Matthews & LeBohec 2019; Acciari et al. 2020). In this context, our group started a number of pilot experiments in 2016 using two modest 1 m size optical telescopes. After the successful observations of temporal and spatial bunching on a few bright stars at 780 nm (Guérin et al. 2017, 2018; Lai et al. 2018; Rivet et al. 2018), we decided to observe emission-line stars. The LBV star P Cyg is a very good candidate due to its strong H and He emission lines.

In the following, we shortly discuss the photometric and spectral variability of P Cyg, especially for its H α line that is relevant to our II observations. We then summarize the three long-baseline interferometric studies available in the literature that shed light on the present results.

Along with η Car, P Cyg is the brightest LBV star in the sky, having undergone a giant eruption in the 17th century and for which evolutionary change has been recorded from its apparent magnitude by Lamers & de Groot (1992) over three centuries. More recently, P Cyg was studied by Markova et al. (2001) using *U*, *B*,

* E-mail: rivet@oca.eu (J-PR); william.guerin@inphyni.cnrs.fr (WG)

V photometry and H α emission, including equivalent width (EW) monitoring over 13.8 yr from 1985 to 1999. These authors find that P Cyg undergoes a slow 7.4 yr variation in its V magnitude, where the star becomes redder when it brightens, and vice versa. They also show that the H α EW changes in correlation with the photometric trend and conclude that the variable wind increases the photospheric radius while the effective temperature is decreasing. Markova et al. (2001) concluded that the wind mass-loss rate of P Cyg increased of ~ 19 per cent over a period of about 7 yr. This increase in mass-loss rate implies an apparent stellar radius (pseudo-photosphere) larger by ~ 7 per cent. Thus, angular diameter observations of this star also need to be monitored by spectrometry of the H α line and simultaneous photometry (Pollmann & Vollmann 2013) in order to correctly analyse and interpret the interferometric data. This work meets the H α spectroscopy criterion.

Milliarcsec (mas) resolution observations of P Cyg trace back to GI2T spectrally resolved interferometry based on visibility and differential phase of the H α emission line (Vakili et al. 1997). These quantities were determined as a function of the Doppler-shift across the H α line profile and gave the first angular diameter of P Cyg's envelope as well as a limit to its extent in He I line. In addition, the signature of an asymmetry in the wind of P Cyg was concluded from a differential phase occurring at the blue absorption component of the H α line. It is worth noting that Vakili et al. (1997) estimated the diameter of P Cyg in H α as 5.52 ± 0.47 mas assuming a simple equivalent uniform disc, without separating the star photosphere and its envelope emission. This single shot observation and study of P Cyg was followed in 1997 by adaptive optics imaging in the H α line through a 1 nm filter and in its continuum vicinity with a 1.5 m telescope, corresponding to 0.1 arcsec diffraction limit resolution (Chesneau et al. 2000). This adaptive optics imaging aimed at first to determine the large-scale extent of P Cyg's envelope as it had been previously witnessed by *Hubble Space Telescope* observations (Nota et al. 1995), and secondly, to detect, if possible, the propagation after 4 yr of the heterogeneities of P Cyg's wind detected by the GI2T. The latter expectation was roughly confirmed whilst it was also clearly confirmed that any high angular resolution observation of P Cyg should consider the central LBV engine, its mass-loss envelope out to thousands of stellar radii, even though dilution factor would make this a high-contrast imaging challenge.

P Cyg was then observed between 2005 and 2008 with the Navy Precision Optical Interferometer (NPOI) interferometer (Balan et al. 2010) with simultaneous spectroscopy to relate any angular diameter variation with the H α line profile and/or emission strength. These observations used a much broader filter than the above-mentioned studies and modelling of the envelope was conducted for the equivalent H α width emission using different circular shapes. Finally, the authors concluded that the data are best fitted with a double Gaussian structure of 5.64 ± 0.21 and 1.80 ± 0.13 mas for P Cyg's envelope. In addition, they found no asymmetry of the envelope and less than 10 per cent variation in size between 2005 and 2008. To make NPOI results comparable to previous GI2T measures, Balan et al. (2010) also considered the simple model of a uniform disc for P Cyg's emission envelope including indifferently the photosphere as well as its envelope. They found uniform disc angular diameters ranging from 8.4 to 10.2 mas on the seasonal observations between 2005 and 2008, a result that significantly differs from those by the GI2T single baseline data. Balan et al. finally concluded that this discrepancy might result from photospheric flux variability and opacity changes through the multiple wind layers of P Cyg.

More recent long baseline interferometry of P Cyg, covering the period of 2006–2010, has been reported by Richardson et al. (2013) using the CHARA interferometer at Mount Wilson. These observations were accompanied by simultaneous infrared (IR) photometry and spectroscopy to monitor any change in the angular size of P Cyg related to the activity at the base of the wind and its impact on eventual fine structures within the mass-loss. These observations differ from previous studies since they have been performed in the IR at 1.6 μm (*H* band), but can still compare to GI2T and NPOI observations. A first important issue of CHARA-MIRC conclusions consists of setting an angular diameter of 0.96 ± 0.02 mas for the wind component of P Cyg at its photospheric base with about 45 per cent of the *H*-band flux. This angular diameter is significantly larger than the 0.41 mas (Najarro, Hillier & Stahl 1997) that was adopted for P Cyg photospheric diameter used by the GI2T paper for instance (Vakili et al. 1997). Additionally, multiple baseline performed with CHARA-MIRC at two epochs in 2010 August and 2011 September were used by Richardson et al. (2013) to reconstruct an image of P Cyg from the Earth rotation synthesis data. Furthermore, these authors used the non-LTE radiative transfer code CMFGEN (spherically symmetric wind) to compare the observed visibility curve of P Cyg to the predicted one. Whilst no significant departure was found from circular symmetry, Richardson et al. concluded that P Cyg is best explained by a two-component model consisting of a uniform disc photosphere unresolved by CHARA at its 0.56 mas resolution in the *H* band and a 0.96 ± 0.02 mas Gaussian halo emitted from the inner regions of the stellar wind of P Cyg. The difference between this result and the 5.5 mas size found by Vakili et al. (1997) can be explained by a larger wind-emitting volume because of its higher optical depth in H α diameter. Besides these interferometric studies, such a spherically symmetric wind around P Cyg is also supported by H α spectroscopy (Richardson et al. 2011).

Due to their limited spatial frequency content, interferometric observations require a model for their interpretation and as shown by the review of these high-resolution results, models that introduce the least amount of a priori information (e.g. uniform disc or Gaussian profile) are usually chosen, yielding limited information, such as the apparent diameter. For our II campaign reported herein, we chose an alternative approach, using the best physical parameters of P Cyg from the CMFGEN code (Hillier & Miller 1998) that reproduce high-resolution spectrometry of the star obtained quasi-simultaneously to our II campaign, to compute the intensity distribution (and its associated visibility) of P Cyg in the emission line, which can be directly compared to our measured visibilities. This additional information constrains the physical size of P Cyg and allows us to estimate the only remaining free parameter, which is its distance. We believe that the association of physical modelling of stellar parameters of LBVs from spectroscopy with interferometric observations has the potential to be a powerful method to refine the first few rungs of the cosmological distance ladder.

The paper is organized as follows. In the next section, we describe our experimental setup and the observing conditions. In Section 3, we show the results of our single-telescope observations, which can be used to calibrate the visibility at zero baseline. This also corresponds to measuring the *temporal* intensity correlation, related to the width of the spectral line. Then, in Section 4, we present the *spatial* intensity correlation measurements performed with two telescopes separated by 15 m. We observe a reduction of the contrast of the correlation, demonstrating a partial resolution of the emitting envelope. Finally, in Section 5, we present our CMFGEN best model to compare the expected and the measured visibilities using the star

distance as the only free parameter. We then conclude and draw some perspectives.

2 EXPERIMENTAL SETUP

2.1 Principle

Stellar intensity interferometry is based on the measurement of the temporal and spatial correlations between the fluctuations of light collected by two telescopes distant by r . The quantity of interest is the intensity correlation function given by

$$g^{(2)}(r, \tau) = \frac{\langle I(t, 0)I(t + \tau, r) \rangle}{\langle I(t, 0) \rangle \langle I(t, r) \rangle}, \quad (1)$$

where the brackets denote the average over time t . For a classical (non-quantum) source of light, correlations are maximum at zero delay ($\tau = 0$) and zero separation ($r = 0$). For a ‘chaotic’ (incoherent) source, Gaussian statistics on the field fluctuations leads to $g^{(2)}(0, 0) = 2$. On the contrary, at large separation r and delay τ , the fluctuations become uncorrelated and the $g^{(2)}(\tau, r)$ tends to 1. The decrease from 2 to 1 of the $g^{(2)}$ function with the time delay τ is related to the temporal coherence time τ_c , which is inversely proportional to the spectrum width. The decrease of the $g^{(2)}$ function with the separation r is related to the spatial coherence of the source, i.e. the usual ‘visibility’ $V(r)$ measured in direct (amplitude) stellar interferometry (Labeyrie, Lipson & Nisenson 2006).

We can therefore use the following equation, valid for chaotic light (Loudon 1973),

$$g^{(2)}(r, \tau) = 1 + |V(r)|^2 |g^{(1)}(\tau)|^2, \quad (2)$$

where $g^{(1)}(\tau)$ is the first-order (field–field) temporal correlation function, related to the optical spectrum $S(\omega)$ by a Fourier transform (Wiener–Khinchin theorem),

$$S(\omega) \propto \mathfrak{F}[g^{(1)}(\tau)]. \quad (3)$$

Similarly, the visibility is related to the brightness distribution of the source by a Fourier transform, like in direct interferometry. Note that we suppose here that the detected light is polarized, otherwise it amounts at reducing the visibility by a factor 2.

In practice, the coherence time τ_c , which gives the width of the $g^{(2)}(\tau)$ function, is often too short to be resolved by the electronic detection chain, whose finite timing resolution τ_{el} introduces an uncertainty on the arrival time of each photon. In that case, the measured ‘bunching peak’ $g^{(2)}(\tau)$ has a width given by $\tau_{el} \gg \tau_c$, and a height, which we call the contrast $C = g^{(2)}(0, 0) - 1$, reduced from $C = 1$ to $C \sim \tau_c/\tau_{el} \ll 1$. This contrast has to be calibrated as it corresponds to the maximum (zero-baseline) squared visibility.

2.2 Instrumental setup

Our experimental setup has been described in detail in previous publications (Guerin et al. 2017, 2018). In short, it consists first in a coupling assembly (CA) set at the focus of the telescope, which allows injecting light into a multimode fiber (MMF) of diameter 100 μm . Then, we use single-photon avalanche photodiodes (SPADs) to detect light in the photon-counting regime and digital electronics in order to compute the $g^{(2)}$ function. The SPADs have a timing jitter of $\simeq 450$ ps each, which gives a temporal resolution $\tau_{el} \simeq \sqrt{2} \times 450 \simeq 640$ ps for the correlation function.

Compared to our previous experiments (Guerin et al. 2017, 2018), we have modified the CA in order to collimate the optical beam before its transmission through the filter, in order to have a more

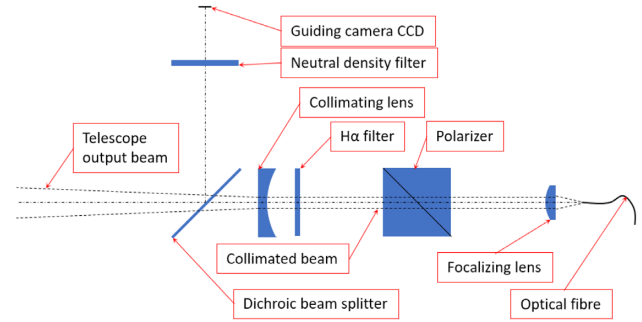


Figure 1. Scheme of the coupling assembly set at the telescope focus in order to perform spectral and polarization filtering, and injection into an MMF, which transports the light to the detection chain. The H α 1 nm filter operates in nominal conditions, i.e. on a collimated beam.

precise control on the filter width and central wavelength. This is indeed more critical when one wants to select a specific spectral line. The new CA is described in Fig. 1. As previously, there is first a dichroic mirror that reflects part of the light to a guiding camera. The transmitted light is then collimated by a diverging lens (focal length $f = -50$ mm). The collimated beam goes through a filter of width $\Delta\lambda = 1$ nm (FWHM), centred at $\lambda = 656.3$ nm (H α line), with a peak transmission of 95 percent, and then to a polarizer, before being focused by a converging lens ($f = 20$ mm) on the fiber tip.

The observations have been performed at the C2PU facility at the Plateau de Calern site of Observatoire de la Côte d’Azur (OCA). The two, quasi-identical, telescopes have a diameter of 1.04 m with an $F/12.5$ aperture in a Cassegrain configuration. With the CA, the total equivalent focal length is 5.2 m. The two CAs are identical and we have checked, using an artificial star in the lab, that they produce identical correlation functions.

2.3 Observation conditions

The observations of P Cyg were performed in 2018 August over eight nights. The main characteristics of the observing runs are summarized in Table 1.

The observing time was used in two configurations. In the first one, we used only one telescope (always the same), in order to measure the temporal intensity correlation function $g^{(2)}(\tau)$ at zero baseline, as in Guerin et al. (2017). In principle, the contrast of the correlation function allows calibrating the visibility measured with two telescopes, which is the second configuration we used, as in Guerin et al. (2018).

3 TEMPORAL INTENSITY CORRELATION

Performing intensity interferometry on an emission line puts an important constraint on the measurement procedure. Indeed, since the $g^{(2)}$ function depends on the spectrum, it is not possible to use a distant, unresolved star as calibrator for the visibility measurement, because this calibrator would have a different spectrum from the science target. For the same reason, it is not possible to calibrate the visibility with an artificial star in the laboratory, as in Guerin et al. (2018). As a consequence, there are two possibilities. The first is to measure the actual spectrum, use equations (2) and (3) and, knowing the temporal resolution of the detection chain, infer the expected bunching contrast for maximum visibility. The second is to perform a temporal intensity correlation measurement with

Table 1. Main circumstances for the observing runs performed on P Cyg over eight nights. ‘Configuration’ indicates the performed experiment, either $g^{(2)}(\tau)$ (single-telescope experiment) or $g^{(2)}(r)$ (two-telescope experiment). Begin and end dates are in UTC (*ISO 8601* compact format). a is the airmass range. The seeing information is provided by the GDIMM instrument (Ziad et al. 2012; Aristidi et al. 2014) of the CATS station (Calern Atmospheric Turbulence Station) (Chabé et al. 2016). The numbers are given as median values over the whole nights.

Configuration	Begin	End	a	Seeing (arcsec)
$g^{(2)}(\tau)$	20180801T2102Z	20180802T0111Z	1.00–1.10	1.29
$g^{(2)}(\tau)$	20180802T2025Z	20180803T0154Z	1.00–1.18	0.66
$g^{(2)}(\tau)$	20180804T0040Z	20180804T0309Z	1.06–1.44	1.10
$g^{(2)}(\tau)$	20180806T1943Z	20180806T2205Z	1.02–1.22	0.56
$g^{(2)}(r)$	20180807T0054Z	20180807T0356Z	1.10–1.79	0.56
$g^{(2)}(r)$	20180807T2212Z	20180808T0353Z	1.00–1.80	0.60
$g^{(2)}(r)$	20180808T2011Z	20180809T0350Z	1.00–1.81	0.74
$g^{(2)}(r)$	20180809T2311Z	20180810T0332Z	1.01–1.71	n.a.
$g^{(2)}(r)$	20180810T1940Z	20180811T0327Z	1.00–1.70	1.19

a single telescope, as in Guerin et al. (2017), which serves as the zero-baseline visibility calibration. We do both in the following.

3.1 $H\alpha$ spectrum of P Cyg and expected temporal correlation

Thanks to its strong $H\alpha$ emission line, P Cyg is a classical target for amateur spectroscopy, which enabled us to obtain a spectrum recorded only a few days after our observations in the ARAS spectral data base (ARAS 2018). This spectrum (resolution: 9000, 4053 Å < λ < 7763 Å) was recorded by J. Guarro i Fló on 2018 August 14.

We show in Fig. 2(a) the measured spectrum centred on the $H\alpha$ line, as well as the transmission spectrum of the 1 nm filter set in the CA, as provided by the manufacturer. Multiplying the two spectra, we obtain the spectrum of the detected light (Fig. 2b). Note that at this scale, the variation with the wavelength of the other elements (reflectivity of mirrors, transmission of the atmosphere and of the dichroic plate, quantum efficiency of the detectors) is negligible.

From the filtered spectrum, one can numerically compute the $g^{(2)}(\tau)$ function by using equations (2) and (3). This theoretical $g^{(2)}(\tau)$ function has a 100 per cent contrast and a width on the order of the picosecond (Fig. 2c). Experimentally we measure this function convolved by the response of the instrument, dominated by the jitter of the SPADs. The resulting expected $g^{(2)}(\tau)$ function is depicted in Fig. 2(d). Note the change of scales compared to Fig. 2(c). The expected contrast is now $C_0 = 3.8 \times 10^{-3}$.

3.2 Measured temporal correlation

We present in this section the measurement of $g^{(2)}(\tau)$ with a single telescope observing P Cyg. In this configuration the flux collected by the telescope is separated into two SPADs in order to overcome the dead time of the detectors (Guerin et al. 2017). This leads to some spurious correlations due to optical and electronic cross-talk between the detectors. These spurious correlations have to be characterized with a white source, for which the expected $g^{(2)}(\tau)$ function is flat, and then removed from the signal (Guerin et al. 2017). The ‘white’ signal has been measured in the lab after the observing run with a similar count rate.

The count rate was in average 3.8×10^5 counts per second (hereafter cps) per detector. The total observation time on P Cyg was 14 h over four nights (Table 1). The obtained $g^{(2)}(\tau)$ functions are shown in Fig. 3, with the direct measurements (P Cyg and

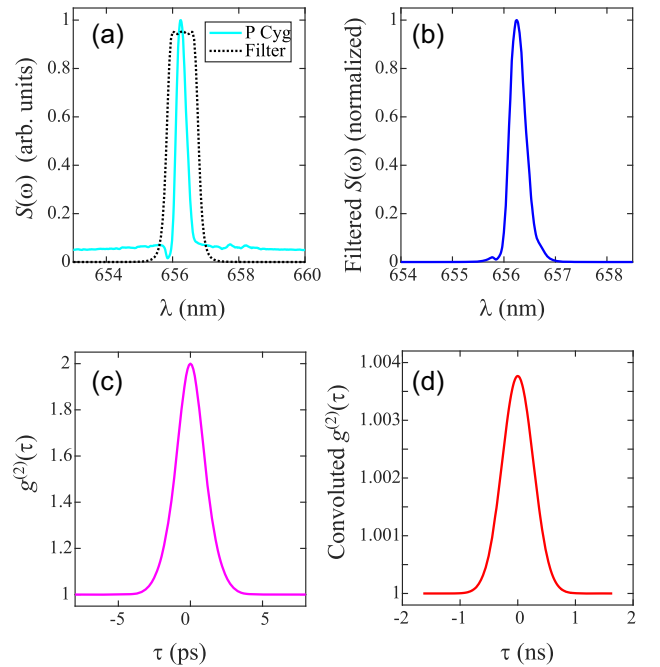


Figure 2. Spectrum and $g^{(2)}(\tau)$ function. (a) Spectrum of P Cyg zoomed-in on the $H\alpha$ emission line and transmission spectrum T of the filter (simulations provided by the manufacturer). (b) Filtered spectrum computed by multiplying the spectra of the star and of the filter. (c) Computed $g^{(2)}(\tau)$ from the filtered spectrum using equations (2) and (3) and supposing maximum visibility. (d) Convolved $g^{(2)}(\tau)$ with the timing resolution of our acquisition chain. We have taken a Gaussian jitter of 450 ps (FWHM) per detector.

‘white’) in panel (a), and the corrected correlation function (after division by the ‘white’ signal to remove the spurious correlations) in panel (b).

The height of the bunching peak, defined as the maximum of the peak, is $C = (4.8 \pm 0.9) \times 10^{-3}$, in fair agreement with the expectation (Fig. 2d) given the uncertainty, estimated from the *rms* noise in the flat areas of the $g^{(2)}(\tau)$ function. Note that a small systematic effect may also be present due to an imperfect removing of spurious correlations and explain a slightly higher value than

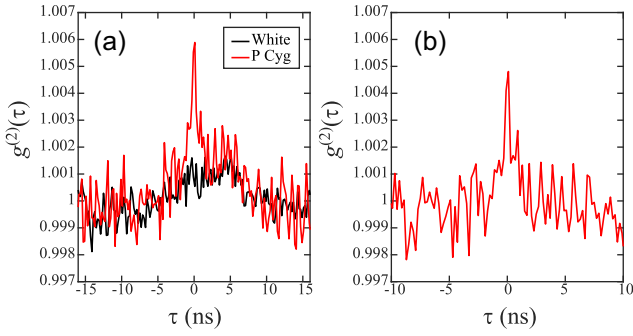


Figure 3. Measured temporal intensity correlation function. (a) Signal on the star and ‘white’ acquired in the lab. (b) $g^{(2)}(\tau)$ after removing the spurious correlations. The binning is 200 ps.

expected ($C_0 = 3.8 \times 10^{-3}$). For this reason, in Section 5.3.2, we will use the computed C_0 value to normalize the visibility data.

Besides providing a zero-baseline calibration for the spatial correlation measurement detailed in the next section, another important aspect of this temporal correlation experiment on an emission line is that the resulting $g^{(2)}(\tau)$ function provides information on the emission line itself via the contrast $C \sim \tau_c/\tau_{el}$. Knowing the response function of the instrument (and thus τ_{el}) and with some assumption on the shape of the line, we can deduce the width $\Delta\lambda$ of the emission line via $\tau_c = \lambda_0^2/c\Delta\lambda$. Here, approximating the line shape by a Gaussian, the temporal correlation measurement corresponds to a line width of FWHM $\Delta\lambda \simeq 0.3$ nm, in agreement with the actual spectrum. Note also that the contrast of the $g^{(2)}(\tau)$ function measured here is significantly higher than what it would be if it were determined by the 1-nm filter (the contrast would be $\sim 1.4 \times 10^{-3}$), which would be the case in the continuum (Guerin et al. 2017). This ‘intensity-correlation spectroscopy’ technique (Goldberger, Lewis & Watson 1966; Phillips, Kleinman & Davis 1967; Tan & Kurtsiefer 2017) would be relevant for exotic, very narrow lines, that would be hard to characterize with standard spectroscopic techniques. With intensity correlation, the narrower the line, the higher the contrast.

4 SPATIAL INTENSITY CORRELATION

We now turn to the spatial correlation experiment, performed with two nearly identical telescopes separated by 15 m on an East–West basis (Guerin et al. 2018). The flux collected at each telescope is filtered and coupled to the MMF with an identical CA and detected by a SPAD. The count rate per detector was in average 8.8×10^5 cps with a total acquisition time of 27 h over five nights (Table 1).

The cross-correlation between the arrival time of photons at the two detectors is computed in real time by the TDC using exposure times of 10 s. After the acquisition, the $g^{(2)}(\tau)$ functions are averaged together after being time shifted from the computed sidereal optical delay between the telescopes (Guerin et al. 2018).

Since the projected baseline also changes due to the Earth’s rotation, several partial averaging of the data as a function of the computed baseline allow us to obtain several $g^{(2)}(\tau)$ functions for different projected baselines. Here, the limited signal-to-noise ratio of the data allows us to obtain only two significant curves, for projected baseline $9.5 < r < 12$ m and $12 < r < 15$ corresponding, respectively, to averaged baselines of 10.7 and 13.9 m. These measurements are reported in Fig. 4(b,c), along with the single-telescope correlation function (Figs 3b and 4a) for comparison.

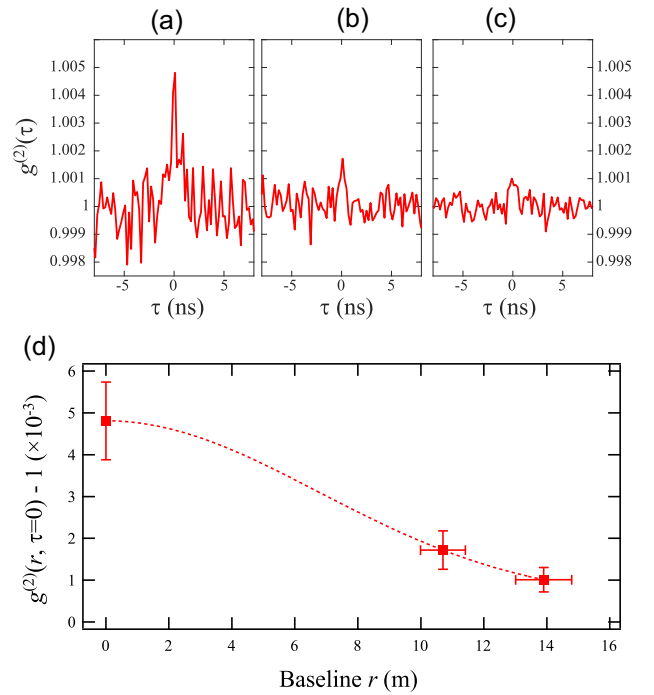


Figure 4. Top row, experimental curves $g^{(2)}(\tau)$ for different baselines: (a) single telescope experiment; (b) two-telescope data for all baselines $r < 12$ m, the average baseline is $r = 10.7$ m; (c) the same for $r > 12$ m, average baseline $r = 13.9$ m. (d) Contrast of the $g^{(2)}(\tau)$ function as a function of the baseline. The vertical error bars indicate the rms noise and the horizontal error bars the rms width of the distribution of projected baselines during the integration time, neglecting the aperture of the telescopes. The line is only a guide to the eye.

The effect of the partial resolution of P Cyg’s emitting envelope is well visible via the contrast of the $g^{(2)}(\tau)$ function, which is much smaller. This contrast, plotted as a function of the baseline, gives the spatial intensity correlation function $g^{(2)}(r, \tau = 0)$, plotted in Fig. 4(d). This contrast gives the squared visibility $|V(r)|^2$ (equation 2) after proper normalization, such that $|V(0)|^2 = 1$ at zero baseline. We can use two normalization methods. The most direct method is to divide the contrast measured at $r \neq 0$ by the contrast measured with a single telescope ($r \approx 0$). However, the statistical noise as well as any systematic noise due to residual spurious correlations affect the results. The other method is to make use of the measured spectrum and, knowing the temporal resolution of the detection chain, compute the expected zero-baseline contrast, see Fig. 2(d). This method introduces much less noise but relies on the good characterization of the instrumental setup (filter and temporal resolution), which can be done in the lab. We show the results of the two methods in Table 2 and use the spectrum-based method in Fig. 7 at the end of the next section.

5 MODEL OF P CYG AND COMPARISON WITH THE EXPERIMENT

5.1 Atmosphere models: code CMFGEN

In order to analyse the visibility curve of P Cyg, we used state-of-the-art atmosphere models computed with the non-LTE (local thermodynamic equilibrium) radiative transfer code CMFGEN (Hillier & Miller 1998). It solves the coupled problem of the radiative transfer, statistical, and radiative equilibrium equations

Table 2. Summary of the observation results. r is the average projected baseline (its uncertainty is the rms width of the baseline distribution), T is the total integration time, F is the detected count rate per detector averaged over the total integration time. It is roughly twice lower in the single-telescope experiment because the flux has to be divided into two detectors. The contrast $C = g^{(2)}(0) - 1$ is the value of the correlation at zero delay given by the amplitude of the bunching peak, its uncertainty is the rms noise on the data. The two last columns correspond to the two possible normalization methods ($C_0 = 3.8 \times 10^{-3}$ is the zero-baseline contrast expected from the measured spectrum).

r (m)	T (h)	F ($\times 10^3$ cps)	$C(r)$ ($\times 10^{-3}$)	$C(r)/C(0)$	$C(r)/C_0$
0	14.5	380	4.80 ± 0.93	1	1.26 ± 0.24
10.7 ± 0.7	8	826	1.72 ± 0.46	0.36 ± 0.12	0.45 ± 0.12
13.9 ± 0.9	19	905	1.01 ± 0.29	0.21 ± 0.07	0.27 ± 0.08

in a spherically symmetric outflow. CMFGEN has been widely used in the literature to analyse central stars of planetary nebula (Marcolino et al. 2007), OB-type (Bouret et al. 2012), LBV (Groh et al. 2012), Wolf-Rayet stars (Tramper et al. 2013), and also core-collapse supernovae (Dessart et al. 2016). It includes, for example, effects of line-blanketing, wind clumping, and Auger ionization by X-rays, thus providing realistic spectra for hot stars from the ultraviolet (UV) to the mid-IR.

The code requires an initial estimate of the hydrostatic structure. For this purpose, we used the BSTAR2006 (Lanz & Hubeny 2007) grid of non-LTE plane-parallel models calculated with the code TLUSTY (Hubeny & Lanz 1995). This grid provides pure-photospheric models with effective temperature $15\,000\text{ K} \leq T_{\text{eff}} \leq 30\,000\text{ K}$ and surface gravity $1.75 \leq \log(g) \leq 3.00$. Up to date, CMFGEN does not allow to calculate hydrodynamically self-consistent models, thus the wind velocity needs to be parametrized. For the wind, we employed a standard β velocity law

$$v(r) = v_{\infty} \left(1 - \frac{R_{\star}}{r}\right)^{\beta}, \quad (4)$$

where R_{\star} is the stellar radius and v_{∞} is the wind terminal velocity. The wind velocity structure is smoothly connected to the hydrostatic structure just above the sonic point.

Clumping was included by default in the models. In CMFGEN, a volume filling factor is used to parametrize the effect of clumping (microclumping approximation) in the wind density structure as follows,

$$f(r) = f_{\infty} + (1 - f_{\infty})e^{-\frac{v(r)}{v_{\text{initial}}}}, \quad (5)$$

where v_{initial} is the onset velocity of clumping, corresponding to the distance in the wind where inhomogeneity starts to be relevant, and f_{∞} is the filling factor value at $r \rightarrow \infty$. Thus, the density structure is parametrized, including the factor $f(r)$, as follows (\dot{M} is the mass-loss rate):

$$\rho(r) = \frac{\dot{M}}{4\pi r^2 v(r) f(r)}. \quad (6)$$

We did not include Auger ionization by X-rays in the models since P Cyg is known to present a very low X-ray luminosity. The X-ray survey on Galactic LBVs of Nazé, Rauw & Hutsemékers (2012) could just provide an upper limit of $\log(L_X/L_{\text{BOL}}) < -9.4$ for P Cyg, including this star in their sub-sample for non-detection of X-ray emission. For comparison, O-type stars typically present $\log(L_X/L_{\text{BOL}}) \sim -7.0$ (Rauw et al. 2015).

Table 3. Number of levels, super-levels, and bound-bound transitions for each atomic species included in our CMFGEN reference model.

Ion	Full-levels	Super-levels	b-b transitions
H I	30	30	435
He I	69	69	905
He II	30	30	435
C II	100	44	1064
C III	99	99	5528
C IV	64	64	1446
N I	104	44	855
N II	144	62	1401
N III	287	57	6223
O I	90	35	615
O II	123	54	1375
O III	104	36	761
Mg II	44	36	348
Al II	44	26	171
Al III	65	21	1452
Si II	62	34	365
Si III	50	50	232
Si IV	66	66	1090
S II	88	27	796
S III	41	21	177
S IV	92	37	708
Ca II	19	12	65
Fe II	510	111	7357
Fe III	607	65	5482
Fe IV	1000	100	25 241
Fe V	1000	139	25 173

5.2 Stellar and wind parameters

CMFGEN is well suited for analysing P Cyg since previous spectroscopic and interferometric studies showed that its wind is almost spherical (see Section 1). Following the approach of Richardson et al. (2013), we analysed CMFGEN models based on the stellar and wind parameters derived by Najarro (2001). Also using CMFGEN, Najarro (2001) performed a detailed multiwavelength spectroscopic analysis of P Cyg from the UV up to the mid-IR region.

In Table 3, we show the atomic species included in the models together with the number of energy levels¹ and bound-bound transitions. These model atoms are similar to those used by Najarro (2001), providing a rather robust model to reproduce the spectrum of

¹Super-level approach (grouping of energy levels) is introduced in CMFGEN for a faster computational treatment. See Hillier & Miller (1998) for further details.

Table 4. Summary of the main stellar and wind parameters of our CMFGEN reference model.

L_* (L_\odot)	610 000
T_{eff} (K)	18 700
$\log g$	2.25
R_* (R_\odot)	75
M_* (M_\odot)	37
\dot{M} ($M_\odot \text{ yr}^{-1}$)	4.0×10^{-5}
f_∞	0.5
v_∞ (km s^{-1})	185
β	2.3

P Cyg in the UV, visible, and IR regions. We also assumed the same chemical abundances as Najarro (2001). Since P Cyg has ended the hydrogen core-burning phase (Langer et al. 1994), the assumption of solar chemical abundances (Z_\odot) must overestimate the intensity in the $H\alpha$ line (considering a fixed set of physical parameters in the model). Most important for the comparison with the observed visible spectrum, the abundances of H, He, C, N, and O were set to 0.66, 1.86, 0.31, 6.5, and 0.18 Z_\odot , respectively.

In Table 4, we present the physical stellar and wind parameters of our CMFGEN reference model. These are the main parameters to define the atmosphere model: stellar luminosity (L_*), effective temperature (T_{eff}), gravity surface acceleration ($\log g$), radius (R_*), mass (M_*), mass-loss rate (\dot{M}), wind clumping factor (f_∞), terminal velocity (v_∞), and the wind velocity law exponent (β). Except for the surface gravity $\log g$, all the other parameters are equal or close to the ones derived by Najarro (2001). We set $\beta = 2.3$ in our reference model due to numerical issues with $\beta = 2.5$ (Najarro 2001). As will be discussed in Section 5.3.1, we set $\dot{M} = 4.0 \times 10^{-5} M_\odot \text{ yr}^{-1}$ instead of $\dot{M} = 2.4 \times 10^{-5} M_\odot \text{ yr}^{-1}$ (Najarro 2001). Instead of $\log g = 1.20$, as in Najarro (2001), we assumed $\log g = 2.25$ since this is the lower value of $\log g$ in the TLUSTY models, according to the used effective temperature ($T_{\text{eff}} = 18\,700$ K). Nevertheless, as pointed out by de Jager (2001), the determination of this parameter for P Cyg is quite uncertain, with a discrepancy up to a factor of 10 from different works in the literature. For example, Pauldrach & Puls (1990) derived 2.04 for the surface gravity of P Cyg.

5.3 Results of the simulations

5.3.1 Comparison to spectroscopic data

Before analysing our interferometric data, we compare, in Fig. 5, the synthetic spectrum calculated from our CMFGEN reference model (Tables 3 and 4) to the observed spectrum of P Cyg in the visible region, obtained from the ARAS Spectral Data Base. This comparison allows a physical validation, in terms of the spectroscopic appearance, of our adopted atmosphere model. Due to the effect of radial velocity, the observed spectrum was shifted in wavelength in order to match the synthetic spectrum.

Fig. 5 shows that our reference model is able to reproduce well the observed visible spectrum of P Cyg, showing intense P Cygni profiles in the Balmer and helium lines. Overall, the weak spectral features due to metals, such as C II $\lambda\lambda 6580$ and 6585 (close to $H\alpha$), are also fairly reproduced. Initially, we assumed the same value for the mass-loss rate as Najarro (2001), i.e. $\dot{M} = 2.4 \times 10^{-5} M_\odot \text{ yr}^{-1}$ with $f_\infty = 0.5$. Since the emission component of $H\alpha$ is highly sensitive to the variation of the mass-loss rate, we followed the simplest approach of only varying this fundamental parameter of the wind. The Balmer lines, in particular $H\alpha$, seems to be better

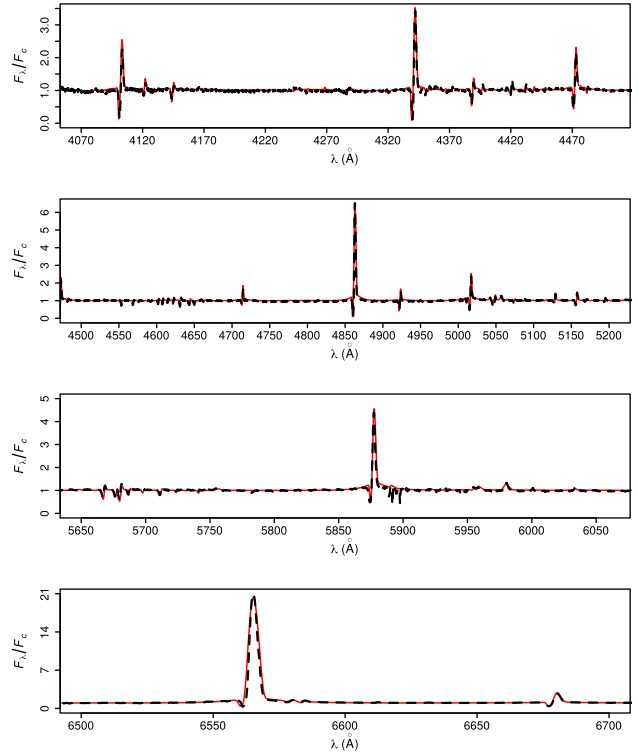


Figure 5. Comparison between the observed spectrum of P Cyg (black dashes) and the spectrum of the CMFGEN reference model (red line) used to analyse the interferometric data. The mass-loss rate of our reference model ($\dot{M} = 4.0 \times 10^{-5} M_\odot \text{ yr}^{-1}$) is close to the one derived by Najarro (2001) of $\dot{M} = 2.4 \times 10^{-5} M_\odot \text{ yr}^{-1}$. This model provides a fairly reasonable overall match to the spectrum.

reproduced using a slightly higher value for the mass-loss rate ($\dot{M} = 4.0 \times 10^{-5} M_\odot \text{ yr}^{-1}$ with $f_\infty = 0.5$). This difference is encompassed by the typical uncertainties on \dot{M} found from spectroscopic analysis of massive stars in literature (see e.g. de Almeida et al. 2019). In addition, it is very unlikely to have a physical cause, as this difference is much larger than the mass-loss rate variability of P Cyg (Markova et al. 2001).

It is beyond the scope of this paper to derive the stellar and wind parameters of P Cyg, as performed by Najarro (2001). Nevertheless, the ability of our CMFGEN reference model to reproduce the visible spectroscopic appearance of P Cyg makes us confident to adopt this model in order to interpret our II observed visibilities.

5.3.2 Comparison to normalized II visibilities

To compare the reference CMFGEN model of P Cyg to the normalized II visibilities, we need to compute the effective radial intensity profile $I_{\text{eff}}(\varpi)$ corresponding to the observed spectral region within the $H\alpha$ filter,

$$I_{\text{eff}}(\varpi) = \frac{\int I(\lambda, \varpi) T(\lambda) d\lambda}{\int T(\lambda) d\lambda}, \quad (7)$$

where $I(\lambda, \varpi)$ is the 1D monochromatic specific intensity, provided by CMFGEN, as a function of the radial coordinate ϖ (impact parameter). The effective wavelength λ_{eff} corresponding to I_{eff} for the reference CMFGEN model is given by

$$\lambda_{\text{eff}} = \frac{\int \lambda F(\lambda) T(\lambda) d\lambda}{\int F(\lambda) T(\lambda) d\lambda} = 6562.9 \text{ \AA}. \quad (8)$$

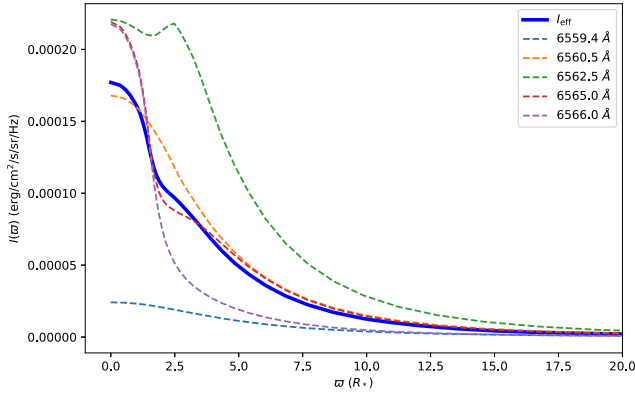


Figure 6. Effective H α radial profile $I_{\text{eff}}(\varpi)$ (equation 7) of the reference CMFGEN model (thick solid blue) as a function of the radial coordinate ϖ given in units of the stellar photospheric radius (clipped at $20R_*$ for better visualization). For comparison, the dashed curves show the model specific intensity profiles $I(\lambda, \varpi)$ for selected wavelengths within the H α emission line and in the region where the filter transmission is high. In particular, we show the profile at $\lambda = 6562.5 \text{ \AA}$, nearly at the maximum of the model H α spectrum. We note that these selected profiles were not multiplied by the filter transmission.

As before, $F(\lambda)$ and $T(\lambda)$ are the observed spectrum and the transmission filter, respectively (see Fig. 2). The effective H α radial profile $I_{\text{eff}}(\varpi)$ of the reference CMFGEN model is shown in Fig. 6, together with radial profiles at some selected wavelengths for comparison.

The normalized squared visibility $|V|^2$ (or simply V^2) associated with the reference CMFGEN model is computed, thanks to the Hankel transform of $I_{\text{eff}}(\varpi)$, normalized by the corresponding spectral flux, as

$$V^2 = \left| \frac{\int_0^\infty I_{\text{eff}}(\rho) J_0(2\pi\rho q) 2\pi\rho d\rho}{\int_0^\infty I_{\text{eff}}(\rho) 2\pi\rho d\rho} \right|^2, \quad (9)$$

where J_0 is the zeroth-order Bessel function of the first kind, $\rho = \varpi/d$ is the radial angular coordinate, with d being the distance to the target. The radial spatial frequency coordinate associated with ρ is $q = r/\lambda_{\text{eff}}$, i.e. the II average projected baseline r divided by the effective wavelength of the observations λ_{eff} . The Hankel transform is used here because of the circular symmetry of the model.

To interpret the II observations, we used the above equations to compute the V^2 corresponding to our reference CMFGEN model, which we assume to be a *bona fide* representation of P Cyg, since it well reproduces the observed visible spectrum, as shown in the previous subsection. Under this assumption, the only remaining free parameter is the distance d . We have thus used a PYTHON-SCIPY non-linear least-squares routine to fit the reference model V^2 to our II data, which allowed us to estimate the distance to P Cyg as $d = 1.56 \pm 0.25 \text{ kpc}$. The fit has been performed on the visibility data normalized by the zero-baseline visibility computed from the measured spectrum (Fig. 2d and Table 2), as those data are less subjected to spurious correlations than the measured single-telescope correlation function. The latter has thus not been used. The observed and best-fitting model V^2 is shown in Fig. 7. These results and the interpretation of the measured d are discussed in the following section.

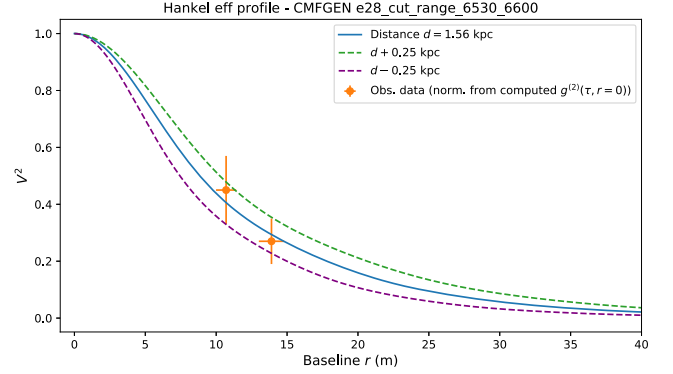


Figure 7. The data points are the measured squared visibility (Section 4) normalized by the contrast computed from the measured spectrum (Fig. 2d). They are fitted (solid blue line) using equation (9) with the distance d to P Cyg as the only free parameter (further details in the text). The curves correspond to the best-fitting d (solid) and associated $\pm 1\sigma$ uncertainties (dashed).

6 DISCUSSION AND CONCLUSION

P Cyg, together with η Car, are the brightest and most studied LBV stars for their spectrometric and photometric observational aspects, which have largely served to determine their physical properties (Najarro 2001). More recently, high angular resolution data, especially from long-baseline interferometry, have shed a new light on the fine spatial details of their mass-loss and geometries in general (Weigelt et al. 2007). As for P Cyg, GI2T, NPOI, and CHARA interferometers provided valuable estimates of the star parameters at the level of mas or a few mas angular resolutions. Although their results agree qualitatively, the numbers differ on the extent of the H α emitting envelope, for instance, which might be due to the variability of P Cyg on time-scales of a few months to year.

The method to determine the extent of P Cyg has often used analytical models such as uniform, limb-darkened discs or multiple Gaussians, whilst authors adopt distance values from different techniques, e.g. O–B association membership (Lamers, de Groot & Cassatella 1983; Turner et al. 2001), to interpret measured visibility points. The distance controversy for P Cyg is well known, with distances determined from $\sim 1.2 \text{ kpc}$ up to 2.3 kpc (see e.g. table 1 of Turner et al. 2001). For instance, CHARA studies (Richardson et al. 2013) adopted a 1.7 kpc distance of P Cyg to match synthetic visibilities based on the CMFGEN stellar atmospheric model and basic parameters (Najarro 2001) to their observed visibilities. The more accurate distance for P Cyg, $d_G = 1.36 \pm 0.24 \text{ kpc}$, from the *Gaia* global astrometry mission and its second data release DR2 (Gaia Collaboration et al. 2018), could also be used. However, *Gaia* has been designed for sources fainter than 11th magnitude in the visible, where the parallax determination is limited by the photon noise. P Cyg has a visual magnitude of 4.5, which is too bright for the normal scanning operation at the focal detector of *Gaia* (Mignard, private communication). Therefore, the question of the exact parallax of P Cyg remains a real issue.

In this context, we have followed a different route by fixing the linear size of P Cyg in agreement with detailed multi wavelength spectroscopic studies in the literature (see Section 5). Our adopted model reproduces fairly well several lines of different atomic species, allowing us to adopt the linear radius of P Cyg photosphere as $75 R_\odot$ and deliver synthesized visibilities and finally determine the distance of P Cyg as $d_{\text{II}} = 1.56 \pm 0.25 \text{ kpc}$. Note that for

such an approach to be effective, it would be useful to monitor interferometric measurements by simultaneous (and preferably U , B , V) photometry. For P Cyg, the variability can originate from effective temperature and radius changes of 10 per cent and 7 per cent, respectively, as concluded by Markova et al. (2001).

With this rather unusual interpretation of long baseline interferometry data, we propose a method to check and improve the so-called *wind momentum versus luminosity relation* (W-LR hereafter) introduced by Kudritzki, Lennon & Puls (1994), which relates the momentum flow of the wind from the star to its linear size times its luminosity,

$$\dot{M}v_{\infty} \propto R_{\star}^{-1/2} L_{\star}^{-1/\alpha_{\text{eff}}}, \quad (10)$$

where α_{eff} reflects all the spectral lines that drive the wind, with a typical value of 2/3, varying according to the spectral type (see e.g. table 2 of Kudritzki & Puls 2000).

The W-LR method consists in recording medium- or high-resolution spectra of the most luminous stars such as O, B, A supergiants, B[e] and LBV stars of the nearby galaxies, or the local Universe if possible, and determine their intrinsic luminosity from quantitative spectroscopy. Despite the good agreement between the theoretical and empirical (derived from spectroscopic analyses) W-LR for the most luminous massive stars (as the ones mentioned above), O-type dwarfs and giants with $\log L_{\star}/L_{\odot} \leq 5.2$ present much lower values of mass-loss rate, up to two orders of magnitude, than the theoretical values, affecting the WL-R (Martins et al. 2005; Marcolino et al. 2009; de Almeida et al. 2019). This shows the current need to check independently the WL-R.

To our knowledge, CMFGEN radiative transfer code represents a robust model to carry such a quantitative spectroscopy of the most luminous stars with their emission lines that often possess P Cyg profiles, i.e. a strong emission red wing and a blue absorption component corresponding to the projection of the wind components on the line of sight. The comparison of the apparent magnitude to the absolute luminosity would then estimate the distance of the luminous star to us even at Megaparsec levels.

As suggested by Vakili et al. (1998), such a method could be further improved by carrying the quantitative spectroscopy of a star observed by long-baseline interferometry and matching synthesized visibilities based on linear diameter of the star versus the measured visibility so as to determine the star's distance. This approach could be furthermore improved by observing luminous stars of Magellanic Clouds with different chemical abundances, i.e. Large Magellanic Cloud versus Short Magellanic Cloud. The brightest stellar members of Magellanic Clouds have apparent magnitudes in the range of 12–15 in the visible and their visibilities could be measured with future extremely long-baseline optical interferometers such as the intensity interferometric mode of the CTA array (Dravins 2016) or connecting large optical telescopes on existing observatories (Lai et al. 2018), such as Mauna Kea or Paranal, which will offer better than 10 μas angular resolution, compatible with the range of angular diameters of the brightest stars of the Magellanic Clouds. Therefore, this work constitutes the first successful step towards settling the quantitative spectroscopy of luminous stars and the W-LR relation, which may serve as an independent calibration technique of cosmological distances comparable to the Cepheid or post-AGB methods (Whitelock 2012).

ACKNOWLEDGEMENTS

We thank P. Weiss for participating in the observations, G. Labeyrie for fruitful discussions, and the MéO Team (Géozur Laboratory)

for their hospitality and help during the tentative session in 2018 November. We also thank F. Thévenin, P. Bériou, and the Observatoire de la Côte d'Azur for financial support. We acknowledge the CATS team (Calern Atmospheric Turbulence Station, <https://cats.oca.eu/>) for providing turbulence real-time measurements and Swabian Instruments for very reactive technical support. We are also grateful to the ARAS data base community members, especially to J. Guarro i Flô, for their high quality spectra of P Cyg. This work is supported by the UCA-JEDI project ANR-15-IDEX-01, the Doebelin Federation, and the OPTIMAL platform. ESGdeA thanks OCA and the 'Ville de Nice' (Nice, France) for the financial support to this work through the 'Bourse Doctorale Olivier Chesneau' during the period of 2016–2019. In memoriam of Paul Nuñez with whom all this adventure started in 2014.

REFERENCES

- Acciari V. A. et al., 2020, *MNRAS*, 491, 1540
 ARAS, 2018, ARAS Spectral Database. Public data available at: <http://www.astrourf.com/aras/>.
 Aristidi E., Fanteï-Caujolle Y., Ziad A., Dimur C., Chabé J., Roland B., 2014, in Stepp L. M., Gilmozzi R., Hall H. J., eds, Proc. SPIE Conf. Ser. Vol. 9145, Ground-based and Airborne Telescopes V. SPIE, Bellingham, p. 91453G
 Balan A., Tycner C., Zavala R. T., Benson J. A., Hutter D. J., Templeton M., 2010, *AJ*, 139, 2269
 Bouret J. C., Hillier D. J., Lanz T., Fullerton A. W., 2012, *A&A*, 544, A67
 Chabé J., Ziad A., Fanteï-Caujolle Y., Aristidi E., Renaud C., Blary F., Marjani M., 2016, in Hall H. J., Gilmozzi R., Marshall H. K., eds, Proc. SPIE Conf. Ser. Vol. 9906, Ground-Based and Airborne Telescopes VI. SPIE, Bellingham, p. 99064Z
 Chesneau O. et al., 2000, *A&AS*, 144, 523
 de Almeida E. S. G., Marcolino W. L. F., Bouret J. C., Pereira C. B., 2019, *A&A*, 628, A36
 de Jager C., 2001, in de Groot M., Sterken C., eds, ASP Conf. Ser. Vol. 233, P Cygni 2000: 400 Years of Progress. Astron. Soc. Pac., San Francisco, p. 215
 Dessart L., Hillier D. J., Audit E., Livne E., Waldman R., 2016, *MNRAS*, 458, 2094
 Dravins D., 2016, in Malbet F., Creech-Eakman M. J., Tuthill P. G., eds, Proc. SPIE Conf. Ser. Vol. 9907, Optical and Infrared Interferometry and Imaging V. SPIE, Bellingham, p. 99070M
 Gaia Collaboration, 2018, *A&A*, 616, A1
 Goldberger M. L., Lewis H. W., Watson K. M., 1966, *Phys. Rev.*, 142, 25
 Groh J. H., Hillier D. J., Madura T. I., Weigelt G., 2012, *MNRAS*, 423, 1623
 Guerin W., Dussaux A., Fouché M., Labeyrie G., Rivet J.-P., Vernet D., Vakili F., Kaiser R., 2017, *MNRAS*, 472, 4126
 Guerin W., Rivet J.-P., Fouché M., Labeyrie G., Vernet D., Vakili F., Kaiser R., 2018, *MNRAS*, 480, 245
 Hanbury Brown R., 1974, *The Intensity Interferometer: Its Application to Astronomy*. Taylor & Francis, London
 Hanbury Brown R., Twiss R. Q., 1956, *Nature*, 178, 1046
 Hanbury Brown R., Davis J., Herbison-Evans D., Allen L. R., 1970, *MNRAS*, 148, 103
 Hanbury Brown R., Davis J., Allen L. R., 1974, *MNRAS*, 167, 121
 Herbison-Evans D., Hanbury Brown R., Davis J., Allen L. R., 1971, *MNRAS*, 151, 161
 Hillier D. J., Miller D. L., 1998, *ApJ*, 496, 407
 Hubeny I., Lanz T., 1995, *ApJ*, 439, 875
 Kieda D. et al., 2019a, State of the Profession: Intensity Interferometry, Astro2020 Science White Paper, p. 227
 Kieda D. et al., 2019b, Science Opportunities Enabled by the Era of Visible Band Stellar Imaging with Sub-100 $\mu\text{arc-sec}$ Angular Resolution, Astro2020 Science White Paper, p. 275
 Kudritzki R.-P., Puls J., 2000, *ARA&A*, 38, 613

- Kudritzki R., Lennon D., Puls J., 1994, in Walsh J., Danziger I., eds, Proceedings of the ESO Workshop, Science with the VLT. Springer, Berlin, p. 246
- Labeyrie A., Lipson S. G., Nisenson P., 2006, An Introduction to Optical Stellar Interferometry. Cambridge Univ. Press, Cambridge
- Lai O. et al., 2018, in Creech-Eakman M. J., Tuthill P. G., Mérand A., eds, Proc. SPIE Conf. Ser. Vol. 1070, SPIE Astronomical Telescopes + Instrumentation. SPIE, Bellingham, p. 1070121
- Lamers H., de Groot M., 1992, *A&A*, 535, A67
- Lamers H. J. G. L. M., de Groot M., Cassatella A., 1983, *A&A*, 128, 299
- Langer N., Hamann W. R., Lennon M., Najarro F., Pauldrach A. W. A., Puls J., 1994, *A&A*, 290, 819
- Lanz T., Hubeny I., 2007, *ApJS*, 169, 83
- Loudon R., 1973, The Quantum Theory of Light. Oxford Science Publications, Oxford
- Marcolino W. L. F., Hillier D. J., de Araujo F. X., Pereira C. B., 2007, *ApJ*, 654, 1068
- Marcolino W. L. F., Bouret J. C., Martins F., Hillier D. J., Lanz T., Escolano C., 2009, *A&A*, 498, 837
- Markova N. et al., 2001, *A&A*, 376, 898
- Martins F., Schaerer D., Hillier D. J., Meynadier F., Heydari-Malayeri M., Walborn N. R., 2005, *A&A*, 441, 735
- Matthews N., LeBohec S., 2019, in PoS 358, 740, 36th International Cosmic Ray Conference, Sissa Medialab, Trieste, Italy
- Najarro F., 2001, in de Groot M., Sterken C., eds, ASP Conf. Ser. Vol. 233, *P Cygni 2000: 400 Years of Progress*. Astron. Soc. Pac., San Francisco, p. 133
- Najarro F., Hillier D. J., Stahl O., 1997, *A&A*, 326, 1117
- Nazé Y., Rauw G., Hutsemékers D., 2012, *A&A*, 538, A47
- Nota A., Livio M., Clampin M., Schulte-Ladbeck R., 1995, *ApJ*, 448, 788
- Pauldrach A. W. A., Puls J., 1990, *A&A*, 237, 409
- Phillips D. T., Kleinman H., Davis S. P., 1967, *Phys. Rev.*, 153, 113
- Pollmann E., Vollmann W., 2013, *J. Am. Assoc. Var. Star Obs.*, 41, 24
- Rauw G. et al., 2015, *ApJS*, 221, 1
- Richardson N. D., Morrison N. D., Gies D. R., Markova N., Hesselbach E. N., Percy J. R., 2011, *AJ*, 141, 120
- Richardson N. D. et al., 2013, *ApJ*, 769, 118
- Rivet J.-P., Vakili F., Lai O., Vernet D., Fouché M., Guerin W., Labeyrie G., Kaiser R., 2018, *Exp. Astron.*, 46, 531
- Tan P. K., Kurtstiefer C., 2017, *MNRAS*, 469, 1617
- Tramper F. et al., 2013, *A&A*, 559, A72
- Turner D., Welch G., Graham M., Fairweather D., 2001, *J. Am. Assoc. Var. Star Obs.*, 29, 73
- Vakili F., Mourard D., Bonneau D., Morand F., Stee P., 1997, *A&A*, 323, 183
- Vakili F., Mourard D., Stee P., Bonneau D., 1998, in Wolf B., Stahl O., Fullerton A., eds, Proc. IAU Colloquium No. 169, Variable and Non-spherical Stellar Winds in Luminous Hot Stars. Springer, Berlin, p. 87
- Weigelt G. et al., 2007, *A&A*, 464, 87
- Whitelock P. A., 2012, *Astrophys. Space Sci.*, 341, 123
- Ziad A., Borgnino J., Dali Ali W., Berdja A., Maire J., Martin F., 2012, *J. Opt.*, 14, 045705

This paper has been typeset from a $\text{\TeX}/\text{\LaTeX}$ file prepared by the author.

6.3 The Be-shell star *o* Aquarii

6.3.1 Probing the Be phenomenon: why study *o* Aquarii with interferometry?

Understanding the origin of the decretion disks around Be stars is one of the current challenges in astrophysics. In particular, a central puzzle on the Be phenomenon regards the physical mechanisms underlying the formation of their circumstellar disks.

Unlike the more massive objects, such as O-type and LBVs stars, which have rotational velocities far-below their critical values, fast rotation plays a key role in the process of mass loss in Be stars. Moreover, their Keplerian decretion disks are efficient sources of angular momentum transport, when compared with the momentum loss due to their stellar winds (e.g., Krtićka et al. 2011). However, and discussed in Chap. 1, how close Be stars are indeed to the break-up limit is still an open question in the literature, and it is an important question regarding the Be phenomenon itself.

Most Be stars appear to rotate below the critical value, showing rotational rates as low as $\sim 30\text{-}40\%$ in some cases (e.g., Cranmer 2005; Zorec et al. 2016). This means that other channels in addition to rotation are needed to remove material from the stellar surface, as provided by pulsations, magnetic fields, and the own radiative force for the earlier Be stars. In addition, more recently, binary effects are understood to be important in the process of spin-up of Be stars, which can show rotational rates very close to the critical value, requiring the search for binary companions among these stars (e.g., Klement et al. 2019; Hastings et al. 2020).

o Aquarii (HD 209409, type B7IVe) is a good target to probe the Be phenomenon, especially through interferometry, since it is quite near ($d = 144$ pc from Gaia Collaboration et al. 2018) and bright ($V = 4.7$). Interestingly, Rivinius et al. (2006) identified the presence of a central quasi-emission (CQE) feature in the Mg II $\lambda 4481$ line of *o* Aquarii. As discussed in Sect. 1.4.2, this is a purely-geometric effect that can arise due to circumstellar disks seen close to the edge-on orientation, this being the case of *o* Aquarii, as discussed below. This means that the kinematics and physical conditions of its disk can be better probed by interferometry since such an edge-on view results in clear specific signatures in the interferometric quantities. For instance, see, again, in Fig. 5.6, the S-shape differential phase that is found for a disk seen edge-on.

The first spectro-interferometric analysis of *o* Aquarii was performed by Meilland et al. (2012), using the kinematic code (Sect. 5.3) to model VLTI/AMBER (K-band) observations of eight bright Be stars. Despite the very limited number of observations for *o* Aquarii (just one measurement), and the also low quality data, these authors were able to constrain its inclination angle, as $i = 70 \pm 20^\circ$. In addition, they determined

6.3. The Be-shell star *o* Aquarii

a disk extension of $\text{FWHM} = 14 \pm 1 D_\star$ in the $\text{Br}\gamma$ line and a rotational rate (see Sect. 1.3.2) of $\Omega/\Omega_{\text{crit}} = 0.93_{-0.17}^{+0.06}$.

This study was followed-up by Cochetti et al. (2019), also analysing *o* Aquarii with the kinematic code, in their large AMBER survey of Be stars (26 objects). Due to the larger and good quality data (8 measurements) for this star, Cochetti et al. (2019) better constrained the disk extension in $\text{Br}\gamma$ and the inclination angle, $\text{FWHM} = 8 \pm 0.5 D_\star$ and $i = 70 \pm 5^\circ$, and then improving the precision on the determination of *o* Aquarii's rotation rate as $\Omega/\Omega_{\text{crit}} = 0.93 \pm 0.07$. From that, the results found by these authors indicate that *o* Aquarii must be a Be star rotating nearly close to the break-up limit.

To date, Sigut et al. (2015) provided one of the most comprehensive picture of *o* Aquarii's disk, employing radiative transfer modeling with the code BEDISK (Sect. 4.2). Unlike in Meilland et al. (2012), these authors did not use spectro-interferometric observations, but they combined large band (15 nm) interferometric data (period of 2007-2014) centered on $\text{H}\alpha$, obtained from the Navy Precision Optical Interferometer, with $\text{H}\alpha$ spectroscopy from the Lowell Observatory Solar/Stellar Spectrograph (2005-2014).

Sigut et al. (2015) managed to reproduce different types of observables from their unified physical model for the disk: absolute visibility, $\text{H}\alpha$ line profile, spectral energy distribution, and also provided a qualitative explanation for the CQE feature observed in the $\text{Mg II } \lambda 4481$ line. They found that the $\text{H}\alpha$ *EW* is quite stable (within about 5%) up to about ten years. Besides that, they also could not detect disk variability from the analysis of the interferometric data considering different time spans within ten years. Another interesting result noted by Sigut et al. (2015) is that the disk extension in $\text{H}\alpha$ (Gaussian $\text{FWHM} \sim 13 D_\star$) found by their analysis is comparable to the one determined by Meilland et al. (2012) in $\text{Br}\gamma$ ($\sim 14 D_\star$). This result deserves to be better investigated because it is commonly thought that Be disks show a larger extension in the $\text{H}\alpha$ line than in $\text{Br}\gamma$, as discussed in Sect. 1.5.2.

6.3.2 Observing *o* Aquarii in the AMBER and VEGA Be surveys

In addition to the VLTI/AMBER data already analysed in the surveys of Meilland et al. (2012) and Cochetti et al. (2019), we performed new observations of *o* Aquarii using the CHARA/VEGA beam-combiner, centered at $\text{H}\alpha$, in order to obtain a detailed interferometric picture of this star, both in the visible and in the infrared.

Taking advantage of the longer baselines provided by the CHARA Array, compared with the ones from VLTI, we were able to archive a higher level of spatial resolution of *o*

6.3. The Be-shell star *o* Aquarii

Aquarii and its environment, allowing us to partially resolve them in different spectral channel using the VEGA instrument (see Fig. 2 of Paper III).

During my PhD, I was engaged in the remote observations of the VEGA team, performing observations of 20 nights in total. In particular, with respect to *o* Aquarii data, I observed in remote mode the 2016 VEGA data analysed in this thesis. In total, we observed *o* Aquarii 50 times with the VEGA instrument between 2012 and 2016, as part of four different programs of the VEGA team at Laboratoire Lagrange/Observatoire de la Côte d’Azur (PI: D. Mourard), as follows:

- (i) V51: 2nd Be stars small survey (2012 - one measurement).
- (ii) V56: Connecting stellar surface and circumstellar environment of Be stars (2013, 8 measurements).
- (iii) V62: Critical rotation and mass-loss: new insights from the study of edge-on Be stars (2014, 38 measurements).
- (iv) V66: Be stars large survey (2016, 3 measurements).

6.3.3 A multi-technique modeling approach: from analytical to numerical models

As pointed out above, these VEGA observations of *o* Aquarii are part of a larger program to study the photosphere and circumstellar environment of Be stars (to date program V66, PI: A. Meilland).

In addition to our interest to achieve a better characterization of physical properties of *o* Aquarii and its disks, this study also aimed to set a more systematic modeling method using both the called kinematic model and the BeAtlas grid of HDUST radiative transfer models, as discussed in the following.

To date, our study presents the largest spectro-interferometric dataset analysed for one Be star, encompassing different spectral channels. For this purpose, we used modeling methods of increasing complexity in order to explain our data, and then allowing us to probe different properties of *o* Aquarii:

- (i) Using the LITpro fitting-tool (Sect. 5.2), simple geometric models for fitting the calibrated visibility measurements: morphology of the central star and the disk.
- (ii) Kinematic models for fitting the differential visibility and phase measurements: morphology of the central star and the disk, as well as their kinematics (as the stellar rotation rate and disk velocity law).

6.3. The Be-shell star *o* Aquarii

- (iii) Radiative transfer models calculated with the HDUST code (BeAtlas grid) for fitting all the observables: morphology of the central star and the disk, as well as their kinematics, in addition to the physics of the disk (as the disk mass density distribution).

For the analysis using the numerical models, that is, calculated using the kinematic and HDUST codes, I wrote several scripts in Python, IDL, and R language. For example, using the library PYHDUST⁶, I wrote scripts in Python for extracting in an automatic way the image cubes in .FITS files from the BeAtlas grid. Details on the PYHDUST library can be found in Sect. 2.1.4 of Faes (2015). Fig. 4.7 illustrated image cubes around the Br γ line of BeAtlas models, as the predicted visibility (simulated to AMBER observations). The predicted interferometric quantities from each BeAtlas image is then calculated using the Discrete Fourier transform (scripts written in IDL) in order to obtain the reduced χ^2 between the model and the VEGA and AMBER datasets. Given the automatic computing of model χ^2 for all the BeAtlas grid, I wrote script mainly in R language in order to visualize the results and calculation statistics of interest. For instance, Fig. 9 of Paper III shows the lowest χ^2 of BeAtlas from fitting our VEGA and AMBER data as a function of model parameters, and statistics from the HDUST parameters are shown in Table 4 of Paper III.

Furthermore, for first time, an automatic modeling fitting procedure was implemented to fit spectro-interferometric with the kinematic code using a MCMC approach (Sect. 5.4.2). From that, I was able to precisely constrain the following parameters for *o* Aquarii: stellar inclination angle, stellar rotation velocity, disk position angle, disk emitting extension, and the disk rotational velocity law exponent.

In short, despite being written in different computing languages, these scripts conjointly provide a somewhat automatic interferometric analysis of any VEGA or AMBER data for Be stars using the BeAtlas grid, ultimately finding the group of BeAtlas models that better explain the datasets in terms of reduced χ^2 , and also in terms of the kinematic code using a MCMC fitting-model procedure. This successful attempt of modeling the VEGA and AMBER data in our study, providing robust model parameters and associated uncertainties for *o* Aquarii, paved the way for a systematic analysis of Be stars using spectro-interferometric data from multiple instruments, such as AMBER, VEGA, MATISSE (Sect. 7.2.2).

6.3.4 Results and conclusions

From the simplest modeling approach using geometric modeling (LITpro) to fit the VEGA calibrated squared visibility, we constrained the stellar radius of *o* Aquarii with

6. Publicly available at <https://pyhdust.readthedocs.io/en/latest/>.

6.3. The Be-shell star *o* Aquarii

a 8% accuracy, that is, $R_{\star} = 4.0 \pm 0.3 R_{\odot}$, from our best-fit two-component uniform disk model to the VEGA data in the $H\alpha$ band (Table 1 of Paper III).

This value of stellar radius is significantly larger than the one adopted in the study Sigut et al. (2015) of $3.2 R_{\odot}$ (polar radius for a B7 dwarf from Townsend et al. 2004). We point out that this could be expected as *o* Aquarii is likely flattened due to its fast rotation, and then our measurement here for its radius represents a mean value between its polar and equatorial radii. Indeed, we were not able to detect any effect of oblateness from this simple geometric analysis, but the situation is quite different when looking the differential data modeled with HDUST (see Tables 4 and 5 of Paper III).

Table 2 of Paper III summarizes our results found using the kinematic code to fit both the differential VEGA and AMBER datasets in separate way, and Fig. 4 shows the MCMC histogram distributions and correlation plots of our best-fit kinematic models. Interestingly, we found that the $H\alpha$ (from fitting VEGA) and $Br\gamma$ (from fitting AMBER) emitting disk sizes presents a quite similar extension of $\sim 11-12 D_{\star}$. This provided a more robust constraint on the previous results found by Meilland et al. (2012) and Sigut et al. (2015), that performed independent analysis of *o* Aquarii in the near-infrared (AMBER) and $H\alpha$ (NPOI), as discussed above. As discussed in Sect. 8.1 of Paper III, this result could be explained in terms of the high inclination angle of *o* Aquarii, but it is one of the open issues that should be addressed by analysing a large sample of Be stars (Sect. 7.2.2).

Furthermore, the inclination angle derived from fitting our VEGA data with the kinematic code is quite lower than the one derived from AMBER, in about 15° . Such a lower value of i is also supported by our analysis with the BeAtlas grid (again, see Fig. 9 and Table 4 of Paper III). This result deserves further investigations, but one possibility to explain that relies on non-isothermal effect arising from *o* Aquarii's disk, as discussed in Sect. 8.2 of Paper III.

In Fig. 6.1, we provide a very simple and preliminary analysis on this question above. We show the major-axis FWHM Gaussian size fitted from each HDUST model, similarly to the analysis provided in Fig. 13 of Paper III, but here we also consider non-parametric HDUST models of the BeAtlas grid (with viscosity parameter α fixed at 0.5). These models are no longer parameterized by Σ_0 and m (see Eq. 1.73), as discussed in Sect. 4.4. In addition, we also show our results based on our best-fit HDUST model (Table 5 of Paper III) from the BeAtlas, that is, the disk density exponent law is fixed at $m = 3.0$.

From that, one sees that the circumstellar disk extension (major-axis FWHM Gaussian) presents a very similar response to the variation in i for the group of non-isothermal models, and then it could be expected to derive closer value for i from VEGA and AMBER, when compared with the parametric case with $m = 3.0$. Therefore, compared

6.3. The Be-shell star *o* Aquarii

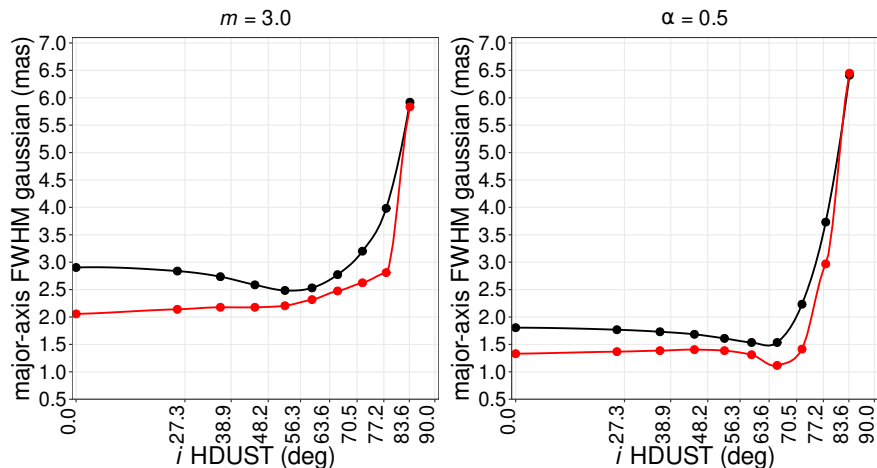


Figure 6.1 – Comparison between parametric HDUST models ($m = 3.0$, left panels) and steady-state non-isothermal HDUST models (non-parametric models, right panels). The major-axis FWHM from a Gaussian fit to each HDUST image is shown as a function of HDUST inclination angle. Notice that, unlike the parametric case with $m = 3.0$, the FWHM extension is very similar in both H α (black) and Br γ (red) when considering the non-isothermal HDUST models in the grid. See text for discussion.

with our best-fit model ($m = 3.0$), we would be able to obtain a better agreement between i derived from the fit to VEGA and AMBER, when considering the group of non-isothermal models in the BeAtlas. On the other hand, in this case of non-parametric models, the fit to AMBER is largely affected ($\chi_r^2 \sim 15$). Notice, from Table 4, that the χ^2 of the best-fit HDUST to AMBER is quite lower than that ($\chi_r^2 \sim 4.7$), being this a parametric model. Finally, we remind the reader the BeAtlas grid is currently quite limited in terms of these self-consistent models (Sect. 4.4), and additional calculations, exploring different values of disk viscosity, are needed in order to verify if the different values of i found by our study from H α and Br γ arise due to non-isothermal effects on the vertical structure of *o* Aquarii’s disk.

In conclusion, our study shows that *o* Aquarii seems to fit in the global picture of Be stars, when looking at the continuum and Br γ line, that is, a Keplerian rotation disk well-described by the so-called VDD model (Sect. 1.5). However, the H α data cannot be fully understood in the framework of the VDD model: it seems needed to consider a super-Keplerian disk, that is, β higher (more positive) than -0.5, to explain the H α interferometric data, the same being indicated considering the H α line profile. This shows that more complex physical processes in Be disks are needed to be taken into account when modeling quantities measured in H α in comparison to Br γ .

Apart from these biases regarding H α , we were able to successively model using the BeAtlas grid both the VEGA and AMBER data with the same physical description for the circumstellar disk, finding a base disk surface density $\Sigma_0 = 0.12 \text{ g cm}^{-2}$ and a radial density law exponent $m = 3.0$. Our best-fit HDUST model, purely found from adjusting interferometric data, is able to reproduce other different types of observables

6.3. The Be-shell star *o* Aquarii

of *o* Aquarii well, the spectral energy distribution, the H α and Br α line profile (Sect. 7 of Paper III), and also to predict fairly well the level of intrinsic polarization in the V-band, namely, 0.41% from our physical model in comparison with 0.49 ± 0.03 % that is derived from our polarimetric data (Sect. 8.4.3 of Paper III).

Furthermore, based on multi-technique observations (spectroscopy, interferometry, and polarimetry), our results supports that *o* Aquarii presents a globally stable disk structure for several years (up to two decades). Interestingly, from the modeling both of our visible and near-infrared interferometric data, our best-fit physical model (BeAtlas grid) presents a volume disk density exponent m lower than the canonical value of 3.5 for the steady-state regime in the VDD model, namely, $m = 3.0$. As discussed in details in Sect. 8.4.4. of Paper III, others stable Be stars with stable disks also present values of m lower than 3.5, such as β Canis Minoris (B8Ve), α Arae (B2Vne), and α Columbae (B9Ve). Since $m = 3.5$ stands for the simplified scenario of the single Be stars with a isothermal vertical height scale disk, this could indicate binary or non-isothermal effects on Be disks.

One possibility to explain such a long-term stability of *o* Aquarii's disk relies on its own high stellar rotational rate, very close ($\sim 96\%$) to the critical value (391 ± 27 km s $^{-1}$). Thus, apart from other possible known mechanisms of mass loss in Be stars (Sect. 1.3.4), this could provide a nearly constant rate of mass-injection in the disk of *o* Aquarii.

Lastly, the high temporal disk stability and rotational rate found for *o* Aquarii (B7IV) are consistent with the more recent scenario proposed in the literature that late-type Be stars are more likely to have stable disks and rotate near to the break-up limit, when compared with early-type Be stars (e.g., Cranmer 2005; Vieira et al. 2017).

Visible and near-infrared spectro-interferometric analysis of the edge-on Be star *o* Aquarii

E. S. G. de Almeida¹, A. Meilland¹, A. Domiciano de Souza¹, P. Stee¹, D. Mourard¹, N. Nardetto¹, R. Ligi², I. Tallon-Bosc³, D. M. Faes⁴, A. C. Carciofi⁴, D. Bednarski⁴, B. C. Mota⁴, N. Turner⁵, and T. A. ten Brummelaar⁵

¹ Université Côte d’Azur, Observatoire de la Côte d’Azur, CNRS, Laboratoire Lagrange, France
e-mail: elisson.saldanha@oca.eu

² INAF – Osservatorio Astronomico di Brera, Via E. Bianchi 46, 23807 Merate, Italy

³ Univ. Lyon, Univ. Lyon1, ENS de Lyon, CNRS, Centre de Recherche Astrophysique de Lyon UMR5574, 69230 Saint-Genis-Laval, France

⁴ Instituto de Astronomia, Geofísica e Ciências Atmosféricas, Universidade de São Paulo, São Paulo, Brazil

⁵ CHARA Array – Georgia State University, Mount Wilson, CA, USA

Received 6 June 2019 / Accepted 6 February 2020

ABSTRACT

Aims. We present a detailed visible and near-infrared spectro-interferometric analysis of the Be-shell star *o* Aquarii from quasi-contemporaneous CHARA/VEGA and VLTI/AMBER observations.

Methods. We analyzed spectro-interferometric data in the H α (VEGA) and Br γ (AMBER) lines using models of increasing complexity: simple geometric models, kinematic models, and radiative transfer models computed with the 3D non-LTE code HDUST.

Results. We measured the stellar radius of *o* Aquarii in the visible with a precision of 8%: $4.0 \pm 0.3 R_{\odot}$. We constrained the circumstellar disk geometry and kinematics using a kinematic model and a MCMC fitting procedure. The emitting disk sizes in the H α and Br γ lines were found to be similar, at ~ 10 – 12 stellar diameters, which is uncommon since most results for Be stars indicate a larger extension in H α than in Br γ . We found that the inclination angle i derived from H α is significantly lower ($\sim 15^{\circ}$) than the one derived from Br γ : $i \sim 61.2^{\circ}$ and 75.9° , respectively. While the two lines originate from a similar region of the disk, the disk kinematics were found to be near to the Keplerian rotation (i.e., $\beta = -0.5$) in Br γ ($\beta \sim -0.43$), but not in H α ($\beta \sim -0.30$). After analyzing all our data using a grid of HDUST models (BeAtlas), we found a common physical description for the circumstellar disk in both lines: a base disk surface density $\Sigma_0 = 0.12 \text{ g cm}^{-2}$ and a radial density law exponent $m = 3.0$. The same kind of discrepancy, as with the kinematic model, is found in the determination of i using the BeAtlas grid. The stellar rotational rate was found to be very close ($\sim 96\%$) to the critical value. Despite being derived purely from the fit to interferometric data, our best-fit HDUST model provides a very reasonable match to non-interferometric observables of *o* Aquarii: the observed spectral energy distribution, H α and Br γ line profiles, and polarimetric quantities. Finally, our analysis of multi-epoch H α profiles and imaging polarimetry indicates that the disk structure has been (globally) stable for at least 20 yr.

Conclusions. Looking at the visible continuum and Br γ emission line only, *o* Aquarii fits in the global scheme of Be stars and their circumstellar disk: a (nearly) Keplerian rotating disk well described by the viscous decretion disk (VDD) model. However, the data in the H α line shows a substantially different picture that cannot fully be understood using the current generation of physical models of Be star disks. The Be star *o* Aquarii presents a stable disk (close to the steady-state), but, as in previous analyses, the measured m is lower than the standard value in the VDD model for the steady-state regime ($m = 3.5$). This suggests that some assumptions of this model should be reconsidered. Also, such long-term disk stability could be understood in terms of the high rotational rate that we measured for this star, the rate being a main source for the mass injection in the disk. Our results on the stellar rotation and disk stability are consistent with results in the literature showing that late-type Be stars are more likely to be fast rotators and have stable disks.

Key words. stars: individual: *o* Aquarii – stars: emission-line, Be – circumstellar matter – techniques: interferometric

1. Introduction

Classical Be stars are main-sequence B-type stars that show (or showed at some time) Balmer lines in emission and infrared excess in their spectral energy distribution. The Be phenomenon is found among the entire spectral range of B stars (e.g., Townsend et al. 2004): M_{\star} from $\sim 3 M_{\odot}$ (B9, $T_{\text{eff}} \sim 12\,000$ K), up to $\sim 18 M_{\odot}$ (B0, $T_{\text{eff}} \sim 30\,000$ K). These observational characteristics are well explained as arising from a dust-free gaseous disk that is supported by rotation with a slow radial velocity (see, e.g., Rivinius et al. 2013). The most successful theory to explain the evolution of the disk structure is the so-called viscous decretion disk (VDD) model, where its dynamics are driven by viscosity (e.g., Lee et al. 1991; Okazaki 2001; Bjorkman & Carciofi 2005).

It is widely accepted that fast rotation plays an important role in the formation of the Be star disk. However, while interferometric analyses typically provide rotational rates $v_{\text{rot}}/v_{\text{crit}} \gtrsim 0.7$ (e.g., Meilland et al. 2012; Cochetti et al. 2019), some statistical studies show rates ranging from ~ 0.3 up to 1.0 (e.g., Cranmer 2005; Zorec et al. 2016). Moreover, it is still not clear whether the rotational rate is correlated to other stellar parameters such as the effective temperature (e.g., Cochetti et al. 2019). Hence, despite the success of the VDD model, the physical mechanism(s) driving the mass injection remains unclear and a detailed physical characterization for the central star and the disk structure is mandatory to better understand the Be phenomenon. By gaining access to geometry on the milliarcsecond scale and kinematics on a few tens of km s^{-1} scale, spectro-interferometry offers a

unique opportunity to probe the circumstellar environment and stellar surfaces of Be stars (see, e.g., Chesneau et al. 2012; Stee & Meilland 2012).

The bright, late-type Be star (type B7IVe) α Aquarii (HD 209409) is known to have a fairly stable disk (Sigut et al. 2015). The stability of the circumstellar disk is evidenced by the quasi-constant equivalent width in the $H\alpha$ line, double-peak separation, and the absence of long-term violet-to-red (V/R) peak variations (e.g., Rivinius et al. 2006; Sigut et al. 2015). This star shows a high value of $v \sin i \sim 282 \text{ km s}^{-1}$ (Frémat et al. 2005) and a shell absorption in $H\alpha$, thus indicating a high stellar inclination angle of about 70° , as discussed below.

Meilland et al. (2012) presented the first spectro-interferometric analysis of α Aquarii with the VLTI/AMBER instrument as part of their AMBER survey of eight bright Be stars. Despite the low data quality and very limited number of observations (just one measurement), they were able to significantly constrain the disk geometry and kinematics. They found that the disk emission in the $\text{Br}\gamma$ line, modeled as an elliptical Gaussian distribution, had a FWHM of $14 \pm 1 D_\star$ (with $R_\star = 4.4 R_\odot$), where D_\star and R_\star are, respectively, the stellar diameter and radius. They estimated the inclination angle as $i = 70 \pm 20^\circ$ and found a stellar rotational rate of $v_{\text{rot}}/v_{\text{crit}} = 0.77 \pm 0.21$ ($\Omega/\Omega_c = 0.93^{+0.06}_{-0.17}$), where v_{crit} and Ω_{crit} are, respectively, the linear and angular critical velocity. New VLTI/AMBER spectro-interferometric measurements of α Aquarii were presented in the Be star survey of Cochetti et al. (2019). Here, they obtained seven good-quality measurements for α Aquarii (i.e., 21 baselines). Using a similar model as in Meilland et al. (2012), they found a $\text{Br}\gamma$ emission FWHM significantly smaller than in Meilland et al. (2012), $8 \pm 0.5 D_\star$ (with $R_\star = 4.4 R_\odot$), and better constrained the object inclination angle ($70 \pm 5^\circ$).

A detailed analysis of α Aquarii using $H\alpha$ spectroscopy and interferometry was performed by Sigut et al. (2015). These authors combined large band (15 nm) interferometric data centered on $H\alpha$, obtained from the Navy Precision Optical Interferometer (NPOI), with $H\alpha$ spectroscopy from the Lowell Observatory Solar-Stellar Spectrograph. Using the radiative transfer code BEDISK (Sigut & Jones 2007), they were able to reproduce simultaneously the visibility, $H\alpha$ line profile, and spectral energy distribution (SED), and showed that the disk is quite stable for up to about ten years. Interestingly, they found a disk extension in $H\alpha$ (Gaussian FWHM of $12.0 \pm 0.5 D_\star$) close to the one determined by Meilland et al. (2012) in $\text{Br}\gamma$ (FWHM of $14 \pm 1 D_\star$). They concluded that this is uncommon since most previously studied Be stars exhibit a larger (up to two times) disk emission region in $H\alpha$ than in $\text{Br}\gamma$.

In this paper, we present new CHARA/VEGA spectro-interferometric measurements of α Aquarii centered on the $H\alpha$ emission line ($\lambda = 0.656 \mu\text{m}$). They are analyzed conjointly with the AMBER $\text{Br}\gamma$ line ($\lambda = 2.166 \mu\text{m}$) measurements from Meilland et al. (2012) and Cochetti et al. (2019), using models of increasing complexity: simple geometric models, kinematic models, and radiative transfer models. This is the first time the code HDUST has been used to model simultaneously spectro-interferometric data from $H\alpha$ and $\text{Br}\gamma$. It is the second time for the kinematic model (i.e., after the δ Scorpii data published in Meilland et al. 2011). This multi-wavelength and multi-line approach allows us to draw a more complete picture of the stellar surface and circumstellar environment of the Be star α Aquarii.

This paper is organized as follows. In Sect. 2, we present the observations and the data reduction process. Our analysis using geometric models of the VEGA calibrated (absolute) visibility is shown in Sect. 3. In Sect. 4, we fit the VEGA and AMBER

differential visibility and phase with a kinematic model using a Markov chain Monte Carlo (MCMC) model fitting method. In Sect. 5, all the interferometric data are analyzed in terms of 3D non-LTE radiative transfer models. Our kinematic and radiative transfer models are discussed in Sect. 6. In Sect. 7, our best-fit models are compared to non-interferometric observables: the spectral energy distribution and line profiles ($H\alpha$ and $\text{Br}\gamma$). The comparison with polarimetric data is performed in Sect. 8.4.3 in the context of the disk stability. In Sect. 8, we discuss the morphological, kinematic, and physical descriptions for α Aquarii and its circumstellar disk. Our conclusions are summarized in Sect. 9.

2. Observations

2.1. CHARA/VEGA

The VEGA instrument (Mourard et al. 2009) is one of the two visible beam combiners on the CHARA Array (ten Brummelaar et al. 2005). It can simultaneously combine up to four beams, operating at different wavelengths from 450 to 850 nm. VEGA is equipped with two cameras (blue and red detectors) that can observe in two different spectral domains simultaneously (around the $H\beta$ and the $H\alpha$ lines). Currently, it is the only instrument at the CHARA Array with a spectral resolution high enough to resolve narrow spectral features such as atomic and molecular lines. It offers 3 spectral modes: $R = 1000$ (LR), $R = 6000$ (MR), and $R = 30\,000$ (HR).

α Aquarii was observed 50 times with VEGA between 2012 and 2016 in MR mode centered on the $H\alpha$ emission line at $0.656 \mu\text{m}$. The 2012 and 2016 observations were focused on the disk geometry and kinematics and data were taken with small baselines (up to 105 m) and without stellar calibrators. On the other hand, the 2013 and 2014 campaigns were aimed at constraining not only the $H\alpha$ emission, but also the R -band continuum geometry. Consequently, observations were carried out with longer baselines (up to 330 m) with a standard calibration plan alternating observations of the science target and few calibrator stars chosen using the SearchCal (Bonneau et al. 2006) tool developed by the Jean-Marie Mariotti Center (JMMC)¹. Table A.1 shows useful information about the stars used as interferometric calibrators during these campaigns. The complete log of observations is presented in Table A.2 and the corresponding uv plane coverage for the VEGA observations is plotted in Fig. 1.

Data were reduced using the standard VEGA data reduction software² described in Mourard et al. (2012). For all programs, differential visibility and phases were computed from the inter-correlation between a fixed 15 nm window centered on $H\alpha$ and a sliding smaller window (i.e. 1, 2, or 5 Å, depending on the data quality). For the 2013 and 2014 data, the raw squared visibility was computed for α Aquarii, and its calibrators, using the auto-correlation method on a 15 nm band centered on the $H\alpha$ emission line (649–664 nm) and another band in the close-by continuum (635–650 nm). Then the transfer function was estimated assuming the diameter of the calibrators recorded before and after the science target observation, and its uncertainty using a weighted standard deviation. Finally, for each measurement, the calibrated squared visibility was derived by dividing α Aquarii's raw squared visibility by the estimated transfer function.

¹ <https://www.jmmc.fr/english/tools/proposal-preparation/search-cal/>

² See VEGA group page at <https://lagrange.oca.eu/fr/vega>.

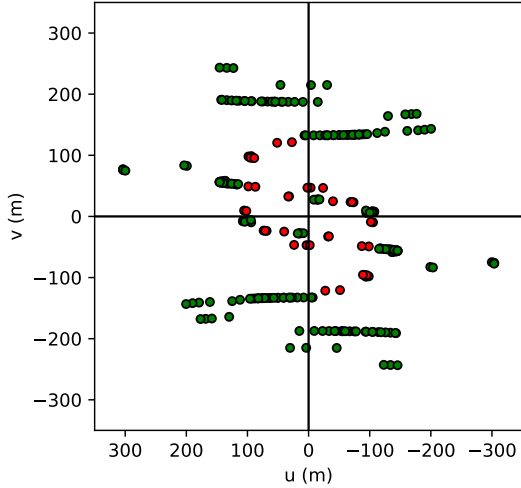


Fig. 1. uv plan coverage obtained around $H\alpha$ ($0.656 \mu\text{m}$) with CHARA/VEGA (green) and $\text{Br}\gamma$ ($2.166 \mu\text{m}$) with VLTI/AMBER (red).

2.2. VLTI/AMBER

The AMBER instrument (Petrov et al. 2007) was a three-beam combiner (decommissioned in 2018) at the Very Large Telescope Interferometer (VLTI). It operated in the H - and K -bands with three spectral resolutions: $R=35$ (LR), $R=1500$ (MR), and $R=12\,000$ (HR). It offered the highest spectral resolution at the VLTI, being the most adapted for studying the gaseous environment in emission lines.

o Aquarii was observed with AMBER during two observing surveys of Be stars in 2011 (ESO program 087.D-0311) and in 2014 (ESO program 094.D-0140). The observations were performed in HR mode in K -band centered on the $\text{Br}\gamma$ emission line at $2.166 \mu\text{m}$. The data from 2011 was published in Meilland et al. (2012) and the 2014 data in Cochetti et al. (2019). During this second survey, seven measurements were acquired for *o* Aquarii with three different triplets. The log of AMBER observations is also presented in Table A.2 and the corresponding uv plane coverage is plotted in Fig. 1.

Calibration was performed using similar methods as the one described for VEGA. However, AMBER measurements were often affected by a highly variable transfer function mainly due to the variable quality of the fringe tracking performed by the FINITO fringe tracker, during the long exposure time needed to perform HR mode observations. As it was the case during our *o* Aquarii observations, we present in this paper only the analysis of differential measurements obtained using the standard AMBER data reduction software amdlib (Tatulli et al. 2007; Chelli et al. 2009).

3. Geometric modeling: VEGA calibrated visibility

In this section, we fit the $H\alpha$ and continuum squared visibilities (V^2) from the VEGA observations where calibrators were observed. We note that as the AMBER data were not calibrated, such analysis cannot be performed on the K -band continuum and $\text{Br}\gamma$ line.

To determine if we can separate the circumstellar disk and the stellar photosphere emissions and constrain their geometry independently, we fitted our data with geometric models of increasing complexity: one-component models (uniform disk, UD, or a uniform ellipse) and two-component models (UD plus UD, Gaussian disk, or uniform or Gaussian ellipse).

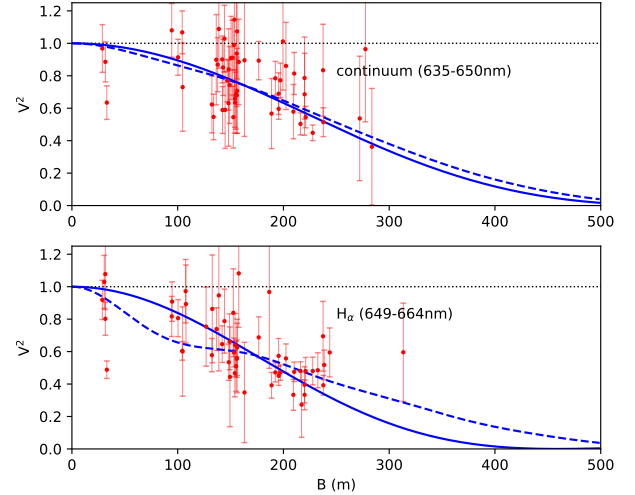


Fig. 2. VEGA V^2 measurements in the close-by continuum band (*top*) and in the $H\alpha$ band (*bottom*) are shown in red points. Our best-fit models consisting of one (solid line) and two (dashed line) uniform disks are overplotted in blue. See Table 1 and text for discussion.

Here, the first component represents the stellar surface and the second one the circumstellar disk. To perform our fit, we used the LITpro model fitting software (Tallon-Bosc et al. 2008) for optical and infrared interferometric observations developed by the Jean-Marie Mariotti Center (JMMC)³.

In Fig. 2, we show the comparison between the visibility curves of our best-fit models to the VEGA data both in the continuum and $H\alpha$ bands. One sees that the object is partially resolved in the continuum and the $H\alpha$ line. The lower level of the visibility in the band centered on the $H\alpha$ line clearly shows that the object is larger in $H\alpha$ than in the close-by continuum region. Assuming that the emission originates from both the stellar photosphere and a circumstellar disk, the lower visibility in $H\alpha$ is due to a larger fraction of the $H\alpha$ flux coming from the disk than from the star. In contrast, the flux contribution from the star is greater than that from the disk in the continuum R -band.

Our main results are summarized in Table 1. We only show our results using UD models since there is no improvement in terms of reduced χ^2 (χ_r^2) when considering more complex models, that is, with a higher number of free parameters. For the continuum band, there is no significant improvement in terms of reduced χ^2 between a simple UD and a two-component UD model. The central star is clearly resolved by the longer baselines and its extension is significantly constrained with a UD diameter of $\theta = 0.28 \pm 0.01$ mas ($\chi_r^2 \sim 1.1$). This value corresponds to an upper limit to the stellar diameter measurements neglecting the putative contribution of the circumstellar disk in the R -band continuum. Adding a second component to the model only marginally reduces the extension of the first component. The contribution of the second component, representing the circumstellar disk, is small ($F_2 = 0.03 \pm 0.03$), thus the extension of the disk cannot be constrained.

Unlike the continuum case, the situation is quite different in the band centered on the $H\alpha$ line. The single uniform disk gives a significantly higher $\chi_r^2 \sim 2.8$ for a best-fit model with $\theta = 0.36$ mas. In this case, adding a second component reduces χ_r^2 by a factor of two, leading to $\chi_r^2 \sim 1.3$. Using a model with two uniform disks, we converge to a diameter of the first

³ LITpro software is available at <https://www.jmmc.fr/english/tools/data-analysis/litpro/>

Table 1. Results from the geometric modeling of the VEGA V^2 data in the close-by continuum band (635–650 nm) and in the band centered on $H\alpha$ (649–664 nm).

Model	Continuum (635–650 nm)				$H\alpha$ (649–664 nm)			
	θ_1 (mas)	θ_2 (mas)	F_2	χ_r^2	θ_1 (mas)	θ_2 (mas)	F_2	χ_r^2
1 UD	0.28 ± 0.01	–	–	1.1	0.36 ± 0.01	–	–	2.8
2 UDs	0.27 ± 0.02	23^{+82}_{-23}	0.03 ± 0.03	1.1	0.26 ± 0.02	6.5 ± 2.1	0.15 ± 0.03	1.3

Notes. For each band, many models were tested, but only these composed of one and two uniform disks (UD) are presented here. The angular diameter of each UD component is denoted as θ_1 and θ_2 . The normalized flux contribution of the first and second model components are, respectively, F_1 and F_2 ($F_1 + F_2 = 1$). All parameters were free in our modeling.

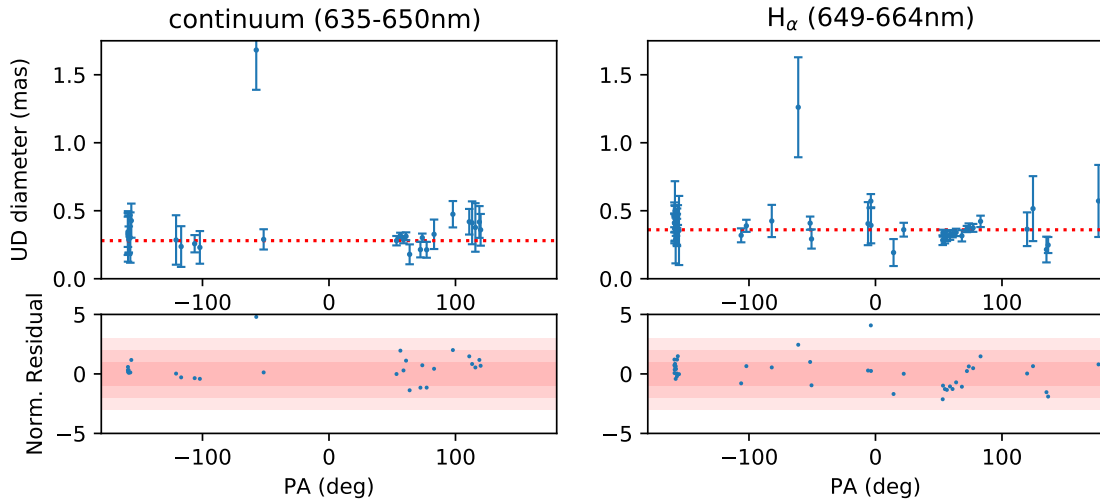


Fig. 3. Top panels: uniform disk diameter derived from each individual VEGA V^2 measurements (continuum band in the left and $H\alpha$ band in the right) plotted as a function of the baseline position angle (PA). The red dotted line represents the best-fit diameter from modeling all the data in each band ($\theta = 0.28$ mas in the continuum and $\theta = 0.36$ mas in the $H\alpha$ band). Bottom panels: corresponding normalized residuals.

component similar to the one found from the continuum, that is, 0.26 ± 0.02 mas. The flux contribution of the second component and its extension are significantly constrained. However, the uncertainty remains quite large, that is, $F_2 = 0.15 \pm 0.03$ and $\theta_2 = 6.5 \pm 2.1$ mas (see Table 1).

Considering that the first component of our model represents the stellar photosphere, our measurement is slightly higher than the value assumed in the work of Sigut et al. (2015) of 0.22 mas. However, their adoption for the stellar angular diameter is based on a spectral type-radius relation for B dwarf stars (Townsend et al. 2004). Moreover, this value of 0.22 mas represents the polar radius. α Aquarii is a fast rotator likely to be significantly flattened, and our measurements are spread over different orientations, so that we end up measuring a mean radius of the star projected on the sky. Assuming a distance of 144 pc (derived from the Gaia DR2 parallaxes, Gaia Collaboration 2018), $\theta_1 = 0.26 \pm 0.02$ mas corresponds to a stellar radius $R_\star = 4.0 \pm 0.3 R_\odot$.

Finally, to try to detect any possible stellar or circumstellar disk flattening from the squared visibility measurements, we also computed individual uniform disk equivalent diameter for each V^2 measurement. This analysis of the uniform disk diameter for α Aquarii, as a function of the VEGA baseline orientation, is shown in Fig. 3. As expected from our analysis (considering uniform elliptical models), we do not find any evidences of flattening from modeling our V^2 dataset since no clear trends are found in the model residual as varying the baseline position angle.

4. Kinematic modeling: VEGA and AMBER differential data

To constrain the geometry and kinematics of the circumstellar gas in the $H\alpha$ and $\text{Br}\gamma$ lines, we fit the VEGA and AMBER differential visibility and phase measurements using a simple bi-dimensional kinematic model for a rotating disk⁴.

4.1. The kinematic model

This kinematic model was already used in a series of papers about spectro-interferometric modeling of Be stars, including Delaa et al. (2011), Meilland et al. (2012), and Cochetti et al. (2019), and is presented in detail in these references.

In short, the intensity map for the central star is modeled as a uniform disk, and the circumstellar disk as two elliptical Gaussian distributions, one for the flux in continuum, and the other one for the flux in line. The disk is geometrically thin so that the ellipse flattening ratio is set to $1/\cos i$, where i is the inclination angle. The disk intensity map in the line is computed taking into account the Doppler effect due to the disk rotational velocity in the considered spectral channels. The parameters of our kinematic model are the following:

(i) The simulation parameters: size in pixels (n_{xy}), field of view in stellar diameters (f_{ov}), number of wavelength points

⁴ Available at the JMMC service AMHRA: <https://amhra.oca.eu/AMHRA/>

(n_λ), central wavelength of the emission line (λ_0), step size in wavelength ($\delta\lambda$), and spectral resolution ($\Delta\lambda$).

(ii) The global geometric parameters: stellar radius (R_\star), distance (d), inclination angle (i), and disk major-axis position angle (PA).

(iii) The disk continuum parameters: disk major-axis FWHM in the continuum (a_c), disk continuum flux normalized by the total continuum flux (F_c).

(iv) The disk emission line parameters: disk major-axis FWHM in the line (a_{line}) and line equivalent width (EW).

(v) The kinematic parameters: rotational velocity (v_{rot}) at $1.5 R_p$ (polar radius) and exponent of the rotational velocity power-law (β).

4.2. Model fitting using the MCMC method

To perform our model fitting, we used the code emcee (Foreman-Mackey et al. 2013). This is an implementation in Python of the MCMC method from Goodman & Weare (2010). Some recent works on stellar interferometry used this code (see., e.g., Monnier et al. 2012; Domiciano de Souza et al. 2014, 2018; Sanchez-Bermudez et al. 2017).

The simulation parameters were set as follows: $n_{xy} = 256$, $fov = 60 D_\star$, $n_\lambda = 60$ (VEGA) and 110 (AMBER), $\lambda_0 = 6563 \text{ \AA}$ (VEGA) and $21\,661 \text{ \AA}$ (AMBER), $\delta\lambda = 2.5 \text{ \AA}$ (VEGA) and 1.0 \AA (AMBER), and $\Delta\lambda = 5.0 \text{ \AA}$ (VEGA) and 1.8 \AA (AMBER). To reduce the number of free parameters, we set $R_\star = 4.0 R_\odot$ and $d = 144 \text{ pc}$. We also fixed the disk continuum extension a_c and flux F_c to 0 for VEGA (i.e., neglecting the disk contribution in the continuum, based on our analysis of the VEGA V^2 data). In the AMBER analysis, we adopted $a_c = 3 D_\star$ and $F_c = 0.2$ from Cochetti et al. (2019). The line equivalent width was set to 19.9 \AA in $H\alpha$ (Sigut et al. 2015). For Bry, we computed the EW using the AMBER spectra from all observations and found a mean value of $13.6 \pm 1.1 \text{ \AA}$, which is compatible with the value from Meilland et al. (2012), 12.6 \AA , but not with the result from Cochetti et al. (2019) of 18.1 \AA . Finally, from the ten parameters of the kinematic model, the fitting of the VEGA and AMBER data were performed with at most five free parameters: i , PA, a_{line} , v_{rot} , and β .

The likelihood function (p_{like}) of the MCMC procedure was chosen as $\ln(p_{\text{like}}) = -\chi_{\text{total}}^2/2$, where χ_{total}^2 is the sum of the χ^2 computed for the differential visibility and the differential phase. Thus, our attempt to converge to samples of parameters that maximizes the likelihood function means the minimization of the total χ^2 between our interferometric data and the kinematic model.

We performed three different model fitting tests with different constraints on the value of v_{rot} :

(i) Five free parameters: i , PA, a_{line} , v_{rot} , and β . Without the inclusion of any prior probability function in the analysis.

(ii) Four free parameters: i , PA, a_{line} , and β . The stellar rotational velocity v_{rot} is fixed on the critical value of 391 km s^{-1} (Frémat et al. 2005).

(iii) Five free parameters: i , PA, a_{line} , v_{rot} , and β . We take into account a prior probability function p_{prior} on $v \sin i$. Adopting $\mu = 282 \text{ km s}^{-1}$ and $\sigma = 20 \text{ km s}^{-1}$, from the measured $v \sin i = 282 \pm 20 \text{ km s}^{-1}$ (Frémat et al. 2005), we have the following expression for p_{prior} :

$$\ln(p_{\text{prior}}) = \frac{-(v \sin i - \mu)^2}{2\sigma^2}, \quad (1)$$

where $v \sin i$ is calculated from the sampled MCMC values for the stellar rotational velocity and inclination angle.

Table 2. Best-fit kinematic models from test (iii) for our VEGA ($H\alpha$) and AMBER (Bry) differential data.

Parameter	VEGA diff.	AMBER diff.
i (deg)	$61.2_{-1.8}^{+1.6}$	$75.9_{-0.4}^{+0.4}$
PA (deg)	$108.4_{-1.9}^{+1.9}$	$110.0_{-0.3}^{+0.3}$
a_{line} (D_\star)	$10.5_{-0.3}^{+0.3}$	$11.5_{-0.1}^{+0.1}$
v_{rot} (km s^{-1})	325_{-6}^{+6}	303_{-2}^{+2}
β	$-0.30_{-0.01}^{+0.01}$	$-0.426_{-0.003}^{+0.003}$
R_\star (R_\odot)	$\equiv 4.0^{(a,b)}$	$\equiv 4.0^{(a,b)}$
d (pc)	$\equiv 144^{(c)}$	$\equiv 144^{(c)}$
a_c (D_\star)	$\equiv 0^{(a)}$	$\equiv 3^{(d)}$
F_c	$\equiv 0^{(a)}$	$\equiv 0.2^{(d)}$
EW (\AA)	$\equiv 19.9^{(e)}$	$\equiv 13.6^{(f)}$
χ_r^2	4.04	1.57

Notes. We show the median and the first and third quartiles for each parameter derived from the MCMC analysis. Adopted parameters stand by “ \equiv ”. ^(a)Based on our fit to the VEGA squared visibility. ^(b)Radius derived considering the distance adopted from Gaia Collaboration (2018). ^(c)Distance adopted from Gaia Collaboration (2018). ^(d)Adopted from Cochetti et al. (2019). ^(e)Adopted from Sigut et al. (2015). ^(f)Measured from our AMBER observations.

Hence, considering a high weight on p_{prior} , the following quantity for the posterior probability function p_{post} is maximized:

$$\ln(p_{\text{post}}) = -100 \left(\frac{(v \sin i - \mu)^2}{2\sigma^2} \right) - \frac{\chi^2}{2}. \quad (2)$$

Note that this is equivalent to the case of equal weights for p_{prior} and p_{like} , but considering a lower error bar on $v \sin i$, namely, $\sigma = 2 \text{ km s}^{-1}$.

We typically used several hundreds of walkers (~ 300 – 900) for the MCMC run. Convergence was obtained for about 50 to 100 iteration steps in each walker, but we used a conservative value of 150 steps in the burn-in phase and 50 in the main phase to estimate the parameters values and uncertainties. Overall, we found a mean acceptance fraction of ~ 0.5 – 0.6 in our MCMC tests. This is close to the optimal range for this parameter of ~ 0.2 – 0.5 (see, e.g., Foreman-Mackey et al. 2013).

4.3. Best-fits in $H\alpha$ and Bry

We modeled a total of 117 (VEGA) and 24 (AMBER) measurements of differential visibility and phase. The best-fit parameters for the MCMC fit with a prior on $v \sin i$ (test iii, described above) are presented in Table 2. The corresponding histograms and the two-by-two parameter correlations from this MCMC run (one for VEGA and other for AMBER) are shown in Fig. 4. The corresponding histograms and correlation plots for the other two fits (tests i and ii) are shown in Figs. B.1 and B.2. One sees that the values of i , PA, and a_{line} , derived from each emission line, differ only marginally in all the fitting tests, showing the robustness of the solution for these parameters.

In Fig. 5, we show examples of VEGA and AMBER data in comparison to our best-fit kinematic models. For later discussion in Sect. 6, the visibility and phase from our best-fit HDUST model is also presented here. Our best-fit kinematic models are able to reproduce both the VEGA and AMBER differential data

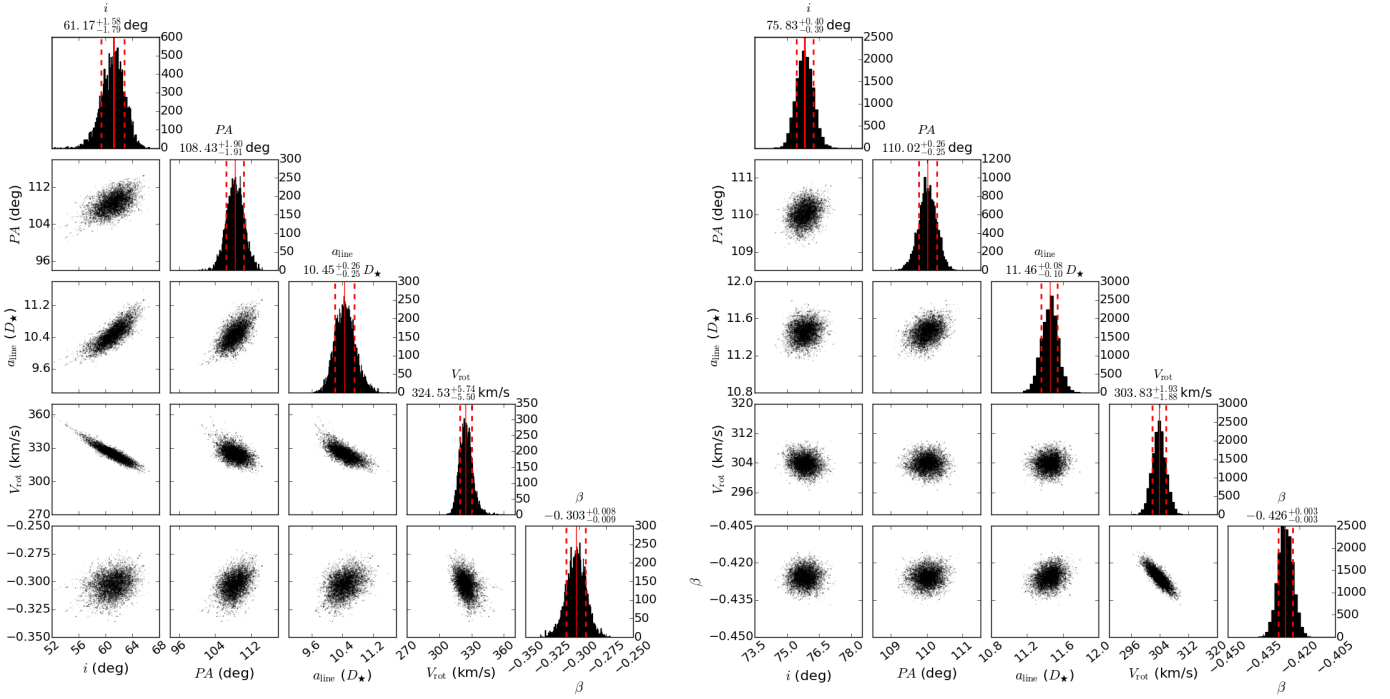


Fig. 4. Histogram distributions and two-by-two correlations (after the burn-in phase) for the free parameters of our best-fit kinematic models using MCMC for the VEGA (*left panel*) and AMBER (*right panel*) differential data. The median values are shown in solid red lines and the first and third quartiles in dashed red lines. The median and the first and third quartiles estimated for the parameters of our best-fit models (VEGA and AMBER) are presented in Table 2. In the correlation plots, darker points correspond to models with lower values of χ^2 . See text for discussion.

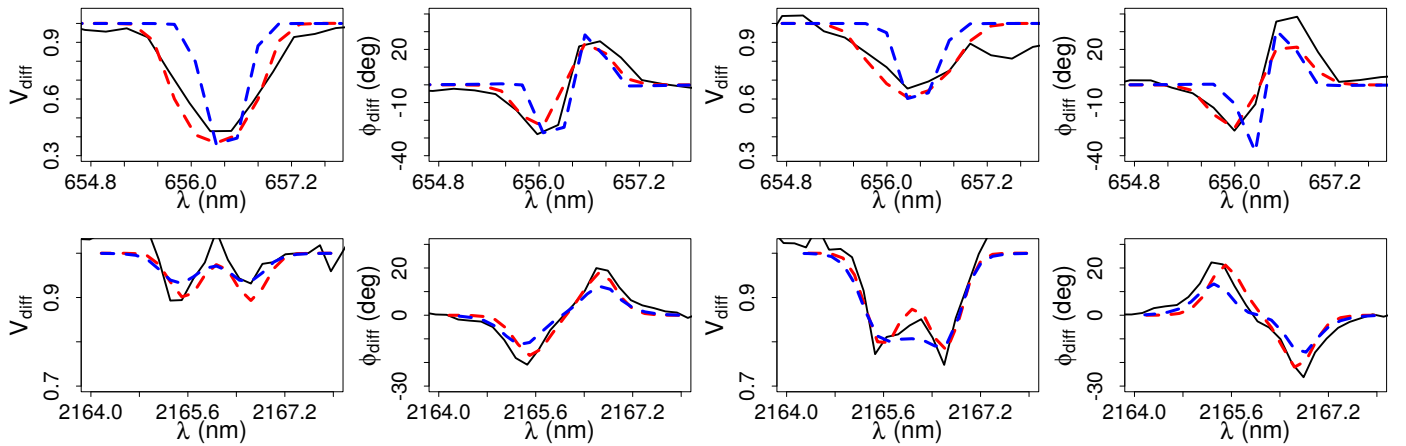


Fig. 5. Comparison between our best-fit kinematic models (dashed red; Table 2) and two different VEGA (*top panels*) and AMBER (*bottom panels*) measurements (black line). Our best-fit HDUST model is also shown (dashed blue; Table 5; discussion in Sect. 6). $\delta\lambda$ of the kinematic model and AMBER data is increased to 1.8 Å in order to compare them to the HDUST model ($\delta\lambda$ fixed to 1.8 Å).

well. We found a reduced χ^2 of ~ 4.0 and 1.6 from fitting, in a separate way, respectively, the VEGA and AMBER datasets.

We derived compatible values for the disk PA ($\sim 110^\circ$) from fitting the VEGA and AMBER data with an uncertainty up to $\sim 2^\circ$. This result agrees well with previous studies (e.g., Meilland et al. 2012; Touhami et al. 2013; Sigut et al. 2015; Cochetti et al. 2019). On the other hand, the inclination angle determined from the fit to the VEGA data is significantly smaller ($i = 61.2 \pm 1.8^\circ$) in comparison to the one determined from fitting AMBER ($i = 75.9 \pm 0.4^\circ$). This latter value is in good agreement with the results for i found by Meilland et al. (2012) and Cochetti et al. (2019). We also constrain the disk extension with a good precision: $a_{\text{line}} = 10.5 \pm 0.3 D_\star$ in the H α line and $a_{\text{line}} = 11.5 \pm 0.1 D_\star$

in the Bry line. These values are compatible with the ones determined by Sigut et al. (2015) in H α and Meilland et al. (2012) in Bry.

Another aspect concerning the disk extension in Bry is the significant discrepancy seen in comparison to $a_{\text{line}} = 8.0 \pm 0.5 D_\star$ from Cochetti et al. (2019). However, these authors used a larger value for the stellar radius of $4.4 R_\odot$ and a closer distance of 134 pc (van Leeuwen 2007), having thus the angular size of the stellar diameter larger in $\sim 19\%$ than the one assumed in our kinematic analysis from our results in Sect. 3. Considering all the other parameters fixed, this results in a smaller disk extension in $\sim 19\%$ than one found from our analysis. Nevertheless, the largest contribution to this discrepancy between our results and the ones

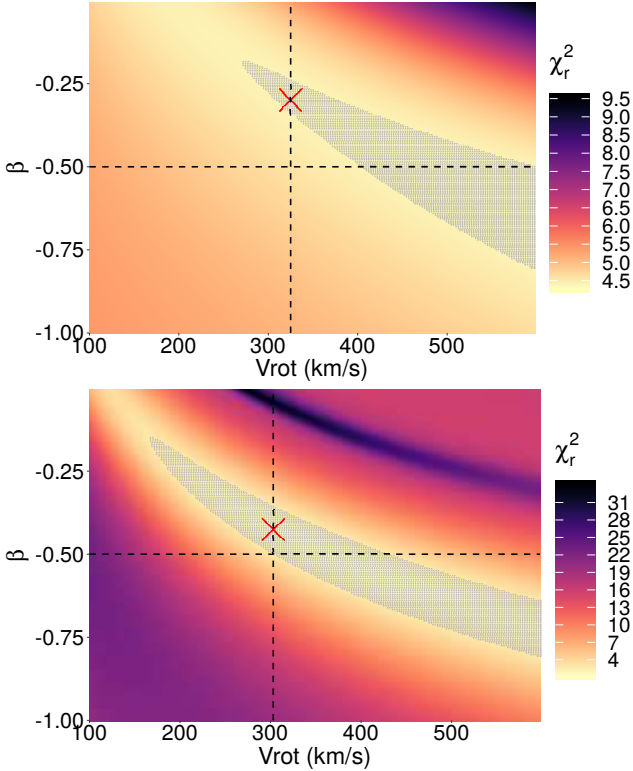


Fig. 6. χ_r^2 maps of 40 000 kinematic models as a function of v_{rot} and β from the fit to VEGA (*top panel*) and AMBER (*bottom panel*) differential data. Only these two parameters were varied in a regular step in the intervals shown here. The other parameters are fixed (Table 2). Our results found from the MCMC analysis for v_{rot} and β are indicated with red crosses. In order to highlight the correlation between β and v_{rot} , the gray region corresponds to an arbitrary number of models, encompassing about the 5000 best models in both cases. The value of $\beta = -0.5$ (Keplerian disk) and our determination for v_{rot} are marked in dashed black line. Note the strong correlation between the stellar rotational velocity and the disk velocity law exponent in both the cases. Also, note that a Keplerian disk is found from modeling the AMBER data, but not from VEGA.

from Cochetti et al. (2019) is due to their high value of equivalent width in the Br γ line of 18.1 Å, as discussed in Sect. 4.2, that also implies in a smaller disk extension in this line.

From our various tests, we showed that β and v_{rot} are strongly correlated. To precisely determine their dependence, we computed a grid of kinematic models varying just these two parameters in a regular step size. The values for i , PA, a_{line} are fixed from Table 2. The resulting χ_r^2 maps are shown in Fig. 6. As expected, one sees that v_{rot} and β are highly correlated for the VEGA and AMBER data. This high degeneracy can be understood since these two parameters provide the rotational velocity structure in the disk: it is hard to distinguish the effects of each one on the modeling of spectro-interferometric (and spectroscopic) data.

Furthermore, we see that $\beta = -0.5$ (Keplerian disk) provides unrealistically high values for the stellar rotational velocity ($\gtrsim 400 \text{ km s}^{-1}$; gray region) of *o* Aquarii (VEGA analysis). For AMBER, v_{rot} is significantly reduced to about 300–400 km s^{-1} . As shown in Fig. 6, our results from AMBER are consistent with a nearly Keplerian rotating disk ($\beta \sim 0.43$). However, it is conspicuous that the β value calculated from the VEGA data ($\beta \sim 0.30$) shows such a large departure from the Keplerian case.

Cochetti et al. (2019) derived a stellar rotational velocity of $355 \pm 50 \text{ km s}^{-1}$ and $\beta = -0.45 \pm 0.03$. This is in fair agreement

with our results for both v_{rot} and β . Considering our MCMC test (ii), where v_{rot} is fixed to the critical value and β is a free parameter, the results for β are shifted to higher values (more positive) with $\beta \sim -0.42$ (VEGA) and -0.54 (AMBER).

Therefore, regardless the MCMC fitting considered here, we verify a discrepancy of about 0.1 between the value of β derived from the H α and Br γ lines. Our results from the AMBER analysis (Br γ) seems to be consistent with a nearly Keplerian rotating disk, but we verified a larger departure from $\beta = -0.5$ for the VEGA analysis (H α).

5. Radiative transfer modeling

5.1. The code HDUST

We used the 3D non-LTE radiative transfer code HDUST⁵ (Carciofi & Bjorkman 2006, 2008) to perform a deeper physical analysis of *o* Aquarii. In addition to geometric and kinematic parameters, we seek to derive the density and temperature distributions in the disk, and the spectral energy distribution (SED), none of which was provided by the two simpler models considered in the two previous sections. HDUST uses a Monte Carlo method to solve the radiative transfer, statistical and radiative equilibrium equations for arbitrary density and velocity distributions in gaseous (pure hydrogen) or dusty circumstellar environments.

This code is well-suited to model the circumstellar environment of Be stars as it implements the VDD model. Thus, the disk velocity law is assumed to be Keplerian (β fixed to -0.5). Many previous studies explored formal solutions of the VDD model in several limiting cases. For example, Bjorkman & Carciofi (2005) investigated the isothermal, steady-state case of a disk formed by a steady mass injection rate over a long time. Effects due to non-isothermal temperature structure were studied by Carciofi & Bjorkman (2008). Haubois et al. (2012) studied the temporal evolution of the disk structure that is subject to variable mass injection rates. Finally, the effects of a binary companion on the disk were studied by Okazaki et al. (2002), Oudmaijer & Parr (2010), Panoglou et al. (2016), and Cyr et al. (2017), among others.

From these studies, the radial density profile in Be star disks is found to be quite complex, for example, depending on the disk age, dynamical state, or presence of a binary companion. Despite this complexity, several studies have shown that the global behavior of this density profile is successfully approximated by a simple radial power-law (e.g., Touhami et al. 2009; Vieira et al. 2017). Considering also that the vertical density structure is that of an isothermal disk (hydrostatic assumption in the z -axis), the disk density can be parameterized as follows:

$$\rho(r, z) = \rho_0 \left(\frac{R_{\text{eq}}}{r} \right)^m \exp \left(\frac{-z^2}{2H(r)^2} \right), \quad (3)$$

where ρ_0 is the disk base density, R_{eq} is the equatorial radius, and $H(r)$ is the (isothermal) disk scale height given by:

$$H(r) = H_0 \left(\frac{r}{R_{\text{eq}}} \right)^{3/2}, \quad (4)$$

and H_0 is the scale height at the disk base,

$$H_0 = c_s R_{\text{eq}} \left(\frac{GM_{\star}}{R_{\text{eq}}} \right)^{-1/2}, \quad (5)$$

⁵ For access and collaborations with HDUST, please contact A. C. Carciofi.

Table 3. HDUST parameters in the BeAtlas grid.

Parameter	Value
Spectral type	B0.5, B1, B1.5, B2, B2.5, B3, B4, B5, B6, B7, B8
$M_\star (M_\odot)$	14.6, 12.5, 10.8, 9.6, 8.6, 7.7, 6.4, 5.5, 4.8, 4.2, 3.8
i (deg)	0.0, 27.3, 38.9, 48.2, 56.3, 63.6, 70.5, 77.2, 83.6, 90.0
Oblateness (R_{eq}/R_p)	1.1, 1.2, 1.3, 1.4, 1.45
Σ_0 (g cm^{-2}) ^(a)	0.02, 0.05, 0.12, 0.28, 0.68, 1.65, 4.00
m ^(b)	3.0, 3.5, 4.0, 4.5

Notes. First row indicates the spectral type corresponding to the stellar mass (Townsend et al. 2004). Models are calculated with the following fixed parameters: fraction of H in the core $X_c = 0.30$, metallicity $Z = 0.014$, and disk radius = $50 R_{\text{eq}}$.^(a)Surface density at the base of the disk. ^(b)Disk mass density law exponent.

where M_\star is the stellar mass, G the gravitational constant, and c_s the sound speed velocity which depends on the local disk temperature T :

$$c_s = \sqrt{\frac{k_B T}{\mu m_H}}, \quad (6)$$

where k_B is the Boltzmann constant, μ is the mean molecular weight of the gas, m_H is the hydrogen mass, and T is adopted as $0.72T_{\text{pol}}$, where T_{pol} is the polar effective temperature (see Correia Mota 2019).

HDUST has been used a few times to model spectro-interferometric observations (e.g., Carciofi et al. 2009; Klement et al. 2015; Faes 2015). From the solution of the radiative transfer problem, we are able to calculate synthetic spectra and intensity maps as a function of the wavelength around specific spectral lines. We estimated the stellar and circumstellar disk parameters from the comparison of our spectro-interferometric observations (visible and near-infrared) with synthetic observables computed from the Fourier transform of HDUST monochromatic intensity maps.

5.2. BeAtlas grid

Since a few hours are needed to compute a single HDUST model, it is not possible to perform an iterative model fitting procedure similar to the one described in Sect. 4. To overcome this issue, we used a pre-computed grid of HDUST models called BeAtlas (Faes 2015; Correia Mota 2019). The BeAtlas grid is presented and described in detail by these references. It consists of $\sim 14\,000$ models with images (specific intensity maps), SEDs, and spectra calculated in natural and polarized spectra, over several spectral regions, including the $H\alpha$ and $\text{Br}\gamma$ lines that are of interest for the analysis of our VEGA and AMBER dataset.

In Table 3, we show the parameter space covered by BeAtlas. Five physical parameters are varying in the grid. The stellar mass M_\star , the inclination angle i , and the stellar oblateness R_{eq}/R_p , fully describe the star. Other stellar parameters such as the stellar polar radius (R_p), rotational velocity (v_{rot}) and linear and angular rotational rates ($v_{\text{rot}}/v_{\text{crit}}$ and $\Omega/\Omega_{\text{crit}}$) can be computed from M_\star and R_{eq}/R_p assuming rigid rotation under the Roche model (see, e.g., Carciofi & Bjorkman 2008). The two last parameters in

Table 3 describe the circumstellar disk structure and are parameterizations of the VDD model: the base surface density (Σ_0) and the radial density exponent (m).

The previously described volume mass density (Eq. (3)) and the surface mass density are related as follows:

$$\Sigma(r) \equiv \int_{-\infty}^{+\infty} \rho(r, z) dz, \quad (7)$$

$$\rho(r, z) = \frac{\Sigma(r)}{H(r)\sqrt{2\pi}} \exp\left(\frac{-z^2}{2H(r)^2}\right). \quad (8)$$

From that, to facilitate the comparison to other disk models, we note that the relation between the volume and surface mass densities at the base of the disk is given by:

$$\rho_0 = \Sigma_0 \sqrt{\frac{GM_\star}{2\pi c_s^2 R_{\text{eq}}^3}}. \quad (9)$$

The range of values for Σ_0 and m in the grid encompasses somewhat extreme cases in the literature for the circumstellar disk of Be stars. For example, see Fig. 7 of Vieira et al. (2017). The listed values of Σ_0 correspond to ρ_0 from $\sim 10^{-12}$ g cm^{-3} to $\sim 10^{-10}$ g cm^{-3} . Parametric models with $m = 3.5$ are equivalent to the steady-state solution of the viscous diffusion equation considering an isothermal disk scale height. Thus, concerning the mass density law exponent m , models with $m > 3.5$ would represent a disk in an accretion phase, while the ones with $m < 3.5$ a disk in an ongoing process of dissipation (see, e.g., Haubois et al. 2012; Vieira et al. 2017).

5.3. Results

We performed four different analyses of our data using different subsets. For that, the reduced χ^2 between the predicted interferometric observables from each HDUST model and the data was calculated as follows:

- (i) calibrated VEGA V^2 in the 642.5 nm band (close-by continuum to $H\alpha$).
- (ii) VEGA differential visibility and phase ($H\alpha$ line).
- (iii) AMBER differential visibility and phase ($\text{Br}\gamma$ line).
- (iv) All the quantities above analyzed together.

Analysis (i) was performed to evaluate the constraint on the stellar mass M_\star and oblateness R_{eq}/R_p . In Fig. 7, we show the lowest value of χ_r^2 for each value of stellar oblateness and mass from fitting the VEGA V^2 data in the continuum band. The predicted V^2 from our best-fit BeAtlas model (with $M_\star = 4.2 M_\odot$; Table 5) is overplotted to the VEGA measurements. For comparison, the predicted visibility curve from the BeAtlas model with the highest stellar mass, $M_\star = 14.6 M_\odot$, is also overplotted to the data. These two models have the same values of i , R_{eq}/R_p , Σ_0 , and m . In Sect. 3, we presented a similar analysis, but in terms of simple geometric models. For better visualisation, we show in Fig. 7 the local regression fits of χ_r^2 as a function of R_{eq}/R_p and M_\star . Like all such calculations in this paper, all these regression fits of χ_r^2 are performed with the LOESS method⁶.

As in the analysis with geometric models, we cannot constrain the stellar oblateness using VEGA V^2 data. On the other hand, the mass is better constrained with $M_\star \sim 4.8 M_\odot$ (B6 dwarf). From Fig. 7, one sees how the measured V^2 are mismatched by the HDUST model with $M_\star = 14.6 M_\odot$ (unrealistic mass value for σ Aquarii) due to the larger polar radius of

⁶ As implemented in R: <https://stat.ethz.ch/R-manual/R-devel/library/stats/html/loess.html>

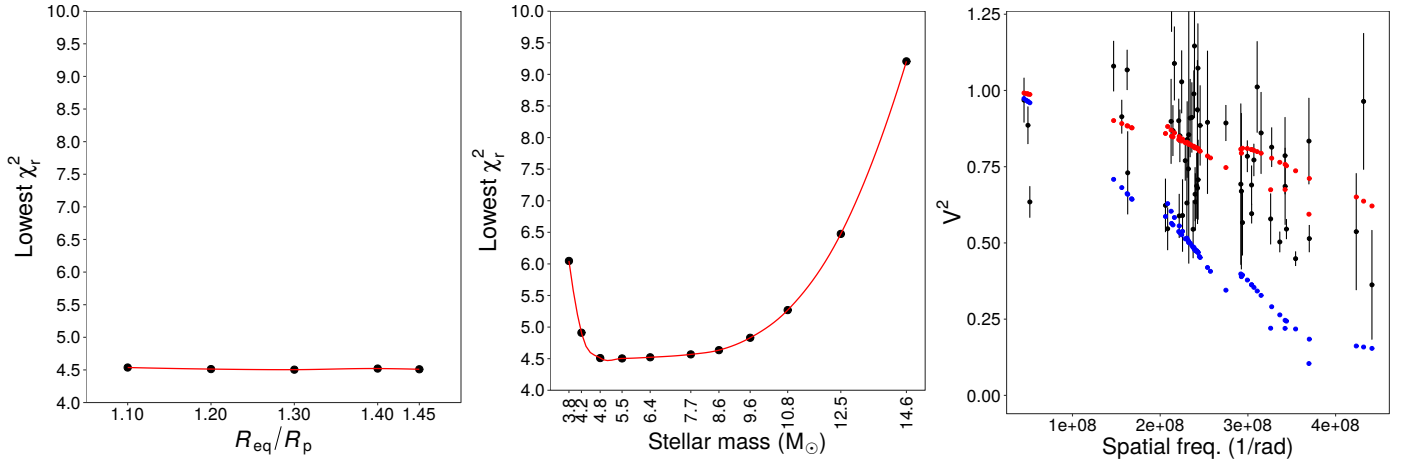


Fig. 7. Analysis (i): lowest value of reduced χ^2 (χ_r^2) for each value of R_{eq}/R_p (left panel) and stellar mass (middle panel) from the HDUST fit to the VEGA V^2 data (642.5 nm band). Local regression fits to χ_r^2 , as a function of the parameter values, are shown in red line. In the right panel, the predicted visibility from our best-fit HDUST model (red points; Table 5) is compared to the VEGA V^2 measurements in the continuum band (black points). The predicted visibility from the HDUST model with the highest mass in the BeAtlas grid ($14.6 M_\odot$, highest χ_r^2 in the middle panel) is shown in blue points.

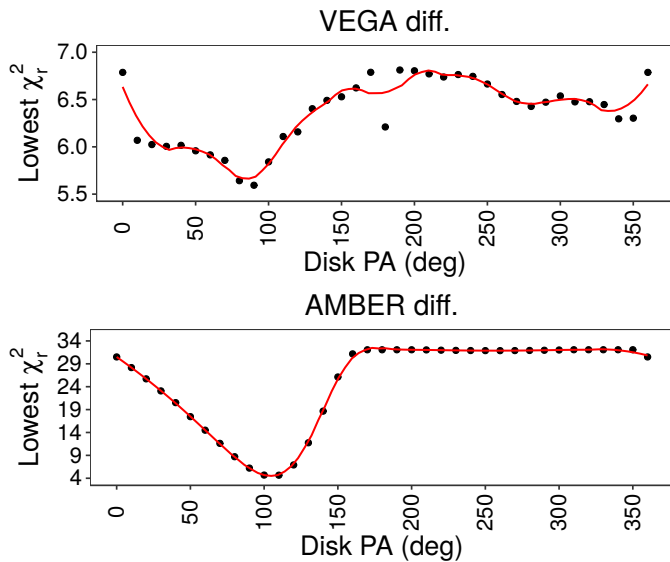


Fig. 8. Lowest value of χ_r^2 for each value of disk major-axis position angle from the HDUST fit to the VEGA (top panel, analysis (ii)) and AMBER (bottom panel, analysis (iii)) differential visibility and phase. Local regression fits of χ_r^2 as a function of the disk PA are shown as a red line.

$\sim 7.4 R_\odot$ in this model. Among all the values for M_\star in the grid, $M_\star = 4.2 M_\odot$ corresponds to a B7 dwarf star (Townsend et al. 2004). Since *o* Aquarii shows luminosity class III-IV, it could be expected to have a mass somewhat higher than a dwarf of same spectral type, which is compatible with our results.

In Fig. 8, we show the lowest χ_r^2 for each value of disk major-axis position angle PA from the fit to the VEGA and AMBER differential visibilities and phases: analyses (ii) and (iii). Here, the stellar mass is fixed to $M_\star = 4.2 M_\odot$ from analysis (i), which also allows a better comparison to other studies of *o* Aquarii (e.g. Sigut et al. 2015). In both cases, χ_r^2 of the models is minimized around $\text{PA} = 110^\circ$, a value that we adopt in the remaining of this section. This is in good agreement to our results found with the kinematic model in Sect. 4.

In Fig. 9, we present our results from modeling the VEGA and AMBER differential visibility and phase in a separate way – analyses (ii) and (iii) – as well as from the simultaneous fit to all the interferometric data (analysis (iv)). The lowest χ_r^2 is shown as a function of the following HDUST parameters: the inclination angle, stellar oblateness, base disk surface density, and the radial disk density law exponent. In Table 4, we show the statistics from these parameters calculated from the HDUST models within a certain threshold of χ_r^2 , which, in each case, is chosen to match a similar number of models (~ 15 – 20 best-models). In Table 4, the parameters for the models with the lowest value of χ_r^2 are also shown. In Table 5, we show the parameters for the best BeAtlas model to explain simultaneously all our different interferometric datasets.

Since our HDUST analysis is limited to the pre-computed BeAtlas grid (limited parameter space and selected parameter values), we stress that the results presented here do not correspond to the real χ^2 minimum to explain our datasets in the framework of HDUST. Furthermore, the values for the standard deviation are shown in parenthesis in Table 4 since these are not determinations for the error bars on the parameters. They are just an evaluation for the dispersion on the parameters values of the BeAtlas best-models (within in a certain threshold of χ_r^2). For example, from fitting AMBER, we found that all the BeAtlas models have $\Sigma_0 = 0.12 \text{ g cm}^{-2}$, and $m = 3.0$, up to, respectively, the top 207% and top 240% best-models. For this reason, it is shown, in this case, null standard deviation in Table 4 for these parameters (top 54% best-models).

From the separate analysis of the VEGA and AMBER differential datasets, we are able to describe the stellar and disk parameters, in H α and Br γ , by the same HDUST model with: $R_{\text{eq}}/R_p = 1.45$, $\Sigma_0 = 0.12 \text{ g cm}^{-2}$, and $m = 3.0$. One clear exception is found for the inclination angle. From the H α analysis, χ_r^2 is minimized for $i = 56.3^\circ$. On the other hand, this is achieved with $i = 77.2^\circ$ in the Br γ line. Such discrepancy of $\sim 20^\circ$ is in agreement with the one found from our kinematic modeling. As expected, the joint analysis to all the data provides an intermediate mean value of $\sim 65^\circ$ for the inclination angle, showing a larger dispersion (higher standard deviation) in comparison to the results found from the separate analysis for VEGA and

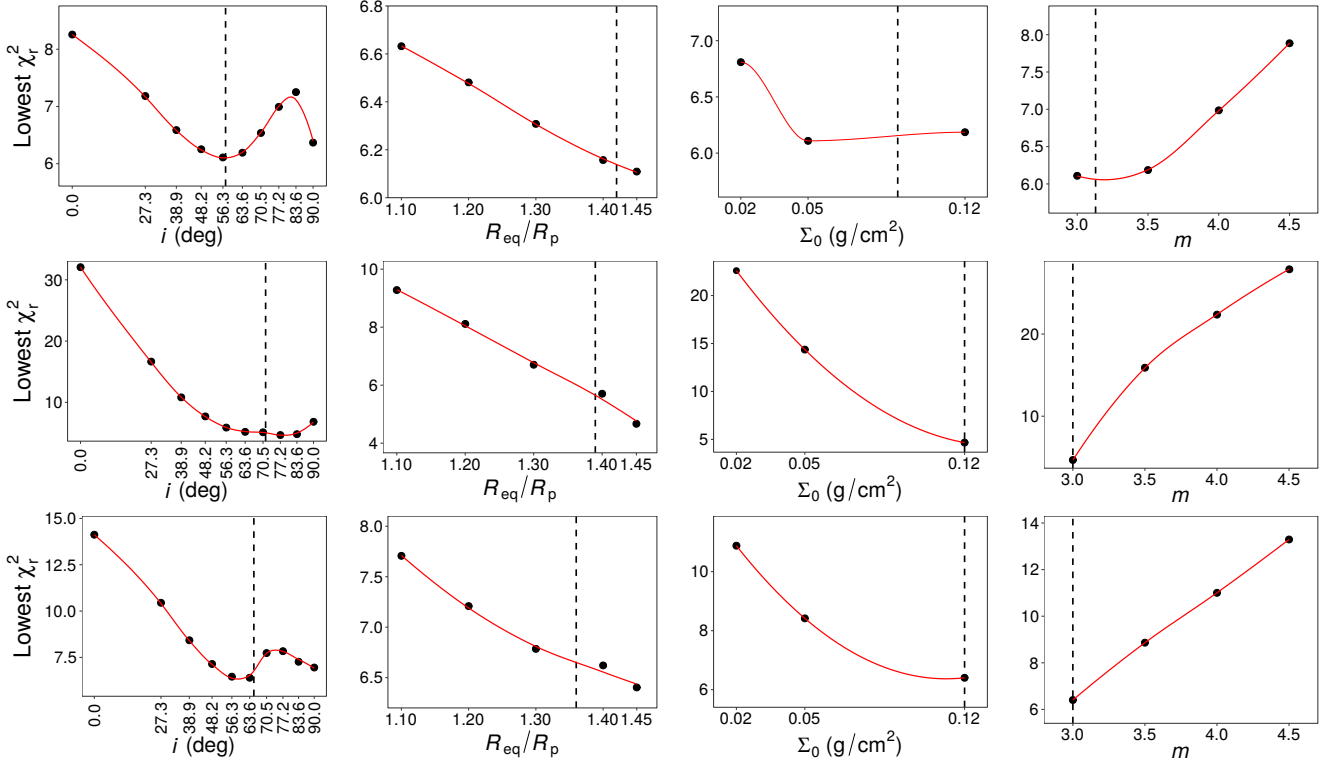


Fig. 9. Lowest value of χ_r^2 for each value of stellar inclination angle, oblateness, base disk surface density, and disk density law exponent from the HDUST fit to the: VEGA differential data (*top*, analysis (ii)), AMBER differential data (*middle*, analysis (iii)), and all the interferometric data considered in this section (*bottom panel*, analysis (iv)). The stellar mass is fixed to $4.2 M_\odot$ and disk PA to 110° . Local regression fits to χ_r^2 , as a function of the parameter values, are shown as a red line. The mean parameter values for the sets of best models (Table 4) are marked in dashed black line. Our best-fit BeAtlas model to fit all the interferometric data is shown in Table 5. See text for discussion.

Table 4. First three columns: mean and standard deviation values for each HDUST parameter of the BeAtlas grid: from analysis (ii) (19 best-fit HDUST models), analysis (iii) (16 best-fit HDUST models), and analysis (iv) (17 best-fit HDUST models).

Parameter	VEGA diff. (19 best models) ^(a)	AMBER diff. (16 best models) ^(a)	All interf. (17 best models) ^(a)	VEGA diff. ($\chi_{\min,r}^2$)	AMBER diff. ($\chi_{\min,r}^2$)	All interf. ($\chi_{\min,r}^2$)
i (deg)	57.3 (5.3)	71.5 (10.8)	65.3 (15.8)	56.3	77.2	63.6
R_{eq}/R_p	1.42 (0.05)	1.39 (0.07)	1.36 (0.09)	1.45	1.45	1.45
Σ_0 (g cm ⁻²)	0.09 (0.05)	0.12 (0.00)	0.12 (0.00)	0.05	0.12	0.12
m	3.13 (0.22) ^(b)	3.00 (0.00)	3.00 (0.00)	3.0	3.0	3.0
χ_r^2	[6.11,6.35]	[4.67,7.19]	[6.40,7.68]	6.11	4.67	6.40
Top A% best ^(c)	4%	54%	20%	–	–	–

Notes. In the bottom rows, there are shown the intervals of χ_r^2 between the minimum value $\chi_{\min,r}^2$ and a certain threshold A ($\chi_{\min,r}^2 + A\%$). From modeling the AMBER data, all models have $\Sigma_0 = 0.12$ g cm⁻² and $m = 3.0$ up to, respectively, $\chi_{\min,r}^2 + 207\%$ and 240% , thus the standard deviation shown here is null. The parameters of the HDUST models with $\chi_{\min,r}^2$ are given in the last three columns. The stellar mass is fixed to $4.2 M_\odot$ and disk PA = 110° . ^(a)These values of standard deviation are given in parenthesis since they are not error bars on the parameters. ^(b)Mean and standard deviation calculated from 16 models since three out of 19 models, in this χ_r^2 threshold, are non-parametric models of the BeAtlas grid. ^(c)“Top A% best” stands by the HDUST models with $\chi_{\min,r}^2 \leq \chi_r^2 \leq \chi_{\min,r}^2 + A\%$, where $\chi_{\min,r}^2$ is the minimum χ_r^2 . These thresholds are chosen to encompass about the same number of HDUST models (~ 15 – 20 models).

Table 5. Parameters of our best-fit HDUST model in the BeAtlas grid to explain the joint analysis of our interferometric data: VEGA calibrated and differential data and AMBER differential data.

M_\star (M_\odot)	R_{eq}/R_p	i (deg)	PA (deg)	Σ_0 (g cm ⁻²)	m	R_p (R_\odot)	v_{rot} (km s ⁻¹)	$v_{\text{rot}}/v_{\text{crit}}$
4.2	1.45	63.6	110	0.12	3.0	3.7	368	0.96

Notes. A part of these parameter values are presented in the last column of Table 4. The polar radius and the stellar rotational velocity are obtained from M_\star and R_{eq}/R_p . The linear rotational rate is also shown here (v_{crit} from Frémat et al. 2005).

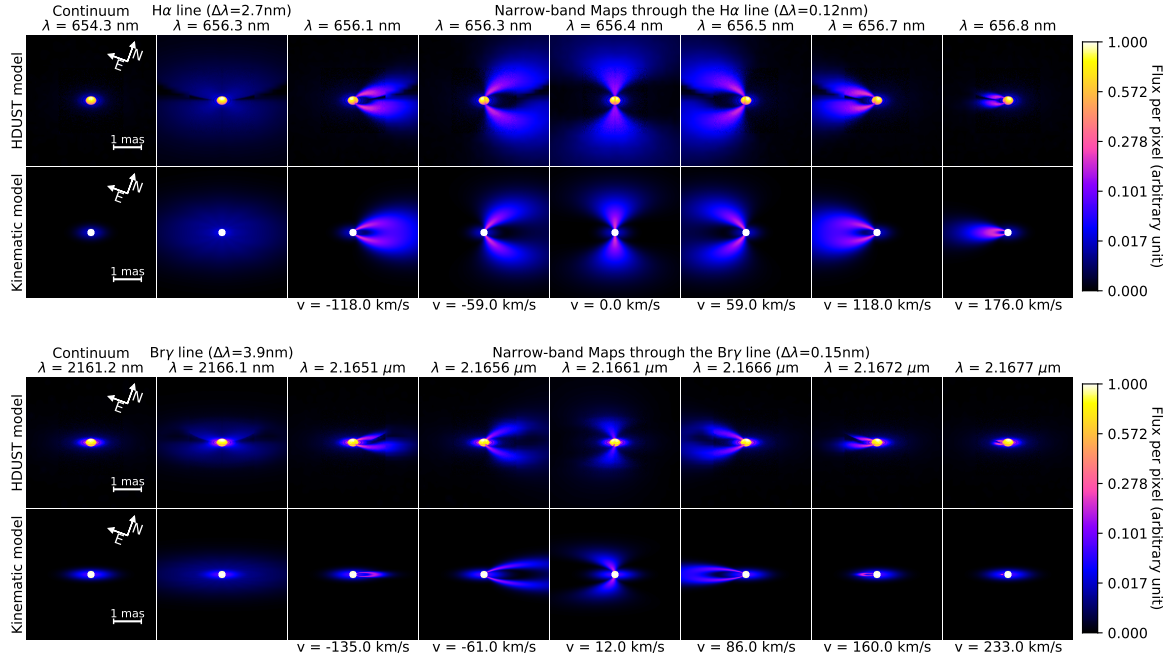


Fig. 10. Intensity maps of our best-fit HDUST and kinematic models at different wavelengths around the $H\alpha$ line (*first two rows*) and the $B\gamma$ line (*last two rows*). Flux/pixel is in arbitrary units with the same scale in $H\alpha$ and $B\gamma$. The image integrated in wavelength around each of these lines ($\Delta\lambda = 2.7$ nm around $H\alpha$ and 3.9 nm around $B\gamma$) are shown in the second column.

AMBER. One sees that the mean value for stellar oblateness is somewhat decreased, when considering all the datasets. However, in this case, the dispersion is significantly increased (± 0.09) when compared to the separate VEGA and AMBER differential fits (± 0.05 – 0.07). This happens due to the inclusion of the calibrated VEGA data in the joint analysis that do not allow us to properly infer this parameter (see, again, Fig. 7).

6. Comparison between kinematic and HDUST best-fit models

In Fig. 5, we compare the synthetic differential visibility and phase from our best-fit kinematic and HDUST models to the actual VEGA and AMBER data for a few baselines. Comparisons to non-interferometric observables (spectral energy distribution and line profiles) are presented in Sect. 7. Our best-fit models are compared to all the AMBER data in Fig. C.1. One sees that our best-fit kinematic models do a better job of reproducing both the VEGA and AMBER data. From the separate kinematic modeling of the VEGA and AMBER differential data, the χ_r^2 of the model is lower than with HDUST (BeAtlas grid). Fixing the stellar mass to a reliable value for *o* Aquarii ($4.2 M_\odot$), our best-fit HDUST model has $\chi_r^2 \sim 6.1$ and 4.7 for VEGA and AMBER, respectively. From the kinematic modeling, we found $\chi_r^2 \sim 4.0$ and 1.6 to explain these same datasets.

For VEGA, in particular, our best-fit HDUST model adjustment for the measured visibility width is worse than with the kinematic model. This particular issue in modeling the VEGA data can be explained; in HDUST, the disk velocity law exponent is fixed by $\beta = -0.5$ (Keplerian disk rotation), while in the kinematic model it is a free parameter. As shown in Sect. 4.3, we find values for β that are higher than -0.5 , and this is accentuated from the analysis of the VEGA data ($\beta \sim -0.3$).

Apart from this issue regarding the analysis in $H\alpha$, we are able to describe well the disk density with the same physical

parameters in both the $H\alpha$ and $B\gamma$ lines: $\Sigma_0 = 0.12 \text{ g cm}^{-2}$ and $m = 3.0$. As will be later discussed, this result found using HDUST is consistent with the ones presented in Sect. 4.3, showing a similar disk extension in these lines.

In Fig. 10, the intensity maps for each model are shown at the close-by continuum region and at different wavelength values in both the $H\alpha$ and $B\gamma$ emission lines. The integrated intensity map (around each of these lines) is also presented. For a more realistic comparison, here we consider our best-fit kinematic model with a small flux contribution of 5% from the disk in the continuum nearby to $H\alpha$ and $a_c = 2 D_\star$. As shown in Table 2, these parameters were adopted as null in the kinematic analysis for the VEGA data, since we were not able to resolve the disk from our analysis of VEGA V^2 measurements in the continuum band (Sect. 3). Regarding the continuum region close to $B\gamma$, the disk extension and flux contribution are given in Table 2 for the AMBER analysis.

The major difference between the intensity maps in $H\alpha$ and $B\gamma$ is the disk flattening which is due to the different inclination angle derived from these two regions, $i \sim 57^\circ$ ($H\alpha$) and $\sim 72^\circ$ ($B\gamma$), from the best models provided in Table 4. Moreover, as seen in the images, the stellar flattening is taken into account in the HDUST modeling, but not in the kinematic model (the star is modeled as a uniform disk). Apart from these departures, we see that our best-fit HDUST model presents a fairly similar distribution to the one computed with the kinematic code: a Gaussian distribution represents the circumstellar disk. This can be better noted considering the full integrated images around the emission lines.

7. Comparison to non-interferometric observables

In this section, we compare our best-fit models, found from the analysis of interferometric observables, to the observed spectral energy distribution (SED) and line profiles ($H\alpha$ and $B\gamma$)

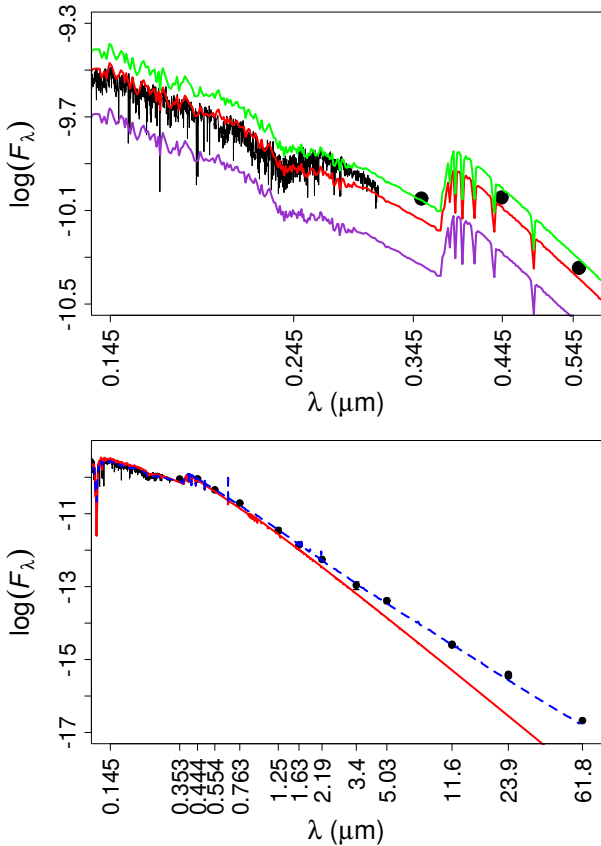


Fig. 11. Comparison between the observed *o* Aquarii and model SEDs from the ultraviolet to the far-infrared region. Flux unit is in $\text{erg cm}^{-2} \text{s}^{-1} \text{\AA}^{-1}$ and wavelength is shown in logarithmic scale. IUE/SWP and IUE/LWP spectra are shown in black line and photometric data in black points. *Top panel:* purely photospheric models (color lines) with variation in the stellar radius (no inclusion of geometrical oblateness): $R_{\star} = 3.2 R_{\odot}$ (orchid), $4.0 R_{\odot}$ (red), and $4.4 R_{\odot}$ (green). *Bottom panel:* photospheric model with $4.0 R_{\odot}$ (red) and our best-fit HDUST model from fitting all the interferometric data (dashed blue line; Table 5). Note that the *UBV*-bands are better reproduced with $R_{\star} = 4.0\text{--}4.4 R_{\odot}$. Our best HDUST model reproduces the observed IR excess due to the circumstellar disk well.

of *o* Aquarii. With respect to polarimetric data, it is discussed in Sect. 8.4.3 when addressing the disk stability.

7.1. Spectral energy distribution

In Fig. 11, we present the spectral energy distribution (SED) of *o* Aquarii from the ultraviolet (IUE/SWP and IUE/LWP spectra⁷) to the far-infrared region. References for the photometric data are given as follows: *UBVJHK*-bands (Anderson & Francis 2012), *i*-band (Henden et al. 2016), *LM*-bands (Bourges et al. 2017), and IRAS 12, 25, and 60 μm bands (Abrahamyan et al. 2015).

For the spectral region up to the *V*-band, we compare the data to the SEDs of purely photospheric atmosphere models with solar metallicity (Castelli & Kurucz 2004). In this region, the circumstellar disk flux level is much lower than the photospheric flux, thus allowing a proper probe of the stellar radius (e.g., Meilland et al. 2009). The surface gravity was fixed at $\log g = 4.0$, this being the closest value in Castelli & Kurucz (2004) to $\log g = 3.9$ that is given by our results of $M_{\star} = 4.2 M_{\odot}$

⁷ Public data available in the Barbara A. Mikulski Archive for Space Telescopes (MAST): <https://archive.stsci.edu/iue/>

and $R_{\star} = 4.0 R_{\odot}$. The effective temperature was fixed at 13 000 K, following Cochetti et al. (2019). As in the previous sections, we consider the distance to be 144 pc, from the *Gaia* DR2 parallax.

These synthetic SEDs were calculated for three different stellar radius values, R_{\star} : $3.2 R_{\odot}$ (Sigut et al. 2015), $4.0 R_{\odot}$, and $4.4 R_{\odot}$ (Cochetti et al. 2019). The value of $4.0 R_{\odot}$ corresponds to the stellar radius determined from the fit to the VEGA V^2 data using a two-component model: $4.0 \pm 0.3 R_{\odot}$. The effect of interstellar medium extinction is not included in these models since it is negligible for *o* Aquarii. Assuming a total to selective extinction ratio of $R_V = 3.1$, Touhami et al. (2013) derived a color excess of $E(B-V) = 0.015 \pm 0.008$ for this star from their fit to the SED. This means the observed flux is $\sim 96\%$ of the intrinsic one in the *V*-band (lower by ~ 0.02 dex). It is beyond the scope of this paper to estimate the extinction due to the circumstellar disk, however, from the comparison to purely photospheric models, we see in Fig. 11 that the effect of extinction (due to the interstellar and circumstellar matter) is conspicuously weak on the 0.220 μm bump.

From Fig. 11, we see that the UV and visible regions are better reproduced for a stellar radius of about $4.0\text{--}4.4 R_{\odot}$, when compared to $3.2 R_{\odot}$, adopted in Sigut et al. (2015), which corresponds to the expected polar radius for a B7 dwarf. We stress that the radius derived by Cochetti et al. (2019) is closer to our results from the fit to the VEGA V^2 data (Sect. 3). Their result of $R_{\star} = 4.4 R_{\odot}$ corresponds to a uniform disk diameter of $\theta \sim 0.28$ mas ($d = 144$ pc). A better comparison to Cochetti et al. (2019) is hard since they do not provide error bars on R_{\star} from fitting the SED. Furthermore, they derived $R_{\star} = 4.4 R_{\odot}$ for *o* Aquarii using a distance of 134 pc from van Leeuwen (2007), rather than the value of 144 pc adopted here. From Fig. 11, this implies a larger discrepancy between the observed and synthetic SED for $R_{\star} = 4.4 R_{\odot}$, overestimating the observed flux.

We also compare the predicted SED of our best-fit HDUST model (Table 5) to the SED of the purely photospheric model with $4.0 R_{\odot}$. Despite being able to reproduce the *UBV*-bands well, one sees that a purely photospheric model clearly underestimates the observed flux beyond the near-infrared due to the flux contribution from the circumstellar disk (e.g., Poeckert & Marlborough 1978; Waters 1986). From Fig. 11, it is evident that the SED is much better reproduced up to the far-infrared region when taking into account the IR excess from the gaseous circumstellar disk present in our best-fit HDUST model.

7.2. $H\alpha$ and $Br\gamma$ profiles

Our $H\alpha$ spectra taken with the VEGA instrument (20 spectra, period from 2012 to 2016) are not analyzed in this work since they are saturated. This is a known effect seen in previous works on Be stars and correlated to the magnitude of the object. We stress that this instrumental saturation effect does not impact the visibilities and phases extracted from the fringes measured with VEGA (see, e.g., Delaa et al. 2011). To overcome this problem we used $H\alpha$ line profiles from the BeSOS⁸ catalog (Arcos et al. 2018; Vanzi et al. 2012), obtained between 2012 and 2015, and thus covering a similar period to our VEGA observations. The typical spectral resolution of the BeSOS spectra is $\sim 0.1 \text{\AA}$.

In Fig. 12, we compare the $H\alpha$ and $Br\gamma$ profiles from our best-fit models to observed profiles, namely, the mean $H\alpha$ line profiles from BeSOS (7 profiles⁹) and the mean $Br\gamma$ line profiles from our AMBER observations (8 profiles). The observed

⁸ Be Stars Observation Survey.

⁹ Public data available at: <http://besos.ifa.uv.cl>

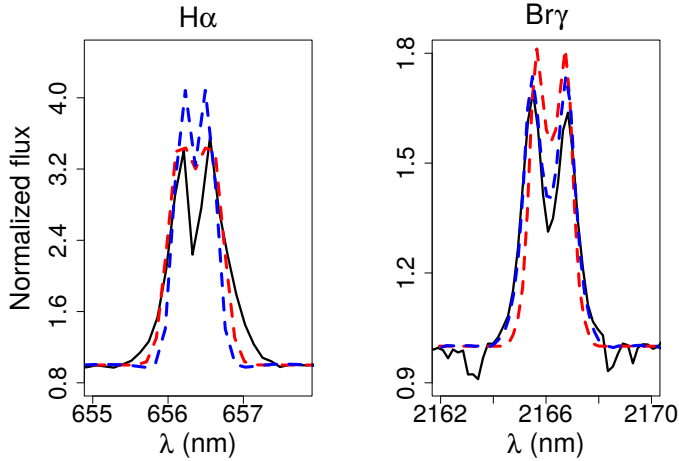


Fig. 12. Comparison between our best-fit kinematic models (dashed red; Table 2) and HDUST model (dashed blue, Table 5) in the $H\alpha$ and $Br\gamma$ line profiles. Mean observed line profiles of $H\alpha$ (BeSOS) and $Br\gamma$ (AMBER) are shown in black line. Our best-fit kinematic and HDUST models provide reasonable synthetic profiles to the observed ones in both $H\alpha$ and $Br\gamma$.

profiles in Fig. 12 were binned in wavelength in order to have a spectral resolution equal to one of the synthetic profiles from the kinematic and HDUST models: 1.3 \AA ($H\alpha$) and 1.8 \AA ($Br\gamma$). The mean EW in $H\alpha$ from the BeSOS data is 19.1 \AA . This is in agreement with the mean value of 19.9 \AA found in Sigut et al. (2015), based on contemporaneous spectra, and adopted in our analysis with the kinematic code (Sect. 4.3).

First, we note that our best-fit kinematic and HDUST models provide a fairly reasonable match to the observed $H\alpha$ and $Br\gamma$ line profiles. The kinematic models correspond to our best-fits obtained from modeling the VEGA and AMBER differential data separately (Sect. 4). On the other hand, our best-fit HDUST model shown in $H\alpha$ and $Br\gamma$ is derived from the simultaneous fit to all our interferometric data (Table 5). Moreover, we stress the difficulty found by Sigut et al. (2015), using the radiative transfer code BEDISK, to reproduce the line wings and central absorption in the $H\alpha$ profile of *o* Aquarii (see their Fig. 5).

However, it can be seen in Fig. 12 that both our best-fit kinematic and HDUST model are not able to properly reproduce, in particular, the wings of the $H\alpha$ profile. On the other hand, the wings of the $Br\gamma$ profile are fairly well reproduced by both of them, especially with HDUST.

Therefore, this inability to reproduce the wings of the $H\alpha$ profile well is likely due to physical processes in the disk that are not taken into account in our models. It is known that the $H\alpha$ profile wings of Be stars can be highly affected by non-coherent scattering, thus resulting in non-kinematic line-broadening in this transition (see, e.g., Hummel & Dachs 1992; Delaa et al. 2011). It is beyond the scope of this paper to quantify this possible effect in the $H\alpha$ line of *o* Aquarii.

8. Discussion

8.1. Disk extension in $H\alpha$ and $Br\gamma$

In Sect. 4.3, we showed that the disk extension is similar in the $H\alpha$ and $Br\gamma$ lines. Interestingly, from previous studies, we could expect to find a larger disk extension in $H\alpha$ than $Br\gamma$. For example, Meilland et al. (2011) found that δ Scorpii (B0.3IV), which was also observed with the VEGA and AMBER

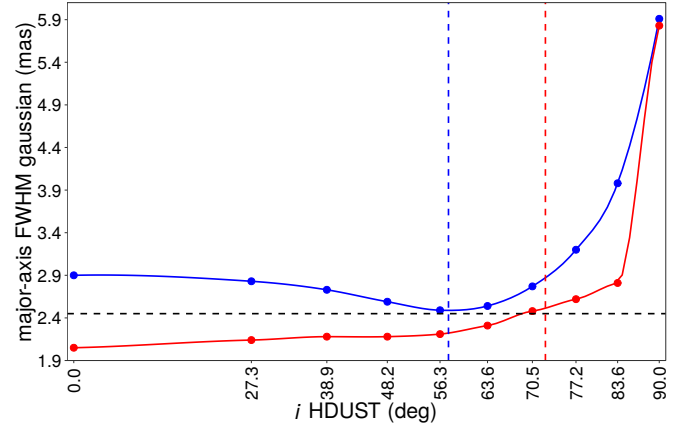


Fig. 13. Major-axis FWHM of Gaussian distribution (fitted from our best-fit HDUST model) as a function of the HDUST inclination angle. All the other HDUST parameters are fixed. Blue points correspond to the fit in $H\alpha$ and red points in $Br\gamma$. The vertical dashed lines mark our values for inclination angle derived from the HDUST analysis, fitting the data in $H\alpha$ (blue) and $Br\gamma$ (red). Note that the equivalent Gaussian fits show a similar extension (2.45 mas, marked in horizontal dashed line) for these values of i .

instruments, shows a circumstellar disk 1.65 times larger in $H\alpha$ than in $Br\gamma$. Furthermore, Gies et al. (2007) derived the angular sizes of four Be stars (γ Cassiopeiae, ϕ Persei, ζ Tauri, and κ Draconis) in the K -band region using interferometric data from the CHARA/CLASSIC instrument. They showed that the disk of these stars was significantly larger (up to ~ 1.5 – 2.0 times) in the $H\alpha$ line than in the K -band. However, Carciofi (2011) investigated theoretically, using the code HDUST, the formation loci of $H\alpha$ and $Br\gamma$, and found them to be quite similar at least in the parameter space explored by the authors (see their Fig. 1). Moreover, Stee & Bittar (2001), using the code SIMECA, found that Be star disks can be larger (up to two times) in $Br\gamma$ than in $H\alpha$.

For a quantitative comparison of the disk extension in $H\alpha$ and $Br\gamma$, we fitted simple Gaussian distributions to the intensity map of our best-fit HDUST model for all the values of inclination angle in BeAtlas. In order to remove the contribution from the star and disk continuum, we removed the image from the continuum before performing the fit and we hide the central part of the image which is affected by the stellar contribution.

In Fig. 13, we show the major-axis FWHM from our fit as a function of the inclination angle for the $H\alpha$ and $Br\gamma$ lines. First, one sees that the disk size-extension (major-axis FWHM) varies differently in the $H\alpha$ and $Br\gamma$ lines as a function of the inclination angle. The disk extension increases in $Br\gamma$ with the inclination angle. On the other hand, it decreases significantly in $H\alpha$ up to $i \sim 56^\circ$ and increases after this value. One sees that the ratio between the extension in these lines decreases from about 1.50 at zero inclination to about 1.05 at 63.5° . Furthermore, we note that the disk extensions in these lines are very close to each other for $i \sim 56^\circ$ ($H\alpha$) and $i \sim 72^\circ$ ($Br\gamma$): major-axis FWHM ~ 2.45 mas. Considering $d = 144$ pc, the disk size is $\sim 10 D_\star$ (close to our findings from the kinematic modeling).

Therefore, from this simple analysis using HDUST models, we verify our findings using the kinematic model: a similar circumstellar disk extension in $H\alpha$ and $Br\gamma$. This arises since the (equivalent) Gaussian disk to our best-fit HDUST model presents quite different changes on its extension in these lines as a function of the inclination angle. Based on that, we can also explain the difference between δ Scorpii and *o* Aquarii. The former is

seen under a low inclination angle ($\sim 30^\circ$) and exhibits a high ratio between the $H\alpha$ and $\text{Br}\gamma$ disk sizes. The latter is seen under a higher inclination angle and shows similar disk sizes in both lines. On the other hand, as discussed above, ϕ Persei and ζ Tau show larger disks in $H\alpha$ than in the K -band and these stars are seen close to edge-on with $i = 78^\circ$ (Mourard et al. 2015) and 85° (Carciofi et al. 2009), respectively. Thus, this similarity in the disk extensions, found for quite different values of inclination angle, could indicate a more complex physical structure of the circumstellar disk than the one assumed by our best-fit HDUST model (based on a vertically isothermal disk).

8.2. Inclination angle and vertical disk structure

From our $H\alpha$ and $\text{Br}\gamma$ differential data analysis, using the kinematic model, we achieved good precision in the determination of the stellar inclination angle: $i \sim 61.2 \pm 1.8^\circ$ (VEGA) and $i = 75.9 \pm 0.4^\circ$ (AMBER). Nevertheless, there is a clear discrepancy between the inclination angle found from fitting the VEGA and AMBER datasets. The value determined from VEGA is about 15° lower than the one found in the analysis of the AMBER data. We can show that this issue does not stem from an intrinsic limitation of the kinematic code (2D model) for Be stars seen under high inclination angle ($i \gtrsim 60^\circ$). Indeed, by using a sophisticated 3D radiative transfer model (HDUST), not subjected to such a limitation, we verified the same discrepancy on i from the fit to these datasets separately (see, again, in Fig. 9, the trend of χ_r^2 , as a function of i).

It may be argued that the difference found in inclination angle is hiding a difference in the disk thickness in these lines. Assuming a non-geometrically thin disk, for an ellipse with major and minor axes denoted, respectively, by a and b , the ratio between a and b , the circumstellar disk flattening, is given by (see, e.g., Meilland et al. 2007b):

$$\frac{a}{b} = \frac{1}{\cos i + 2 \sin \frac{\Theta}{4} \sin \left(i - \frac{\Theta}{4} \right)}, \quad (10)$$

where i is the stellar inclination angle and Θ the disk opening angle. Since the i derived from $H\alpha$ using our physical models is much lower than from $\text{Br}\gamma$ (a reliable value when compared to other results in the literature), this would imply a disk thicker (higher opening angle Θ) in $H\alpha$ than in $\text{Br}\gamma$. Considering the values described above, the disk opening angle in $H\alpha$ would be $\Theta \sim 37^\circ$ larger in $H\alpha$ than in $\text{Br}\gamma$ (assuming a geometrically thin disk in $\text{Br}\gamma$). Such a high value of opening angle is far beyond what is measured and expected by the VDD model, typically less than $\sim 10^\circ$ (cf. Rivinius et al. 2013). This might indicate the necessity of more complex physical assumptions in the physical properties of our disk model.

Since the code HDUST provides a pure hydrogen modeling for the photosphere plus disk regions, this disagreement between the VEGA ($H\alpha$) and AMBER ($\text{Br}\gamma$) analyses in the determination of i could be due to an opacity effect. It is well-known that the inclusion of heavy elements can impact the density and temperature stratifications in the circumstellar disk of Be stars by shielding emission from the star. (see, e.g., Sigut & Jones 2007). Furthermore, we stress that our best-fit HDUST model is a parametric model (based on a vertically isothermal structure). Departures from vertically isothermal disks are well-known in the literature. For example, using the radiative transfer code BEDISK, Sigut et al. (2009) verified that isothermal and self-consistent hydrostatic models can present large differences regarding the temperature stratification in the disk of Be stars.

Using HDUST, Carciofi & Bjorkman (2008) also found that non-isothermal effects can be significant for denser Be star disks. Thus, further investigation is needed concerning this effect on the determination of i for o Aquarii, but that is beyond the scope of this paper.

Finally, another possibility to explain the difference in apparent inclination angle found in our modeling could be a non-negligible contribution of a polar wind. Clues of the presence of polar wind, or at least of circumstellar material in the polar regions, have been found by Kervella & Domiciano de Souza (2006) and Meilland et al. (2007a). In our models, we assume that all the circumstellar material is in the thin equatorial disk. If a non negligible fraction of the material is located near the poles, although we would expect it to be quite diluted and optically thin (at least in the continuum), it might affect the line emission with a different magnitude in $H\alpha$ and in $\text{Br}\gamma$. If one assumes that the hydrogen level populations favor $H\alpha$ emission over $\text{Br}\gamma$, the polar contribution of $H\alpha$ would be higher, and the environment might look less flattened in this line than in $\text{Br}\gamma$.

8.3. Stellar and disk rotation

In Sect. 5, our results are presented in terms of the stellar oblateness R_{eq}/R_p (denoted by f in Eq. (11)). First, we give the relation between the oblateness and the angular $\Omega/\Omega_{\text{crit}}$ and linear $v_{\text{rot}}/v_{\text{crit}}$ rotational rates as follows:

$$\frac{\Omega}{\Omega_{\text{crit}}} = \frac{v_{\text{rot}}}{v_{\text{crit}}} \frac{R_{\text{eq,crit}}}{R_{\text{eq}}} = \left(\frac{3}{2} \right)^{3/2} \left[\frac{2(f-1)}{f^3} \right]^{1/2}, \quad (11)$$

where $R_{\text{eq,crit}}$ and R_{eq} (in units of polar radius) are, respectively, the stellar equatorial radius in the case of critical velocity and the actual one (see, e.g., Frémat et al. 2005; Ekström et al. 2008).

Considering only the uncertainties on v_{rot} (Table 2), with the critical velocity v_{crit} fixed to 391 km s^{-1} (Frémat et al. 2005), we obtain a linear rotational rate of $v_{\text{rot}}/v_{\text{crit}} = 0.83 \pm 0.02$ ($v_{\text{rot}} = 325 \pm 6 \text{ km s}^{-1}$, VEGA) and 0.775 ± 0.005 ($v_{\text{rot}} = 303 \pm 2 \text{ km s}^{-1}$, AMBER). From the HDUST analysis, we find $v_{\text{rot}}/v_{\text{crit}} = 0.96$ (VEGA and AMBER) from our best-fit model (no error bars). This difference between the kinematic and HDUST analysis can be explained since the β exponent (velocity law in the disk) is fixed in the HDUST analysis (Keplerian disk, $\beta = -0.5$), while it is a free parameter in the kinematic model. We derived values for β from the kinematic analysis that are significantly higher (more positive) than -0.5 (see Table 2).

Apart from these differences, our analysis is consistent with a high rotational rate for o Aquarii, showing $v_{\text{rot}}/v_{\text{crit}}$ from ~ 0.8 up to 1.0, depending on the particular analysis considered. The BeAtlas fits to the VEGA and AMBER differential data are significantly worsened (Fig. 9), when considering $R_{\text{eq}}/R_p = 1.20$ – 1.30 ($\Omega/\Omega_{\text{crit}} = 0.88$ – 0.96). Thus, our HDUST analysis indicates that o Aquarii rotates faster than $\Omega/\Omega_{\text{crit}} = 0.96$, disfavoring the lower range of $\Omega/\Omega_{\text{crit}}$ between 0.86 and 0.93 that is derived by Cochetti et al. (2019).

In Sect. 4.3, we found a strong correlation between the velocity at the base of the disk and the β exponent of the rotation law β . The inferred degeneracy, stronger in the case of the VEGA data, which have a lower spectral-resolution with higher uncertainties, prevents us from independently constraining these two parameters with our kinematic model when fitting only our spectro-interferometric data. However, the addition of an external constraint, the measured $v \sin i$, removed this degeneracy, allowing us to derive a more accurate value of β in comparison to the other MCMC fitting tests (Appendix B).

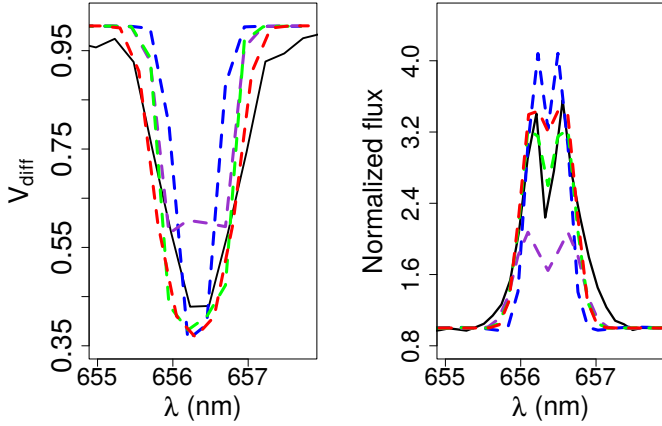


Fig. 14. Bias effect of the disk velocity on $H\alpha$ modeling. One VEGA measurement and observed $H\alpha$ profile (BeSOS, as in Fig. 12) are shown in black lines. Our best-fit kinematic (dashed red) and HDUST (dashed blue) models are shown in $H\alpha$ visibility and line profile. They are compared to HDUST models with a higher mass of $10.8 M_{\odot}$ with: $\Sigma_0 = 0.12 \text{ g cm}^{-2}$ (dashed orchid) and $\Sigma_0 = 0.28 \text{ g cm}^{-2}$ (dashed green). See text for discussion.

From our MCMC fit to the AMBER dataset, with a preset $v \sin i$, we derived a β of -0.426 ± 0.003 . Thus, the disk appears to be rotating in a nearly Keplerian fashion. Despite this very low error on β , note that the error bars on β change with respect to the presented MCMC tests, up to ± 0.008 (see Fig. B.2). On the other hand, the value derived from the fit of the VEGA data is about 0.1 higher than from AMBER. We stress that this discrepancy cannot be explained by a radial dependent rotational law because both lines roughly stem from the same region in the disk (similar disk extensions in these lines).

Moreover, this apparent higher value of β in $H\alpha$ was also the origin of some biases that we found when modeling the VEGA differential data alone using HDUST. Without fixing M_{\star} , the VEGA analysis with HDUST favours unrealistically high values of stellar mass up to $\sim 11 M_{\odot}$. This happened due to the fact the higher mass models also correspond to higher rotational velocity at the base of the disk. As the value of β is fixed to -0.5 in the BeAtlas grid of models, this was the only way to increase the rotational velocity in the disk. In Fig. 14, our best-fit kinematic and HDUST models are compared to a higher mass HDUST model for one VEGA differential measurement and the $H\alpha$ profile. When compared to our best HDUST model (mass fixed to $4.2 M_{\odot}$), the visibility drop and the $H\alpha$ profile are better reproduced with HDUST models with higher value of mass, but also considering a larger value of Σ_0 (0.28 g cm^{-2}). This happens since the stellar radius is also increased for a higher mass model and the flux contribution from the star is larger in the line. In this case, our BeAtlas model is able to produce more similar synthetic $H\alpha$ visibility and profile to the ones from our best-fit kinematic model.

One possible explanation for the discrepancy between the value of β determined from $H\alpha$ and $\text{Br}\gamma$ could be the higher effects of non-kinematic broadening on $H\alpha$. This is already evidenced by the larger wings, in terms of Doppler shift, for this emission line. Such effects are known to be due to non-coherent scattering in the circumstellar environment, as explained, for example, in Auer & Mihalas (1968). Global effects on interferometric data were discussed by Stee et al. (2012) in the case of the Be star γ Cassiopeiae observed with VEGA. These authors used a similar kinematic model, but with two additional parameters

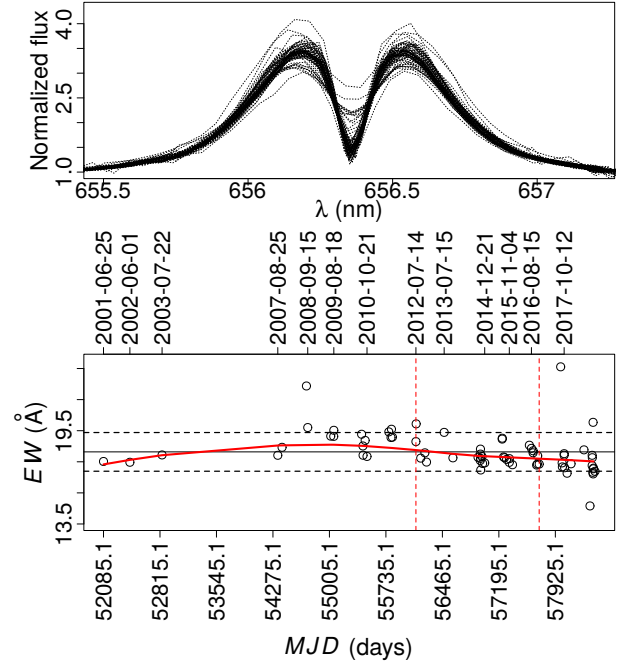


Fig. 15. Top panel: 70 observed $H\alpha$ profiles of *o* Aquarii from the BeSS database, covering about 17 yr of observations (2001–2018). Bottom panel: $H\alpha$ equivalent width as a function of the observation time (modified Julian date). Civil dates are indicated for a part of the measured EW. The mean EW (solid) within the standard deviation (dashed lines) is marked in black. Local regression fit of EW, as a function of time, is shown as a solid red line. The time interval covered by our interferometric observations (VEGA) is indicated with dashed red lines. See text for discussion.

to quantify the non-coherent scattering and found that about half the flux in the line was affected by such an effect. Nevertheless, the possible bias on the measurement of β in a line strongly affected by such non-kinematic broadening should be investigated further.

We also note that a possible close companion could influence v_{rot} , as well as the disk structure, as previously mentioned. However, the presence of a close companion with a detectable influence on the measured parameters seems excluded from the observed calibrated V^2 , and in particular from the spectro-interferometric differential observables, which both show signatures well reproduced by a symmetric rotating disk.

8.4. Disk variability: a multi-technique analysis

8.4.1. Spectroscopy

The Be star *o* Aquarii is known to possess a stable $H\alpha$ line profile for up to several years. For example, Sigut et al. (2015) verified that the EW in the $H\alpha$ line is stable (within about 5%) up to about nine years (from 2005 to 2014).

To go further in the analysis of the disk stability, we analyzed 70 $H\alpha$ line profiles, spanning from 2001 to 2018, from the BeSS database¹⁰ (Neiner et al. 2011). Since these observations are performed with several instruments, the line profiles shown here are interpolated to have spectral resolution of 0.5 \AA (lowest resolution in the dataset). From these observations, we calculated the equivalent width (EW) in the $H\alpha$ line. In Fig. 15, we show the

¹⁰ Public data available at: <http://basebe.obspm.fr>

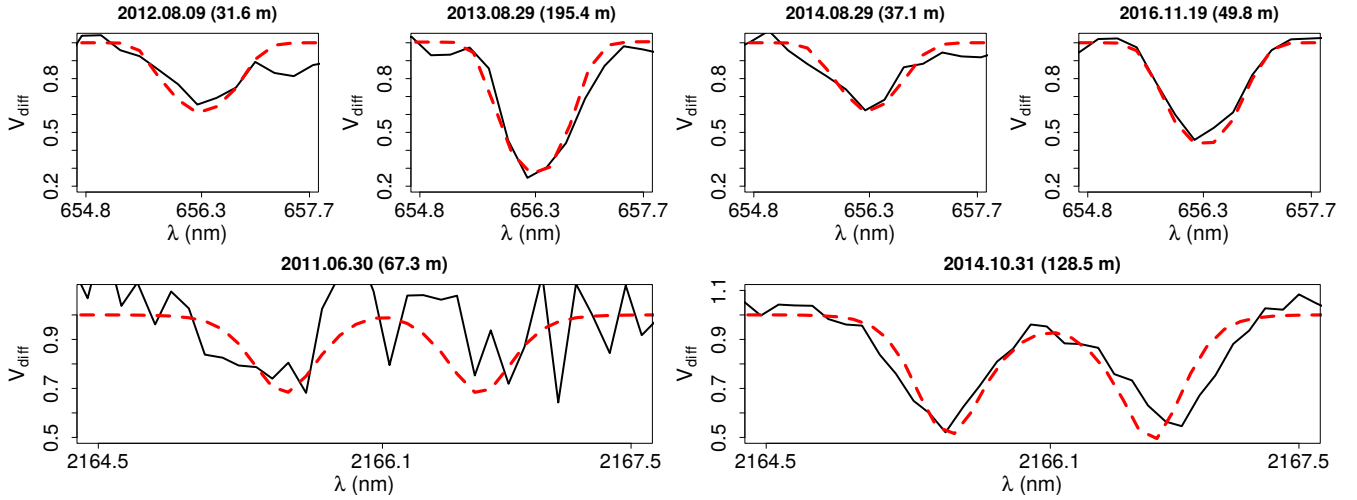


Fig. 16. VEGA (*top panels*) and AMBER (*bottom panels*) differential visibilities extracted from observations at different epochs (black line). VEGA measurements span four years and the AMBER ones span three years. The observation date and the baseline length (projected onto the sky) are indicated in the top of each panel. Our best-fit kinematic models derived from the fit, in a separate way, to each dataset (VEGA and AMBER) are shown in dashed red line. Note that our best-fit kinematic models match well to the differential visibilities obtained at different epochs.

analyzed $H\alpha$ spectra together to the temporal evolution of the $H\alpha$ EW.

We found that the disk is fairly stable over this 17-yr time span with a mean value of $\overline{EW} = 18.1 \pm 1.2 \text{ \AA}$. This value agrees well to older results in the literature. Slettebak & Reynolds (1978) measured $H\alpha$ EW = $18.80 \pm 0.11 \text{ \AA}$ in 1975 and $18.58 \pm 0.21 \text{ \AA}$ in 1976. From the $H\alpha$ profile observed in 1981, Andriolat (1983) measured EW = 17.2 \AA . Thus, this supports an even longer global disk stability up to at least 40 yr. However, a slight increasing trend in EW is seen between 2001 and 2012. This could suggest an augmentation in the disk density of *o* Aquarii in this period. Considering the period of our interferometric observations (from 2012 to 2016), it is hard to observe any trend of $H\alpha$ EW as a function of time.

8.4.2. Interferometry

These results are consistent with our ability to model, with the same model parameters, simultaneously all our VEGA and AMBER data regardless of the epoch. In Fig. 16, we present a temporal evaluation of our spectro-interferometric data in the $H\alpha$ and $\text{Br}\gamma$ lines. Since the drop in visibility is expected to change due to possible variations in the disk extension, we only show here the differential visibilities from the VEGA and AMBER observations. These measurements are chosen to cover the whole period of our observations from 2011 to 2016. For a more robust comparison, we chose measurements obtained with different baseline lengths (projected onto the sky), and, thus, covering different levels of spatial resolution.

One sees that, regardless of the period of time of the observations, our final kinematic models provide a very reasonable match to both the VEGA and AMBER data. Thus, considering our interferometric data, we are not able to detect any conspicuous variation of the circumstellar disk extension within a period up to five years (from 2011 to 2016). This is in agreement with previous interferometric studies of *o* Aquarii by Sigut et al. (2015). Besides that, this analysis supports our approach of fitting each one of the interferometric datasets (VEGA and AMBER) without imposing any discrimination based on the observation time.

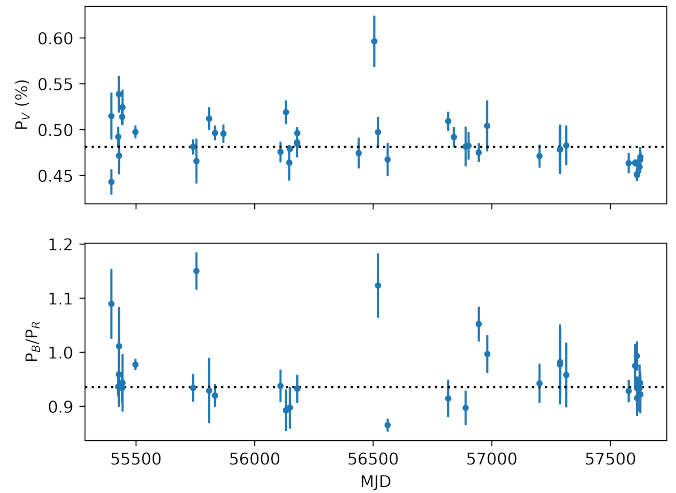


Fig. 17. Polarimetric quantities of *o* Aquarii, as a function of the observation time, spanning about six years. *Top panel:* observed V -band polarization (44 measurements). *Bottom panel:* ratio between the observed B - and R -bands polarization (40 measurements). The mean values of these quantities are shown in dashed line. See text for discussion.

8.4.3. Polarimetry

Additional multi-epoch polarimetric data also support our findings of a stable disk for *o* Aquarii, close to the steady-state regime. In Fig. 17, we show the temporal evolution of broad-band linear polarimetry in the V -band (P_V) of *o* Aquarii, as well as the ratio between the B - and R -bands polarization (P_B/P_R).

These data were obtained over 43 nights, from June 2010 to August 2016, with the IAGPOL polarimeter (Magalhães et al. 1996), mounted on the 0.6 m Boller & Chivens telescope at Observatório do Pico dos Dias (OPD/LNA). This polarimeter is composed by a rotating half-wave retarder and a Savart Plate used as analyser to provide the modulation of the light polarization, and then the polarimetric quantities. Details of data reduction are found in Magalhães et al. (1984) and Bednarski (2016).

Table 6. Interstellar parameters derived for *o* Aquarii: the Serkowski parameters, P_{\max} and λ_{\max} , with the polarization angle PA_{IS} .

P_{\max} (%)	λ_{\max} (μm)	PA_{IS} (deg)
0.11 ± 0.01	0.49 ± 0.18	132 ± 4

From Fig. 17, the mean value of the observed *V*-band polarization is $\overline{P_V} = 0.48 \pm 0.03\%$. This value, derived from the mean and standard deviation of the Stokes *Q* and *U* parameters, is compatible to the one determined by Yudin (2001), namely, $0.52 \pm 0.05\%$. Since the observations from Yudin (2001) predate our OPD/LNA observations by more than a decade, we conclude that the polarization values of *o* Aquarii remained very constant for over 20 yr.

In order to determine the intrinsic value of polarization, the interstellar contribution to the observed values quoted above must be removed. For that, we observed four main sequence stars, in the *BVRI*-bands, which are angularly close to *o* Aquarii. A MCMC method was implemented to process the four *BVRI* data of each field star, generating a sample of the likelihood function in terms of the interstellar Serkowski parameters P_{\max} and λ_{\max} (Serkowski et al. 1975; Wilking et al. 1982). The best estimates for these parameters are shown in Table D.1.

There is a good agreement among the PA values of the field stars. Moreover, by using *Gaia* DR2 distances, we found that P_{\max} increases linearly along the line of sight of *o* Aquarii (see Fig. D.1). In this case, it suggests that the alignment of the grains at the interstellar medium is nearly homogeneous (e.g., McLean & Clarke 1979). Thus, from a simple linear fit to P_{\max} vs. distance for the field fields, we determined P_{\max} for *o* Aquarii. The derived interstellar polarization parameters for *o* Aquarii are shown in Table 6, which are in reasonable agreement with the ones reported in Yudin (2001) of $P_{\max} = 0.20\%$ and $\text{PA}_{\text{IS}} = 125^\circ$ (no error bars).

Taking into account our results for the interstellar polarization components, we found for the intrinsic *V*-band polarization and position angle $P_V^{\text{int}} = 0.49 \pm 0.03\%$ and $\text{PA}^{\text{int}} = 2.5 \pm 2.7^\circ$, respectively. Yudin (2001) determined $P_V^{\text{int}} = 0.60\%$ with $\text{PA}^{\text{int}} = 6.0^\circ$, which is close to our PA^{int} value. Moreover, both estimates for PA^{int} are consistent with our determination for the disk major-axis position angle ($\sim 110^\circ$), being almost perpendicular to the polarization vector, as expected.

Furthermore, our best-fit HDUST model (Table 5) predicts a polarization degree of 0.41% in the *V*-band. This agrees well with our measurement for the average intrinsic polarization of the OPD/LNA data. Therefore, besides the independent checks provided by the SED and spectroscopic data (Sect. 7), our polarimetric data also support our physical model for *o* Aquarii, which was derived purely from the fit to interferometric data (as discussed in Sect. 5.3).

Lastly, Fig. 17 shows that both the polarization degree in the *V*-band and the ratio between the *B*- and *R*-bands are almost constant in time, showing a small scatter around the mean value. In particular, this latter quantity is related to the density scale at the inner portion of the disk (Haubois et al. 2014). From the theoretical investigation of Panoglou et al. (2019), the variation on the polarization degree in the *V*-band (ΔP_V) can reach up to about 0.1% due to asymmetries in the disk density structure, caused by a binary companion. Moreover, Haubois et al. (2014) predicted ΔP_V of up to 2% due to temporal changes in the mass decretion

rate. The standard deviation of our P_V distribution (approximately Gaussian), namely, $\sim 0.03\%$, is quite a bit lower than the above values. It is well explained in terms of the precision of our polarimetric data, as the typical error bar on P_V is $\sim 0.01\text{--}0.02\%$ (Fig. 17).

8.4.4. A stable disk

Besides the analysis of the $\text{H}\alpha$ EW and broad-band polarimetric quantities, our modeling with the code HDUST indicates that the disk must be close to the steady-state regime: having a radial density law exponent of 3.0 (e.g. Haubois et al. 2012; Vieira et al. 2017). Other studies of *o* Aquarii are in fair agreement to our findings from HDUST. Using the radiative transfer code BEDISK, Silaj et al. (2010) derived $m = 3.5$ from the fit to the $\text{H}\alpha$ profile, while Sigut et al. (2015) found $m = 2.7$ as a representative value from the analysis of all the different observables.

Previous and ongoing studies of Be stars with stable disks found similar results to ours. For example, Klement et al. (2015) found $m = 2.9$ for the late-type Be star β Canis Minoris (B8Ve). Correia Mota (2019) derived $m = 2.44^{+0.27}_{-0.16}$ for α Arae (B2Vne). The B9Ve star α Columbae shows $m = 2.54^{+0.06}_{-0.13}$ (A. Rubio, priv. comm.). Thus, the radial density exponent is consistently equal or somewhat less than 3.0 for these Be stars with stable disks. Also, from analysing the temporal variation of the disk density, Vieira et al. (2017) identified a slightly extended range of m (between ~ 3.0 and ~ 3.5) for the steady-state regime, in comparison to the canonical value of 3.5. As pointed out by these authors, this canonical value is based on simplifications of the standard theory, which assumes, for example, vertically isothermal disks and isolated systems (single stars). One possibility to explain the measured m lower than 3.5 could thus rely on non-isothermal effects in the disk structure (see, e.g., Carciofi & Bjorkman 2008).

Finally, we note that such long-term stability of *o* Aquarii's disk is consistent with other results in the literature: late-type Be stars are more likely to have more stable disks than earlier Be stars (e.g., Vieira et al. 2017; Labadie-Bartz et al. 2018; Rímulo et al. 2018). As discussed in Sect. 8.3, the stellar rotation seems to be very close ($\sim 96\%$) to the critical value ($391 \pm 27 \text{ km s}^{-1}$ from Frémat et al. 2005), in particular regarding the HDUST analysis: $v_{\text{rot}} = 368 \text{ km s}^{-1}$ (Table 5). This is consistent with the results from Cranmer (2005): Be stars with lower effective temperature $T_{\text{eff}} \lesssim 21\,000 \text{ K}$ – that is, later spectral types such as our target – are more likely to have a rotation rate close to one than the earlier Be stars. Thus, one possibility to explain such a long-term stability of the disk of *o* Aquarii could rely on its fast rotation, ensuring in this case a nearly constant mass-injection rate into the disk.

9. Conclusions

We analyzed VEGA V^2 , as well as VEGA and AMBER differential visibility and phase of the Be-shell star *o* Aquarii. To date, the spectro-interferometric dataset analyzed in this paper is the largest for a Be star, considering quasi-contemporaneous observations in both the $\text{H}\alpha$ (VEGA) and $\text{Br}\gamma$ (AMBER) lines.

For the first time, we measured *o* Aquarii's stellar radius ($R_\star = 4.0 \pm 0.3 R_\odot$) and determined the disk extension in the $\text{H}\alpha$ and $\text{Br}\gamma$ lines as, respectively, $10.5 \pm 0.3 D_\star$ and $11.5 \pm 0.1 D_\star$. Using radiative transfer models computed with the code HDUST, we explained the quasi-identical extension of the emission in these lines by an opacity effect found for disks seen under a high inclination angle.

We showed that the inclination angle derived from $H\alpha$ is about 15° lower than the one determined in B_{ry} , when analysing each line separately with HDUST. More complex physical models, for example, with non-isothermal vertical scaling of the disk or the addition of heavier elements, could resolve this issue and should be investigated in the future.

Our simple kinematic model highlighted the high correlation between the rotational velocity at the base of the disk and the rotational law exponent β . Assuming external constraints, such as $v \sin i$, we managed to constrain this parameter and showed that the disk rotation is nearly Keplerian ($\beta \sim 0.43$) from the analysis in the B_{ry} emission line. As for the inclination angle, the determination of β , using the $H\alpha$ line ($\beta \sim 0.30$), seems to be significantly biased. Other studies also verified such a large deviation from the Keplerian rotation for Be stars when analysing interferometric quantities measured in $H\alpha$ (see, e.g., Delaa et al. 2011). One possible explanation would be the higher effect of non-coherent scattering on the $H\alpha$ line formation than on B_{ry} .

Despite being derived purely from the fit to interferometric data, our best-fit HDUST model provides a very reasonable match to non-interferometric observables of σ Aquarii: the observed SED, $H\alpha$ and B_{ry} line profiles, and polarimetric quantities. Thus, this cross-check provides an independent validation of our best-fit physical model. We found using HDUST a satisfying common physical description for the circumstellar disk in both $H\alpha$ and B_{ry} : a base disk surface density $\Sigma_0 = 0.12 \text{ g cm}^{-2}$ ($\rho_0 = 5.0 \times 10^{-12} \text{ g cm}^{-3}$) and a radial density law exponent $m = 3.0$, that is, close to the steady-state regime according to the VDD model ($m = 3.5$). This result agrees with recent studies of other Be stars with stable disks, and may indicate the necessity to revise $m = 3.5$ (steady-state standing for single stars with vertically isothermal disks) that is predicted by the VDD theory. Otherwise, this could indicate non-isothermal effects on the disk vertical structure of σ Aquarii. The long-term stability of the σ Aquarii's disk is verified by our analysis of a large sample of $H\alpha$ profiles and polarimetric data, spanning about 20 and six years, respectively. Combined with older results in the literature, a longer global disk stability is suggested for up to at least 40 yr.

The stellar rotation seems to be very close ($\sim 96\%$) to the critical value (391 km s^{-1}), in particular accordingly to our HDUST analysis: $v_{\text{rot}} = 368 \text{ km s}^{-1}$ from the best-fit HDUST model with fixed $M_\star = 4.2 M_\odot$ (cf., Sects. 5.2 and 5.3). One possibility to explain such a long-term stability in the disk of σ Aquarii could rely on its own high stellar rotation, being, in this case, a main source for the mass injection from the stellar surface to the disk. Thus, apart from the mass decretion due to other possible mechanisms in Be stars, this would provide a constant rate of mass injection. In short, our results on the stellar rotation and on the disk stability are consistent with the literature results showing that late-type Be stars are more likely to be fast rotators and have stable disks (see Sect. 8.4.4).

Finally, to further investigate these issues, our multi-wavelength and multi-emission line modeling approach must be performed on a larger sample of Be stars with disks of different densities and seen under different inclination angles. The implementation of a MCMC model fitting procedure with the kinematic model, and the use of our grid of HDUST models (BeAtlas), are very promising for the spectro-interferometric analysis of a large survey of Be stars, providing robust model parameters and associated uncertainties. A future project will attempt this task on a few dozen objects observed with VEGA and AMBER.

Acknowledgements. We thank the anonymous referee for helping to improve this paper. E.S.G.de.A. thanks OCA and the “Ville de Nice” (Nice, France) for the financial support to this work through the “Bourse Doctorale Olivier Chesneau” during the period of 2016–2019. E.S.G.de.A. acknowledges A. Rubio for relevant information about her work on α Columbae. R.L. has received funding from the European Union’s Horizon 2020 research and innovation program under the Marie Skłodowska-Curie grant agreement n. 664931. D.M.F. acknowledges FAPESP (grant 2016/16844-1). A.C.C. acknowledges support from CNPq (grant 307594/2015-7). This work was supported by the “Programme National de Physique Stellaire” (PNPS) of CNRS/INSU co-funded by CEA and CNES. This work made use of the computing facilities of the Laboratory of Astromatics (IAG/USP, NAT/Unicisul), whose purchase was made possible by the Brazilian agency FAPESP (grant 2009/54006-4) and the INCT-A. This work is based upon observations obtained with the Georgia State University Center for High Angular Resolution Astronomy Array at Mount Wilson Observatory. The CHARA Array is supported by the National Science Foundation under Grants No. AST-1211929 and AST-1411654. This work used BeSOS Catalogue, operated by the Instituto de Física y Astronomía, Universidad de Valparaíso, Chile: <http://besos.ifa.uv.cl> and funded by Fondecyt iniciación N 11130702. Based on observations collected at the European Southern Observatory under ESO programmes 087.D-0311 and 094.D-0140. This work has made use of the BeSS database, operated at LESIA, Observatoire de Meudon, France: <http://basebe.obspm.fr>. Some of the data presented in this paper were obtained from the Mikulski Archive for Space Telescopes (MAST). STScI is operated by the Association of Universities for Research in Astronomy, Inc., under NASA contract NAS5-26555. Support for MAST for non-HST data is provided by the NASA Office of Space Science via grant NNX13AC07G and by other grants and contracts. This research has made use of the Jean-Marie Mariotti Center (JMCC) services LITpro, SearchCal, and AMHRA, co-developed by CRAL, IPAG and Lagrange. This work has made use of the SIMBAD and VizieR databases, operated at CDS, Strasbourg, France.

References

- Abrahamyan, H. V., Mickaelian, A. M., & Knyazyan, A. V. 2015, *Astron. Comput.*, **10**, 99
- Anderson, E., & Francis, C. 2012, *Astron. Lett.*, **38**, 331
- Andrillat, Y. 1983, *A&AS*, **53**, 319
- Arcos, C., Kanaan, S., Chávez, J., et al. 2018, *MNRAS*, **474**, 5287
- Auer, L. H., & Mihalas, D. 1968, *ApJ*, **153**, 245
- Bednarski, D. 2016, Master thesis, Universidade de São Paulo, Brazil
- Bjorkman, J. E., & Carciofi, A. C. 2005, *ASP Conf. Ser.*, **337**, 75
- Bonneau, D., Clausse, J.-M., Delfosse, X., et al. 2006, *A&A*, **456**, 789
- Bourges, L., Mella, G., Lafrasse, S., et al. 2017, *VizieR Online Data Catalog*: **II/346**
- Carciofi, A. C. 2011, *IAU Symp.*, **272**, 325
- Carciofi, A. C., & Bjorkman, J. E. 2006, *ApJ*, **639**, 1081
- Carciofi, A. C., & Bjorkman, J. E. 2008, *ApJ*, **684**, 1374
- Carciofi, A. C., Okazaki, A. T., Le Bouquin, J.-B., et al. 2009, *A&A*, **504**, 915
- Castelli, F., & Kurucz, R. L. 2004, ArXiv e-prints [arXiv:astro-ph/0405087]
- Chelli, A., Utrera, O. H., & Duvert, G. 2009, *A&A*, **502**, 705
- Chesneau, O., Lagarde, E., Otulakowska-Hypka, M., et al. 2012, *A&A*, **545**, A63
- Cochetti, Y. R., Arcos, C., Kanaan, S., et al. 2019, *A&A*, **621**, A123
- Correia Mota, B. 2019, PhD thesis, Universidade de São Paulo, Brazil
- Cranmer, S. R. 2005, *ApJ*, **634**, 585
- Cyr, I. H., Jones, C. E., Panoglou, D., Carciofi, A. C., & Okazaki, A. T. 2017, *MNRAS*, **471**, 596
- Delaa, O., Stee, P., Meilland, A., et al. 2011, *A&A*, **529**, A87
- Domiciano de Souza, A., Kervella, P., Moser Faes, D., et al. 2014, *A&A*, **569**, A10
- Domiciano de Souza, A., Bouchaud, K., Rieutord, M., Espinosa Lara, F., & Putigny, B. 2018, *A&A*, **619**, A167
- Ekström, S., Meynet, G., Maeder, A., & Barblan, F. 2008, *A&A*, **478**, 467
- Faes, D. M. 2015, PhD thesis, IAG-Universidade de Sao Paulo, Brazil, Lagrange-Université de Nice, France
- Foreman-Mackey, D., Hogg, D. W., Lang, D., & Goodman, J. 2013, *PASP*, **125**, 306
- Frémat, Y., Zorec, J., Hubert, A.-M., & Floquet, M. 2005, *A&A*, **440**, 305
- Gaia Collaboration (Brown, A. G. A., et al.) 2018, *A&A*, **616**, A1
- Gies, D. R., Bagnuolo, Jr. W. G., Baines, E. K., et al. 2007, *ApJ*, **654**, 527
- Goodman, J., & Weare, J. 2010, *Comm. App. Math. Comp. Sci.*, **5**, 65
- Haubois, X., Carciofi, A. C., Rivinius, T., Okazaki, A. T., & Bjorkman, J. E. 2012, *ApJ*, **756**, 156

- Haubois, X., Mota, B. C., Carciofi, A. C., et al. 2014, *ApJ*, **785**, 12
- Henden, A. A., Templeton, M., Terrell, D., et al. 2016, *VizieR Online Data Catalog*: II/336
- Hummel, W., & Dachs, J. 1992, *A&A*, **262**, L17
- Kervella, P., & Domiciano de Souza, A. 2006, *A&A*, **453**, 1059
- Klement, R., Carciofi, A. C., Rivinius, T., et al. 2015, *A&A*, **584**, A85
- Labadie-Bartz, J., Chojnowski, S. D., Whelan, D. G., et al. 2018, *AJ*, **155**, 53
- Lee, U., Osaki, Y., & Saio, H. 1991, *MNRAS*, **250**, 432
- Magalhães, A. M., Benedetti, E., & Roland, E. H. 1984, *PASP*, **96**, 383
- Magalhães, A. M., Rodrigues, C. V., Margoniner, V. E., Pereyra, A., & Heathcote, S. 1996, *ASP Conf. Ser.*, **97**, 118
- McLean, I. S., & Clarke, D. 1979, *MNRAS*, **186**, 245
- Meilland, A., Millour, F., Stee, P., et al. 2007a, *A&A*, **464**, 73
- Meilland, A., Stee, P., Vannier, M., et al. 2007b, *A&A*, **464**, 59
- Meilland, A., Stee, P., Chesneau, O., & Jones, C. 2009, *A&A*, **505**, 687
- Meilland, A., Delaa, O., Stee, P., et al. 2011, *A&A*, **532**, A80
- Meilland, A., Millour, F., Kanaan, S., et al. 2012, *A&A*, **538**, A110
- Monnier, J. D., Che, X., Zhao, M., et al. 2012, *ApJ*, **761**, L3
- Mourard, D., Clausse, J. M., Marcotto, A., et al. 2009, *A&A*, **508**, 1073
- Mourard, D., Challouf, M., Ligi, R., et al. 2012, *Proc. SPIE*, **8445**, 84450K
- Mourard, D., Monnier, J. D., Meilland, A., et al. 2015, *A&A*, **577**, A51
- Neiner, C., de Batz, B., Cochard, F., et al. 2011, *AJ*, **142**, 149
- Okazaki, A. T. 2001, *PASJ*, **53**, 119
- Okazaki, A. T., Bate, M. R., Ogilvie, G. I., & Pringle, J. E. 2002, *MNRAS*, **337**, 967
- Oudmajer, R. D., & Parr, A. M. 2010, *MNRAS*, **405**, 2439
- Panoglou, D., Carciofi, A. C., Vieira, R. G., et al. 2016, *MNRAS*, **461**, 2616
- Panoglou, D., Borges Fernandes, M., Baade, D., et al. 2019, *MNRAS*, **486**, 5139
- Petrov, R. G., Malbet, F., Weigelt, G., et al. 2007, *A&A*, **464**, 1
- Poecckert, R., & Marlborough, J. M. 1978, *ApJS*, **38**, 229
- Rímulo, L. R., Carciofi, A. C., Vieira, R. G., et al. 2018, *MNRAS*, **476**, 3555
- Rivinius, T., Štefl, S., & Baade, D. 2006, *A&A*, **459**, 137
- Rivinius, T., Carciofi, A. C., & Martayan, C. 2013, *A&ARv*, **21**, 69
- Sanchez-Bermudez, J., Alberdi, A., Barbá, R., et al. 2017, *ApJ*, **845**, 57
- Serkowski, K., Mathewson, D. S., & Ford, V. L. 1975, *ApJ*, **196**, 261
- Sigut, T. A. A., & Jones, C. E. 2007, *ApJ*, **668**, 481
- Sigut, T. A. A., McGill, M. A., & Jones, C. E. 2009, *ApJ*, **699**, 1973
- Sigut, T. A. A., Tycner, C., Jansen, B., & Zavala, R. T. 2015, *ApJ*, **814**, 159
- Silaj, J., Jones, C. E., Tycner, C., Sigut, T. A. A., & Smith, A. D. 2010, *ApJS*, **187**, 228
- Slettebak, A., & Reynolds, R. C. 1978, *ApJS*, **38**, 205
- Stee, P., & Bittar, J. 2001, *A&A*, **367**, 532
- Stee, P., & Meilland, A. 2012, *ASP Conf. Ser.*, **464**, 167
- Stee, P., Delaa, O., Monnier, J. D., et al. 2012, *A&A*, **545**, A59
- Tallon-Bosc, I., Tallon, M., Thiébaud, E., et al. 2008, *Proc. SPIE*, **7013**, 70131J
- Tatulli, E., Millour, F., Chelli, A., et al. 2007, *A&A*, **464**, 29
- ten Brummelaar, T. A., McAlister, H. A., Ridgway, S. T., et al. 2005, *ApJ*, **628**, 453
- Touhami, Y., Gies, D., Coudé du Foresto, V., & Schaefer, G. 2009, *AAS Meeting Abstracts*, **213**, 409.18
- Touhami, Y., Gies, D. R., Schaefer, G. H., et al. 2013, *ApJ*, **768**, 128
- Townsend, R. H. D., Owocki, S. P., & Howarth, I. D. 2004, *MNRAS*, **350**, 189
- van Leeuwen, F. 2007, *A&A*, **474**, 653
- Vanzi, L., Chacon, J., Helminiak, K. G., et al. 2012, *MNRAS*, **424**, 2770
- Vieira, R. G., Carciofi, A. C., Bjorkman, J. E., et al. 2017, *MNRAS*, **464**, 3071
- Waters, L. B. F. M. 1986, *A&A*, **162**, 121
- Wilking, B. A., Lebofsky, M. J., & Rieke, G. H. 1982, *AJ*, **87**, 695
- Yudin, R. V. 2001, *A&A*, **368**, 912
- Zorec, J., Frémat, Y., Domiciano de Souza, A., et al. 2016, *A&A*, **595**, A132

Appendix A: Observational logs**Table A.1.** Stellar calibrators used for the VEGA observations.

Star (HD)	Spec. type	<i>R</i> (mag)	<i>K</i> (mag)	Diameter (mas)
194244	B9V	6.1	6.1	0.161 ± 0.011
210424	B5III	5.5	5.7	0.177 ± 0.012
211924	B5IV	5.4	5.5	0.219 ± 0.015
224926	B7III-IV	5.2	5.4	0.197 ± 0.014

Table A.2. VEGA and AMBER observations.

UTC (date)	UTC (hh:mm)	N° of measur.	Tel. conf.
VEGA			
2012-08-28	09:40	1	S1-S2
2013-08-28	09:07–09:43	2	S2-S1-E2
2013-08-28	07:05	1	W2-W1-E1
2013-08-30	10:35	1	S2-S1-W2
2013-10-31	05:45	1	W2-W1
2013-08-29	07:55	1	S2-S1-E2
2013-08-29	06:35	1	W2-W1-E1
2014-07-03	10:38–11:27	2	E2-E1
2014-07-04	08:24–11:32	3	E2-S2-W2
2014-07-06	08:06	1	E2-E1
2014-07-08	10:57–11:49	4	E2-S2-W2
2014-07-10	08:07–11:57	9	E2-S2-W2
2014-08-22	07:12–07:41	2	E2-S2-W2
2014-08-23	06:19–06:49	2	E2-S2-W2
2014-08-25	06:40	1	E2-E1
2014-08-28	07:19–09:39	3	W2-W1
2014-08-29	06:41–09:51	3	E2-E1
2014-10-17	03:52	1	S1-E1-W1
2014-10-19	03:40–05:32	4	W2-S2-W1
2014-10-20	02:38	1	W2-S2-W1
2014-10-23	03:13–03:43	2	S1-E1-W1
2016-11-19	01:44–04:53	3	E2-E1
AMBER			
2011-06-20	10:08	1	D0-I1-H0
2014-10-29	00:48–01:27	2	A1-G1-I1
2014-10-30	01:06–03:31	2	A1-G1-J3
2014-10-31	00:25–03:39	3	A1-K0-J3

Notes. In the third column, the number of measurements are shown accordingly to the presented UT interval (second column). CHARA (VEGA) and VLTI (AMBER) telescope configurations are shown in the fourth column.

Appendix B: MCMC fitting tests: fits to the VEGA and AMBER data with the kinematic model

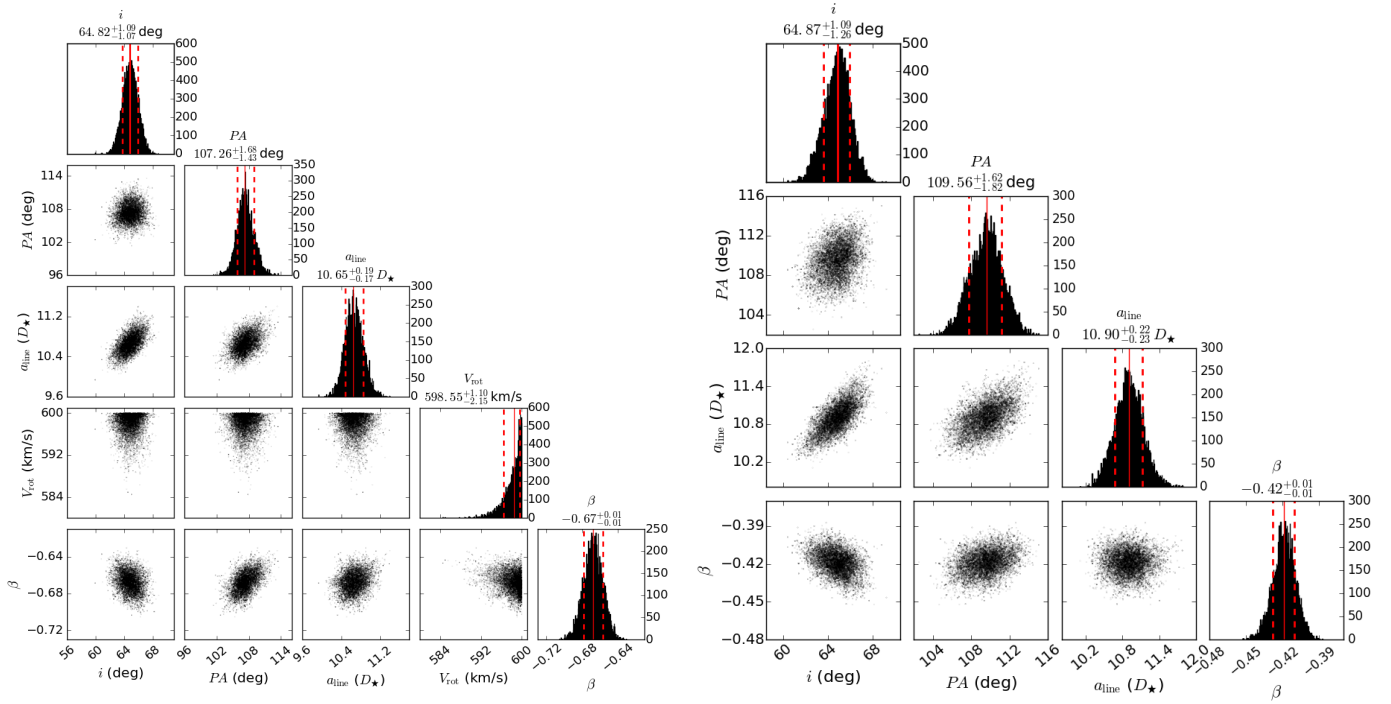


Fig. B.1. As in Fig. 4, but for the other MCMC fitting tests (test i in the *left* and test ii in the *right*) to fit the VEGA differential data.

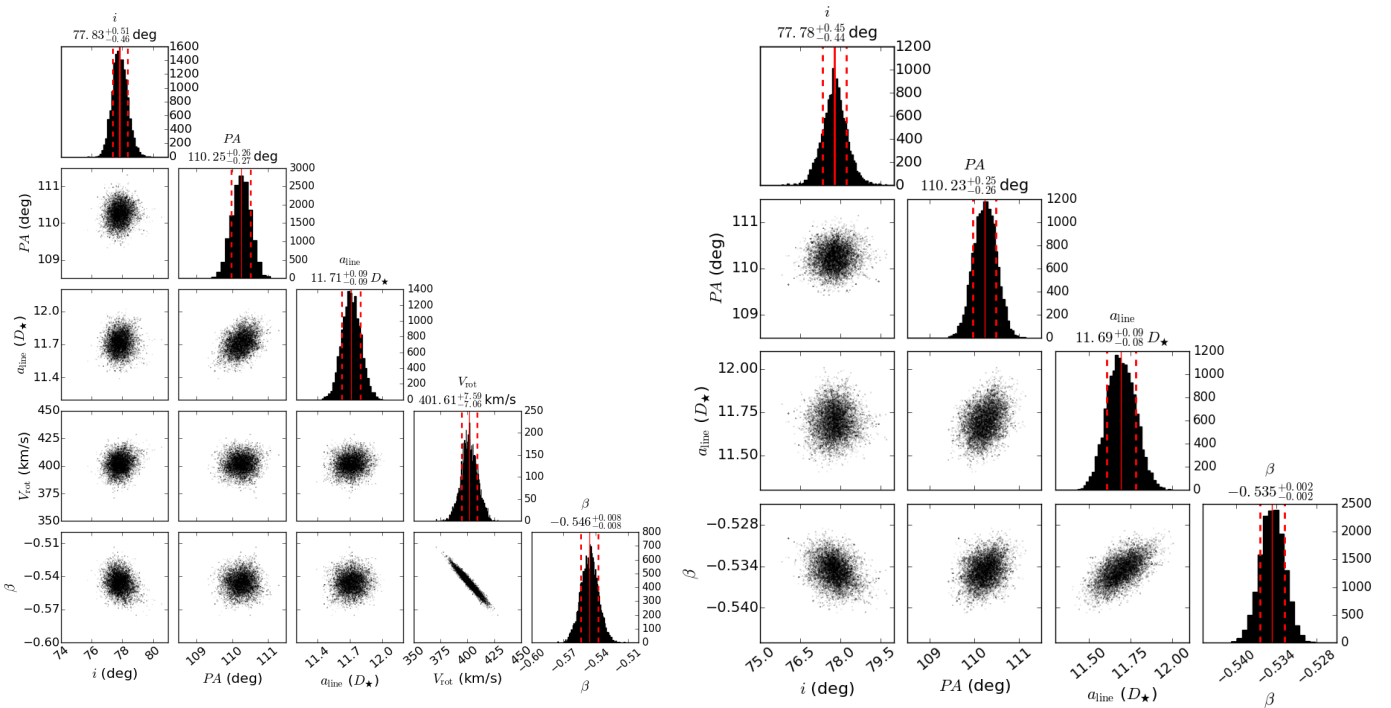


Fig. B.2. As in Fig. 4, but for the other MCMC fitting tests (test i in the *left* and test ii in the *right*) to fit the AMBER differential data.

Appendix C: Best-fit kinematic and HDUST models: AMBER

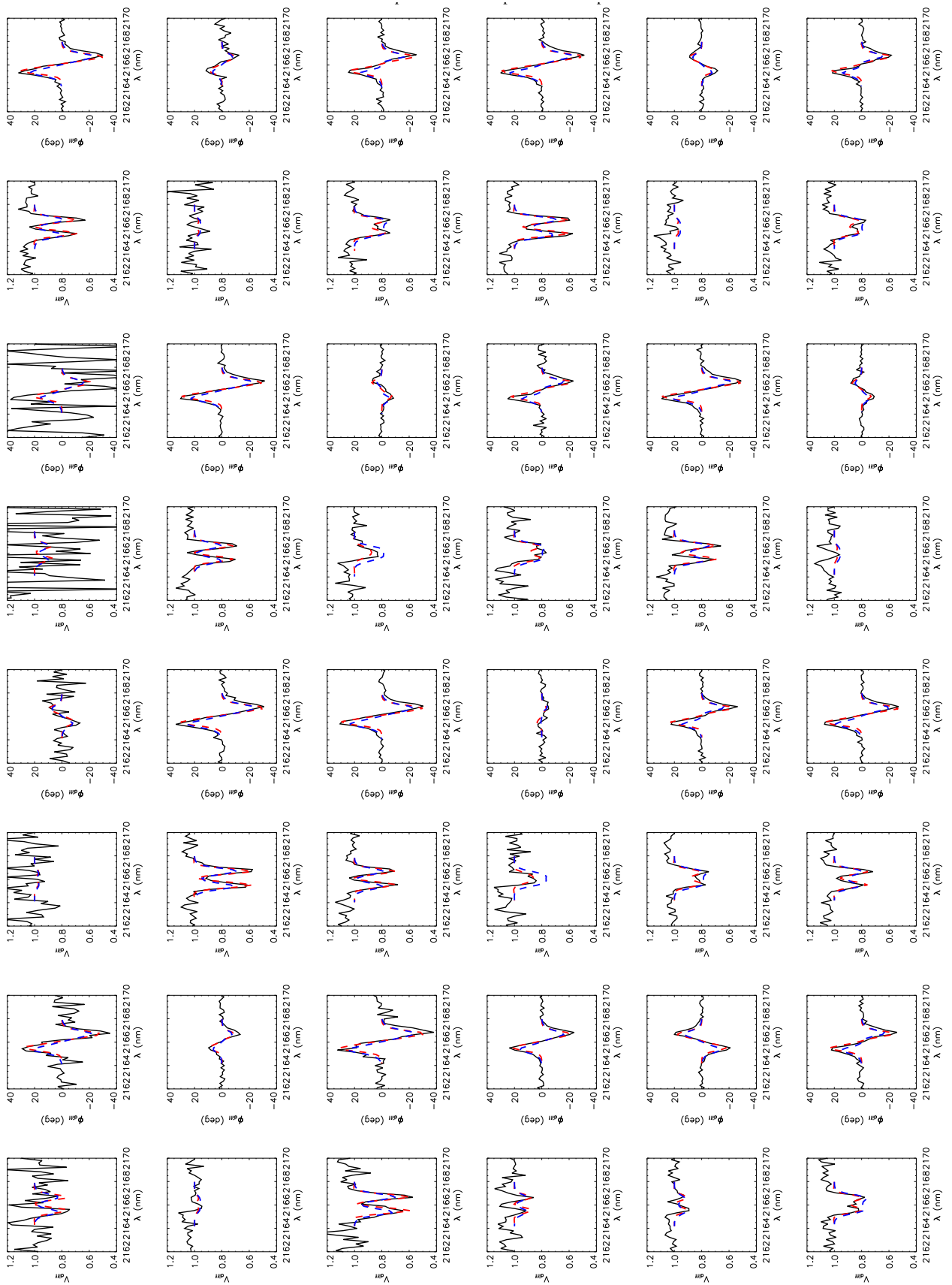


Fig. C.1. Comparison between our best-fit kinematic (dashed red; Table 2) and HDUST (dashed blue; Table 5) models to all the AMBER measurements (black).

Appendix D: Interstellar polarization**Table D.1.** Fitted Serkowski parameters, with the polarization angle, for the field stars used to derive the interstellar polarization of α Aquarii.

Star	RA (J2000) (hh:mm:ss)	Dec (J2000) (deg:arcmin:arcsec)	P_{\max} (%)	λ_{\max} (μm)	$\langle PA_{\text{IS}} \rangle$ (deg)
HD 208719	21 58 20.0	-01 49 46.7	$0.095^{+0.006}_{-0.005}$	$0.75^{+0.05}_{-0.06}$	130.7 ± 2.9
HD 209348	22 02 48.4	-02 28 44.4	$0.012^{+0.005}_{-0.005}$	$0.40^{+0.34}_{-0.24}$	128 ± 44
2MASS J22025363-0229207	22 02 53.6	-02 29 20.7	$0.88^{+0.17}_{-0.18}$	$0.34^{+0.21}_{-0.17}$	135.4 ± 9.1
2MASS J22025544-0230058	22 02 55.4	-02 30 05.8	$0.975^{+0.017}_{-0.014}$	$0.49^{+0.02}_{-0.02}$	136.8 ± 0.6

Notes. We show the median and the 15.87th and 84.13th percentiles for P_{\max} and λ_{\max} from the MCMC analysis (more details in [Bednarski 2016](#)). The interstellar polarization angle estimated for each field star is the mean value among the observations in the $BVRI$ -bands ($\langle PA_{\text{IS}} \rangle$).

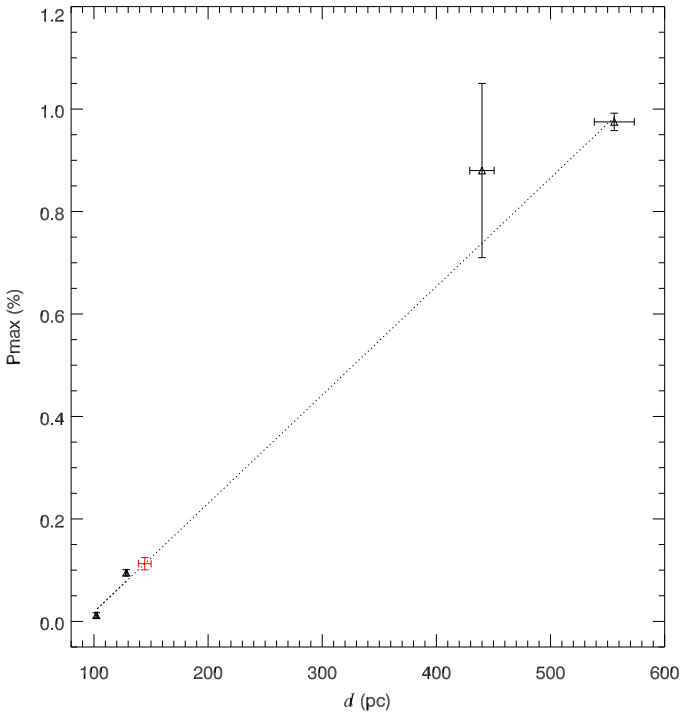


Fig. D.1. Fitted P_{\max} for the field stars (Table D.1, open triangles) as a function of the *Gaia* DR2 distance. From the linear fit to P_{\max} vs. d for the field stars (dotted line), we determined P_{\max} for α Aquarii (red cross).

Chapter 7

Ongoing studies

Contents

7.1	The radiative line-driven wind of Rigel	238
7.1.1	Rigel: an evolved massive star	238
7.1.2	Multi-band spectro-interferometry: CHARA and VLTI	239
7.1.3	H α intensity interferometry: I2C team	243
7.1.4	Direct imaging: VLT/SPHERE	245
7.2	Classical Be stars	246
7.2.1	Drawing a big picture of Be disks	246
7.2.2	The VEGA and AMBER large surveys	247
7.2.3	First observations with MATISSE	249
7.2.4	Toward a detailed view on Be stars (other than <i>o</i> Aquarii)	251

My ongoing and near-future studies on the two main lines of research of this thesis are discussed here: radiative line-driven winds and disks of massive hot stars.

Sect. 7.1 discusses in details my work on the fundamental wind parameters of the blue supergiant star Rigel through a multi-wavelength interferometric approach (visible, near-infrared, and mid-infrared), while Sect. 7.2 is devoted to the study of Be disks also by means of interferometry at multi-spectral channels.

7.1 The radiative line-driven wind of Rigel

7.1.1 Rigel: an evolved massive star

Rigel (β Orionis, HD 34085) is the MK-standard of spectral type B8Ia. This B supergiant star belongs to class of α Cygni stars, presenting variability at different time-scales, ranging from ~ 1.2 to ~ 74.7 days, due to non-radial pulsations (e.g., Kaufer et al. 1996, 1997; Moravveji et al. 2012a,b). Rigel is thought to have an initial mass

7.1. The radiative line-driven wind of Rigel

of $\sim 25 M_{\odot}$ (O-type star) and to have already passed by a red supergiant phase before the blue-loop in the HR diagram (Saio et al. 2013).

The circumstellar environment of Rigel was analysed through spectro-interferometry observations in the visible ($H\alpha$) with CHARA/VEGA (Chesneau et al. 2010) and in the near-infrared ($Br\gamma$) with VLTI/AMBER (Chesneau et al. 2014). This latter study performed one of the largest interferometric campaigns of Rigel with observation collected in the periods of 2006-2007 and 2009-2010.

One of the main findings of Chesneau et al. (2014) is the wind variability of Rigel with the mass-loss rate changing in $\sim 20\%$ in the time-scale of one year (periods of 2006-2007 and 2009-2010). These authors found a mean mass-loss rate of $\sim 9.4 \times 10^{-7} M_{\odot} \text{ yr}^{-1}$ in the period of 2006-2007, while it is $\sim 7.6 \times 10^{-7} M_{\odot} \text{ yr}^{-1}$ in the latter one from modeling AMBER visibilities (measured in $Br\gamma$). In addition, they verified a substantial discrepancy between the mass-loss rate derived from the $H\alpha$ transition ($\sim 1.5 \times 10^{-7} M_{\odot} M_{\odot} \text{ yr}^{-1}$), when compared with one found from $Br\gamma$ (up to about one order of magnitude).

Thus, further investigations on the wind parameters of Rigel are still necessary, allowing us to have a better picture of the winds around OBA supergiants. As discussed above, these stars show interesting photospheric phenomena, such as pulsations, which are undoubtedly connected to their wind properties (e.g., Kraus et al. 2015; Haucke et al. 2018, and references within). They also impose a current challenge to the standard CAK-theory of line-driven winds (see again our discussion on the wind acceleration of hot supergiants in Sect. 1.2.2).

7.1.2 Multi-band spectro-interferometry: CHARA and VLTI

Rigel is one the brightest ($V \sim 0.13$) massive stars, and thus an ideal target to further tests on the capability of the recent operating GRAVITY instrument (K-band region, VLTI second generation, Sect. 3.7.3) to probe the structure and intensity of radiative line-driven winds around massive stars. Commissioned in 2016, GRAVITY has been successfully used to probe the circumstellar environments of massive stars, such as the study of wind-wind collision regions of η Carinae (Gravity Collaboration et al. 2018) and HD 93206 A (Sanchez-Bermudez et al. 2017).

The main objective of this project is investigate the mass-loss rate of Rigel through interferometric data obtained with VLTI/GRAVITY, in the K-band, conjointly with data from CHARA/VEGA (visible), VLTI/AMBER (near-infrared), and VLTI/MATISSE (mid-infrared). Part of our AMBER data was already analysed by (Chesneau et al. 2014), as discussed above. In addition, we have new unpublished AMBER data obtained from our team at Laboratoire Lagrange, covering the period of 2006-2016

7.1. The radiative line-driven wind of Rigel

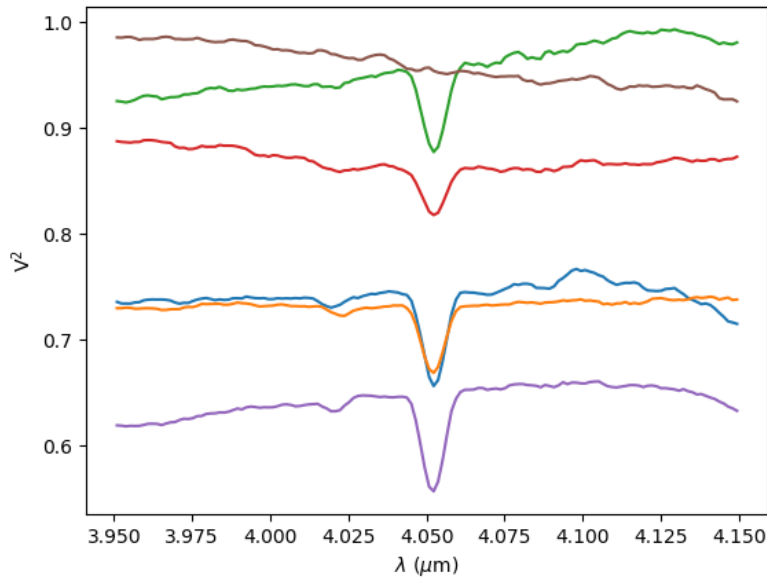


Figure 7.1 – VLTI/MATISSE observation of Rigel performed on September 25, 2019. The squared visibility for each baseline is shown as a function of wavelength around the $\text{Br}\alpha$ line. Note the large visibility drop in the $\text{Br}\alpha$ line due to the larger flux contribution from the wind in this line, when compared with the continuum.

in total. At the end of 2019, Rigel was also observed by our team using the new VLTI mid-infrared beam-combiner MATISSE¹ (Lopez et al. 2014), during its Commissioning/Science Verification phase. Fig. 7.1 illustrate our MATISSE observations of Rigel (calibrated visibility around the $\text{Br}\alpha$ line) using different VLTI baseline configurations. Then we aim to address the wind variability of Rigel in terms of more recent multi-wavelength spectro-interferometric data covering the period of 2016-2019.

Together with my PhD advisors and other collaborators from Laboratoire Lagrange, I proposed to observe Rigel with the VLTI/GRAVITY instrument, as the PI of the ESO program 0100.D-0332². Our proposal was approved (ESO period 100, 6h of observation in the total) and all the observations were performed in service mode, between October 2017 and March 2018, using the high spectral resolution mode of GRAVITY ($R = 4000$). To obtain different levels of spatial resolution of Rigel, covering both small and high frequencies in the Fourier plan, our observations were performed with all the possible auxiliary telescope quadruplets at VLTI, A0-B2-C1-D0, D0-G2-J3-K0, and A0-G1-J2-J3, allowing us to reach larger baseline lengths, respectively.

For preparing this observational proposal, I computed a small grid of atmosphere models using the code CMFGEN (1-D non-ELT radiative transfer) for different values

1. Acronym for “Multi AperTure mid-Infrared SpectroScopic Experiment”.

2. co-PIs: A. Meilland, A. Domiciano de Souza, M. Carbillet, S. Kannan, E. Lagadec, F. Millour, and P. Stee.

7.1. The radiative line-driven wind of Rigel

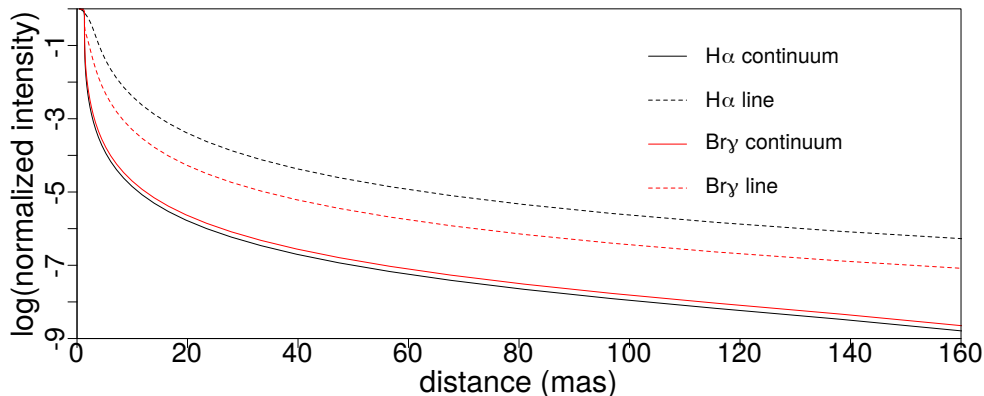


Figure 7.2 – Intensity profiles from one of our adopted CMFGEN models for Rigel, used as a reference model in our VLTI/GRAVITY proposal. These profiles are calculated at different spectral regions, in the H α and Br γ lines, and in their close-by continuum regions. The intensity is shown as a function of distance from the center of the star (in milliarcsecond).

of mass-loss rate, taking as reference the value of \dot{M} tested by Chesneau et al. (2014). Also (partially) based on Chesneau’ study about Rigel, the other parameters in our model are fixed as follows: $\log L_{\star}/L_{\odot} = 5.45$, $T_{\text{eff}} = 20000$ K, $\log g = 2.6$, $R_{\star} = 44.4 R_{\odot}$, and $v_{\infty} = 300$ km s $^{-1}$.

We see a notable difference between the CMFGEN model intensity in both the H α (VEGA) and Br γ (AMBER and GRAVITY) lines, when compared with their close-by continuum regions, up to large distances from the photosphere (Fig. 7.2). Such difference is highly dependent on the mass-loss rate used in the models due to the larger opacity of the wind in these lines than in the continuum. Fixing the other model parameters allows us to predict the drop in visibility in these lines for a certain value of \dot{M} , as shown in Fig. 7.3. As expected, higher values of mass-loss rates yield a larger drop in the Br γ visibility, and also a more intense Br γ line profile.

Fig. 7.4 shows an example of our GRAVITY data (calibrated V^2) for one observational night, taken using the K0-G2-D0-J3 quadruplet (six different baselines). Unfortunately, information on the visibilities measured in the He I lines is lost due to atmospheric effects. Nevertheless, the data quality is good with a clear signal of drop in Br γ visibility, being this transition our principal interest in this project (well-known wind diagnostic, as discussed in Sect. 2.3).

As a preliminary analysis, also shown in Fig. 7.4, we compare one of our CMFGEN model ($\dot{M} = 4 \times 10^{-7} M_{\odot} \text{ yr}^{-1}$) to calibrated V^2 data of Rigel from all the observations with GRAVITY (shown as a function of spatial frequency, instead of wavelength). In this case, our predicted visibility of the model is calculated considering a stellar diameter of 2.72 mas from Bourges et al. (2017).

First, from just looking the calibrated GRAVITY visibility, we are able to almost

7.1. The radiative line-driven wind of Rigel

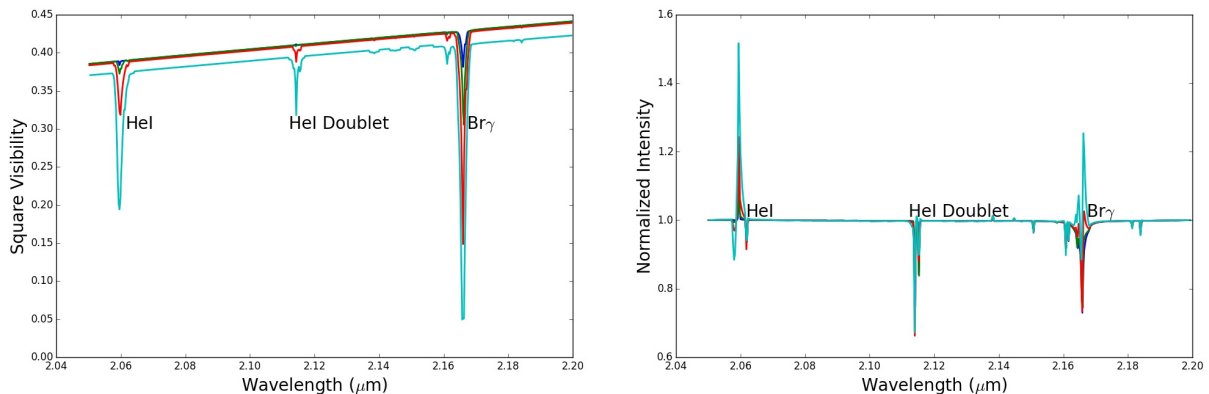


Figure 7.3 – Simulated visibilities (left panel) and spectra (right panel) in the K-band (GRAVITY wavelength region) from CMFGEN models with different values of mass-loss rate: $\dot{M} = 1 \times 10^{-7}$ (blue), 2×10^{-7} (green), 4×10^{-7} (red), and 8×10^{-7} (cyan) $M_{\odot} \text{ yr}^{-1}$. All the other parameters are fixed as discussed in the text.

resolve the stellar diameter with the longer baselines. Comparing our adopted CMFGEN model to data, we see that the assumed value of stellar diameter overestimates the overall drop in the continuum visibility, indicating a somewhat smaller value for the photosphere size of Rigel. In addition, this model also seems to overestimate the observed visibility drop in the $\text{Br}\gamma$, and then indicating a value of mass-loss rate lower than $4 \times 10^{-7} M_{\odot} \text{ yr}^{-1}$.

Using the LITpro tool, I almost finished the work regarding the geometric modeling of calibrated GRAVITY visibility. These results are summarized in Fig. 7.5. The GRAVITY visibility of Rigel is shown in the continuum region close to $\text{Br}\gamma$ (2.165–2.168 μm), and in the core of this line. As suggested by the analysis shown in Fig. 7.4, it is needed a smaller extension for the stellar diameter, a uniform disk with a diameter of ~ 2.6 mas. However, the best-fit uniform disk found from fitting the V^2 measured in the core of $\text{Br}\gamma$ is significantly larger than this value from the continuum, with a diameter of ~ 3.1 mas, due to the larger flux contribution from the wind in the $\text{Br}\gamma$ line. Therefore, this preliminary analysis from our GRAVITY data allows us to detect the wind of Rigel.

Further work is in progress on this study about Rigel. In particular, I finished the reduction of all the GRAVITY observations, using the standard GRAVITY data reduction pipeline³ provided by ESO (Lapeyrere et al. 2014), and the analysis of calibrated visibility using geometric models is well-advanced, as discussed above.

Nevertheless, I still need to improve the grid of CMFGEN models for a proper analysis of these data. Our reference model has a substantially higher effective temperature ($T_{\text{eff}} = 20000$ K) than a reliable value for Rigel with $T_{\text{eff}} \sim 12000$ (e.g., Przybilla

3. Publicly available at <https://www.eso.org/sci/facilities/paranal/instruments/gravity/tools.html>

7.1. The radiative line-driven wind of Rigel

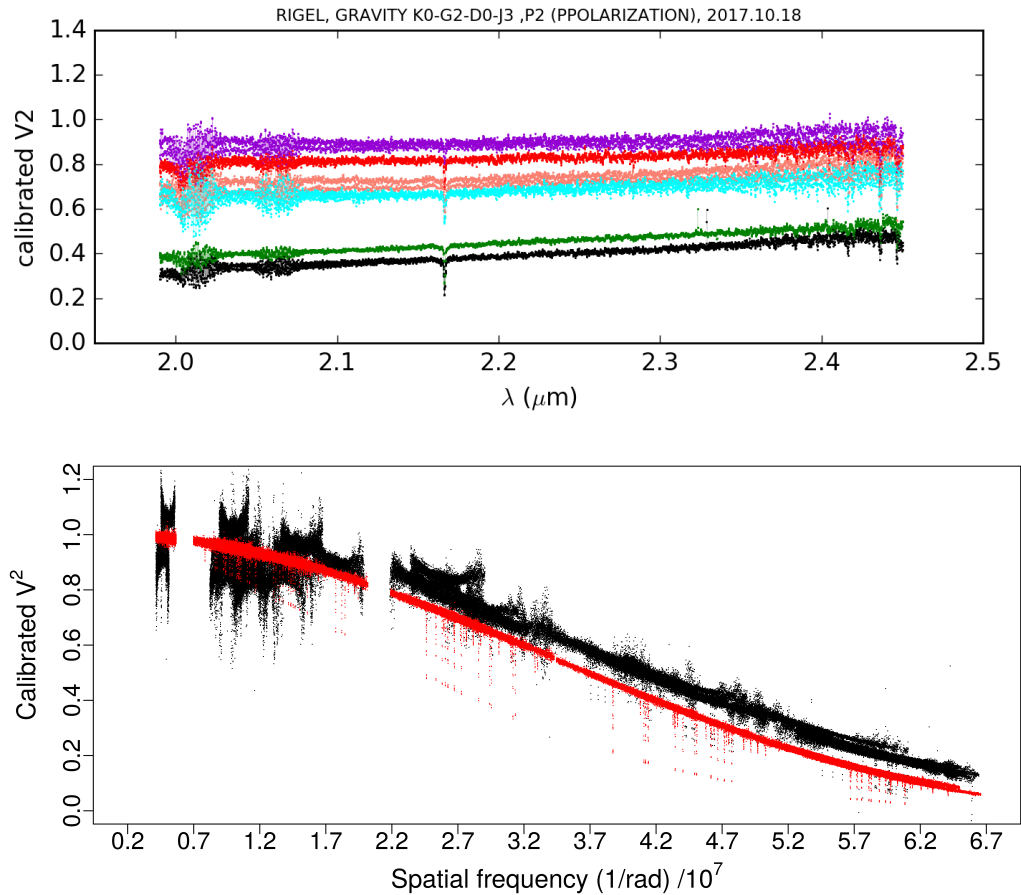


Figure 7.4 – Top panel: an example of reduced GRAVITY data for Rigel, observed in one night (18/10/2017) using the VLTI quadruplet K0-G2-D0-J3, as a function of wavelength (K-band). The baselines configurations are shown in different colors. Bottom panel: our complete GRAVITY dataset (8 nights, 6 h of observations in total) as function of spatial frequency (black), compared with the same CMFGEN shown in Fig. 7.2 (red). See text for discussion.

et al. 2006; Chesneau et al. 2014). This difference comes from the fact that I started to work on models for Rigel based on my CMFGEN grid for O-type stars (Paper I), combined with the deadline for submitting our proposal to ESO. To have a fixed value of luminosity from Chesneau et al. (2014), our reference model has a quite smaller stellar radius of $\sim 44 R_{\odot}$, instead of the value adopted by these authors ($115 R_{\odot}$). In addition, the model for Rigel presented here has the same chemical composition of the basic CMFGEN models of Paper I, and I have been working to improve this later point for the case of a late B supergiant as Rigel (B8Ia). In short, it is still a “dirty” CMFGEN model for Rigel.

7.1.3 H α intensity interferometry: I2C team

Furthermore, the I2C team observed Rigel (total of ~ 50 h of observations) in a campaign performed from January 27 to February 14, 2020. Also as a short-term

7.1. The radiative line-driven wind of Rigel

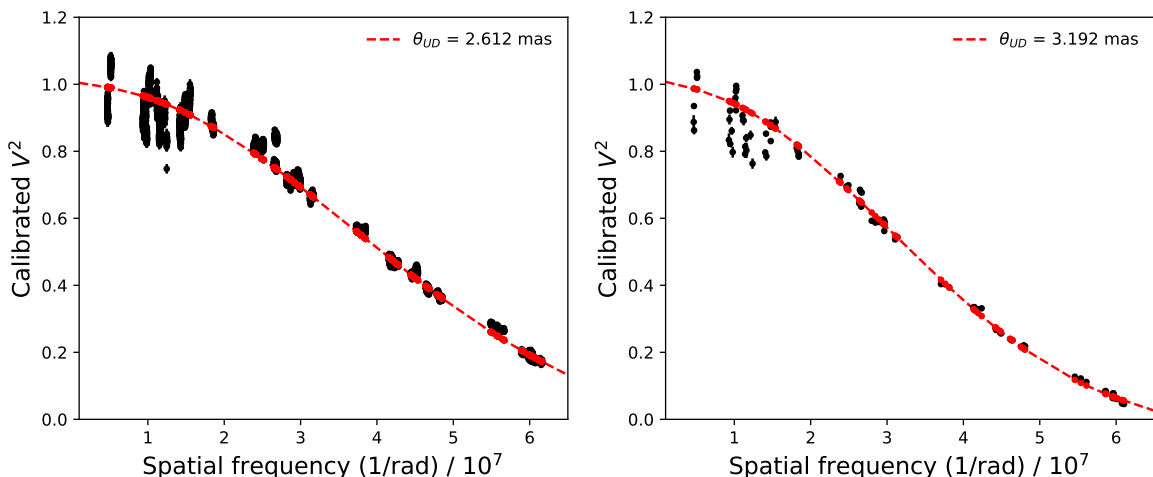


Figure 7.5 – LITpro best-fit uniform disk models found from fitting our GRAVITY data for Rigel, in the continuum region close to $\text{Br}\gamma$ (left panel) and in the core of $\text{Br}\gamma$ (right panel). Note the larger size of the fitted uniform disk when looking at the $\text{Br}\gamma$ line, compared with its close-by continuum.

perspective, we aim to use our best-fit CMFGEN model for Rigel also to interpret these new $\text{H}\alpha$ -band intensity interferometric data, applying on Rigel the same method used in Paper II for deriving the distance of P Cygni.

In conclusion, we plan to write two papers based on these interferometric observations of Rigel, in both of them using the code CMFGEN, but with different aims, that is, investigating its wind parameters from spectro-interferometric data (VEGA, AMBER, GRAVITY, and MATISSE) and estimating its distance from $\text{H}\alpha$ intensity interferometry. We point out that Rigel’s distance is estimated to be ~ 265 pc with $\sim 10\%$ of uncertainty based on Hipparcos parallax measurements (van Leeuwen 2007). Then, such an interferometric study of Rigel allows us to constrain its distance based on a different distance determination method. In addition, depending on the quality of these new $\text{H}\alpha$ intensity interferometric observations of Rigel, we could try to test our results for the wind mass-loss rate found from the best-fit model to the spectro-interferometric datasets.

Also using CMFGEN models, we intend to analyse a large sample of hot supergiants in the framework of this distance determination method. In addition to the importance of more accurate and precise distance determinations on many branches of astrophysics, such a large survey of OBA supergiants allows us to provide an independent check on the modified-wind momentum luminosity relation for massive stars, and then directly touching on our understanding about their wind properties.

7.1. The radiative line-driven wind of Rigel

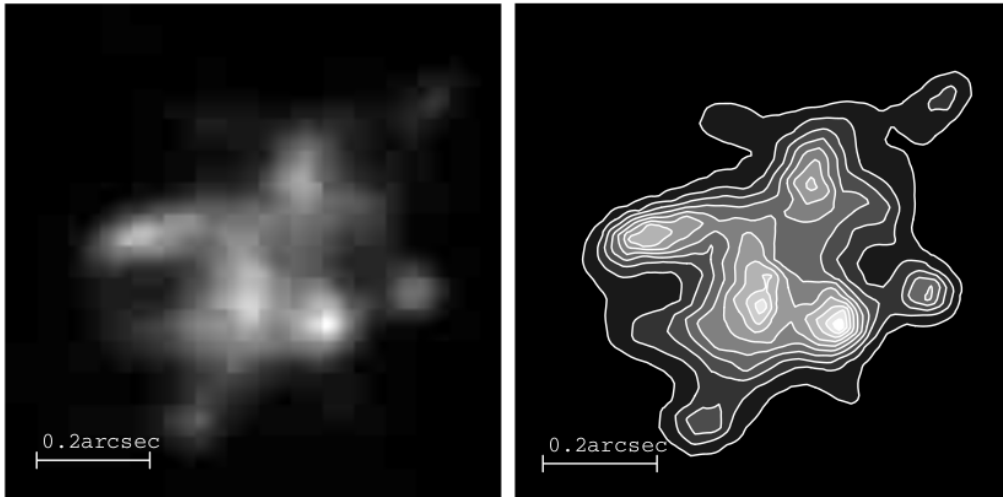


Figure 7.6 – Image reconstruction by Chesneau et al. (2000) of P Cygni large-scale circumstellar environment (up to $\sim 1000 R_{\star}$) using Observatoire de Haute-Provence (OHP) observations with adaptive optics. The central star has an angular diameter of about 0.2 mas. Reproduced from Chesneau et al. (2000).

7.1.4 Direct imaging: VLT/SPHERE

Besides the power provided by interferometry to probe the structure of massive stars winds, another very interesting observational technique relies on direct imaging. For instance, based on near-diffraction limited observations, using adaptive optical system, Chesneau et al. (2000) were able to resolve the $H\alpha$ -emitting region of P Cygni and to detect clear signatures of clumps in the wind of P Cygni from the inner ($\sim 20 R_{\star}$) up to the outer wind region ($\sim 1000 R_{\star}$) (see Fig. 7.6).

The VLT/SPHERE instrument is the current state-of-the-art of the technique of high dynamical coronagraphic imaging, giving us access on how the circumstellar environment is distributed up to larger distance from the stellar surface. Despite being more widely used for studies on exoplanet and evolved cool stars, observation of massive stars with SPHERE are for sure of great interest, for example, when looking for departures of spherical symmetry in their radiative line-driven winds.

Fig. 7.7 shows our simulations of SPHERE observations (in $Pa\beta$ and $Br\gamma$) based on our reference CMFGEN for Rigel. I calculated this model in the framework of my small set of CMFGEN models for preparing an observational proposal of Rigel with GRAVITY and SPHERE. Thus, using SPHERE, we would be able to detect the wind of Rigel both in $Pa\beta$ and $Br\gamma$ and constrain its geometry at a larger scale than using long-baseline interferometry, as with GRAVITY, allowing us to determine the mass-loss rate of Rigel’s wind at different scales.

Unlike our request with GRAVITY (discussed in Sect. 7.1.2), unfortunately our last request for observing Rigel with SPHERE was denied. Nevertheless, this science

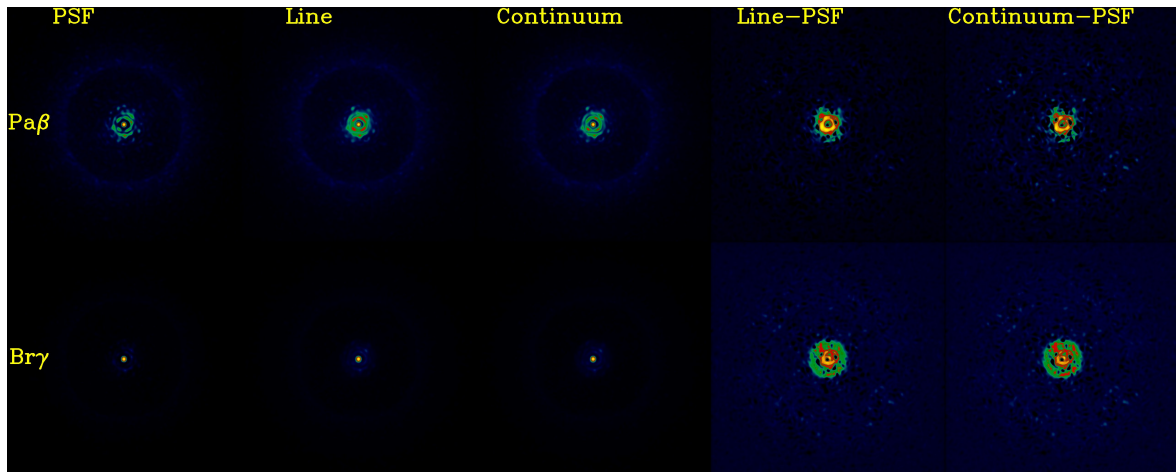


Figure 7.7 – SPHERE simulated observations (raw images) from our reference CMFGEN model for Rigel (with mass-loss rate of $4 \times 10^{-7} M_{\odot}\text{yr}^{-1}$). Note the difference between the PSF and the line/continuum image in both lines (Pa β and Br γ).

case about Rigel shows the current large potential for studying the morphology and physical conditions on massive stars winds using high angular resolution techniques other than interferometry. Of course, these simulations for the wind of Rigel encourage us to request again time to observe this star with VLT/SPHERE in the near-future.

7.2 Classical Be stars

7.2.1 Drawing a big picture of Be disks

Our detailed analysis of the Be star *o* Aquarii (Sect. 6.3; Paper III) helped us to constrain its parameters, as the equatorial rotation velocity and the kinematical and physical condition of its disk, and draw a unified picture of this star and its environment in the visible and near-infrared region.

My work on *o* Aquarii paved the way for a more systematic analysis of Be stars, based on the same methodology used in Paper III. This means to use the kinematic model with a MCMC mode fitting procedure and also a large grid of pre-calculated HDUST models (BeAtlas grid), together with my routines for data analysis, to model spectro-interferometric data measured at different transitions.

We aim to analyse a large sample of Be stars, based both on published and new spectro-interferometric data taken by our group at OCA. Such a multi-wavelength interferometric Be survey allows us to find a more complete description on the morphology, kinematics, and physical properties of both the cooler and hotter Be stars with disks seen under different directions. For instance, this should help us to test more firmly, in a statistical way, the picture proposed in Paper III that the quite similar disk extension of *o* Aquarii in both H α and Br γ arises due to its nearly edge-on view.

7.2. Classical Be stars

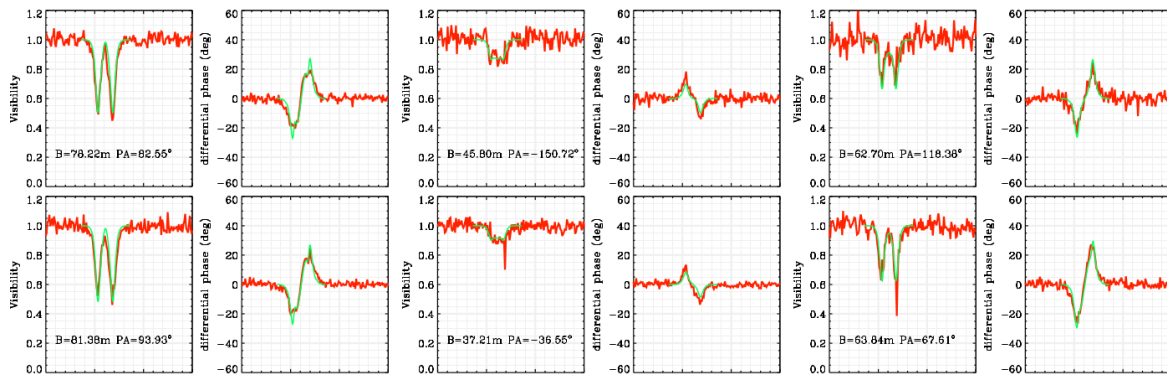


Figure 7.8 – Example of AMBER differential data (red line) of α Arae observed in the Be survey of Meilland et al. (2012). The best-fit kinematic model found by these authors is shown in green line. Adapted from Meilland et al. (2012).

In Sect. 7.2.2, we present a very brief discussion on our VEGA and AMBER Be stars datasets, and Sect. 7.2.3 discusses our very preliminary observations of Be stars using the new VLTI mid-infrared beam combiner MATISSE. Lastly, Sect. 7.2.4 summarizes some of our on-going studies about individual objects.

7.2.2 The VEGA and AMBER large surveys

Regarding the K-band region, all the AMBER data for this project was already published in the Be surveys of Meilland et al. (2012) (8 objects) and Cochetti et al. (2019) (26 objects). Details on their star samples can be found in Tables 1 and 2 of Meilland et al. (2012) and Cochetti et al. (2019), respectively.

For instance, the $\text{Br}\gamma$ profiles of the sample analysed by Cochetti et al. (2019) are shown in Fig. 7.9. In addition, Fig. 7.8 shows part of the AMBER dataset of α Arae (HD 158427, B2Vne) from Meilland et al. (2012) together with the best-fit kinematic model found by these authors to fit their AMBER data to this star. Interestingly, as discussed in Sect. 1.5.1, the AMBER study of Meilland et al. (2007b) on this star provided the first direct detection of a Keplerian rotating disk in Be stars, in addition to find evidences of an enhanced polar wind in α Arae, that is, contributing to the flux distribution of its environment along the rotational axis.

We remind the reader that these studies are based purely on the kinematic code, but without the implementation of an automatic fitting procedure as performed in this thesis using the code EMCEE. Furthermore, as these authors do not employ radiative transfer models on their analysis, we have the opportunity to model their AMBER datasets using our BeAtlas grid of HDUST models to derive the disk density parameters of the objects in their samples.

In complement to the analysis in the $\text{Br}\gamma$ line, A. Meilland has been leading a large observational program of Be stars with the VEGA instrument since about 2015

7.2. Classical Be stars

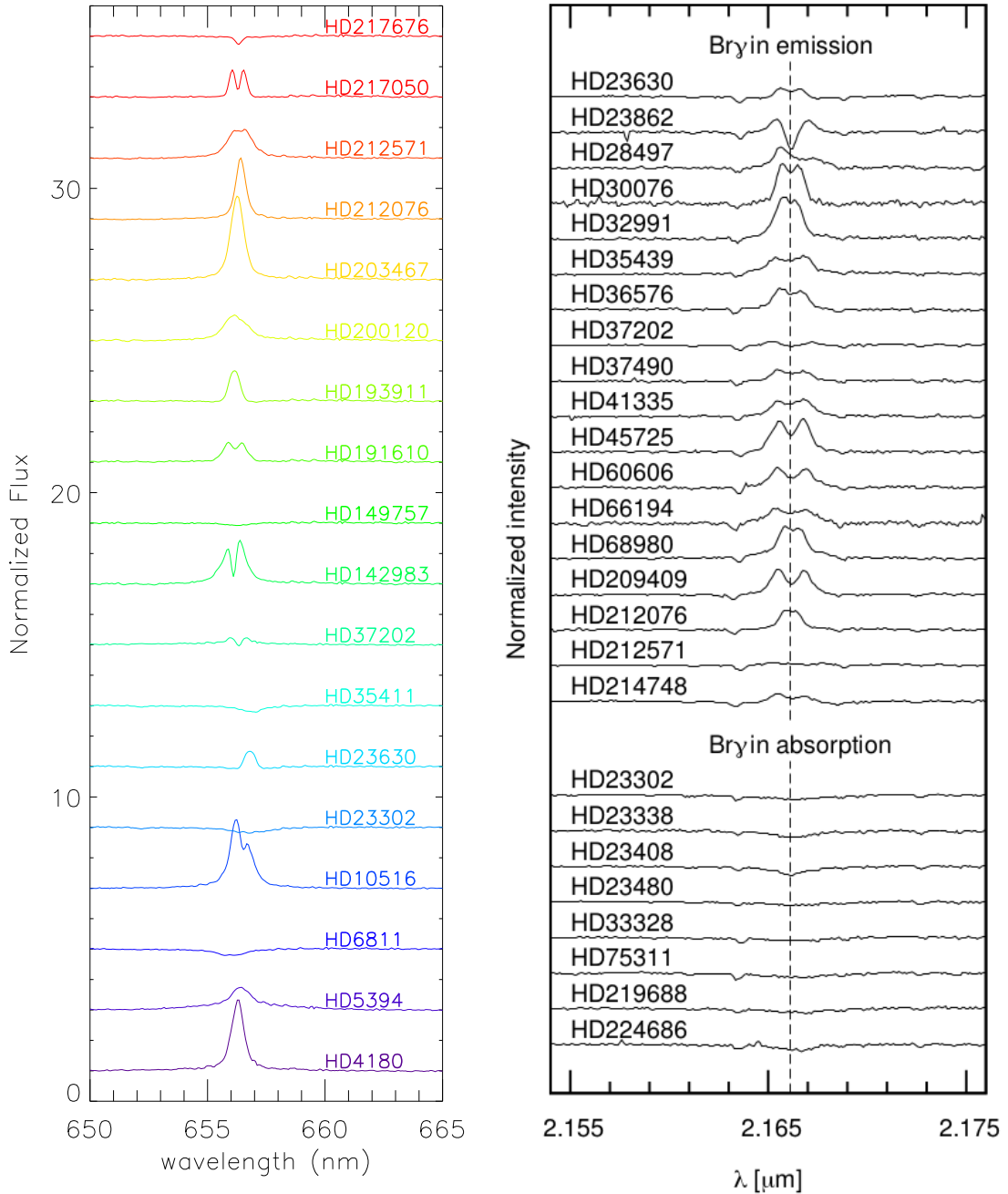


Figure 7.9 – Left: example of H α line profiles observed with the VEGA instrument for 17 Be stars of our VEGA survey (34 objects observed in total). Right: Br γ line profiles of the Be star sample (26 objects) analysed by Cochetti et al. (2019). The right panel is reproduced from Cochetti et al. (2019).

(observations centered at H α).

To date, we have observed 34 Be stars using VEGA, in particular, almost choosing the CHARA two-telescope configurations with different lengths and orientations, S1S2 (~ 34 m), E1E2 (~ 66 m), W1W2 (~ 108 m), allowing us to resolve our targets with different levels of angular resolution. This program is almost finished, only missing

7.2. Classical Be stars

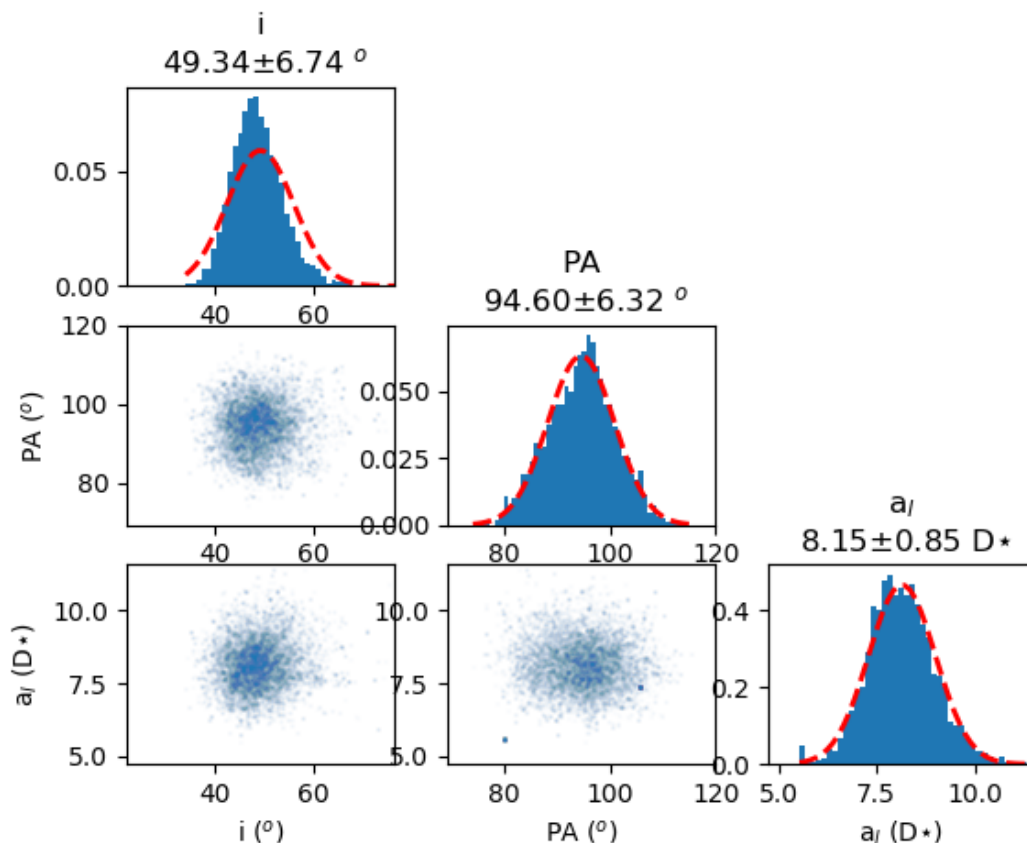


Figure 7.11 – Preliminary MCMC analysis of VLTI/MATISSE differential data (in the $\text{Br}\alpha$ line) of the Be star α Arae, fitted using the kinematic code with three free parameters: stellar inclination angle, disk major-axis position angle, and the disk major-axis FWHM in $\text{Br}\alpha$. See text for discussion.

Fig. 7.10 shows observations of δ Centauri with MATISSE in the L- and M-bands (from ~ 3.0 to $5.0 \mu\text{m}$). The observed spectrum is shown here in addition to the measured interferometric fringes and the computed quantities (visibility and differential phase). This illustrates how rich is the mid-infrared spectral region of Be stars, showing several emission-lines being the $\text{Br}\alpha$ and $\text{Pf}\gamma$ the strongest ones. As discussed in Sect. 2.3, $\text{Br}\alpha$ and $\text{Pf}\gamma$ are usually the best lines to trace the density structure of the environments in massive stars (e.g, Lenorzer et al. 2004; Najarro et al. 2011). Indeed, from Fig. 7.10 the largest visibility drops (when comparing to the nearby continuum) are found in these transitions.

As a very preliminary analysis of these MATISSE data, Fig. 7.11 shows a simple evaluation of our MCMC kinematic model fitting code to fit differential MATISSE data (in the $\text{Br}\alpha$ line) of α Arae. Despite being a simple initial test, we were able to constrain the three kinematic model parameters that were free in the fitting fairly-well: inclination angle of $\sim 49^\circ$, disk major-axis position angle of $\sim 95^\circ$, and the disk size in $\text{Br}\alpha$ of $\sim 8 D_\star$.

We point out that this star was also analysed in the AMBER Be surveys of Meilland

7.2. Classical Be stars

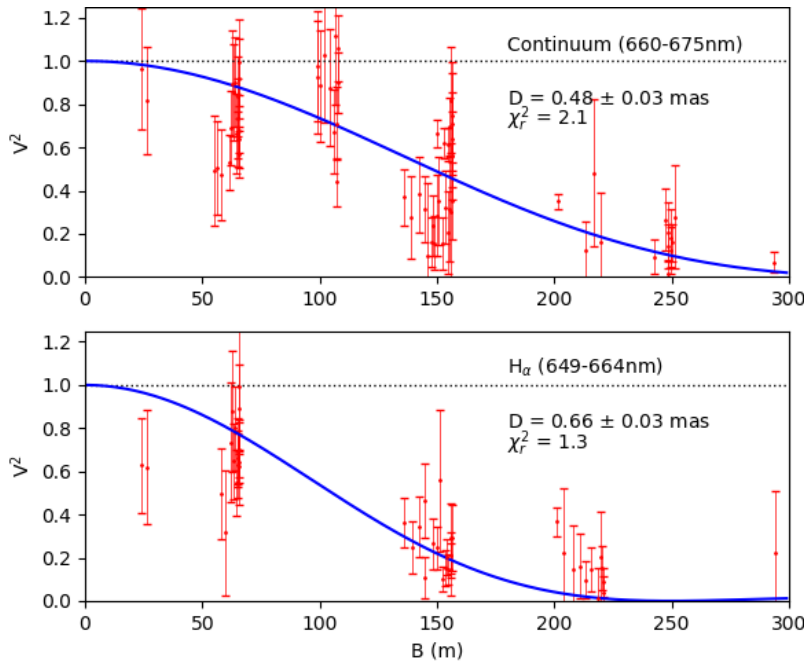


Figure 7.12 – Geometric modeling of VEGA squared visibilities of the late-type Be star κ Draconis (B6IIIe). Note that the VEGA visibility is quite lower in the $H\alpha$ -band, in comparison with the close-by continuum band, and then a larger uniform disk is found in the $H\alpha$ -band.

et al. (2012) and Cochetti et al. (2019), and they determined these parameters as follows: $i = 45 \pm 5^\circ$, disk $PA = 88 \pm 2^\circ$, and $a_{\text{line}}(\text{Br}\gamma) = 5.8 \pm 0.5 D_\star$. Then our results presented here for the inclination angle and the disk position angle seems to be in line with the values derived these authors.

From Fig. 7.11, we note that the disk extension seems to be substantially larger about 1.4 time) in $\text{Br}\alpha$ than in $\text{Br}\gamma$. A deeper analysis is needed due to the preliminary status of our results, but this could result from a possible larger flux contribution of α Arae’s disk in the mid-infrared, when compared with shorter wavelengths, and it shows the current importance of investigating Be disks at different spectral bands.

7.2.4 Toward a detailed view on Be stars (other than *o* Aquarii)

Lastly, besides the large spectro-interferometric programs of Be stars described above, our modeling approach in Paper III is very useful to provide a more robust analysis of specific objects, as for the case of *o* Aquarii.

In the following, we present a non-extensive list of old and new data of Be stars that have been currently investigated by our group and collaborators:

- (i) Published VEGA and MIRC data of ϕ Persei by Mourard et al. (2015). In spite of using image reconstruction models and the kinematic code, it still lacks an interpretation of their data with physical models, and this can be done using the BeAtlas grid.

- (ii) New 2016 VEGA and FRIEND data of γ Cassiopeiae observed in four-telescope configuration.
- (iii) VEGA imaging program on κ Draconis (PI: A. Meilland; 2015-2019). This program was finished and the analysis is going-on. Fig. 7.12 shows the geometric modeling of the calibrated VEGA data in two different bands: continuum band (close to $H\alpha$) and $H\alpha$ -band.
- (iv) VEGA imaging program on β Canis Majoris (PI: R. Klement; 2017-present). This program is close to be finished. β Canis Majoris is known to have a stable disk and was recently investigated in details by Klement et al. (2015) with multi-instrument spectroscopic and interferometric data, interpreted using the code HDUST, and it shows evidences of a truncated disk by an unseen binary companion.

Chapter 8

Conclusions and perspectives

The objective of this thesis was to study the mechanisms of mass loss in different types of massive hot stars. In addition to the own physical properties of their environments (e.g., the mass-loss rate and the density law profile), this task demands a detailed analysis of their photospheric parameters, such as the effective temperature and rotational rates, as performed in this thesis.

This means that we investigated both the less massive hot stars showing relevant extended atmospheres (as the Be stars), for which the stellar rotation is understood to be (at least partially) a key mechanism to form their circumstellar disks, as well as the more massive hot stars (as the O and LBV stars), which show larger lost material from their surfaces through strong radiative line-driven winds arising from their very high luminosities and effective temperatures.

For this purpose, we combined different observational methods, mainly focusing on interferometry and spectroscopy at different wavelength regions (UV, visible, and infrared). In Paper I, spectroscopic data taken with multiple instruments was used to constrain the photospheric and wind parameters of a small sample of late-type O giants in the Galaxy. In Paper II, the LBV star P Cygni was studied using H α intensity interferometry. Finally, Paper III studied quasi-simultaneous spectro-interferometric observations of the Be star *σ Aquarii* in the visible (CHARA/VEGA) and in the near-infrared (VLTI/AMBER).

Besides the particular modeling methods used in each one of these studies, such as the multi-tool approach by Paper III, non-LTE radiative transfer models are key among all of them: CMFGEN (Papers I and II), one of the state-of-the-art codes for hot stars with intense radiative line-driven winds, and HDUST that is well-suited for hot stars with highly asymmetrical environments as in Be stars (Paper III). Our studies evidence the success of these forefront codes to model different types of observables in hot stars: photometry, polarimetry, spectroscopy, and interferometry.

Based on different observational methods and spectral bands, we were then able to

draw a unified picture of the physical conditions on the surface and environments of massive stars using these codes. Apart of constraining their fundamental parameters, radiative transfer modeling of interferometry can also be explored to constrain other quantities of interest, as shown by Paper II, allowing us to estimate distances to these stars in an independent way to other methods.

We tried hard to completely conciliate the UV and H α mass-loss rates of O giant stars, but it was not possible for all the stars of our sample. Nevertheless, we clearly showed that the theoretical mass-loss rates for the most part of our sample fail to match simultaneously the observed UV and visible spectra, and this departure is much more explicit than in the case of late O dwarfs.

We showed for first time that more evolved massive stars, late O giants, present the weak wind phenomenon (originally found in late O dwarfs). Our derived mass-loss rates are much lower (by up to 10^2) than the values found by theoretical studies. The luminosity region around $\log(L_\star/L_\odot) \sim 5.2$ is indeed critical for the onset of weak winds in O stars.

In short, our study suggests that weak winds are unlikely linked to evolutionary effects in O stars, and weak winds should occur along the H-burning phase of less luminous O stars ($\log(L_\star/L_\odot) \lesssim 5.2$). This means that the majority of state-of-the-art stellar evolution models are taking severely overestimated mass-loss rates into account for these stars. Further investigations should evaluate the impact of weak winds on their physical properties, probably affecting their rotation and surface chemistry during their evolutionary stages.

To date, our interferometric study on *o* Aquarii allowed us to draw one of the most complete pictures of a Be star and its disk both in the visible and the near-infrared. From that, we were able to precisely constrain both the central star and disk parameters of *o* Aquarii. We showed that its disk extension is quite similar in both H α and Br γ . Such a quite uncommon feature for Be disks could be explained in terms of an opacity effect in these lines for Be stars seen under high inclination angles, and it deserves further investigations. We showed that the disk density is well-described by a common physical model, that is, the same values for the disk density parameters in the H α and Br γ lines, and this result is linked to the similar disk extension found at these lines.

We found that *o* Aquarii has a stable disk over a very long period: combined to older literature studies, our results suggest a global disk stability for up to at least 40 years. Such a long-term disk stability can be interpreted in terms of our results showing that *o* Aquarii has a rotational rate very close to the break-up limit. This means that the rotational rate could be a main source of mass injection in the disk of *o* Aquarii.

Despite being a result for an individual star, it matches well the more recently suggested picture of the Be phenomenon that late-type Be stars, such as *o* Aquarii, are

more likely to have a quasi-critical rotation and long-term stable disks, when compared with the earlier Be stars. In comparison with the later Be stars, early-type Be stars present a more relevant contribution from the radiative force to break the hydrostatic equilibrium at the photosphere, and then the rotational rate should be less important for the process of mass loss in more massive Be stars.

In short, *o* Aquarii fits in the global scheme of Be stars and their circumstellar disk, that is, a Keplerian rotating disk well described by the VDD model when looking at the Br γ emission line. However, the determination of the disk kinematics seems to be significantly biased when looking at H α , apart from our efforts to conciliate our picture of its kinematics at these lines simultaneously. As indicated by some previous studies on Be stars, this bias could arise due to a higher effect of non-coherent scattering on the H α line formation than in Br γ .

The findings of this thesis clarified some issues regarding the environments of massive hot stars, but, of course, future investigations are needed to constrain their fundamental parameters. The results found for the mass-loss rates of line-driven winds in massive stars diverge, when looking to their winds at several spectral bands (X-ray, UV, visible, and infrared regions). Furthermore, it is still not firmly understood how the stellar properties of Be stars, such as the effective temperature and the rotational rate, correlate among themselves, and consequently are linked to the formation of the envelopes in these stars. Chap. 7 presented my ongoing and near-future studies on some of these open issues: it clearly shows the current need to continue to study both winds and disks of massive hot stars at different spectral regions.

Finally, the infrared region should be more explored to constrain the fundamental parameters of the environments of these stars: the spectral lines in this region are less investigated when compared with more traditional wind diagnostics, as H α , in the visible (e.g., Lenorzer et al. 2004; Najarro et al. 2011; Marcolino et al. 2017). A quantitative spectroscopic analysis of a significant sample of O stars simultaneously in the UV, visible, near- and mid-infrared regions is still missing. As pointed out by Najarro et al. (2011), together with other lines in the L-band, as Pf γ (3.731 μm), the Br α (4.051 μm) line is very sensitive to the wind mass-loss rate of massive stars. In particular, Br α seems to be a very promising mass loss diagnostic for low-density winds. Then Br α is an interesting diagnostic to probe the weak wind phenomenon in the infrared region. Despite being more suited for studying dusty environments, the VLTI/MATISSE spectro-interferometric instrument (operating at the L-, M-, and N-bands) just have started to investigate at these lines the morphology and physical conditions of the environments around Be, O, and B supergiant stars. Moreover, in the following years, the instruments at the James Webb Space Telescope will allow us to investigate their physical properties by means of spectroscopy at even longer

wavelengths up to $\sim 30 \mu\text{m}$.

Bibliography

- Abbott, B. P., Abbott, R., Abbott, T. D., et al. 2016, *ApJ*, 818, L22
- Abbott, D. C. 1979, in *IAU Symposium*, Vol. 83, *Mass Loss and Evolution of O-Type Stars*, ed. P. S. Conti & C. W. H. De Loore, 237–239
- Abbott, D. C. 1982a, *ApJ*, 263, 723
- Abbott, D. C. 1982b, *ApJ*, 259, 282
- Abramowitz M., S. I. e. 1972, *Handbook of mathematical functions*, 10th edn. (US Dept. of Commerce)
- Abt, H. A., Meinel, A. B., Morgan W. W., & Tapscott I. W. 1968, *An Atlas of low-dispersion grating stellar spectra*
- Adam, C. & Ohnaka, K. 2019, *A&A*, 628, A132
- Alencar, S. H. P. & Basri, G. 2000, *AJ*, 119, 1881
- Allard, F. & Hauschildt, P. H. 1995, *ApJ*, 445, 433
- Amarsi, A. M., Grevesse, N., Grumer, J., et al. 2020, *The 3D non-LTE solar nitrogen abundance from atomic lines*
- Anugu, N., Le Bouquin, J.-B., Monnier, J. D., et al. 2018, in *Society of Photo-Optical Instrumentation Engineers (SPIE) Conference Series*, Vol. 10701, *Proc. SPIE*, 1070124
- Arcos, C., Jones, C. E., Sigut, T. A. A., Kanaan, S., & Curé, M. 2017, *ApJ*, 842, 48
- Arcos, C., Kanaan, S., Chávez, J., et al. 2018, *MNRAS*, 474, 5287
- Austin, M. J. 2011, PhD thesis, University of London, University College London (United Kingdom)
- Baade, D., Rivinius, T., Pigulski, A., et al. 2016, *A&A*, 588, A56

BIBLIOGRAPHY

- Babel, J. 1995, *A&A*, 301, 823
- Babel, J. 1996, *A&A*, 309, 867
- Bagnulo, S., Landstreet, J. D., Fossati, L., & Kochukhov, O. 2012, *A&A*, 538, A129
- Balbus, S. A. 2003, *ARA&A*, 41, 555
- Beals, C. S. 1929, *MNRAS*, 90, 202
- Beals, C. S. 1930, *Publications of the Dominion Astrophysical Observatory Victoria*, 4, 271
- Beals, C. S. 1932, *MNRAS*, 92, 677
- Beals, C. S. 1935, *MNRAS*, 95, 580
- Beals, C. S. 1953, *Publications of the Dominion Astrophysical Observatory Victoria*, 9, 1
- Beckers, J. M. 1993, *ARA&A*, 31, 13
- Berger, J.-P. 2003, *EAS Publications Series*, 6, 23
- Beuzit, J. L., Vigan, A., Mouillet, D., et al. 2019, *A&A*, 631, A155
- Bianchi, L. & Garcia, M. 2002, *ApJ*, 581, 610
- Bjorkman, J. E. & Carciofi, A. C. 2005, in *Astronomical Society of the Pacific Conference Series*, Vol. 337, *The Nature and Evolution of Disks Around Hot Stars*, ed. R. Ignace & K. G. Gayley, 75
- Bjorkman, J. E. & Cassinelli, J. P. 1993, *ApJ*, 409, 429
- Blaauw, A. 1991, *Journal for the History of Astronomy*, 22, 87
- Bode, M. F. & Evans, A. 2008, *Classical Novae*, Vol. 43
- Bodensteiner, J., Sana, H., Mahy, L., et al. 2020, *A&A*, 634, A51
- Bohlender, D. 2016, in *Astronomical Society of the Pacific Conference Series*, Vol. 506, *Bright Emissaries: Be Stars as Messengers of Star-Disk Physics*, ed. T. A. A. Sigut & C. E. Jones, 275
- Böhm-Vitense, E. 1989, *Introduction to stellar astrophysics*. Vol. 2. *Stellar atmospheres.*, Vol. 2

BIBLIOGRAPHY

- Bouchaud, K., Domiciano de Souza, A., Rieutord, M., Reese, D. R., & Kervella, P. 2020, *A&A*, 633, A78
- Bouret, J.-C., Hillier, D. J., Lanz, T., & Fullerton, A. W. 2012, *A&A*, 544, A67
- Bouret, J.-C., Lanz, T., & Hillier, D. J. 2005, *A&A*, 438, 301
- Bouret, J.-C., Lanz, T., Hillier, D. J., et al. 2003, *ApJ*, 595, 1182
- Bouret, J. C., Lanz, T., Hillier, D. J., et al. 2015, *MNRAS*, 449, 1545
- Bouret, J.-C., Lanz, T., Martins, F., et al. 2013, *A&A*, 555, A1
- Bourges, L., Mella, G., Lafrasse, S., et al. 2017, *VizieR Online Data Catalog*, II/346
- Bowen, G. H. & Willson, L. A. 1991, *ApJ*, 375, L53
- Brott, I., de Mink, S. E., Cantiello, M., et al. 2011, *A&A*, 530, A115
- Brown, R. H. & Twiss, R. Q. 1956, *Nature*, 177, 27
- Burbidge, E. M. & Burbidge, G. R. 1955, *ApJ*, 122, 89
- Busche, J. R. & Hillier, D. J. 2005, *AJ*, 129, 454
- Carciofi, A. C. 2011, in *IAU Symposium*, Vol. 272, *Active OB Stars: Structure, Evolution, Mass Loss, and Critical Limits*, ed. C. Neiner, G. Wade, G. Meynet, & G. Peters, 325–336
- Carciofi, A. C. & Bjorkman, J. E. 2006, *The Astrophysical Journal*, 639, 1081
- Carciofi, A. C. & Bjorkman, J. E. 2008, *ApJ*, 684, 1374
- Carciofi, A. C., Bjorkman, J. E., & Magalhães, A. M. 2004, *ApJ*, 604, 238
- Carciofi, A. C., Bjorkman, J. E., & Zsargó, J. 2017, in *IAU Symposium*, Vol. 329, *The Lives and Death-Throes of Massive Stars*, ed. J. J. Eldridge, J. C. Bray, L. A. S. McClelland, & L. Xiao, 390–390
- Carciofi, A. C., Miroshnichenko, A. S., & Bjorkman, J. E. 2010, *ApJ*, 721, 1079
- Cassinelli, J. P., Brown, J. C., Maheswaran, M., Miller, N. A., & Telfer, D. C. 2002, *ApJ*, 578, 951
- Cassinelli, J. P. & Lamers, H. J. G. L. M. 1987, in *Astrophysics and Space Science Library*, Vol. 129, *Exploring the Universe with the IUE Satellite*, ed. Y. Kondo & W. Wamsteker, 139

BIBLIOGRAPHY

- Cassinelli, J. P. & Olson, G. L. 1979, *ApJ*, 229, 304
- Castor, J. I. 1993, in *Astronomical Society of the Pacific Conference Series*, Vol. 35, *Massive Stars: Their Lives in the Interstellar Medium*, ed. J. P. Cassinelli & E. B. Churchwell, 297–306
- Castor, J. I., Abbott, D. C., & Klein, R. I. 1975, *ApJ*, 195, 157
- Cauley, P. W. & Johns-Krull, C. M. 2014, *ApJ*, 797, 112
- Cerruti-Sola, M. & Perinotto, M. 1985, *ApJ*, 291, 237
- Chené, A.-N., Schnurr, O., Crowther, P. A., Fernández-Lajús, E., & Moffat, A. F. J. 2011, in *IAU Symposium*, Vol. 272, *Active OB Stars: Structure, Evolution, Mass Loss, and Critical Limits*, ed. C. Neiner, G. Wade, G. Meynet, & G. Peters, 497–498
- Chesneau, O., Dessart, L., Mourard, D., et al. 2010, *A&A*, 521, A5
- Chesneau, O., Kaufer, A., Stahl, O., et al. 2014, *A&A*, 566, A125
- Chesneau, O., Lagadec, E., Otulakowska-Hypka, M., et al. 2012, *A&A*, 545, A63
- Chesneau, O., Meilland, A., Banerjee, D. P. K., et al. 2011, *A&A*, 534, L11
- Chesneau, O., Nardetto, N., Millour, F., et al. 2007, *A&A*, 464, 119
- Chesneau, O., Roche, M., Boccaletti, A., et al. 2000, *A&AS*, 144, 523
- Clark, J. S., Tarasov, A. E., & Panko, E. A. 2003, *A&A*, 403, 239
- Cochetti, Y. R., Arcos, C., Kanaan, S., et al. 2019, *A&A*, 621, A123
- Code, A. D., Bless, R. C., Davis, J., & Brown, R. H. 1976, *ApJ*, 203, 417
- Cohen, D. H., Wollman, E. E., Leutenegger, M. A., et al. 2014, *MNRAS*, 439, 908
- Conti, P. S. 1975, *Memoires of the Societe Royale des Sciences de Liege*, 9, 193
- Conti, P. S. & Alschuler, W. R. 1971, *ApJ*, 170, 325
- Conti, P. S. & Massey, P. 1989, *ApJ*, 337, 251
- Correia Mota, B. 2019, PhD thesis, Universidade de São Paulo
- Cote, J. & Waters, L. B. F. M. 1987, *A&A*, 176, 93

BIBLIOGRAPHY

- Coudé du Foresto, V., Borde, P. J., Merand, A., et al. 2003, in Society of Photo-Optical Instrumentation Engineers (SPIE) Conference Series, Vol. 4838, Proc. SPIE, ed. W. A. Traub, 280–285
- Cox, A. N., Guzik, J. A., Soukup, M. S., & Despain, K. M. 1998, Astronomical Society of the Pacific Conference Series, Vol. 135, Pulsations and Outbursts of Luminous Blue Variables, ed. P. A. Bradley & J. A. Guzik, 302
- Coyne, G. V. 1976, in IAU Symposium, Vol. 70, Be and Shell Stars, ed. A. Slettebak, 233
- Cranmer, S. R. 2005, *ApJ*, 634, 585
- Crivellari, L., Simón-Díaz, S., & Arévalo, M. 2019, Radiative Transfer in Stellar and Planetary Atmospheres, Canary Islands Winter School of Astrophysics (Cambridge University Press)
- Crowther, P. A. 2007, *ARA&A*, 45, 177
- Crowther, P. A., Lennon, D. J., & Walborn, N. R. 2006, *A&A*, 446, 279
- Crowther, P. A., Schnurr, O., Hirschi, R., et al. 2010, *MNRAS*, 408, 731
- Cummings, J. D., Kalirai, J. S., Tremblay, P. E., & Ramirez-Ruiz, E. 2016, *ApJ*, 818, 84
- Curé, M., Cidale, L., & Granada, A. 2011, *ApJ*, 737, 18
- Curé, M. & Rial, D. F. 2004, *A&A*, 428, 545
- Cyr, I. H., Jones, C. E., Panoglou, D., Carciofi, A. C., & Okazaki, A. T. 2017, *MNRAS*, 471, 596
- da G. de Almeida, E. S., Marcolino, W. L. F., & Pereira, C. B. 2017, in Revista Mexicana de Astronomia y Astrofisica Conference Series, Vol. 49, Revista Mexicana de Astronomia y Astrofisica Conference Series, 82–82
- Dachs, J., Hanuschik, R., Kaiser, D., et al. 1986, *A&AS*, 63, 87
- Dalla Vedova, G., Millour, F., Domiciano de Souza, A., et al. 2017, *A&A*, 601, A118
- Davies, R. & Kasper, M. 2012, *ARA&A*, 50, 305
- Davis, J., Morton, D. C., Allen, L. R., & Hanbury Brown, R. 1970, *MNRAS*, 150, 45

BIBLIOGRAPHY

- de Almeida, E. S. G. 2016, Master's thesis, Observatório do Valongo – Universidade Federal do Rio de Janeiro
- de Almeida, E. S. G., Marcolino, W. L. F., Bouret, J. C., & Pereira, C. B. 2019, *A&A*, 628, A36
- de Almeida, E. S. G., Meilland, A., Domiciano de Souza, A., et al. 2020, *A&A*, 636, A110
- de Groot, M. J. H. & Lamers, H. J. G. L. M. 1992, *Nature*, 355, 422
- de Jager, C., Nieuwenhuijzen, H., & van der Hucht, K. A. 1988, *A&AS*, 72, 259
- de Mink, S. E., Sana, H., Langer, N., Izzard, R. G., & Schneider, F. R. N. 2014, *ApJ*, 782, 7
- Decin, L., Hony, S., de Koter, A., et al. 2006, *A&A*, 456, 549
- Delaa, O., Stee, P., Meilland, A., et al. 2011, *A&A*, 529, A87
- Deleuil, M., Lecavelier des Etangs, A., Bouret, J. C., et al. 2004, *A&A*, 418, 577
- Dessart, L., Crowther, P. A., Hillier, D. J., et al. 2000, *MNRAS*, 315, 407
- Dessart, L., Hillier, D. J., Audit, E., Livne, E., & Waldman, R. 2016, *MNRAS*, 458, 2094
- Domiciano de Souza, A., Borges Fernandes, M., Carciofi, A. C., & Chesneau, O. 2015, in *IAU Symposium*, Vol. 307, *New Windows on Massive Stars*, ed. G. Meynet, C. Georgy, J. Groh, & P. Stee, 291–292
- Domiciano de Souza, A., Bouchaud, K., Rieutord, M., Espinosa Lara, F., & Putigny, B. 2018, *A&A*, 619, A167
- Domiciano de Souza, A., Driebe, T., Chesneau, O., et al. 2007, *A&A*, 464, 81
- Domiciano de Souza, A., Hadjara, M., Vakili, F., et al. 2012, *A&A*, 545, A130
- Domiciano de Souza, A., Kervella, P., Jankov, S., et al. 2003, *A&A*, 407, L47
- Domiciano de Souza, A., Kervella, P., Jankov, S., et al. 2005, *A&A*, 442, 567
- Domiciano de Souza, A., Kervella, P., Moser Faes, D., et al. 2014, *A&A*, 569, A10
- Domiciano de Souza, A., Vakili, F., Jankov, S., Janot-Pacheco, E., & Abe, L. 2002, *A&A*, 393, 345

BIBLIOGRAPHY

- Domiciano de Souza, A., Zorec, J., Jankov, S., et al. 2004, *A&A*, 418, 781
- Doran, E. I., Crowther, P. A., de Koter, A., et al. 2013, *A&A*, 558, A134
- Eddington, A. S. 1925, *The Observatory*, 48, 73
- Eddington, A. S. 1926, *The Internal Constitution of the Stars*
- Ekström, S., Georgy, C., Eggenberger, P., et al. 2012, *A&A*, 537, A146
- Ekström, S., Georgy, C., Meynet, G., Groh, J., & Granada, A. 2013, in *EAS Publications Series*, Vol. 60, *EAS Publications Series*, ed. P. Kervella, T. Le Bertre, & G. Perrin, 31–41
- Ekström, S., Meynet, G., Maeder, A., & Barblan, F. 2008, *A&A*, 478, 467
- El Eid, M. F. & Hartmann, D. H. 1993, *ApJ*, 404, 271
- Espinosa Lara, F. & Rieutord, M. 2011, *A&A*, 533, A43
- Eversberg, T., Lépine, S., & Moffat, A. F. J. 1998, *ApJ*, 494, 799
- Faes, D. M. 2015, PhD thesis, IAG-Universidade de Sao Paulo (Brazil), Lagrange-Université de Nice (France)
- Feigelson, E. D. & Babu, G. J. 2012, *Modern Statistical Methods for Astronomy*
- Fierro, C. R., Borissova, J., Zsargó, J., et al. 2015, *PASP*, 127, 428
- Figer, D. F., McLean, I. S., & Najarro, F. 1997, *ApJ*, 486, 420
- Foreman-Mackey, D., Hogg, D. W., Lang, D., & Goodman, J. 2013, *PASP*, 125, 306
- Frémat, Y., Zorec, J., Hubert, A. M., & Floquet, M. 2005, *A&A*, 440, 305
- Gaia Collaboration, Brown, A. G. A., Vallenari, A., et al. 2018, *A&A*, 616, A1
- Gall, C., Andersen, A. C., & Hjorth, J. 2011a, *Astronomy and Astrophysics*, 528, A13
- Gall, C., Hjorth, J., & Andersen, A. C. 2011b, *A&A Rev.*, 19, 43
- Garmany, C. D., Conti, P. S., & Chiosi, C. 1982, *ApJ*, 263, 777
- Gehrels, N. & Razzaque, S. 2013, *Frontiers of Physics*, 8, 661
- Gehrz, R. D., Hackwell, J. A., & Jones, T. W. 1974, *ApJ*, 191, 675

BIBLIOGRAPHY

- Gies, D. R., Bagnuolo, W. G., J., Baines, E. K., et al. 2007, *The Astrophysical Journal*, 654, 527
- Glindemann, A., Bauvir, B., Van Boekel, R., et al. 2002, in *Scientific Drivers for ESO Future VLT/VLTI Instrumentation*, ed. J. Bergeron & G. Monnet, 279
- Golden-Marx, J. B., Oey, M. S., Lamb, J. B., Graus, A. S., & White, A. S. 2016, *ApJ*, 819, 55
- Goodman, J. & Weare, J. 2010, *Communications in Applied Mathematics and Computational Science*, Vol. 5, No. 1, p. 65-80, 2010, 5, 65
- Gräfener, G., Koesterke, L., & Hamann, W. R. 2002, *A&A*, 387, 244
- Granada, A., Ekström, S., Georgy, C., et al. 2013, *A&A*, 553, A25
- Gravity Collaboration, Abuter, R., Accardo, M., et al. 2017, *A&A*, 602, A94
- Gravity Collaboration, Sanchez-Bermudez, J., Weigelt, G., et al. 2018, *A&A*, 618, A125
- Gray, R. O. & Corbally, J., C. 2009, *Stellar Spectral Classification*
- Grevesse, N., Asplund, M., Sauval, A. J., & Scott, P. 2010, *Ap&SS*, 328, 179
- Grevesse, N., Asplund, M., Sauval, A. J., & Scott, P. 2012, *Astronomical Society of the Pacific Conference Series*, Vol. 462, *The New Solar Chemical Composition — from $Z = 0.02$ to $Z = 0.013$* , ed. H. Shibahashi, M. Takata, & A. E. Lynas-Gray, 41
- Groh, J. H. 2011, in *Journal of Physics Conference Series*, Vol. 328, *Journal of Physics Conference Series*, 012020
- Groh, J. H., Meynet, G., Ekström, S., & Georgy, C. 2014, *A&A*, 564, A30
- Guerin, W., Dussaux, A., Fouché, M., et al. 2017, *MNRAS*, 472, 4126
- Guerin, W., Rivet, J. P., Fouché, M., et al. 2018, *MNRAS*, 480, 245
- Guzik, J. A., Cox, A. N., Despain, K. M., & Soukup, M. S. 1997, *Astronomical Society of the Pacific Conference Series*, Vol. 120, *A Nonlinear Study of LBVs and Possible Outbursts*, ed. A. Nota & H. Lamers, 138
- Hadjara, M. 2017, arXiv e-prints, arXiv:1709.07334
- Hadjara, M., Cruzalèbes, P., Nitschelm, C., et al. 2019, *MNRAS*, 489, 2595
- Hadjara, M., Petrov, R. G., Jankov, S., et al. 2018, *MNRAS*, 480, 1263

BIBLIOGRAPHY

- Halonen, R. J., Jones, C. E., & Sigut, T. A. A. 2010, in *Revista Mexicana de Astronomia y Astrofisica Conference Series*, Vol. 38, *Revista Mexicana de Astronomia y Astrofisica Conference Series*, 85–86
- Hamann, W. R. 1985, *A&A*, 148, 364
- Hamann, W. R. 1986, *A&A*, 160, 347
- Hamann, W. R. & Gräfener, G. 2003, *A&A*, 410, 993
- Hamann, W.-R., Oskinova, L. M., & Feldmeier, A. 2008, in *Clumping in Hot-Star Winds*, ed. W.-R. Hamann, A. Feldmeier, & L. M. Oskinova, 75
- Hanbury Brown, R. 1956, *Nature*, 178, 1046
- Hanbury Brown, R., Davis, J., & Allen, L. R. 1967a, *MNRAS*, 137, 375
- Hanbury Brown, R., Davis, J., & Allen, L. R. 1974, *MNRAS*, 167, 121
- Hanbury Brown, R., Davis, J., Allen, L. R., & Rome, J. M. 1967b, *MNRAS*, 137, 393
- Hanbury Brown, R., Davis, J., Herbison-Evans, D., & Allen, L. R. 1970, *MNRAS*, 148, 103
- Hanuschik, R. W. 1995, *A&A*, 295, 423
- Hastings, B., Wang, C., & Langer, N. 2020, *A&A*, 633, A165
- Haubois, X., Carciofi, A. C., Rivinius, T., Okazaki, A. T., & Bjorkman, J. E. 2012, *ApJ*, 756, 156
- Haucke, M., Cidale, L. S., Venero, R. O. J., et al. 2018, *A&A*, 614, A91
- Heck, A. 1987, in *Astrophysics and Space Science Library*, Vol. 129, *Exploring the Universe with the IUE Satellite*, ed. Y. Kondo & W. Wamsteker, 121
- Heger, A., Fryer, C. L., Woosley, S. E., Langer, N., & Hartmann, D. H. 2003, *ApJ*, 591, 288
- Henrichs, H. F., Hammerschlag-Hensberge, G., Howarth, I. D., & Barr, P. 1983, *ApJ*, 268, 807
- Herald, J. E. & Bianchi, L. 2011, *MNRAS*, 417, 2440
- Herwig, F. 2005, *ARA&A*, 43, 435

BIBLIOGRAPHY

- Hillier, D. J. 2012, in IAU Symposium, Vol. 282, From Interacting Binaries to Exoplanets: Essential Modeling Tools, ed. M. T. Richards & I. Hubeny, 229–234
- Hillier, D. J. 2020, *Galaxies*, 8, 60
- Hillier, D. J., Davidson, K., Ishibashi, K., & Gull, T. 2001, *ApJ*, 553, 837
- Hillier, D. J., Lanz, T., Heap, S. R., et al. 2003, *ApJ*, 588, 1039
- Hillier, D. J. & Miller, D. L. 1998, *ApJ*, 496, 407
- Hillier, D. J. & Miller, D. L. 1999, *ApJ*, 519, 354
- Hirata, R. 2007, in *Astronomical Society of the Pacific Conference Series*, Vol. 361, Active OB-Stars: Laboratories for Stellar and Circumstellar Physics, ed. A. T. Okazaki, S. P. Owocki, & S. Stefl, 267
- Höfner, S. & Andersen, A. C. 2007, *A&A*, 465, L39
- Höfner, S. & Olofsson, H. 2018, *A&A Rev.*, 26, 1
- Holgado, G., Simón-Díaz, S., Barbá, R. H., et al. 2018, *A&A*, 613, A65
- Holweger, H. 1967, *ZAp*, 65, 365
- Howarth, I. D. & Prinja, R. K. 1989, *ApJS*, 69, 527
- Huang, W., Gies, D. R., & McSwain, M. V. 2010, *ApJ*, 722, 605
- Hubeny, I. & Lanz, T. 1995, *ApJ*, 439, 875
- Huenemoerder, D. P., Oskinova, L. M., Ignace, R., et al. 2012, *ApJ*, 756, L34
- Hummel, W. & Dachs, J. 1992, *A&A*, 262, L17
- Hummel, W. & Vrancken, M. 2000, *Astronomy and Astrophysics*, 359, 1075
- Humphreys, R. M. 2003, in IAU Symposium, Vol. 212, A Massive Star Odyssey: From Main Sequence to Supernova, ed. K. van der Hucht, A. Herrero, & C. Esteban, 38
- Humphreys, R. M. & Davidson, K. 1994, *PASP*, 106, 1025
- Humphreys, R. M., Gordon, M. S., Martin, J. C., Weis, K., & Hahn, D. 2017, *ApJ*, 836, 64
- Ireland, M. J., Mérand, A., ten Brummelaar, T. A., et al. 2008, in *Society of Photo-Optical Instrumentation Engineers (SPIE) Conference Series*, Vol. 7013, Proc. SPIE, 701324

BIBLIOGRAPHY

- Israelian, G. & de Groot, M. 1999, *Space Sci. Rev.*, 90, 493
- Jamialahmadi, N., Berio, P., Meilland, A., et al. 2015, *A&A*, 579, A81
- Johnson, H. L. & Morgan, W. W. 1953, *ApJ*, 117, 313
- Jones, C. E., Tycner, C., & Smith, A. D. 2011, *AJ*, 141, 150
- Jones, S., Hirschi, R., Nomoto, K., et al. 2013, *ApJ*, 772, 150
- Kaufer, A., Stahl, O., Wolf, B., et al. 1997, *A&A*, 320, 273
- Kaufer, A., Stahl, O., Wolf, B., et al. 1996, *A&A*, 314, 599
- Keenan, P. C. 1971, *Contributions from the Kitt Peak National Observatory*, 554, 35
- Keenan, P. C. 1973, in *IAU Symposium, Vol. 54, Problems of Calibration of Absolute Magnitudes and Temperature of Stars*, ed. B. Hauck & B. E. Westerlund, 68
- Keller, G. R., Herald, J. E., Bianchi, L., Maciel, W. J., & Bohlin, R. C. 2011, *MNRAS*, 418, 705
- Kervella, P. 2007, *A&A*, 464, 1045
- Kervella, P., Coudé du Foresto, V., Glindemann, A., & Hofmann, R. 2000, in *Society of Photo-Optical Instrumentation Engineers (SPIE) Conference Series, Vol. 4006, Proc. SPIE*, ed. P. Léna & A. Quirrenbach, 31–42
- Kervella, P., Montargès, M., Lagadec, E., et al. 2015, *A&A*, 578, A77
- Khouri, T., Maercker, M., Waters, L. B. F. M., et al. 2016, *A&A*, 591, A70
- Kilian, J., Becker, S. R., Gehren, T., & Nissen, P. E. 1991a, *A&A*, 244, 419
- Kilian, J., Montenbruck, O., & Nissen, P. E. 1991b, *A&AS*, 88, 101
- Kirkpatrick, J. D. 2005, *ARA&A*, 43, 195
- Klement, R., Carciofi, A. C., Rivinius, T., et al. 2019, *ApJ*, 885, 147
- Klement, R., Carciofi, A. C., Rivinius, T., et al. 2015, *A&A*, 584, A85
- Koechlin, L., Bonneau, D., & Vakili, F. 1979, *A&A*, 80, L13
- Koutoulaki, M., Garcia Lopez, R., Natta, A., et al. 2018, *A&A*, 614, A90
- Kraus, M., Haucke, M., Cidale, L. S., et al. 2015, *A&A*, 581, A75

BIBLIOGRAPHY

- Krtička, J. 2014, *A&A*, 564, A70
- Krtička, J., Owocki, S. P., & Meynet, G. 2011, *A&A*, 527, A84
- Kudritzki, R. P. 2002, *ApJ*, 577, 389
- Kudritzki, R.-P., Lennon, D. J., & Puls, J. 1995, in *Science with the VLT*, ed. J. R. Walsh & I. J. Danziger, 246
- Kudritzki, R. P., Puls, J., Lennon, D. J., et al. 1999, *A&A*, 350, 970
- Kurucz, R. L. 1991, in *NATO Advanced Science Institutes (ASI) Series C, Vol. 341*, *NATO Advanced Science Institutes (ASI) Series C*, ed. L. Crivellari, I. Hubeny, & D. G. Hummer, 441
- Kurucz, R. L. 2005, *Memorie della Societa Astronomica Italiana Supplementi*, 8, 189
- Labeyrie, A. 1975, *ApJ*, 196, L71
- Labeyrie, A., Lipson, S. G., & Nisenson, P. 2006, *An Introduction to Optical Stellar Interferometry* (Cambridge University Press)
- Lai, O., Guerin, W., Vakili, F., et al. 2018, in *Society of Photo-Optical Instrumentation Engineers (SPIE) Conference Series*, Vol. 10701, *Proc. SPIE*, 1070121
- Lamers, H. J. G. L. M. 1995, *Astronomical Society of the Pacific Conference Series*, Vol. 83, *Observations and Interpretation of Luminous Blue Variables*, ed. R. S. Stobie & P. A. Whitelock, 176
- Lamers, H. J. G. L. M. & Cassinelli, J. P. 1999, *Introduction to Stellar Winds*
- Lamers, H. J. G. L. M., de Groot, M., & Cassatella, A. 1983, *A&A*, 128, 299
- Lamers, H. J. G. L. M., Haser, S., de Koter, A., & Leitherer, C. 1999, *ApJ*, 516, 872
- Lamers, H. J. G. L. M., Zickgraf, F.-J., de Winter, D., Houziaux, L., & Zorec, J. 1998, *A&A*, 340, 117
- Lanz, T. & Hubeny, I. 2003, *ApJS*, 146, 417
- Lanz, T. & Hubeny, I. 2007, *ApJS*, 169, 83
- Lapeyrere, V., Kervella, P., Lacour, S., et al. 2014, *Society of Photo-Optical Instrumentation Engineers (SPIE) Conference Series*, Vol. 9146, *GRAVITY data reduction software*, 91462D

BIBLIOGRAPHY

- Lawson, P. R. 2000, in *Principles of Long Baseline Stellar Interferometry*, ed. P. R. Lawson, 325
- Le Bouquin, J. B., Berger, J. P., Lazareff, B., et al. 2011, *A&A*, 535, A67
- Lee, U., Osaki, Y., & Saio, H. 1991, *MNRAS*, 250, 432
- Léna, P. 2014, in *EAS Publications Series*, Vol. 69-70, 3–13
- Lenorzer, A., Mokiem, M. R., de Koter, A., & Puls, J. 2004, *A&A*, 422, 275
- Lépine, S. & Moffat, A. F. J. 2008, *AJ*, 136, 548
- Levesque, E. M., Massey, P., Olsen, K. A. G., et al. 2005, *ApJ*, 628, 973
- Li, G.-W., Shi, J.-R., Yanny, B., et al. 2018, *ApJ*, 863, 70
- Lopez, B., Lagarde, S., Jaffe, W., et al. 2014, *The Messenger*, 157, 5
- Lucy, L. B. 1967, *ZAp*, 65, 89
- Lucy, L. B. 2002, *A&A*, 384, 725
- Lucy, L. B. 2003, *A&A*, 403, 261
- Lucy, L. B. 2005, *A&A*, 429, 19
- Lucy, L. B. 2007, *A&A*, 468, 649
- Lucy, L. B. 2010a, *A&A*, 524, A41
- Lucy, L. B. 2010b, *A&A*, 512, A33
- Lucy, L. B. 2012, *A&A*, 543, A18
- Lucy, L. B. & Solomon, P. M. 1970, *ApJ*, 159, 879
- Maeder, A. 1992, *Astronomy and Astrophysics*, 264, 105
- Maeder, A. 2009, *Physics, Formation and Evolution of Rotating Stars*
- Maeder, A. & Meynet, G. 2005, *A&A*, 440, 1041
- Mahy, L., Rauw, G., De Becker, M., Eenens, P., & Flores, C. A. 2015, *A&A*, 577, A23
- Maíz Apellániz, J., Pantaleoni González, M., Barbá, R. H., et al. 2018, *A&A*, 616, A149
- Maíz Apellániz, J., Sota, A., Arias, J. I., et al. 2016, *ApJS*, 224, 4

BIBLIOGRAPHY

- Maíz Apellániz, J., Sota, A., Morrell, N. I., et al. 2013, in *Massive Stars: From alpha to Omega*, 198
- Maíz Apellániz, J., Sota, A., Walborn, N. R., et al. 2011, in *Highlights of Spanish Astrophysics VI*, ed. M. R. Zapatero Osorio, J. Gorgas, J. Maíz Apellániz, J. R. Pardo, & A. Gil de Paz, 467–472
- Marcolino, W. L. F., Bouret, J. C., Lanz, T., Maia, D. S., & Audard, M. 2017, *MNRAS*, 470, 2710
- Marcolino, W. L. F., Bouret, J.-C., Martins, F., et al. 2009, *A&A*, 498, 837
- Marcolino, W. L. F., Hillier, D. J., de Araujo, F. X., & Pereira, C. B. 2007, *ApJ*, 654, 1068
- Markova, N., Morrison, N., Kolka, I., & Markov, H. 2001a, *A&A*, 376, 898
- Markova, N., Puls, J., Scuderi, S., & Markov, H. 2005, *A&A*, 440, 1133
- Markova, N., Scuderi, S., de Groot, M., Markov, H., & Panagia, N. 2001b, *A&A*, 366, 935
- Martayan, C., Floquet, M., Hubert, A. M., et al. 2007a, *A&A*, 472, 577
- Martayan, C., Frémat, Y., Hubert, A. M., et al. 2006, *A&A*, 452, 273
- Martayan, C., Hubert, A. M., Floquet, M., et al. 2007b, in *Astronomical Society of the Pacific Conference Series, Vol. 361, Active OB-Stars: Laboratories for Stellar and Circumstellar Physics*, ed. A. T. Okazaki, S. P. Owocki, & S. Stefl, 356
- Martayan, C., Rivinius, T., Baade, D., Hubert, A.-M., & Zorec, J. 2011, in *IAU Symposium, Vol. 272, Active OB Stars: Structure, Evolution, Mass Loss, and Critical Limits*, ed. C. Neiner, G. Wade, G. Meynet, & G. Peters, 242–253
- Martinod, M. A., Mourard, D., Bério, P., et al. 2018, *A&A*, 618, A153
- Martins, F. 2004, PhD thesis, UNIVERSITE PAUL SABATIER - OBSERVATOIRE MIDI-PYRENEES, Toulouse, France
- Martins, F. 2011, *Bulletin de la Societe Royale des Sciences de Liege*, 80, 29
- Martins, F. 2018, *A&A*, 616, A135
- Martins, F., Marcolino, W., Hillier, D. J., Donati, J.-F., & Bouret, J.-C. 2015, *A&A*, 574, A142

BIBLIOGRAPHY

- Martins, F., Schaerer, D., & Hillier, D. J. 2005a, *A&A*, 436, 1049
- Martins, F., Schaerer, D., Hillier, D. J., & Heydari-Malayeri, M. 2004, *A&A*, 420, 1087
- Martins, F., Schaerer, D., Hillier, D. J., et al. 2005b, *A&A*, 441, 735
- Maryeva, O. & Abolmasov, P. 2012, *MNRAS*, 421, 1189
- Massey, P., Neugent, K. F., Hillier, D. J., & Puls, J. 2013, *ApJ*, 768, 6
- Mathys, G. 1989, *A&AS*, 81, 237
- McCrea, W. H. 1929, *Zeitschrift fur Physik*, 57, 367
- McDonald, A. B. 2016, *Reviews of Modern Physics*, 88, 030502
- Meilland, A., Delaa, O., Stee, P., et al. 2011, *A&A*, 532, A80
- Meilland, A., Millour, F., Kanaan, S., et al. 2012, *A&A*, 538, A110
- Meilland, A., Millour, F., Stee, P., et al. 2007a, *A&A*, 464, 73
- Meilland, A. & Stee, P. 2014, in *EAS Publications Series*, Vol. 69-70, 209–226
- Meilland, A., Stee, P., Vannier, M., et al. 2007b, *A&A*, 464, 59
- Mennickent, R. E. 1991, *A&AS*, 88, 1
- Messineo, M., Zhu, Q., Menten, K. M., et al. 2018, *VizieR Online Data Catalog*, J/ApJ/822/L5
- Meynet, G., Chomienne, V., Ekström, S., et al. 2015, *A&A*, 575, A60
- Meynet, G., Georgy, C., Hirschi, R., et al. 2011, *Bulletin de la Societe Royale des Sciences de Liege*, 80, 266
- Meynet, G. & Maeder, A. 2000, *A&A*, 361, 101
- Michelson, A. A. 1890, *The London, Edinburgh, and Dublin Philosophical Magazine and Journal of Science*, 30, 1
- Michelson, A. A. 1891, *Nature*, 45, 160
- Michelson, A. A. & Pease, F. G. 1921, *ApJ*, 53, 249
- Mihalas, D. 1978, *Stellar atmospheres*
- Mihalas, D. & Hummer, D. G. 1973, *ApJ*, 179, 827

BIBLIOGRAPHY

- Millour, F. 2014, in EAS Publications Series, Vol. 69-70, EAS Publications Series, 17–52
- Millour, F., Mourard, D., Woillez, J., et al. 2018, *Experimental Astronomy*, 46, 497
- Millour, F. A., Vannier, M., & Meilland, A. 2012, Society of Photo-Optical Instrumentation Engineers (SPIE) Conference Series, Vol. 8445, Three recipes for improving the image quality with optical long-baseline interferometers: BFMC, LFF, and DPSC, 84451B
- Mokiem, M. R., de Koter, A., Evans, C. J., et al. 2007a, *A&A*, 465, 1003
- Mokiem, M. R., de Koter, A., Vink, J. S., et al. 2007b, *A&A*, 473, 603
- Monin, D. N., Wade, G. A., & Fabrika, S. N. 2003, *A&A*, 411, 197
- Monnier, J. D. 2000, in *Principles of Long Baseline Stellar Interferometry*, ed. P. R. Lawson, 203
- Monnier, J. D. 2003a, in EAS Publications Series, Vol. 6, EAS Publications Series, ed. G. Perrin & F. Malbet, 213
- Monnier, J. D. 2003b, *Reports on Progress in Physics*, 66, 789
- Monnier, J. D. & Allen, R. J. 2013, *Radio and Optical Interferometry: Basic Observing Techniques and Data Analysis*, ed. T. D. Oswalt & H. E. Bond, 325
- Monnier, J. D., Berger, J.-P., Millan-Gabet, R., & ten Brummelaar, T. A. 2004, in Society of Photo-Optical Instrumentation Engineers (SPIE) Conference Series, Vol. 5491, *Proc. SPIE*, ed. W. A. Traub, 1370
- Monnier, J. D., Che, X., Zhao, M., et al. 2012, *ApJ*, 761, L3
- Monnier, J. D., Zhao, M., Pedretti, E., et al. 2007, *Science*, 317, 342
- Moravveji, E., Guinan, E. F., Shultz, M., Williamson, M. H., & Moya, A. 2012a, *ApJ*, 747, 108
- Moravveji, E., Moya, A., & Guinan, E. F. 2012b, *ApJ*, 749, 74
- Morel, T., Castro, N., Fossati, L., et al. 2015, in *IAU Symposium*, Vol. 307, *New Windows on Massive Stars*, ed. G. Meynet, C. Georgy, J. Groh, & P. Stee, 342–347
- Morgan, W. W., Abt, H. A., & Tapscott, J. W. 1978, *Revised MK Spectral Atlas for stars earlier than the sun*

BIBLIOGRAPHY

- Morgan, W. W. & Keenan, P. C. 1973, *ARA&A*, 11, 29
- Morgan, W. W., Keenan, P. C., & Kellman, E. 1943, *An atlas of stellar spectra, with an outline of spectral classification*
- Morton, D. C. 1967a, *ApJ*, 150, 535
- Morton, D. C. 1967b, *ApJ*, 147, 1017
- Morton, D. C. 1976, *ApJ*, 203, 386
- Mossoux, E., Mahy, L., & Rauw, G. 2018, *A&A*, 615, A19
- Mourard, D., B erio, P., Perraut, K., et al. 2017, *Journal of the Optical Society of America A*, 34, A37
- Mourard, D., Bosc, I., Labeyrie, A., Koechlin, L., & Saha, S. 1989, *Nature*, 342, 520
- Mourard, D., Challouf, M., Ligi, R., et al. 2012, in *Society of Photo-Optical Instrumentation Engineers (SPIE) Conference Series*, Vol. 8445, Proc. SPIE, 84450K
- Mourard, D., Clause, J. M., Marcotto, A., et al. 2009, *A&A*, 508, 1073
- Mourard, D., Monnier, J. D., Meilland, A., et al. 2015, *A&A*, 577, A51
- Mourard, D. & Nardetto, N. 2019, *Optical Long Baseline Interferometry - Principles and Instrumentation*, 105–146
- Muijres, L. E., Vink, J. S., de Koter, A., M uller, P. E., & Langer, N. 2012, *A&A*, 537, A37
- M uller, P. E. & Vink, J. S. 2014, *A&A*, 564, A57
- Najarro, F. 2001, in *ASP Conference Proceeding*, Vol. 233, *P Cygni 2000: 400 years of progress*, ed. M. de Groot & C. Sterken (San Francisco: Astronomical Society of the Pacific), 133
- Najarro, F., Hanson, M. M., & Puls, J. 2011, *A&A*, 535, A32
- Najarro, F., Hillier, D. J., Puls, J., Lanz, T., & Martins, F. 2006, *A&A*, 456, 659
- Najarro, F., Hillier, D. J., & Stahl, O. 1997, *A&A*, 326, 1117
- Nardetto, N., M erand, A., Mourard, D., et al. 2016, *A&A*, 593, A45
- Negueruela, I., Steele, I. A., & Bernabeu, G. 2004, *Astronomische Nachrichten*, 325, 749

BIBLIOGRAPHY

- Neiner, C., Mathis, S., Alecian, E., et al. 2015, in IAU Symposium, Vol. 305, Polarimetry, ed. K. N. Nagendra, S. Bagnulo, R. Centeno, & M. Jesús Martínez González, 61–66
- Nemravová, J., Harmanec, P., Kubát, J., et al. 2010, *A&A*, 516, A80
- Neugent, K. F., Massey, P., Skiff, B., et al. 2010, *ApJ*, 719, 1784
- Noble, L. M. & Scarf, F. L. 1963, *ApJ*, 138, 1169
- Nomoto, K. 1984, *ApJ*, 277, 791
- Nomoto, K. 1987, *ApJ*, 322, 206
- Ohnaka, K., Weigelt, G., & Hofmann, K. H. 2016, *A&A*, 589, A91
- Ohnaka, K., Weigelt, G., & Hofmann, K.-H. 2019, *ApJ*, 883, 89
- Okazaki, A. T. 1991, *PASJ*, 43, 75
- Okazaki, A. T. 1997, *A&A*, 318, 548
- Okazaki, A. T. 2001, *PASJ*, 53, 119
- Okazaki, A. T. 2007, in *Astronomical Society of the Pacific Conference Series*, Vol. 361, *Active OB-Stars: Laboratories for Stellar and Circumstellar Physics*, ed. A. T. Okazaki, S. P. Owocki, & S. Stefl, 230
- Olson, G. L. & Castor, J. I. 1981, *ApJ*, 244, 179
- Oskinova, L. M. 2016, *Advances in Space Research*, 58, 739
- Owocki, S. P. 1992, *Instabilities in hot-star winds: Basic physics and recent developments*, ed. U. Heber & C. S. Jeffery, Vol. 401, 393
- Owocki, S. P., Castor, J. I., & Rybicki, G. B. 1988, *ApJ*, 335, 914
- Owocki, S. P., Cranmer, S. R., & Gayley, K. G. 1996, *ApJ*, 472, L115
- Owocki, S. P., Cranmer, S. R., & Gayley, K. G. 1998, *Ap&SS*, 260, 149
- Pannekoek, A. 1961, *A history of astronomy*.
- Panoglou, D., Carciofi, A. C., Vieira, R. G., et al. 2016, *MNRAS*, 461, 2616
- Parker, E. N. 1958, *ApJ*, 128, 664
- Pauldrach, A., Puls, J., & Kudritzki, R. P. 1986, *A&A*, 164, 86

BIBLIOGRAPHY

- Pauldrach, A. W. A., Hoffmann, T. L., & Lennon, M. 2001, *A&A*, 375, 161
- Pauls, T. A., Young, J. S., Cotton, W. D., & Monnier, J. D. 2005, *PASP*, 117, 1255
- Payne, C. H. 1925, PhD thesis, RADCLIFFE COLLEGE.
- Percheron, I. 2008, *New A Rev.*, 52, 186
- Percy, J. R., Harlow, C. D. W., & Wu, A. P. S. 2004, *PASP*, 116, 178
- Petrov, R. G. 1989, in *NATO Advanced Science Institutes (ASI) Series C*, Vol. 274, NATO Advanced Science Institutes (ASI) Series C, ed. D. M. Alloin & J. M. Mariotti, 249
- Petrov, R. G., Malbet, F., Weigelt, G., et al. 2007, *A&A*, 464, 1
- Plaskett, J. S. & Pearce, J. A. 1931, *Publications of the Dominion Astrophysical Observatory Victoria*, 5, 1
- Pollmann, E. 2018, *Information Bulletin on Variable Stars*, 6239, 1
- Porter, J. M. & Rivinius, T. 2003, *PASP*, 115, 1153
- Pringle, J. E. 1981, *ARA&A*, 19, 137
- Prinja, R. K. 1989, *MNRAS*, 241, 721
- Prinja, R. K. 1990, *A&A*, 232, 119
- Prinja, R. K. & Howarth, I. D. 1986, *ApJS*, 61, 357
- Proga, D., Stone, J. M., & Kallman, T. R. 2000, *ApJ*, 543, 686
- Przybilla, N., Butler, K., Becker, S. R., & Kudritzki, R. P. 2006, *A&A*, 445, 1099
- Puls, J. 2017, in *IAU Symposium*, Vol. 329, *The Lives and Death-Throes of Massive Stars*, ed. J. J. Eldridge, J. C. Bray, L. A. S. McClelland, & L. Xiao, 435–435
- Puls, J., Kudritzki, R.-P., Herrero, A., et al. 1996, *A&A*, 305, 171
- Puls, J., Owocki, S. P., & Fullerton, A. W. 1993, *A&A*, 279, 457
- Puls, J., Sundqvist, J. O., Najarro, F., & Hanson, M. M. 2009, in *American Institute of Physics Conference Series*, Vol. 1171, *American Institute of Physics Conference Series*, ed. I. Hubeny, J. M. Stone, K. MacGregor, & K. Werner, 123–135
- Puls, J., Urbaneja, M. A., Venero, R., et al. 2005, *A&A*, 435, 669

BIBLIOGRAPHY

- Puls, J., Vink, J. S., & Najarro, F. 2008, *A&A Rev.*, 16, 209
- Quirrenbach, A., Bjorkman, K. S., Bjorkman, J. E., et al. 1997, *ApJ*, 479, 477
- Renzini, A. 1981, in *Astrophysics and Space Science Library*, Vol. 88, *Physical Processes in Red Giants*, ed. J. Iben, I. & A. Renzini, 431–446
- Repolust, T., Puls, J., & Herrero, A. 2004, *A&A*, 415, 349
- Richardson, N. D., Morrison, N. D., Gies, D. R., et al. 2011, *AJ*, 141, 120
- Richardson, N. D., Schaefer, G. H., Gies, D. R., et al. 2013, *ApJ*, 769, 118
- Richichi, A. & Percheron, I. 2005, *A&A*, 434, 1201
- Rieutord, M. & Espinosa Lara, F. 2009, *Communications in Asteroseismology*, 158, 99
- Rivet, J. P., Siciak, A., de Almeida, E. S. G., et al. 2020, *MNRAS*, 494, 218
- Rivet, J.-P., Vakili, F., Lai, O., et al. 2018, *Experimental Astronomy*, 46, 531
- Rivinius, T., Baade, D., & Štefl, S. 2003, *A&A*, 411, 229
- Rivinius, T., Carciofi, A. C., & Martayan, C. 2013, *A&A Rev.*, 21, 69
- Rivinius, T., Štefl, S., & Baade, D. 1999, *A&A*, 348, 831
- Rivinius, T., Štefl, S., & Baade, D. 2006, *A&A*, 459, 137
- Rountree, J. & Sonneborn, G. 1991, *ApJ*, 369, 515
- Rybicki, G. B. & Lightman, A. P. 1986, *Radiative Processes in Astrophysics*
- Ryle, M. 1950, *Reports on Progress in Physics*, 13, 184
- Saio, H., Georgy, C., & Meynet, G. 2013, *MNRAS*, 433, 1246
- Salpeter, E. E. 1955, *ApJ*, 121, 161
- Sana, H., de Koter, A., de Mink, S. E., et al. 2013a, *A&A*, 550, A107
- Sana, H., de Koter, A., de Mink, S. E., et al. 2013b, *A&A*, 550, A107
- Sana, H., de Mink, S. E., de Koter, A., et al. 2012, *Science*, 337, 444
- Sana, H., de Mink, S. E., de Koter, A., et al. 2013c, in *Astronomical Society of the Pacific Conference Series*, Vol. 470, *370 Years of Astronomy in Utrecht*, ed. G. Pugliese, A. de Koter, & M. Wijburg, 141

BIBLIOGRAPHY

- Sanchez-Bermudez, J., Alberdi, A., Barbá, R., et al. 2017, *ApJ*, 845, 57
- Sander, A., Shenar, T., Hainich, R., et al. 2015, *A&A*, 577, A13
- Sander, A. A. C. 2017, in *IAU Symposium*, Vol. 329, *The Lives and Death-Throes of Massive Stars*, ed. J. J. Eldridge, J. C. Bray, L. A. S. McClelland, & L. Xiao, 215–222
- Sander, A. A. C., Hamann, W. R., Todt, H., Hainich, R., & Shenar, T. 2017, *A&A*, 603, A86
- Santolaya-Rey, A. E., Puls, J., & Herrero, A. 1997, *A&A*, 323, 488
- Schatzman, E. 1962, *Annales d’Astrophysique*, 25, 18
- Scott, N. J., Millan-Gabet, R., Lhomé, E., et al. 2013, *Journal of Astronomical Instrumentation*, 2, 1340005
- Secchi, A. 1866, *Astronomische Nachrichten*, 68, 63
- Shakura, N. I. & Sunyaev, R. A. 1973, *A&A*, 500, 33
- Shimada, M. R., Ito, M., Hirata, B., & Horaguchi, T. 1994, in *IAU Symposium*, Vol. 162, *Pulsation; Rotation; and Mass Loss in Early-Type Stars*, ed. L. A. Balona, H. F. Henrichs, & J. M. Le Contel, 487
- Shlosman, I., Vitello, P. A., & Shaviv, G. 1985, *ApJ*, 294, 96
- Shultz, M. E., Wade, G. A., Rivinius, T., et al. 2018, *MNRAS*, 475, 5144
- Sigut, T. A. A. 2011, in *IAU Symposium*, Vol. 272, *Active OB Stars: Structure, Evolution, Mass Loss, and Critical Limits*, ed. C. Neiner, G. Wade, G. Meynet, & G. Peters, 426–427
- Sigut, T. A. A. 2018, *Astronomical Society of the Pacific Conference Series*, Vol. 515, *The Bedisk and Beray Circumstellar Disk Codes*, 213
- Sigut, T. A. A. & Jones, C. E. 2007, *ApJ*, 668, 481
- Sigut, T. A. A., Tycner, C., Jansen, B., & Zavala, R. T. 2015, *ApJ*, 814, 159
- Silaj, J., Jones, C. E., Tycner, C., Sigut, T. A. A., & Smith, A. D. 2010, *ApJS*, 187, 228
- Slettebak, A. 1966, *ApJ*, 145, 121

BIBLIOGRAPHY

- Slettebak, A. 1970, in IAU Colloq. 4: Stellar Rotation, ed. A. Slettebak, 3
- Smith, L. F. 1968, MNRAS, 138, 109
- Smith, N. 2014, ARA&A, 52, 487
- Smith, N., Humphreys, R. M., Davidson, K., et al. 2001, AJ, 121, 1111
- Smith, N. & Owocki, S. P. 2006, ApJ, 645, L45
- Snow, T. P., J. & Morton, D. C. 1976, ApJS, 32, 429
- Snow, T. P. & Stalio, R. 1987, in Astrophysics and Space Science Library, Vol. 129, Exploring the Universe with the IUE Satellite, ed. Y. Kondo & W. Wamsteker, 183
- Sobolev, V. V. 1960, Moving envelopes of stars
- Sota, A., Maíz Apellániz, J., Morrell, N. I., et al. 2014, ApJS, 211, 10
- Sota, A., Maíz Apellániz, J., Walborn, N. R., et al. 2011, ApJS, 193, 24
- Stee, P. 2011, in Active OB Stars: Structure, Evolution, Mass Loss, and Critical Limits, ed. C. Neiner, G. Wade, G. Meynet, & G. Peters, Vol. 272, 313–324
- Stee, P. & Bittar, J. 2001, Astronomy and Astrophysics, 367, 532
- Stee, P. & de Araujo, F. X. 1994, A&A, 292, 221
- Stee, P., de Araujo, F. X., Vakili, F., et al. 1995, A&A, 300, 219
- Stee, P., Delaa, O., Monnier, J. D., et al. 2012, A&A, 545, A59
- Stee, P. & Meilland, A. 2012, in Astronomical Society of the Pacific Conference Series, Vol. 464, Circumstellar Dynamics at High Resolution, ed. A. C. Carciofi & T. Rivinius, 167
- Stee, P., Meilland, A., & Kanaan, S. 2008, in EAS Publications Series, Vol. 28, EAS Publications Series, ed. S. Wolf, F. Allard, & P. Stee, 135–144
- Strassmeier, K. G. 2002, Astronomische Nachrichten, 323, 309
- Struve, O. 1931, ApJ, 73, 94
- Struve, O. 1935, ApJ, 81, 66
- Struve, O. & Roach, F. E. 1939, ApJ, 90, 727

BIBLIOGRAPHY

- Sturrock, P. A., Holzer, T. E., Mihalas, D. M., Ulrich, R. K., & Parker, E. N. 1986, *Nature*, 323, 210
- Sundqvist, J. O., Puls, J., Feldmeier, A., & Owocki, S. P. 2011, *A&A*, 528, A64
- Surdej, J. 2019, Introduction to optical/IR interferometry: history and basic principles, 56–103
- Tallon-Bosc, I., Tallon, M., Thiébaud, E., et al. 2008, in *Proc. SPIE*, Vol. 7013, Optical and Infrared Interferometry, 70131J
- ten Brummelaar, T. A. 1995, *Appl. Opt.*, 34, 2214
- ten Brummelaar, T. A., McAlister, H. A., Ridgway, S. T., et al. 2005, *ApJ*, 628, 453
- Ten Brummelaar, T. A., Sturmman, J., Ridgway, S. T., et al. 2013, *Journal of Astronomical Instrumentation*, 2, 1340004
- Thiébaud, É. & Young, J. 2017, *Journal of the Optical Society of America A*, 34, 904
- Thom, C., Granes, P., & Vakili, F. 1986, *A&A*, 165, L13
- Touhami, Y., Gies, D. R., & Schaefer, G. H. 2011, *The Astrophysical Journal*, 729, 17
- Touhami, Y., Gies, D. R., Schaefer, G. H., et al. 2013, *ApJ*, 768, 128
- Townsend, R. H. D., Owocki, S. P., & Howarth, I. D. 2004, *MNRAS*, 350, 189
- Tramper, F., Sana, H., de Koter, A., Kaper, L., & Ramírez-Agudelo, O. H. 2014, *A&A*, 572, A36
- Tramper, F., Straal, S. M., Sanyal, D., et al. 2015, *A&A*, 581, A110
- Turner, D., Welch, G., Graham, M., & Fairweather, D. 2001, *JAAVSO*, 29, 73
- Tycner, C., Gilbreath, G. C., Zavala, R. T., et al. 2006, *AJ*, 131, 2710
- Underhill, A. B. 1958, in *Liege International Astrophysical Colloquia*, Vol. 8, 91–97
- Underhill, A. B. 1975, *ApJ*, 199, 691
- Vakili, F., Mourard, D., Bonneau, D., Morand, F., & Stee, P. 1997, *A&A*, 323, 183
- Valiante, R., Schneider, R., Bianchi, S., & Andersen, A. C. 2009, *Monthly Notices of the Royal Astronomical Society*, 397, 1661
- van Belle, G. T., Ciardi, D. R., ten Brummelaar, T., et al. 2006, *ApJ*, 637, 494

BIBLIOGRAPHY

- van Cittert, P. H. 1934, *Physica*, 1, 201
- van der Hucht, K. A., Conti, P. S., Lundstrom, I., & Stenholm, B. 1981, *Space Sci. Rev.*, 28, 227
- van Leeuwen, F. 2007, *A&A*, 474, 653
- van Loon, J. T., Cioni, M. R. L., Zijlstra, A. A., & Loup, C. 2005, *A&A*, 438, 273
- Vieira, R. G., Carciofi, A. C., Bjorkman, J. E., et al. 2017, *MNRAS*, 464, 3071
- Vilhu, O. & Kallman, T. R. 2019, arXiv e-prints, arXiv:1906.05581
- Vink, J. S., Davies, B., Harries, T. J., Oudmaijer, R. D., & Walborn, N. R. 2009, *A&A*, 505, 743
- Vink, J. S., de Koter, A., & Lamers, H. J. G. L. M. 2000, *A&A*, 362, 295
- Vink, J. S., de Koter, A., & Lamers, H. J. G. L. M. 2001, *A&A*, 369, 574
- Vink, J. S., Drew, J. E., Harries, T. J., & Oudmaijer, R. D. 2002, *MNRAS*, 337, 356
- Vogt, S. S., Penrod, G. D., & Hatzes, A. P. 1987, *ApJ*, 321, 496
- von Zeipel, H. 1924, *MNRAS*, 84, 665
- Wade, G. A. & Neiner, C. 2018, *Contributions of the Astronomical Observatory Skalnaté Pleso*, 48, 106
- Wade, G. A., Neiner, C., Alecian, E., et al. 2016a, *MNRAS*, 456, 2
- Wade, G. A., Petit, V., Grunhut, J. H., Neiner, C., & MiMeS Collaboration. 2016b, in *Astronomical Society of the Pacific Conference Series*, Vol. 506, *Bright Emissaries: Be Stars as Messengers of Star-Disk Physics*, ed. T. A. A. Sigut & C. E. Jones, 207
- Walborn, N. R. 1971, *ApJ*, 167, L31
- Walborn, N. R. 2008, in *Revista Mexicana de Astronomia y Astrofisica Conference Series*, Vol. 33, *Revista Mexicana de Astronomia y Astrofisica Conference Series*, 5–14
- Walborn, N. R. & Fitzpatrick, E. L. 1990, *PASP*, 102, 379
- Walborn, N. R., Howarth, I. D., Lennon, D. J., et al. 2002, *AJ*, 123, 2754
- Walborn, N. R., Morrell, N. I., Howarth, I. D., et al. 2004, *ApJ*, 608, 1028

BIBLIOGRAPHY

- Walborn, N. R., Nichols-Bohlin, J., & Panek, R. J. 1985, NASA Reference Publication, 1155
- Walborn, N. R., Parker, J. W., & Nichols, J. S. 1995, NASA Reference Publication, 1363, 0
- Waters, L. B. F. M., van der Veen, W. E. C. J., Taylor, A. R., Marlborough, J. M., & Dougherty, S. M. 1991, *A&A*, 244, 120
- Weber, E. J. & Davis, Leverett, J. 1967, *ApJ*, 148, 217
- Weigelt, G., Hofmann, K. H., Schertl, D., et al. 2016, *A&A*, 594, A106
- Weigelt, G., Kraus, S., Driebe, T., et al. 2007, *A&A*, 464, 87
- Willis, A. J. & Garmany, C. D. 1987, in *Astrophysics and Space Science Library*, Vol. 129, *Exploring the Universe with the IUE Satellite*, ed. Y. Kondo & W. Wamsteker, 157
- Wilson, R. 1958, in *Liege International Astrophysical Colloquia*, Vol. 8, 85–90
- Willez, J., Akeson, R., Colavita, M., et al. 2012, *PASP*, 124, 51
- Wood, K., Bjorkman, K. S., & Bjorkman, J. E. 1997, *ApJ*, 477, 926
- Yudin, R. V., Hubrig, S., Pogodin, M. A., & Schoeller, M. 2011, in *IAU Symposium*, Vol. 272, *Active OB Stars: Structure, Evolution, Mass Loss, and Critical Limits*, ed. C. Neiner, G. Wade, G. Meynet, & G. Peters, 222–223
- Zernike, F. 1938, *Physica*, 5, 785
- Zickgraf, F. J., Wolf, B., Stahl, O., Leitherer, C., & Appenzeller, I. 1986, *A&A*, 163, 119
- Zorec, J. & Briot, D. 1997, *A&A*, 318, 443
- Zorec, J., Frémat, Y., Domiciano de Souza, A., et al. 2016, *A&A*, 595, A132
- Zsargo, J., Arrieta, A., Fierro, C., et al. 2017, *Astronomical Society of the Pacific Conference Series*, Vol. 508, *A Mega-Grid of CMFGEN Model Atmospheres for Rapid Analysis of Stellar Spectra*, ed. A. Miroshnichenko, S. Zharikov, D. Korčáková, & M. Wolf, 407
- Zsargo, J., Georgiev, L. N., Hillier, D. J., et al. 2013, in *Massive Stars: From alpha to Omega*, 110

BIBLIOGRAPHY